FULLY DEVELOPED TURBULENT FLOW

IN

RECTANGULAR INTERRUPTED-PLATE DUCTS

by

Robert Kevin McBrien

Department of Mechanical Engineering

McGill University, Montreal

November 1989

A Thesis submitted to the Faculty of Graduate Studies and Research

in partial fulfillment of the requirements for the degree of

Doctor of Philosophy

ABSTRACT

Experimental and numerical investigations of turbulent spatially-periodic fully developed flows in straight ducts of rectangular cross section, with interrupted-plate inserts, are presented in this thesis. A computer code, based on a finite volume method and incorporating a low-Reynolds-number k-ϵ turbulence model, for the simulation of two-dimensional, steady, spatially-periodic fully developed flows in interrupted-plate channels was developed, tested, and used in the numerical investigation. The experimental work was complementary to the numerical work. It was aimed at obtaining accurate and complete data that would allow fair evaluation of the numerical model and lead to an enhanced understanding of spatially-periodic fully developed turbulent flows.

Turbulent spatially-periodic fully developed flows in three different interrupted-plate ducts, each having different plate thicknesses, were investigated, with module Reynolds numbers in the range $5x10^3 \leq Re_m \leq 33.5x10^3$. The results presented include (i) module friction factor versus Reynolds number plots; (ii) plots of intramodular time-mean wall static pressure distributions; (iii) plate surface streamline photographs; and (iv) a variety of numerical results, including plots of streamlines, and distributions of plate shear stress, wall shear stress, axial momentum flux, axial velocities, mean turbulence kinetic energy and turbulence Reynolds numbers. The details and implications of these results are discussed in this thesis.

SOMMAIRE

Cette thèse présente les résultats de recherches expérimentales et numériques sur des écoulements pleinement développées et spatiallement périodiques dans des conduites rectilignes de section rectangulaire, dans lesquelles sont insérées des plaques interruptrices. Un programme informatique, basé sur une méthode de volume délimité et incorporant un modèle de turbulence du type "k-ε" pour faible nombre de Reynolds , a été développé pour la simulation des écoulements bidimensionnels, permanents, pleinement développées et spatiallement périodiques dans des conduites rectilignes contenant des plaques interruptrices. La recherche expérimentale a eu pour but d'obtenir des résultats précis permettant une évaluation juste du modèle numérique et menant à une meilleure compréhension des écoulements turbulents pleinement développées et spatiallement périodiques.

Les écoulements turbulents pleinement développées et spatiallement périodiques ont été étudiés dans trois conduites rectilignes contenant des plaques interruptrices d'épaisseur différentes pour des valeurs du nombre de Reynolds comprises entre $5x10^3$ et $33.5x10^3$. Les résultats qui sont présentés incluent: (i) des graphiques du facteur de friction modulaire en fonction du nombre de Reynolds; (ii) des graphiques de la distribution intramodulaire de la moyenne temporelle de la pression statique murale; (iii) des photos montrant la trajectoire de l'écoulement à la surface des plaques; et (iv) une série de graphiques tirés des résultats numériques qui montrent: les lignes de courant, les distributions des contraintes de cisaillement sur la paroi des plaques ainsi que sur la paroi des conduites, le flux de quantité de mouvement axial, les

vitesses axiales, l'énergie cinétique turbulente moyenne et les nombres de Reynolds turbulents. Les détails et les implications de ces résultats sont élaborés dans cette thèse.

ACKNOWLEDGEMENTS

I would like to sincerely thank my supervisor, Professor B.R. Baliga, for the considerable guidance and support he has provided throughout the course of this research work. He has helped make this work a rewarding and enjoyable learning experience.

I received partial financial support from the Department of Mechanical Engineering at McGill, in the form of Graduate Research and Teaching Assistantships. I was awarded a two-year Postgraduate Scholarship by NSERC and also received support through an NSERC Individual Operating Grant awarded to Professor Baliga. In addition, a significant portion of the computational work reported in this thesis was done at the Centre for Large Scale Computation at the University of Toronto, under the auspices of a NSERC Supercomputer Time Allocation Grant to Professor Baliga. I am grateful to NSERC and the Department of Mechanical Engineering at McGill for the above-mentioned financial support.

The support services and facilities provided by the Centre for Large Scale Computation at the University of Toronto are gratefully acknowledged.

During the construction and setup of the experimental facility, many people provided technical skills and advice. For these services I would like to express my appreciation to Arthur Clément, Donald Borland, and the rest of the staff of the Machine Shop, Jack Kelly and his staff of

the Undergraduate Laboratory, Steve Markhauser of the Aerodynamics Laboratory, and George Dedic and George Tewfik of the DATAC Laboratory, all from the Department of Mechanical Engineering. In addition, I would also like to thank Michel Bilodeau, Steven Devries, and Thomas Marshall for their help. Assembly and disassembly of the various experimental test sections could not be physically done by one person. For the effort and time spent in helping with this I would like to express a special note of thanks to my friends, Neil Hookey and Michel Bernier.

I would also like to thank Michel Bernier for his time spent discussing experimental procedures and uncertainty analysis.

Finally, I would like to thank my wife, Ginette, my two sons, Alex and Sean, and my parents for their support, patience, and understanding throughout the course of my graduate studies and research.

TABLE OF CONTENTS

PAGE

PAGE

PAGE

PAGE

PAGE

PAGE

NOMENCLATURE

SYMBOL	DESCRIPTION
A	total flow area [= 2Hb]
A_c	minimum flow area of a module [= (b(H - t)]
A_{ft}	area of the flow metering cross section
A_w	total wall area of a module [= (2L + s)b + 2(L + s)(H - t) + 2ts]
b	width of a rectangular flow passage
B	empirical constant appearing in the logarithmic velocity profile equation (Eq. 3-29) [= 9.0 for smooth walls]
$C_{1\epsilon}, C_{2\epsilon}, C_{3\epsilon}, C_\mu$	empirical constants in the k-ϵ turbulence models
D_h	nominal hydraulic diameter of a module [= (4Hb/(2H + 2b)]
D_{hd}	hydraulic diameter of a rectangular duct [= $4A/P_w$]
D_{hk}	hydraulic diameter of a module [= $4(A_c/A_w)(L+s)$]
D_k, D_ϵ	rate of dissipation of k and ϵ, respectively
E_k, E_ϵ	empirical correction terms appearing in the low-Reynolds-number versions of the k-ϵ turbulence models
$f_{c1\epsilon}, f_{c2e}, f_{c\mu}$	empirical functions of turbulence Reynolds numbers in the k-ϵ turbulence models
f_d	Darcy friction factor [= $(-\partial P/\partial x)\, D_{hd} \,/\, (\frac{1}{2}\, \rho\, \overline{U_d}^2)$]
f_k	module friction factor based on $\overline{U_k}$ and D_{hk}
f_m	module friction factor based on $\overline{U_m}$ and D_h
H	half-height of rectangular duct
k	mean kinetic energy of the turbulence velocity fluctuations
l_t	a length scale characteristic of the large-scale turbulent motion

SYMBOL	DESCRIPTION
L	length of plate in interrupted-plate ducts
L^*	nondimensional value of L [= L/H]
L1	total number of x-direction grid points
$\dot{m}$	total mass flow rate in the duct
M^*	nondimensional axial momentum flux {Eq. (9-4)}
M1	total number of y-direction grid points
p	fluctuating part of $\tilde{p}$
$\tilde{p}$	instantaneous pressure [= P + p]
P	time-mean value of $\tilde{p}$
P_{dyn}	time-mean dynamic pressure
P_i	initial value of P in a module
P_k, P_ϵ	modelled forms of the rate of production of k and ϵ, respectively
P_{k1}, P_{k2}	contributions to P_k due to shear strains and normal strains, respectively
P_o	reference value of P
P_{stag}	time-mean stagnation pressure
P_{static}	time-mean averaged value of the wall static pressure measurements in the flow metering cross section
P_t	rate of production of k
P_w	wetted perimeter of a rectangular duct [= 4H + 2b]
P^*	nondimensional value of P $\{= P / (\frac{1}{2} \rho \bar{U}^2)\}$
$\hat{P}$	periodically varying part of P
Re_d	Reynolds number for a rectangular duct $[= \rho U_d D_{hd} / \mu]$
Re_{fric}	friction-velocity Reynolds number based on U_τ and D_{hd}
Re_k	module Reynolds number based on $\bar{U}_k$ and D_{hk}

SYMBOL	DESCRIPTION
Re_m	nominal module Reynolds number based on $\bar{U}_m$ and D_h
Re_p	plate Reynolds number based on $\bar{U}_k$ and t
Re_t	turbulence Reynolds number based on k and ϵ
Re_y	turbulence Reynolds number based on k and the perpendicular distance from the wall (y)
Re^*	laminar equivalent Reynolds number of Jones [54]
s	plate spacing
s_{ij}	the strain rate of the fluctuating turbulence velocities
s^*	nondimensional value of s [=s/H]
S_i	standard deviation of a sample set, i {(Eq. 6-5)}
S_{pooled}	pooled standard deviation calculated from values of S_i {Eq. 6-6)}
$S^u, S^v, S^k, S^\epsilon$	volumetric source terms in the U, V, k and ϵ equations, respectively
$\bar{S}^u, \bar{S}^v, \bar{S}^k, \bar{S}^\epsilon$	discretized forms of S^u, S^v, S^k, and S^ϵ
St	Strouhal number [= $2t\omega/\bar{U}_m$]
t	half-thickness of plate
t^*	nondimensional value of t [=t/H]
u_j	fluctuating part of $\tilde{u_j}$
u_t	a velocity scale characteristic of the large-scale turbulent motion
u_τ	module friction velocity [= $(\beta H / \rho)^{1/2}$]
$\tilde{u_j}$	instantaneous velocity component in the x_j (i=1, 2, or 3) direction [= $U_j + u_j$]
U	[= U_1]
U_j	time-mean value of $\tilde{u}_j$
U_{ft}	cross-sectional average value of U based on A_{ft}
U_w	resultant velocity parallel to a wall

SYMBOL	DESCRIPTION
U_τ	friction velocity [= $\{(-\partial P/\partial x\ H)/\rho\}^{1/2}$]
$\overline{U}_d$	cross-sectional average value of U based on $\dot{m}$ and A
$\overline{U}_k$	module cross-sectional average value of U based on $\dot{m}$ and A_c
$\overline{U}_m$	nominal module cross-sectional average value of U based on $\dot{m}/2$, b and H
v	[= u_2]
V	[= U_2]
V_{dp}	voltage output signal from the Barocel pressure transducer for a measured air-flow pressure differential
V_{zero}	voltage output signal for a zeroed pressure reading from the Barocel pressure transducer
w	[= u_3]
W	[= U_3]
x	[= x_1]
x_i	initial value of x in a module
x_j	Cartesian coordinate directions, j= 1 to 3 (Fig. 1)
x_o	reference value of x
x_R	streamwise length of a recirculation zone
XL	total length of a calculation domain in the x dimension
y	[= x_2]
y^+	dimensionless normal distance from a wall [=$\rho\ U_\tau\ y\ /\ \mu$]
YL	total length of a calculation domain in the y dimension
z	[= x_3]

GREEK SYMBOL	DESCRIPTION
β	modular pressure drop [per unit length]
Γ_u, Γ_k, Γ_ϵ	diffusion coefficients in the momentum, k, and ϵ equations, respectively
δ_{ij}	Kronecker delta [= 0 if i = j; = 1 otherwise]
δV_{cal}	fixed uncertainty in voltage output signal of the Barocel pressure transducer
δV_{dP}, δV_{zero}	random uncertainty in voltage output signal of the Barocel pressure transducer for measurements of air-flow pressure differentials and zeroed pressure readings, respectively
δx, δy	local dimensions in the grid (Figs. 7 and 10)
$\Delta X, \Delta Y$	local dimensions in the grid (Figs. 7 and 10)
ϵ	the rate of viscous dissipation of k
κ	von Karman constant [= 0.41]
λ	aspect ratio of a module in the periodic fully developed flow regime [= b/H]
μ	dynamic viscosity of the fluid
μ_t	dynamic turbulent eddy viscosity
ξ	aspect ratio of a rectangular duct [= b/(2H)]
ρ	mass density of the fluid
τ_w	shear stress at the wall surface
τ^*_p	nondimensional shear stress at the plate surface {Eq. (9-6)}
τ^*_w	nondimensional shear stress at the wall surface {Eq. (9-7)}
ψ	time
ω	frequency of vortex shedding

SUBSCRIPTS	DESCRIPTION
d	pertains to ducts or channels without interrupted-plate inserts
m	pertains to a module in the periodic fully developed flow regime of a duct or channel with interrupted-plate inserts

CHAPTER I

INTRODUCTION

1.1 AIMS OF THE THESIS

The research undertaken in this thesis involves numerical and experimental investigations of turbulent fluid flow in rectangular interrupted-plate ducts, such as that shown in Fig. 1. The ducts of interest are characterized by geometrically identical modules, as illustrated in the cross-sectional view given in Fig. 2. At a distance greater than about ten geometric modules downstream from the inlet plane, the turbulent fluid flows in such ducts start to repeat identically from one periodic module to another. Attention in this thesis is focused on such spatially-periodic fully developed flows. The geometric parameters and Reynolds numbers investigated in this research are similar to those found in compact heat exchangers [1-4].

The principal aims in the numerical investigation are the following: (1) implement and test a finite volume method (FVM) applicable to steady, two-dimensional, spatially fully developed flows in rectangular interrupted-surface geometries; (2) study available turbulence models, select one suitable for engineering predictions of turbulent flows in spatially-periodic interrupted geometries, and incorporate it into the aforementioned FVM; and (3) use the proposed FVM and turbulence model to study the flows of interest. The experimental work is complementary to the numerical work. It is aimed at obtaining accurate and complete data that would enhance current understanding of spatially-periodic fully developed turbulent flows and allow fair evaluations of the numerical

predictions. Specifically, the experiments are designed to obtain overall friction factor versus Reynolds number results, intramodular wall static pressure distributions, and plate surface streamline flow visualizations.

Rectangular flow passages with interrupted-surface configurations are often encountered in heat transfer equipment [1-10]. One example of such equipment is compact heat exchanger cores. These have a high ratio of heat transfer surface area to core volume, usually in excess of 700 m^2/m^3, and are characterized by high heat transfer performance, small size, and light weight [1-3]. They are widely used in automobiles, aircrafts, spacecrafts, and a multitude of applications in the power and process industries [1-3]. The high surface to volume ratios of these heat exchangers is commonly achieved by inserting fins between the plates in their cores. This practice often creates plate-fin flow passages of rectangular cross section, as shown in Fig. 3. Interrupted-surface configurations, such as the rectangular offset-fin geometry illustrated in Fig. 4a, are among the most popular plate-fin core designs used in compact heat exchangers. Another example of interrupted-surface flow passages in heat transfer equipment is forced convection cooling of electronic equipment such as modern digital computers and switching units used in telecommunications [5-9]. Advances in the field of electronic component technology, coupled with the ever present desire to enhance machine performance, has led to smaller and more powerful electronic devices, or modules, being deployed in greater densities onto circuit boards that are often closely stacked in parallel [6-8], as illustrated in Fig. 4b. Forced convection cooling by air or other suitable gases, is a common means of removing the dissipated heat

from these devices so as to ensure that critical temperature levels, for component reliability, will not be exceeded [6-8,10].

The interruptions in the flow passages of the type of equipment illustrated in Fig. 4 cause a continual restarting of the thermal boundary layers on the heat transfer surfaces, and this leads to high heat transfer coefficients. This enhanced heat transfer performance is, however, accompanied by pressure drops that are higher than those encountered in uninterrupted-surface configurations, due to the restartings of the velocity boundary layers. It is necessary, therefore, to achieve optimal designs of the interrupted-surface flow passages encountered in such equipment. To do this, in the context of the usual multitude of design criteria, it is imperative to develop numerical methods, and the corresponding turbulence models and computer codes, capable of predicting turbulent flow and heat transfer in such flow passages. It is also necessary to test these numerical models and establish their capabilities and limitations by conducting thorough checks of their predictions against the results of well-planned and carefully executed experiments.

A longitudinal cross section of an interrupted-plate rectangular duct is shown in Fig. 2. As was stated earlier, turbulent flows in ducts of this kind attain a spatially-periodic behaviour after a relatively short entrance region, which may extend at the most to eight ranks of plates [11,12]. In this spatially-periodic fully developed regime, the flow repeats itself identically in successive geometrical modules, such as ABCDE in Fig. 2. It is possible to numerically predict the flow in such a module directly without doing any entrance region calculations [13,14]. Indeed, for the design of heat transfer equipment

consisting of a large number of modules, it is sufficient to know the flow and heat transfer characteristics for a typical module in the periodic fully developed regime. The developing flow behaviour that occurs in the first few modules of the entrance region is relatively unimportant. It is for this reason that attention in this thesis is concentrated on the periodic fully developed regime.

The results of several numerical studies concerned with the prediction of flow and heat transfer phenomena in periodically interrupted geometries are available in the literature [12-23]. With the exception of [23], all these numerical investigations are limited to laminar flows. At the time that the research for this thesis was being completed, Ref. [23] appeared in the literature. The numerical model in [23] was developed for the study of flows in rectangular ducts with walls having rectangular grooves that are periodically spaced with respect to the main flow direction. The particular form of the turbulence model used in [23] had already been considered and judged not to be the most appropriate model for the type of geometries investigated in this research. The emphasis in this research is on studying the various turbulence models available in the literature, incorporating one suitable for cost-effective engineering predictions of spatially-periodic flows, and using it to investigate the flows of interest.

Experimental data on overall heat transfer and pressure drops in full-scale heat exchanger models that incorporate interrupted-surface geometries have been reported in the literature [1,4,24]. These data are of direct utility in the design of specific heat exchange devices, but they cannot be used as critical tests of numerical predictions

because they lack the necessary accuracy and local details. The results of several laboratory investigations of fluid flow and heat transfer in rectangular interrupted-surface flow passages are also available in the literature [8,9,11,25-31], but there is still a severe shortage of detailed and accurate data on local heat transfer and pressure drops in such geometries. The experimental work presented in this thesis is an effort to fulfill a part of this need. Attention is limited to the measurement of wall static pressure distributions and surface streamline flow visualization in ducts similar to those shown in Fig. 1. Details of the velocity and temperature fields are not within the scope of this thesis, rather they are suggested as extensions of this work and expected to be the subjects of future investigations.

The interrupted-surface passages that are employed in practical heat transfer equipment can be quite complex geometrically, as shown in Fig. 4. It is very difficult to obtain accurate pressure drop and flow visualization data in such passages. To obtain data suitable for enhancing the understanding of such flows and for evaluating the capabilities of numerical methods, however, it is not necessary to experiment with full-scale heat exchanger cores. It is sufficient to conduct experiments with ducts that are relatively less difficult to construct and instrument for detailed pressure measurements and flow visualization data, but generate similar complexities in the flow as those generated by interrupted-surface passages in heat transfer equipment. An example of such an experimentally convenient flow passage is the straight rectangular duct with an interrupted-plate insert illustrated in Fig. 1. Attention in this thesis is focussed primarily on such ducts. They generate flow complexities that are similar to those that would be generated in the

cores of compact heat exchangers, such as the one illustrated in Fig. 4a.

1.2 SYNOPSIS OF RELATED INVESTIGATIONS

Numerous investigations of fluid flow and heat transfer in ducts have been reported in the published literature. A comprehensive survey of all these investigations is not the purpose of this section. Detailed reviews and discussions of many of these investigations are already available in reference handbooks and archival journals. A thorough survey of studies pertaining to laminar flow and heat transfer in ducts has been published by Shah and London [32]. Kays and Perkins [33] have presented a comprehensive survey of laminar and turbulent forced convection in ducts. Extensive data and numerous empirical correlations for turbulent flow and heat transfer in ducts have been reported by Kays and London [1]. In-depth discussions of duct flow and heat transfer phenomena can be found in textbooks by Schlichting [34], Kays and Crawford [35], and White [36]. The physics of turbulent flow and mathematical models of turbulence are discussed at length in books by Hinze [37], Tennekes and Lumley [38], Launder and Spalding [39], and Bradshaw et al. [40]. Details about the derivation and implementation of numerical methods that are used for prediction of fluid flow and heat transfer can be found in publications by Patankar [41], Raithby and Schneider [42], and Anderson et al. [43].

The application of the physical laws of fluid mechanics to measurement techniques, differential pressure measurements, and volume flow measurements have been discussed in articles by Eckert, Blake, and

Mattingly, respectively, in a book edited by Goldstein [44]. Pitot and static tube techniques for measuring the flow of air in pipes of circular cross section have been described and critically reviewed by Winternitz and Fischl [45] and Ower and Pankhurst [46]. Detailed descriptions of some well established and commonly used methods of flow visualization for air flows are presented in an article by Maltby and Keating [47]. Discussions describing the importance and the methodology of uncertainty analysis, for use in the initial planning and final data presentation of engineering experiments, can be found in articles by Kline and McClintock [48], Moffat [49,50], Kline [51], and Abernethy et al. [52].

The literature review in this section is limited to those investigations that were directly used in (1) the planning and definition of the scope of this thesis, (2) the theoretical and practical considerations used in the initial evaluation of both the numerical models and experimental facility used in this work, and (3) the interpretation and discussion of results presented in this thesis. The discussion is divided into the following subsections: fully developed turbulent flow in straight rectangular ducts; modelling and simulation of turbulent flows; experimental investigations of fluid flow in interrupted-plate passages; and numerical investigations of fluid flow in interrupted-plate passages.

1.2.1 Fully Developed Turbulent Flow in Straight Rectangular Ducts

There have been numerous experimental studies of turbulent fully developed flow in straight ducts of rectangular cross section. Hartnett

et al. [53] and Jones [54] have critically reviewed many of the investigations dealing with the measurement of friction factors, including the pioneering works of Stanton and Pannell [55], Davies and White [56], Cornish [57], Nikuradse [58], and Colebrook [59]. Using ducts of aspect ratios 1, 5, and 10, Hartnett et al. [53] also conducted their own friction factor measurements for turbulent flows. In addition, they used the semi-analytical method of Deissler and Taylor [60] to calculate the friction factor. The calculated and measured results were in agreement for ducts having large aspect ratios. At aspect ratios less than 5, the predicted values of friction factors were lower than the experimental data, with a maximum difference of 12 percent evident for the square duct. They also concluded that the circular tube correlations accurately predict the friction factors for flow through rectangular ducts of any aspect ratio at Reynolds numbers, based on average flow velocity and the duct hydraulic diameter, between $6x10^3$ and $5x10^5$.

Jones [54] has done a detailed examination of published friction factor data for turbulent flow in rectangular ducts. Data for smooth rectangular ducts having aspect ratios between 1 and 39 were obtained in the literature and examined, in conjunction with his own experimental data. He determined that at constant Reynolds number, based on duct hydraulic diameter, the friction factor increases monotonically with increasing aspect ratio. In addition, Jones concluded that the hydraulic diameter is not the proper length dimension to use in the Reynolds number to ensure similarity between the results for circular and rectangular ducts. Instead, he proposed a modified Reynolds number, Re^*, that ensured the laminar flow results for rectangular ducts of any aspect ratio could be predicted by using the well-known result for the

circular tube, $f = 64/Re^*$. Jones then showed that this "laminar equivalent Reynolds number", Re^*, also provided good agreement between rectangular and circular duct results in fully developed turbulent flow.

One of the first comprehensive investigations and discussions of two-dimensional turbulent channel flow was done by Laufer [61]. He took detailed hot-wire measurements of the fields of time-mean and fluctuating quantities for turbulent flow in a straight rectangular duct, 0.127 m wide with an aspect ratio (height to width) of 12, and length to half-width ratio of 86. The flow was considered to be two dimensional and measurements were taken at three Reynolds numbers, 12300, 30800, and 61600, based on the duct half-width and the maximum mean velocity. Time-mean velocity and axial-fluctuation measurements were made in the fully turbulent regions and well into the viscous sublayer. Using his experimental data, Laufer established the validity of his semi-analytical predictions concerning the extent of the viscous sublayer.

It is to be noted that in this thesis, unless otherwise stated, the use of the adjectives "mean" and "time-mean" will be used interchangeably to infer the temporal average of a quantity. The spatial average of a quantity will be indicated by the use of the adjective "average".

The work of Laufer [61] was extended by Comte-Bellot [62], who conducted a detailed experimental investigation of turbulent flow in a channel. She used hot-wire anemometry to study turbulent flow in a straight rectangular duct of width 0.18 m, with aspect ratio of 13.3 and a length to half-width ratio of 122. Flows at Reynolds numbers of 57000, 120000, and 230000, based on the duct half-width and average flow

velocity, were examined. In particular, she studied the structure of the large eddies, the probability distribution of the velocity fluctuations, the local isotropy of the small eddies, the structure of the viscous sublayer, and the establishment of fully developed duct flow.

The works of Laufer [61] and Comte-Bellot [62] were further extended by Clark [63] who studied fully developed incompressible turbulent flow in a 0.127 m wide channel with aspect ratio of 12 and a length to half-width ratio of 120. Reynolds numbers examined ranged from 15000 to 45600, based on duct half-width and maximum mean velocity. Clark used constant-temperature hot-wire anemometry, with particular attention to measurements well into the viscous sublayer. He used the measured mean velocity distribution in the sublayer to estimate the skin friction coefficient.

Hussain and Reynolds [64] also used constant-temperature hot-wire anemometry to study fully developed turbulent channel flow in a straight rectangular duct, 0.0635 m wide with aspect ratio of 18 and a length to half-width ratio of 450. They obtained distributions of mean and streamwise turbulence velocities, well into the viscous sublayer, as well as frequency spectra and calculated eddy viscosity distributions. In doing a detailed comparison of their results to those of Laufer [61], Comte-Bellot [62], and Clark [63], they found some differences in near-wall turbulence intensity distributions. Hussain and Reynolds attributed this to the fact that the increased aspect ratio and length-to-half-width dimensions of their duct, ensured full development of the turbulence structure: The flow was thus cioser to a true two-dimensional fully developed turbulent channel flow than that in the

previously mentioned investigations.

More recent detailed experimental investigations of turbulent fully developed flow in rectangular ducts have concentrated on turbulence-induced secondary flows in the duct cross sections. Prandtl [65] gave some explanation of the origins of these secondary motions, but it was not until the work of Brundrett and Baines [66] that a fairly complete description of such flows was provided. They showed that gradients in Reynolds stresses in the plane of the cross section were responsible for generating streamwise vorticity. Their work included hot-wire measurements of all six independent components of the Reynolds stress tensor. From these data, they deduced that in rectangular ducts with axes chosen parallel to the sides, it was predominantly the normal-stress gradients that generated the secondary flows in the plane of the cross section. In a complementary experimental work, Gessner and Jones [67] examined several aspects of turbulent fully developed flow in a 0.203 m square duct, with Reynolds numbers in the range 75000 to 300000, and in a 0.203 m x 0.102 m rectangular duct, with Reynolds numbers in the range 50000 to 300000. They concluded that within the Reynolds number range of their investigations, the secondary-flow velocities, when nondimensionalized by either the bulk velocity or the axial mean velocity at the duct centerline, decrease with an increase in Reynolds number. The greatest skewness of local wall shear stress vectors was shown to occur in the vicinity of corners where secondary flow was maximum. Finally, through an experimental evaluation of terms in a momentum balance along a typical secondary-flow streamline, they showed that the secondary flow is the result of small differences in the magnitudes of opposing forces exerted by the Reynolds stresses and static pressure gradients in planes

normal to the axial flow direction.

The studies of Brundrett and Baines [66] and Gessner and Jones [67] were extended by Launder and Ying [68], who studied turbulence-induced secondary flows in a straight square duct with equally roughened sides. They showed that the secondary flow in a duct with rough sides is a substantially larger proportion of the axial flow than that in smooth-walled ducts. With secondary velocities normalized by the friction velocity, however, the resultant profiles for smooth-walled and rough-walled ducts were shown to be the same, within the precision of the measurements.

Early investigations, such as those by Laufer [61], Comte-Bellot [62], and Clark [63], were concerned with fully developed symmetric turbulent channel flow. One of the first detailed experimental examinations of asymmetric fully developed turbulent channel flow was done by Hanjalic and Launder [69]. The asymmetry in the flow was introduced by roughening one plate and leaving the other smooth. The rough plate to smooth plate shear stress ratio was about 4:1. Flows at Reynolds numbers, based on duct half-width and maximum mean velocity, ranging from 18470 to 76690 were investigated for channel aspect ratios of 6 and 12. The main emphasis of the work was on establishing the turbulence structure of the flow, particularly in the central region where the two dissimilar wall boundary layers interacted. In this central region, it was found that the boundary layer interactions are characterized by strong diffusional transport of turbulent shear stress and kinetic energy from the rough wall region towards the smooth wall region. This can give rise to an appreciable separation between the planes of zero shear

stress and maximum mean velocity in the flow. They found that in regions close to either wall, the velocity profiles became universal when nondimensionalized with length and velocity scales appropriate for the particular wall region.

The work of Hanjalic and Launder [69] was extended by that of Telbany and Reynolds [70,71]. They examined plane channel flows where one wall of the channel could move relative to the other. This allowed the overall stress gradient, the difference of the two wall shear stresses divided by the distance between the walls, to be easily varied, and its effect on the flow structure could be studied. They studied twenty-six different fully developed flows, of both Couette and Poiseuille type, at Reynolds numbers ranging from 10^4 to 10^5, based on the average flow velocity and half the distance between the two channel walls. Measurements were taken of time-mean velocities [70], the three components of velocity fluctuation intensities, and shear stresses [71]. From these data, they were able to develop empirical correlations to describe the wall and core regions of such flows. It was noted that the turbulence structure responded to an increased stress gradient sooner than the mean velocity distribution, and the pattern of turbulence production changed before the intensities did. This leads to a core region behaviour for Poiseuille type flows similar to that observed by Launder and Hanjalic [69]: As the stress gradient increases, the locations of the maximum mean velocity and zero shear stress shift towards the lower-stress wall, with the shift in the location of zero shear stress being more rapid than that of the maximum mean velocity.

In addition to the aforementioned experimental investigations, there

have been numerous semi-analytical and numerical studies of turbulent fully developed flow in straight ducts of rectangular cross section. The semi-analytical studies have been primarily concerned with fully developed turbulent flows in two-dimensional channels, and are based on the so-called three-layer concept: (1) an inner, or wall, layer, where viscous shear stress is dominant; (2) an outer layer, where turbulent shear stress is dominant; and (3) an overlap, or buffer, layer, where both are significant. Detailed discussions of such semi-analytical studies, including the pioneering works of Prandtl, von Karman, Millikan, Rotta, Reichardt, Deissler, Clauser, van Driest, and Spalding, are available in books by Schlichting [34] and White [36], so they will not be repeated here. White [36] has demonstrated that friction factor predictions based on an inner law proposed by Spalding are in excellent agreement with experimental data for turbulent fully developed flow in channels, and similar predictions based on the work of Prandtl are also quite accurate, except at Reynolds numbers near transition. As already mentioned, Hartnett et al. [53] have proposed a semi-empirical correlation that gives the friction factor as a function of Reynolds number for fully developed turbulent flow in square-sectioned and rectangular-sectioned ducts.

Numerical studies of turbulent fully developed flow in straight ducts of rectangular cross section involve the use of turbulence models which are reviewed in the next section.

1.2.2 Modelling and Simulation of Turbulent Flows

Turbulence models can be classified in several ways. Using the

classification system adopted for the 1980-81 Stanford Conference on Complex Turbulent Flows [72], most turbulence models can be considered as belonging to one of six classes: (1) correlations; (2) integral methods; (3) one-point closures; (4) two-point closures; (5) large eddy simulations; or (6) full simulations.

Empirical correlations, such as friction factor correlations for duct flows can be obtained from experimental data. These can be very accurate, but usually only for a narrow range of flow and geometrical parameters. In addition, they are generally limited to simple cases involving only a few parameters. Prior to the mid 1960's, most "advanced" turbulence modelling of boundary layer type flows was done using integral methods [73]. These involve the use of empirical profile equations that allow the governing partial differential equations to be approximately integrated in the cross-flow direction, and reduced to ordinary differential equations in the streamwise direction. During the last twenty-five years, however, emphasis has been on the development of turbulence models based on the governing partial differential equations for the turbulent flow field [73]. This approach has led to the evolution of more complex and supposedly more general approaches to turbulence modelling, ranging from one-point closures to full simulation of the governing Navier-Stokes equations.

One-point closures deal with single-point statistics of the turbulent flow, such as Reynolds stresses or turbulent kinetic energy [74], and are concerned with the solution of the time-averaged Navier-Stokes equations. The turbulent Reynolds stresses that appear in these equations are approximated using either algebraic models or various turbulence

transport equations. The number of differential equations solved, in addition to the time-averaged momentum and continuity equations, is commonly used to categorize the various one-point closure models as being: (1) zero-equation models; (2) one-equation models; (3) two-equation models; or (4) stress transport models [40,72,73,75,76].

Two-point closure methods involve the solution of the Navier-Stokes equations in the spectral domain [74,77]. Direct information about turbulent length scales and knowledge of how eddies of different sizes affect the turbulent motion can only be obtained from multi-point statistics. To keep the complexity of the turbulence model from becoming overwhelming, it is assumed that two-point statistics will give sufficient information [74]. A common practice with this type of model is to Fourier transform the Navier-Stokes equations, and use these transformations to derive the governing equations of two-point statistics in Fourier space [74]. While this may allow more accurate and general modelling of some complex turbulent flows, the resulting model is also more complex with an increased number of unknowns compared to one-point closures [75]. A general outline of two-point closures, and their use in the evaluation of one-point closures, can be found in an article by Aupoix [74].

Large eddy simulation involves direct computation of the large-scale turbulence structure, and calculation of the small-scale structure using relatively simple models [77,78]. The rationale for this is that the characteristics of large eddies in turbulent flow tend to vary significantly from flow to flow, while the small eddies are more universal in nature and therefore easier to model [77,78]. These types of simulations

can provide important detailed information about turbulent flows, and this can be used to evaluate and enhance less sophisticated turbulence models [78]. At present, however, they are still computationally very expensive and therefore impractical for general engineering applications. Laurence [77] gives an overview of some common one-point closures and describes how the results of large eddy simulations can be used to enhance the one-point closure models.

Direct or full simulation of the entire turbulent flow field has recently become possible using modern supercomputers. These types of simulations are providing an important new means for studying turbulence. However, because the energy at large scales and dissipation at small scales must be resolved, very fine grids are required, and the applications are presently limited to relatively low-Reynolds-number flows in simple geometries such as straight rectangular ducts and channels [78].

At the present time, the one-point closure methods provide a degree of accuracy that is acceptable for many engineering applications, with a computational efficiency that far exceeds the more advanced turbulence modelling methods [77]. For this reason, one-point closures are currently the most widely used class of turbulence models for engineering predictions. Therefore, further discussion of the turbulence models available in the published literature will be limited to the models of this class, with particular emphasis on the most popular category, the so-called two-equation k-ϵ models [76,77].

Numerous reviews that describe and discuss the performance of

various one-point closure models have been published in recent years. These include works by Launder and Spalding [39], Reynolds [73], Rodi [75], Bradshaw et al. [40], and Nallasamy [76]. Each publication critically reviews zero equation, one equation, two equation, and Reynolds stress models, describing details and discussing advantages and disadvantages of the various models. In particular, the works by Bradshaw et al. [40], Rodi [75], and Nallasamy [76] give several examples in order to evaluate the predictive capability of the different models. Rodi [75] emphasizes applications to hydraulic flow problems, while Bradshaw et al. [40] concentrate on external flows over wings and airfoils, and Nallasamy [76] looks at several plane and axisymmetric two- and three-dimensional internal flows. In addition to these publications, at the 1980-81 Stanford conference on complex turbulent flows [79], computations were compared with carefully compiled experimental data for several flows of engineering interest: The majority of these computations were based on one-point closure models, and many internal flows that were classified as being either attached or separated were considered.

Most zero-equation, one-equation and two-equation turbulence models are based on Boussinesq's eddy viscosity concept: Turbulent stresses are made proportional to the mean velocity gradients. Furthermore, the Kolmogorov relation is used, in which the eddy viscosity is assumed proportional to turbulent velocity and length scales [40,75]. Of these models, the zero equation models are the simplest, using an empirically determined turbulent length scale, l_t, and mean velocity gradients to calculate the eddy viscosities [40,73,75,76]. The biggest problem that arises in the use of these models is the determination of an accurate length scale expression, for other than the simplest shear flows. A

transport equation for the turbulence kinetic energy, k, is solved in one equation models, and $k^{1/2}$ is assumed proportional to the turbulent velocity scales [40,73,75,76]. The problem of calculating the turbulent length scale, l_t, still remains, however. In addition to a transport equation for k, two equation models employ a transport equation for l_t or a variable that is a function of both k and l_t. The most commonly used equation is that for the turbulence energy dissipation rate, $\epsilon = k^{3/2}/l_t$, suggested by Jones and Launder [80]. Transport equations for other combinations of k and l_t have been used, but the ϵ equation has become the most popular of these equations, because in near-wall regions it performs better than other equations and it is also less complicated than the other equations [75,81].

It is now well known that numerical methods based on the turbulent eddy viscosity concept and the mixing length, one-equation, or two-equation models of turbulence fail to predict the turbulence-induced secondary flow in the developing or fully developed regions of straight rectangular ducts [40,75,76]. The main reason for this is the assumption of an isotropic eddy viscosity [40,75,76]. Reynolds stress models have been developed in an effort to overcome this problem. In these models, the Reynolds stresses that appear in the time-averaged momentum equations are calculated from appropriate stress transport equations. A brief overview of numerical methods and turbulence models that are capable of predicting turbulence-induced secondary flows in ducts of rectangular cross section is available in a paper by Gosman and Rapley [82]. Reynolds stress models could require the simultaneous solution of up to eleven coupled nonlinear partial differential equations [83]: Axial momentum, cross-plane momentum and continuity equations account for four

of these partial differential equations, and the other seven, which include an equation for ϵ, are required for the calculation of the Reynolds stresses that appear in the momentum equations. In addition, empirical inputs are still needed to invoke closure for triple-correlations that appear in the Reynolds stress equations. The number of partial differential equations can be reduced by employing the algebraic stress transport model (ASTM), in which simplified algebraic approximations to the Reynolds stress transport equations are employed. The ASTM was first derived by Launder and Ying [84] for the calculation of fully developed flows in square ducts, and was then further developed and analyzed by Gessner and Emery [85]: It is based on a set of approximate algebraic equations that enable the calculation of the entire Reynolds stress tensor in terms of axial velocity gradients, the turbulence kinetic energy, k, and its dissipation rate, ϵ. Examples of the application of such methods to the prediction of turbulent flow in ducts of rectangular cross section include the works of Launder and Ying [84], Gessner and Emery [85], Gosman and Rapley [82], Rapley [86], and Nakayama et al. [87].

The majority of 2-D turbulent flow calculations appearing in the literature have been done using the two-equation k-ϵ model of turbulence [76]. While this model has several limitations, the most restrictive being the assumption of isotropic eddy viscosity and some ad hoc assumptions in the derivation of the ϵ equation, it has been used extensively in engineering calculations [75,76]. The computational cost of the k-ϵ model is relatively low when compared to the more elaborate higher order models and, in practice, it seems to give quite satisfactory results for many present-day complex industrial applications [77]. For these

reasons, it was decided in this work to investigate the ability of the k-ϵ model to predict periodic fully developed turbulent flow phenomena in interrupted-surface geometries. The remainder of this discussion of turbulence models will therefore focus on the various forms of the k-ϵ model of turbulence.

Jones and Launder [80] presented a turbulence model based on approximate forms of the k and ϵ equations that Hanjalic [88] had found promising for the prediction of high-Reynolds-number flows near to and remote from walls. The standard, or high-Reynolds-number, form of the k-ϵ model that is commonly used today is also based on these equations. The phrase "high-Reynolds-number flows" refers to flows in which the direct effect of molecular viscosity is negligible, implying that the local turbulence Reynolds number is high. In the high-Reynolds-number k-ϵ model, there appear five constants, two diffusion constants that relate the eddy viscosity to the turbulent diffusion coefficient for the k and ϵ equations, a proportionality constant which appears in the Prandtl-Kolmogorov relation for eddy viscosity, and two proportionality constants in the ϵ equation, $C_{1\epsilon}$ and $C_{2\epsilon}$, that appear in terms for the production and the dissipation of ϵ, respectively. The values of these constants are determined using measurements in grid-generated turbulence and thin equilibrium shear layers, in conjunction with computer optimizations [75]. Various values of $C_{1\epsilon}$ and $C_{2\epsilon}$ are used by different modelers, which may be justified based on their particular form of k-ϵ model, but Hanjalic [81] points out that values for $C_{2\epsilon}$ should be determined only from the experimental data on the law of the decay of grid turbulence. At walls, boundary conditions for the governing equations are obtained in the near-wall region of the flow by using "universal"

wall functions [75]. These wall functions relate surface boundary conditions to points in the fluid outside the region next to the wall where molecular viscosity has a direct influence. This removes the need to integrate the model equations through the viscous sublayer region where, because of the very steep velocity gradients, very fine computational grids would be required, and result in increased computational costs [75].

For many complex engineering flows, which include recirculating regions, sudden changes in boundary conditions, and low Reynolds numbers, the wall function approach to boundary condition specification is not adequate. Jones and Launder [80] extended the high-Reynolds-number form of the k-ϵ model to make provision for modelling of flow regions where the turbulence Reynolds number is low, such as the viscous sublayer region near a wall boundary. They achieved this by 1) including the viscous diffusion of k and ϵ; 2) making the eddy viscosity constant, C_μ, and the $C_{2\epsilon}$ constant of the ϵ equation dependent on the local turbulence Reynolds number; and 3) adding additional source terms, one each to the k and ϵ equations, to allow ϵ to be set to zero at solid boundaries for computational convenience. They applied this model to the prediction of wall boundary-layer flows that were subjected to strong streamwise accelerations so as to cause partial relaminarization of the turbulent boundary layer. They reported close agreement of the predicted boundary layer development with measured behaviour.

Jones and Launder [89] also applied their k-ϵ model of turbulence to low-Reynolds-number pipe and channel flows, and wall boundary layers with favourable streamwise pressure gradient and wall injection.

Friction factor data and streamwise mean velocity profiles for the pipe and channel flow showed good agreement with measured values in the fully turbulent region, although transition from laminar to turbulent flow was predicted at lower Reynolds numbers than measured values. Flows with acceleration and blowing showed greater differences between predictions and measurements.

Since the publication of the low-Reynolds-number k-ϵ model of Jones and Launder [80,89], several other low-Reynolds-number two-equation models of turbulence have appeared in the literature. The performance of eight of these models has been examined by Patel et al. [90]. Their review of each model includes a statement of the model assumptions and an evaluation of the damping functions that were employed to account for low-Reynolds-number and wall proximity effects. Two-dimensional incompressible fluid flow calculations were performed for a flat-plate boundary layer, an equilibrium adverse pressure gradient boundary layer, a strong favourable pressure gradient boundary layer, and sink-flow boundary layers. Using these results, each model was evaluated based on its ability to (i) reproduce results of its parent high-Reynolds-number model for the flows not dominated by low turbulence Reynolds numbers, and (ii) give predictions that showed acceptable agreement with experimental data for wall regions and flows where low turbulence Reynolds numbers dominate. Based on these evaluations, Patel et al. [90] concluded that the k-ϵ models of Launder and Sharma [91], Chien [92], and Lam and Bremhorst [93], and a k-ω (ω refers to a turbulence pseudovorticity) model by Wilcox and Rubesin [94], gave acceptable performance. Even for these four models, however, it was concluded that there is still a need for improving the damping functions for turbulent viscosity

and the source terms in the ϵ equation in order to obtain better agreement with the experimental data in near-wall regions. In addition, it was suggested that modifications to the original high-Reynolds-number form of the models be made so as to improve their prediction capabilities in adverse pressure gradient flows.

Launder and Sharma [91] used the low-Reynolds-number model of Jones and Launder [80,89] for the prediction of swirling flows generated by a rotating disc in a quiescent environment. The governing equations were derived for a two-dimensional coordinate system, in the radial and normal directions. As a result of reoptimizations, minor changes were made to the values of model constants and the form of the viscosity damping function used by Jones and Launder [80,89]. However, it was reported that these changes made no noticeable difference when the revised model was used to redo some of the predictions presented in [80,89]. Launder and Sharma [91] concluded that the basic form of the low-Reynolds-number k-ϵ model developed by Launder and Jones [80,89] could accurately predict flow, heat, and mass transfer in the vicinity of a rotating disc.

The low-Reynolds-number k-ϵ model of Chien [92] follows the same general approach as the Jones and Launder [80,89] model. However, the forms of the damping functions and the additional source terms required in the k and ϵ equations, as a result of setting ϵ to zero at solid boundaries, are quite different. Chien used the Taylor series expansion technique to study the behaviour of turbulent shear stress and turbulence kinetic energy and its rate of dissipation near a wall. The damping function he arrived at for the turbulent viscosity is dependent on the normal distance from the wall boundary and the local shear stress at

that same wall. The additional k and ϵ equation source terms that appear in this form of the low-Reynolds-number model are also dependent on the normal distance from the nearest wall. Chien applied his model to fully developed turbulent channel flow and to flat plate boundary layers. He reported good agreement with experimental measurements and with the results of the Jones and Launder model [80,89]. However, the calculated peak turbulence kinetic energy is closer to actual measured values than that predicted with the Jones and Launder model.

Unlike the low-Reynolds-number k-ϵ models of Jones and Launder [80,89], Launder and Sharma [91], and Chien [92], the k-ϵ model of Lam and Bremhorst [93] sets ϵ to a calculated value at a solid boundary, rather than setting it to zero for computational convenience. Thus there is no need for adding additional source terms to the k and ϵ equations. In the near-wall region, Lam and Bremhorst expressed the variation of k and ϵ by expansion in a Taylor series. Using such an expression for ϵ and the resulting form of the k equation at a wall boundary, they obtain a boundary value expression for ϵ. Lam and Bremhorst also postulated that the turbulent viscosity damping function should be dependent not only on the local turbulence Reynolds number but also on the normal distance from the wall. In addition, they assumed that the coefficient appearing in the generation term of the ϵ equation should be greater than unity near a wall, unlike the models presented in [80,89,91,92]. This causes an increase in predicted dissipation rates and hence reduces predicted near-wall turbulence levels, and gives better agreement with experimental data. The coefficients in the ϵ equation generation term was made a function of the viscosity damping function, and is therefore dependent on the normal distance from the wall

boundary. Lam and Bremhorst tested their model by doing predictions of fully turbulent, semi-laminar, and laminar regions of fully developed pipe flow. They reported predictions that are in good agreement with experimental data. This model also allowed the comparison of predicted and measured ϵ values in the near-wall region. Measured near-wall ϵ values given in [37] showed as much as 45 percent disagreement with computed values in [93]. However, Lam and Bremhorst [95] claim that the experimental values from [37] are approximately 1.9 times too high. They conclude in [93] that more accurate experimental information on near-wall ϵ profiles is needed to allow a more thorough evaluation of their numerical results.

Patel et al. [90] used a variation of the Lam and Bremhorst model [93] in which the gradient of ϵ is set to zero at a wall boundary. This boundary condition is easie. to apply than that used by Lam and Bremhorst. They reported [90] that results were still in good agreement with experimental results.

Hanjalic and Launder [96] suggested a modification for the standard high-Reynolds-number k-ϵ model so that it would give more accurate predictions in both adverse pressure gradient flows and flows that experienced strong disturbances. From their initial investigations and previous studies, they concluded that the ϵ equation was the main cause of errors in predictions of these types of flows. Hanjalic and Launder pointed out that irrotational straining plays an important role in the spectral transport from the large energy containing eddies to the small energy dissipating eddies. In its general form, the generation term appearing in the ϵ equation involves both rotational and irrotational

strain rates. To bring the irrotational strain rate term into prominence, Hanjalic and Launder multiplied it by a larger empirical coefficient than the rotational term. For a plane jet, round jet, and adverse pressure gradient boundary layers, they reported improved agreement of calculated results, obtained using this simple modification of the ϵ equation, with experimental data.

Rodi and Scheuerer [97] examined the performance of the Lam and Bremhorst low-Reynolds-number k-ϵ model [93] for adverse pressure gradient boundary layers. They also reported unsatisfactory results for this model in this type of flow. An analytical analysis of the log-law region was done to show that the generation term in the ϵ equation should be increased to give better agreement with experiments for adverse pressure gradient conditions. Rodi and Sheuerer [97], in turn, employed the modification of Hanjalic and Launder [96] and reported improved predictions for both moderately and strongly decelerated boundary layer flows.

When detailed calculation of the near-wall flow region is necessary, an alternative to low-Reynolds-number k-ϵ models are multi-layer near-wall models that can be used with the standard k-ϵ model of turbulence. Examples of such models are those of Chieng and Launder [98], Amano [99], and Patel and Chen [100]. The basic idea behind this type of modelling is that rather than model the governing transport equations through the near-wall region, which requires a large number of grid points, this region is subdivided into two or three layers, and semi-empirical and empirical profile distributions are used to calculate flow variables in these layers. This allows for more detailed and accurate

near-wall modelling than the standard wall-function approach commonly used with the high-Reynolds-number k-ϵ model, especially in complex flows.

Chieng and Launder [98] modelled the near-wall region as two layers, a viscous sublayer and a logarithmic, or fully turbulent, layer. A parabolic profile distribution of k was assumed over the viscous sublayer and a linear distribution was assumed over the logarithmic layer, where a logarithmic profile was assumed for the velocity parallel to the wall. The two-layer and three-layer near-wall models of Amano [99] follow the same approach as the Chieng and Launder model [98], except that each term in the ϵ equation for the near-wall region was evaluated in accordance with the k equation rather than approximated under local equilibrium conditions. In Amano's three-layer model, an attempt is made to approximate experimental velocity profiles more accurately by modelling the near-wall region as three layers: a viscous sublayer, a buffer layer, and a logarithmic layer. Amano reports better results with the three-layer model. Nallasamy [76] states that while the near-wall models in [98,100] have allowed some significant improvements in prediction of wall heat transfer rates, the flow field predictions are not noticeably different from those of the standard k-ϵ model.

Patel and Chen [100] and Chen and Patel [101] have developed near-wall models that are simpler and more efficient, in some flows, than the low-Reynolds-number k-ϵ modelling approach. The computational domain is divided into two regions, an outer region where the standard k-ϵ model is used and an inner, or wall, region comprised of the viscous sublayer, the buffer layer, and part of the logarithmic layer. In both the earlier

[100] and later [101] versions of the model, momentum transport equations are solved through the inner layer to the wall, and the inner-layer eddy viscosity is determined by using a mixing length formula. In [100], inner-layer values of k and ϵ were calculated from empirical expressions obtained from curve fits of the data summarized in [90], however, the transport equation for k was retained and ϵ was calculated from a length-scale formulation for the inner layer of [101]. In [100], Patel and Chen performed calculations of turbulent flow over the trailing end and in the wake of a flat plate. They reported satisfactory agreement with experimental data and with solutions obtained previously using boundary layer equations, except in the far-wake region where the rate of decay of turbulence was underpredicted. In [101], Chen and Patel examined the performance of the Lam and Bremhorst low-Reynolds-number k-ϵ model [93], their two-layer k-ϵ model [101], and the standard k-ϵ model using a two-point wall function approach [100]. They carried out calculations for test cases that included strong pressure gradients, surface curvatures, boundary layers and wakes, viscous-inviscid interaction, and separation. The two-layer modelling approach of [101], was reported to be quite successful in resolving the most important features of these complex flows and computationally less expensive and easier to implement than the low-Reynolds-number k-ϵ model of Lam and Bremhorst [93]. It was also concluded that the standard wall-function approach is not suitable for separated flows, and its extension to three-dimensional and unsteady flows requires additional assumptions that appear to have no sound physical basis.

In order to further evaluate the performance of the standard k-ϵ model and the two-layer Chen and Patel [101] k-ϵ models, Patel and

Richmond [102] performed a detailed numerical investigation of the effects of pressure gradients and surface curvatures in two-dimensional flows. Within the extremes of laminarization and separation caused by favourable and adverse pressure gradient flows on flat surfaces, respectively, they found the performance of the two-layer model quite satisfactory and superior to that of the standard k-ϵ model. For flows over curved surfaces, their results were not so conclusive: The main features of these flows were reproduced, but the turbulent shear stress was either over or under predicted for convex or concave walls, respectively.

Iacovides and Launder [103] have used a "Parabolic Sublayer" (PSL) scheme in an attempt to simplify the modelling of the near wall region in an elliptic turbulent flow. Next to the wall, they assume a thin parabolic sublayer where the static pressure variation is assumed to be negligible, or calculated from equilibrium conditions for a curved wall. Velocities normal to the wall are calculated using continuity requirements over computational control volumes rather than by solving the respective momentum equation. Computations are reduced from that of a low-Reynolds-number model, but a fine computational grid is still needed. Eliminating the use of wall functions makes this approach particularly attractive for three-dimensional flows, although its computational benefits are much reduced for complex flows with recirculation and separation [103].

1.2.3 Experimental Investigations of Fluid Flow in Interrupted-Plate Passages

The enhancement of heat transfer with fluid flow along a succession of discrete plate segments compared to that for flow along a continuous wall was first demonstrated by the pioneering experiments of Norris and Spofford [104]. They dealt with air flows through actual or model heat exchangers consisting of an array of discrete plates aligned parallel to the flow. The discrete plates, which were fins that bridged between the walls of the heat exchanger passages, were arranged in parallel columns, with streamwise gaps between the plates in each column. Condensing steam served as the hot fluid in most of these experiments. Similar experiments with model or actual heat exchanger cores involving interrupted-plate passages have also been carried out by Manson [105], Kays and London [1], London and Shah [24], Wieting [4], and Mochizuki and Yoshinao [106]. The emphasis in these experiments was on overall results. Measurements typically included air temperatures and pressures at the inlet and exit ports of the core, the air flow rate, the steam temperature and pressure, and the steam condensation rate. The overall results obtained proved very useful in the design of specific heat exchange devices [1], but they do not provide insights into the details of the complex flow phenomena that occur inside interrupted-plate passages.

More detailed measurements than those reported in [1,4,24,104-106] have been conducted by Adarkar and Kays [107], Roadman and Loehrke [27], Zelenka and Loehrke [28], Cur and Sparrow [11,25], Sparrow and Hajiloo [26], Loehrke and Lane [29], Mullisen and Loehrke [30], and Joshi and

Webb [31] for flow and heat transfer in simple interrupted-plate passages, with configurations ranging from two colinear plates to a multi-column array of plates.

The initial experiments of Cur and Sparrow [25] were performed to determine pressure drop and heat transfer characteristics for each plate of a two-plate colinear array aligned parallel to the air flow direction in a flat rectangular duct having a cross-sectional aspect ratio of 5. The plate length was kept fixed while the plate thickness and interplate spacing were parametrically varied, and the Reynolds number was varied in the range 1000 to 14000. The results showed that the pressure drop increase caused by increasing plate thickness was greater than the largest thickness-related increase in the Nusselt number. Cur and Sparrow [25] also observed that the interplate gap affects the Nusselt number for both plates, but it affects the second plate to a greater extent than it does the first plate.

Cur and Sparrow [11] studied heat transfer and pressure drop characteristics of an array of eight colinear plates, equally spaced and aligned parallel to the air flow in a flat rectangular duct with a cross-sectional aspect ratio of 6. The thickness of the plates in the array was varied parametrically, and the Reynolds number was also varied in the range 1000 to 14000. It was found that the Nusselt number increases with plate thickness: Up to 65 percent increases were recorded in the periodic fully developed regime, which was typically achieved before the last geometrically similar module. The presence of the interruption was also found to augment heat transfer: In the fully turbulent regime of Reynolds numbers, the heat transfer coefficients

were about twice those for a conventional duct. Modular pressure drops were also recorded, and it was determined that they increase with increasing plate thickness. Pressure distributions were not obtained for regions within geometrically similar modules.

Sparrow and Hajiloo [26] studied heat transfer and pressure drop characteristics of a multicolumn array of staggered plates aligned parallel to the direction of a forced convection air flow. Plate thicknesses equal to 4, 8, and 12 percent of the plate length were used, and the Reynolds number, based on the Kays and London definition [1], was varied in the range 1000 to 9000. Periodic fully developed conditions for heat transfer were achieved within a streamwise length of two geometrically similar modules from the inlet plane. It was found that the thicker plates gave rise to higher pressure drops and higher heat transfer coefficients. The pressure measurements were conducted along the length of the discrete plate array and also in the upstream and downstream duct work. Those measurements enabled the determination of a net per-row pressure loss coefficient and an apparent friction factor for the array. No pressure distributions were obtained for regions within geometrically similar modules. For the thickest plates, the apparent friction factor was found to be essentially independent of the Reynolds number.

Roadman and Loehrke [27] investigated the flow between a pair of flat colinear plates at low Reynolds numbers in both water and air flows. Their main objective was to establish the conditions for transition from steady to unsteady laminar flow between the plates. In a 7.6 cm square cross-section water channel, hydrogen bubble and dye

injection flow visualization experiments were performed, and measurements of wake oscillation frequency and amplitude were made using a cylindrical hot-film probe positioned near the leading edge of the second plate. In order to extend the range of parametric variation, runs were also conducted in a 33 cm diameter low speed wind tunnel in which the mean velocity was uniform over the central 90 percent of the tunnel. Hot-wire measurements, comparable to the hot-film measurements, were made in air. Plates with streamwise length to thickness ratios ranging from 4 to 159 were used. From their experiments, Roadman and Loehrke [27] determined that there was a critical velocity at which periodic oscillations in the flow between plates was first observed. This critical velocity depended strongly on plate spacing, plate length, and plate thickness, but only weakly on the free-stream turbulence level. The downstream plate was observed to have a noticeable influence on this critical velocity value.

In [28], Zelenka and Loehrke observed the effects of leading-edge bluntness, plate spacing, and Reynolds number on the average heat transfer from each plate of a two-plate colinear array aligned parallel to an air flow. Steady laminar and transitional flow regimes were investigated. Each plate was heated by means of an internal resistance heating strip, and average plate heat transfer coefficients were calculated using the total power dissipated, total plate surface area, and the difference between temperatures of upstream air and the plate center. Zelenka and Loehrke found that the leading-edge shape of the first plate had an effect on heat transfer from the second plate if the interplate spacing was small enough and the wake of the first plate did not become unsteady. An unsteady wake allows increased mixing of the flow in the

interplate gap before it hits the second plate, thereby diminishing the effects of a leading-edge separation on the first plate. The heat transfer from the second plate was often found to be greater than that of the first plate.

Loehrke and Lane [29] extended the work done in [27] to the investigation of flow through a two-dimensional array of parallel plates aligned with the flow direction. Flow visualization experiments were done in water flows for both staggered and in-line arrangements of plate arrays with streamwise plate spacing equal to streamwise plate length, and plate spacing in the direction perpendicular to the main flow direction equal to one half the streamwise plate length. It was observed that the wake behind each plate in each array became unsteady at a Reynolds number, based on plate thickness and average open channel velocity, that was comparable to that which causes the onset of unsteady flow between an array of only two colinear plates [27]. Measurements of total core pressure drops for the various arrays tested suggested that the onset of this periodic unsteady flow between plates leads to friction factor distributions similar to those in steady fully turbulent flows: The slope of the overall friction factor versus Reynolds number curve changed abruptly as it does for a parallel plate channel when the flow undergoes a laminar-to-turbulent transition. This behaviour was also evident from measurements of the spectra of the flow noise emitted from a closely packed array that was tested in air. Loehrke and Lane [29] observed that the critical Reynolds number for transition from this laminar to turbulent behaviour in a parallel-plate array can be significantly increased if the streamwise gaps between plates are made sufficiently small.

More recently, Mullisen and Loehrke [30] have performed an experimental study of flow and heat transfer in in-line and staggered parallel plate arrays, and in perpendicular plate arrays. Air flow Reynolds numbers, based on a form of the Kays and London definition [1], ranged from 100 to 10000. Various values of plate length, streamwise plate spacing, and plate thickness were examined for plate arrays having three to six streamwise columns for in-line configurations, and six or twelve streamwise columns for staggered configurations. Overall friction factors were obtained from measurements of the total pressure drop across a core. Plates were heated using a resistance heater located within the plates, and a transient heating technique was used to determine overall heat transfer rates. Fluid flow phenomena were identified using the Schlieren visualization technique. Steady, general unsteady, and periodic unsteady flow regimes were observed in the cores of in-line and staggered parallel plates. The periodic unsteady regime was characterized by periodic, synchronized, vortex shedding from the trailing edges of upstream plates, and it was accompanied by an audible tone. No periodic regime was detected for arrays with plates perpendicular to the main flow direction. Mullisen and Loehrke [30] found that the transition from steady to unsteady flow is best correlated by a Reynolds number based on plate-wake width rather than by a Reynolds number based on passage hydraulic diameter. They also reported that enhancements of over 100 percent in the average heat transfer coefficient for some parallel-plate cores may be obtained by interrupting the plate surfaces.

Joshi and Webb [31] carried out an experimental investigation of periodic fully developed flows through offset strip-fin heat exchanger geometries. They studied water flows through test cores having five

rows of fifteen colinear fins aligned in the flow direction. Various values of plate thickness, plate length (equal to streamwise plate spacing), and perpendicular separation distance between parallel plates were used in eight different scaled-up geometries. Reynolds numbers, based on minimum flow area average velocity and hydraulic diameter for the strip-fin channel, ranged from 200 to 4000. Dye injection flow visualization experiments showed that transition from laminar to turbulent flow coincided with the onset of oscillating velocities in the wake, although it was reported that the plate boundary layers remained laminar. Based on previous friction factor and heat transfer coefficient data in the literature for offset fin geometries, Joshi and Webb correlated the value of the wake-width Reynolds numbers with nondimensional plate thickness and spacing ratios, and obtained an equation to predict the transition from laminar to turbulent flow. They also developed analytical models to predict the heat transfer coefficients and friction factors in offset strip-fin geometries. Curve fits to the numerical data of Sparrow and Liu [15], with corrections incorporated to account for fin thickness and three-dimensional aspect ratios, were obtained for laminar flows. A semi-empirical method was used for turbulent flows. Using these analytical models, Joshi and Webb reported that predictions for Nusselt number and friction factor were within ±20 percent when compared to their experimental data and the available data on actual heat exchangers.

Flow visualization has also been used by Mochizuki and Yagi [108] to study the vortex shedding characteristics of staggered-plate arrays. They used a combined dye injection and hydrogen bubble technique to visualize the fluid flow through scaled-up models of heat exchanger

cores. Thirteen scaled-up models, from single plate to eighteen-stage cascade plates in staggered arrangement, were systematically tested for a wide range of Reynolds number. The flow patterns were recorded by both still and video cameras, and a hot-wire technique was used to measure the frequency of vortex shedding. The data were used by the authors as the basis of a qualitative discussion of the vortex shedding characteristics as a function of fin arrangement and the Reynolds number.

The experimental work in this thesis dealt with detailed and accurate local and overall pressure drop measurements and plate surface streamline flow visualization in the periodic fully developed region of turbulent flows in interrupted-plate rectangular ducts, similar to that shown in Fig. 1. These measurements were done using a specially designed experimental facility [109]. The ability of this facility to generate periodic fully developed turbulent flows has been demonstrated from the results of overall and intramodular pressure measurements taken in the early stages of this research and discussed in [110]. The experimental research presented in this thesis is concerned with the effect of plate thickness and flow rate on the overall and local flow field. The test section consisted of a minimum of 23 geometrically similar modules, for all cases considered, so as to ensure the attainment of the periodic fully developed flow regime. Reynolds numbers ranged from $5x10^3$ to $30x10^3$. This experimental work therefore complements and extends the investigations reported in [11,25-31].

1.2.4 Numerical Investigations of Fluid Flow in Interrupted-Plate Passages

Since the early 1970's, the widespread availability of high-speed digital computers, the development of powerful numerical methods for the prediction of fluid flow and heat transfer, and the advent of microprocessor-based automatic data acquisition and processing systems have enabled several detailed numerical and experimental investigations of the flow and heat transfer phenomena inside interrupted-plate passages. The numerical studies include works of Sparrow et al. [12], Sparrow and Liu [15], Patankar et al. [13], Patankar and Prakash [14], and Choudhury [16]. All these numerical investigations were limited to laminar flows, and invoked various other assumptions to simplify the flow and heat transfer problems. Despite these limitations, however, these numerical studies have provided a considerable amount of insight and useful mathematical models of the complex fluid flow and heat transfer phenomena encountered in interrupted-plate passages.

The numerical study of Sparrow et al. [12] involved offset-fin surfaces similar to that shown in Fig. 4a. They assumed two-dimensional laminar behaviour of the flow, and restricted their analysis to geometries with negligible plate thickness. When the plate thickness is neglected, the impingement region on the leading edge of the plate and the recirculation region behind its trailing edge are absent. Therefore, the analysis in [12] could be done using a parabolic, or boundary layer type, numerical procedure, in which the solution could be obtained by marching step-by-step from the inlet plane to successive downstream locations. Detailed velocity and temperature distributions, heat

transfer coefficients, and pressure drop data were obtained for a range of Reynolds numbers and for several values of a dimensionless geometrical parameter that characterized the streamwise length of the interrupted plates. The Prandtl number was fixed at 0.7 for all computations. These results were used to investigate whether an interrupted-plate channel experienced an augmented heat transfer rate compared with that for a parallel-plate channel. For conditions of equal heat transfer surface area and equal pumping power, it was found that appreciably higher heat transfer rates prevailed in the interrupted-wall channel for a wide range of operating conditions. The results in [12] also demonstrated that at sufficiently large distances downstream from the inlet plane, typically beyond the first 5 to 10 geometrically similar modules of the interrupted-plate array, the velocity and suitably nondimensionalized temperature profiles repeated their values in successive modules, and the modular pressure drop and an average modular heat transfer coefficient took on constant values. The term periodic fully developed regime was used to characterize such regions. The analysis and results of Sparrow et al. [12] were later extended by Sparrow and Liu [15], who obtained heat transfer, pressure drop, and performance relations for two-dimensional laminar flow in in-line, staggered, and continuous-plate heat exchangers.

Patankar and Prakash [14] also conducted a numerical investigation of two-dimensional laminar flow in offset-fin passages, but they focused attention on the effect of plate thickness. This was done because, in practice, a certain minimum thickness of the plates is required for structural integrity: This thickness could significantly influence the fluid flow and heat transfer if the spacing between plates in a column

is made small in order to achieve compact heat exchanger cores. The thick plate analysis requires the solution of an elliptic problem: In other words, downstream events can have a noticeable influence on upstream flow phenomena and vice versa. Patankar and Prakash [14] solved this elliptic problem in the periodic fully developed regions of several offset-plate arrays, using the methodology proposed by Patankar et al. [13]. The results in [14] show that the finite-thickness plates give rise to complex flow patterns involving impingement and recirculation zones and flow deflections. Furthermore, they show that compared to the results for passages with plates of negligible thickness, the thick-plate passages lead to significantly larger pressure drops, but the heat transfer does not improve proportionally despite increased average velocities and greater surface areas.

Choudhury [16] has developed a computational scheme for predicting three-dimensional laminar flow and temperature fields in cases where two of the dimensions of the flow domain, in the x and y coordinate directions for example, are relatively large compared to the third dimension, in the z coordinate direction. He points out that this type of flow passage is particularly characteristic of many heat exchanger configurations where the flow tends to be dominated by two-dimensional effects although the "weak" flow field in the third dimension still may have a noticeable influence on the overall flow field. In his scheme, Choudhury uses a quasi-three-dimensional "gap-integral" form of the governing equations. The three-dimensional form of the continuity and the momentum equations are integrated over the gap in the shorter z dimension. Across this gap, it is assumed that the velocity profile takes on the parabolic form of a fully developed laminar flow between parallel

plates. The result is a quasi-three-dimensional mathematical model for fluid flow that is expressed in terms of the continuity equation and the x and y momentum equations containing "gap-integrated' variables of the u and v velocities, pressure, and "gap-integrated" constants. Using the same line of reasoning, a "gap-integrated" energy equation was also derived. One of the test cases Choudhury applied his model to was that of periodic fully developed flow and heat transfer in an interrupted-plate passage. Calculations for zero and two other plate thickness values were done for Reynolds numbers, based on average flow velocity and two-dimensional hydraulic diameter, ranging from 200 to 2000. Aspect ratios (defined here as the y-direction distance between the continuous plates divided by the z-direction gap width) of 2,5,15 and 20 were used. Generally, good agreement was reported between results from this model and those obtained using a full field model, with agreement between the two models improving as the aspect ratio increased. It was also shown that two-dimensional model velocity calculations were in greater error when compared with the full three-dimensional model calculations than were calculations done with this quasi-three-dimensional model. Choudhury concluded that for flows where three-dimensional effects are relatively weak, his model gives improved results over two-dimensional models and reasonably good agreement with full three-dimensional models, while providing a considerable saving in computational cost over the later.

In recent years, several other numerical investigations have been done for flows through periodically varying geometries other than interrupted-plate configurations. Sparrow and Prata [17] and Prata and Sparrow [18] examined laminar flow and heat transfer in periodically

converging and diverging pipes and annuli, respectively. Ghaddar et al. [19,20] used spectral element methods to study laminar flow in a two-dimensional channel with periodically spaced rectangular grooves along one wall. Kelkar and Patankar [21] simulated laminar flow and heat transfer in two-dimensional finned passages, where the flat fin surface was perpendicular rather than parallel to the main flow direction. Choudhury and Karki [22] have analyzed two-dimensional periodic fully developed laminar fluid flow and heat transfer in a parallel plate channel with periodically spaced dimples, using generalized curvilinear coordinates. Near the time that the research for this thesis was being completed, a study by Knight and Crawford [23] that included a numerical analysis of turbulent periodic fully developed flow was published. Except for this publication, to the best of this author's knowledge, no other works dealing with this type of turbulent flow have appeared in the literature.

Knight and Crawford [23] performed a numerical analysis of two-dimensional periodic fully developed flows in parallel plate ducts having periodically spaced rectangular grooves along one wall. Reynolds numbers, based on average flow velocity and hydraulic diameter for the minimum duct flow area, ranged from 250 to 1500 for laminar flows and from 2000 to 5000 for turbulent flows. The two momentum equations governing the flow field were reformulated in a stream function-vorticity form. The effect of turbulence was accounted for by using the Chien [92] low-Reynolds-number k-ϵ model of turbulence. In this model, the viscous damping function for eddy viscosity depends on both the normal distance to the boundary wall and the value of the corresponding local wall shear stress. In or near regions of recirculation, such as would be

expected in the periodic grooves, it was necessary to redefine this wall shear stress as the maximum shear stress occurring at that particular streamwise location. Using this adjustment, Knight and Crawford [23] reported good agreement with experimental data for flows involving heat transfer in recirculating flows. With other modifications of the model for convergence monitoring, they reported that periodic fully developed turbulent flow and heat transfer calculations for these grooved channels could be done on mid-sized computers in several hours of computer time.

The numerical investigation undertaken in this thesis involved the development of a computer code that implements a low-Reynolds number k-ϵ turbulence model to predict periodic fully developed turbulent fluid flow in interrupted-plate geometries. Numerical predictions were done for the configurations examined experimentally in this work in order to (1) evaluate the performance of the numerical model used, and (2) gain further insight into the complex fluid flow phenomena occurring in interrupted-plate geometries. This numerical work complements and extends the works in [12-16] for flows in interrupted-plate geometries.

1.3 SURVEY OF THE THESIS

The aims of the thesis and a synopsis of published investigations relevant to this work have already been presented in the earlier sections of this chapter. There are a total of ten chapters in this thesis. The contents of the remaining nine chapters are summarized in the next paragraph.

In Chapter II, the theoretical considerations which are employed in

the mathematical description of turbulent air flows of interest in this thesis, in the recording and processing of the experimental data, and in the interpretation of both numerical and experimental results, are presented concisely. In Chapter III, modelled forms of the turbulent flow governing equations, described in Chapter II, are presented and discussed. The numerical method used to solve the modelled flow equations is concisely described in Chapter IV. The final choice and implementation of a turbulence model, suitable for the flows of interest in this thesis, are discussed in Chapter V. In Chapter VI, descriptions of the experimental apparatus, instrumentation, and procedures are given. The results of initial experimental and numerical investigations are presented and discussed in Chapter VII. Presentation of the experimental results for the interrupted-plated duct flows investigated in this thesis is done in Chapter VIII. The results of the corresponding numerical investigation, in the context of the experimental results given in Chapter VIII, are presented and discussed in Chapter IX. In the concluding chapter, Chapter X, the contributions of this work are summarized, and suggestions for improvements and extensions are presented.

CHAPTER II

THEORETICAL CONSIDERATIONS

2.1 PROBLEM STATEMENT AND ASSUMPTIONS

The mathematical description of three-dimensional turbulent flows is the subject matter of this chapter. Attention is limited to the type of flows investigated in this work, namely, turbulent air flows through ducts of rectangular cross section with and without an array of colinear interrupted-plates, as shown in Figs. 1 and 5, respectively. The mathematical models used for computations of one-dimensional turbulent fully developed channel flow and two-dimensional turbulent periodic fully developed interrupted-plate channel flow are obtained from the three-dimensional governing equations presented in this chapter. These mathematical models are discussed in Chapters III and V.

All the turbulent flow experiments performed in this research were done under essentially isothermal conditions, and the Mach number was always less than 0.1. For the theoretical considerations presented in this chapter, therefore, the fluid is assumed to be incompressible and to have constant thermophysical properties. Since the experiments were conducted with air at pressures close to atmospheric and temperatures between 16 °C and 28 °C, the fluid is also assumed to be Newtonian.

The equations that govern unsteady three-dimensional turbulent flows are presented first in this chapter. Following that, the time-averaged forms of these equations and relevant nondimensional parameters are presented and discussed. In this thesis, a low-Reynolds-number k-ϵ model

of turbulence is used to invoke closure of the time-averaged flow equations. Details of this model, including governing equations for the mean turbulence kinetic energy, k, and its rate of dissipation, ϵ, are, presented and discussed in Chapter III.

2.2 THREE-DIMENSIONAL TURBULENT FLOW: FULL FORMS OF THE GOVERNING EQUATIONS

In the context of the assumptions mentioned in Section 2.1, three-dimensional elliptic turbulent flow of air can be described mathematically by the following forms of the Navier-Stokes and continuity equations [37-40]:

momentum

$$\rho \left(\frac{\partial \tilde{u}_i}{\partial \psi} + \tilde{u}_j \frac{\partial \tilde{u}_i}{\partial x_j}\right) = - \frac{\partial \tilde{p}}{\partial x_i} + \mu \left(\frac{\partial}{\partial x_j} \frac{\partial \tilde{u}_i}{\partial x_j}\right) \qquad (2\text{-}1)$$

continuity

$$\frac{\partial \tilde{u}_i}{\partial x_i} = 0 \qquad (2\text{-}2)$$

Here, the indices i and j can take the values 1, 2, and 3, and repeated indices in any term indicate a summation over all three values of the index. It should be noted that these governing equations are written with respect to the Cartesian coordinate system shown in Figs. 1 and 5, where x, y, and z, are equivalent to x_1, x_2, and x_3, respectively, and similarly u, v, and w velocities are equivalent to u_1, u_2, and u_3 velocities, respectively. These notations will be used interchangeably throughout this thesis. In Eqs. (2-1) and (2-2), $\tilde{u}_i$ denotes the instantaneous velocity component in the i direction, ρ is the mass

density of the fluid, μ is the dynamic viscosity, $\tilde{p}$ is the instantaneous pressure, and ψ denotes time.

In addition to Eqs. (2-1) and (2-2), boundary conditions and initial conditions for the dependent variables, $\tilde{u}_i$ and $\tilde{p}$, specific to the problems of interest, are needed to complete the mathematical model. Boundary conditions for fully developed turbulent flow and periodic fully developed turbulent flow in rectangular ducts without and with interrupted plates, respectively, are discussed in later sections of this chapter.

2.3 THREE-DIMENSIONAL ELLIPTIC TURBULENT FLOW: TIME-AVERAGED FORMS OF THE GOVERNING EQUATIONS

In principle, the solutions of Eqs. (2-1) and (2-2), subject to appropriate initial and boundary conditions, would provide a complete description of the turbulent flow problems of interest in this thesis. Such solutions are, however, impractical at present. The reason for this is that such direct simulations of turbulent flows, accurate for all temporal and spatial scales of motion, require proper resolution of the large- and small-scale turbulent motion. The small-scale motion is typically of the order of 10^3 times smaller than the extent of the flow domain [75]. The numerical solution of Eqs. (2-1) and (2-2) would thus require the calculation of the dependent variables at 10^9 grid points or more. This would stretch the storage capacity of even the most modern supercomputers, and the excessive computing times required would make such computations prohibitively expensive.

Fortunately, only the time-averaged effects of the turbulent flow are important for most engineering problems. Compared to the instantaneous small-scale structure of turbulent flows, the time-averaged properties vary relatively gradually in space, allowing the number of calculation points to be reduced substantially from those required if all the details of the turbulence were needed. In this section, the time-averaged forms of Eqs. (2-1) and (2-2) are presented. It should be noted that in interrupted-plate geometries, similar to that illustrated in Fig. 1, certain combinations of Reynolds number and plate thickness can give rise to vortex shedding [27,29-31,108]. In this section, however, this vortex shedding phenomena is not considered, and it is assumed that the turbulent flows of interest are in a statistically steady state [37,38].

In turbulent flows, following the procedure of Reynolds, the instantaneous velocities and pressure which appear in Eqs. (2-1) and (2-2) can be decomposed into time-mean and fluctuating components [34,36-40,75]:

$$\tilde{u}_i = U_i + u_i \tag{2-3}$$

$$\tilde{p} = P + p \tag{2-4}$$

where the lower-case bold type denotes the fluctuating components. The time-mean values of the fluctuating components are zero, by definition, but the time-averaged values of the products of correlated fluctuating components are not zero [38]. For example:

$$\overline{\tilde{u}_i \tilde{u}_j} = U_i U_j + \overline{u_i u_j} \tag{2-5}$$

Using Eqs. (2-3) to (2-5), the time averaged forms of Eqs. (2-1) and (2-2) can be written as follows [34,36-40,75]:

momentum

$$\rho\left(U_j\frac{\partial U_i}{\partial x_j}\right) = -\frac{\partial P}{\partial x_i} + \frac{\partial}{\partial x_j}\left(\mu\frac{\partial U_i}{\partial x_j} - \rho\overline{u_i u_j}\right) \qquad (2\text{-}6)$$

continuity

$$\frac{\partial U_i}{\partial x_i} = 0 \qquad (2\text{-}7)$$

The $\rho\overline{u_i u_j}$ term in Eq. (2-6) can be thought of as the contribution of the turbulent motion to the mean stress tensor [38], and its components are referred to as Reynolds stresses. The Reynolds stress tensor is comprised of nine components, of which only six are independent, as the tensor is symmetric [34,37,38]. In many flows, the terms representing the turbulent normal stresses, $-\rho\overline{uu}$, $-\rho\overline{vv}$, and $-\rho\overline{ww}$, contribute little to the transport of the mean momentum [38]. The terms $-\rho\overline{uv}$, $-\rho\overline{uw}$, and $-\rho\overline{vw}$ represent turbulent shear stresses, and they play a dominant role in the transport of mean momentum by turbulent motion [38].

Equations (2-6) and (2-7) represent a system of four coupled governing equations that contains ten unknowns: U, V, W, P, and the six independent components of the Reynolds stress tensor. There is no direct way of calculating the Reynolds stresses. If additional equations for the Reynolds stresses are obtained, by appropriate manipulations and averaging of the original Navier-Stokes equations, more unknowns such as $\rho\overline{u_i u_j u_j}$ are generated by the nonlinear inertia terms [38]. This illustrates the so-called "closure problem" that is characteristic of

all nonlinear stochastic systems. To overcome the closure problem of turbulence, the Reynolds stresses are approximated or "modelled" in terms of quantities that can be directly determined. Details of how closure was achieved for the numerical models used in this thesis are given in Chapter III. Before this is done, particular forms of Eqs. (2-6) and (2-7), relevant to the types of flows studied in this thesis, will be presented and discussed in this chapter.

2.4 TURBULENT FULLY DEVELOPED FLOW IN RECTANGULAR DUCTS: TIME-AVERAGED GOVERNING EQUATIONS

In straight ducts of uniform cross section, fully developed flows are characterized by a velocity field that is invariant in the main flow direction, shown as the x direction in Fig. 5. If no cross-stream velocities exist, and the pressure is constant over a cross section and varies linearly with x, the flow is classified as being simple fully developed [32,33]: $U = U(y,z)$, $V = W = 0$, and dP/dx = constant. Laminar fully developed flow, with no body forces, in a straight duct of uniform cross section is one example of simple fully developed flow. In a complex fully developed flow, the flow field is also invariant with x and the pressure varies linearly with x, but the pressure varies over a cross section and cross stream velocities (secondary flows) are present [66-68]: thus $U = U(y,z)$, $V = V(y,z)$, $W = W(y,z)$, and $\partial P/\partial x$ = constant. Turbulent fully developed flow, with no body forces, in a straight rectangular duct is an example of complex fully developed flow. In such flows, the Reynolds stresses play an important role in the physical mechanisms that extract the energy from the main flow and provide it to the secondary flow, thereby sustaining the secondary flow in the fully

developed regions [66-68].

In the Cartesian coordinate system of Fig. 5, turbulent fully developed flow in straight rectangular ducts is governed by the following forms of the time-averaged Navier-Stokes and continuity equations:

x momentum

$$\rho\left(V\frac{\partial U}{\partial y} + W\frac{\partial U}{\partial z}\right) = -\frac{\partial P}{\partial x} + \frac{\partial}{\partial y}\left(\mu\frac{\partial U}{\partial y} - \rho\overline{uv}\right) + \frac{\partial}{\partial z}\left(\mu\frac{\partial U}{\partial z} - \rho\overline{uw}\right) \qquad (2\text{-}8)$$

y momentum

$$\rho\left(V\frac{\partial V}{\partial y} + W\frac{\partial V}{\partial z}\right) = -\frac{\partial P}{\partial y} + \frac{\partial}{\partial y}\left(\mu\frac{\partial V}{\partial y} - \rho\overline{vv}\right) + \frac{\partial}{\partial z}\left(\mu\frac{\partial V}{\partial z} - \rho\overline{vw}\right) \qquad (2\text{-}9)$$

z momentum

$$\rho\left(V\frac{\partial W}{\partial y} + W\frac{\partial W}{\partial z}\right) = -\frac{\partial P}{\partial z} + \frac{\partial}{\partial y}\left(\mu\frac{\partial W}{\partial y} - \rho\overline{vw}\right) + \frac{\partial}{\partial z}\left(\mu\frac{\partial W}{\partial z} - \rho\overline{ww}\right) \qquad (2\text{-}10)$$

continuity

$$\frac{\partial V}{\partial y} + \frac{\partial W}{\partial z} = 0 \qquad (2\text{-}11)$$

The impermeability and no-slip boundary conditions apply at the walls of the ducts for the cases considered in this thesis. With reference to Fig. 5, therefore, at the walls of the rectangular ducts:

$$U = V = W = 0 \qquad (2\text{-}12)$$

$$\overline{uu} = \overline{vv} = \overline{ww} = \overline{uv} = \overline{uw} = \overline{vw} = 0 \qquad (2\text{-}13)$$

A complete mathematical model of the fully developed duct flows considered in this thesis is obtained when an appropriate turbulence model is used in conjunction with Eqs. (2-8) to (2-13). This is done in Chapter III.

2.5 TURBULENT PERIODIC FULLY DEVELOPED FLOW IN INTERRUPTED-PLATE RECTANGULAR DUCTS: TIME-AVERAGED GOVERNING EQUATIONS

A fully developed turbulent flow regime, in which the flow field is invariant in the main flow, or x, direction, does not occur in interrupted-plate rectangular ducts, similar to that in shown in Fig. 1. In such ducts, the flow continually changes in the x direction, but attains a periodic fully developed behaviour after 5 to 10 ranks of plates downstream of the inlet section [11,12,14,26]. The interrupted-plate duct illustrated in Fig. 1 can be subdivided into geometrically similar modules: The cross section of one such module, ABCDE, is shown by the dashed lines in Fig. 2. In the periodic fully developed flow regime, the time-mean velocity field repeats itself identically in each of the geometrically similar modules: with reference to Figs. 1 and 2,

$$U(x,y,z) = U(x+L+s,y,z) = U(x+2L+2s,y,z) = \ldots \quad (2\text{-}14)$$

$$V(x,y,z) = V(x+L+s,y,z) = V(x+2L+2s,y,z) = \ldots \quad (2\text{-}15)$$

$$W(x,y,z) = W(x+L+s,y,z) = W(x+2L+2s,y,z) = \ldots \quad (2\text{-}16)$$

Thus in the periodic fully developed regime, the variation of U, V, and W, in a module of periodic length (L+s), can be studied independently, without reference to the flow field in the entrance region or in adjacent modules [13,14].

An analysis of the flow field in the periodic fully developed regime also requires an understanding of the pressure field. In order to have

a net mass flow in the positive x direction, the pressure must decrease as x increases. Thus the time-mean pressure cannot have the same type of periodicity as expressed by Eqs. (2-14) to (2-16) for the velocities, but it exhibits another type of periodicity in the periodic fully developed region.

To understand the behaviour of the time-mean pressure in the periodic fully developed region, its distribution over two cross sections in this region will be considered, one located at x and one at (x+L+s). While the shape of the time-mean pressure distribution at both cross sections will be identical, the pressure distribution at (x+L+s) will be lower than that at x by a uniform amount over the whole cross section. Similarly, the shape of the pressure distribution at (x+2L+2s) will be the same as that at (x+L+s), but it will be lower than the distribution at (x+L+s) by the same uniform amount over the whole cross section as the distribution at (x+L+s) was from that at x. This behaviour of the time-mean pressure field in the periodic fully developed flow regime can be expressed as follows:

$$\{ P(x,y,z) - P(x+L+s,y,z) \} = \{ P(x+L+s,y,z) - P(x+2L+2s,y,z) \}$$
$$= \{P(x+2L+2s,y,z) - P(x+3L+3s,y,z)\} = \ldots \qquad (2\text{-}17)$$

A time-mean pressure gradient, responsible for the overall mass flow rate in the positive x-direction, can be defined from the time-mean pressure drops expressed in Eq. (2-17):

$$\beta = \frac{(P(x,y,z) - P(x+L+s,y,z))}{(L + s)} \qquad (2\text{-}18)$$

β is a constant in the periodic fully developed region, and the

time-mean pressure field can be expressed as:

$$P(x,y,z) = -\beta x + \hat{P}(x,y,z) \tag{2-19}$$

where $-\beta x$ is related to the overall mass flow rate and $\hat{P}(x,y,z)$ is related to the details of the local flow field in each geometrically similar module located in the periodic fully developed region. It is evident from Eqs. (2-17) and (2-19) that $\hat{P}(x,y,z)$ is periodic and its behaviour can be expressed in a similar fashion as the velocity field:

$$\hat{P}(x,y,z) = \hat{P}(x+L+s,y,z) = \hat{P}(x+2L+2s,y,z) = \ldots \tag{2-20}$$

This description of the time-mean pressure field in the periodic fully developed flow region of interrupted-plate rectangular ducts is taken from the works of Patankar et al. [13,14]. Experimentally, the value of β for a particular turbulent periodic fully developed flow in such ducts can be determined from measurements of the time-mean static pressure values at several axial locations, with successive locations separated by a periodic distance of (L+s) in the x direction and located at a fixed (y,z) location on the duct wall. The slope of a straight line fitted through these (x,P) points gives a value of β accurate to within the limits of experimental uncertainty.

Using Eqs. (2-6), (2-7), and (2-19), the time averaged forms of the Navier-Stokes and continuity equations that govern periodic fully developed turbulent flow in interrupted-plate ducts, similar to those illustrated in Figs. 1 and 2, can be cast in the following forms:

x momentum

$$\rho\left(U\frac{\partial U}{\partial x} + V\frac{\partial U}{\partial y} + W\frac{\partial U}{\partial z}\right) = \beta - \frac{\partial \hat{P}}{\partial x} + \frac{\partial}{\partial x}\left(\mu\frac{\partial U}{\partial x} - \rho\overline{uu}\right) + \frac{\partial}{\partial y}\left(\mu\frac{\partial U}{\partial y} - \rho\overline{uv}\right) + \frac{\partial}{\partial z}\left(\mu\frac{\partial U}{\partial z} - \rho\overline{uw}\right) \quad (2\text{-}21)$$

y momentum

$$\rho\left(U\frac{\partial V}{\partial x} + V\frac{\partial V}{\partial y} + W\frac{\partial V}{\partial z}\right) = -\frac{\partial \hat{P}}{\partial y} + \frac{\partial}{\partial x}\left(\mu\frac{\partial V}{\partial x} - \rho\overline{uv}\right) + \frac{\partial}{\partial y}\left(\mu\frac{\partial V}{\partial y} - \rho\overline{vv}\right) + \frac{\partial}{\partial z}\left(\mu\frac{\partial V}{\partial z} - \rho\overline{vw}\right) \quad (2\text{-}22)$$

z momentum

$$\rho\left(U\frac{\partial W}{\partial x} + V\frac{\partial W}{\partial y} + W\frac{\partial W}{\partial z}\right) = -\frac{\partial \hat{P}}{\partial z} + \frac{\partial}{\partial x}\left(\mu\frac{\partial W}{\partial x} - \rho\overline{uw}\right) + \frac{\partial}{\partial y}\left(\mu\frac{\partial W}{\partial y} - \rho\overline{vw}\right) + \frac{\partial}{\partial z}\left(\mu\frac{\partial W}{\partial z} - \rho\overline{ww}\right) \quad (2\text{-}23)$$

continuity

$$\frac{\partial U}{\partial x} + \frac{\partial V}{\partial y} + \frac{\partial W}{\partial z} = 0 \quad (2\text{-}24)$$

On the solid surface boundaries:

$$U = V = W = 0 \quad (2\text{-}25)$$

and on the symmetry surface, shown as DC along the y = 0 line in Fig. 2,

$$\frac{\partial U}{\partial y} = \frac{\partial W}{\partial y} = 0 \; ; \quad V = 0 \quad (2\text{-}26)$$

At the upstream and downstream planes of the module, located at x_i and (x_i+L+s), respectively, and denoted by AE and BC in Fig. 2, the periodicity conditions for U, V, W, and $\hat{P}$ apply:

$$\phi(x_i, y, z) = \phi(x_i + L + s, y, z) \; ; \quad \phi = U, V, W, P \tag{2-27}$$

The boundary conditions, given by Eqs. (2-25) to (2-27), along with the governing equations, Eqs. (2-21) to (2-24), and an appropriate model for the Reynolds stresses appearing in these equations, constitute a complete mathematical model for the type of interrupted-plate duct flows investigated in this thesis. The term β in Eq. (2-21) can be assigned a value that will generate a corresponding mass flow rate, or alternatively, the value of β can be adjusted iteratively to obtain a desired mass flow rate.

2.6 NONDIMENSIONAL PARAMETERS

2.6.1 Turbulent Fully Developed Flow in Rectangular Ducts

The independent dimensionless parameters that characterize turbulent fully developed flow in rectangular ducts, similar to the one illustrated in Fig. 5, can be obtained by a formal nondimensionalization of the governing equations, Eqs. (2-8) to (2-11), and the associated boundary conditions. Such a nondimensionalization yielded two independent dimensionless parameters:

(i) Aspect ratio, $\xi = \frac{b}{2H}$ (2-28)

and

(ii) Reynolds number, $Re_d = \frac{\rho \bar{U}_d D_{hd}}{\mu}$ (2-29)

where b is the width of the rectangular duct and H is its half-height, as shown in Fig. 5. $\bar{U}_d$ is the cross-sectional average value of the

time-mean axial velocity, U :

$$\overline{U}_d = \frac{\dot{m}}{\rho A} \tag{2-30}$$

with $\dot{m}$ being the total mass flow rate in the rectangular duct, and A being the total cross-sectional flow area:

$$A = 2Hb \tag{2-31}$$

The term D_{hd} in Eq.(2-29) is the duct hydraulic diameter, defined as:

$$D_{hd} = \frac{4A}{P_w} \tag{2-32}$$

where P_w is the wetted perimeter for the rectangular duct:

$$P_w = 4H + 2b \tag{2-33}$$

In this thesis, pressure drop results for turbulent fully developed duct flow are presented in terms of the Darcy friction factor [32]:

$$f_d = \frac{(-\frac{\partial P}{\partial x})\, D_{hd}}{\frac{1}{2}\rho\, \overline{U}_d^{\,2}} \tag{2-34}$$

2.6.2. Turbulent Periodic Fully Developed Flow in Interrupted-Plate Rectangular Ducts

Nondimensionalization of Eqs. (2-21) to (2-27) that govern turbulent periodic fully developed flow in interrupted-plate ducts, similar to those illustrated in Figs. 1 and 2, yielded five independent dimensionless parameters:

(i) aspect ratio of a periodic module, ABCDE in Fig. 2,

$$\lambda = \frac{b}{H} \tag{2-35}$$

(ii) plate thickness parameter, $t^* = \frac{t}{H}$ (2-36)

(iii) plate length parameter, $L^* = \frac{L}{H}$ (2-37)

(iv) plate spacing parameter, $s^* = \frac{s}{H}$ (2-38)

and

(v) Reynolds number.

Pressure drop results for turbulent periodic fully developed flows in interrupted-plate geometries are generally presented in the form of module friction factor versus Reynolds number graphs [1,11,14,26,31]. There are two sets of friction factor and Reynolds number definitions that are commonly used in the published literature on periodic fully developed flows [1,14]. In this thesis, results corresponding to both these sets of definitions are presented. One set of definitions is that used by Kays and London [1]:

$$Re_k = \frac{\rho \bar{U}_k D_{hk}}{\mu} \tag{2-39}$$

and

$$f_k = \frac{\beta D_{hk}}{\frac{1}{2} \rho \bar{U}_k^2} \tag{2-40}$$

In these equations, $\bar{U}_k$ is the cross-sectional average value of the time-mean axial velocity component, U, based on the minimum flow area in a

periodic module and D_{hk} is a module hydraulic diameter. With reference to Figs. 1 and 2, these terms are defined as follows:

$$\bar{U}_k = \frac{\dot{m}}{2 \rho A_c} \tag{2-41}$$

and

$$D_{hk} = \frac{4A_c(L + s)}{A_w} \tag{2-42}$$

The minimum flow area, A_c, and the total wall area, A_w, of the periodic module are given by:

$$A_c = b(H - t) \tag{2-43}$$

and

$$A_w = (2L + s)b + 2(L + s)(H - t) + 2ts \tag{2-44}$$

The other set of Reynolds number and module friction factor definitions is similar to that used by Patankar and Prakash [14]:

$$Re_m = \frac{\rho \bar{U}_m D_h}{\mu} \tag{2-45}$$

and

$$f_m = \frac{\beta D_h}{\frac{1}{2} \rho \bar{U}_m^2} \tag{2-46}$$

In Eqs. (2-45) and (2-46), $\bar{U}_m$ is based on the nominal cross-sectional flow area of a periodic module and D_h is a nominal hydraulic diameter:

$$\bar{U}_m = \frac{\dot{m}}{2\rho bH} \tag{2-47}$$

and

$$D_h = \frac{4bH}{2H + 2b} \tag{2-48}$$

The time-averaged forms of the governing equations for turbulent periodic fully developed flow, Eqs. (2-21) to (2-24), have been presented in the context of statistically steady turbulent flows. Investigations concerned mainly with the laminar and transitional flow regimes have shown, however, that vortex shedding may occur for certain combinations of Reynolds number and plate-thickness parameter [27,29-31,108]. If this vortex shedding phenomena is considered, a nondimensional analysis of turbulent flow in interrupted-plate rectangular ducts would yield an additional dimensionless parameter. This parameter, the Strouhal number, could be defined as [108]:

$$St = \frac{2t\omega}{\bar{U}_m} \tag{2-49}$$

where ω is the frequency of vortex shedding.

2.7 CLOSING REMARKS

In this chapter, the governing equations, the appropriate boundary conditions, and the independent dimensionless parameters that characterize the flows investigated in this thesis have been presented. Attention has been focussed on the three-dimensional mathematical description of these flows. To model the Reynolds stresses, thereby achieving

closure of the time-averaged governing equations, a suitable version of the k-ϵ model of turbulence is used. Details of the various k-ϵ models are discussed in Chapter III.

CHAPTER III

TWO-EQUATION (k-ϵ) MODELS OF TURBULENCE

Turbulent flows of the types investigated in this thesis can be modelled mathematically using the time-averaged form of the Navier-Stokes and continuity equations, given by Eqs. (2-6) and (2-7). To achieve closure of this set of equations, the Reynolds stress terms, $-\rho\overline{u_i u_j}$ appearing in the momentum equations, Eq. (2-6), need to be approximated or modelled. In this research, an eddy-viscosity based two-equation k-ϵ model of turbulence has been used to model Reynolds stresses. The reasons for the selection of this particular form of turbulence model and a discussion of other turbulence models were presented in the literature survey of Section 1.2.2.

The purpose of this chapter is to present and discuss the modelled forms of the flow governing equations presented in Chapter II, and to then present these modelled equations in the context of the flows considered in the numerical investigation of this thesis.

3.1 MODELLED FORMS OF THE FLOW EQUATIONS

The Reynolds stresses in Eq. (2-6) are modelled using the Boussinesq eddy-viscosity concept in which it is assumed, in analogy to the relations for viscous stresses in laminar flow, that the Reynolds stress tensor is proportional to the mean-flow rate of strain tensor. The expression used to model the Reynolds stresses is given as [75]:

$$-\rho\overline{u_i u_j} = \mu_t \left(\frac{\partial U_i}{\partial x_j} + \frac{\partial U_j}{\partial x_i}\right) - \frac{2}{3}k\delta_{ij} \qquad (3\text{-}1)$$

where μ_T is a turbulent, or eddy, viscosity and δ_{ij} is the Kronecker delta which has a value of one when i = j and a value of zero otherwise. k, the time-mean kinetic energy of the turbulence velocity fluctuations, is defined as [37-40,75]:

$$k = \frac{1}{2}\overline{u_i u_i} \tag{3-2}$$

The eddy viscosity, μ_t, is not a fluid property, unlike the molecular viscosity, μ, rather it depends on the state of the turbulence and may vary significantly throughout the flow field. For this reason, a turbulence model is required to calculate the turbulent viscosity field. In this research, a low-Reynolds-number version of the k-ϵ model of turbulence was used, and it is discussed in Section 3.4. The last term in Eq. (3-1) is included to ensure that the sum of the normal Reynolds stresses will be equal to twice the turbulence kinetic energy. Without this term, the sum of the normal stresses, calculated from Eq. (3-1), would be zero, taking into account the mean-flow continuity equation.

Using Eq. (3-1) and the continuity equation, Eq. (2-7), the general form of the time-mean governing momentum equations, Eq. (2-6), can be written as:

$$\rho\left(U_j\frac{\partial U_i}{\partial x_j}\right) = -\frac{\partial P}{\partial x_i} + \frac{\partial}{\partial x_j}\left\{\Gamma_u\left(\frac{\partial U_i}{\partial x_j} + \frac{\partial U_j}{\partial x_i}\right)\right\} \tag{3-3}$$

where the diffusion coefficient, Γ_u, is given as:

$$\Gamma_u = \mu + \mu_t \tag{3-4}$$

The last term of Eq. (3-1) has been absorbed in the pressure gradient

term of Eq. (3-3). Like pressure, the (2/3 k) term in Eq. (3-1) is a scalar quantity and can be thought of as being a pressure component. It is common practice, therefore, to model this term in combination with the static pressure term, P, appearing in Eq. (2-6). Thus, the pressure term in Eq. (3-3) actually represents the term (P + 2/3 k) [75]. To achieve closure of Eq. (3-3), the distribution of the isotropic eddy-viscosity field needs only to be determined.

Based on dimensional considerations, it is postulated that μ_t is proportional to a velocity scale, u_t, and a length scale, l_t, both of which are characteristic of the large-scale turbulent motion [75]. Thus:

$$\mu_t \propto \rho u_t l_t \tag{3-5}$$

The relationship in Eq. (3-5) is obtained by assuming an analogy with the molecular motion which leads to a dynamic viscosity proportional to an average velocity and the mean free path of the fluid molecules [75]. The eddy viscosity should depend on the local state of the turbulence and the mean flow [75,111]. However, the relationship given in Eq. (3-5) assumes that μ_t is a scalar quantity related to the local flow in general terms through velocity and length scales that are characteristic of the large-scale turbulence. This assumption of isotropy has been pointed out as one of the deficiencies of the eddy-viscosity concept as put forth in Eq. (3-5). A more detailed discussion of these ideas is presented in [75,111]. The success of using the relationship given in Eq. (3-5) depends critically on the accuracy of approximations for u_t and l_t.

Using a two-equation k-ϵ model of turbulence, the distributions of both u_t and l_t, and their relationship to μ_t, can be approximated well enough to give acceptable results for many types of one- and two-dimensional turbulent flow calculations [75,77]. In this model, the square root of the mean turbulence kinetic energy is assumed to be representative of the characteristic turbulence velocity scale, u_t, and the length scale is represented indirectly by the turbulence energy dissipation rate, ϵ [75]. These relationships can be expressed as:

$$u_t \propto k^{1/2} \tag{3-6}$$

$$\epsilon \propto \frac{k^{3/2}}{l_t} \tag{3-7}$$

Dissipation affects the length scale indirectly by destroying the small-scale turbulence eddies thus effectively increasing the overall eddy size [75]. While dissipation is a viscous process that occurs at the smallest scales of turbulence, the rate of dissipation, ϵ, is also determined by the large-scale motion, as it is this motion that determines the rate at which energy from the mean flow is fed into the turbulent motion. It is from this energy only that the final small-scale motion can receive the energy that it dissipates [75]. When Eqs. (3-6) and (3-7) are used in Eq. (3-5), the following expression for the eddy viscosity is obtained:

$$\mu_t = f_{c\mu} C_\mu \rho \frac{k^2}{\epsilon} \tag{3-8}$$

The value of the proportionality constant, C_μ, is given in Table 1, and $f_{c\mu}$ can be called a viscous damping function which, for purposes of the discussion in the following section, takes on a value of unity. More

will be said about these quantities in following sections where the modelled form of the k and ϵ equations are discussed.

3.2 DIFFERENTIAL TRANSPORT EQUATIONS FOR k AND ϵ

In this section, the differential transport equations for k and ϵ are presented and discussed. Appropriate modelled forms of these equations are discussed in Section 3.3.

The governing differential equation for k can be obtained by: (i) multiplying Eq. (2-6) by U_i to obtain the equation for the kinetic energy of the mean flow; (ii) multiplying the Navier-Stokes equations, Eq. (2-1), by $\tilde{u}_i$ and time averaging all terms; and (iii) subtracting the resulting equation in (i) from the equation obtained in (ii). Substituting Eq. (3-2) into the resulting equation of (iii) yields, for a statistically steady flow, [37,38]:

$$\underset{(I)}{\rho U_j \frac{\partial k}{\partial x_j}} = \underset{(II)}{-\frac{\partial}{\partial x_j}\left(\overline{u_j\left(p + \tfrac{1}{2}\rho u_i u_i\right)}\right)} + \underset{(III)}{\mu \frac{\partial}{\partial x_j}\left(\overline{u_i\left(\frac{\partial u_i}{\partial x_j} + \frac{\partial u_j}{\partial x_i}\right)}\right)}$$

$$\underset{(IV)}{-\rho\overline{u_i u_j}\frac{\partial U_i}{\partial x_j}} \underset{(V)}{- \mu\overline{\left(\frac{\partial u_i}{\partial x_j} + \frac{\partial u_j}{\partial x_i}\right)\frac{\partial u_i}{\partial x_j}}} \qquad (3\text{-}9)$$

In Eq. (3-9), (I) represents the change in the mean kinetic energy of turbulence, per unit of volume and of time, due to the convective transport by the mean motion. This is equal to: (II) the work done by the total pressure of the turbulence per unit volume and time, plus (III) the work done by the viscous shear stresses of the turbulent motion per unit volume and time, plus the deformation-work terms, (IV)

and (V), which are also per unit volume and time. Term (IV) represents the work of deformation of the mean motion by the turbulence stresses. This term also appears, with the opposite sign, in the equation for the kinetic energy of the mean motion. In Eq. (3-9), when $i \neq j$, term (IV) is often positive indicating that the work of deformation of the mean motion by the turbulence shear stresses usually serves to increase the mean turbulence energy at the expense of the mean flow energy. This term is, therefore, commonly referred to as the turbulence production term, P_t [37,38]:

$$P_t = -\rho\overline{u_i u_j}\frac{\partial U_j}{\partial x_j} \tag{3-10}$$

Term (V) in Eq. (3-9) represents the work of deformation on the turbulent strain rate performed by the viscous stresses of the turbulent motion and is always negative, thus indicating a loss of mean turbulent kinetic energy. This term represents the viscous dissipation by the turbulent motion, ϵ, which is defined as [37,38]:

$$\epsilon = \frac{\mu}{\rho}\overline{\left(\frac{\partial u_i}{\partial x_j} + \frac{\partial u_j}{\partial x_i}\right)\frac{\partial u_i}{\partial x_j}} \tag{3-11}$$

The transport equation for ϵ can also be obtained through appropriate manipulations of the Navier-Stokes equations. By subtracting Eq. (2-6) from Eq. (2-1), then differentiating the result with respect to x_q, multiplying by $\partial u_i/\partial x_q$, and time averaging this resulting equation, the following equation can be obtained:

$$\rho U_j \frac{\partial}{\partial x_j}\left\{\frac{1}{2}\overline{\left(\frac{\partial u_i}{\partial x_q}\right)^2}\right\} = \underbrace{-\overline{\frac{\partial u_i}{\partial x_q}\frac{\partial^2 p}{\partial x_q \partial x_i}}}_{(I)} \underbrace{-\rho\overline{\frac{\partial u_i}{\partial x_q}\frac{\partial u_j}{\partial x_q}\frac{\partial u_i}{\partial x_j}}}_{(II)} \underbrace{-\rho\overline{u_j\frac{\partial}{\partial x_j}\left\{\frac{1}{2}\left(\frac{\partial u_i}{\partial x_q}\right)^2\right\}}}_{(III)} \underbrace{-\rho\frac{\partial U_i}{\partial x_j}\overline{\frac{\partial u_i}{\partial x_q}\frac{\partial u_j}{\partial x_q}}}_{(IV)} \underbrace{-\rho\frac{\partial U_j}{\partial x_q}\overline{\frac{\partial u_i}{\partial x_q}\frac{\partial u_i}{\partial x_j}}}_{(V)} \underbrace{+\mu\overline{\frac{\partial u_i}{\partial x_q}\left(\frac{\partial^2}{\partial x_j^2}\frac{\partial u_i}{\partial x_q}\right)}}_{(VI)} \underbrace{-\rho\frac{\partial^2 U_i}{\partial x_q \partial x_j}\overline{u_j\frac{\partial u_i}{\partial x_q}}}_{(VII)} \qquad (3\text{-}12)$$

$$(VIII)$$

If it is assumed that local isotropy prevails, then Eq. (3-11) reduces to:

$$\epsilon = \frac{\mu}{\rho}\overline{\left(\frac{\partial u_i}{\partial x_j}\right)^2} \qquad (3\text{-}13)$$

It can be seen that if Eq. (3-13) were substituted into Eq. (3-12) then ϵ would be the dependent variable of (3-12). Other than the convection term (I) and the dissipation term (VII), the exact meanings of the terms in Eq. (3-12) are unclear and many complex correlations appear for which fairly arbitrary model assumptions must be made to make the equation tractable.

It should be noted here that an assumption of local isotropy is necessary in order to obtain a transport equation for ϵ from Eq. (3-12), and any future reference to ϵ in this thesis will imply the form defined by Eq. (3-13) unless otherwise stated. Details of the modelled forms of the Eqs. (3-9) and (3-12) are given in the next section.

3.3 MODELLED FORMS OF THE k AND ϵ EQUATIONS

As discussed in Section 3.2, differential transport equations for k and ϵ, Eqs. (3-9) and (3-12), can be derived from the Navier-Stokes equations. Several unknown correlations appear in both these equations, so model assumptions must be introduced in order to obtain a closed set of equations. From the discussion in Chapter I, it is evident that there are many versions of the k-ϵ turbulence model that can be used in the numerical calculation of wall bounded shear flows. All these versions are variations of a standard k-ϵ model [40,76,90]. In this section, the modelled forms of the standard k and ϵ equations will be presented in general forms that can be easily specialized to the forms appropriate for the various k-ϵ models.

The turbulence kinetic energy equation, Eq. (3-9), can be modelled as [40]:

$$\rho U_j \frac{\partial k}{\partial x_j} = \frac{\partial}{\partial x_j}\left(\Gamma_k \frac{\partial k}{\partial x_j}\right) + P_k - D_k - E_k \tag{3-14}$$

where

$$\Gamma_k = \mu + \frac{\mu_t}{\sigma_t} \tag{3-15}$$

$$P_k = \mu_t \left(\frac{\partial U_i}{\partial x_j} + \frac{\partial U_j}{\partial x_i}\right)\frac{\partial U_i}{\partial x_j} \tag{3-16}$$

and

$$D_k = \rho \epsilon \tag{3-17}$$

The accompanying modelled form of the ϵ equation, obtained from

Eq. (3-12), can be given as [40]:

$$\rho U_j \frac{\partial \epsilon}{\partial x_j} = \frac{\partial}{\partial x_j}(\Gamma_\epsilon \frac{\partial \epsilon}{\partial x_j}) + P_\epsilon - D_\epsilon + E_\epsilon \tag{3-18}$$

where

$$\Gamma_\epsilon = \mu + \frac{\mu_t}{\sigma_\epsilon} \tag{3-19}$$

$$P_\epsilon = f_{c1\epsilon}\, C_{1\epsilon}\, \frac{\epsilon}{k} P_k \tag{3-20}$$

and

$$D_\epsilon = \rho\, f_{c2\epsilon}\, C_{2\epsilon}\, \frac{\epsilon^2}{k} \tag{3-21}$$

It is the f and E terms in Eqs. (3-14) to (3-21) that can be changed to produce different versions of the k-ϵ model. These terms take on the following values in the <u>standard</u> form of the k-ϵ model [80,89,90]:

$$f_{c\mu} = f_{c1\epsilon} = f_{c2\epsilon} = 1.0 \tag{3-22}$$

$$E_k = E_\epsilon = 0 \tag{3-23}$$

The discussion in the remainder of this section will focus on the description of the <u>standard</u> form of the k and ϵ model equations. Further discussion concerning the E and f terms in Eqs. (3-14) to (3-21) will be presented in the next section.

The Γ, P, and D, terms in Eqs. (3-14) to (3-21) represent the diffusion coefficient, the production term, and the rate of dissipation term, respectively, of either k or ϵ as denoted by their subscript. In Eqs. (3-15) and (3-19), the σ term is an empirical turbulent Prandtl or

Schmidt number that relates the eddy viscosity, μ_t, to the respective k and ϵ equation diffusion coefficients, Γ_k and Γ_ϵ. The constant C and σ terms will be discussed in greater detail after a brief explanation of how the standard form of the model equations were obtained from Eqs. (3-9) and (3 12).

The standard modelled forms of the k and ϵ equations have been derived for high-Reynolds-number flows [39,40,75,76,90]. In such flows, the local Reynolds number of turbulence, Re_t, is generally high throughout most of the flow field. A high value of Re_t indicates that, compared to the Reynolds stresses and the effects of the turbulence motion on the structure of the mean flow, the viscous stresses and the direct viscous effects on the overall flow structure are negligible [111]. The turbulence Reynolds number, Re_t, is defined as [80,89,90]:

$$Re_t = \frac{\rho k^2}{\epsilon \mu} \tag{3-24}$$

Because of the aforementioned characteristics of high-Reynolds-number flows, the work done by the viscous shear stresses of the turbulent motion, term (III) in Eq. (3-9) for k, is negligible and is therefore not modelled in Eq. (3-14). The major assumption used to obtain Eq. (3-14) is that the diffusion flux of k, or the work done by the total dynamic pressure of the turbulence, term (II) in Eq. (3-9), can be assumed proportional to the gradient of k such that:

$$\overline{u_j \left(p + \tfrac{1}{2} \rho u_i u_i\right)} = \Gamma_k \frac{\partial k}{\partial x_j} \tag{3-25}$$

Bradshaw [40] points out that since the $\overline{u_j p}$ term cannot be measured

directly, the relationship expressed in Eq. (3-25) cannot be tested independently and may be questionable. Despite this, the relationship expressed in Eq. (3-25) performs adequately, as witnessed by the relative success of the k-ϵ model in providing acceptable predictions for many types of flows [75-77].

The production term P_k, Eq. (3-16), is the modelled form of P_t, Eq. (3-10), obtained by using Eq. (3-1). The dissipation term D_k, Eq. (3-17), is simply $(\rho\epsilon)$ in which, for modelling purposes, ϵ is defined by Eq. (3-13).

To make the equation for the rate of dissipation of the mean turbulence energy, ϵ, tractable, many "drastic" model assumptions need to be employed [75]. The differential conservation equation given by Eq. (3-12) can be regarded as an equation for ϵ if local isotropy prevails, as it generally does for high-Reynolds-number flows [38,111]. The reason for this is explained in the following paragraphs.

It can be shown, by dimensional and order of magnitude considerations, that as a turbulence Reynolds number, Re_t for example, increases so does the difference between the small-scale and large-scale turbulent motion in terms of characteristic time, velocity, and length scales [38]. The strain rate of the mean flow tends to cause the turbulent motion to be oriented in the same direction as the mean flow. This is particularly true in the case of the large-scale turbulent eddies which have time, velocity, and length scales similar to those of the mean flow: The large-scale turbulent eddies exhibit a steady anisotropy [38]. When the local turbulence Reynolds number of the flow is large,

the small-scale eddies are characterized by small time scales and large fluctuating, or turbulent, strain rates compared to the motion of the large-scale turbulence and the mean flow. Because of these relatively short time scales and the random fluctuating nature of this small-scale turbulence motion, the time that small-scale turbulent eddies remain aligned with the strain rate imposed by the larger-scale motion is relatively short: The small-scale motion tends to quickly return to an isotropic state. With respect to the rest of the flow, the small-scale turbulent motion is in a statistically isotropic state commonly referred to as local isotropy [38,111]. The point where the motion can start to be considered as "small scale" and in a state of local isotropy depends on the flow field itself, however, it does include the smallest turbulent scales where most of the dissipation of the mean turbulence kinetic energy occurs, the so-called Kolmogorov microscales [38].

The assumption of local isotropy of the small-scale turbulence motion is only valid if the local value of Re_t is large enough such that there exists a noticeable difference in the time, length, and velocity scales of the large- and small-scale turbulence motion. Tennekes and Lumley [38] have estimated that an Re_t in the order of at least 100 is required. Local isotropy can be assumed to prevail for high-Reynolds-number flows, since Re_t in such flows is generally large throughout most of the flow field.

The expression for ϵ given by Eq. (3-11) can be recast in the following form:

$$\epsilon = \frac{\mu}{\rho} \overline{2s_{ij}s_{ij}} \qquad (3\text{-}26)$$

where s_{ij} is the strain rate of the fluctuating turbulence velocities and is given as:

$$s_{ij} = \frac{1}{2}\left(\frac{\partial u_i}{\partial x_j} + \frac{\partial u_j}{\partial x_i}\right) \tag{3-27}$$

In regions of a flow where local isotropy prevails, it can be shown that the mean of the square of the fluctuating strain rate can be approximated by the mean of the square of the vorticity fluctuations [38] such that:

$$\overline{2s_{ij}s_{ij}} \approx \overline{\left(\frac{\partial u_i}{\partial x_j}\frac{\partial u_i}{\partial x_j}\right)} \tag{3-28}$$

Substitution of Eq. (3-28) into (3-26) yields the expression given by Eq. (3-13) for ϵ that can be used when the assumption of local isotropy of the turbulence motion is valid.

Since the amount of dissipation that occurs at larger scales, where statistical isotropy does not prevail, is insignificant compared to that occurring at the smaller scales where the turbulence is statistically isotropic, it is valid to assume that ϵ can be represented by Eq. (3-13), when deriving the model form of the ϵ equation for the case of high-Reynolds-number flows. To obtain Eq. (3-18) from Eq. (3-12), the recommendations given by Bradshaw [40] are used: terms II, III, and IV in Eq. (3-12) have been combined and modelled as a gradient diffusion term, appearing on the immediate left of the equal sign in Eq. (3-18); terms V and VI have been combined to represent production of ϵ, P_ϵ; term VIII has been neglected; and the convection and dissipation terms are

obtained from terms I and VII respectively, of Eq. (3-12).

The k and ϵ equations, Eqs. (3-14) and (3-18), and the expressions for the terms appearing in these two equations, Eqs. (3-15) to (3-17) and (3-19) to (3-21), along with the modelled forms of the momentum, continuity, and eddy viscosity equations given by Eqs. (3-3), (2-7), and (3-8), respectively, form a set of equations that can be solved numerically when the values of the constant terms are specified and the appropriate boundary conditions for U_i, k, and ϵ are given.

In the expressions given by Eqs. (3-8), (3-15), (3-19) to (3-21), the following empirical constants appear: C_μ in Eq. (3-8); σ_k and σ_ϵ in Eqs. (3-15) and (3-19); and $C_{1\epsilon}$ and $C_{2\epsilon}$ in Eqs. (3-20) and (3-21), respectively. Values of these constants have been determined for the standard form of the k-ϵ model [75,89,90,112]. The values of σ_k and σ_ϵ are assumed to be close to one and final values have been obtained by computer optimization [75,89,90,112]. Using Eqs. (3-14) and (3-18), the value of C_μ is determined from measurements of $\rho\overline{uv}$ and k in equilibrium shear layers, and the value of, $C_{2\epsilon}$ is obtained from the measured rate of decay of k behind a grid [75,89]. With the values of $C_{2\epsilon}$, σ_ϵ, C_μ, and the resulting form of Eq. (3-18) for the near-wall flow region where local equilibrium exists, an expression for the value of $C_{1\epsilon}$ is obtained. It should be noted that rate of change of ϵ is particularly sensitive to the difference in the values of $C_{1\epsilon}$ and $C_{2\epsilon}$ [81]. Due to slightly different approaches by different modelers, there are often slightly different values of these constants used, although, as pointed out by Hanjalic [81], the experimental evidence indicates that $C_{2\epsilon}$ should always have a value less than 2 and equal to or greater than 1.8.

In this thesis, the particular values used for these constants, for all versions of the k-ϵ model, are those recommended by Launder and Spalding [112] and are given in Table 1.

In the case of wall bounded shear flows, at the solid wall boundary the no-slip condition prevails, implying that all mean and fluctuating velocities, hence k, have values of zero. However, ϵ has a finite value that requires calculation. Nevertheless, if possible, it is desirable to avoid use of the standard k-ϵ model in this near-wall region. In high-Reynolds-number flows, the effect of dynamic viscosity on the flow field is negligible except in a small region of the flow adjacent to wall boundaries: the viscous sublayer and so-called buffer layer. In this region, the direct effects of viscosity become progressively larger, compared to the turbulence, as the wall is approached. In the viscous sublayer, the viscous effects are so dominant that the turbulence is unable to sustain itself [38]. The assumption of high turbulence Reynolds number and the corresponding local isotropy used in the derivation of the k and ϵ model equations is not valid in this region, thus making the standard form of the model equations inappropriate here. In addition, if the equations are solved all the way to the wall, the very steep gradients of turbulence properties that prevail in the viscous sublayer, in a direction normal to the wall boundary, require that a large number of grid points be placed in this region, which in turn increase computational costs. For many high-Reynolds-number wall bounded shear flows, integration of the model equations through the viscous sublayer and the buffer layer can be avoided by using existing empirical correlations, often referred to as universal wall functions [90], that relate surface boundary conditions to points in the fluid outside the

viscous sublayer and the buffer layer.

The near-wall region of wall bounded turbulent shear flows consists of a viscous sublayer where the effects of viscous stresses dominate; a buffer layer where both the viscous and turbulent stresses are important; and an inertial sublayer where the effects of viscosity can be neglected and the mean flow velocity follows a logarithmic profile. The velocity in this so-called logarithmic region of wall bounded shear flows can be expressed as [75]:

$$\frac{U_w}{U_\tau} = \frac{1}{\kappa} \ln(y^+ B) \tag{3-29}$$

where U_w is the resultant velocity parallel to the wall. The von Karman constant, κ, and the roughness parameter, B, are empirically determined constants. Their values and resultant friction velocity, U_τ, and the dimensionless normal distance from the wall, y^+, are given as [75]:

$$U_\tau = \left(\frac{\tau_w}{\rho}\right)^{1/2} \tag{3-30}$$

$$y^+ = \frac{\rho U_\tau y}{\mu} \tag{3-31}$$

$$\kappa = 0.41 \tag{3-32}$$

$$B = 9.0 \quad \text{(for smooth walls)} \tag{3-33}$$

Equation (3-29) is derived for the y^+ region where the large-scale turbulence motion is proportional to the normal distance, y, from the wall, the mean-flow velocity component normal to the wall is considered to be negligible compared to that parallel to it, and the effective

shear stress is essentially constant and equal to the wall shear stress, τ_w. Therefore, to be sufficiently accurate, the equation should be used at locations where $30 \lesssim y^+ \lesssim 100$ [75]. In this region, the U_w velocity profile is given by Eq. (3-29) for flows with a strongly adverse pressure gradient to flows involving a strongly favourable pressure gradient, but it is not applicable to separated flows [36]. For the aforementioned y^+ range, the flow can also be considered to be in local equilibrium, in that the net convective and diffusive transport of turbulence quantities, such as k, are negligible. This implies from Eq. (3-14) and (3-17) that:

$$P_k = \rho \epsilon \tag{3-34}$$

These assumptions, along with Eqs. (3-29) and (3-8), lead to the following expressions for k and ϵ at points located in the above-mentioned y^+ region [75]:

$$k = \frac{U_\tau^2}{c_\mu^{1/2}} \tag{3-35}$$

$$\epsilon = \frac{U_\tau^3}{\kappa\, y} \tag{3-36}$$

The y^+ range for which these boundary equations are applicable corresponds to a turbulence Reynolds number range of $145 \lesssim Re_t \lesssim 455$. The normal distance, y, from a wall to the corresponding boundary grid point where Eqs. (3-29), (3-35), and (3-36) are applied, should be a small fraction of the total extent of the flow domain in the y-coordinate direction.

3.4 LOW-REYNOLDS-NUMBER VERSIONS OF THE k-ϵ MODEL

In the high-Reynolds-number, or standard, k-ϵ model, universal wall functions are used to relate wall surface boundary conditions to grid points located in the $30 \leq y^+ \leq 100$ region of the flow, thus removing the need to solve the modelled equations through the viscous sublayer and the buffer layer, located adjacent to a wall surface. This practice is acceptable if the Reynolds number of the flow is sufficiently high so as to make the viscous effects on the overall flow field unimportant, and if, of course, it has been established that the universal wall functions provide an adequate means of linking conditions at grid points outside the viscous flow region to conditions at the wall surface. The near-wall velocity profiles of unsteady or separated turbulent flows are poorly predicted by Eq. (3-29) [36], and thus the use of universal wall functions is inappropriate for such flows. In high-Reynolds-number flows, the flow region $y^+ < 30$ typically occupies 2 percent [36] or less of the flow field. In low-Reynolds-number flows, however, this same y^+ region may occupy as much as 30 to 40 percent, or even more, of the flow field, and thus neglecting its effect, hence the effect of viscosity, on overall flow field calculations may lead to significant errors in the final flow solution.

As discussed in Section 1.2.2, many of the alternate versions of the k-ϵ turbulence models attempt to deal with the above-mentioned problems by proposing and solving appropriate model equations through the buffer layer and the viscous sublayer regions of wall bounded shear flows, thereby removing the need for using wall functions. This requires some extensions of the standard k-ϵ model equations. In the

more advanced forms of the k-ϵ model, these extensions incorporate either a wall damping effect or the direct effect of dynamic viscosity, or both, on the empirical constants and on certain functions in the turbulence model equations [90].

The direct effect of dynamic viscosity has already been incorporated into the diffusion coefficients, Γ's, appearing in Eqs. (3-3), (3-14), and (3-18) and defined by Eqs. (3-4), (3-15), and (3-19). It should be noted that the effect of dynamic viscosity, μ, is often not included in the Γ terms of the high-Reynolds-number model equations as it is negligible compared to μ_t. Because it is negligible for high Reynolds numbers, however, the inclusion of μ in the Γ terms does not effectively change the performance of the model equations . Therefore, in this thesis, μ is kept in the Γ's of the standard form of the k-ϵ model equations so as to keep them as general as possible. In the immediate vicinity of a wall, the direct viscous effects begin to dominate over the turbulent stresses, hence the effect of the eddy viscosity in this region becomes insignificant, compared to those of the viscous stresses, as the wall is approached. In addition, certain terms in the k and ϵ equations must also be made sensitive to the effects of dynamic viscosity in such viscous dominated flow regions. It is the differences in the modelling of μ_t, and the k and ϵ equations, in these regions that give rise to the many versions of the so-called low-Reynolds-number or near-wall k-ϵ model discussed in Chapter I.

In low-Reynolds-number k-ϵ models, the so-called wall damping effect imposed on the turbulence in the viscous dominated flow regions is accounted for by the f and E terms appearing in Eqs. (3-8) and (3-14) to

(3-21). The expressions for these terms vary from model to model, and most of them have been based largely on numerical experiments and comparisons between calculated and experimental global parameters: There is still a lack of reliable turbulence data for flow at low turbulence Reynolds numbers such as those found in the immediate vicinity of a wall [90].

As discussed in Chapter I, Patel et al. [90] did a systematic evaluation of eight low-Reynolds-number two-equation turbulence models and found that k-ϵ model versions proposed by Launder and Sharma [91], Chien [92], and Lam and Bremhorst [93], gave acceptable performances. These three models and the original form of the low-Reynolds-number k-ϵ model presented by Jones and Launder [80,89] are examined here.

The Launder and Sharma [91] model is a revised version of the original Jones and Launder [80,89] model. A reoptimization of model coefficients was done in [91] which led to the coefficient values given in Table 1. These differ slightly from those used in the original model version of Jones and Launder [80,89]. The values in Table 1 are widely used, and these are the values used in the Jones and Launder k-ϵ model [80,89] used in this thesis. The only difference, then, in the Jones and Launder [80,89] and the Launder and Sharma [91] k-ϵ models used here is the form of the viscous damping function $f_{c\mu}$. The performance of both these models, in the context of fully developed and spatially fully developed turbulent flows, is examined in this thesis.

In the remainder of this section, the four low-Reynolds-number k-ϵ models, mentioned above, are presented so as to set the basis for the

discussion in the following chapters. A more detailed discussion of these models, as they relate to the specific numerical investigation undertaken in this work, is presented in Chapter V.

The functional forms of the terms $f_{c\mu}$, $f_{c1\epsilon}$, $f_{c2\epsilon}$, E_k, and E_ϵ, appearing in Eqs. (3-8) and (3-14) to (3-21), for the various low-Reynolds-number k-ϵ models considered are given in Table 2. Since the expression used for E_k depends on the wall boundary condition specified for ϵ, this ϵ boundary condition is also given in the table. As indicated in Table 2, the Jones and Launder; Launder and Sharma; Chien; and Lam and Bremhorst k-ϵ model versions will be denoted as JL, LS, CH, and LB, respectively.

The purpose of the $f_{c\mu}$ function in the eddy-viscosity relation, Eq. (3-8), is to model the direct effect of the dynamic viscosity on the turbulent stresses. It is thus correlated as a function of a turbulence Reynolds number, Re_t, Re_y, or the nondimensional wall distance y^+. The terms Re_t and y^+ are defined by Eqs. (3-24) and (3-31), respectively. The expression for Re_y is given as [90]:

$$Re_y = \frac{\rho\, k^{1/2} y}{\mu} \tag{3-37}$$

From Table 2, it is seen that $f_{c\mu}$ is correlated as an exponential function of Re_t for the JL and LS models; y^+ for the CH model; and Re_y for the LB model. Launder points out that the near-wall turbulent shear stress is also reduced by the fluctuating pressure field [112], however, this process is to a first approximation independent of dynamic viscosity and cannot be correlated in the same fashion as the viscous

effects. Nevertheless, the $f_{c\mu}$ function is used to approximate the combined effects of dynamic viscosity and the pressure fluctuations [90]. The behaviour of this function should be such that in regions where the effect of dynamic viscosity is noticeable, the value of $f_{c\mu}$ becomes smaller, tending to zero as a wall boundary is reached. On the other hand, in the fully turbulent flow region, where dynamic viscosity can be neglected, $f_{c\mu}$ should become unity. Patel et al. [90] indicate that, based on experimental data, $f_{c\mu}$ can be expected to increase in an almost linear fashion, from close to zero at a wall to about 0.8 at $y^+ \simeq 50$, after which it is expected to asymptote to a maximum value near unity in the fully turbulent region. As it turns out, none of the models completely simulates this "experimental" $f_{c\mu}$ behaviour: The JL and LS models give $f_{c\mu}$ values that rise too rapidly in the viscous region, although they predict the fully turbulent behaviour adequately, and the CH and LB model $f_{c\mu}$'s rise too slowly outside the viscous region thus underpredicting the values for $f_{c\mu}$ in the fully turbulent region. The CH model also underpredicts $f_{c\mu}$ in the viscous region but the LB model approximates the expected $f_{c\mu}$ behaviour well in this region where $y^+ < 40$ [90].

Low-Reynolds-number effects are incorporated into the rate of dissipation term in the ϵ equation, D_ϵ, by means of the $f_{c2\epsilon}$ term. This term is chosen so that the resulting calculated model values will agree with experimental measurements for the case of the decay of grid turbulence in high-Reynolds-number and low-Reynolds-number flows [80,89,92]. All the formulas for $f_{c2\epsilon}$, presented in Table 2, reach their asymptotic values of unity at Re_t values less than 15, indicating that the effect of this function can be considered as being limited to the viscous sublayer

region [90]. In all the low-Reynolds-number models considered here, $f_{C2\epsilon}$ is modelled as an exponential function, asymptoting to one as Re_t becomes large.

In the LB k-ϵ model, the $f_{C1\epsilon}$ term appearing in the ϵ equation production term, P_ϵ, takes on a functional form that depends on the value of $f_{C\mu}$ in the manner expressed in Table 2. This is done in order to increase the predicted dissipation rate in the near-wall region, thus causing the predicted turbulence level to be reduced in this region. The result should be a predicted k distribution in the near-wall region that gives better agreement with experiment. In the JL, LS, and CH k-ϵ models, $f_{C1\epsilon}$ is left as unity but additional terms are added to the k and ϵ equations to give the proper distribution of k close to a wall. The LB version of the k-ϵ model sets the boundary value of ϵ to the value that is obtained when Eq. (3-14), for k, is applied at the wall. In this case, the second derivative of k with respect to the normal distance y at the wall is calculated by performing a Taylor series expansion of k near the wall [93]. By using this treatment for specifying ϵ at the wall boundary, and by incorporating a functional form for $f_{1C\epsilon}$ that serves to correct the near-wall k distribution, no additional terms are required in the LB model equations, and thus the values of E_k and E_ϵ are zero.

In the case of the JL, LS, and CH k-ϵ models, the value of ϵ at the wall boundary is set to zero [89,91,92]. This practice is computationally more convenient than calculating the wall boundary value of ϵ, as is done in the LB model. In setting ϵ at the wall to zero, however, it is necessary to add an additional term to the k equation. This term

represents the actual finite value of ϵ at the wall and it is needed to balance the molecular diffusion term in Eq. (3-14), which is not zero at the wall [80,89,92]. The E_k term, appearing in the k equation of the JL, LS, and CH k-ϵ models, serves this purpose. The values of E_k should take on significant values near the wall and become negligible, compared to D_k (= $\rho\epsilon$) values, in the fully turbulent or logarithmic regions [90].

The E_ϵ term used in the CH k-ϵ model is introduced in order to yield a quadratic growth of ϵ with distance from the wall, in the near-wall region. Chien has presented arguments based on Taylor series expansion of the ϵ equation near the wall and length scale assumptions that indicate that the ϵ should vary as y^2 close to the wall [92]. The E_ϵ term in the JL and LS k-ϵ models is added so that the distribution of k in the regions near a wall would be in reasonable accord with experimental measurements [80,89]. This term becomes negligible in the viscous sublayer and decreases as y^4 in the logarithmic region, with the maximum value occurring in the buffer layer [90]. The result is an increase in the dissipation rate of the turbulence energy in this region, thereby reducing the peak values of k and giving better agreement with experiment.

Different approaches by modelers have led to different expressions for the f and E terms in Eqs. (3-8) and (3-14) to (3-21). In the case of the CH k-ϵ model, two of the model constants are also different from those that are generally used and presented in Table 1: $C_{1\epsilon}$ and $C_{2\epsilon}$ are given values of 1.35 and 1.0, respectively, by Chien [92].

3.5 OTHER NEAR-WALL VERSIONS OF THE k-ϵ MODEL

An alternative to the low-Reynolds-number k-ϵ models discussed in the preceding section is near-wall models that can be used with the standard k-ϵ model of turbulence to allow calculation of the near-wall flow region. Rather than model the governing equations through this region, which requires many grid points to ensure proper resolution of the flow field, semi-empirical and empirical profile distributions are use to calculate the flow field close to the wall. For complex flows, this may allow more detailed and accurate modelling than can be achieved by using the standard wall function approach of the high-Reynolds-number k-ϵ model. There are, however, obvious limitations that may arise in flows for which correlations are not well established, such as unsteady or separated flows.

Such models were discussed briefly in Chapter I. The models by Chieng and Launder [98] and Amano [99] attempt to model the near-wall shear stress, velocity, k, and ϵ profiles accurately by considering separate near-wall regions: a viscous sublayer, a logarithmic layer, and in the case of Amano's three layer model, a buffer layer as well. While profile assumptions are used in the viscous sublayer and buffer regions, universal wall functions are still used to model the logarithmic region. One of the advantages of the low-Reynolds-number k-ϵ model equations, namely the ability to use the equations in flows where wall functions are not well established, is not present with these particular models [98,99]. Nallasamy [76] has pointed out that the flow predictions obtained using these near-wall models are not noticeably different form those of the standard k-ϵ model. For these reasons, the aforementioned

near-wall models were not given further consideration for use in the numerical investigation performed in this research.

Chen and Patel [101] have developed a more detailed form of near-wall turbulence model based on the high-Reynolds-number k-ϵ model. In their "two-layer" model, only the momentum and k equations are solved all the way to the wall, as they are in low-Reynolds-number models. However, in the viscous sublayer, the buffer layer and part of the logarithmic layer, values of μ_t and ϵ are determined using length-scale relations. In the remaining region of the flow, the standard k-ϵ model equations are solved. The relations for μ_t and ϵ in the near-wall region are given as [101]:

$$\epsilon = \frac{k^{3/2}}{l_\epsilon} \tag{3-38}$$

$$\mu_t = \rho\, C_\mu\, k^{1/2}\, l_\mu \tag{3-39}$$

The viscous damping effects that are experienced in the near-wall region are provided by the dependence of the length scales, l_ϵ and l_μ, on the turbulence Reynolds number Re_y, defined by Eq. (3-37). These length scales are given as [101]:

$$l_\epsilon = C_l\, y\, \{1 - \exp\{-\frac{Re_y}{A_\epsilon}\}\} \tag{3-40}$$

$$l_\mu = C_l\, y\, \{1 - \exp(-\frac{Re_y}{A_\mu})\} \tag{3-41}$$

where

$$C_l = \kappa\, C_\mu^{-3/4} \tag{3-42}$$

$$A_\epsilon = 2\, C_l \tag{3-43}$$

$$A_\mu = 70 \qquad (3\text{-}44)$$

The basis for the choice of these various parameters is discussed in [101] and will not be repeated here.

Patel and Richmond [102] found the performance of the two-layer model, just described, to be satisfactory within the extremes of laminarization and separation caused by favourable and adverse pressure gradients on flat surfaces. The results for flows over curved surfaces were not as good, with turbulent shear stress being over or under predicted for convex or concave surfaces, respectively [102]. Based on these results, the two-layer near-wall k-ϵ model of Chen and Patel [101] was, along with the previously discussed low Reynolds number k-ϵ models, considered for possible use in this research. Further attention to this matter will be given in Chapter V.

3.6 k-ϵ MODEL FOR ADVERSE PRESSURE GRADIENT FLOWS

From their investigation in [90], Patel et al. concluded that modifications would be required to improve the prediction capabilities of the standard k-ϵ turbulence model, or any of its extensions, in adverse pressure gradient flows. Hanjalic and Launder [96] have proposed such a modification.

From initial investigations and previous studies, it was concluded by Hanjalic and Launder [96] and Rodi and Scheuerer [97], that the ϵ equation was the main cause of errors in the predictions of flows that experience strong disturbances or adverse pressure gradients. Hanjalic

and Launder [96] suggested that irrotational straining plays an important role in the spectral transport from the large energy-containing eddies to the small energy-dissipating eddies of the turbulent flow. Since the energy that is transferred from the large-scale to the small-scale turbulent motion ends up as dissipated energy, they concluded that in the ϵ equation, there should be a term that favours higher rates of dissipation for irrotational strains compared to that for rotational strains. This is accomplished by breaking the production term P_ϵ, in Eqs. (3-18) and (3-20), into two parts: The first part contains contributions to P_ϵ due to shear strains, and the second part contains contributions due to normal strains. Prominence is given to the normal strain component by multiplying it by a larger empirical coefficient than the $C_{1\epsilon}$ value, which now multiplies only the shear strain term but previously multiplied the entire P_ϵ term of Eq. (3-20). With this modification, Eq. (3-20) for P_ϵ know takes on the form:

$$P_\epsilon = \frac{\epsilon}{k}\ \mu_t\ \{\ f_{C1\epsilon}\ C_{1\epsilon}\ (\frac{\partial U_i}{\partial x_j} + \frac{\partial U_j}{\partial x_i})\frac{\partial U_i}{\partial x_j}\ (1-\delta_{ij}) + C_{3\epsilon}\ (\frac{\partial U_i}{\partial x_j} + \frac{\partial U_j}{\partial x_i})\frac{\partial U_i}{\partial x_j}\ \delta_{ij}\ \} \qquad (3\text{-}45)$$

where all terms, except $C_{3\epsilon}$, have been previously defined in this chapter. The δ_{ij} is the Kronecker delta, and the value for $C_{3\epsilon}$ is given as [96]:

$$C_{3\epsilon} = 4.44 \qquad (3\text{-}46)$$

Rodi and Scheuerer [97] performed an analysis of the logarithmic region of such flows and came to the same conclusion as Hanjalic and Launder [96] concerning the need to increase the generation term, P_ϵ, in

Eq. (3-18). Rodi and Scheuerer [97] in turn used the modification put forth in [96]. After this modification was made, in the investigations of [96] and [97], improved predictions were reported for both moderately and strongly decelerated boundary layer flows.

In view of the results of these two investigations, it would appear useful to include the modification in [96] to any form of k-ϵ model in flow where adverse pressure gradients or strong disturbances might occur. It should be noted that in cases where there is relatively little or no change of the flow in the mean flow direction, such as in fully developed duct flows, Eq. (3-45) will become equivalent to Eq. (3-20), as the normal strain terms will be small or nonexistent.

3.7 CLOSING REMARKS

In this chapter, the equations for a k-ϵ model of turbulence have been presented in a general three-dimensional form. These equations are reduced to the particular forms suitable for the simulation of fully developed and periodic fully developed turbulent flow in rectangular ducts without and with interrupted-plate ducts, respectively, in Chapter V.

CHAPTER IV

FORMULATION OF THE NUMERICAL METHOD

Mathematical models of the turbulent flows of interest in this thesis were presented in Chapters II and III. The formulation of a control-volume-based finite difference method that was used to solve the governing equations of these models is presented in this chapter. This numerical method and related ideas are borrowed from the works of Patankar et al. [13,41], Van Doormaal and Raithby [113], and Settari and Aziz [114]. Therefore, the emphasis in this chapter will be on a concise presentation of this method, rather than on detailed discussions of its key ideas.

4.1 SOLUTION METHOD FOR CONVECTION-DIFFUSION PROBLEMS

In convection-diffusion problems, the task is to solve for the distribution of scalar quantities as they are transported by convection and diffusion in the presence of a known velocity field [41]. It is to be noted that the transport of momentum is strongly dependent on convection and diffusion processes. Therefore, a solution method for convection-diffusion problems is a prerequisite for the formulation of a solution method for fluid flow [41].

4.1.1 Governing Equations

In the Cartesian coordinate system, the equations which govern steady convection and diffusion of a scalar quantity, ϕ, in the presence of steady turbulent fluid flow, can be cast in the following form:

$$\frac{\partial J_i}{\partial x_i} = S \tag{4-1}$$

where J_i is given by:

$$J_i = \rho u_i \phi - \Gamma \frac{\partial \phi}{\partial x_i} \tag{4-2}$$

In Eqs. (4-1) and (4-2), ϕ is a general scalar dependent variable, Γ is the corresponding generalized diffusion coefficient, S is a volumetric source term of ϕ, and u_i represents the component of the velocity in the i direction. The purpose of the source term is to represent the actual production or dissipation of ϕ, however, to ensure the generality of Eq. (4-1), all terms that do not take the form of the convection or diffusion term in Eq. (4-2) can also be included in S [41].

The mass density and velocity field in Eq. (4-2) must also satisfy the continuity equation:

$$\frac{\partial}{\partial x_1}(\rho u_1) = 0 \tag{4-3}$$

4.1.2 Domain Discretization

In the numerical method used, the values of the dependent variables are calculated at a finite number of points in the calculation domain. These points are called grid points. The grid-point values of the dependent variables are obtained by solving sets of algebraic equations called discretization equations. The discretization equations are obtained by first integrating the governing differential equations over

a subdomain, or control volume, surrounding each grid point, and then deriving algebraic approximations to the resulting integral conservation equations.

Grid points and their associated control volumes can be defined in several ways, as discussed by Patankar [41]. The practice adopted here is depicted in Fig. 6. The calculation domain is first divided into control volumes: The dashed lines denote the control-volume boundaries. Then, grid points are placed at the geometric centers of the control volumes: The dots in Fig. 6 denote grid points. For the two-dimensional situation illustrated, a given grid point is connected to a maximum of four neighbouring grid points by grid lines, shown as the solid lines, passing through the four faces of the associated control volume.

An example of a grid point and its associated control volume is shown by point P and the shaded area in Fig. 6. It can be seen that point P communicates with its four neighbour grid points, E, W, N, and S across its four control volume faces, e, w, n, and s, respectively. The E, W, N, and S notations denote east, west, north, and south grid-point neighbours, respectively, and the corresponding control-volume faces are designated as e, w, n, and s. The boundary points, shown as hollow dots, are located at the center of the control-volume face of the near-boundary control volume, illustrated by the shaded area around the grid point B in Fig. 6. With respect to the nomenclature presented in Fig. 7, if P were located on a vertical boundary then $\Delta X_p = 0$, and if P were located on a horizontal boundary then $\Delta Y_p = 0$.

4.1.3 Conservation Equation for the Control Volume

The discretization equation is an algebraic equation that relates ϕ at a particular grid point P to the ϕ's at the four neighbouring grid points, E, W, N, and S, shown in Fig. 6. This algebraic equation is obtained by integrating Eq. (4-1) over a control volume and approximating (algebraically) the various terms in the integral conservation equation. The resulting equation is [41]:

$$J_e A_e - J_w A_w + J_n A_n - J_s A_s = \bar{S}\Delta V \tag{4-4}$$

where ΔV is the volume of the control volume, A's and J's represent areas and total convection-diffusion fluxes, respectively, and the subscripts e, w, n, and s denote locations at these particular control-volume faces, as shown in Fig. 6. The term $\bar{S}$ is a volumetric average source term for the control volume.

4.1.4 Discretization of the Total Flux

Patankar [41] has shown that the fluxes in Eq. (4-4) may be expressed in terms of the dependent variable ϕ at the grid points P, E, W, N, and S, using solutions to locally one-dimensional convection-diffusion problems along appropriate grid lines. Thus the flux J_e may be expressed as follows [41]:

$$J_e A_e = F_e\left(\phi_p + \frac{\phi_p - \phi_E}{\exp(Pe_e) - 1}\right) \tag{4-5}$$

where Pe_e is a dimensionless grid Peclet number defined as:

$$Pe_e = \frac{F_e}{D_e} \tag{4-6}$$

Here, F_e is the flow rate $(\rho u)_e A_e$, and D_e is the diffusion conductance. The diffusion coefficient Γ is regarded as uniform over each control volume, and following the rationale in [41], the appropriate expression for D_e is given by:

$$D_e = A_e \left\{ \frac{(\delta x)_{e-}}{\Gamma_P} + \frac{(\delta x)_{e+}}{\Gamma_E} \right\}^{-1} \tag{4-7}$$

where $(\delta x)_{e-}$ and $(\delta x)_{e+}$ are the distances shown in the control volume depicted in Fig. 7.

Exponential functions are computationally time-consuming, so many approximations, or simplifications, have been proposed for the flux relation in Eq. (4-5). A general representation of these schemes can be arrived at by rewriting Eq. (4-5) as follows [41]:

$$J_e A_e = F_e \phi_P + \{ D_e A(|Pe_e|) + \| -F_e, 0 \| \} (\phi_P - \phi_E) \tag{4-8}$$

where $\|a,b\|$ is used to denote the greater of a and b. Appropriate forms of $A(|Pe|)$ for several different approximations are given in [41]. Of these, the so-called power-law scheme gives the best approximation to the actual exponential function in Eq. (4-5) [41]. The power-law scheme was therefore used in this thesis. It can be obtained by using [41]:

$$A(|P_e|) = \| 0, (1-0.1|P_e|)^5 \| \tag{4-9}$$

It should be noted that flow-oriented difference schemes, such as the SUD scheme of Raithby [115] and the QUICK scheme of Leonard [116], are available in the literature. These schemes are more accurate than

the power-law-difference scheme (PLDS), because they incur less false diffusion than PLDS [117]. However, the SUD and QUICK schemes are less robust than the PLDS, in terms of their ability to yield converged solutions with the iterative solution methods used in this thesis. Therefore, PLDS was used in this work. Representative grid-independence checks were undertaken, in conjunction with the extrapolation procedure presented by de Vahl Davis [118], to obtain estimates of the accuracy of the numerical results. These results will be discussed in detail in later chapters.

4.1.5 Source Term Linearization

If the source term $\overline{S}$ in Eq. (4-4) depends nonlinearly on the variable ϕ, it is desirable to make this dependence linear, at least nominally, so that the discretization equation remains linear: Iterative updating is then used to solve the nonlinear problem. In general, therefore, $\overline{S}$ is formulated as [41]:

$$\overline{S} = \overline{S_C} + \overline{S_P}\phi_P \tag{4-10}$$

where $\overline{S_P}$ is the coefficient of ϕ_P, and $\overline{S_C}$ is the part of $\overline{S}$ that does not explicitly depend on ϕ_P. When $\overline{S}$ is linearized in this manner, the $\overline{S_P}$ term must always be less than zero in order to ensure that instabilities and physically unrealistic solutions do not occur [41].

The best formulation for $\overline{S_C}$ and $\overline{S_P}$ depends on the particular expression for S and the particular type of problem being dealt with. This is also true for the source terms in the turbulence model equations, and

details of the various treatments used in this research will be given in Chapter V.

4.1.6 Final Discretization Equation

Using expressions analogous to those given by Eqs. (4-8) and (4-10), Eq. (4-4) can be cast in the following discretized form:

$$a_P\phi_P = a_E\phi_E + a_W\phi_W + a_N\phi_N + a_S\phi_S + b \tag{4-11}$$

Equation (4-11) can be rewritten more compactly as:

$$a_P\phi_P = \Sigma a_{nb}\phi_{nb} + b \tag{4-11a}$$

In Eq. (4-11):

$$a_E = D_eA(|Pe_e|) + \|-F_e,0\| \tag{4-12}$$

$$a_W = D_WA(|Pe_W|) + \|F_W,0\| \tag{4-13}$$

$$a_N = D_nA(|Pe_n|) + \|-F_n,0\| \tag{4-14}$$

$$a_S = D_sA(|Pe_s|) + \|F_s,0\| \tag{4-15}$$

$$b = \overline{S_C}\Delta V \tag{4-16}$$

$$a_P = a_E + a_W + a_N + a_S - \overline{S_P}\Delta V \tag{4-17}$$

The terms a_E, a_W, a_N, and a_S are the coefficients of the E, W, N, and S neighbour grid points, respectively, and the remaining terms are defined analogously to those in Eqs. (4-6), (4-7), and (4-9). In Eq. (4-11a), the subscript nb denotes a neighbour grid point of P, and the summation is to be taken over all neighbours.

4.1.7 Solution of the Discretization Equations

Collectively, the discretization equations comprise a set of simultaneous algebraic equations for the dependent variables, ϕ, at the internal grid points. These equations are in general nonlinear and coupled. The solution of these equations was achieved by using an iterative method. In this method, the equations are first decoupled and linearized using available values of ϕ, either from a guessed field or from the solution generated during a previous iteration. The resulting set of nominally linear and decoupled equations are diagonally dominant, thereby satisfying the Scarborough criterion for the convergence of successive over-relaxation iterative solution methods [41]. Line-by-line tri-diagonal-matrix algorithms (TDMA) and cyclic tri-diagonal-matrix algorithms (CTDMA) were used to solve the nominally linear and decoupled sets of discretization equations.

The line-by-line TDMA solution technique is described in detail by Patankar [41]. The line-by-line CTDMA solution technique is required in cases where periodicity boundary conditions are encountered. Such conditions are characteristic of spatially-periodic fully developed flows. For example, the velocity components and the periodic part of the pressure field, $\hat{P}(x,y)$, are identical at the inlet and outlet boundaries, shown by the lines AE and BC in Fig. 2, of the calculation module in the periodic fully developed region of the turbulent interrupted-plate duct flows investigated in this thesis. A detailed discussion of the line-by-line CTDMA technique is available in Patankar et al. [13].

To ensure convergence of the overall iterative scheme,

underrelaxation is usually necessary. On the other hand, the rate of convergence of the line-by-line TDMA and CTDMA techniques for the solution of the nominally linear and decoupled sets of discretization equations may be enhanced by using a block correction procedure.

Underrelaxation

In this research, the implicit underrelaxation procedure of Patankar [41] was used. In this procedure, the change in ϕ from iteration to iteration can be reduced by introducing an underrelaxation factor, α ($0 < \alpha < 1$), into Eq. (4-11a). This equation can then be recast in the form:

$$(\frac{a_P}{\alpha})\phi_P = \Sigma a_{nb}\phi_{nb} + b + (1 - \alpha)\frac{a_P \phi_P^*}{\alpha} \qquad (4\text{-}18)$$

where ϕ_P^* denotes the value of ϕ_P from the previous iteration. It should be noted that when convergence is achieved, $\phi_P = \phi_P^*$, and Eq. (4-18) becomes equivalent to Eq. (4-11a).

Block Correction Procedure

To enhance the rate of convergence of the line-by-line TDMA and CTDMA procedures, an additive correction method, described by Settari and Aziz [114] and known as the block correction method, was used. This method will be briefly outlined with reference to Fig. 8, where I and J denote grid-point locations in the x and y directions, respectively. The main idea of this procedure is to correct the unconverged ϕ_{IJ}^* field, during the line-by-line iterative solution of the nominally linear discretization equations, by adding uniform corrections $\overline{\phi_I}$ to all grid-point values of ϕ_{IJ}^* along the corresponding I^{th} grid line (or

adding uniform corrections $\overline{\phi_J}$ to all grid-point values of ϕ^*_{IJ} along the corresponding J^{th} grid line). Thus:

$$\phi_{IJ} = \phi^*_{IJ} + \overline{\phi_I} \tag{4-19}$$

In Eq. (4-19), the corrections $\overline{\phi_I}$ are chosen to ensure integral conservation over blocks around lines of constant I, as shown in Fig. 8.

First, Eq. (4-11) is recast in the general form:

$$a_{IJ}\phi_{IJ} = b_{IJ}\phi_{I+1,J} + c_{IJ}\phi_{I-1,J} + d_{IJ}\phi_{I,J+1} + e_{IJ}\phi_{I,J-1} + f_{IJ} \tag{4-20}$$

Then Eq. (4-19) is used to express the ϕ values in this equation in terms of ϕ^* and $\overline{\phi}$ values. The resulting equation is then summed over all J values, except for known boundary values, and an equation for $\overline{\phi_I}$ is obtained:

$$A_I\overline{\phi_I} = B_I\overline{\phi_{I+1}} + C_i\overline{\phi_{I-1}} + D_I \tag{4-21}$$

where

$$A_I = \Sigma(a_{IJ} - d_{IJ} - e_{IJ}) \tag{4-22}$$

$$B_I = \Sigma\, b_{IJ} \tag{4-23}$$

$$C_I = \Sigma\, c_{IJ} \tag{4-24}$$

$$D_I = \Sigma(b_{IJ}\phi^*_{I+1,J} + c_{IJ}\phi^*_{I-1,J} + d_{IJ}\phi^*_{I,J+1} + e_{IJ}\phi^*_{I,J-1} + f_{IJ} - a_{IJ}\phi^*_{IJ}) \tag{4-25}$$

The set of equations for $\overline{\phi_I}$ is solved by the TDMA or the CTDMA, as is appropriate for the problem of interest. Equation (4-19) is then used to correct the ϕ^*_{IJ} values, before the application of line-by-line TDMA

and CTDMA procedures to obtain an updated $\phi_{I,J}$ field. Block corrections along grid lines of constant J are done analogously.

4.2 SOLUTION OF THE FLUID FLOW EQUATIONS

The time-averaged equations which govern the steady, two-dimensional, turbulent flows of interest in this thesis can be cast in the following forms:

x momentum

$$\frac{\partial}{\partial x}(\rho UU) + \frac{\partial}{\partial y}(\rho VU) = - \frac{\partial P}{\partial x} + \frac{\partial}{\partial x}\left(\Gamma_u \frac{\partial U}{\partial x}\right) + \frac{\partial}{\partial y}\left(\Gamma_u \frac{\partial U}{\partial y}\right) + S^u \qquad (4\text{-}26)$$

y momentum

$$\frac{\partial}{\partial x}(\rho UV) + \frac{\partial}{\partial y}(\rho VV) = - \frac{\partial P}{\partial y} + \frac{\partial}{\partial x}\left(\Gamma_u \frac{\partial V}{\partial x}\right) + \frac{\partial}{\partial y}\left(\Gamma_u \frac{\partial V}{\partial y}\right) + S^v \qquad (4\text{-}27)$$

continuity

$$\frac{\partial U}{\partial x} + \frac{\partial V}{\partial y} = 0 \qquad (4\text{-}28)$$

If the pressure field, P, is known, then it is evident that equations (4-26) and (4-27) are particular cases of the general convection-diffusion equation, Eq. (4-1), with $\Gamma = \Gamma_u$ (Γ_u is given by Eq. (3-4)), and ϕ and S set to U and ($S^u - \partial P/\partial x$) or V and ($S_v - \partial P/\partial y$), respectively. In such a case, the solution of these equations can be achieved by means of the procedure outlined in the preceding sections of this chapter.

The pressure field, however, is not known a priori. It is specified indirectly by the governing continuity equation in conjunction with the momentum equations. When solving the momentum equations, the correct

pressure field is required in order that the resulting velocity field will satisfy the continuity equation. For computational purposes, it is desirable to have a direct method for determining the pressure. Thus additional considerations and techniques are required for calculating the flow field [41]. In this thesis, the Semi-Implicit-Method-for-Pressure-Linked-Equations-Consistent (SIMPLEC) proposed by Van Doormaal and Raithby [113], was used to solve the discretized momentum and continuity equations. A concise description of the procedure used to solve the fluid flow equations is presented in this section.

4.2.1 Staggered Grid

If the velocity components and pressure are calculated at the same grid-point locations, physically unrealistic oscillatory solutions may result [41]. These difficulties are avoided by using the staggered-grid method [41], in which the pressures and all other variables, except the velocity components, are calculated at main-grid locations. The velocity components are calculated at staggered locations, as shown in Fig. 9: The short arrows in x and y directions represent the U and V velocity components, respectively, the dashed lines are main-grid control-volume faces, and the dots are the main-grid points . The velocities are located on the main-grid control-volume faces that are perpendicular to their direction. With respect to the main grid, the grid for U is displaced in the x direction and the grid for V is displaced in the y direction [41]. The resulting staggered momentum control volumes are illustrated in Fig. 10.

4.2.2 Discretized Momentum Equations

Using the same approach that was used to obtain Eq. (4-11) from Eq. (4-1), the discretized form of the x-momentum equation, with respect to the U control volume shown in Fig. 10(c), can be written as [41]:

$$a_e U_e = \Sigma a_{nb} U_{nb} + b + A_e (P_P - P_E) \qquad (4\text{-}29)$$

where b includes all source terms other than the pressure gradient term. A_e is the area over which the pressure force in the x direction acts: It is equal to the area of the main-grid control-volume face at e. The expressions for a_{nb}, a_e, and b are calculated in a manner similar to that used to obtain corresponding terms in Eq. (4-11a): The only difference is that the staggered-grid geometry must be taken into account when calculating the D and F terms. The discretization equation for the V velocities is obtained in a similar manner. Details of these expressions can be found in the book by Patankar [41].

4.2.3 Pressure Correction Equation

Using an estimated pressure field, denoted by P^*, the set of equations represented by Eq. (4-29) can be used to calculate a corresponding velocity field, U^*, that satisfies the equation:

$$a_e U_e^* = \Sigma a_{nb} U_{nb}^* + b + A_e (P_P^* - P_E^*) \qquad (4\text{-}30)$$

Similarly, the corresponding V^* field can be obtained.

Unless the estimated P^* values happen to be the correct P values needed in the discretized momentum equation, the U^* and V^* velocities

will not satisfy the continuity equation . The estimated pressure field must, therefore, be corrected by an amount P' that will result in corresponding corrections in the velocities, U' and V', so that they will satisfy the continuity equation. This implies that:

$$U = U^* + U' \tag{4-31}$$

$$V = V^* + V' \tag{4-32}$$

and

$$P = P^* + P' \tag{4-33}$$

By subtracting Eq. (4-30) from Eq. (4-29) and substituting Eqs. (4-31) and (4-33) into the result, an equation for U'_e is obtained [41]:

$$a_e U'_e = \Sigma a_{nb} U'_{nb} + A_e (P'_P - P'_E) \tag{4-34}$$

In this equation, it can be assumed that the U'_e velocity corrections are of the same order of magnitude as the U'_{nb} corrections [113]. In the SIMPLEC procedure, the term $(\Sigma a_{nb} U'_e)$ is subtracted from each side of Eq. (4-34), and it is assumed that the net magnitude of the summation terms on the right hand side of the resulting equation is negligible. The result is a simplified equation that expresses U'_e in terms of only the P' corrections. This can be expressed as follows [113]:

$$U_e = U^*_e + d_e (P'_P - P'_E) \tag{4-35}$$

where

$$d_e = \frac{A_e}{(a_e - \Sigma a_{nb})} \tag{4-36}$$

Correction equations for the V velocity components can be obtained similarly.

With respect to the main-grid control volume surrounding a particular node, P, in the interior of the calculation domain, the discretized form of the continuity equation is the following [41]:

$$F_e - F_w + F_n - F_s = 0 \tag{4-37}$$

The velocity correction equations, such as Eq. (4-35), are substituted into the discretized continuity equations, such as Eq. (4-37), to obtain the pressure correction equations [41,113]:

$$a_P P'_P = a_E P'_E + a_W P'_W + a_N P'_N + a_S P'_S + b' \tag{4-38}$$

where

$$a_E = \rho A_e d_e \tag{4-39}$$

$$a_W = \rho A_w d_w \tag{4-40}$$

$$a_N = \rho A_n d_n \tag{4-41}$$

$$a_S = \rho A_s d_s \tag{4-42}$$

$$a_P = a_E + a_W + a_N + a_S \tag{4-43}$$

$$b' = \rho U^*_w A_w - \rho U^*_e A_e + \rho U^*_s A_s - \rho U^*_n A_n \tag{4-44}$$

The term b' represents an apparent mass source, caused by the U^* and V^* fields when they do not satisfy continuity requirements. The pressure correction, P', is used to correct the U^* and V^* fields, via equations such as Eq. (4-35), in order to remove this apparent mass source term. The pressure field is updated using Eq. (4-33).

4.2.4 Synopsis of the SIMPLEC Procedure

When using the SIMPLEC procedure, it is necessary to use implicit underrelaxation in the discretized momentum equations, otherwise, if the $\overline{S_p}$ source term is zero, the denominator in Eq. (4-36) will become zero. On the other hand, the pressure correction equation should not be underrelaxed [113], otherwise the corrected velocity fields will not necessarily satisfy the continuity equation during the iterations.

The various steps in the SIMPLEC procedure are summarized below [113]:

1. Guess the pressure and velocity fields, P^*, U^*, and V^*.
2. Evaluate the coefficients in the discretized momentum equations, and solve them to obtain new U^* and V^* values.
3. Calculate the coefficients in Eq. (4-38), and solve for the P' field.
4. Correct the velocity field using the velocity correction equations, and update the pressure field using Eq. (4-33).
5. Solve the discretization equations for other ϕ's, if necessary.
6. Use the P obtained in step 4 as the new P^*, return to step 2, and repeat this procedure until convergence is achieved.

CHAPTER V

IMPLEMENTATION OF SUITABLE k-ϵ MODELS FOR THE FLOWS INVESTIGATED

5.1 CHOICE OF A k-ϵ MODEL

The numerical investigation undertaken in this research is concerned primarily with steady, spatially-periodic, two-dimensional turbulent flows through interrupted-plate rectangular ducts. The flows of interest are governed by geometric parameters, such as aspect ratio, nondimensional plate spacing and plate thickness parameters, and the module Reynolds number. In this work, these parameters are assigned values similar to those that might be found in actual heat exchange equipment. Therefore, turbulent flows with relatively low Reynolds numbers were considered in this study: Nominal values for module Reynolds numbers ranged from $5x10^3$ to $30x10^3$.

As explained in Chapter II, for periodic fully developed flow in an interrupted-plate rectangular duct, only the flow through one of the geometrically similar modules, such as ABCDE in Fig. 2, need be considered. As the flow enters module ABCDE, at the line AE, it will undergo an acceleration due to the presence of the plate. For purposes of numerical modelling, this flow between the plate and the wall could be treated as a developing turbulent duct flow and modelled using the standard k-ϵ model of turbulence [75]. In flow regions near the duct wall and the surface of the plate, the viscous effects cannot be neglected. In the standard k-ϵ model, the solution of the governing differential

equations in the near-wall regions is avoided by the use of "universal wall functions", as discussed in Chapter III.

For the use of wall functions to be appropriate, it is necessary that there is no, or only a very small, leading-edge separation zone over the plate. This is not the case when the plate thickness parameter is large. In addition, since the turbulent flows investigated here have relatively low Reynolds numbers, it is expected that the local turbulence Reynolds number, Re_t, will be low throughout much of the flow region. As discussed in Chapter III, in such circumstances, it is also desirable to avoid the use of wall functions and solve model differential equations that are appropriate all the way to the wall. Thus the standard k-ϵ model used in conjunction with wall functions to handle near-wall regions is inappropriate for this numerical investigation. Alternative approaches for the numerical simulation of the flows of interest include one of the four low-Reynolds-number k-ϵ models [89,91,92,93] , or the two-layer k-ϵ model of Chen and Patel [101], presented in Chapter III.

The task is now to determine which of these five extensions of the standard k-ϵ model is most appropriate for the numerical investigation undertaken in this thesis. To facilitate the following discussion, the geometric flow module, ABCDE in Fig. 2, has been redrawn so that certain positions and distances within the module are clearly indicated: This has been done in Fig. 11, where short dashed lines indicate spatial locations in the fluid region and solid lines with arrows indicate distances. The dashed line ab represents a location in the flow just above the plate surface. The distance $\overline{ae}$ represents the normal distance from

line ab to the plate surface. The line bc/ is a continuation of line ab into the flow region downstream of the plate trailing edge. $\overline{Bc/}$ is the normal distance from the surface of the upper duct wall to the line bc/. The lines db/ and dc are extensions of the vertical and horizontal plate surface lines, respectively.

For the five k-ϵ models being considered [89,91,92,93,101], attention will first be focussed on the ability of each to properly simulate the turbulent eddy viscosity in the near-wall regions and in the vicinity of the trailing edge of the plate. Each model incorporates a viscosity damping function that serves to appropriately decrease or damp out the eddy viscosity, μ_t, in regions where viscous effects become dominant, such as in the vicinity of a wall. In the flow region close to the plate surface, represented by abde in Fig. 11, the values of Re_t are expected to be small and, because the distance $\overline{ae}$ is also small, the values of Re_y and y^+ are expected to be small. As seen in Table 2 and from Eqs. (3-8), (3-39) and (3-41), this will result in small values of μ_t for all the models, as would be expected in this near-wall region. It should be emphasized here that, in the expressions for y^+, Re_y, and l_μ, given by Eqs. (3-31), (3-37), and (3-41), respectively, the y variable is the shortest distance normal to a solid surface. As the fluid just upstream of bd, in Fig. 11, flows past the trailing edge of the plate, the shortest distance normal to a wall changes from $\overline{ae}$ to $\overline{Bc/}$, the distance to the upper duct wall at AB. The difference between $\overline{ae}$ and $\overline{Bc/}$ is large, so there will be large changes in the values of y^+, and Re_y. Correspondingly, the values of μ_t, calculated in the Chien [92], Lam and Bremhorst [93], and Chen and Patel [101] k-ϵ models, will also change suddenly from a very low value, just upstream of bd, to a

relatively large value immediately downstream of bd. Furthermore, in the case of the Chien model [92], $f_{C\mu}$ is dependent on y^+, and hence on both y and the local wall shear stress, τ_w. Just downstream of bd, τ_w will also change suddenly from the value at the plate surface to the value at the upper duct wall. In the actual flow, because of convection and diffusion processes, sudden transitions in the value of μ_t would not occur immediately downstream of bd. A gradual and continuous transition process would be expected, with the flow along bc' becoming more like the core region of a fully turbulent duct flow as the downstream distance from bd becomes greater. In the Jones and Launder [89] and the Launder and Sharma [91] k-ϵ models, calculation of $f_{C\mu}$ depends on Re_t which is, in turn, dependent only on the local values of k and ϵ in the flow, and not the normal distance to the nearest wall. Therefore, the sudden changes in μ_t that occur in the other models [92,93,101] in the vicinity of the plate trailing edge, do not occur with these two models [89,91].

Difficulties similar to those encountered in the calculation of μ_t are expected to arise in the calculation of E_ϵ and E_k in the Chien model [92], in the calculation of $f_{C1\epsilon}$ in the Lam and Bremhorst model [93], and in the calculation of l_ϵ in the Chen and Patel model [101]. If the region in which μ_t is comparable to or smaller than μ is very small, the error in the overall flow calculations caused by assuming an abrupt transition to fully turbulent flow, in the region immediately downstream of bd, may be small or negligible. However, since the flows investigated in this work are low-Reynolds-number turbulent flows, the viscous affected flow region is expected to be large relative to the rest of the flow field. In such a case, significant errors can occur if sudden

changes in μ_t are allowed to occur in the vicinity of bd.

For the reasons just discussed, only the Jones and Launder [89] and the Launder and Sharma [91] low-Reynolds-number k-ϵ turbulence models were given further consideration for use in this numerical study. It will be noticed in Table 2 that the only difference between these two models is in the form of the viscous damping function, $f_{c\mu}$. The performance of each of these models was evaluated by doing some initial numerical calculations of two-dimensional simple fully developed turbulent flows in straight channels. The corresponding numerical formulation is discussed in the Section 5.3.

From the results of initial experimental investigations carried out in this work [110], it was evident that some regions of the flow through a periodic module experience locally adverse pressure gradients. With this in mind, it was decided that once a choice was made between the Jones and Launder [89] and the Launder and Sharma [91] k-ϵ models, the effect of using the modification suggested by Hanjalic and Launder [96] would be examined. In the investigations reported in Refs. [96,97], use of k-ϵ models incorporating this modification led to improved predictions for flows subjected to adverse pressure gradients. The details have been discussed in Chapter III, and the modification is given by Eqs. (3-45) and (3-46).

5.2 NUMERICAL TREATMENT OF THE MODEL EQUATIONS FOR TWO-DIMENSIONAL PERIODIC FULLY DEVELOPED FLOWS

This section of Chapter V deals with the numerical solution of the

k-ϵ turbulence model equations for two-dimensional periodic fully developed flows, in the context of the numerical formulation presented in Chapter IV. Domain discretization, presentation of model equations, the iterative solution procedure used, treatment of boundary surfaces and plate regions, handling of source terms, and the overall convergence criteria are discussed here.

5.2.1 Domain Discretization

As described in Section 4.1.2, the geometric module, ABCDE, in Figs. 2 and 11 is discretized by subdividing the calculation domain into rectangular control volumes, and grid points are then located at the geometric centers of the control volumes. All dependent variables, except velocities, are stored at the main-grid points, shown in Fig. 6. The U and V velocities are stored at the appropriate staggered-grid points, as shown in Fig. 9.

When discretizing a calculation domain, it is convenient to place main-grid control-volume faces at locations where discontinuities in the flow field or boundary conditions occur. Therefore, in discretizing the geometric module shown in Fig. 11, control-volume faces have been positioned not only along the boundaries designated by AB, BC, CE, and EA, but also along the plate surfaces, shown by the lines ed and dD, located within the boundaries of the domain. The control volumes of the main-grid points, located inside the plate region, will thus lie entirely within this region's boundaries, edDE in Fig. 11.

Staggered-grid points for the U and V velocities are located along

the vertical and horizontal plate surfaces, respectively. The velocity components that are located on a surface are perpendicular to that surface, as seen in Fig. 12. In this figure, the corner of a plate surface corresponds to the corner of a main-grid control volume. There are no main-grid or staggered-grid points located at such a location. This is another desirable feature of the present domain discretization. Since no grid points are located at the plate corners, no dependent variable values need to be specified or calculated at these locations.

Figures 6 to 10, and 12, have been drawn for uniform grids. However, in the present numerical investigation, the final flow calculations were done with nonuniform grid spacing. This enabled efficient use of grid points, by allowing a greater number of grid points to be deployed in regions where the variation of the dependent variables was greatest. Thus improved accuracy could be obtained with fewer total grid points, compared to calculations done with uniform grid spacing, thereby allowing substantial savings in computing costs. As a result, a greater number of geometric parameter values and flow rates could be investigated numerically with the financial resources available for this research. The nonuniform grid spacing used will be discussed next.

At the solid surfaces, AB and ed in Fig. 11, the no-slip boundary condition prevails and the flow is brought to rest. Along the line edc and EDC there is a discontinuous change from a no-slip to a free-flow boundary condition when the end of the plate is reached at dD. At the inlet and exit of module ABCDE, and at the center of the module, along Db′, the cross-sectional flow area suddenly changes due to the presence of the interrupted-plate and causes substantial changes and steep

gradients in the flow field. Thus, grid points have to be more densely packed in these regions of the calculation domain, compared to the rest of the calculation domain. In the proposed discretization scheme, the geometric module shown in Fig. 11 is divided into four zones: two zones in the y coordinate direction, a lower and an upper zone; and two zones in the x coordinate direction, an upstream and a downstream zone. With reference to Fig. 11, the upper y zone is bounded by AB at its top boundary and by ec at its lower limit, and the lower zone is bounded by ec and EC. The upstream x zone is bounded by AE on the left and Db′ on the right, and the downstream region is bounded by Db′ and BC. Within the y-grid zones, the distribution of grid points in the y-coordinate direction is most dense near the zone boundaries and becomes coarser towards the center of the zone. The upper half of a y zone is the mirror image of the lower half of that same zone, in terms of grid-point distribution density. In the x-coordinate direction of the x zones, the distribution of grid points is done in the same manner as for the y-directional distribution in the y zones. Further details of this discretization scheme are given in Appendix 1. The nonuniform grids used with the three different interrupted-plate duct geometries of this research are shown in Figs. 13, 14, and 15.

The procedures for dealing with the discretization equations at grid points located within the plate region of the calculation domain are discussed in Section 5.2.4.

5.2.2 Two-Dimensional Form of the Model Equations

Using the Reynolds stress model given by Eq. (3-1), the two-dimensional form of the equations governing turbulent periodic fully developed flow in interrupted-plate ducts, Eqs. (2-21) to (2-24), can be written as follows:

x momentum

$$\frac{\partial}{\partial x}(\rho UU) + \frac{\partial}{\partial y}(\rho UV) = \frac{\partial}{\partial x}(\Gamma_u \frac{\partial U}{\partial x}) + \frac{\partial}{\partial y}(\Gamma_u \frac{\partial U}{\partial y}) - \frac{\partial \hat{P}}{\partial x} + S^u \qquad (5\text{-}1)$$

y momentum

$$\frac{\partial}{\partial x}(\rho UV) + \frac{\partial}{\partial y}(\rho VV) = \frac{\partial}{\partial x}(\Gamma_u \frac{\partial V}{\partial x}) + \frac{\partial}{\partial y}(\Gamma_u \frac{\partial V}{\partial y}) - \frac{\partial \hat{P}}{\partial y} + S^v \qquad (5\text{-}2)$$

where the source terms S^u and S^v are given by

$$S^u = \beta + \frac{\partial \mu_t}{\partial x}\frac{\partial U}{\partial x} + \frac{\partial \mu_t}{\partial y}\frac{\partial V}{\partial x} \qquad (5\text{-}3)$$

$$S^v = \frac{\partial \mu_t}{\partial x}\frac{\partial U}{\partial y} + \frac{\partial \mu_t}{\partial y}\frac{\partial V}{\partial y} \qquad (5\text{-}4)$$

In Eqs. (5-1) and (5-2), the diffusion coefficient, Γ_u, is given by Eq. (3-4).

Equations (5-1) and (5-2) are in the same general form as Eqs. (4-26) and (4-27). They can thus be easily incorporated into the numerical formulation used for the solution of the flow equations, as

presented in Chapter IV. It should also be noted that the pressure gradient term of the x momentum equation consists of two parts, the gradient of the unknown periodic component of time-mean pressure, $\hat{P}$, defined by Eq. (2-20), and the constant pressure gradient term, β, defined by Eq. (2-18). Since β is a constant value, which is specified at the start of each computer simulation, it can be included in the S^u term of Eq. (5-1).

In the context of the Jones and Launder [89], and Launder and Sharma [91], k-ϵ models that incorporate the Hanjalic and Launder [96] modification for adverse pressure gradient flows, the two-dimensional forms of the k and ϵ equations can be written in the form of the general convection-diffusion equation, Eq. (4-1).

The two-dimensional form of the k equation, Eq. (3-14), is:

$$\frac{\partial}{\partial x}(\rho U k) + \frac{\partial}{\partial y}(\rho V k) = \frac{\partial}{\partial x}(\Gamma_k \frac{\partial k}{\partial x}) + \frac{\partial}{\partial y}(\Gamma_k \frac{\partial k}{\partial y}) + S^k \qquad (5\text{-}5)$$

where

$$S^k = P_{k1} + P_{k2} - D_k - E_k \qquad (5\text{-}6)$$

and

$$P_{k1} = \mu_t \left(\frac{\partial U}{\partial y} + \frac{\partial V}{\partial x} \right)^2 \qquad (5\text{-}7)$$

$$P_{k2} = 2 \mu_t \left\{ \left(\frac{\partial U}{\partial x}\right)^2 + \left(\frac{\partial V}{\partial y}\right)^2 \right\} \qquad (5\text{-}8)$$

$$E_k = 2 \mu \left[\left\{ \frac{\partial}{\partial x}(k^{1/2}) \right\}^2 + \left\{ \frac{\partial}{\partial y}(k^{1/2}) \right\}^2 \right] \qquad (5\text{-}9)$$

The expressions for Γ_k and D_k have already been given in Eqs. (3-15) and (3-17), respectively. The turbulence production term, P_k, in Eq. (3-14), is modelled as the sum of two terms in Eq. (5-6). These terms, P_{k1} and P_{k2}, represent the contributions to P_K due to shear strains and normal strains, respectively. The reason for modelling P_k in this manner is to facilitate the introduction of the Hanjalic and Launder [96] modification of the ϵ equation production term, P_ϵ, for adverse pressure gradient flows. Equation (5-9) for E_k, is taken from Table 2 for the JL [89] and LS [91] low-Reynolds-number k-ϵ models.

The two-dimensional form of the ϵ equation, Eq. (3-18), is given as:

$$\frac{\partial}{\partial x}(\rho U \epsilon) + \frac{\partial}{\partial y}(\rho V \epsilon) = \frac{\partial}{\partial x}(\Gamma_\epsilon \frac{\partial \epsilon}{\partial x}) + \frac{\partial}{\partial y}(\Gamma_\epsilon \frac{\partial \epsilon}{\partial y}) + S\epsilon \qquad (5\text{-}10)$$

where

$$S\epsilon = P_\epsilon - D_\epsilon + E_\epsilon \qquad (5\text{-}11)$$

and

$$P_\epsilon = \frac{\epsilon}{k} (C_{1\epsilon} P_{k1} + C_{3\epsilon} P_{k2}) \qquad (5\text{-}12)$$

$$E_\epsilon = \frac{2\mu\mu_t}{\rho} \left[\left\{ \frac{\partial}{\partial x}\left(\frac{\partial U}{\partial x} \right) \right\}^2 + \left\{ \frac{\partial}{\partial y}\left(\frac{\partial V}{\partial y} \right) \right\}^2 \right.$$

$$+ \left\{ \frac{\partial}{\partial y}\left(\frac{\partial U}{\partial y} \right) \right\}^2 + \left\{ \frac{\partial}{\partial x}\left(\frac{\partial V}{\partial x} \right) \right\}^2$$

$$\left. + 2 \left\{ \frac{\partial}{\partial y}\left(\frac{\partial U}{\partial x} \right) \right\}^2 + 2 \left\{ \frac{\partial}{\partial x}\left(\frac{\partial V}{\partial y} \right) \right\}^2 \right] \qquad (5\text{-}13)$$

The Γ_ϵ and D_ϵ terms in the above equations are given by Eqs. (3-19) and (3-21), respectively, with the $f_{C2\epsilon}$ function in Eq. (3-21) taking the form appropriate for either the JL [89] or LS [91] k-ϵ models, as shown in Table 2. The production term, P_ϵ, given by Eq. (5-12), has been obtained by substitution of Eqs. (5-7) and (5-8) into Eq. (3-45). The $f_{C1\epsilon}$ function, in Eq. (3-45), has been omitted as it has a value of one for the k-ϵ models being considered for use in this research [89,91]. The values of $C_{1\epsilon}$ and $C_{3\epsilon}$ are given in Table 1 and by Eq. (3-46), respectively. The expression for E_ϵ is also taken from Table 2 for the JL [89] and LS [91] models.

5.2.3 Boundary Condition Specification

Boundary conditions for the flow and turbulence equations must be specified at grid points located along the geometric module boundaries AB and CDE, shown in Figs. 2 and 11. At the duct wall boundary, AB, values of U, V, and k are zero due to the no-slip and impermeability conditions which prevail at solid surfaces. At such surfaces, in the low-Reynolds-number k-ϵ models [89,91] used here, the value of ϵ is also set to zero. As seen in Fig. 2, the module boundary at line CDE is a geometrical symmetry line for the interrupted-plate duct. For the periodic fully developed flows investigated numerically in this thesis, this line is also a flow symmetry line. The part of this boundary shown by line DE passes through the center of the plate, and all flow and turbulence variables along this boundary line can thus be set to zero. Along the line CD, symmetry boundary conditions are specified for U, V, k, and ϵ.

For periodic fully developed flows, the values of U, V, k, and ϵ, at similar vertical locations on the AE and BC boundary lines, in Figs. 2 and 11, are identical. Thus the cyclic tri-diagonal-matrix algorithm (CTDMA), discussed in Chapter IV, can be employed to solve the discretization equations along the x-coordinate direction. This removes the need to specify boundary values along AE and BC.

As was discussed in Chapter IV, the absolute level of the pressure (and pressure correction) is not important in the calculation of incompressible flows, because it is the pressure gradient that drives the velocity field. In this work, however, to avoid computational difficulties that could arise if the absolute level of the P field is allowed to float, and possibly achieve very large values, the values of P and P' at a specified node within the flow field were fixed at zero.

The treatment of the flow and turbulence equations at grid points inside the solid plate region of the module, will be discussed in the next section.

5.2.4 Treatment of the Plate Region

The values of dependent variables, such as U, V, k, and ϵ, at grid points located on, or inside, the solid plate region of the geometric module, shown as edDE in Fig. 11, are set to zero by overwriting the coefficients in the appropriate discretization equations. At main grid points, the a_{nb} coefficients and the b term in Eq. (4-11a) are overwritten to zero while a_p is set to unity. Similarly, at staggered-velocity

locations, the a_{nb} coefficients and the $\{b+A_e(P_P-P_E)\}$ term are set to zero and a_e is set to one, in Eq. (4-29), and d_e in Eq. (4-35) is set to zero.

The solid plate region can be thought of as a part of the flow domain having essentially infinite viscosity [41]. This can be modelled in Eqs. (5-1), (5-2), (5-5) and (5-10), by setting all diffusion coefficients to large values ($\Gamma \simeq 10^{30}$) at grid points inside the plate region. In this connection, it should be noted that the harmonic mean interpolation scheme, given by Eq. (4-7), ensures that the large change that occurs in Γ's at the plate-fluid interface is properly handled [41].

By following the procedures just mentioned, no further adaptations and specializations are necessary when using the line-by-line CTDMA and TDMA solvers. General versions of these solvers can be used to solve discretization equations at all grid points, regardless of whether they lie in the solid plate region or in the fluid region.

5.2.5 Iterative Solution Procedure

Using Eqs. (5-1) and (5-2) and following the numerical formulation in Chapter IV, algebraic discretization equations are obtained for the U and V velocity fields. Similarly, using Eqs. (5-5) and (5-10), two sets of discretization equations are also obtained for k and ϵ. Finally, the discretized momentum and continuity equations are used to obtain a set of algebraic equations for the pressure correction field, as discussed in Chapter IV. An iterative procedure used for the solution of these five sets of coupled discretization equations will be outlined next. An

understanding of this procedure will facilitate the discussions presented in following sections.

1. To start the calculation process, values of the relaxation parameters, α in Eq. (4-18), and suitable convergence criteria are specified, and guess values of U, V, P, k, and ϵ are supplied.
2. Calculate values of μ_t using available values of k and ϵ.
3. Using the available values of μ_t, U, V, and P, calculate the coefficients and source terms in the discretized U momentum equations, relax them ($\alpha_U = 0.9$), and then solve to obtain the U^* field.
4. Using the available values of μ_t, U, V, and P, calculate the coefficients and source terms in the discretized V momentum equations, relax them ($\alpha_V = 0.9$), and then solve to obtain the V^* field.
5. Set the initial guess values of P' to zero.
6. Use the U^* and V^* values from Steps 3 and 4 to calculate the mass source term, b', in Eq. (4-38), and solve for the P' field.
7. Correct the velocity field using the velocity correction equations, Eq. (4-35), and correct the pressure field using Eq. (4-33).
8. Repeat Steps 3 to 7, which will be referred to as a velocity-field iteration, a specified number of times to ensure that the velocity field reaches an acceptable level of convergence before proceeding to solve the k and ϵ equations.
9. Calculate the coefficients and source terms in the k equation, using the values of U and V from Step 8, and the same values of k and ϵ as those used in Step 2, and then solve for an updated k field.
10. Calculate the coefficients and source terms in the ϵ equation, using values of U and V from Step 8, and the same k and ϵ values as used in Step 2 (do not use the k values from Step 9), and solve

for an updated ϵ field.

11. Steps 2 to 10 constitute one iteration of the overall solution procedure. Return to step 2 and repeat the procedure, until convergence is achieved.

In Steps 3, 4, 6, 9, and 10, the nominally linear discretization equations are solved using the iterative TDMA/CTDMA procedure with block correction, as described in Section 4.1.7. During each of these steps, the line-by-line TDMA/CTDMA sweeps of the calculation domain are done a specified number of times, updating the dependent variable field each time, thus obtaining a partially converged field for the dependent variable with a given set of coefficient values. It is not necessary to obtain complete convergence of the nominally linear and decoupled sets of discretization equations in each of the above-mentioned steps during the overall iterative procedure as it does not enhance the overall rate of convergence significantly [41].

5.2.6 Treatment of Source Terms

As was mentioned in Section 4.1.5, the volume-averaged forms of the source terms in Eq. (5-1), (5-2), (5-5), and (5-10), are linearized as done in Eq. (4-10). In such a linearization, the $\overline{S_P}$ term must always be less than or equal to zero to ensure that the a_p coefficient, in Eq. (4-11), and the a_e coefficient, in Eq. (4-29), do not become negative. If these coefficients were to become negative, instabilities and physically unrealistic solutions could occur [41].

Momentum equations

The S^u source term, Eq. (5-3), is only dependent on the U velocity distribution through gradients of U. This dependence on U cannot be easily expressed in a linear form, similar to that of the $(\overline{S_P}\phi_P)$ term in Eq. (4-10). In addition, even if such a linearization were possible, it is not certain that the corresponding $\overline{S_P{}^u}$ term would always remain less than or equal to zero. The same may be said of the S^v source term. Therefore, with respect to the staggered-grid control volumes for the U_e and V_n velocities, shown in Figs. 10(a) and (b), volume-averaged values of S^u and S^v, are formulated as given in the following equations.

$(\overline{S^u})_e$ is written as:

$$(\overline{S^u})_e = (\overline{S_C{}^u})_e + (\overline{S_P{}^u})_e \, U_e \tag{5-14}$$

where

$$(\overline{S_C{}^u})_e = (\beta + \frac{\partial \mu_t}{\partial x}\frac{\partial U}{\partial x} + \frac{\partial \mu_t}{\partial y}\frac{\partial V}{\partial x})_e \tag{5-15}$$

$$(\overline{S_P{}^u})_e = 0 \tag{5-16}$$

$(\overline{S^v})_n$ is expressed as:

$$(\overline{S^v})_n = (\overline{S_C{}^v})_n + (\overline{S_P{}^v})_n \, V_n \tag{5-17}$$

where

$$(\overline{S_C{}^v})_n = (\frac{\partial \mu_t}{\partial x}\frac{\partial U}{\partial y} + \frac{\partial \mu_t}{\partial y}\frac{\partial V}{\partial y})_n \tag{5-18}$$

$$(\overline{S_P{}^v})_n = 0 \tag{5-19}$$

With reference to Figs. 10(a) and (b), the e and n subscripts appearing

in the above equations indicate the e or n velocity grid-point locations. The β term is a constant, and its value is specified for the particular problem of interest. However, the gradients of velocity components and μ_t need to be calculated, and the methods used to do this will now be described.

If values of a variable are required at a grid-point location other than the one where they are normally calculated and stored, they are calculated as a volume-weighted average of the values at neighbouring grid points, where the variable is stored. For example, if the variable, ϕ, is stored at main-grid-point locations its value at a staggered-grid point location, say e in Figs. 7 and 10(c), is obtained from the following relation:

$$(\phi)_e = \frac{\{\phi_P * (\delta x)_{e-} + \phi_E * (\delta x)_{e+}\}}{(\delta x)_e} \qquad (5\text{-}20)$$

where the lengths $(\delta x)_{e-}$, $(\delta x)_{e+}$, and $(\delta x)_e$, are as shown in Fig. 7. The length ΔY_p is also used in the volume-averaging calculation, but it appears in both the numerator and denominator of Eq. (5-20) and is, therefore, not shown as it has no effect on the final form of the expression.

The x-direction gradient of ϕ at the staggered-grid locations, such as e in Figs. 7 and 10(c), is given as:

$$\left(\frac{\partial \phi}{\partial x}\right)_e = \frac{\phi_E - \phi_P}{(\delta x)_e} \qquad (5\text{-}21)$$

The x-direction gradient of ϕ at main-grid nodes is calculated as the volume-weighted average of the gradients of ϕ at a control-volume

face, in the fashion analogous to the calculation of $(\phi)_e$ in Eq. (5-20). Thus at the node P in Figs. 7 and 10(c):

$$(\frac{\partial \phi}{\partial x})_P = \{(\frac{\partial \phi}{\partial x})_e \frac{\Delta X_P}{2} + (\frac{\partial \phi}{\partial x})_w \frac{\Delta X_P}{2} \} / \Delta X_P$$

$$= \{(\frac{\partial \phi}{\partial x})_e + (\frac{\partial \phi}{\partial x})_w\} / 2 \qquad (5\text{-}22)$$

Using the same methodology as that employed to obtain Eqs. (5-20) to (5-22), the gradient terms in $(\overline{S_C{}^u})_e$, Eq. (5-15), were calculated. With reference to the terminology presented in Figs. 7 and 10(c), at a staggered-grid-point location, such as e, these terms were expressed as:

$$(\frac{\partial U}{\partial x})_e = \frac{(U_{ee} - U_w)}{(\delta x)_e} / 2 \qquad (5\text{-}23)$$

$$(\frac{\partial V}{\partial x})_e = \{\frac{(V_{nE} + V_{sE})}{2} - \frac{(V_n + V_s)}{2} \} / (\delta x)_e \qquad (5\text{-}24)$$

$$(\frac{\partial \mu_t}{\partial x})_e = \frac{\{(\mu_t)_E - (\mu_t)_P\}}{(\delta x)_e} \qquad (5\text{-}25)$$

and

$$(\frac{\partial \mu_t}{\partial y})_e = \{(\frac{\partial \mu_t}{\partial y})_P (\delta x)_{e-} + (\frac{\partial \mu_t}{\partial y})_E (\delta x)_{e+}\} / (\delta x)_e \qquad (5\text{-}26)$$

where

$$(\frac{\partial \mu_t}{\partial y})_P = \frac{\{(\mu_t)_n - (\mu_t)_s\}}{\Delta Y_P} \qquad (5\text{-}27)$$

and $(\partial \mu_t / \partial y)_E$ was calculated in a similar fashion. Since μ_t is a diffusion coefficient, values of μ_t at staggered-grid point locations were calculated as the harmonic mean, Eq. (4-7), of the μ_t values stored at adjacent main-grid nodes: For example, $(\mu_t)_n$ in Eq. (5-27) was calculated as the harmonic mean of the μ_t values stored at the P and N nodes

in Fig. 10(c).

Using procedures analogous to those just described for determining the gradient terms in $\overline{S_C{}^u}$, the gradient terms in $\overline{S_C{}^v}$, Eq. (5-17), were calculated for the V velocity staggered grid, depicted in Fig. 10(b).

k and ϵ equations

Careful consideration must be given to the linearization of the k and ϵ equation source terms, S^k and S^ϵ, of Eqs. (5-6) and (5-11). Physically, k and ϵ are scalar quantities that can only have positive or zero values. To ensure this during the computations, any terms that could cause the volume-averaged values of S^k or S^ϵ to become negative are modified and included in the respective $(\overline{S_P{}^k}\ k)$ or $(\overline{S_P{}^\epsilon}\ \epsilon)$ terms of $\overline{S^k}$ and $\overline{S^\epsilon}$. This is done following procedures similar to those suggested by Raithby and Schneider [42]. Numerical studies by Raithby have indicated that these procedures ensure and promote the rate of convergence of the solution procedure for the complete set of discretization equations, as outlined in Section 5.2.5.

The source term S^k is given by Eq. (5-6). With respect to the main-grid control volume shown in Fig. 6, the volume-averaged form of S^k at the node P, is expressed as follows:

$$(\overline{S^k})_P = (\overline{S_C{}^k})_P + (\overline{S_P{}^k})_P\ k_P \qquad (5\text{-}28)$$

where

$$(\overline{S_C{}^k})_P = (P_{k1} + P_{k2})_P \qquad (5\text{-}29)$$

$$(\overline{S_P{}^k})_P = - \frac{(D_k + E_k)_P}{k_P} \quad . \tag{5-30}$$

The expressions for P_{k1}, P_{k2}, E_k, and D_k are given by Eqs. (5-7), (5-8), (5-9), and (3-17), respectively. Since the D_k and E_k terms in Eq. (5-6) always make a negative contribution to the value of S^k, an artificial linear dependence on k is created by multiplying them both by (k_P/k_P), and they are put in the $\{(\overline{S_P{}^k})\ k\}_P$ part of $(\overline{S^k})_P$. The resulting form of the $(\overline{S_P{}^k})_P$ term is then given by Eq. (5-30). The value of k_P in Eq. (5-30) is taken as the value from the previous iteration, and is not changed till the beginning of the next iteration, as stated in Section 5.2.5.

As seen from Eqs. (5-7) to (5-9) and (3-17), values of μ, μ_t, ρ, ϵ, and the x and y gradients of U, V, and $k^{1/2}$ are required at main-grid points in the calculation of $\overline{S_P{}^k}$. The values used for μ, μ_t, ρ, and ϵ are those already stored at P. The gradients of variables, at main-grid points, are calculated following analogous procedures to the those described earlier for the calculation of gradients at staggered-grid points. The $k^{1/2}$ values are obtained from the k values stored at main-grid points, and these square root values are used for calculation of the x and y gradient terms of $k^{1/2}$. When calculating $(\overline{S^k})_P$, all gradients at P are first calculated and then squared, if required.

For the main-grid point P, in Fig. 6, $(\overline{S^\epsilon})_P$ is written as:

$$(\overline{S^\epsilon})_P = (\overline{S_C{}^\epsilon})_P + (\overline{S_P{}^\epsilon})_P \ \epsilon_P \tag{5-31}$$

where

$$(\overline{S_C{}^{\epsilon}})_P = (P_\epsilon + E_\epsilon)_P \quad . \tag{5-32}$$

$$(\overline{S^{P\epsilon}})_P = - \frac{(\rho\, f_{C2\epsilon}\, C_{2\epsilon}\, \epsilon)_P}{k_P} \tag{5-33}$$

The expressions for P_ϵ and E_ϵ are given by Eqs. (5-12) and (5-13). The JL and LS model forms of $f_{C2\epsilon}$, as given in Table 2, are used, and the value of $C_{2\epsilon}$ is that given in Table 1. As for $\overline{S^k}$, all k and ϵ values appearing in $\overline{S_C{}^{\epsilon}}$ and $\overline{S_P{}^{\epsilon}}$ are set to the values from the previous iteration, as mentioned in Section 5.2.5.

P_{k1} and P_{k2}, in Eq. (5-12) for P_ϵ, are the same as those calculated for $\overline{S_C{}^k}$. Procedures analogous to those already described for the calculation of gradient terms in $\overline{S^u}$ are used to calculate the second derivative velocity terms appearing in E_ϵ, Eq. (5-13). To do this, the first derivative terms, enclosed by the inner brackets, are calculated, and then the gradients of these terms are found to obtain the second derivatives at node P. These are then squared as indicated in Eq. (5-13).

The procedures described in this section for the calculation of gradient terms must be modified slightly when used to obtain gradients at a staggered-grid point that is located on a plate surface. For example, normally, the distance between the two main-grid locations is used in the denominator of Eq. (5-21). However, when point e lies at the interface between the plate and the flow region, the distance between the main-grid point, located in the flow, and the staggered-grid point, located on the plate surface, is used to calculate the gradient.

5.2.7 Final Convergence Criteria

The iterative solution procedure described in Section 5.2.5, is repeated until a specified convergence tolerance is achieved. To determine when this occurs, the relative change in U, V, k, and ϵ values is monitored. The absolute value of the change in the magnitude of each of these variables, from the preceding iteration to the current iteration, relative to the current iteration value, is calculated at each grid point along a designated vertical grid line in the calculation domain: The relative changes in the U and V velocities are calculated at the corresponding staggered-grid point locations. The maximum relative change, in each of the variables monitored, is then determined for each iteration. When the sum of the maximum relative changes from the two most recent iterations, for each variable monitored, is less than a specified tolerance, convergence of the flow and turbulence equations is considered to have been achieved. Unless otherwise stated, in this work, the convergence criteria used was that, for each dependent variable monitored , the sum of maximum relative changes over two successive iterations had to be less than 10^{-6}.

Initial monitoring of other quantities, such as the relative change in calculated mass flux, the average of absolute residual values, the "mass source" term in the P' equation, and of the absolute relative changes in variables at all grid points, indicated that the above-mentioned convergence criterion was satisfactory.

5.3 NUMERICAL TREATMENT OF THE MODEL EQUATIONS FOR TWO-DIMENSIONAL SIMPLE FULLY DEVELOPED FLOWS

For reasons discussed in Section 5.1, the low-Reynolds-number k-ϵ turbulence models of Jones and Launder [89], and Launder and Sharma [91] were selected for use in the numerical investigation of this thesis. The only difference in the forms of these two models is in the expression for the viscous damping function, $f_{c\mu}$, as shown in Table 2. To gain insight as to which model would be most appropriate for the type of flows being studied in this work, both were used to simulate turbulent two-dimensional simple fully developed flows in straight channels. Such flows can be simulated using one-dimensional forms of the k-ϵ turbulence model equations, and allow an economical performance evaluation of the two low-Reynolds-number k-ϵ turbulence models under consideration. This is due to the reduced computational effort required to solve a one-dimensional flow problem, compared to that needed to solve the two-dimensional model equations for interrupted-plate duct flows.

The Reynolds number, Re_d, values for the fully developed duct flows studied covered the same range as the nominal flow Reynolds number, Re_m, of the two-dimensional periodic fully developed duct flows of interest here. In addition, flows having higher Reynolds numbers were simulated to determine at what point the low-Reynolds-number k-ϵ models would become equivalent to the standard, or high-Reynolds-number, version of the k-ϵ model. To do this, flow results were also obtained using the standard k-ϵ turbulence model.

5.3.1 Model Equations

In turbulent two-dimensional simple fully developed duct flows, the time-mean velocity field is invariant in the flow direction and has no cross-stream component. The gradient of the time-mean pressure is constant in the flow direction and zero in the cross-stream direction. Such a flow can be modc'led using the following one-dimensional forms of the low-Reynolds-number k-ϵ model equations, presented in Chapter III:

x momentum equation

$$0 = \frac{\partial}{\partial y}(\Gamma_u \frac{\partial U}{\partial y}) + S^u \qquad (5\text{-}34)$$

k equation

$$0 = \frac{\partial}{\partial y}(\Gamma_k \frac{\partial k}{\partial y}) + S^k \qquad (5\text{-}35)$$

ϵ equation

$$0 = \frac{\partial}{\partial y}(\Gamma_\epsilon \frac{\partial \epsilon}{\partial y}) + S^\epsilon \qquad (5\text{-}36)$$

The expressions for Γ_u, Γ_k, and Γ_ϵ are given by Eqs. (3-4), (3-15), and (3-19), respectively.

In the x-momentum equation, the pressure gradient term , which is constant and is specified as a problem parameter, is placed in S^u so that:

$$S^u = - (\frac{\partial P}{\partial x}) \qquad (5\text{-}37)$$

The corresponding forms of $\overline{S_C{}^u}$ and $\overline{S_P{}^u}$ in $\overline{S^u}$ are:

$$\overline{S_C{}^u} = - \left(\frac{\partial P}{\partial x}\right) \tag{5-38}$$

$$\overline{S_P{}^u} = 0 \tag{5-39}$$

The form of S^k, in Eq. (5-35), is:

$$S^k = P_{k1d} - D_k - E_{k1d} \tag{5-40}$$

where D_k is given by Eq. (3-17), and:

$$P_{k1d} = \mu_t \left(\frac{\partial U}{\partial y} \right)^2 \tag{5-41}$$

$$E_{k1d} = 2 \mu \left[\left\{ \frac{\partial}{\partial y}(k^{1/2}) \right\}^2 \right] \tag{5-42}$$

In Eq. (5-36), S^ϵ is:

$$S^\epsilon = P_{\epsilon 1d} - D_\epsilon + E_{\epsilon 1d} \tag{5-43}$$

with D_ϵ given by Eq. (3-21), and:

$$P_{\epsilon 1d} = \frac{\epsilon}{k} \left(C_{1\epsilon} P_{k1d} \right) \tag{5-44}$$

$$E_{\epsilon 1d} = \frac{2\mu\mu_t}{\rho} \left\{ \frac{\partial}{\partial y}\left(\frac{\partial U}{\partial y} \right) \right\}^2 \tag{5-45}$$

The treatment of the S^k and S^ϵ terms requires some special consideration, as mentioned in Section 5.2.6, and will be discussed shortly. Since there are no unknown pressure terms in Eq. (5-34), all three model equations, (5-34) to (5-36), can be treated as convection-diffusion type

equations, with convection terms set to zero, and solved using procedures akin to those described for Eq. (4-1). This means that all variables, including U velocities, are stored at main-grid points. Gradients of variables, appearing in the source terms of the model equations, are calculated using procedures analogous to those used for determining similar gradients in Section 5.2.6.

5.3.2 Domain Discretization

From the discussion in Chapter III, it will be recalled that the principle difference between the low-Reynolds-number and standard k-ϵ turbulence models is in the handling of the near-wall regions. In the standard k-ϵ model, boundary conditions are not specified at wall surfaces but rather at grid points that are located in the fluid at a non-dimensional perpendicular distance from the wall of $30 \leq y^+ \leq 100$ [75]: In this investigation a value of $y^+ = 30$ is used. When using low-Reynolds-number turbulence models, the U, k, and ϵ equations are solved all the way to the wall boundary points. This requires that a large number of grid points be placed in the $y^+ < 30$ region, in order to ensure adequate resolution of the steep gradients of the turbulence properties that occur there, particularly through the viscous sublayer. The one-dimensional grids for fully developed duct flows were generated such that a designated number of grid points were always located in the near-wall regions where $y^+ < 30$, regardless of the value of U_τ, which, for the same duct dimensions, increases with increasing flow rate. From Eq. (3-31), it can be seen that as U_τ increases, the aforementioned near-wall regions will occupy less of the total calculation domain, and the core-flow region located between these near-wall regions will be

correspondingly larger. In such a case, more grid points were placed within the central core region, resulting in a greater total number of grid points, although the number of grid-points within the near-wall regions ($y^+ < 30$) was not changed. On average, for the entire range of flow rates investigated, approximately 40 to 50 percent of all the grid points were located in such near-wall regions. A more detailed description of the grid-generation procedure is given in Appendix 1.

5.3.3 Formulation of the k and ϵ Source Terms

The manner in which a source term is linearized can have a significant effect on the rate of convergence of the iterative solution of the discretization equations [41]. There are many ways that the expression for $\overline{S^k}$ can be split into $\overline{S_C{}^k}$ and $(\overline{S_P{}^k}\ k)$. The same may also be said of the expression for $\overline{S^\epsilon}$. During preliminary testing, using the one-dimensional k-ϵ model equations, the source term formulation suggested in Ref. [42] was compared to several other formulations that had been used by the present author and found to work well for one-dimensional flow calculations. In particular, two different formulations for $\overline{S^k}$ and $\overline{S^\epsilon}$ were used, and the effect that these had on the overall rate of convergence of the solution to the coupled sets of U, k, and ϵ discretization equations was evaluated.

$\overline{S^k}$ Treatment (1): $\overline{S^k}_1$

This formulation is the one suggested in [42] and used for the two-dimensional form of $\overline{S^k}$, in Section 5.2.6. At a grid point P, $(\overline{S^k})_P$ is given by Eq. (5-28). For turbulent simple fully developed duct flow:

$$(\overline{S_C{}^k})_P = (P_{k1d})_P \tag{5-46}$$

$$(\overline{S_P{}^k})_P = - \frac{(D_k + E_{k1d})_P}{k_P} \tag{5-47}$$

P_{k1d}, D_k, and E_{k1d} are as defined in Section 5.3.1.

$\overline{S^k}$ Treatment (2): $\overline{S^k}_2$

In Treatment (1) for $\overline{S^k}$, the negative terms in $(\overline{S^k})_P$ are multiplied by (k_P/k_P) to make them linearly dependent on k_P, in an artificial manner. The resulting form of $(\overline{S_P{}^k})_P$ is shown in Eq. (5-47). By doing this, $(\overline{S_C{}^k})_P$ and $(\overline{S_P{}^k})_P$ will always be positive and negative, respectively, thus ensuring that k_P is always positive [41]. If, during the iterative solution procedure, k_P becomes very small, the artificial $(\overline{S_P{}^k})_P$ term, given by Eq. (5-47), can become large, compared to the other terms in the discretization equation for k_P. $(\overline{S_P{}^k})_P$ would then make a_P, in Eq. (4-11), correspondingly large and result in an even lower value of k_P. Such an event can occur during the early stages of the iterative solution process when, due to a poor initial guess for the values of the dependent variables, it could take several iterations before the distribution of U, k, and ϵ assume forms similar to those of the converged solution profiles. A small value of k_P, caused by an artificially large $(\overline{S_P{}^k})_P$, could substantially increase the number of iterations needed before proper profile trends for k are obtained. For this reason, it was decided to try the following alternative procedure for calculating k source terms and solving the k equations.

Step 1:

Formulate $(\overline{S_C{}^k})_P$ and $(\overline{S_P{}^k})_P$ as:

$$(\overline{S_C{}^k})_P = (P_{k1d} - D_k - E_{k1d})_P \tag{5-48}$$

$$(\overline{S_P{}^k})_P = 0 \tag{5-49}$$

Step 2:

Store the k field values from the previous iteration. Then solve the k equations using these previous iteration values for the initial k field distribution.

Step 3:

If a value of the newly calculated k field from Step 2, say k_P, is less than zero, reformulate $(\overline{S_C{}^k})_P$ and $(\overline{S_P{}^k})_P$ in the same manner as that in Treatment (1) for $\overline{S^k}$, using Eqs. (5-46) and (5-47), at that particular P location only. In Eq. (5-47), the previous iteration value of k_P is to be used, not the negative value just calculated.

Step 4:

Repeat Steps 2 and 3 until all k values calculated in Step 2 are positive. When this occurs, use these values as the current iteration values of k and proceed to solve for ϵ.

When a value, k_P, calculated in Step 2, is less than zero, it means that $(\overline{S_C{}^k})_P$ was negative and large enough in magnitude to cause the value of k_P to become negative. Usually, this iterative process, between Steps 2 and 3, is only required in the initial few iterations of the solution procedure. Once the calculated k field begins to take the shape of the converged solution, the source term treatment of Eq. (5-48) does not result in negative values of k_P.

$\overline{S^\epsilon}$ Treatment (1): $\overline{S^\epsilon}_1$

As with Treatment (1) for $\overline{S^k}$, this formulation of $\overline{S^\epsilon}$ is based on the one suggested in [42] and used in Section 5.2.6. At a grid point P, the source term expression $(\overline{S^\epsilon})_P$ is given by Eq. (5-31), and for the one-dimensional form of the ϵ equation, $(\overline{S_C{}^\epsilon})_P$ and $(\overline{S_P{}^\epsilon})_P$ are:

$$(\overline{S_C{}^\epsilon})_P = (P_{\epsilon 1d} + E_{\epsilon 1d})_P \tag{5-50}$$

$$(\overline{S_P{}^\epsilon})_P = - \frac{(\rho\, f_{C2\epsilon}\, C_{2\epsilon}\, \epsilon)_P}{k_P} \tag{5-51}$$

$P_{\epsilon 1d}$ and $E_{\epsilon 1d}$ are as defined in Section 5.3.1, and $C_{2\epsilon}$ and $f_{C2\epsilon}$ are given in Tables 1 and 2, respectively.

$\overline{S^\epsilon}$ Treatment (2): $\overline{S^\epsilon}_2$

In Eq. (5-43), since D_ϵ contains an ϵ^2 term, S^ϵ is a nonlinear function of ϵ. Following the recommendation of Patankar [41], at a grid point P, $\overline{S^\epsilon}$ is linearized as:

$$\begin{aligned}(\overline{S^\epsilon})_P &= \left(\frac{\partial \overline{S^\epsilon}}{\partial \epsilon}\right)^{\circ}_P (\epsilon - \epsilon^\circ)_P + (\overline{S^{\epsilon\circ}})_P \\ &= (D_\epsilon{}^\circ + E_{\epsilon 1d})_P + (A_\epsilon - B_\epsilon{}^\circ)_P\, \epsilon_P \end{aligned} \tag{5-52}$$

where

$$(A_\epsilon)_P = \left\{ C_{1\epsilon}\, \frac{\mu_t}{k} \left(\frac{\partial U}{\partial y} \right)^2 \right\}_P \tag{5-53}$$

$$(B_\epsilon{}^\circ)_P = \left\{ 2\, \rho\, f_{C2\epsilon}\, C_{2\epsilon}\, \frac{\epsilon^\circ}{k} \right\}_P \tag{5-54}$$

The superscript ^{o} appearing on ϵ or terms containing ϵ, indicates that the value of ϵ from the previous iteration is to be used. The other terms appearing in these equations are as defined previously in this chapter. In order to ensure that the $\overline{S_C^{\epsilon}}$ and $\overline{S_P^{\epsilon}}$ terms are always positive and negative, respectively, they are calculated, following the recommendation in [41], as:

If $(A_\epsilon < B_\epsilon^{o})_P$ then

$$(\overline{S_C^{\epsilon}})_P = (D_\epsilon^{o} + E_{\epsilon 1d})_P \tag{5-55}$$

$$(\overline{S_P^{\epsilon}})_P = (A_\epsilon - B_\epsilon^{o})_P \tag{5-56}$$

otherwise

$$(\overline{S_C^{\epsilon}})_P = (D_\epsilon^{o} + E_{\epsilon 1d})_P + (A_\epsilon\ \epsilon^{o})_P \tag{5-57}$$

$$(\overline{S_P^{\epsilon}})_P = -\ (B_\epsilon^{o})_P \tag{5-58}$$

Calculation of $\overline{S_C}$ and $\overline{S_P}$: Procedure A

In the formulation given by Treatment (1) for both the k and ϵ source terms, Raithby and Schneider [42] state that convergence is accelerated if the previous iteration values of k_P and ϵ_P are used wherever they appear in $(\overline{S_C})_P$ and $(\overline{S_P})_P$ terms. This practice is denoted as Procedure A.

Calculation of $\overline{S_C}$ and $\overline{S_P}$: Procedure B

The other procedure that can be employed when calculating k and ϵ source terms at a grid point, P, is to use the most recent values of k_P and ϵ_P. Therefore, the previous iteration values of k_P and ϵ_P are used to calculate $(\overline{S_C^{k}})_P$ and $(\overline{S_P^{k}})_P$. For the analogous terms in $\overline{S^{\epsilon}}$, the newly calculated values of k_P in the current iteration are used along with the previous iteration values of ϵ_P.

The effect of using both procedures, A and B, for specifying k_p and ϵ_p were also evaluated for the different source term formulations presented in this section. Particular source term combinations will be designated according to the treatment and procedure used in the formulation: For example, a source term combination consisting of the Treatment (1) formulations for both $\overline{S^k}$ and $\overline{S^\epsilon}$ using Procedure A will be designated as $S^k{}_1$-$S^\epsilon{}_1$-A. Tests were undertaken to determine which formulations yield the best rate of convergence. The results of these tests will be discussed in Chapter VII.

5.3.4 Use of the Standard k-ϵ Model

Results were also obtained using the standard k-ϵ turbulence model. These were then compared to the low-Reynolds-number model results. The model equations and source term formulations are the same as those presented in Section 5.3.1, except that E_{k1d} and $E_{\epsilon 1d}$ in Eqs. (5-40) and (5-43), respectively, are set to zero, and $f_{c2\epsilon}$ in Eq. (3-21) for D_ϵ becomes one.

The grids used are the same as those used for corresponding low-Reynolds-number calculations, except, of course, they exclude all grid points in the near-wall regions where $y^+ < 30$. Details of grid generation are given in Appendix 1. The specification of near-wall boundary conditions for the standard k-ϵ model are explained in Section 3.3.

CHAPTER VI

EXPERIMENTAL APPARATUS AND PROCEDURES

An experimental facility was specially designed and constructed in an initial phase of this research effort [109]. A schematic representation of this facility is shown in Fig. 16. Most of the flow circuit can be seen in Fig. 17: The air flow direction is from right to left in the photograph. The flow facility consists of the following key elements: (i) a test section; (ii) a flow transition section; (iii) a flow metering section; (iv) a flow control, generation, and exhaust section; and (v) a data acquisition and processing system. Brief descriptions of these key elements and the experimental procedures used are given in the following sections of this chapter: Detailed descriptions of all sections and the procedures used in the initial testing and calibration of the experimental facility are available in [109]. Some modifications have been made to improve the facility described in [109], and these are noted and described in this chapter.

6.1 TEST SECTION

The experimental facility was designed so that the test section could easily be detached, disassembled, reconfigured, and reattached to the rest of the flow circuit. This allowed three different interrupted-plate rectangular duct configurations to be investigated. The final configurations of the test sections were arrived at by using representative compact heat exchanger dimensions and overall pressure drop data available in [1-5,11,24-26,53,54], in the context of the capabilities of the rest of the flow circuit. As was mentioned in Chapter I, one of the

objectives of this work is to investigate the effect on the flow of the thickness of the plates in an interrupted-plate duct. Each of the three interrupted-plate duct test sections used, which will be referred to as Ducts 1 to 3 in the remainder of this thesis, was obtained by using the same overall rectangular-duct section and inserting plates of a desired thickness along its centerline. The actual dimensions measured from the final, assembled, test sections are presented in Table 3. With reference to the nomenclature given in Fig. 2, the nominal dimensions for Ducts 1 to 3 are given below.

All of Ducts 1 to 3:

Overall length, ℓ = 2133.6 mm

Width, b = 152.4 mm

Half Height, H = 12.7 mm

Plate Length, L = 25.4 mm

Interplate spacing, s = 25.4 mm

Module Aspect Ratio, λ = b/H = 12.0

Full-Duct Aspect Ratio, ς = b/(2H) = 6.00

Plate Length Ratio, L^* = L/H = 2

Plate Spacing Ratio, s^* = s/H = 2

Duct 1:

Half-thickness of plate, t = 0.400 mm

Plate thickness ratio, t^* = t/H = 0.0315

Duct 2:

Half-thickness of plate, t = 0.800 mm

Plate thickness ratio, $t^* = t/H$ = 0.0630

Duct 3:

Half-thickness of plate, t = 1.60 mm

Plate thickness ratio, $t^* = t/H$ = 0.126

The test sections used in this study were comprised of two rectangular interrupted-plate duct sections connected in series: (1) a leading section, 1524.0 mm long, made of aluminum, and instrumented for wall static pressure measurements; and (2) a flow visualization section, 609.6 mm long, and made of clear acrylic. The interrupted-plate duct test-section geometry was continuous from the first plate of the aluminum duct through to the last plate in the acrylic duct. With the above-mentioned length, a minimum of 23 geometrically similar modules, such as ABCDE in Fig. 2, could be configured in the leading aluminum duct. Thus periodic fully developed flow could be considered to prevail over at least the last 13 modules of the aluminum duct and all the modules of the acrylic duct, for each test section.

6.1.1 Aluminum Duct Details

An exploded view of the aluminum section of Duct 3 is shown in Fig. 18. The top and bottom walls, ① and ② , are machined from 1524.0 mm long, 12.7 mm thick, and 203.2 mm wide aluminum plates. Two sets of adjacent shoulders, ③ and ④ , are milled along the edges of these plates, to a depth of 6.8 mm over their entire length. These

shoulders are used for proper location and alignment of three sets of side walls, ⑤ , ⑥ , and ⑦ , which are machined from flat aluminum bars. The outer set of side walls, ⑦ , are each 12.7 mm thick, 38.1 mm high, and 1524.0 mm long. Both sets of inner side walls, ⑤ and ⑥ , are 12.7 mm thick, 19.05 mm high, and 1524.0 mm long. The bottom set of these walls, ⑥ , have a total of 239 holes, 3.2 mm in diameter and 6.4 mm deep, drilled along their centerline, with a uniform spacing of 6.35 mm between the centers of adjacent holes. To obtain a desired plate spacing, steel dowel pins, ⑧ , 3.2 mm in diameter and 12.7 mm long, are fitted into the appropriate holes in the bottom inner side walls. Suitable positioning holes are drilled 5.0 mm in from the end of each plate, ⑨ , of the colinear array. This ensures accurate positioning of the plates, which are made of precision ground steel cut to a cross-flow width of 175.0 mm and guaranteed by the manufacturer to have the following dimensions and tolerances: with reference to the notations in Fig. 2, $L = 25.40 \pm 0.025$ mm and, for Duct 3, $2t = 3.175 \pm 0.025$ mm. To allow the upper set of inner side walls, ⑤ , to sit on top of the dowel pins protruding through the array of colinear interrupted plates, a groove, 4 mm wide and 6.4 mm deep, has been milled along the centerline over the whole length of these walls, on the side facing the dowel pins. Interplate spacers, not shown in Fig. 18, are placed on the top surface of the inner side walls, filling in the gaps between the trailing and leading edges of two successive plates. These 25 mm long spacers are 12.7 mm wide, with the same thickness as the plates, and they are accurately positioned in the same manner as the plates: A positioning hole, through which a steel dowel pin can be passed, is drilled through the center of each spacer.

Screws are used to fasten the inner side walls, ⑤ and ⑥ , to the respective upper and lower plates, ① and ②. The entire duct is assembled and held together using machine screws and nuts that pass through holes drilled through the outer side walls, along their centerline, and corresponding holes drilled along the centerlines of the outer shoulders, ④ , of the top and bottom plates, ① and ②. Aluminum angles, ⑩ , are attached to each end of the duct section and, with the use of bolts and nuts, they are used to connect the aluminum duct to the downstream acrylic duct section. When completely assembled and connected to the flow facility, the edges of all joints where two or more parts of the duct mated were sealed with two layers of ducting tape. This ensured airtight joints along the entire test section.

Axial pressure distributions were measured with the aid of 221 taps, ⑪ , each with a hole diameter of 0.5 mm, deployed along the centerline of the bottom plate of the aluminum duct section. The first and last of these pressure taps were drilled 63.5 mm from each end of the bottom plate and the other holes were drilled at regular intervals, with a distance of 6.35 mm between the centers of adjacent holes. The measured locations of these holes with respect to the downstream end of the aluminum duct section, are given in Table 4. With the L and s dimensions given in Section 6.1, the spacing of the pressure taps ensures that 8 uniformly spaced wall static pressure measurements are obtained along the length of a geometric module, at the locations shown and labelled in Fig. 19: LE is located over the leading edge of the plate; LC is located over the plate, midway between its leading edge and center; CP is located over the center of the plate; CT is located over the plate, midway between its center and trailing edge; TE is located over the

trailing edge of the plate; G1 is the first point downstream of TE, midway between TE and the center of the interplate gap; G2 is located over the center of the interplate gap; and G3 is located midway between the G2 and the leading edge of the first plate in the next downstream module. It should be noted here that the bottom wall in Fig. 18, with pressure taps located along its centerline, corresponds to the top duct wall shown in Figs. 17 and 19.

The construction details of Ducts 1 and 2 differ from those of Duct 3, just presented, only in that the plate thickness is decreased: halved from Duct 3 to 2, and halved again from Duct 2 to 1. To maintain the same value of module aspect ratio , λ, aluminum shims of the appropriate thickness, 0.80 mm for Duct 2 and 1.19 mm for Duct 1, were placed along the length of the Duct side walls, ⑤ and ⑥ , on the horizontal surfaces that mated with the top and bottom aluminum plates. This ensured that the height of the duct, 2H, remained the same for Ducts 1, 2, and 3. In this connection, the thickness of the interplate spacers was also changed as the plate thickness changed.

A photograph of an assembled interrupted-plate rectangular duct test section, appropriately mounted and fitted to the rest of the flow circuit, is shown in Fig. 20. The inlet, or upstream end, of the aluminum duct is seen at the lower-right edge of the picture. The static pressure taps, the machine screws that hold the duct together, and the connection to the downstream acrylic duct are all clearly seen. A photograph of the top and bottom plates of the aluminum duct, showing the inner and outer side walls and the array of colinear interrupted plates, is given in Fig. 21.

Further details on the design of the interrupted-plate aluminum duct, including the construction of the pressure taps, are available in [109].

6.1.2 Acrylic Duct Details

The interrupted-plate acrylic duct section is a continuation of the interrupted-plate configuration in the aluminum duct sect on. It allows plate-surface flow visualization studies to be performed. The dimensions and construction details of this duct are similar to those presented for the aluminum duct in Section 6.1.1, with the following exceptions: (i) all the walls of this section are made from clear acrylic, except for the lower inner side walls which are made of aluminum; (ii) the length of the duct is 609.6 mm instead of 1524.0 mm; (iii) there are no static pressure taps along the length of the duct; (iv) the colinear array of plates are painted with a thin layer of flat-black paint to allow good contrast with surface flow visualization paint patterns; and (v) a section of the top plate can be removed after the entire duct has been assembled and connected to the flow circuit.

The top acrylic plate of the acrylic duct consists of three parts: two 114.3 mm long sections at the upstream and downstream ends of the duct, and a 381.0 mm long central section. The upper inner side walls are also sectioned so that the appropriate lengths are fastened to each upper plate section. The two end sections of the upper plate and the rest of the acrylic duct, except for the central upper plate section, are assembled and held together using machine screws and nuts. The

machine screws pass through holes in the outer side walls and the outer shoulders of the top end plates and the bottom plate. When the duct is assembled, the two end sections of the top plate provide a sliding fit for the central section of this plate. During an experimental run, the joints between the central section of the upper plate and the rest of the duct are sealed with two layers of ducting tape to ensure an air-tight seal, as with all other locations where two surfaces mate. The removable central portion of the upper plate allows ready access to the array of interrupted-plates while the rest of the acrylic duct section is still fastened to the flow circuit. This facilitates the removal of the plates when they need to be prepared for flow visualization studies.

In Figs. 17, 20, and 22, the acrylic, or flow visualization, portion of the interrupted-plate rectangular duct test section is seen connected to the downstream end of the aluminum duct section. A close-up view of this acrylic section, given in Fig. 22, clearly shows the colinear array of plates along its length, the connection to the upstream aluminum section on the right, and the connection to the downstream flow transition section. The access to the array of plates that is allowed by the removal of the central top-plate section of the duct is demonstrated in Figs. 23 to 25. In these figures, the surfaces of the fourth, fifth, and sixth plates downstream from the inlet of the acrylic duct section have been painted for the flow visualization study. Figure 25, in which the fifth plate has been removed, shows details of the inner side walls, the plates and dowel pins used to construct the colinear interrupted-plate array, and the interplate spacers used to fill the gaps between plates along the inner side walls. These details have been described in Section 6.1.1, and they are common to both the aluminum and the acrylic

sections of the interrupted-plate duct test section.

6.2 FLOW METERING SECTION

The main flow passage in the flow metering section is a 88.9 mm I.D. and 1244.6 mm long tube made of clear acrylic. This section can be seen at the far-left side of Fig. 17. The flow rates are obtained using stagnation pressure measurements from a traversing pitot tube and static pressure measurements from two taps in the flow tube wall. The pitot tube can be positioned to an accuracy of ± 0.02 mm. Volumetric flow rates are determined by employing the ten-point log-linear method of Winternitz and Fischl [45]. In the design, construction, and assembly of the flow metering section, the recommendations of Ower and Pankhurst [46] and Shaw [119] were followed as closely as possible, in order to minimize the errors in the stagnation and static pressure measurements. Further details are given in [109].

6.3 FLOW TRANSITION SECTION

The flow transition section can be seen in Fig. 17, attached to the downstream end of the interrupted-plate rectangular duct test section on one side and to the upstream end of the flow metering tube on the opposite side. This section consists of two main parts: a flow redevelopment duct of rectangular cross section and a flow adjustment box. The rectangular flow redevelopment duct attaches to the downstream end of the interrupted-plate rectangular duct test section on one end and to the flow adjustment box on the other end. It is used to ensure that the flow in the test section is, as much as possible, free of the effects

caused by the transition from a duct of rectangular cross section to the circular cross section tube of the flow metering section. The flow adjustment box allows the air leaving the rectangular redevelopment duct to redistribute itself and enter the circular cross section flow metering tube axisymmetrically. Design and construction details are given in [109].

6.4 FLOW CONTROL, GENERATION, AND EXHAUST SECTION

Some black colored rubber and plastic ducts, and two flow control valves, which constitute a part of this section can be seen in the upper left corner of Fig. 17. A centrifugal-type, constant-speed, blower (Regenair R7100a), driven by a 10 HP AC motor with a rotor speed of 3450 rpm, was used in the suction mode to generate the air flow. The blower was mounted in a room adjacent to the Heat Transfer Laboratory, on the opposite side of the wall shown in Fig. 17. Additional details and operational characteristics of the blower are given in Appendix 2. The exhaust air coming out of the blower was passed to the outdoor environment to ensure that it did not disturb the air entering the test section. The use of two flow control valves, as shown in Figs. 16 and 17, made it possible to supply the blower with an adequate supply of air over the whole range of test-section flow rates considered in this thesis.

6.5 SUPPORTING EQUIPMENT, INSTRUMENTATION, AND MATERIALS

Brief descriptions of the key components of the equipment and instrumentation used to measure, record, and process the experimental

data, and materials used in the flow visualization studies, are given in this section.

6.5.1 Pressure Measurement Instrumentation

Measurements of atmospheric, static, and dynamic pressures were required in the investigation.

The atmospheric pressure was measured using a Fortin-type mercury-in-glass barometer that was accurate to ± 0.2 mm of mercury.

Static gauge pressures in the flow metering section and all other differential pressures greater than 1 kPa were measured using an inclinable reservoir-type manometer (Type 5 Airflow Manometer, Airflow Developments, Canada, Ltd.). The manufacturer's specifications state that the manometer fluid, a dyed blend of Paraffin, has a specific gravity of 0.784 at 20°C and that the manometer is accurate to ± 1% of the reading or ± 0.13 mm vertical height, whichever is larger. A calibration of the manometer, performed in the Heat Transfer Laboratory, confirmed these specifications.

All differential static pressures of less than 1 kPa were measured using an integral Barocel pressure transducer (Datametrics, Model 590-D-1kPa-2Q8-V1X-4D). Its output is a 0 to 10 volts DC signal that is linearly proportional to positive differential pressures applied across its diaphragm over a full scale range of 0 to 1 kPa. It was determined that the unit is accurate to within ± 0.05 Pa, which is accounted for by assuming an uncertainty in the output signal of $\delta V_{cal} = \pm 500\ \mu V$, when

measuring positive pressure differentials ranging from 0.2 Pa to 1 kPa. Details of this calibration procedure are given in Appendix 3. More detailed descriptions of the transducer and its incorporation into the overall experimental flow facility are available in [109].

Differential pressure measurements from the numerous static pressure taps of the test section were done using an Scanivalve mechanical multiplexor (Scanivalve Corp., Model 48D9-1/2) driven by a solenoid drive (Scanivalve Corp., Model DS4-48) that was controlled by a Scanivalve controller unit (Scanivalve Corp., Model CTLR10P/S2-S6) This Scanivalve mechanical multiplexor has a 48-port detachable pneumatic connector which allows as many as 48 pressure lines, made of 1.6 mm vinyl tubing (Scanivalve Corp., VINL-063 vinyl tubing), to be connected to the Scanivalve. This enabled a sequential connection of 48 pressure ports, one at a time, to the Barocel pressure transducer: The use of two such connectors allowed a total of 96 pressure lines to be handled by one Scanivalve unit and one Barocel transducer. The reader is referred to [109] if more detailed information is required.

6.5.2 Temperature Measurements

The air temperature in the flow metering cross section was measured using a chromel-constantan thermocouple, made of 30-gauge chromel and constantan wires insulated with teflon (Omega TT-E-30). Thermocouple attachments were done using a two-part epoxy adhesive (Omegabond 101). This thermocouple was mounted on a traversing thermocouple probe and connected to an electronic digital thermometer (Omega, Model 410A) with an internal reference junction and a temperature resolution of 0.1 °C.

Measurements of the ambient air temperature were done using an alcohol-in-glass thermometer having a temperature resolution of 0.2 °C.

6.5.3 Dimension Measurements

The cross-sectional dimensions of the assembled test sections and the interplate spacings of the colinear plate arrays were measured using a vernier caliper having a resolution of 0.02 mm.

6.5.4 Data Acquisition and Processing System

Most of the pressure measurements made in this work were recorded and processed using a microprocessor-based data acquisition unit (Hewlett-Packard Model 3497A). This unit was used to receive, display, store, and transfer to the main controller unit the 0 to 10 V DC output signal from the Barocel pressure transducer. The digital voltmeter of this unit has an accuracy of $\pm$ 1 μV DC. The controller unit of the Scanivalve was also controlled by the data acquisition unit, via commands sent from the main controller unit.

The main controller unit was a desk-top scientific microcomputer (Hewlett-Packard Model 86B) which interfaced to the aforementioned data acquisition unit. Software to operate this data acquisition and control system was written in the BASIC computer language. This software allowed all the experimental data to be processed and stored for future retrieval, analysis, and hardcopy output.

Additional details concerning the data acquisition unit, the main controller unit, and the computer software written for the main controller unit, are available in [109].

6.5.5 Materials Used for Surface Flow Visualization

In this work, after some initial testing of various surface flow visualization techniques presented in [47,120], it was decided that plate-surface streamline patterns could be best obtained using a surface oil-flow technique. This technique involves coating the surface of a plate with a paint made of a powdered pigment mixed with a suitable oil. When put in an air flow, details of the flow in the immediate vicinity of the plate are shown by the surface streamline patterns formed. The reader is referred to [47] for a description of the physics of this process.

Two types of kerosene based paints were used in this work: Titanium Dioxide (TiO_2), an opaque fine white powder, was used as the pigment in one paint; and a fluorescent orange pigment (Day-glo Color Corp., A-15-N Blaze Orange) was used in the other paint. In addition, when required, Oleic acid ($C_{18}H_{34}O_2$) was used as an additive to control the extent of flocculation by pigment particles in the kerosene: This allowed well defined streaks to be produced. The properties of these substances are listed in Appendix 4. The amounts of different materials required to create a suitable paint varied, depending on the flow rate, and will be discussed in Section 6.6.4.

A paint brush with a flat one-inch wide sable-hair tip was used in

the application of the flow visualization paint to the surface of the plate.

As was mentioned in Section 6.1, each plate in the colinear array of plates in the flow visualization duct section was spray painted with a thin layer of flat-black paint. This served to provide high contrast between the plate surface and the paint pigment, particularly in the case of the white TiO_2 pigment, and thereby facilitated photography of the resulting streak patterns.

Two 250 W tungsten lamps were used to illuminate the streaks formed by the TiO_2 pigment. Photographs of dried TiO_2 streamline patterns were taken using high contrast Kodak Ektagraphic HC slide film (ASA 8). Some photographs of wet streamline patterns were taken while the plates were still in the flow, and before the TiO_2 flow visualization paint had dried, using tungsten balanced Kodak Ektachrome slide film (ASA 160).

The streaks formed by the fluorescent Day-glo pigment were illuminated in a dark enclosure using a long-wave black light (Panosonic Blacklight Blue - F15 T8/BL-B), and they were photographed using Kodak Ektachrome Daylight slide film (ASA 100).

6.6 EXPERIMENTAL PROCEDURES

In this section, brief descriptions are given of the procedures used to obtain differential static pressure measurements, the air flow rate in the flow metering section, plate-surface streamline patterns, and reported experimental uncertainties. Following that, a step-by-step

description of the overall procedure used to run this experiment is presented.

6.6.1 Differential Static Pressure Measurements

Wall static pressure measurements in the aluminum duct portion of the test section were made in the differential mode, with reference to the static pressure at a suitable initial reference port. The gauge static pressure at this reference port, and the gauge static pressures in the flow metering section were measured using the inclinable manometer mentioned earlier in Section 6.5.1.

Differential static pressures of less than 1 kPa, were measured using the integral Barocel pressure transducer described in Section 6.5 1. In order to minimize output signal fluctuations caused by electrical noise, a very stable DC power supply to the Barocel transducer was used, and all signal cables were shielded by several wraps of aluminum foil. Cyclical fluctuations in the output signal of the Barocel, caused by the inherent static pressure fluctuations in turbulent flows and flows generated by centrifugal blowers, and by low-level 60 Hz AC noise, were filtered out by using the following time-averaging procedure. For each measurement, the data acquisition system was programmed to take 60 discrete readings of the Barocel output over a period of 13 seconds, compute the arithmetic mean of these readings, and record this value. In test runs, it was established that this procedure provided a good degree of repeatability [109]. A quantitative estimate of this repeatability, using the procedure described later in Section 6.6.3, was made for each flow rate and duct combination studied,

and included in the calculation of the uncertainty in the final results.

Over a period of 24 hours, the zero-drift in the Barocel output signal was found to be as much as ± 0.003 V. However, the time required to complete one data run was between one and two hours, and the problem of zero-drift could be overcome by using the following procedure. For each run, five zero readings were taken before the start of the run and five zero readings were taken at the end of the run. The average of the ten zero readings was then subtracted from all other differential pressure readings taken during the run to obtain their correct values. It was found that this procedure reduced the zero-drift to acceptable levels [109]. A quantitative measure of the zero-drift was calculated for each set of pressure measurements, using the method outlined later in Section 6.6.3, and this value was accounted for in the calculation of overall experimental uncertainties.

6.6.2 Air Flow Rate Measurements

In the flow metering cross section, measurements of time-mean stagnation pressures at designated measuring points and measurements of time-mean wall static pressure were used to calculate local values of time-mean dynamic pressure, P_{dyn}:

$$P_{dyn} = P_{stag} - P_{static} \qquad (6\text{-}1)$$

where P_{static} is the time-mean average value of the wall static pressure measurements and P_{stag} is the time-mean stagnation pressure measured at the point of interest. The location of the P_{stag} measuring points was determined by using the ten-point log-linear rule of Winternitz and

Fischl [45]. The measured values of air temperature and time-mean average wall static pressure in the flow metering cross section were used with standard air tables [121] to obtain the corresponding time-mean density of the air. The local values of U at the stagnation-pressure locations were calculated from:

$$U = \left(\frac{2\,P_{dyn}}{\rho}\right)^{1/2} \qquad (6\text{-}2)$$

Using the method of Winternitz and Fischl [45], the local values of U were integrated over the flow tube cross section to obtain an average velocity through the flow tube, U_{ft}. The values of U_{ft} and ρ were used to calculate the corresponding mass flow rate, $\dot{m}$, which is also the mass flow rate through the entire length of the flow circuit upstream of the flow metering cross section:

$$\dot{m} = \rho\, U_{ft}\, A_{ft} \qquad (6\text{-}3)$$

where A_{ft} is the area of the flow metering cross section.

The value of the dynamic viscosity, μ, used in the calculation of Reynolds numbers was obtained from standard air tables [121] as a function of the air temperature measured in the flow metering cross section.

A sample calculation of flow rate is presented in Appendix 5.

6.6.3 Calculation of Experimental Uncertainty

In this thesis, uncertainties in the values of individual measurements were combined appropriately to obtain the overall uncertainty of

final results calculated from these measurements: The method of Constant Odds Combination [49] first presented by Kline and McClintock [48] was employed. Using this method, if a final result, Ψ, is expressed as a function of N number of random variables or measurements, η_i, where i = 1 to N, having associated uncertainties of $\pm \delta\eta_i$ for the same odds, the uncertainty in Ψ, $\pm \delta\Psi$, can be calculated for the same odds from the relation [48,49]:

$$\delta\Psi = \{ \left(\frac{\partial\Psi}{\partial\eta_1}\delta\eta_1\right)^2 + \left(\frac{\partial\Psi}{\partial\eta_2}\delta\eta_2\right)^2 + \ldots \left(\frac{\partial\Psi}{\partial\eta_N}\delta\eta_N\right)^2 \}^{1/2} \qquad (6\text{-}4)$$

It was assumed that each η_i is independent and normally distributed, and the odds for each $\delta\eta_i$ are the same (20 to 1). It has been shown in [48] that when these three assumptions are valid, the overall uncertainty in a result can be given with good accuracy by Eq. (6-4). Ideally, an experimental run should be repeated several times to obtain enough samples of a given quantity, η_i, so that the true standard deviation, σ_i, of the population can be estimated [48-51]. For 20 to 1 odds, $\delta\eta_i$ is given by $2\sigma_i$ [49,52], and for a normal distribution, σ_i can be estimated from the standaid deviation of the sample set, S_i, given by [122]:

$$S_i = \left[\frac{\sum_{j=1}^{M} (\eta^o{}_j - \eta_i)^2}{M-1} \right]_i^{1/2} \qquad (6\text{-}5)$$

M represents the number of sample readings of $\eta^o{}_j$ that are taken to calculate the average of these sample values, η_i.

However, as in many engineering experiments [48], because of time

and money constraints, the final experimental runs in this investigation were single-sample [48] in nature: Not enough repeated measurements could be done to allow a proper statistical analysis of the data. In such experiments, the uncertainty in the measured values must be estimated before the final measurements are taken [48,49]. This estimation of uncertainties was based on (i) the theory of the operation of the equipment in the conditions of this work; and (ii) the sensitivity and fluctuations in instrument readings as specified by the manufacturers and confirmed in preliminary experimental runs: These include results obtained from instrument calibrations and the initial flow facility tests that were performed both for this work and in [109].

The differential pressure measurements taken with the Barocel pressure transducer were used in deriving the final experimental flow and pressure distributions presented in this thesis. The random uncertainty in such measurements was estimated from a statistical analysis of sample readings taken before each experimental run. These measurements were taken after the desired flow rate had been setup in the test section and just before the final data taking process was initiated. This particular method for estimating uncertainties was part of the experimental procedure for each run, and it is outlined briefly in the following paragraph. Particular details concerning the complete calculation procedure used to derive the overall uncertainty in a final result are given in the example of Appendix 5.

In the flow metering section, the measured value of P_{dyn} is expected to be largest at the center of the flow metering cross section and, consequently, the magnitude of the random uncertainty in this measured

value is expected to be correspondingly large relative to the values measured at other locations. In the interrupted-plate duct test section, if there is unsteadiness in the periodic fully developed flow field it is expected to be greatest in the region immediately downstream of the trailing edge of a plate: The uncertainty in the measured pressure difference between any two successive wall pressure-tap locations is, therefore, expected to be greatest between the TE and G1 locations shown in Fig. 19. For the aforementioned reasons, the uncertainty in the measured pressure differences pertaining to these two "worst-case" locations, one in the flow metering section and one in the test section, were used as a conservative estimate of the uncertainty for all differential pressure measurements. The procedure used to calculate these uncertainties was as follows: (i) the Barocel pressure transducer was connected so as to measure the pressure difference at the appropriate flow metering or test section location; (ii) over a period of 10 to 11 minutes, using the time-averaging procedure described in Section 6.6.1, 30 successive time-averaged measurements of the differential pressure were taken (the corresponding voltage output signal, V_{dP}, from the Barocel was recorded using the instrumentation and software of the data acquisition system); (iii) the sample standard deviation of the 30 measurements taken in (ii) was then calculated; (iv) the value calculated in (iii) was doubled and used as the uncertainty, $\pm \delta V_{dP}$, in the Barocel output signal for all values of differential pressures measured.

As described in Section 6.6.1, the zero-drift in the output signal of the Barocel pressure transducer was corrected by calculating the average output signal for a zero pressure differential and subtracting this value, V_{zero}, from the value measured for a pressure difference,

V_{dp}. Ten individual zero output readings were recorded and used to calculate V_{zero}. Using the time-averaging procedure described in Section 6.6.1, each individual reading was the average of 60 readings taken over a period of 13 seconds. It was assumed that over such a short time period, the average zero output signal of the Barocel could be assumed static, and twice the standard deviation of these 60 sample readings was assumed to be a good estimate of the uncertainty in that value. The uncertainty in each of the ten zeroed-values was then combined, as in Eq. (6-4), to obtain the overall uncertainty in V_{zero}, δV_{zero}. In other words, δV_{zero} was twice the pooled standard deviation, S_{pooled}, of the ten zeroed values, expressed as [122]:

$$S_{pooled} = \left[\frac{\sum_{i=1}^{N} (S_i)^2}{N} \right]^{1/2} \qquad (6\text{-}6)$$

The values of δV_{cal}, discussed in Section 6.5.1, δV_{dp}, and δV_{zero} were used in the calculation of the overall uncertainty of the measured pressure differences. An example calculation is given in Appendix 5.

6.6.4 Flow Visualization Technique

As stated in Section 6.5.5, two kerosene based flow visualization paints were used: Titanium dioxide, TiO_2, was used as the pigment in one and a fluorescent "Blaze Orange" Day-glo pigment was used in the other. In order to obtain consistently good streak patterns with increasing flow rates, the concentration of Day-glo pigment, relative to the kerosene, had to be increased to make a stiffer paint. Over the

range of flow rates investigated, three Day-glo paints, referred to as DG1, DG2, and DG3, were used, with the paint stiffness increasing from DG1 to DG3. Only one TiO_2 paint was used, and it will simply be referred to as the TiO_2 paint. The detailed recipes for these paints are given in Appendix 4. The methods used to apply these paints to a plate surface are discussed next.

The flow visualization paints were applied to the top surface of three plates in the clear acrylic flow visualization section, usually the fourth, fifth, and sixth plates downstream from the inlet of this section. To ensure that the surfaces of the plates were clean, they were wiped with a soft cloth dampened with kerosene. For flows in which the nominal value of the module Reynolds number, Re_m, was less than $25x10^3$, the paint brush described in Section 6.5.5 was wetted with kerosene and brushed across the plate surface. This left a thin visible layer of kerosene that thoroughly wetted the surface. The range of flow rates over which a given paint would give acceptable streamline patterns, could be extended by varying the thickness of this initial kerosene coating. The kerosene would mix with the flow visualization paint that was applied and act to reduce the stiffness of the paint (the ease with which the paint flowed): The degree of this reduction in stiffness would vary depending on the amount of kerosene and paint applied to the surface. At higher flow rates, when this thin "pre-coating" of kerosene mixed with the flow visualization paint, the paint would flow too readily: When placed in the air stream it would flow completely to the trailing edge of the plate, leaving no streaks. For high flow rates, therefore, the paint was applied directly to the plate surface, without pre-coating it with kerosene.

In the case where the plate surface was pre-coated with kerosene, the paint was applied in the following manner: (i) the paint brush was wetted with the flow visualization paint; (ii) the flat surface of the wetted paint brush was then pushed against the surface of the plate at one end, near the dowel-pin positioning hole, so as to squeeze the paint out of the brush onto the plate; (iii) by holding the plate at each end, and tilting it from side-to-side and forward-and-backward several times, the paint deposited in (ii) could be made to flow, and form a uniform layer, over the whole upper surface of the plate. The plate was then ready to be placed into the flow visualization section.

At the higher flow rates, $Re_m \geq 25x10^3$, the paint brush was wetted with flow visualization paint and lightly brushed, once or twice, across the plate, traversing it in a cross-flow direction from one end to the other, with the one-inch wide tip of the brush extending over the length of the plate, L. This thin, almost transparent, layer of paint yielded very fine streak patterns when the plate was placed in the air flow.

While the TiO_2 paint was used over the whole range of flow rates investigated, the DG1 paint was used only for $Re_m < 25x10^3$. For $Re_m \simeq 25x10^3$ and $\simeq 30x10^3$, the DG2 and DG3 paints were used, respectively.

This process of applying the flow visualization paints depended on the author's ability to visually estimate when the correct amount of paint and kerosene had been applied to the surface of a plate for a given flow rate. Several attempts were often required before the proper

combinations were found, but the ability to obtain these successful combinations improved as experience was gained.

The procedure to prepare a plate for flow visualization experiments can be summarized as follows: (i) when the desired flow rate through the interrupted-plate duct test section is established, remove the central portion of the top plate in the acrylic flow visualization duct; (ii) remove the plates of the interrupted-colinear array that are to be painted with the flow visualization paint; (iii) paint the plates as described in the preceding paragraphs of this subsection; (iv) carefully put the plates back into their proper locations in the colinear array; (v) fit the removable top section of the acrylic duct back into its appropriate location; and (vi) seal the joints at locations where this section mates with the rest of the duct. There is a short time delay from when the top section of flow visualization duct is replaced to when periodic fully developed flow conditions occur. From observations of the variations in the time-mean wall static pressure measurements and the behaviour in the flow of paint on the plates, this short delay was estimated to be less than three seconds, and it does not noticeably affect the final patterns of the dried streaks: The time required for the paint to flow from the leading-edge region to the trailing-edge region of a plate is of the order of fifteen to thirty seconds for the higher flow rates, and as long as two or three minutes for the lower flow rates. The time for the paint to dry is of the order of one to two hours, again depending on the overall flow rate.

6.6.5 Synopsis of the Overall Experimental Procedure

After the assembly of the test section with the desired plates, measurement of its dimensions, and its attachment to the rest of the flow circuit, the following step-by-step procedure was used to obtain the desired flow rates, the corresponding pressure drop data, and the plate-surface flow visualization results.

1. Power-up all electrical systems, except the air blower, and allow a two-hour warm-up period.
2. Set the flow control by-pass valve to its full-open position, turn on the blower, and allow a one-hour warm-up period.
3. Position the pitot-stagnation tube at the center of the flow metering cross section, and locate the traversing thermocouple probe immediately beneath it.
4. After the stipulated warm-up periods in Steps 1 and 2, set the flow control valves to obtain the maximum flow rate: Open the main flow valve completely and close the by-pass valve. Allow five to ten minutes to achieve a stable flow rate.
5. Making sure that one of the two flow control valves is always fully open, adjust the air flow rate through the test section to obtain the desired maximum Reynolds number value in the test section. To do this, it is necessary to measure the test section Reynolds number for the maximum air flow rate in Step 4 along with the corresponding value of P_{dyn} at the center of the flow metering cross section. By connecting the P_{stag} and P_{static} pressure lines to the Barocel pressure transducer, the data acquisition system can be used to monitor the change in this P_{dyn} as the flow rate is changed. The following

equation can be used as a rough guide to determine what value of P_{dyn} corresponds to the desired flow rate:

$$(P_{dyn})_{desired} = (P_{dyn})_{old} \left(\frac{Re_{desired}}{Re_{old}} \right)^2 \qquad (6\text{-}7)$$

6. Allow five to ten minutes for the new flow rate to stabilize.
7. Following the procedures described in Section 6.6.4, open the flow visualization section, remove and paint the desired plates, replace them, and close and seal the flow visualization section.
8. Following the procedures described in Section 6.6.3, determine the value of the random uncertainty to be specified for the differential pressure measurements taken in the flow metering section.
9. Following the procedures described in Section 6.6.3, determine the value of the random uncertainty to be specified for the differential pressure measurements taken in the interrupted-plate duct test section.
10. Initialize the data-taking procedure for the flow measurements by running the appropriate computer software developed for this task.
11. Take measurements of (i) barometric pressure (mm Hg); (ii) ambient air temperature (°C); (iii) air temperature in the flow metering cross section (°C); and (iv) gauge time-mean static pressure in the flow metering cross section (mm manometer fluid).
12. Input (i) the dimensions of the test section, 2H, b, L, s, and t in meters; (ii) the measurements taken in Step 11; and (iii) the estimated random uncertainty in the dynamic pressure measurements, from Step 8, as prompted for by the computer software developed to manage the flow-measurement task.

13. When prompted by the computer, open both ports of the Barocel to atmosphere and then signal the program to continue and take five zero readings.
14. Connect the P_{stag} and P_{static} pressure lines of the flow metering section to the respective high-pressure and low-pressure ports of the Barocel pressure transducer, and conduct a ten-point log-linear traverse of the flow metering cross section, in accordance with the instructions produced by the computer software written for this task.
15. Upon the completion of Step 14, repeat Step 13.
16. Using the computer software developed for the flow-measurement task, process, print, and store the air flow rate data.
17. Initialize the computer software developed to manage the task of recording and processing the time-mean wall static pressure measurements along the aluminum duct portion of the test section. When prompted by the computer software, input (i) the name of data sets containing the flow metering data, (ii) the identification numbers of the static pressure taps to be monitored; (iii) the identification number of the pressure tap chosen to be the reference port; (iv) the gauge value of the time-mean static pressure in the reference port chosen in (iii); and (v) the estimated random uncertainty, from Step 9, in the measurements of the differential time-mean wall static pressures.
18. Repeat Step 13.
19. Connect the pressure line from the dummy transducer of the Scanivalve mechanical multiplexor to the low-pressure port of the Barocel pressure transducer; connect the pressure line from the reference pressure port chosen in Step 17 to the high pressure port

of the Barocel pressure transducer; and then in response to the prompts produced by the computer software, initiate the automatic scanning and recording of differential pressure values for each of the chosen pressure ports downstream of the reference port chosen in Step 17.

20. Upon completion of Step 19, repeat step 13.
21. Using the computer software developed for this task, process, print and store the time-mean static pressure data. An inspection of this data should be done at this time to verify that no unexpected fluctuations have occurred during the run. If such anomalies have occurred, try to identify the problem, solve it, and repeat Steps 7 to 21.
22. Check to see that the streamline patterns formed from the paint applied in Step 7 have dried. When the paint has dried, remove the painted plates, photograph the dried streamline patterns, clean the dried paint off the plates with a kerosene dampened cloth, and put the plates back into the acrylic flow visualization duct.
23. Repeat Steps 5 to 22, until all the desired Reynolds numbers have been investigated. In Step 5, the Reynolds number value for the experimental run just completed is used as the value of Re_{old}.

CHAPTER VII

RESULTS OF INITIAL INVESTIGATIONS

In this chapter, the results of initial experimental and numerical investigations undertaken as a part of this research are presented.

7.1 INITIAL EXPERIMENTAL RESULTS: FULLY DEVELOPED TURBULENT FLOW

This section presents the results of a preliminary experimental investigation undertaken to establish that the experimental facility and procedures used in this work are capable of providing repeatable and accurate differential time-mean wall static pressure measurements. This study was done for fully developed turbulent flows in a straight rectangular duct, without interrupted-plate inserts. The same rectangular duct test section, with interrupted-plate inserts, and the same range of flow rates were later used for the periodic fully developed flow investigation. The reason for performing these initial studies for fully developed rectangular duct flow is that friction factor - Reynolds number results can be obtained and compared with corresponding data that is available in the published literature [54]. As a result, the suitability of the basic test section and the capabilities of the pressure and flow measurement procedures can be verified before proceeding to study the more complex problem of periodic fully developed duct flows.

Measurements were taken for seven different flows rates, over a nominal Reynolds number range of $10 \times 10^3 \leq Re_d \leq 60 \times 10^3$. It has already

been determined from the calibration checks presented in [109] that the flow facility used for this work is capable of generating steady, repeatable, and symmetric flows in the flow metering section, over the range of Reynolds numbers investigated. The test section used for this work is not the same as that used in [109], hence, calibration tests were performed for this section. Construction details of the test section have been described in Chapter VI. The locations of the static pressure taps and the measured duct dimensions are given in Tables 4 and 5, respectively. The duct has an aspect ratio of 5.309 ± 0.010.

Checks to determine the repeatability of time-mean static pressure measurements were carried out at the maximum and minimum flow rates used in this work. The results of these checks are presented in Figs. 26(a) and (b) in terms of $(P^*_o - P^*)_d$ versus $(x^* - x^*_o)_d$ plots where:

$$(P^*_o - P^*)_d = \frac{(P_o - P)}{\frac{1}{2} \rho \bar{U}_d^2} \tag{7-1}$$

and

$$(x^* - x^*_o)_d = \frac{(x - x_o)}{D_{hd}} \tag{7-2}$$

$\bar{U}_d$ and D_{hd} are defined by Eqs. (2-30) and (2-32), respectively, P_o is the time-mean static pressure at a suitably chosen reference pressure tap, and x_o is the axial distance of the reference pressure tap from the inlet plane of the duct. The reference pressure tap, or port, was chosen sufficiently downstream from the inlet plane of the duct so that fully developed flow conditions could be assumed to prevail from the reference port to the outlet of the rectangular duct test section. In

all of the seven flows rates considered for this initial study, port number 97 was chosen as the reference port. From the data reported in Tables 4 and 5, it is seen that this reference port is located 17.60 hydraulic diameters, D_{hd}'s, downstream of the duct inlet.

In Figs. 26(a) and (b), results of the primary and repeatability runs are denoted by the symbols ○ and □ , respectively. Each run required 90 minutes to 120 minutes to complete, and 10 minutes to 15 minutes after a primary run, the corresponding repeatability run was performed. The maximum uncertainty in the $(P^*_o - P^*)_d$ values is ± 0.012 in Fig. 26(a), and ± 0.024 in Fig. 26(b), and the uncertainties in the $(x^* - x^*_o)_d$ values are all less than ± 0.019 in both figures. The results from the primary and repeated runs for the maximum flow rate, shown in Fig. 26(a), are very close. The results for the minimum flow rate, presented in Fig. 26(b), also show good agreement, although not as good as those in Fig. 26(a). This is because the nondimensional data plotted in Fig. 26(b) are calculated from lower flow rates and smaller pressure differentials than those used for the results in Fig. 26(a). Any measurement errors in these dimensional quantities will lead to proportionally greater errors in the $(P^*_o - P^*)_d$ values of Fig. 26(b) than for the higher flow rate values shown in Fig. 26(a). However, both sets of data in Fig. 26(b) do agree within the limits of the experimental uncertainty of the measurements.

A more quantitative indication of the repeatability of the data presented in Figs. 26(a) and (b) can be obtained by comparing friction factor - Reynolds number values. The method of least squares was used to fit straight lines to the data of Figs. 26(a) and (b): The slopes of

these lines are the values of the Darcy friction factor, f_d, defined in Eq. (2-34). Correlation coefficients [123] were also calculated for use as a measure of the linearity of these lines: a perfectly linear variation of $(P^*_o-P^*)_d$ with $(x^*-x^*_o)_d$ being indicated by a correlation coefficient of one.

The correlation coefficients for the least-squares straight lines fitted to the data in Figs. 26(a) and (b) are all better than 0.9978, as seen in Table 6. A visual appreciation of the linearity indicated by this value can be obtained by examination of Fig. 27, where the data from the initial run presented in Fig. 26(a) is shown with a plot of the corresponding least-squares straight line. The linear behaviour of the data indicates that fully developed turbulent flows are established over the portion of the rectangular duct test section located downstream of the reference pressure tap located at port 97: This section of the duct is the one of interest for this work. In Table 6, the deviation of f_d values for the second run from those of the first run are shown to be less than $\pm$ 2.4 percent, and the deviation in the corresponding Reynolds numbers is less than $\pm$ 0.8 percent. The uncertainty in the friction factors is less than $\pm$ 5.0 percent of the f_d values reported in Table 6, and the uncertainty in the Re_d values is less than $\pm$ 2.4 percent. Based on these results, it was concluded that the experimental facility and procedures used are capable of providing repeatable time-mean wall static pressure measurements.

To establish the accuracy of the time-mean wall static pressure data, the friction factor - Reynolds number results for all seven flow rates were compared with corresponding results in the published

literature. As discussed in Chapter I, Jones [54] has done an in-depth study of published friction factor data for fully developed turbulent flows in straight rectangular ducts. Using this data, in conjunction with his own experimental data, Jones proposed a modified form of "Prandtl's formula" [36] for wall friction in turbulent pipe flow, which expresses friction factor as a function of Reynolds number. This correlation, hereafter referred to as the PJ (Prandtl-Jones) correlation, is applicable to turbulent flow in straight rectangular ducts and is written as:

$$\frac{1}{\sqrt{f_d}} = 2.0 \log_{10} (Re^* \sqrt{f_d}) - 0.8 \qquad (7\text{-}3)$$

where Re^* is a "laminar equivalent Reynolds number" [54], and is given by the following expressions:

$$Re^* = \phi^* Re_d \qquad (7\text{-}4)$$

$$\phi^* = \frac{2}{3} + \frac{11}{24} \left(\frac{2H}{b}\right) \left\{2 - \left(\frac{2H}{b}\right)\right\} \qquad (7\text{-}5)$$

The deviation of the friction factors predicted by the PJ correlation from the corresponding values obtained from the best of the published experimental data is about ± 5 percent [54].

The friction factor - Reynolds number data obtained from the measurements made in this work are compared, in Fig. 28 and Table 7, with the corresponding results obtained from Eq. (7-3). In Fig. 28, the PJ correlation results are plotted as the solid curve and the ± 5 percent error band of these results is shown by the dashed curve. It is seen that all the experimental results from this work fall in between

these dashed lines, indicating good agreement with the PJ values. Table 7 shows that the experimental value of f_d deviates from the corresponding PJ correlation value by less than $\pm$ 2.7 percent in all cases.

On the basis of the results presented in this section, it was concluded that the experimental facility and procedures used in this work, are capable of producing accurate results. Quantitatively, it may be stated that the friction factor results of this investigation have an uncertainty of less than $\pm$ 5 percent.

7.2 INITIAL NUMERICAL INVESTIGATION: FULLY DEVELOPED TURBULENT FLOW

Initial evaluations of the numerical predictions based on the Jones and Launder [89] and the Launder and Sharma [91] low-Reynolds-number k-ϵ turbulence models are presented in this section. In addition, the different formulations for incorporating $\overline{S^k}$ and $\overline{S^\epsilon}$ in the discretization equations, as put forth in Section 5.3.3, are evaluated in terms of their effect on the rate of convergence of the overall solution procedure for U, k, and ϵ. For the reasons discussed in Section 5.3, these initial studies were done for the case of fully developed, turbulent, two-dimensional flow in a channel. To facilitate the presentation of the remaining text in this thesis, the Jones and Launder version [89], the Launder and Sharma version [91], and the standard version [75] of the k-ϵ model will often be referred to as the JL, LS, and ST models, respectively. Details of the corresponding numerical method were given in Chapter IV. The results presented in Sections 7.2.1 and 7.2.2 were obtained by using an IBM 3090 computer, operated by the

McGill University Computing Centre.

7.2.1 Preliminary Performance Evaluation of the k-ϵ Turbulence Models

Background

The performance of the JL [89] and the LS [91] low-Reynolds-number k-ϵ turbulence models was evaluated for eight cases of turbulent fully developed flow in a two-dimensional duct, or channel. For such a duct, the width, b in Fig. 5 , is infinite, and the mass flow rate, $\dot{m}$, is specified in terms of the mass flow rate per unit width of the duct. Accordingly, the appropriate forms of $\overline{U}_d$ and D_{hd} used in the calculation of the nondimensional parameters for turbulent duct flows, as presented in Section 2.6.1, are:

$$\overline{U}_d = \frac{\dot{m}}{\rho\ (2H)} \tag{7-6}$$

and

$$D_{hd} = 4H \tag{7-7}$$

The eight nominal, or desired, values of flow Reynolds number, Re_d, for the turbulent one-dimensional fully developed channel flow studied were 5.00×10^3, 10.0×10^3, 15.0×10^3, 25.0×10^3, 56.2×10^3, 92.8×10^3, 129×10^3, and 228×10^3. The lower end of this range, $5.00\times10^3 \leq (Re_d)_{nom} \leq 25.0\times10^3$, covers the same range as the modular Reynolds number values, Re_m, for the two-dimensional periodic fully developed duct flows that are discussed later in this thesis. Therefore, the performance of both turbulence models in this Reynolds number

range is of particular interest. The upper end of the range, $56.2 \times 10^3 \leq (Re_d)_{nom} \leq 228 \times 10^3$, was investigated to determine at what point the low-Reynolds-number turbulence models give results similar to those of the standard, or high-Reynolds-number, version of the k-ϵ turbulence model. In this connection, calculations for the eight flow rates were also performed using the ST k-ϵ turbulence model.

In this investigation, the $(-\partial P/\partial x)$ values specified for each desired, or nominal, value of Reynolds number, $(Re_d)_{nom}$, were calculated in the following manner: (i) the value of $(Re_d)_{nom}$ was used in the PJ correlation, Eq. (7-3), to calculate $(f_d)_{PJ}$ for a two-dimensional duct, $\xi = \infty$; (ii) Eqs. (2-34), (2-29), and (7-7) were then used to obtain the corresponding value of $(-\partial P/\partial x)$. This value generally yielded a numerically calculated value of Re_d that was slightly different from the nominal or desired value of Re_d. An iterative procedure could have been used to modify the specified value of $(-\partial P/\partial x)$ until the calculated Re_d was equal to $(Re_d)_{nom}$. For the purposes of this investigation, however, it was not important to have a calculated value of Re_d that was exactly the same as the corresponding nominal value.

For fully developed turbulent flow in a two-dimensional channel of height 2H, the wall shear stress, τ_w, can be obtained by integrating Eq. (5-34) from y = 0 to y = H:

$$\tau_w = \left(-\frac{\partial P}{\partial x} H\right) \tag{7-8}$$

Substitution of this equation into Eq. (3-30) gives the expression for the friction velocity, U_τ, as a function of $(-\partial P/\partial x)$:

$$U_\tau = \{(-\frac{\partial P}{\partial x} H) \; / \; \rho \}^{1/2} \qquad (7\text{-}9)$$

The value of U_τ is needed to specify boundary conditions for U, k, and ϵ in the ST k-ϵ model, via the "universal" wall functions approach [75], and it is also used in the nondimensionalization of U, k, ϵ, and other variables. The specified values of $(-\partial P/\partial x)$ used in this work are presented in terms of U_τ through the use of a friction-velocity Reynolds number, Re_{fric}, defined as:

$$Re_{fric} = \frac{\rho \; U_\tau \; D_{hd}}{\mu} \qquad (7\text{-}10)$$

where, for a channel, D_{hd} takes on the form given in Eq. (7-7). The values of Re_{fric} used in this investigation are given in column 2 of Table 8 and are used in the following discussion to identify each of the eight channel flows studied. From the table it is seen that the friction-velocity Reynolds number range of $3.72 \times 10^2 \leq Re_{fric} \leq 10.5 \times 10^3$ corresponds to the nominal, or desired, duct Reynolds number range of $5.00 \times 10^3 \leq (Re_d)_{nom} \leq 228 \times 10^3$.

Following the procedure described in Section 5.2.7, the relative change in each of the grid-point values of U, k, and ϵ was monitored over the two most recent iterations of the overall solution procedure. When this change was less than 10^{-8} for all variables, at all interior nodes, the solution of the discretization equations for U, k, and ϵ was considered to have converged.

Using the k and ϵ source term treatment designations presented in Section 5.3.3, the $S^k{}_1$-$S^\epsilon{}_1$-A source term treatment was used to obtain

all performance evaluation data presented in this section. More will be said about the other possible source term treatments in Section 7.2.2.

The value of the underrelaxation parameter, α, appearing in the general discretization equation, Eq. (4-18), was set to 1.0 for the U discretization equations and to 0.9 for the k and ϵ discretization equations when either of the two low-Reynolds-number turbulence models was employed. Underrelaxation of the k and ϵ equations was required in order to achieve a stable, converged, solution, and the above-mentioned values of α gave the most rapid convergence. No underrelaxation was required, all α's = 1.0, when calculations where done using the ST k-ϵ model equations.

Grid Checks

To determine the accuracy of the numerical solutions obtained using the various turbulence models employed in this work, grid-independent solutions were obtained and compared to experimental data and established semi-analytical correlations whenever possible. The numerical solution is said to be grid independent when it no longer changes as finer and finer grids are used. In theory, the exact grid-independent solution requires a computational grid for which the grid-point spacing approaches zero. Fortunately, the grid-independent solution can often be well approximated from solutions obtained with finite grid spacing by using suitable extrapolation procedures. De Vahl Davis [118] has presented an extrapolation procedure that can be used to approximate grid-independent solutions. This technique involves obtaining solutions from at least three different grid distributions for which the grid points

are uniformly spaced and separated by distances which are small enough to ensure that the grid-independent solution is more closely approached with each successively finer grid. Such uniform-grid solutions for the fully developed turbulent duct flows examined in this investigation, using the JL [89] and LS [91] low-Reynolds-number turbulence models, were found to be impractical because of the large number of grid points and computational effort required. On the other hand, the use of nonuniform grids allows more efficient distribution of grid points, and a grid-independent solution can be approached with the use of considerably fewer grid points and for greatly reduced computational effort and expense. A qualitative estimate of when a grid-independent solution has been reached can be obtained by plotting the profiles of variables that have been calculated using different grids. When such profile plots of a variable show little or no change from one grid to a finer grid, it is assumed that grid independence has been reached. This method was used to determine the final grid distributions that were employed for the one-dimensional turbulent flow calculations in this thesis.

It has been this author's experience that in order to obtain a stable and converged solution when using low-Reynolds-number k-ϵ turbulence models, it is necessary to use a sufficient number of grid points in the near-wall region, $y^+ < 30$, to ensure adequate resolution of the steep gradients of turbulence properties in this region. For a given duct, the physical y dimension of this near-wall region decreases as Re_{fric} increases, the corresponding gradients of the turbulence properties become even greater, and it is expected that the number of grid points required in the near-wall region will increase. Therefore, it is assumed that a grid distribution that is fine enough to give a

grid-independent solution for a large value of Reynolds number will also give a grid-independent solution for smaller values of Reynolds number. For this reason, the same type of grid that gave a grid-independent solution for the maximum Reynolds number examined, $Re_{fric} = 10.5 \times 10^3$ which corresponds to $(Re_d)_{nom} = 228 \times 10^3$, was also used for all other flows.

The results of the grid-independence checks done using the JL [89] model are presented in Figs. 29(a), (b), (c) and (d). In these figures, plots of nondimensional values of U, k, and ϵ versus nondimensional y distance from the wall, $0 \leq y \leq H$, are shown. Results obtained from four different nonuniform grids, generated using the procedure described in Appendix 1 and having a total number of grid points, M1, of 93, 133, 153, and 193, are presented. The close agreement between the various profiles for common variables indicates that it can be conservatively assumed that grid-independent results have been achieved with a grid of M1 = 193.

This same type of grid distribution was used for all the one-dimensional turbulent flow calculations. It should be noted, however, that with the grid generating procedure described in Section 5.3.2 and Appendix 1, the total number of grid points located in the near-wall regions, $y^+ < 30$, will remain constant, but the physical dimension of the core-flow region located between the wall regions decreases as Re_{fric} decreases and, hence, the total number of grid points also decreases. The corresponding number of grid points used for each value of Re_{fric} are shown in column three of Table 8. The number of grid points located in each near wall region, $y^+ < 30$, is 41 for a total of

82 near-wall grid points. Results of grid-independence checks for $Re_{fric} = 3.72x10^2$, the minimum value used, are shown in Figs. 30(a), (b), and (c). Again, the close agreement between the U, k, and ϵ profiles for the various grids verify that grid-independent results have been achieved by using the same type of grid as that used for the maximum Reynolds number, $Re_{fric} = 10.5x10^3$.

To enable a one-to-one comparison of the prediction capabilities of the JL [89], LS [91], and the ST [75] k-ϵ turbulence models, the same grids were used with all models. The standard k-ϵ model solves the discretization equations at grid points outside the near-wall regions: So with this model, all grid points located in the wall regions, $y^+ < 30$, were excluded from the calculations. This is the reason for the lower number of grid points shown for this model in column 4 of Table 8.

Results

The numerical results for turbulent fully developed two-dimensional channel flows using the JL [89], LS [91], and ST [75] k-ϵ model of turbulence were compared to each other and, when possible, to experimental data and established correlations available in the literature. The results and conclusions of this study are presented in this subsection. It is to be remembered that to calculate a value of Re_d using the JL, LS, and ST models, the same value of Re_{fric} is specified for all three models. For this reason, different Reynolds number runs will be identified by the particular value of Re_{fric} specified. As Re_{fric} increases, the value of Re_d also increases, so that reference to high Re_{fric} values also implies that the corresponding value of Re_d is high, as shown in

Table 8.

As mentioned in Chapter III, it is the functional forms of the terms $f_{C\mu}$, $f_{C1\epsilon}$, $f_{C2\epsilon}$, E_k, and E_ϵ, appearing in Eqs. (3-8), and (3-14) to (3-21), that determine the differences between the various low-Reynolds-number k-ϵ models and the standard k-ϵ model. In regions of the flow where the turbulence Reynolds number, Re_t, is large ($Re_t > 445$), the low-Reynolds-number k-ϵ models are expected to take on the form of the standard k-ϵ model, and hence all f's should asymptote to 1, and the effects of E_k and E_ϵ should become negligible. In order to evaluate the performance of the JL and LS models, relative to each other, the behaviour of these E and f terms, as well as local and overall calculated flow data, are examined over the whole range of Reynolds numbers investigated.

Behaviour of E_k and E_ϵ

Although ϵ has a finite value greater than zero at a wall boundary, ϵ has been set to zero at such boundaries for computational convenience in both the JL and LS models, as discussed in Chapter III. This results in the D_k term, Eq. (3-17), in the k equation, Eq. (3-14), going artificially to zero as a wall boundary is approached. To compensate for this, an additional term, E_k, was added to Eq. (5-6), to ensure that S^k behaves in the proper fashion near the wall. In Figs. 31(a) and (b), the ratio of E_k/D_k for the JL and LS models is plotted against the non-dimensional wall distance, y^+, for the maximum and minimum extremes of the Reynolds number range investigated. In Fig. 31(a), where $Re_{fric} = 10.5x10^3$, and in Fig. 31(b), where $Re_{fric} = 3.72x10^2$, E_k/D_k behaves in the same manner for both the JL and LS models and, as

expected, the ratio is significant only very close to the wall, $y^+ < 10$, well into the viscous dominated near-wall flow region.

The inclusion of E_ϵ in the ϵ equation, Eq. (3-18), of the JL and LS models is necessary to ensure that the calculated k distribution peaks in the near-wall region, $y^+ \simeq 20$, thus giving better accord with experimental observations for wall bounded shear flows [80,89] . The effect of E_ϵ on the performance the JL and LS models is, therefore, best evaluated by examining the k profiles calculated using these models. This will be done later on in this section.

Behaviour of $f_{C1\epsilon}$ and $f_{C2\epsilon}$

The $f_{C1\epsilon}$ term does not affect the relative performance of the JL, LS, and ST models, as it has a constant value of one.

The $f_{C2\epsilon}$ term is formulated in the same manner for both the JL and LS models, as shown in Table 2. The behavior of this function as a function of Re_t, the turbulence Reynolds number, is shown in Fig. 32. From this figure, it is seen that $f_{C2\epsilon}$ asymptotes to its ST model value of one for $Re_t > 3$. For the fully developed channel flows considered in this work, this implies that $f_{C2\epsilon}$ has a damping effect only within the viscous sublayer region, $y^+ < 5$.

Behaviour of $f_{C\mu}$

The damping effect imposed on the Reynolds stresses in the viscous dominated flow regions is modelled using the $f_{C\mu}$ term in the expression for μ_t, Eq. (3-8). As seen in Table 2, this function is dependent on Re_t, the turbulence Reynolds number, and is formulated differently for

the JL and LS models. These two formulations are illustrated in Figs. 33(a) and (b). Figure 33(a) shows the behaviour of $f_{c\mu}$ at low values of Re_t (< 50), as would be expected to occur very close to a channel wall. In this figure, it is seen that the LS model $f_{c\mu}$ formulation initially gives a lower value than the JL formulation, but for Re_t > 18, $f_{c\mu}$ of the LS model increases at a greater rate and becomes larger in magnitude than that of the JL model. It is observed in Fig. 33(b) that, as Re_t increases to fully turbulent values, the $f_{c\mu}$ in the LS formulation approaches the value of one (the ST model value) noticeably faster than that in the JL formulation. For Re_t values of 145, 445, 610, and 850, $f_{c\mu}$ has corresponding values of 0.80, 0.97, 0.98, and 0.99 for the LS formulation, and respective values of 0.53, 0.78, 0.83, and 0.87 for the JL formulation. Even at Re_t = 3000, close to the upper limit of Re_t for the fully developed channel flows studied in this investigation, the JL model value of $f_{c\mu}$ only reaches 0.96.

Plots of Re_t versus y/H, and y^+, are shown in Figs. 34(a) and (b) for the maximum and minimum values of Re_{fric} used in this investigation. Values obtained using the JL, LS, and ST models are presented. From these two figures, as expected, it is seen that for the larger Re_{fric}, y^+ is larger at the same y/H distance from the wall: For example, y^+ values of 2.62×10^3 and 93.0 occur at y/H = 1.0 for Re_{fric} values of 10.5×10^3 and 3.72×10^2, respectively. For fully developed channel flows having a large Re_{fric}, the rapid increase in values of Re_t compared to y/H verifies that the flow can be considered fully turbulent over most of the flow domain. In Fig. 34(a), the region $y^+ < 30$ occupies less than 1.2 percent of the flow domain, and for y/H = 0.1, Re_t is large enough so that $f_{c\mu}$ of the LS model reaches 99 percent of the ST model

value of one , as can be seen by viewing the plots in Fig. 35(a). It is seen in Fig. 35(a) that $f_{c\mu}$ of the JL model only reaches a value of 0.90 and 0.96 at y/H locations of 0.1 and 1.0, respectively. For the low-Reynolds-number fully developed turbulent channel flow with $Re_{fric} = 3.72 \times 10^2$, there is a noticeable difference in the values of Re_t from model to model, as observed in Fig. 34(b). Despite this difference, relative to the Re_t values occurring in high-Reynolds-number turbulent flows, illustrated by Fig. 34(a), the values of Re_t remain low throughout the calculation domain: Values of Re_t are less than 120 for the JL model and less than 90 for the LS model. Even for the ST model, the Re_t values are all lower than 142, and they are even less than the boundary-point value of 136, located at $y^+ = 30.6$, in over 75 percent of the calculation domain. The $f_{c\mu}$ profiles calculated using the JL and LS models for $Re_{fric} = 3.72 \times 10^2$, shown in Fig. 35(b), also reflect the fact that neither model indicates the presence of a fully turbulent flow region, where μ can be neglected relative to μ_t. In addition, the near-wall region where the $f_{c\mu}$ term of the JL model is greater is just over 10 percent of the total calculation domain.

Figure 35(b) also shows that by locating the calculation domain boundary points at $y^+ \simeq 30$ in the ST model, over 30 percent of the flow domain is handled by the use of wall functions. It is expected that use of the wall functions over such a large physical region of the flow domain could lead to a significant decrease in the accuracy of the overall flow and turbulence calculations.

Model Predictions

Plots of nondimensional velocity, U/U_τ, versus nondimensional

distance from the channel wall, y^+ and y/H, are presented in Fig. 36 and Figs. 37(a) to (f). In the viscous sublayer region of wall bounded shear flows, $0 \leq y^+ \leq 5$, the mean velocity can be expressed using the so-called "law of the wall" [63]:

$$\frac{U}{U_\tau} = y^+ \tag{7-11}$$

The mean velocity in the logarithmic region of these flows, $30 < y^+ < 100$, is given by Eq. (3-29). In Fig. 36 and all of Figs. 37, Eq. (7-11) is plotted as the solid curved line from $0 \leq y^+ \leq 11.5$ and Eq. (3-29) is plotted as the solid straight line for $y^+ > 11.5$. Turbulent velocity profiles are not expected to fall along either of these curves through the buffer region, $5 < y^+ < 30$. The logarithmic profile of Eq. (3-29) is, however, often characteristic of the velocity profiles exhibited up to y^+ values in the range of 500 to 1000. These semi-analytical correlations are used to give an indication of the accuracy of the numerical data shown in Figs. 37(a) to (f).

In Fig. 36, fully developed velocity profiles from three different experimental investigations of turbulent duct flows are presented and compared to Eqs. (7-11) and (3-29). The experimental data of Comte-Bellot [62], Clark [63], and Hussain and Reynolds [64], were taken in ducts with aspect ratios of 13.3, 12, and 18, respectively. The corresponding flow Reynolds numbers were $Re_H = 57.0 \times 10^3$ [62], $Re_{max} = 15.2 \times 10^3$ [63], and $Re_{max} = 13.8 \times 10^3$ [64]. The purpose of presenting the data in Fig. 36 was to (1) illustrate that the nondimensionalized mean velocity profile does exhibit a Reynolds number dependence, and (2) show that there is no one set of data or correlation that

can be used as a definitive means of determining the quantitative accuracy of the numerical results to be presented for the fully developed channel flows investigated. In the literature, no local experimental data of flow and turbulence properties was found for comparison with the numerical data in the range $3.72\text{x}10^2 \leq Re_{fric} \leq 1.48\text{x}10^3$. For this low-Reynolds-number range, comparison with the velocity profiles given by the semi-analytical expressions of Eqs. (7-11) and (3-29) was the only means of obtaining a measure of the accuracy of the local numerical data.

Values of U/U_τ, versus y^+ and y/H, obtained using the JL, LS, and ST models are plotted for Re_{fric} values of $3.72\text{x}10^2$, $6.69\text{x}10^2$, $9.48\text{x}10^2$, $1.48\text{x}10^3$, $3.00\text{x}10^3$, and $10.5\text{x}10^3$ in Figs. 37(a) to (f), respectively. Equations (7-11) and (3-29) are also plotted in all these figures. The experimental data of Clark [63] and Hussain and Reynolds [64] correspond to Reynolds number values that are approximately the same as those calculated numerically for $Re_{fric} = 3.00\text{x}10^3$ and are therefore plotted in Fig. 37(e) as well. For similar reasons, the experimental data of Comte-Bellot [62] is plotted in Fig. 37(f). In all these figures, the actual grid-point values of the numerical data are shown, rather than a best-fit curve, in order to avoid confusion with the curves plotted for the semi-analytical and experimental profiles.

In all cases, except for the minimum Re_{fric} value of $3.72\text{x}10^2$ shown in Fig. 37(a), the ST model velocities follow the logarithmic profile, Eq. (3-29), from $30 < y^+ < 100$. For $y^+ > 100$, the U/U_τ generally increases slightly above the logarithmic profile.

In the viscous sublayer region, both the JL and LS models show agreement with the velocity profile given by Eq. (7-11) over the full range of Re_{fric} investigated in this thesis, as seen in all of Figs. 37. Outside the viscous sublayer region, the LS model predicts higher values of U/U_τ than the JL model in all cases plotted. For the low-Reynolds-number flows shown in Figs. 37(a) to (d), $3.72x10^2 \leq Re_{fric} \leq 1.48x10^3$, the JL model gives better agreement overall with the ST model results and the logarithmic profile. However, for the higher-Reynolds-number flow shown in Fig. 37(e), $Re_{fric} = 3.0x10^3$, the $y^+ > 30$ values of U/U_τ calculated using the LS model are close to those of the ST model, and they follow the experimental data of Clark [63] right through the buffer zone, $5 < y^+ < 30$. The JL model on the other hand, gives a U/U_τ profile that is lower in magnitude than the corresponding LS, ST, and logarithmic profiles for $10 \leq y^+ \leq 200$. For $y^+ > 100$, the JL data agrees with the experimental U/U_τ values of Hussain and Reynolds [64], but underpredicts this data for $10 \leq y^+ \leq 100$, whereas the values of the LS model follow the experimental data from $y^+ < 30$. At even higher Reynolds numbers, as shown for $Re_{fric} = 10.5x10^3$ in Fig. 37(f), the agreement between the LS and ST models for $y^+ > 30$ is good, although it underpredicts the experimental data of Comte-Bellot [62] in this region. The JL model is seen to give velocity values that are again somewhat lower that those of the other two models.

In Figs. 35(a) and (b), it was shown that values of $f_{c\mu}$ for the LS model are larger than those of the JL model over approximately 99 percent and 90 percent of the calculation domain with $Re_{fric} = 10.5x10^3$, and $3.72x10^2$, respectively. From Eq. (3-8) for the turbulent viscosity, it appears that the same type of relationship would also exist between

corresponding μ_t values of both models, resulting in the LS model having larger values of μ_t over most of the flow domain, compared to the JL model. At first thought, it might be expected that the larger μ_t values of the LS model would lead to smaller values of U/U_τ compared to the JL model. However, exactly the opposite trend is observed in Fig. 37(a) to (f). Because of the strong coupling between the governing U, k, and ϵ equations, and the dependence of both $f_{C\mu}$ and μ_t on k and ϵ values, it is difficult to predict the behaviour of μ_t simply by considering the behaviour of $f_{C\mu}$ for each model. Plots of the μ_t/μ profiles for the JL and LS models are shown in Figs. 38(a) and (b) for the respective extremes of $Re_{fric} = 10.5x10^3$ and $3.72x10^2$. In these figures, the same trends are observed as for the $f_{C\mu}$ function: The JL model values of μ_t are larger than the corresponding LS values in the near-wall region where $y^+ < 24$ and 29, for the respective maximum and minimum Re_{fric} values, and smaller outside this region . The difference between the μ_t values of each model is, however, relatively small compared to that of the corresponding $f_{C\mu}$ values, particularly for $Re_{fric} = 10.5x10^3$, in Fig. 38(a), where both models give values of μ_t very close to each other when $y^+ > 30$. It is thus concluded that, even for the high Reynolds number case, with $Re_{fric} = 10.5x10^3$, where the region corresponding to $y^+ < 30$ makes up less than one percent of the total flow domain, the modelling of the flow in the near-wall region can have a noticeable effect on the magnitude of the velocity profiles outside the region. This can be explained by examining the expression for $\partial U/\partial y$ that is obtained by substitution of Eqs. (5-37) and (3-4) into Eq. (5-34), integrating the expression over the duct half-height, H, and rearranging the result to give:

$$\frac{\partial U}{\partial y} = - \left(\frac{\partial P}{\partial x}\right) \frac{(H - y)}{(\mu + \mu_t)} \qquad (7\text{-}12)$$

From Eq. (7-12), it can be shown that in the near-wall viscous region, where μ_t values are smallest, the largest velocity gradients of the flow will occur, as verified by experimental observations. In the near-wall region of $y^+ < 24$, μ_t of the LS model is smaller than that of the JL model for all flows investigated in this work. This means that the U velocity profile calculated using the LS model will increase, from its wall value of zero, at a greater rate than that of the JL model. At the cross-over point where μ_t of the LS model becomes larger than that of the JL model, the rate of increase of the LS velocity profile will become less than that of the JL profile, but the level of the LS model U profile is higher than that of the JL model. There is enough of a difference in these two levels that the LS model velocities remain greater than those of the JL model throughout the fully turbulent flow region. The near-wall velocity gradients are so large that at $y^+ = 30$, for both JL and LS models, U/U_τ reaches just over 50 percent of its maximum value for $Re_{fric} = 10.5 \times 10^3$, at a physical distance from the wall that is only one percent of the total flow domain. Therefore, even for high-Reynolds-number flows, the performance of the turbulence model in the near-wall region, $y^+ < 30$, has a significant influence on the overall flow calculations. As Re_{fric} is decreased, the effect of this region is even more important, as witnessed by the even larger differences in the U/U_τ profiles shown in Fig. 37(a).

From the preceding discussion, it can be concluded that an important factor in determining the accuracy of a low-Reynolds-number turbulence model is its ability to properly simulate the flow and turbulence in the

near-wall viscous region, $y^+ < 30$. From the comparisons with the semi-analytical expressions, Eqs. (7-11) and (3-29), and local experimental data for U/U_τ, presented in Figs. 37(e) and (f), it appears that the LS model has better prediction capabilities for high-Reynolds-number flows, $Re_{fric} \geq 3.00 \times 10^3$. However, a similar comparison of the nondimensional turbulent kinetic energy profiles, presented in Figs. 39 and 40 for the corresponding Re_{fric} values of 3.00×10^3 and 10.5×10^3, shows that in the near-wall region, the JL model gives marginally better agreement with the experimental results [62-64] compared to the LS model. Further from the walls there is little difference between the two profiles and the ST model profile. It will also be noticed from these two plots that k peaks at $y^+ \simeq 20$, indicating that the E_ϵ term is having the desired influence on the k profiles. The plot of nondimensional kinetic energy for $Re_{fric} = 3.72 \times 10^2$, shown in Fig. 41, illustrates again that, as Re_{fric} becomes smaller, the differences increase between values of common variables calculated using the JL, LS, and ST models. At low Reynolds numbers, $3.72 \times 10^2 \leq Re_{fric} \leq 1.48 \times 20^3$, one may conclude, based on qualitative agreement with Eq. (3-29), that the JL model is better than the LS model. However, at small values of Re_{fric} where the $y^+ < 30$ region occupies a significant portion of the flow, as much as 30 percent at $Re_{fric} = 3.72 \times 10^2$, the overall accuracy of a given model depends to a large extent on its ability to accurately simulate the flow in the buffer region, $5 < y^+ < 30$. A proper performance evaluation of the JL and LS models for the low-Reynolds-number flows of this thesis requires comparison with experimental data in the near-wall viscous flow region. To this author's knowledge, this type of local data is not presently available in the literature.

ST Model: Near-Wall Mass-Flow Calculation

Using the ST model, the boundary value of U is specified at $y^+ \simeq 30$. The common practice in the calculation of the mass flow rate is to assume that this boundary value, determined by Eq. (3-29), prevails over the near-wall boundary control volume which extends all the way to the wall. This will be referred to as the prevailing assumption practice. One of the advantages in using the low-Reynolds-number models is that velocity is calculated all the way to the wall and should therefore result in more accurate calculation of the near-wall portion of the total mass flow rate than if the prevailing assumption practice were used. The overall flow rates were used to calculate Reynolds number, Re_d, values and the corresponding friction factor, f_d, values.

An indication of the overall accuracy of the flow rates calculated using the JL, LS, and ST models was obtained by comparison of f_d values with those calculated by using the corresponding values of Re_d in the PJ correlation for a duct with $\xi = \infty$. The results are presented in Table 9, and plotted in Fig. 42 where the PJ correlation, Eq. (7-3), is shown by the solid curve, and the two dashed lines represent the correlation's $\pm$ 5 percent uncertainty band [54]. It is seen that the f_d values of the JL model fall inside the $\pm$ 5 percent uncertainty band, all being within $\pm$ 2 percent of the corresponding PJ values. The f_d values of both the LS and ST models show poorer agreement, underpredicting the PJ correlation f_d values by 8.59 and 6.75 percent, respectively, at the highest Reynolds numbers and by as much as 14.2 and 10.5 percent, respectively, at the lower Reynolds numbers. It is perhaps surprising that the LS model data shows poorer agreement with the PJ curve than the ST model, particularly in the low-Reynolds-number range of

$5.00 \times 10^3 < Re_d < 30.0 \times 10^3$. From Figs. 37(a) to (d), it is seen that the LS model overpredicts the flow in all regions of the flow domain compared to the ST and JL models. Without accurate experimental data for such low-Reynolds-number flows, it cannot be determined if flow in all regions is being overpredicted, or just that of one region, say the $y^+ < 30$ region. It is also possible that the JL model shows close agreement with the PJ correlation because it underpredicts U values in one region of the flow and overpredicts them in the other region of the flow. Reliable and accurate experimental flow and turbulence data for low-Reynolds-number flows is required to verify which model can best predict the local flow characteristics. Based on the friction factor - Reynolds number data available in the literature, it appears that the JL model is better suited than the LS model for the range of Reynolds numbers investigated in this thesis.

The difference between the f_d values of the ST model and those of the PJ correlation become greater as the Reynolds number decreases, with the ST model values always being lower. It has already been shown that even for the upper range of Reynolds numbers used in this investigation, the value of U at the $y^+ = 30$ boundary-point location of the ST model will be at least 50 percent of the calculated maximum U velocity in the channel. At high Reynolds numbers, the $y^+ < 30$ region comprises only a small fraction of the flow domain, and hence, compared to the total mass flow rate, the mass flow rate calculated in the near-wall region using the prevailing assumption practice is relatively small. For example, at $Re_{fric} = 10.5 \times 10^3$, the near-wall region comprises about one percent of the flow domain and the mass flow rate in this region, calculated using the prevailing assumption practice, is less than 0.75 percent of the

total mass flow rate. An error in the calculated near-wall mass flow rate will cause an error of less than 0.75 percent in the total mass flow rate calculation. At this Reynolds number, the LS and ST models show close agreement in f_d and Re_d values, as seen in Fig. 42.

In the lower-Reynolds-number range, $5.00 \times 10^3 \leq Re_d \leq 30.0 \times 10^3$ corresponding to $3.72 \times 10^2 \leq Re_{fric} \leq 1.48 \times 10^3$, the relative error caused by using the prevailing assumption practice in the calculation of the mass flow rate is greater than at higher Reynolds numbers. This is observed from the results of the ST model compared to those of the JL model and the PJ correlation, as shown in Fig. 42. For instance, at $Re_{fric} = 3.72 \times 10^2$, $Re_d \simeq 5 \times 10^3$, 31 percent of the total mass flow rate occurs within the $y^+ \leq 30$ region, which occupies just over 30 percent of the flow domain. This is an overprediction of the near-wall flow rate and it significantly affects the overall channel mass flow rate calculation. For $y^+ > 30$, the JL model predicts higher U velocities than the ST model, as seen in Fig. 37(a), yet as shown by the lower values of f_d in Fig. 42, the ST model overpredicts the channel mass flow rate due to the error caused by using the prevailing assumption practice.

In order to improve the near-wall mass flow rate calculation of the ST model, particularly for low-Reynolds-number flows, it was assumed that the velocity distribution over the $y^+ \leq 30$ region is given by Eq. (3-29) for $11.5 \leq y^+ \leq 30$ and by Eq. (7-11) for $0 \leq y^+ \leq 11.5$. As seen by comparison with the experimental data in Fig. 36, while such a profile approximation overestimates the flow in the buffer region, it is nevertheless better than the prevailing assumption practice. By integrating the two-piece velocity profile over the appropriate limits,

the calculated mass flow rate for a given Re_{fric} is reduced, and this results in better agreement of the ST model friction factor - Reynolds number data with the PJ correlation values, most noticeably for low Reynolds numbers, as shown in Table 10 and Fig. 43: For $Re_d < 25x10^3$, the ST model friction factors agree with the PJ correlation to within its ± 5 percent uncertainty band. It is also evident from this figure that there is little difference between the mass flow rate values calculated with the prevailing-assumption and the two-piece velocity profile integration over the near-wall region for $50x10^3 < Re_d < 240x10^3$.

7.2.2 Evaluation of Source Term Formulations

In this section, the different formulations proposed for incorporating $\overline{S^k}$ and $\overline{S^\epsilon}$ into the discretization equations, as presented in Section 5.3.3, are evaluated in terms of their effect on the rate of convergence of the overall solution procedure. It is to be noted again at this stage that the only difference in the JL and LS models is the expression used to calculate $f_{c\mu}$: Since the other features of these two models are similar, the effect of one source term treatment relative to the others is expected to be the same when using either model. Therefore, the source term evaluations were done using only the JL k-ϵ turbulence model.

First, the evaluation of the different combinations of source terms, $\overline{S^{k_1}}$, $\overline{S^{k_2}}$, $\overline{S^{\epsilon_1}}$, and $\overline{S^{\epsilon_2}}$, was done using Procedure A, described in Section 5.3.3, in which all $\overline{S_C}$ and $\overline{S_P}$ terms are calculated using the previous iteration values of k and ϵ rather than the most recent values, as done when Procedure B is implemented. Following these tests, the

combination of $\overline{S^k}$ and $\overline{S^\epsilon}$ chosen as the most appropriate was used with each of Procedures A and B to determine the effects of these procedures on the rate of convergence of the overall solution procedure.

Based on the method of classification presented in Section 5.3.3, four combinations of two possible $\overline{S^k}$ and $\overline{S^\epsilon}$ formulations were tested: $S^k{}_1$-$S^\epsilon{}_1$-A, $S^k{}_1$-$S^\epsilon{}_2$-A, $S^k{}_2$-$S^\epsilon{}_1$-A, $S^k{}_2$-$S^\epsilon{}_2$-A. These different source term treatments were evaluated in terms of the number of machine execute units required to achieve the convergence criteria described in Section 7.2.1. Table 11 shows the results for four different Re_{fric} values: For each Re_{fric} value the results are normalized with respect to the number of execute units required to obtain a converged solution when using the $S^k{}_1$-$S^\epsilon{}_1$-A formulation. The four values of Re_{fric} are representative of the Reynolds number range investigated in the performance evaluation presented in Section 7.2.1. For $Re_{fric} = 10.5 \times 10^3$, the results show that with the $S^k{}_1$-$S^\epsilon{}_1$-A formulation a converged solution was reached in 40 percent, or less, of the total time required when using any one of the other three formulations. For the intermediate Re_{fric} values in Table 11, it is evident that there is at least a marginal advantage to be gained by using the $S^k{}_1$-$S^\epsilon{}_1$-A formulation instead of either the $S^k{}_1$-$S^\epsilon{}_2$-A or $S^k{}_2$-$S^\epsilon{}_2$-A formulations. However, the $S^k{}_2$-$S^\epsilon{}_1$-A formulation gives equivalent or, in some cases, even better rates of convergence, as shown by the results for $Re_{fric} = 3.00 \times 10^3$ where convergence is achieved in 84 percent of the time required when using the $S^k{}_1$-$S^\epsilon{}_1$-A formulation. At the lowest end of the Re_{fric} range, $Re_{fric} = 3.72 \times 10^2$, it appears that no significant savings in computation time can be gained by using any one particular formulation. This

is true if the underrelaxation coefficients in the U, k, and ϵ discretization equations are kept at the values of 1.0, 0.9, and 0.9, respectively. These values are required in order to achieve stable converged solutions using any of the four source term formulations, over the entire range of Re_{fric} being investigated. Only with the S^k_1-S^ϵ_1-A formulation, for $Re_{fric} = 3.72 \times 10^2$, was it possible to attain a converged solution without using underrelaxation (i.e. all α's = 1.0): The computing time required in this case was one sixth of that needed when the k and ϵ underrelaxation values of $\alpha = 0.9$ were used. This low-Reynolds-number behaviour indicates that the S^k_1-S^ϵ_1-A formulation leads to greater stability of the iterative solution procedure than the other three formulations.

This desirable behaviour of the S^k_1-S^ϵ_1-A formulation is also demonstrated with the ST model for the case of no underrelaxation, as shown by the results in Table 12: When using the S^k_1-S^ϵ_1-A formulation, a converged solution is obtained for both the minimum and maximum Re_{fric}; when using any of the other three formulations, a converged solution is not obtained for the maximum Re_{fric}; and at the lowest Re_{fric}, the S^k_1-S^ϵ_2-A and S^k_2-S^ϵ_2-A formulations give converged solutions, but they need more than 175 percent of the time required when using the S^k_1-S^ϵ_1-A formulation.

Based on the foregoing discussion, it can be concluded that the S^k_1-S^ϵ_1-A source term formulation should be used to ensure that a converged solution is achieved efficiently for the entire range of Reynolds numbers used in this investigation. It can also be argued that the S^k_1-S^ϵ_1-A formulation will be more efficient than the other

formulations, even for the more complex case of two-dimensional periodic fully developed duct flows investigated in this thesis. Solution of such elliptic flows requires the use of two-dimensional grids, which contain a considerably larger number of grid points than the one-dimensional grids used in this initial evaluation, and line-by-line TDMA/CTDMA iterative procedures for solving the linearized and decoupled sets of discretization equations within one iteration of the overall solution process. In this context, the additional iterative procedures that are required in the implementation of the S^k_2 treatment for the k equation could greatly decrease the computational efficiency of the S^k_2-S^ϵ_1-A formulation. In addition, for the complex interrupted-plate duct flows, it is desirable to use a source term formulation that enhances the stability of the overall iterative process. This characteristic is clearly demonstrated by the S^k_1-S^ϵ_1-A formulation when compared to the S^k_2-S^ϵ_1-A formulation.

The evaluation of the effects of using Procedures A and B for calculating the $\overline{S_C}$ and $\overline{S_P}$ terms of the k and ϵ equations was done with the S^k_1-S^ϵ_1 formulation, for the minimum and maximum Re_{fric} values of 3.72×10^2 and 10.5×10^3, respectively. When underrelaxation coefficients of $\alpha = 0.9$ were used in the k and ϵ discretization equations, the results of the two procedures showed little difference. Converged solutions using Procedure B required only one percent and three percent more time than with Procedure A for the respective minimum and maximum Re_{fric} values. When no underrelaxation was used for $Re_{fric} = 3.72 \times 10^2$, a converged solution using Procedure B required 222 percent more time than when using Procedure A. Thus Procedure A can be considered more efficient than Procedure B.

From the evaluations of the k and ϵ equation source term formulations presented in this section, it was concluded that the S^k_1-S^ϵ_1-A formulation is the most stable and efficient of the four formulations considered.

7.3 INITIAL NUMERICAL INVESTIGATION: PERIODIC FULLY DEVELOPED LAMINAR FLOW

As was stated in Chapter I, a computer code incorporating the numerical formulation described in Chapter IV was developed during the course of this research. In this section, an evaluation of the code's capability to predict two-dimensional periodic fully developed flows is made: Results for laminar flows are presented and compared to results obtained by Patankar and Prakash [14] for similar flows. This was done to verify that the proposed numerical method was correctly implemented in the computer code. Similar checks of the results for turbulent periodic fully developed flows were not possible at the time of this evaluation since no suitable comparison data were available in the published literature.

The results presented in this section were obtained by performing the numerical computations on the CRAY X-MP/22 supercomputer operated by the Centre for Large Scale Computation (CLSC) at the University of Toronto. The FORTRAN source code was compiled using the Cray FORTRAN Compiler (CFT) and all real numbers and variables were specified as real (R), or single precision, type values which allows real numbers in the range $10^{-2466} < R < 10^{2465}$ to be approximated to 14 decimal digits of

precision [124].

7.3.1 Mathematical Model

Patankar and Prakash [14] performed a numerical analysis of periodic fully developed laminar flow in an interrupted-plate passage similar to the one depicted in Fig. 44. As discussed in Chapter II, for periodic fully developed flow, it is sufficient to solve for the flow field in only one geometrically similar module: One such module is shown by the shaded area ABCDEF in Fig. 44. The x and y momentum equations governing this type of flow are given by Eqs. (5-1) and (5-2) when μ_t is set equal to zero. The k and ϵ equations are, of course, not required for laminar flow calculations.

With reference to the nomenclature shown in Fig. 44, a nominal flow Reynolds number, Re_s, and module friction factor, f_s, for the module ABCDEF have been defined in [14] as:

$$Re_s = \frac{\rho\, U_{av}\, (4H)}{\mu} \tag{7-13}$$

$$f_s = \frac{\beta\, (4H)}{(2\, \rho\, U_{av}^2)} \tag{7-14}$$

The average velocity, U_{av} is:

$$U_{av} = \frac{\dot{m}_M}{(\rho\, H)} \tag{7-15}$$

where $\dot{m}_M$ is the mass flow rate through the module ABCDEF.

The mass flow rate through a module is determined by the value specified for the modular pressure gradient, β, in Eq. (5-3). The only quantitative measure of β presented in [14] is in the form of friction factor - Reynolds number, f_s versus Re_s, plots. For L/H = 1.0, t/H = 0.3, and Re_s values of 100, 200, 500, 1000, and 2000, corresponding values of f_s were read from the appropriate figures given in [14]. These values are representative of the full range of Reynolds numbers and the largest plate thickness parameter studied by Patankar and Prakash [14]. From this set of f_s versus Re_s data, the input values of β were determined for the geometric module parameters already given. The values of f_s read from the graphical data in [14] are presented in Table 13.

7.3.2 Numerical Formulation

The periodic fully developed laminar flow in this problem is governed by the continuity equation, Eq. (2-7), and the x and y momentum equations given by Eqs. (5-1) and (5-2), respectively, when all μ_t terms are set to zero. Excluding any steps that involve μ_t, k and ϵ, the same iterative solution procedure summarized in Section 5.2.5 was used to solve the laminar flow equations: Only Steps 1, 3 to 8, and 11 were performed. In Step 1, the relaxation parameters, α's, are set to 0.9 for the U and V momentum discretization equations, and the convergence tolerance was set to 10^{-8}. Convergence is considered to be achieved when the mass source term, b', in the pressure correction equation, Eq. (4-38), was less than the convergence tolerance. The modular pressure gradient term was determined from the data of Table 13. It was found from preliminary tests that some repetitions of the internal

line-by-line TDMA/CTDMA iterations, five times for the U and V momentum discretization equations in Steps 4 and 5, respectively, and fifteen times for the p' discretization equation in Step (6), provided the best overall rate of convergence.

The calculation domain was discretized in the same manner as that described in Section 5.2.1, except that an additional y zone was added at the top of the domain to account for the plate in this region. This ensured that y-direction grid spacing was finer near plate surfaces and the x-direction grid spacing was finer near the leading and trailing edges of a plate. After performing calculations with a number of different grid distributions, generated as described in Appendix 1, it was determined that an x-y grid distribution of 88x73 nodes gives grid-independent results for the range of Reynolds numbers investigated. This grid is shown in Fig. 45, and it was used for all laminar flow computations. The results of these tests are presented in the next section.

The flow field in the module ABCDEF, shown in Fig. 44, repeats itself at the periodic boundaries, AF and CD. A flow symmetry line is assumed at the boundaries along BC and EF. These boundaries and the solid plate regions are treated in the same manner as that described in Sections 5.2.3 and 5.2.4 for similar boundaries and regions in turbulent interrupted-plate duct flow.

7.3.3 Results

Grid Checks

Because of the complex elliptic nature of the laminar periodic fully

developed flows investigated, densely packed uniform grids are required to obtain solutions that can be extrapolated to approximate true grid-independent solutions. As was the case for the turbulent flow studies of Section 7.2, the use of such grids was impractical because of the large computational expense that would be involved. Instead, nonuniform grids of 56x11 to 112x105 were generated using the procedure described in Appendix 1. Computations using grids of 56x11, 88x73, and 112x105, yielded the U velocity profiles at the inlet of the module ABCDEF that are shown in Fig. 46. Little change is observed between the profiles of the two densest grids indicating that for the purposes of this study: The 88x73 grid was to give grid-independent solutions. In order of increasing grid density, the CPU time required to obtain a converged solution ranged from just less then 4 minutes for the coarsest grid to over 60 minutes for the finest grid with the intermediate grid requiring some 30 minutes. This illustrates the importance in determining an optimum grid, for which essentially grid-independent solutions are achieved at reasonable costs: The 88x73 grid can be used at half the cost of the 112x105 grid to give results that are within less than 0.5 percent of each other.

The grid checks presented here were done for the maximum Reynolds number flow. At this Reynolds number the flow is assumed to be of a more complex nature, with greater velocity gradients occurring near plate surfaces and more extensive recirculation zones existing between the trailing and leading edges of plates, compared to the lower-Reynolds-number flows. For this reason, it is valid to assume that the 88x73 grid calculations will give grid-independent results over the whole Reynolds number range considered here.

Friction Factor - Reynolds Number Plots

The friction factor - Reynolds number results of the computations are plotted in Fig. 47 along with the corresponding data of Patankar and Prakash [14]. The curve obtained from the computations done in this work is shifted slightly above that drawn from the data in [14], although both curves show the same trends. It is difficult to explain why this difference exists without having more detailed information than what is given in [14] about the grids employed and the methods used to determine the numerical accuracy of the solutions. A thorough review of the source code used for this work did not reveal any errors, thereby providing confidence in the numerical correctness of the computations. Care was taken to minimize any error that may have occurred in reading the f_s values from the plots in [14]. There is, however, a degree of uncertainty that is inherent in these values due to the fact that they were read from logarithmic plots reduced to allow inclusion in the text of a journal publication. Another plausible explanation is that the mass flow rates calculated using the 88x73 grid of this work are more accurate than the 60x30 grid solutions reported in [14]. This cannot be verified without quantitative information on how the grid in [14] was distributed across the calculation domain. It was found that a 56x11 grid used in the grid checks of this study resulted in a computed R_s value of 2001, compared to the value of 2000 in [14], but with the finer 88x73 grid the computed R_s value increased to a value of 2075.

Streamline Plots

The discussion in the preceding paragraph is somewhat speculative. However, if it is assumed that both the computations of this work and

those in [14] are numerically correct, for the particular grid distributions used, then the results of both sets of computations should exhibit at least qualitative agreement. Such agreement between the calculated flow fields of this investigation and those in [14] is demonstrated by the streamline plots shown in Fig. 48 for the maximum and minimum values of Re_s.

Conclusion

From the results presented for the laminar flow investigation, it was concluded that the numerical method presented in Chapter IV has been properly implemented in the numerical code. This allowed applications of the code to periodic fully developed turbulent flows to be undertaken with confidence.

CHAPTER VIII

RESULTS OF THE EXPERIMENTAL INVESTIGATION

The results of the experimental investigation of turbulent periodic fully developed flow in interrupted-plate rectangular ducts are presented in this chapter. Initial tests were first run to determine that statistically steady periodic fully developed flows are established. The results of these tests are presented and discussed first. Then the results of time-mean wall static pressure measurements and flow visualization studies are presented. In this chapter, the emphasis is on the presentation of the experimental results. A detailed discussion of these results is left for the next chapter, in which the corresponding numerical data are also presented and compared to the experimental data.

8.1 SPECIFICATIONS OF INTERRUPTED-PLATE DUCT TEST SECTIONS

Three interrupted-plate rectangular duct test sections, denoted as Duct 1, Duct 2, and Duct 3, where used in this research. Each test section could be constructed by suitably adapting a common rectangular duct test section, as described in Chapter VI. The nominal values of the dimensions and the geometric parameters of the three interrupted-plate ducts were also given in Chapter VI. The actual measured values of these quantities are presented in Table 3. The wall static pressure taps are located along the centerline of the bottom aluminum plate of each test section. The same aluminum plate is used in all three ducts, and the locations of the centers of the pressure tap holes are given in Table 4.

8.2 CHECKS TO DETERMINE THE ESTABLISHMENT OF TURBULENT PERIODIC FULLY DEVELOPED FLOW

First, checks to determine the repeatability of the time-mean static pressure measurements were done at the maximum and minimum flow rates used in this investigation, for each of Ducts 1 to 3. The results of these checks are shown in Figs. 49(a) and (b) in terms of $(P^*_o - P^*)_m$ versus $(x^* - x^*_o)_m$ plots for the respective maximum and minimum flow rates of Duct 1. The corresponding results for Duct 2 and Duct 3 are shown in Figs. 50(a) and (b), and Figs. 51(a) and (b), respectively. In these figures:

$$(P^*_o - P^*)_m = \frac{(P_o - P)}{\frac{1}{2} \rho \overline{U}_m^2} \tag{8-1}$$

and

$$(x^* - x^*_o)_m = \frac{(x - x_o)}{D_h} \tag{8-2}$$

P^*_o and x^*_o denote nondimensional values of the time-mean wall static pressure and axial coordinate, respectively, at a suitably chosen reference pressure port, or tap. With reference to Figs. 1 and 2, and to the data in Tables 3 and 4, the reference pressure tap for Ducts 1 to 3 was located at port 91, ensuring that there were at least 11 geometrically similar modules upstream. Thus in each duct, periodic fully developed flow conditions were expected to prevail over the geometrically similar modules located downstream of this reference pressure port. Time-mean wall static pressure measurements were taken over the first 11 modules

located downstream of port 91.

The numerical simulations in this thesis are done for two-dimensional flow geometries. In Eq. (8-2), to be consistent with the nondimensional numerical data presented, the two dimensional form of D_h is used for both the numerical and the complementary experimental results. This two-dimensional form of D_h is:

$$D_h = 2H \tag{8-3}$$

In Eq. (8-1), $\bar{U}_m$ is defined by Eq. (2-47):

$$\bar{U}_m = \frac{\dot{m}}{2\rho bH} \tag{2-47}$$

The overall mass flow rate, $\dot{m}$, in the interrupted-plate duct test section is the same mass flow rate that is calculated from the measurements in the flow metering section. Since the air flows investigated are essentially isothermal and incompressible, the density, ρ, was based on the air temperature and the time-mean wall static pressure measured in the flow metering section. For all test runs, the total pressure drop across the section of duct in which pressure measurements were taken, was less than 460 Pa. The difference in the arithmetic mean of the time-mean wall static pressures at the reference port and the last port in the aluminum duct test section, and the time-mean static pressure of the flow metering section, was one percent or less of the former quantity. In addition, for the maximum flow rate, the Mach number based on the average velocity, $\bar{U}_k$, at the minimum flow area in the duct was less than 0.06. These results indicate that the assumption of incompressible, constant property, fluid flow is valid throughout the length

of the flow facility over which pressure measurements were taken.

In each of the Figs. 49(a) to 51(b), the results of the initial and the repeatability test runs are denoted by the symbols ○ and □, respectively. Three types of vertical lines are also shown in each of these figures. They denote the locations of the leading edge (————————), the center (– – – – – – –), and the trailing edge (—— – – ——) of each of the plates in the colinear interrupted-plate array. A geometrically similar module, such as ABCDE in Fig. 2, extends over the region between the leading edge of a plate to the leading edge of an adjacent plate in the colinear interrupted-plate array. Within each module, the region between the trailing edge of the plate to the exit plane of the module comprises the wake region of the flow coming off the plate. With reference to Fig. 19, pressure measurements are taken at LE, LC, CP, CT, TE, G1, G2, and G3 locations in each of the first 11 modules downstream of the reference pressure port, as well as at the LE location of the twelfth module. The plots in Figs. 49(a) to 51(b) show that in each module, there is a drop in the time-mean wall static pressure over the leading-edge region of a plate and a partial recover of this pressure drop in the wake region just downstream of a plate trailing edge. A detailed examination and discussion of this intramodular pressure behaviour is presented in Chapter IX.

Each test run required 90 minutes to 120 minutes to complete, and each repeatability run was performed 10 minutes to 15 minutes after the corresponding initial run. The maximum ± uncertainty in $(P^*_o - P^*)_m$ values is 0.024, 0.046, 0.033, 0.058, .055, and 0.11, in Figs. 49(a), 49(b), 50(a), 50(b), 51(a), and 51(b), respectively. The maximum

uncertainty in $(x^*-x^*_o)_m$ values is $\pm$ 0.041 in all of these figures. A detailed description of the uncertainty analysis used is given in Appendix 5, where a sample calculation of the uncertainty in Re_m is presented. The results from the initial and repeated runs for the maximum flow rates in Ducts 1, 2, and 3, shown in Figs. 49(a), 50(a), and 51(a), respectively, are almost indistinguishable from each other, indicating very good repeatability. The results shown in Figs. 49(b), 50(b), and 51(b) for the minimum flow rates in these three ducts, also show good agreement between the initial and repeated runs, although not as good as those for the maximum flow rates. The measurement errors relative to the magnitude of flow rates and pressure differentials will be larger at lower flow rates than at higher flow rates. However, both initial and repeated sets of data plotted in each of Figs. 49(b), 50(b), and 51(b) do agree within the limits of the experimental uncertainty in the measurements. A better quantitative measure of the overall repeatability of the data presented in Figs. 49(a) to 51(b) can be obtained by comparison of the corresponding modular friction factor - Reynolds number values.

As was discussed in Chapter II, the behaviour of the time-mean static pressure in the periodic fully developed region of turbulent flows in interrupted plate ducts is given by Eqs. (2-17) to (2-19). To facilitate the following discussion, these equations are repeated here:

$$\{ P(x,y,z) - P(x+L+s,y,z) \} = \{ P(x+L+s,y,z) - P(x+2L+2s,y,z) \}$$
$$= \{ P(x+2L+2s,y,z) - P(x+3L+3s,y,z) \} \qquad (2\text{-}17)$$

and

$$P(x,y,z) = -\beta x + \hat{P}(x,y,z) \qquad (2\text{-}19)$$

where

$$\beta = \frac{\{\, P(x,y,z) - P(x+L+s,y,z) \,\}}{(L+s)} \qquad (2\text{-}18)$$

β is related to the pressure drop required to generate the overall mass flow rate in the duct. $\hat{P}(x,y,z)$ is the periodically varying component of the pressure related to the details of the local flow field in each geometrically similar module:

$$\hat{P}(x,y,z) = \hat{P}(x+L+s,y,z) = \hat{P}(x+2L+2s,y,z) = \ldots \qquad (2\text{-}20)$$

This periodicity in the time-mean wall static pressure variation can be seen in the results in Figs. 49(a) to 51(b).

Equations (2-17) and (2-18) imply that the same drop in time-mean static pressure occurs between any two points that have the same (y,z) coordinates and are separated by a periodic distance of (L+s) in the x direction. Therefore, in Figs. 49(a) to 51(b), if periodic fully developed flow conditions prevail downstream of the reference pressure port, then any set of data points having a periodic spacing of (L+s) in the x direction should all fall on a straight line. The method of least squares was used to fit a straight line through each of 8 sets of $(P^*_o - P^*)_m$ versus $(x^* - x^*_o)_m$ data points having a periodic spacing of (L+s): With reference to Fig. 19, lines were fitted through sets of data points located at the LE, LC, CP, CT, TE, G1, G2, and G3 locations of the 11 modules shown in Figs. 49(a) to 51(b). The LE data point of the twelfth module, located at the exit of the eleventh module, is also

included in the LE data set. The correlation coefficient and slope of each line were calculated: The correlation coefficient serves as a measure of the linearity of the $(P^*_o - P^*)_m$ versus $(x^* - x^*_o)_m$ data, and the slope is equal to the module friction factor, f_m, as defined in Eq. (2-46):

$$f_m = \frac{\beta D_h}{\frac{1}{2} \rho \bar{U}_m^2} \tag{2-46}$$

The f_m values reported without any additional subscript are the average of the eight local values, f_{mLE}, f_{mLC}, f_{mCP}, f_{mCT}, f_{mTE}, f_{mG1}, f_{mG2}, and f_{mG3}, calculated for the aforementioned sets of periodically spaced data points. In principle, for each run, all module friction factor values should be the same. A comparison of the eight local module friction factors with the average module friction factor was used as an internal consistency check on the experimental $(P^*_o - P^*)_m$ versus $(x^* - x^*_o)_m$ data obtained for each run, as discussed in the following paragraphs.

The correlation coefficients and f_m values produced by the above mentioned analysis of the data in Figs. 49(a) to 51(b) are presented in Table 14. The correlation coefficient in every case is better than 0.9985. The results also indicate, quantitatively, the repeatability of the data in Figs. 49(a) to 51(b). The deviation in f_m of the repeated run from the initial run is less than ± 2.7 percent for all cases and less than ± 0.7 percent for all the maximum flow rate tests. The corresponding Reynolds number deviations are all less than ± 0.8 percent. These results demonstrate the ability of the flow facility to provide

steady air flow rates and repeatable time-mean wall static pressure measurements in each of the three interrupted-plate duct test sections, over the range of module Reynolds numbers investigated.

For each of Ducts 1 to 3, seven different Reynolds numbers were considered: Thus a total of 21 different combinations of flow rates and interrupted-plate geometries were investigated. The establishment of periodic fully developed flow for each of these combinations can be verified by examining the deviations of the local values, f_{mLE}, f_{mLC} f_{mCP}, f_{mCT}, f_{mTE}, f_{mG1}, f_{mG2}, and f_{mG3}, from the average value of f_m. These are given in Table 15 along with corresponding values of correlation coefficients. The deviation of all local f_m values from the average value for any given Re_m is less than $\pm$ 1.6 percent in all cases. Indeed, in only four instances did any of the local values deviate from the average f_m value by more than $\pm$ 1 percent. These deviation limits are roughly the same as, or better than, the deviation limits obtained from the repeatability checks discussed in the previous paragraph, and all fall within the experimental uncertainty of the corresponding average f_m values reported in Table 16. In addition, all correlation coefficients for local f_m values were better than 0.9985, indicating a good degree of linearity in the sets of periodically spaced points. To provide a visual appreciation of the linearity and internal consistency of the data at periodically spaced points, $(P^*_o-P^*)_m$ versus $(x^*-x^*_o)_m$ data points for the LC, TE, and G3 locations of Duct 3 for the maximum Re_m are presented in Fig. 52, along with the plots of the corresponding least-squares straight lines: The Reynolds number for this run is $Re_m = 32.32 \times 10^3$.

Based on the results presented in this section, it was concluded that steady and repeatable time-mean wall static pressure measurements could be obtained with the experimental facility and procedures used in this work, over the entire range of Reynolds numbers considered. In addition, for this Re_m range, it was concluded that periodic fully developed flows are established in Ducts 1 to 3 downstream of the reference pressure tap located at port 91.

8.3 MODULE FRICTION FACTOR - REYNOLDS NUMBER RESULTS

The module friction factor - Reynolds number results for Ducts 1 to 3 are presented in this section. As was mentioned in the preceding section, a total of 21 different combinations of interrupted-plate duct and flow rates were investigated. As was discussed in Chapter II, for a given flow rate, two different Reynolds numbers can be defined for interrupted-plate ducts: one based on $\bar{U}_m$ and one based on $\bar{U}_k$:

$$Re_m = \frac{\rho \bar{U}_m D_h}{\mu} \tag{2-45}$$

and

$$Re_k = \frac{\rho \bar{U}_k D_{hk}}{\mu} \tag{2-39}$$

with $\bar{U}_m$ and $\bar{U}_k$ given by Eqs. (2-47) and (2-41), respectively. As discussed in Section 8.2, the two dimensional form of D_h is used, Eq. (8-3), and similarly, D_{hk} is given by the two dimensional form of Eq. (2-42):

$$D_{hk} = \frac{4\,(H - t)\,(L + s)}{(2L + s)} \tag{8-4}$$

The method used to calculate the module friction factor, f_m, has already been described in Section 8.2. Another commonly used module friction factor, f_k, was defined in Eq. (2-40), and discussed in Section 2.6.2. It is related to f_m by the following equation:

$$f_k = f_m \left(\frac{D_{hk}}{D_h} \right) \left(\frac{\bar{U}_m}{\bar{U}_k} \right)^2 \qquad (8\text{-}5)$$

The f_m versus Re_m results for Ducts 1 to 3 are shown in Table 16, and the corresponding f_k versus Re_k results are presented in Table 17. The nominal geometric dimensions of modules in Ducts 1 to 3 are equivalent, except for the plate thickness, 2t. Thus, for a given mass flow rate, $\dot{m}$, the only variable which changes in the f_m values for Duct 1, Duct 2, and Duct 3, is the module pressure gradient term, β. However, due to the different values of 2t in Duct 1, Duct 2, and Duct 3, if f_k and Re_k values are considered, the average flow velocity, $\bar{U}_k$, the module hydraulic diameter, D_{hk}, and β are all variable quantities. To facilitate a direct evaluation of the effect of plate thickness on the overall module pressure drop, the discussion in this thesis will be focussed on the f_m versus Re_m data for Ducts 1 to 3. The f_k versus Re_k values are presented for completeness only.

Graphical representation of the f_m versus Re_m results for Ducts 1, 2, and 3 are shown in Fig. 53. As indicated in Table 16, the uncertainty in the f_m values ranges from $\pm$ 12 percent at the lowest Reynolds numbers to less than $\pm$ 2 percent at the higher Reynolds numbers, and it is less than $\pm$ 5 percent for most of the data. The

corresponding uncertainty in Re_m values is less than $\pm$ 2.25 percent in all cases. Within the limits of the experimental uncertainty reported in Table 3, the only difference in the geometries of Ducts 1, 2, and 3 is the plate thickness parameter, t^*, which is approximately doubled from Duct 1 to 2 and from Duct 2 to 3: $t^* = 0.027$ for Duct 1; $t^* = 0.056$ for Duct 2; and $t^* = 0.110$ for Duct 3.

The effects on overall pressure drop caused by changing t^* and Re_m can be seen in the friction factor data plotted in Fig. 53. For all three ducts, the friction factors follow the same general trend: The values of f_m become smaller as Re_m increases, with the decrease in f_m becoming progressively less as Re_m increases. When t^* increases so does the overall pressure drop, as demonstrated by the increase in the levels of f_m from Duct 1 to Duct 2, and the even greater increase in the f_m level from Duct 2 to Duct 3. A more detailed analysis of these results will be deferred until Chapter IX, where the numerical results are also presented.

8.4 INTRAMODULAR TIME-MEAN WALL STATIC PRESSURE RESULTS

In this section, nondimensionalized time-mean wall static pressure distributions within a module are presented. Detailed experimental data on intramodular pressure distributions for periodic fully developed flow in interrupted-plate ducts, or any other periodically interrupted flow passages, have not been reported in the published literature by any other investigators for either laminar or turbulent conditions. Therefore the results presented in this section for various combinations of the plate thickness parameter, t^*, and the module Reynolds number, Re_m,

add new information to the fluid flow data in the published literature, and are considered as an important original contribution of this thesis.

Seven different Reynolds numbers were considered for each of Ducts 1 to 3. The 21 time-mean wall static pressure distributions obtained from this experimental investigation are presented in Figs. 54(a) to (d) and Figs. 55(a) to (c) for Duct 1; Figs. 56(a) to (d) and 57(a) to (c) for Duct 2; and Figs. 58(a) to (d) and Figs. 59(a) to (c) for Duct 3. In these figures, the intramodular time-mean wall static pressure distributions are plotted as $(P^*_1 - P^*)_m$ versus $(x^* - x^*_1)_m$: P's and x's are nondimensionalized by $\{(1/2)\rho\bar{U}_m^2\}$ and D_h, respectively, and the subscript, i, is used to denote quantities pertaining to the wall static pressure tap located over the leading edge of the plate in the periodic fully developed module. The pressure values shown are the arithmetic averages of the nondimensional time-mean wall static pressures at corresponding x locations, having a periodic x spacing of (L+s), in each of the 11 modules where pressure measurements were taken: With reference to Fig. 19, arithmetic averages of pressure measurements at the LE, LC, CP, CT, TE, G1, G2, G3, and LE at the exit of each module, are presented in Figs. 54(a) to 59(c). In these figures, the experimental data points are represented by the symbol o, and the vertical lines denote the locations of the leading edge (————————), the center (— — — — — — —), and the trailing edge (—— — — ——) of the plate. The corresponding plate locations are also the arithmetic averages of the measured LE, CT, TE, and module exit LE locations of the 11 modules in which pressure measurements were taken. In these figures, the maximum uncertainty in $(x^* - x^*_i)_m$ values is less than 1.3×10^{-3}, and the maximum uncertainty in the $(P^*_i - P^*)_m$ values ranges from a minimum of 8.3×10^{-4} for Duct 1 with

$Re_m = 33.49 \times 10^3$, to a maximum of 1.5×10^{-2} for Duct 3 with $Re_m = 4.997 \times 10^3$: The maximum uncertainties of nondimensional pressure values corresponding to each duct and Re_m combination are given in the caption accompanying each of the figures.

From Figs. 54(a) to 59(c), it is observed that for all Reynolds numbers, there is a steep drop in time-mean wall static pressure over the leading-half of the plate, a rise in this pressure over the first half of the interrupted-plate gap, and a drop in the time-mean wall static pressure in the second half of the gap as the next plate leading edge is approached. Over the second half of the plate, the time-mean wall static pressure begins to rise before the trailing edge of the plate is reached in all cases, except for the lowest Reynolds number of Duct 1 where the rise in time-mean wall static pressure does not begin until the flow has entered the interplate gap region. These experimental results shall be examined and discussed in more detail in Chapter IX, after all the experimental and numerical data has first been presented. To aid in the use of the experimental intramodular time-mean wall static pressure distributions in future investigations, the actual values of $(P^*_i - P^*)_m$ versus $(x^* - x^*_i)_m$ data points which correspond to the minimum and maximum flow rates in Ducts 1, 2, and 3 are presented in Table 18.

8.5 INTERRUPTED-PLATE SURFACE STREAMLINE RESULTS

The nature of the flow over the surface of an interrupted-plate in periodic fully developed turbulent flow was investigated using the surface oil-flow technique described in Chapter V'. Initially, two types

of kerosene based paints were used: one containing a Day-glo orange fluorescent pigment and the other containing powdered titanium dioxide (TiO_2). A detailed discussion concerning the paint compositions and application procedures was presented in Section 6.6.4. The results of this surface flow visualization study are presented in the current section.

The clear acrylic flow visualization section used in this work was a continuation of the interrupted-plate geometry of the upstream aluminum duct section. Within the limits of the reported measurement uncertainties, the dimensions of the flow visualization section for Ducts 1 to 3 are the same as those values presented in Table 3 for the corresponding aluminum duct sections. The module-to-module repeatability, characteristic of velocities at periodically spaced (L+s) points in the x direction with the same (y,z) locations, is demonstrated, qualitatively, by the similarity in the surface streamline patterns on the three successive plates shown in Fig. 60 for $Re_m = 8.087x10^3$ in Duct 2. The main-flow direction in this figure is from right to left and, starting from the upstream position, these plates are located in the fourth, fifth and sixth periodic modules downstream of the start of the flow visualization section. This type of repeatability was exhibited for all of the 21 interrupted-plate duct geometry and module Reynolds number combinations investigated.

As explained in Section 6.1.1, each of the plates in Fig. 18 has a total cross-flow width of 175.0 mm, of which the central 152.4 mm makes up the plate width, b, that is located in the turbulent air flow. As seen from the dark streaks that run in the flow-oriented (length-wise)

direction of the three plates shown in Fig. 60, the flow over the surface of each plate can be considered to be two-dimensional over at least the central 80 percent of the aforementioned 152.4 mm width of plate.

The surface streamline patterns in Fig. 60 show three distinct regions from the leading edge to the trailing edge of a plate: (1) a leading-edge region where little or no streaking is observed; (2) a central region where dark streaks are seen extending towards the trailing edge of the plate; and (3) a trailing edge zone which begins where an accumulation of paint is observed. These three regions were observed in each of the 21 different cases considered.

The plate-surface streamline patterns characteristic of the periodic fully developed turbulent flows investigated are presented in Figs. 61 to 81: Results are shown for each value of Re_m, beginning with the minimum value and increasing to the maximum value, in Figs. 61 to 67, Figs. 68 to 74, and Figs. 75 to 81, for Duct 1, Duct 2, and Duct 3, respectively. In each of these photographs, the upper edge of the plate is the leading edge and the bottom edge is the trailing edge. To enhance the details of the streamline patterns, only close-up photographs, which in most cases show the central 70 percent of the plate cross-flow width, b, are presented in Figs. 61 to 81. The streamlines in Figs. 61 to 67 for Duct 1 were obtained using the TiO_2 paint, while the patterns shown in Figs. 68 to 81 were obtained using the Day-glo orange fluorescent paint. The reasons for this are discussed in the next paragraph.

From preliminary tests, it was found that both the Day-glo and TiO_2 paints show similar streamline patterns, but the TiO_2 paint gave a finer resolution of the details than the Day-glo paint in some cases. To determine if the TiO_2 paint would give the best results over the whole range of flow rates investigated, both the TiO_2 and Day-glo paints were used in the experimental runs with Duct 1. Four plates were painted, two with the TiO_2 paint and two with the Day-glo paint, and placed in the flow visualization section at the beginning of each run. After enough time had elapsed to allow the kerosene to evaporate and leave the dried TiO_2 or Day-glo pigment on the plate in the form of the surface streamline patterns, the plates were removed from the flow visualization section and photographed. Figures 66 and 67 are examples of dried TiO_2 flow patterns, and Figs. 68 to 81 are examples of dried Day-glo flow patterns. It was found that the streamline patterns could be more clearly photographed from the dried Day-glo paint patterns than the dried TiO_2 patterns. The TiO_2 streamline patterns appear finer than the Day-glo patterns when visually examined, but the TiO_2 details are more difficult to distinguish in a photograph, at least when dried. On the other hand, the Day-glo pigment is fluorescent when illuminated by ultraviolet light and even faint flow patterns can be made quite visible and easily photographed. The photographs shown in Figs. 61 to 65 are also TiO_2 patterns, but these were taken through the top of the flow visualization section when the plates were still in the air flow and the paint had not yet dried. The detail in these photographs is clearer than those of Figs. 66 and 67, but it was very difficult and tedious to take such photographs with the photographic equipment available for this work. Specifically, it was difficult to position the camera close enough to the plate to capture the details of the flow pattern without

the camera-support stand partially obstructing the view of the plate, as occurred in Fig. 64, or without interfering with the lighting, as is shown by the dark patches caused by shadows in Figs. 61 and 63. Because of the good photographic quality of the surface streamline patterns obtained using the Day-glo fluorescent paint, and the relative ease and efficiency of the procedure used to obtain these photographs, it was decided that the Day-glo paint would be used for the experiments with Ducts 2 and 3. With each of these ducts, the Day-glo paint was applied to the fourth, fifth and sixth plates downstream of the start of the flow visualization section, as shown in Fig. 60.

In Figs. 61 to 81, the streamline patterns over the central region of the plate indicate that the flow over the surface is essentially two-dimensional: There is no indication of cross flows, as all streamlines extend over the entire plate in the x, or main-flow, direction. It is also observed that the accumulation of paint in the trailing-edge region starts further upstream of the trailing edge as the value of Re_m decreases: At the lowest Re_m values, this region begins at an upstream distance that is as much as 20 to 25 percent of the streamwise plate length, L. As the maximum value of Re_m is approached in all ducts, the extent of this trailing-edge zone decreases, and paint accumulation along the plate leading edge is also observed. A detailed analysis of these plate-surface streamline results will be deferred to Chapter IX, after the results of the numerical investigation have been presented.

CHAPTER IX

RESULTS OF THE NUMERICAL INVESTIGATION AND DISCUSSION

In this chapter, the results of the numerical investigation of turbulent two-dimensional periodic fully developed flow in interrupted-plate rectangular ducts are presented and discussed with respect to the corresponding experimental data that was presented in Chapter VIII. There are nine sections in this chapter. The first section describes some of the key features of the numerical investigation, including the results of a performance evaluation done to finalize the k-ϵ model of turbulence used in this study. In the remaining eight sections, the focus is on the presentation and discussion of the results of the numerical investigation, in the context of the experimental results presented in Chapter VIII.

All the numerical results presented in this chapter were obtained by performing the computations on the CRAY X-MP/22 supercomputer operated by the Centre for Large Scale Computation (CLSC) at the University of Toronto. The Cray FORTRAN Compiler (CFT) was used to compile the FORTRAN source code. All real numbers and variables were specified as single precision type. This allowed real numbers between 10^{-2466} and 10^{2465} to be approximated to 14 significant digits of precision [124].

9.1 KEY FEATURES OF THE NUMERICAL INVESTIGATION

9.1.1 Introduction

During the course of this research, a computer code incorporating

the numerical formulation described in Chapter IV was developed. This code was tested, debugged, and validated by applying it to several test problems, including the periodic fully developed laminar flow discussed in Chapter VII. In addition, the Jones and Launder (JL) [89] and the Launder and Sharma (LS) [91] k-ϵ models of turbulence were evaluated in the context of fully developed turbulent flow in a channel. Based on the results presented in Section 7.2.1, it was concluded that the JL k-ϵ model was better than the LS model for low-Reynolds-number, $5.00\text{x}10^3 \leq (Re_d)_{nom} \leq 25.0\text{x}10^3$, fully developed turbulent channel flows. The turbulent periodic fully developed, two-dimensional, interrupted-plate duct flows ($5.00\text{x}10^3 \leq (Re_m)_{nom} \leq 30.0\text{x}10^3$) of this investigation, however, are more complex than fully developed two-dimensional channel flows. Therefore, a final comparison of the JL and LS models was undertaken to see if the JL model is indeed the better one of the two to use for the numerical simulation of such flows. These results are presented in Section 9.1.4.

As was discussed in Section 3.6, in the numerical investigations of Hanjalic and Launder [96] and Rodi and Scheuerer [97], the prediction capabilities of k-ϵ models in adverse pressure gradient turbulent flows were improved by incorporating the Hanjalic and Launder [96] modification to the ϵ equation production term P_ϵ. This modification brings in a term that favours higher dissipation for irrotational strains compared to that for rotational strains. With this modification, the P_ϵ term of S^ϵ, Eq. (5-11), is modelled by Eq. (5-12). In the interrupted-plate duct flows investigated here, due to the sudden change in module cross-sectional area that occurs when the plate ends and the interplate gap begins, it was expected that the flow within a module would experience

an adverse pressure gradient and undergo some deceleration in this region. The experimental values of intramodular time-mean wall static pressure distributions, presented in Figs. 54(a) to 59(c), do indeed indicate an adverse pressure gradient in this region of the module. It was assumed, therefore, that the Hanjalic and Launder modification [96] would be useful when modelling the periodic turbulent flows studied in this thesis. To confirm this, however, results of the JL model [89] with and without the modification were compared to corresponding experimental data. These results are given in Section 9.1.4.

Following these preliminary tests and performance evaluations, the computer code, incorporating the JL model of turbulence [89] with the Hanjalic and Launder modification [96], was used to investigate turbulent, two-dimensional, periodic fully developed flows in interrupted-plate rectangular ducts. The key features of this numerical investigation are discussed in this section.

9.1.2 Problem Description

The problem of interest involves turbulent periodic fully developed flow in a straight rectangular two-dimensional interrupted-plate duct. As was discussed in Chapter II, for such flows, it is possible and sufficient to calculate the flow field in only one geometrically similar module, such as the module ABCDE shown in Fig. 2. The x and y momentum and the continuity equations governing this type of flow are given by Eqs. (5-1), (5-2), and (2-7) . The complete set of governing equations includes Eqs. (5-5) and (5-10) for k and ϵ, respectively, and Eq. (3-8) for the calculation of the μ_t field.

The investigation was performed for three module geometries which are designated as Duct 1, 2, and 3. A schematic representation of these ducts is given in Fig. 2. The nondimensional plate length parameter, L^*, and plate thickness parameter, t^*, for these ducts in the numerical study were the same as those used in the experimental investigation, and they are given in Table 3. Considering the range of measurement uncertainties specified in this table, the values of s^* and L^* can be considered the same. In the numerical formulation of the problem, the value of s^* was, therefore, set equal to the value of L^* specified in Table 3.

Hereafter in this chapter, unless otherwise specified, reference to Duct 1, 2, or 3 will imply one geometric module in the periodic fully developed region of the flow in these ducts. Furthermore, the words duct and module will be used interchangeably.

Four flow rates (with nominal Re_m values of $5x10^3$, $10x10^3$, $15x10^3$ and $25x10^3$) were investigated for each of the three module geometries. The value specified for the modular pressure gradient, β, in Eq. (5-3) determines the mass flow rate through a module. The specified values of β in the numerical investigation were obtained from the experimental module friction factor - Reynolds number, f_m versus Re_m, data for Runs 1, 3, 4, and 6 for each of Ducts 1, 2, and 3, given in Table 16.

9.1.3 Numerical Details

The calculation domain was discretized in the manner described in Section 5.2.1 It was determined that nonuniform x-y grid distributions

of 72x78, 72x100, and 72x100 provided essentially grid-independent results for the module configurations of Ducts 1, 2, and 3, respectively, over the range of Reynolds numbers investigated. Further details are given in Section 9.1.4. These grids are shown in Figs. 13, 14, and 15. It should be noted that the y dimension of the grids in these figures has been expanded to three times its actual size relative to the x dimension. This was done in order to clearly illustrate the relative changes in the y control-volume lengths across the module. Details of the grid generation procedure are given in Appendix 1, and more will be said about how these grids were chosen in Section 9.1.4.

The derivation of the discretized forms of the governing equations was discussed in Chapter IV. The procedures used to specify boundary conditions and the treatment of the blocked-off plate regions were discussed in Sections 5.2.3 and 5.2.4, respectively.

The iterative procedure that was used to solve the discretized governing equations was summarized in Section 5.2.5. In Step 1 of this procedure, the relaxation parameters, α's, were set to 0.9 in the discretized x and y momentum and the k and ϵ equations. In the first run for each of Ducts 1, 2, and 3, the initial guess values of the U velocities were set equal to the value of the cross-sectional average mean-flow velocity, based on the appropriate experimental value of Re_m and the appropriate flow passage cross-sectional dimension of the module. Initial guess values of k and ϵ were also specified as constant values for a given stream-wise location. The guess values of k were arbitrarily set to 3.5 percent of the local mean-flow kinetic energy, and the values of ϵ were determined based on an arbitrary length scale,

chosen as (0.2 x H): The guess values of ϵ were set equal to $k^{3/2}/(0.2\ H)$. The initial values of V and P were set to zero. After the first run, in subsequent runs for a given duct, the converged solutions for U, V, P, k, and ϵ from a previous run, having the value of Re_m closest to the nominal Re_m value of the current run, were used as initial guess values. This resulted in fewer overall iterations to achieve the new converged solutions than the number required if arbitrary constant-value initial values were specified.

The convergence tolerance was set to 10^{-8}, with the convergence criteria stated in Section 5.2.7.

The block correction procedure described in Section 4.1.7 was used in Steps 3, 4, and 6 of the overall iterative solution procedure, when solving for the U^*, V^*, and P' values, but it was turned off in Steps 9 and 10 when solving the k and ϵ equations, respectively. It was found that block correction on k and ϵ did not improve the overall rate of convergence of the solution. The number of internal line-by-line TDMA and CTDMA iterations used when solving the linearized, decoupled, U, V, P', k, and ϵ discretization equations was initially set to 2, 2, 10, 3, and 3, in Steps 3, 4, 6, 9, and 10, respectively. It was found that after an initial fifty iterations these internal iterations could be reduced to 1, 1, 5, 1, and 1, without adversely affecting the overall number of iterations needed to achieve a converged solution.

9.1.4 Preliminary Numerical Results

Notes on Nondimensionalization

The results of grid checks and a final performance evaluation of the JL [89] and LS[91] k-ϵ turbulence models are discussed in this section. These results, and other numerical results in this chapter, are presented in terms of nondimensional values. In most cases, nondimensional variables and parameters are the same as those defined and used in Chapter VIII to present the experimental data. Two dimensional variables which need special mention, however, are the average module velocity, $\overline{U}_m$, and a periodic fully developed friction velocity, u_τ, that are used in the nondimensionalization of the numerical data.

The mass flow rate through a geometric module of height H, such as ABCDE in Figs. 2 and 11, is $\dot{m}/2$. As was discussed in Section 4.1.2 with reference to the nomenclature in Figs. 6 and 10(c), in the discretized calculation domain, the main-grid nodes are located at the intersections of the vertical and horizontal main-grid lines: Such a main-grid node P is located at the intersection of the lines I and J. Two control-volume faces of length ΔY_J are located on the two adjacent U-velocity staggered-grid lines, at i and i+1, adjacent to the main-grid line I shown in Fig. 10(c). The corresponding x-direction mass flow rate across a vertical control-volume face of length ΔY_J on the i grid line can be expressed as $(\rho\, U_{i,J}\, \Delta Y_J)$. Since it is assumed that there is no mass flow in or out of the top or bottom horizontal boundaries of a module, the total mass flow rate through the module is the same across any vertical cross section of the module. This value is calculated by summing the local stream-wise mass flow rate across all ΔY_J

control-volume faces located on the same i grid line:

$$\frac{\dot{m}}{2} = \sum_{J=2}^{M2} (\rho\, U_{i,J}\, \Delta Y_J) \qquad \text{for } 2 \leq i \leq L2 \qquad (9\text{-}1)$$

As was stated in Chapter IV, the boundary values of ΔY_J (ΔY_1 and ΔY_{M1}) are zero, hence, the summation is from 2 to M2, M2 = M1-1. The corresponding two-dimensional value of $\overline{U}_m$, Eq. (2-47) with b = 1, is then calculated using the $\dot{m}/2$ value obtained from Eq. (9-1):

$$\overline{U}_m = \frac{\dot{m}}{2}\ \frac{1}{\rho\, H} \qquad (9\text{-}2)$$

A friction velocity value is used in the nondimensionalization of k and ϵ values presented in this chapter. The friction velocity, U_τ, is defined by Eq. (3-30) as:

$$U_\tau = \left(\frac{\tau_W}{\rho}\right)^{1/2} \qquad (3\text{-}30)$$

which for fully developed turbulent duct flows can be written in the form of Eq. (7-9):

$$U_\tau = \left\{\left(-\frac{\partial P}{\partial x} H\right) / \rho\right\}^{1/2} \qquad (7\text{-}9)$$

In contrast to fully developed duct flows, the value of U_τ given by Eqs. (3-30) and (7-9) is not constant in periodic fully developed duct flows, because $(-\partial P/\partial x)$ is not constant. Since it is desirable to use a constant value of friction velocity in the nondimensionalization of the data for a particular run, in this work, a periodic fully developed friction velocity, u_τ, was defined based on β, the constant part of the module pressure gradient. In analogy to the expression in Eq. (7-9),

the value of u_τ was defined as:

$$u_\tau = \{(\beta H) / \rho\}^{1/2} \qquad (9\text{-}3)$$

Grid Checks

As was stated in Section 9.1.3, the calculation domains of Ducts 1, 2, and 3, were discretized into nonuniform x-y grid distributions of 72x78, 72x100, and 72x100 nodes. These grids were chosen after a careful examination of the values of the computed variables obtained with many different nonuniform grid distributions. These type of grid checks were performed for the maximum Reynolds number flow in each of Ducts 1, 2, and 3. It was assumed that grids which give grid-independent solutions at maximum Reynolds numbers will also give grid-independent solutions over the whole range of Reynolds numbers considered for a particular duct.

A quantitative estimate of the numerical accuracy of the solutions was obtained by determining how well the above-mentioned grids allow truly grid-independent solutions to be approached. As was discussed in Section 7.2.1, grid-independent solutions can often be well approximated using the extrapolation procedure used by de Vahl Davis in [118]. Because of the complex elliptic nature of the turbulent periodic fully developed flows investigated here, densely packed uniform grids were required to obtain solutions that could be extrapolated to the true grid-independent limit. The use of such grids is computationally very expensive, so a quantitative estimate of numerical accuracy was done for only one case, involving the maximum flow rate in Duct 3. This numerical error was assumed to be a conservative estimate of the numerical errors in all other interrupted-plate turbulent flow computations, for

the reasons discussed in the following paragraph.

Steep velocity and turbulence property gradients are expected to occur in regions near solid surface - fluid interfaces. These gradients generally become greater as the flow Reynolds number increases, thus requiring a larger number of grid points to ensure proper resolution of the flow field. Therefore, a grid that gives a grid-independent solution for a large value of flow Reynolds number would be expected to give a grid-independent solution at smaller values of Reynolds number for the same flow-passage configuration. In Ducts 1, 2, and 3, most of the solid surface - fluid interfaces occur parallel to the main-flow, or x, direction, and the y dimension of each corresponding module is about one quarter of the x dimension: As a result, the greatest concentration of grid points, per unit length, is required in the y direction to ensure adequate resolution of the flow properties. The most complex flow regions to be resolved involve recirculation, and these zones are largest in the interplate-gap region, shown by dcCD in Fig. 11, extending in the y direction from y = 0 to the height of the plate, v = t. In this region, the number of grid points in the y direction per unit of the plate thickness parameter, t^*, was the smallest for the grid used in Duct 3: for example, 254 points per unit of t^* compared to 370 for Duct 1 and 393 for Duct 2. For this reason, it was considered that the least accurate solution of the flow field will result for this duct, grid, and maximum flow combination. The numerical accuracy of all the other turbulent periodic fully developed flow solutions would be at least as good as, or better than, the accuracy of the solution obtained for Duct 3 with the maximum value of Re_m.

For Duct 3, with a specified β corresponding to the maximum flow rate, the extrapolated grid-independent value of Re_m was 27.27×10^3. This was obtained by assuming that with fine grids the numerical method used is second order accurate [41,125], and by extrapolating Re_m values obtained with grids of 124x174, 124x201, 146x174, and 146x201 nodes, uniformly spaced in the x and y directions. Full details of how the extrapolated grid-independent solution for Re_m was obtained are given in Appendix 6. The value of Re_m obtained using the nonuniform 72x100 grid distribution, $Re_m = 27.84 \times 10^3$, was within 2 percent of the extrapolated grid-independent value. This is representative of the accuracy of all other overall flow results calculated using this grid.

A visual appreciation of this numerical accuracy can be obtained by examining Figs. 82(a) and (b); and 83(a) to (d). These figures show plots of various nondimensional variables obtained with the nonuniform 72x100 grid and tne uniformly spaced 146x201 grid. The value of Re_m for the 146x201 grid was 27.21×10^3, a difference of less than 0.25 percent from the extrapolated grid independent value of 27.27×10^3. Figure 82(a) shows plots of the nondimensional U velocity profile at the module cross section located at the plate trailing edge. The location of the plate in these plots is shown by the region of zero velocity extending from y/H = 0 to 0.110. Figure 82(b) shows the variation of the cross-stream x-momentum flux with distance along the length of the module: The plate leading-edge, center-point, and trailing-edge locations are denoted by the vertical lines (————————), (— — — — — —), and (—— – – ——), respectively. The cross-stream x-momentum flux will be referred to as the axial momentum flux, and for a given x location, it is defined as follows:

$$M_i^* = \sum_{J=2}^{M2} (U_{i,J}\ U_{1,J}\ \Delta Y_J) \ /\ (\tfrac{1}{2}\ \bar{U}_m\ \bar{U}_m\ D_h) \qquad \text{for } 2 \le i \le L2 \quad (9\text{-}4)$$

where D_h and U_m are defined by Eqs. (8-3) and (9-2), respectively.

Plots of nondimensional k profiles are shown in Figs. 83(a) and (b), and nondimensional ϵ profiles are shown in Figs. 83(c) and (d). These profiles are for module cross sections located over the first half of the plate and the first half of the interplate-gap region, at $(x^*-x^*_i)_m = 0.1414$ and 1.027, respectively. The plots in Figs. 82(a) and (b), and 83(a) to (d) show that there is good agreement between the results obtained with the 146x201 uniform grid and those obtained with the nonuniform 72x100 grid: However, the CPU time required to obtain the solution using the nonuniform grid is in the order of 50 minutes, and this is less than half that required with the uniformly spaced grid. This indicates the computational efficiency attained by using the non-uniform grid distribution.

To summarize, it was concluded that the nonuniform 72x100 grid yielded numerical solutions of overall flow rates that were within 2 percent of the true grid-independent value in the case of Duct 3. For reasons already discussed, this was used as a conservative estimate of the agreement expected between extrapolated grid-independent solutions and the numerical solutions reported for Ducts 1 and 2, using 72x78 and 72x100 node nonuniform grid distributions, respectively.

Turbulence Models: Final Performance Evaluation

The final performance evaluation of the k-ϵ turbulence models

consisted of two-parts: First, the effect of using the Hanjalic and Launder modification [96], discussed in Sections 3.6 and 9.1.1, was examined; and second, the relative performance of the Jones and Launder [89], JL, and Launder and Sharma [91], LS, k-ϵ models of turbulence was evaluated. These evaluations were done by comparing the numerically calculated friction factor - Reynolds number, f_m versus Re_m, values for Duct 1 with those obtained from the corresponding experimental investigation.

The effect of using the Hanjalic and Launder [96] modification for the ϵ equation production term, P_ϵ, was studied using the JL turbulence model. To indicate that this modification has been incorporated into the JL turbulence model, H will be added to the two letters representing the model: In this case, the JL model becomes the JLH model. The results of the computations are shown by the f_m versus Re_m plots in Fig. 84. In this figure, the symbols ● , □ , and ○ denote the experimental results for Duct 1, the solutions obtained with the JL model, and the solutions obtained with the JLH model, respectively. It can be seen that the f_m values calculated using the JL and the JLH models follow the same general trend: At low values of Re_m, $Re_m < 15\times10^3$, the numerical values of f_m are underpredicted with respect to the experimental values; but as the value of Re_m increases, the experimental values of f_m decrease faster than the numerical values, and the numerical values eventually become larger than the experimental values. The cross-over point, where the numerical f_m values become greater than experimental values, occurs at $Re_m \simeq 25\times10^3$ with the JLH model and at $Re_m \simeq 15\times10^3$ with the JL model. From the experimental time-mean wall static pressure measurements for Duct 1, presented in Figs. 54(a) to (d) and 55(a) to

(c), it is observed that the recovery in the time-mean wall static pressure ove· the region extending from just upstream of the plate trailing edge to the center of the interplate gap becomes larger, relative to the total time-mean static pressure drop over the entire module, as Re_m increases. It is not surprising that the difference in the predictions of the JLH and the JL models becomes greater in flows where the relative effect of adverse pressure gradients increases, with the JLH values showing closer agreement with experimental values, as shown in Fig. 84.

As a result of this performance evaluation, it was concluded that the inclusion of the Hanjalic and Launder modification [96] in the k-ϵ turbulence model results in numerical predictions that are generally in better agreement with the experimental data over the range of Reynolds numbers studied in this investigation.

The relative performance of the JL and LS k-ϵ turbulence models was examined for the flows with the maximum and minimum values of Re_m in Duct 1. For this comparison, the Hanjalic and Launder modification [96] was incorporated into both models, and designated as the JLH and LSH models. The results of this study are also shown in Fig. 84 where $\diamond$ denotes the results using the LSH model and, as stated previously, $\circ$ denotes the results using the JLH model. These results confirm the trend that was observed in the turbulent channel flow data presented in Section 7.2: At $Re_m \simeq 25 \times 10^3$ both models give approximately the same results for f_m, but as Re_m decreases, the f_m values calculated using the LSH model show poorer agreement with experimental values than those predicted by the JLH model. It was concluded that for the range of Reynolds numbers of interest in this investigation, the JLH model is

better than the LSH model.

The numerical predictions of turbulent periodic fully developed flow presented in the remainder of this thesis were done using the Jones and Launder [89] k-ϵ model of turbulence with the modification proposed by Hanjalic and Launder [96]. The values of the constants used in this turbulence model are given in Table 1.

9.2 MODULE FRICTION FACTOR - REYNOLDS NUMBER RESULTS

As was previously stated, numerical calculations were done for a total of twelve interrupted-plate duct and flow rate combinations: four flow rates through each of Ducts 1, 2, and 3. In this section, the module friction factor - Reynolds number results obtained from these numerical studies are presented and compared to the corresponding experimental results presented in Section 8.3. A discussion of these f_m versus Re_m results is also presented in this section.

The f_m versus Re_m results of the numerical investigation for Ducts 1, 2, and 3 are given in Table 19. The respective graphical representations of these numerical results along with the corresponding experimental results are shown in Figs. 85(a), (b), and (c). In these figures, the numerical data points are joined by continuous lines, and the corresponding experimental data points are shown with error bars representing the uncertainties reported for these values in Table 16.

In Figs. 53 and 85(a) to (c), it is observed that both the experimental and numerical values exhibit the same general trends: (a) f_m

drops with increasing Re_m for a given duct, but this drop becomes progressively smaller as Re_m increases; and (b) as t^* increases from Duct 1 to Duct 2, and again from Duct 2 to Duct 3, so does the overall level of f_m. These trends can be understood by noting that an overall pressure drop over a module is required to overcome: (i) wall friction, or shear forces, at the walls and plate surfaces of the module; and (ii) the so-called inertial losses [26], that are proportional to $\bar{U}_m^2$ and occur in regions of separation and recirculation at the leading and trailing edge of the plate. At low Reynolds numbers, the contribution of the wall friction to the overall module pressure drop is significant, and the module friction factor, f_m, responds noticeably to changes in the module Reynolds number, Re_m. However, at high Reynolds numbers, the inertial losses dominate the wall friction losses, and f_m, $\{= \beta D_h/(\rho \bar{U}_m^2/2)\}$, becomes relatively insensitive to changes in Re_m. This accounts for the above-mentioned Trend (a). Trend (b) is a result of the decrease in minimum flow area, A_c, caused when t^* is approximately doubled from Duct 1 to Duct 2, and then again from Duct 2 to Duct 3. For the same values of Re_m, as A_c decreases, the flow rate through the plate region of a module increases, and this in turn results in greater frictional losses due to the larger shear stresses on the plate surface and at the duct walls. Furthermore, the increased blockage effect of the plates with increasing t^*, and the accompanying increase in the flow rate for the same Re_m, lead to greater regions of separation and recirculation, causing the inertial losses to also increase in magnitude.

Figures 85(a) to (c) give an indication of the overall accuracy of the numerical predictions obtained in this study. In all cases, the difference between numerical and experimental results is greatest at the

lowest values of Re_m ($\simeq 5x10^3$). As Re_m increases, the experimental values of f_m decrease at a greater rate than the numerical values, and they eventually cross-over, and become lower than, the numerical values for $Re_m > 25x10^3$. Over the range of Re_m investigated, agreement between the numerical and experimental data is best for Duct 1, $t^* = 0.027$, and becomes progressively less satisfactory as t^* increases to 0.056 for Duct 2, and 0.110 for Duct 3, as shown in Figs. 85(a) to (c). A quantitative measure of the differences between the numerical and experimental sets of data is given in Table 20. The differences in the numerically calculated values of Re_m, reported in Table 19, from the corresponding experimental values, reported in Table 16, range from 7.90 percent to -1.94 percent for Duct 1, 7.63 percent to -0.563 percent for Duct 2, and 14.4 percent to 0.00 percent for Duct 3 over the Reynolds number range of $5x10^3 \lesssim Re_m \lesssim 28x10^3$. Considering the range of the uncertainties reported for Re_m in Tables 16 and 20, it may be stated that the numerical and experimental data agree for Reynolds numbers in the range $16x10^3 < Re_m < 28x10^3$. Although the Hanjalic and Launder modification [96] to the ϵ equation production term, P_ϵ, has improved the numerical results at the higher Re_m values, there is a need for further improvement of the JLH model in order to obtain better agreement of the numerical f_m versus Re_m results with those obtained experimentally.

It was demonstrated in [97] that without the Hanjalic and Launder modification [96], the k-ϵ turbulence model gives values of skin friction coefficients that are too high when applied to two-dimensional decelerated thin shear layers. As is evident from Eqs. (5-8) and (5-12), in the presence of large gradients of velocities, $\partial U/\partial x$ or $\partial V/dy$, such as those experienced when strong deceleration or acceleration of the flow

occurs, the modification suggested in [96] will give rise to larger ϵ values than those obtained without the modification, and, as a result, smaller values of k and smaller values of μ_t, are obtained. In turn, the value of the effective viscosity, $(\mu+\mu_t)$, becomes less, and larger flow rates, hence smaller values of f_m, are calculated for a specified modular pressure gradient, β. This is observed in Fig. 84 where the f_m versus Re_m results for the JLH model are shifted downward from the corresponding JL model results, most noticeably for $Re_m > 15x10^3$.

The interrupted-plate duct flows of this investigation are more complex in nature than the two-dimensional decelerated thin shear layers of [96] and [97]. In contrast to the results of those two investigations, where skin friction factors were all overpredicted before the modification of P_ϵ, in the interrupted-plate duct flows of this study, the overprediction in f_m values only occurred at $Re_m \gtrsim 15x10^3$. At these large values of Re_m, as already discussed, the overprediction of the f_m values by the numerical model is due, at least partially, to the underprediction of the effects of irrotational strains on the dissipation of the turbulence kinetic energy in flows experiencing acceleration or deceleration. This has been corrected to a noticeable extent by implementing the Launder and Hanjalic modification [96] to P_ϵ. However, in the results of Duct 1 shown in Fig. 84, a comparison of the f_m values of the JL and JLH models reveals that this modification to P_ϵ has had relatively little effect at low values of Re_m, where frictional losses are significant. One possible explanation of these results may be obtained by examining the streamline patterns on the plates shown in the flow visualization results of Figs. 60 to 81. They indicate that over the central 80 percent of the duct, the mean-flow field can be considered to

be two-dimensional. However, at low values of Re_m, the wall friction makes a significant contribution to the overall module pressure drop. Unlike the ideal two-dimensional flow module used in the numerical calculations, the experimental flow module has side walls that lead to an increase in total wall friction forces, and, hence, a greater module pressure drop is required to obtain the same flow rate as for the ideal two-dimensional situation. It is thus expected that experimental f_m values should be larger than the two-dimensional numerical values, especially at relatively low values of Re_m, when frictional losses become more significant relative to inertial losses.

As a final note in this section, it must be remembered that the ϵ equation, Eq.(3-18), was derived from Eq. (3-12) only after some rather "ad hoc" assumptions, and in its present form, even after the modification to P_ϵ [96], it is still a very simplistic model. Considering the complex nature of turbulent periodic fully developed duct flow, some improvements to the ϵ equation and the viscous damping functions employed in the JL form of the k-ϵ model are necessary before accurate predictions can be achieved over a wide range of Re_m. Specific recommendations for such improvements require detailed analytical and numerical studies, supported by detailed experimental measurements of U, V, k, and Reynolds stresses, using hot-wire and laser-Doppler anemometry. Such studies and measurements are beyond the scope of this thesis.

9.3 DISCUSSION OF SURFACE STREAMLINE RESULTS

The behaviour of the flow over the surface of a plate can be determined by careful examination of the surface streamline results shown in

Figs. 61 to 81. The interpretation of these results has been done after studying surface streamline patterns and discussions presented by Maltby and Keating [47] for separating and reattaching flows.

Regions of surface flow separation are indicated by either dark patches, indicating the absence of paint, or solid bright regions which indicate the accumulation of paint at one location [47]. Regions of paint accumulation in the vicinity of the leading edge of the plate are clearly visible in all of Figs. 61 to 81, except in the case of the lowest Reynolds number runs for each duct, Figs. 61, 68, and 75, and for Runs 2, 3, and 4, (Re_m = 8.806×10^3, 11.22×10^3, and 17.17×10^3, respectively) with Duct 1. In the cases without leading-edge paint accumulation, it cannot be conclusively stated that a leading-edge separation and recirculation zone does not occur, but only that no definite indication of its occurrence appears in the surface streamline data. In the cases where leading-edge paint accumulation does occur, the paint was actually seen to be recirculating in, and confined to, these regions before it dried. Furthermore, it will be noticed that immediately downstream of these leading-edge paint accumulation zones, there is a small region where streaks are not clearly defined or are completely absent. This would indicate a region of low surface shear relative to the region just downstream of this one, where the streaks are very distinct, extending along the length of the plate towards the trailing edge. It is to be expected that just downstream of a separation zone, as the main flow reattaches to the wall, the wall shear will be initially weak as the surface boundary layer will require some distance to strongly reestablish itself [47].

For flows with Re_m less than $20x10^3$, there is another region of separation and recirculation that appears upstream of the plate trailing edge, particularly noticeable at the lowest Re_m values for each Duct. In Figs. 61, 68, and 75, showing the results for Run 1 with Ducts 1 , 2 and 3, respectively, the two-dimensional streamline patterns on the central region of the plates are ended abruptly by a line of accumulated paint that stretches across the width of the plate. This is best seen in the case of Duct 1, Fig. 61, where the paint has accumulated at a location roughly 25 percent of the plate length, $\simeq 0.25$ L, upstream of the trailing edge. Behind this region, is a clear dark region where, initially, paint was observed to be recirculating until it began to dry and accumulate at the indicated location. With the other duct and flow combinations, for $Re_m < 20x10^3$, the same type of phenomena is evident in the streamline patterns, although less distinctly. In some cases, specks of paint broke through the recirculation zone and flowed towards the trailing edge, where a second region of paint accumulation is observed in the streamline photographs. A distinct dark line demarcates the boundary between these two regions. During the experiments, before the paint had dried, it was observed that no paint would cross this dark line, except in the case where specks broke through. It is plausible that the dark line indicates the end of the trailing-edge separation zone, but this could not be definitely confirmed from the results obtained here As the value of Re_m increases, the extent of these trailing-edge recirculation zones decreases, until for $Re_m > 20x10^3$, Figs. 65 to 67, 72 to 74, and 79 to 81, the zones become so small that it is not possible to definitely determine if the accumulation of paint at the trailing edges is due to such zones or is simply the result of paint on the upstream surface of the plate being pushed downstream until it arrives at the trailing

edge.

To summarize, three distinct regions were observed in the streamline patterns on the surface of the plates in turbulent periodic fully developed interrupted-plate duct flows: 1) a leading-edge separation and recirculation zone, followed by a region of low surface shear relative to that on the central region of the plate; 2) a central zone characterized by strong shear in the mean axial-flow direction; and 3) a region adjacent to the trailing edge characterized by paint accumulation and, for $Re_m < 20 \times 10^3$, a zone of surface flow separation and recirculation that extends as much as $\simeq 0.25$ L upstream of the plate trailing edge for the minimum Re_m values. The occurrence of the first two of these regions was anticipated, but the presence of a separation zone upstream of the trailing edge was unexpected, and to the best of this author's knowledge no similar phenomena has been reported in the literature to date. The first step in formulating an explanation for the observed experimental results is to examine the numerical data to see if the same phenomena are predicted.

9.4 STREAMLINE PLOTS

Streamline plots were generated from the numerical solutions obtained for flows through Ducts 1, 2, and 3. Using the terminology adopted in Table 19, the streamline plots for Runs 1, 3, 4, and 6, appear in Figs. 86(a) to (d) for Duct 1, 87(a) to (d) for Duct 2, and 88(a) to (d) for Duct 3. In these figures, the uppermost horizontal line represents the streamline on the upper duct wall, shown by line AB in Fig. 2, and will be denoted as the first streamline. The value of

the stream function values corresponding to the next nine streamlines below it, to the tenth streamline, decrease by equal amounts; and the stream function values of the four streamlines immediately below these, the eleventh to fourteenth streamlines, also decrease by an equal, but smaller, increment. The values of these fourteen stream functions are given in Table 21 for Ducts 1, 2, and 3. The location of the plate within the module is shown by the cross-hatched area, and the zero stream function is shown by the zero streamline located along the plate surface - fluid interface. The flow direction is indicated by the arrows. All recirculation zones are also bounded by the zero streamline.

In the streamline plots shown in Figs. 86(a) to 88(d), flow separation and recirculation is evident immediately downstream of the plate trailing edge in the interplate gap, and, except for Run 1 of Duct 1 in Fig. 86(a), a leading-edge separation and recirculation zone is also seen. This leading-edge separation zone is difficult to see for the results of Duct 1, and Run 1 of Duct 2, because of the small size of the recirculation region compared to the resolution of the plots. The stream-wise extents of these recirculation zones vary as Re_m and t^* increase. The streamwise lengths of the leading-edge and trailing-edge recirculation zones, appearing in Figs. 86(a) to 88(d), are presented in Figs. 89 and 90, respectively, in terms of a nondimensional length, x_R/t, versus a plate Reynolds number, Re_p: x_R is the length of the recirculation zone in the mean-flow, or x, direction, and t is the plate half-thickness, shown by the length of line Dd in Fig. 11. The plate Reynolds number is defined as:

$$Re_p = \frac{\rho \bar{U}_k t}{\mu} \qquad (9\text{-}5)$$

where $\bar{U}_k$, given by Eq. (2-41) with b = 1, is the mean-flow average velocity per unit width based on the minimum flow cross-sectional area, A_c, which occurs in the region where the plate is located. The confining effect of duct walls on the flow around a rectangular plate has been found to cause significant changes in the characteristics of the flow around such a plate [126]. This confinement effect is expected to change as the blockage caused by the plate, indicated by the value of t^*, changes. This is reflected by the differences in the data for Ducts 1 to 3 in Figs. 89 and 90.

The length of a recirculation zone is influenced by the rate of spread of the separated shear layer in the cross-stream, or y, direction [127]. When this shear layer encounters a solid surface and reattaches to it or, in the case of trailing-edge separation in the interplate gap, when it merges with its counterpart that has separated from the opposite surface of the plate, a recirculation zone is established. As the value of Re_p is increased, starting from relatively low values, the streamwise extent of the recirculation zone initially increases, then decreases, and finally becomes essentially constant, as seen in Figs. 89 and 90. At low values of Re_p, the rate at which the separated shear layer diffuses in the cross-stream, or y, direction is determined primarily by viscous diffusion [127-129]. As Re_p increases, it reaches a critical value beyond which the separated shear layer becomes initially unstable, experiencing oscillations in the y direction, and, as the increase in Re_p continues, turbulent mixing also increases [126-128,130,131]: The y direction spread of the separated shear layer tends to be dominated by these latter two processes relative

to the viscous diffusion process. Eventually, at very high values of Re_p, the viscous effects become comparably negligible and the length of the recirculation zone becomes essentially constant, independent of Re_p [126-131]. It must be remembered, however, that the recirculation zones predicted by the numerical model used in this thesis are based on the assumption of statistically-steady time-mean flows. Thus, the numerical model cannot account for instabilities that develop in the separated shear layer. As a result, the critical value of Re_p in Figs. 89 and 90 occurs only when turbulent mixing begins to dominate over the viscous diffusion of the separated shear layer: The critical value of Re_p would be smaller if unsteady effects in the shear layer were also modelled.

Evidence that the reduction in the length of recirculation zones with Re_p, for relatively high Re_p, is caused by the increased effects of turbulence, compared to viscous effects, can also be obtained by examining the levels of the turbulence Reynolds number, Re_t, in regions of the flow where such zones occur. Streamwise profiles of Re_t in the interplate gap are shown in Figs. 91(a) to (c) for Ducts 1 to 3, respectively. These profiles are representative of Re_t levels throughout the interplate-gap region, where $y/H < t^*$. In all cases, as Re_m, and hence Re_p, increases for a given duct, so does the level of Re_t. Of particular interest is the region immediately downstream of the plate, where the trailing-edge recirculation zones, shown in Figs. 86(a) to 88(d), occur: For the minimum flow rates in each duct, the values of Re_t in the recirculation zones are less than 10, 20, and 100 for Ducts 1, 2, and 3, respectively. As Re_m increases, it is clearly seen that the levels of Re_t increase rapidly in the near-plate-wake region.

The flow in the interplate gap between two pairs of colinear rectangular plates was studied experimentally by Roadman and Loehrke [27]. Their results indicated that the downstream plate provided an upstream influence, which has an effect on the "natural" disturbances in the wake of the upstream plate. This caused a decrease in the critical Reynolds number for which unsteadiness in the wake of the upstream plate would occur. It was also observed that this "feedback process" was less evident as the flow rates increased beyond the critical Reynolds number value. A similar sort of unsteady effect, caused by one plate on the next plate located immediately upstream of it, could also contribute to the observed characteristics of the aforementioned recirculation zones that became smaller as flow rates were increased. At higher flow rates, the elliptic nature of the flow is diminished due to the larger flow Peclet numbers, and the effect of a downstream plate on its upstream neighbour is reduced.

9.5 FLOW OVER A PLATE UPSTREAM OF THE TRAILING EDGE

The numerical results show a trailing-edge separation zone only downstream of a plate, in the interplate gap. The flow visualization results for $Re_m < 20x10^3$, however, show that there is a region of separation and recirculation on the surface of the plate upstream of its trailing edge. Since this upstream trailing-edge separation region is not predicted numerically, it was concluded that it is due to some unsteady flow phenomena. In the case of an abrupt channel expansion, where the main flow reattaches to the channel wall downstream of the recirculation zone, unsteady oscillations in the separated shear layer have been observed when the streamwise length of the recirculation zone

stops increasing and begins to decrease with increasing flow rate [127]. The effects of turbulence become important after the initial onset of this instability which causes the length of the recirculation zone to begin decreasing [127]. In the case of the present numerical simulations, since the decrease in recirculation-zone length can only be accounted for by increased turbulent mixing in the flow, it was concluded that when this decrease was observed numerically, the separated shear layer in the actual flow situation would already be experiencing unsteady disturbances. However, the onset of instability in a separated shear layer in the wake of a bluff body, such as a rectangular plate, is usually accompanied by the well-known von Karman vortex street, the phenomenon of periodic vortex shedding from alternate sides of the body [130-132]. Such a periodic shedding of vortices could conceivably cause the separation zone upstream of the plate trailing edge. To confirm this, unsteady flow simulations or local flow measurements using hot-wire or laser-Doppler anemometry are needed. Such investigations are suggested as extensions of the work reported in this thesis.

9.6 FLOW OVER THE CENTRAL REGION OF A PLATE

As previously mentioned, in Figs. 61 to 81, immediately downstream of a plate leading-edge separation zone, there was either an absence of streaks in the surface paint pattern or they were not very distinct. Further downstream, over the central region of a plate, there were very distinct streak patterns indicating that the shear stress on the plate surface was greater here than in the region immediately downstream of the plate leading edge. This observation is confirmed by the numerical results, as shown from the plots of nondimensional plate-surface

shear stress presented in Figs. 92(a), 93(a), and 94(a) for Ducts 1, 2, and 3, respectively. In these figures, the plate leading-edge, center-point and trailing-edge locations are denoted by the vertical lines (————————), (— — — — — —), and (—— – – ——), respectively, and the nondimensional plate-surface shear stress, τ^*_p, has been defined for a given U-velocity staggered-grid line location, i, as:

$$\tau^*_p = \mu \frac{U_{i,Jp}}{\left(\frac{\Delta Y_{Jp}}{2}\right)} \Big/ \left(\frac{1}{2} \rho \bar{U}_m^2\right) \qquad \text{for } 2 \leq i \leq ip \qquad (9\text{-}6)$$

where ip denotes the value of i at the U-velocity staggered-grid line that falls on the trailing edge of the plate, and Jp denotes the horizontal main-grid line located in the flow immediately above the horizontal surface of the plate. $(\Delta Y_{Jp}/2)$ is, therefore, the vertical distance from the location of $U_{i,Jp}$ to the plate surface. $\bar{U}_m$ is obtained from Eq. (9-2).

In all cases of the numerical investigation, except for Run 1 with Duct 1 ($Re_m = 5.764 \times 10^3$), the value of τ^*_p is less than zero at the leading edge of the plate, thus indicating the presence of a leading-edge separation and recirculation zone. τ^*_p increases rapidly along the first upstream quarter of the plate and then increases relatively slowly along the rest of the plate to its trailing edge. Compared to the region where the surface boundary layer reestablishes itself just downstream of a leading-edge recirculation zone, the shear stress over the central region of the plate is large. This behaviour was also evident in the surface streamline results shown in Figs. 61 to 81, further validating the qualitative prediction capabilities of the numerical model. In

the case of the lowest Re_m of Duct 1, in Fig. 92(a), no leading-edge separation was predicted, and the surface shear stress in the immediate vicinity of the leading edge of the plate is larger than that on the central section of plate. This is expected, as large velocity gradients occur when the leading edge of the plate is encountered and the fluid is suddenly brought to rest at its surface, with only a very small or no separation zone.

9.7 PLATE SHEAR STRESS, WALL SHEAR STRESS, AXIAL MOMENTUM FLUX, AND U VELOCITY DISTRIBUTIONS

Profiles of nondimensional shear stress at the plate surface, τ^*_p, the shear stress at the upper-wall surface, τ^*_w, axial momentum flux, M^*, and cross-sectional profile plots of nondimensional U velocities, $U/\overline{U}_m$, are discussed in this section. M^* and τ^*_p have already been defined by Eqs. (9-4) and (9-6), respectively. τ^*_w is defined in an analogous fashion to τ^*_p:

$$\tau^*_w = \mu \frac{U_{1,Jw}}{(\frac{\Delta Y_{Jw}}{2})} / (\tfrac{1}{2} \rho \overline{U}_m^2) \qquad \text{for } 2 \le i \le L2 \quad (9\text{-}7)$$

where the subscript Jw denotes the horizontal main-grid line located immediately below the upper-wall surface, shown by line AB in Fig. 11, and $(\Delta Y_{Jw}/2)$ is the vertical distance from $U_{1,Jw}$ to the wall. The plots of τ^*_p, τ^*_w and M^* are shown, respectively, in Figs. 92(a), (b) and (c) for Duct 1, in Figs. 93(a), (b) and (c) for Duct 2, and in Figs. 94(a), (b) and (c) for Duct 3. To aid in the discussion of these results, at eight $(x^*-x^*_1)_m$ locations along a module, cross-sectional profile plots

of nondimensional U velocities are presented for the minimum and maximum Re_m values in each duct. These eight streamwise locations, denoted as X1, X2, ..., to X8, and are shown in Figs. 95(a) to (c) for Ducts 1 to 3, respectively. In these figures, the plate leading-edge, center-point and trailing-edge locations are denoted by the vertical lines (————————), (— — — — — —), and (—— – – ——), respectively. With reference to the nomenclature in Fig. 19, X1 to X4 are located over the plate at approximately the LE, LC, CP and TE locations, respectively. X5 to X8 are located in the interplate gap: X5 is just downstream of the TE location, and X6, X7, and X8 correspond approximately to the G1, G2, and G3 locations. The corresponding plots of $U/\bar{U}_m$ for the minimum and maximum Re_m values, Runs 1 and 6 in Table 19, appear in Figs. 96 to 101.

The plots of $(P^*_1-P^*)_m$, τ^*_p, τ^*_w, M^*, and $U/\bar{U}_m$ exhibit similar trends for all values of Re_m and t^* in this investigation. Consequently, the discussion of these results will be focused on the data of Duct 3, for the case of Run 6, $Re_m = 27.84 \times 10^3$. The relative changes in velocity profiles at different streamwise locations along the module are greater for this duct and flow combination than for others, and will, therefore, facilitate the following discussion.

The profiles of τ^*_p, τ^*_w, and M^* for $Re_m = 27.84 \times 10^3$ in Duct 3, Figs. 94(a) to (c), can be explained by examining the corresponding cross-sectional profiles of $U/\bar{U}_m$ for the X1 to X4, and X5 to X8 module locations shown in Figs. 101(a) and (b), respectively. Just upstream of a plate, the fluid in the $0 \leq y/H \leq t^*$ region of the interplate gap has a nonzero velocity, as seen by the profile for position X8 in Fig. 101(b). At the inlet plane of a geometric module, the flow encounters

the plate, which has blunt, square, leading and trailing edges. The flow separates at the leading edge of the plate, and, in order to satisfy continuity requirements, undergoes a strong streamwise acceleration in the region just outside the separation zone. This is evident in the velocity profile at X1, in Fig. 101(a): the presence of the plate is indicated by the region of zero velocity for $0 \leq y/H \leq 0.110$; the leading-edge separation is indicated by the negative values of $U/\bar{U}_m$; and the strong acceleration near the plate surface is seen by the steep gradient of $U/\bar{U}_m$ in this region. At a short distance downstream of the leading edge, the flow reattaches to the plate surface and begins to develop in the streamwise direction, as shown by the velocity profiles at X2, X3, and X4 in Fig. 101(a). It can be seen that the presence of the plate causes the flow to be initially deflected towards the upper wall, as displayed by the following features of the velocity profile at X2 compared to that at X1: (i) the upward shift in the location of the maximum velocity and the increase in its magnitude; (ii) the flatter velocity profile in the region near the upper wall; and (iii) the reduced cross-stream gradients in velocity just above the plate. These changes in velocity profile also result in an increase in the axial momentum flux of the flow from X1 to X2, shown by the appropriate M^* profile in Fig. 94(c). As the flow adjusts to the presence of the plate, it begins to redistribute itself in a more symmetric fashion, resulting in a decrease of the maximum velocity, with a slight shift downward in its location, and an increase in the flatness of the velocity profile in the region adjacent to the plate, as can be seen from the relative change in the velocity profiles going from X2 to X3 to X4 These changes in velocity profile are reflected and confirmed in Figs. 94(a), (b), and (c), by the continuous increase of τ^*_p, and the continuous decrease in τ^*_w and M^*,

over the plate from X2 to the trailing edge at X4.

The cross-sectional $U/\bar{U}_m$ velocity profiles in the interplate gap develop as shown by the plots in Fig. 101(b). The flow begins to redistribute itself more towards the centerline of the duct, shown by the symmetry line CDE in Figs. 2 and 11, as it adjusts to the increased flow area resulting from the absence of the plate. In Fig. 101(b), progressing from location X5 through to X8, the magnitude of the maximum velocity continually decreases, the U velocity along the centerline increases, and the velocity gradients near the upper wall become smaller. At location X8, however, the decrease in the maximum velocity levels off, and the fluid begins to accelerate towards the upper half of the module as it approaches the leading edge of the next downstream plate, resulting in steeper velocity gradients along the upper wall. This behaviour is also evident in the corresponding profiles of τ^*_w and M^* shown in Figs. 94(b) and (c).

9.8 INTRAMODULAR TIME-MEAN WALL STATIC PRESSURES

9.8.1 Results

The experimental intramodular time-mean wall static pressure distributions measured for the 21 different combinations of interrupted-plate duct and flow rate have been presented in Figs. 54(a) to 59(c) and described briefly in Section 8.4. With reference to the run numbers in Tables 16 and 19, the corresponding numerical data for Runs 1, 3, 4, and 6 are also presented in Figs. 54(a), (c), (d) and 55(b) for Duct 1; in Figs. 56(a), (c), (d), and 57(b) for Duct 2; and in Figs. 58(a), (b),

(c) and 59(b) for Duct 3, respectively. The numerical data displays good qualitative agreement with the experimental data. For all Reynolds numbers, there is a steep drop in time-mean wall static pressure in the region located over the first half of the plate, followed by a rise in pressure that begins in the region above the last quarter of the plate and continues over the first half of the interplate-gap region. The time-mean wall static pressure begins to drop again over the last half of the interplate-gap region as the next plate is approached. The only instance where the wall static pressure behaviour is slightly different is in the experimental data pertaining to the minimum Re_m in Duct 1, Run 1 displayed in Fig. 54(a): The time-mean wall static pressure decreases all the way to the trailing edge of the plate, albeit mildly over the last quarter, and the pressure recovery, or decrease in $(P^*_i - P^*)_m$, begins only in the region over the interplate gap.

The numerical values of $(P^*_i - P^*)_m$ are lower than the experimental ones, with the difference becoming smaller as Re_m increases. The best agreement between numerical and experimental data is at the maximum Re_m values, as was the case for the f_m versus Re_m data of Section 9.2. The largest difference in the experimental and numerical results occurs in the magnitude of the maximum pressure drop along the wall region located over the plate. With respect to the nomenclature illustrated in Fig. 19, this occurs on the wall at a position corresponding to CT, located midway between the center of the plate and its trailing edge.

Although the quantitative accuracy of the numerical data requires improvement, the qualitative accuracy is generally quite good.

Therefore, the numerical results may be used in a qualitative manner, in conjunction with the experimental data, to gain insight into the turbulent fluid flow phenomena occurring within a periodic fully developed flow module. As was mentioned in Chapter I, in the published literature there is a lack of both detailed numerical and experimental intramodular results for periodic fully developed turbulent flows. Therefore the results presented in this section are considered as an important original contribution of this thesis.

9.8.2 Discussion of Results

The variations observed in the measured values of the intramodular time-mean wall static pressures, presented in Figs. 54(a) to 59(c) for all the 21 combinations of interrupted-plate duct and flow rate combinations, will now be discussed.

An increase in M^*, or an increase in overall frictional losses caused by increases in τ^*_w or τ^*_p, will result in a drop of the time-mean static pressure within a module. For Run 6 of Duct 3, as observed in Figs. 94(b) and (c), τ^*_w and M^* increase in the region immediately downstream of the leading edge of a plate. They then level off and start decreasing slowly towards the trailing edge of the plate, while τ^*_p gradually increases. The corresponding plot in Fig. 59(b) shows that the time-mean wall static pressure undergoes a large drop from LE to LC as the plate is encountered by the flow: This is to be expected because the increase in M^* and τ^*_w in this region overshadows the local effects caused by the rise in static pressure on the plate surface at the leading-edge separation zone. However, the time-mean

wall static pressure is observed to continue dropping, although progressively less, from LC to CP to CT. Since both M^* and τ^*_w decrease gradually over this region of the module, it must be assumed that the observed increase in τ^*_p is large enough to overshadow these drops, resulting in a net increase in overall losses and accounting for the continually decreasing time-mean static pressures experienced at the wall, shown in Fig. 59(b) as increased levels of $(P^*_i - P^*)_m$. From locations CT to TE, in Fig. 59(b), the values of $(P^*_i - P^*)_m$ begin to decrease, indicating that the decreases in M^* and τ^*_w have become large enough to cancel the effects caused by the increase in τ^*_p over this region.

In Fig. 59(b), over the interplate-gap region, from TE to G2, a sharp rise in static pressure is observed to occur. This occurs because the total transport of axial momentum associated with the velocity profiles in this region continues to decrease, as does the wall shear stress, and the elimination of the plate surface results in a sizeable reduction in the overall frictional losses. About halfway along the length of the interplate gap, τ^*_w begins to increase again and the value of M^* begins to level off, as shown in Figs. 94(b) and (c). The net effect of these events is a decrease in static pressure, as seen by the increased drop of wall pressure at G3 in Fig. 59(b). This drop in time-mean static pressure continues as the flow approaches the leading edge of the next plate, and M^* and τ^*_w continue to increase.

Reasoning similar to that presented above to explain time-mean wall static pressure distributions for Run 6 of Duct 3 can be used to explain the results for the other cases investigated and presented in

Figs. 54(a) to 59(c). As the value of Re_m decreases, the most noticeable change in these results is that the recovery of the time-mean wall static pressure over the plate is observed to begin further along the module towards the TE location. The reasons for this can be seen by examining the data plotted in Figs. 92(a) to 94(c). As Re_m decreases: (i) the relative rise in τ^*_p over the plate becomes greater; (ii) along the plate region of the module, the relative decrease in M^* becomes less, or in the case of Run 1 for Duct 1, M^* actually increases over most of the plate region; and (iii) the wall shear stress increases to its maximum value at a point further downstream from the region over the leading edge of the plate but, relative to this increase, its rate of decrease over the last half of the plate is greater. The net effect of (i) and (ii) is to cause the time-mean static pressure to decrease in the region over a plate, but the effect of (iii) over the last half of the plate moderates, and eventually cancels, this decrease, and the time-mean wall static pressure begins to increase. This recovery of time-mean wall static pressure, shown as decreased values of $(P^*_i - P^*)_m$, occurs closer to the trailing edge of the plate as Re_m decreases. In the case of Duct 1, for the minimum value of Re_m, shown in Fig. 54(a), the time-mean wall static pressure continues to drop all the way to the trailing-edge region.

The preceding explanations have been based on the assumption that the numerical solutions accurately represent, at least qualitatively, the time-averaged behaviour of turbulent periodic fully developed flow through an interrupted-plate duct. In the case of the time-mean wall static pressure data, this has been shown to be true. However, the flow visualization data, Figs. 61 to 81, shows a flow separation and

recirculation region that extends upstream from the trailing edge of the plate for $Re_m < 20x10^3$, and the time-averaged numerical model does not predict this. The effect of such a zone is to reduce frictional losses due to τ^*_p, although, it would be expected that the corresponding change in the shape of the velocity profile may act to increase M^* and τ^*_w as well. Quantitatively, the magnitude of these changes and the net effect on the local cross-sectional time-mean static pressure values cannot be determined without measurements of the local flow field. However, based on the qualitative agreement shown between present numerical and experimental pressure data, the local effect of the above-mentioned separation and recirculation region on time-mean wall static pressures appears to be small. In terms of the overall losses through a module, an additional zone of separation and recirculation, and the effective increase in the y-direction extent of the plate wake that could be caused by the periodic shedding of vortices [132], will increase the inertial losses in the flow. As a result, a higher pressure drop across a module is needed to maintain the same flow rate in the presence of these increased losses. This would explain, in part, why the experimental values of Re_m are lower than the numerical values calculated for the same value of module pressure gradient, β, for flow rates corresponding to $Re_m < 20x10^3$.

9.9 TURBULENCE RESULTS

As a final point of interest, the numerically predicted cross-sectional profiles of the turbulence kinetic energy, k, and the turbulence Reynolds number, Re_t, are presented for the minimum and maximum Re_m values in Ducts 1, 2, and 3 at four locations along the module.

These locations correspond approximately to the X1, X4, X5, and X8 positions shown in Figs. 95(a) to (c) and are labelled as such. The exact locations, given in Figs. 102(a) to (c) for Ducts 1 to 3, are slightly different from the corresponding velocity locations, because k and Re_t values are calculated at main-grid points rather than at the staggered U-velocity grid locations.

The profiles of nondimensionalized k values are shown in Figs. 103 to 105, and profiles of Re_t are shown in Figs. 106 to 108, for Ducts 1, 2, and 3, respectively. In Figs. 103 to 105, it is observed that the presence of the plate, or lack of it, has little effect on the k profiles in the proximity of the upper wall for a given duct and flow rate. It may be recalled from Chapter VII, that values of Re_t in the range $100 < Re_t < 400$ corresponded to y^+ values of approximately $30 < y^+ < 100$ for a fully developed turbulent channel flow. This is the region where boundary conditions are specified for the standard k-ϵ turbulence model used in conjunction with wall functions. It was found from the investigation presented in Chapter VII that the standard, or high Reynolds number, k-ϵ model performed poorly, compared to the JL k-ϵ model, in the calculation of overall flow rates when the levels of Re_t were not greater than the above-mentioned range over most of the flow domain. In Figs. 106(a), 107(a), and 108(a) the Re_t profiles for Re_m values of 5.764×10^3 in Duct 1, 5.809×10^3 in Duct 2, and 5.710×10^3 in Duct 3, respectively, show that all these flows exhibit a low level of turbulence: $Re_t < 200$ for Duct 3, and less than 140 in the case of Ducts 1 and 2. The levels of Re_t increase for the maximum Re_m flows, presented in Figs. 106(b), 107(b), and 108(b) corresponding to Re_m values of 27.27×10^3 in Duct 1. 26.47×10^3 in Duct 2, and 27.84×10^3 in Duct 3.

However, even in these flows, the level of Re_t is less than 900, and it is less than 400 over at least 20 percent of the flow domain. These results confirm the reasoning presented in Chapter V and the conclusions reached in Chapter VII that the low-Reynolds-number form of the k-ϵ turbulence model is better suited for the simulation of the flows of interest than the standard, or high-Reynolds-number, model.

This concludes the presentation and discussion of the results of this investigation.

CHAPTER X

CONCLUSION

This chapter is divided into two main sections: In the first section, the main contributions of this thesis are concisely reviewed; and some recommendations for the extension and improvement of this work are presented in the second section.

10.1 CONTRIBUTIONS OF THE THESIS

In this research work, complementary experimental and numerical investigations of turbulent periodic fully developed flows in three different interrupted-plate ducts have been carried out. The results of these investigations include (i) overall pressure drop data presented in the form of module friction factor - Reynolds number plots; (ii) plots of intramodular time-mean wall static pressure distributions in the periodic fully developed regime; (iii) plate surface streamline photographs taken as part of the experiments; and (iv) numerical predictions of streamlines, and distributions of plate shear stress, wall shear stress, axial momentum flux, and axial (U) velocities. In addition, profiles of mean turbulence kinetic energy, k, and turbulence Reynolds numbers, Re_t, have been presented as part of the numerical results.

The main achievements and contributions of the work reported in this thesis are summarized in the following subsections.

10.1.1 Place of this Work in Relationship to Available Literature

Experimental Investigation

A literature review pertaining to experimental investigations of turbulent fully developed flows in rectangular ducts and periodic fully developed flows in interrupted-plate passages was presented in Sections 1.2.1 and 1.2.3, respectively. It was found that experimental data on overall heat transfer and pressure drops in full-scale heat exchanger models have been reported in the published literature, but they are not suitable for use as critical tests of numerical predictions because they lack the necessary accuracy and local details. The results of several laboratory investigations of fluid flow and heat transfer in rectangular interrupted-surface flow passages are also available in the literature, but there is still a shortage of detailed and accurate data on heat transfer and fluid flow in such geometries. The experimental work presented in this thesis is an effort to fulfill a part of this need, and it has also provided new insights into fluid flow in interrupted-plate rectangular ducts.

Numerical Investigation

It is evident from the literature survey presented in Section 1.2.3 that several numerical studies concerned with laminar flows through interrupted-surface passages are available in the literature. It was found, however, that there is an absence of numerical studies that deal with the simulation of low-Reynolds-number turbulent flows in such passages. Such flows are commonly encountered in heat exchange equipment. The module Reynolds numbers ranged from approximately 5×10^3 to 33×10^3 in

this numerical investigation.

Based on the review of turbulence models presented in Section 1.2.2, it was decided that the two equation k-ϵ model of turbulence would be incorporated into the computer code developed as a part of this research. The computational costs associated with this model are relatively low compared to the more elaborate higher-order models. Furthermore, this model has been found to give satisfactory results for many complex two-dimensional turbulent flows encountered in industrial applications. In Section 5.1, it was decided that only the Jones and Launder [89] (JL), and the Launder and Sharma [91] (LS) low-Reynolds-number versions of the k-ϵ model would be considered for use in the simulation of the interrupted-plate duct flows of interest. These two versions of the model possess the desirable feature of having viscous damping functions that are dependent only on local properties of the flow, unlike functions in the other low-Reynolds-number models which are also dependent on the normal distance to the nearest wall, and, therefore, unsuitable for flows in interrupted-surface geometries.

10.1.2 Experimental Facility and Procedures

Initial tests performed with the rectangular duct test section, without an interrupted-plate array, established that the flow facility and procedures used in this research were capable of providing flow rate and time-mean wall static pressure measurements that are repeatable and accurate over the range of Reynolds numbers investigated: $10\times10^3 \leq Re_d \leq 60\times10^3$. The fully developed duct flow data yielded Reynolds number values that have an uncertainty of less than

± 2.4 percent and are repeatable to within less than 1 percent of a previous run at the same flow rate. The friction factor values, f_d, have an uncertainty of less than ± 5.0 percent, they are repeatable to within less than ± 2.5 percent of a previous run at the same flow rate, and they deviate from the corresponding Prandtl-Jones (PJ) correlation [54] values by less than ± 2.7 percent.

From initial tests with each of the three interrupted-plate duct configurations used in this work, it was concluded that the experimental facility was capable of providing flow rate and time-mean pressure measurements that were repeatable to within the following experimental uncertainties: The uncertainty in module Reynolds numbers, Re_m, was less than ± 2.3 percent; and the uncertainty in module friction factors, f_m, ranged from 12 percent at the smallest flow rates ($Re_m \simeq 5x10^3$) to 2 percent or less at the largest flow rates ($Re_m \simeq 33x10^3$). These initial test results, along with surface streamline flow visualization data, also confirmed that periodic fully developed flows were generated throughout the portion of the test section where measurements and observations were made.

Based on the surface streamline flow patterns observed over the central region of a plate in periodic fully developed flow, for the range of Reynolds numbers investigated ($5x10^3 \leq Re_m \leq 33.5x10^3$), it was concluded that the flow over the central 80 percent of the plate surface is essentially two-dimensional: The module aspect ratio was $\lambda \simeq 10.6$, for the three ducts investigated.

10.1.3 Computer Code

A computer code for the simulation of two-dimensional, steady, spatially-periodic fully developed flows in interrupted-plate channels was developed and tested as a part of this work. This code is based on the finite volume method of Patankar [41]. It incorporates the SIMPLEC procedure of Van Doormaal and Raithby [113], along with line-by-line TDMA [41] and CTDMA [13] algorithms and block correction procedures [114], for the solution of the coupled nonlinear discretization equations. The code is written in FORTRAN, and it was run on the CRAY X-MP/22 with the Cray FORTRAN Compiler.

An evaluation of this computer code was undertaken in the context of periodic fully developed laminar flows, before final incorporation of a turbulence model. The results for laminar flows were compared to those obtained by Patankar and Prakash [23] for similar flows. It was concluded that the numerical method formulated in Chapter IV has been properly implemented in this code.

10.1.4 Performance Evaluations of Some k-ϵ Models of Turbulence and Related Implementation Procedures

Performance evaluations were done to determine the suitability of some of the available k-ϵ models of turbulence, and related implementation procedures, for the simulation of the flows considered in this thesis. The standard (ST) [75], the Jones and Launder (JL) [89], and the Launder and Sharma (LS) [91] versions of the k-ϵ model were examined in detail. The low-Reynolds-number JL and LS models were tested with

and without the Hanjalic and Launder modification [96] discussed in Sections 1.2.2, 3.6, and 5.2.2. The sets of numerical results obtained with these models were compared to each other, and, whenever possible, they were also checked against experimental data and correlations available in the literature. These performance evaluations lead to the following conclusions:

(i) In low-Reynolds-number two-dimensional fully developed turbulent flows in a channel ($5x10^3 \leq Re_d \leq 30x10^3$), where a significant portion of the flow field has a low turbulence Reynolds number, Re_t, the overall mass flow calculations, and hence friction factor - Reynolds number predictions, of the ST model [75] can be improved by assuming, and integrating, a simple two-piece velocity profile over the near-wall boundary control volume, rather than using the prevailing assumption practice, as described in Section 7.2.1.

(ii) Of the four different combinations of k and ϵ equation source term linearizations presented in Section 5.3.3, the formulation designated as $S^k{}_1$-$S^\epsilon{}_1$-A ensures that a converged solution is efficiently achieved for the entire range of Reynolds numbers ($5x10^3 \leq Re_d \leq 244x10^3$) used in the numerical investigation of fully developed channel flow. This desirable performance of the $S^k{}_1$-$S^\epsilon{}_1$-A formulation is also realized in the simulation of steady, spatially-periodic, fully developed turbulent flows in interrupted-plate channels.

(iii) In the simulation of fully developed channel flows, the LS model [91] predicts U velocity profiles that are greater in magnitude than those obtained with the JL model [89], over the whole range of Reynolds numbers investigated ($5x10^3 \leq Re_d \leq 244x10^3$). Based on a comparison with experimental and analytical data available in the

literature, it was concluded that the JL model gives better predictions of the flow field than the LS model over the low-Reynolds-number range ($5x10^3 \leq Re_d \leq 30x10^3$). This conclusion was based on the qualitative agreement with the logarithmic velocity profile, Eq. (3-29), and the quantitative agreement of the numerical friction factor results with the PJ correlation [54] values: The friction factor values of the JL model are all within $\pm$ 2 percent of the PJ values, while those of the LS model deviate by as much as -14 percent at the smallest flow rate.

(iv) Of the k-ϵ models of turbulence considered in this evaluation, the JL model [89] with the Hanjalic and Launder modification [96], and the model constants listed in Table 1, is the best suited for the prediction of the steady spatially-periodic fully developed turbulent flows considered in this thesis.

(v) For given values of the module pressure-drop parameter, β, the corresponding flow rates were calculated: The numerically calculated values of Re_m ranged from being as much as 14.4 percent greater than the corresponding experimental values at the lowest flow rates ($Re_m \simeq 5x10^3$), to 1.94 percent lower than experimental values at the highest flow rates ($Re_m \simeq 27x10^3$). In general, as the plate thickness was increased and the flow rate was decreased, the numerical data were qualitatively good, but the quantitative differences between corresponding numerical and experimental data became greater, particularly in the lower range of Reynolds numbers ($5x10^3 \leq Re_m \leq 16x10^3$) where numerical flow rates were higher than the experimental flow rates.

Although the quantitative accuracy of the numerical data requires

improvement, the qualitative accuracy of the numerical results is quite good. It was therefore concluded that computer code developed for this research may be used, in conjunction with the experimental data, to gain an enhanced understanding of turbulent fluid flow phenomena within a periodic fully developed module.

10.1.5 Module Friction Factor - Reynolds Number Results

The module friction factor - Reynolds number results show the following:

(i) At low Reynolds numbers, both the inertial and frictional losses make a significant contribution to the overall pressure drop, and the module friction factor responds noticeably to changes in the module Reynolds number. However, as the Reynolds number increases, the inertial losses begin to dominate the frictional losses, and the module friction factor becomes less sensitive to changes in the Reynolds number.

(ii) As the plate thickness is increased, for the same duct aspect ratio and module Reynolds number, both the flow rate through the plate regions and the effective blockage of the plates increase. This causes an increase in the frictional and inertial losses, respectively, and increases the value of the module friction factor.

10.1.6 Intramodular Time-Mean Wall Static Pressure Distributions

The intramodular time-mean wall static pressure distributions presented in this thesis, along with those in earlier work by the author

[109,110], represent the first contribution of such data to the literature on fluid flow in interrupted-surface geometries. These results show clearly that spatially-periodic time-mean fully developed turbulent flows were indeed obtained in the experiments undertaken in this work. In addition, these results show that there is a steep drop in wall static pressure over the first half of a plate, and there is a significant recovery in this pressure in the initial part of the wake region. Except for the lowest flow and thinnest plate combination, this pressure recovery in wall static pressure starts in the region above the second half of the plate.

10.1.7 Surface Streamline Results

The surface streamline results also show that spatially-periodic fully developed turbulent flows were obtained in this investigation. Furthermore, the flow in the central 80 percent of the ducts was essentially two-dimensional.

The surface streamline results, and the numerical predictions of U velocity and shear stress at the plate surface, show that a small separation zone occurs over the leading-edge region of the plates , except at the lowest flow rate and thinnest plate combination. This separation zone is followed by a region of low surface shear stress, just after reattachment of the air flow to the plate surface.

The surface streamline data has also shown for the first time the existence of a second separation and recirculation region which occurs over the plate immediately upstream of its trailing edge, for values of

module Reynolds numbers in the range $5x10^3 \leq Re_m \leq 20x10^3$. At the lowest flow rates, this region extends upstream of the trailing edge by as much as one quarter of the plate length, and decreases in its upstream extent as the flow rate increases. This region is not predicted by the steady state numerical model. It may thus be concluded that this separation region is caused by some unsteady phenomena in the flow, such as periodic shedding of vortices from the plates.

10.1.8 Turbulence Kinetic Energy and Turbulence Reynolds Number Results

The numerically predicted profiles of mean turbulence kinetic energy, k, and turbulence Reynolds number, Re_t, show that, for the flow rates considered, there can be large regions where the turbulence level is low within a periodic module ($Re_t < 400$). Thus the low-Reynolds-number form of the k-ϵ model is more suitable than the standard form of this turbulence model for the prediction of flows similar to those considered in this research

10.2 SUGGESTIONS FOR EXTENSIONS AND IMPROVEMENTS OF THIS WORK

New insights into the local flow phenomena occurring in a periodic fully developed flow module in an interrupted-plate duct have been obtained as a result of the work presented in this thesis. While this success has been encouraging, there are some extensions and improvements of this work that would be worthwhile to undertake in future research. Some suggestions in this regard are presented in this section.

In the initial performance evaluation of the turbulence models considered for use in this work, it became evident that there is a lack of experimental data available for low-Reynolds-number flows ($5x10^3 \leq Re_d \leq 30x10^3$), especially in the region close to a wall ($y^+ < 30$). In this region, it would be very useful to obtain detailed velocity measurements using techniques such as laser-Doppler and thermal anemometry [133]. Such data are needed in order that a critical performance evaluation, and fine-tuning, of the low-Reynolds-number turbulence models may be carried out. These flow measurement techniques could also be used to obtain local velocity measurements within a periodic module in interrupted-plate duct flows. Such data are also urgently needed, particularly in the region where a separation zone upstream of the trailing edge of the plate has been indicated by the surface streamline results of this investigation.

The results of this research indicate that some improvements to the ϵ equation and the viscous damping functions employed in the JL form [89] of the k-ϵ model are in order. In addition, the surface streamline results of this investigation have indicated the existence of a separation zone upstream of the trailing edge of the plate. To properly simulate this flow, the present steady-state numerical model should be extended to model unsteady flow phenomena. The results obtained by using such a model could be compared to those obtained using the present model to determine the extent of any error that is introduced by modelling only the time-averaged behaviour of the flow. Another logical extension of the numerical investigation would be to incorporate heat transfer into the present computer code. The two-dimensional numerical

formulation used in this work could also be expanded to a three-dimensional one.

In conjunction with the above-mentioned extensions of the numerical research, additional experimental research could include the study of heat transfer, and three-dimensional flows in interrupted-plate passages. An experimental investigation of periodic fully developed heat transfer in such ducts could be directed towards obtaining, first, average Nusselt number data and, then, local Nusselt number data. Such local heat transfer data could be acquired by using electrically heated thin films of gold or stainless steel [134,135], or by using mass transfer experiments and the analogy between convective transport of mass and the convective transport of thermal energy [136]. The naphthalene sublimation studies of Sparrow et al. [12-14] are examples of heat transfer studies based on mass transfer experiments. Flows through modules with small aspect ratios, for example $1 \leq \lambda \leq 5$, could be studied to obtain three-dimensional flow and heat transfer data.

Both the experimental and numerical investigations could also be extended to include turbulent periodic fully developed flows in other interrupted-surface flow passages that are used in heat transfer devices. Such flow passages include louvered plate-fin ducts, rod or tube arrays, and shrouded pin-fin arrays [1]. The test section used in this experimental study could be reconfigured to allow simulation of flows through such passages. The numerical model would require semiautomatic curvilinear grid-generation procedures [137], and modifications similar to those elaborated by Raithby and Schneider [42]. Following that, the numerical simulation of fluid flow and heat transfer in actual

heat transfer equipment having interrupted-surface flow passages [1,2] could be undertaken.

In conclusion, it is hoped that the work presented in this thesis will lead to a better understanding of the fluid flow and heat transfer phenomena that occur in interrupted-surface flow passages, and enable improvements of the numerical methods suitable for the prediction of these phenomena.

REFERENCES

1. Kays, W.M. and London, A.L., **Compact Heat Exchangers**, 2nd ed., McGraw-Hill, New York, 1964.

2. Shah, R.K., Classification of heat exchangers, in **Heat Exchangers: Thermo-Hydraulic Fundamentals and Design** (Eds. S. Kakac, A.E. Bergles, and F. Mayinger), Hemisphere Publishing Corp., New York, pp. 9-46, 1981.

3. Shah, R.K., Compact Heat Exchangers, in **Heat Exchangers: Hydraulic Fundamentals and Design** (Eds. S. Kakac, A.E. Bergles, and F. Mayinger), Hemisphere Publishing Corp., New York, pp. 111-151, 1981.

4. Wieting, A.R., Empirical correlations for heat transfer and flow friction characteristics of rectangular offset-fin plate-fin heat exchangers, **ASME J. Heat Transfer**, Vol. 97, pp. 488-490, 1975.

5. Bergles, A.E., Principles of heat transfer augmentation. I: Single-phase heat transfer, in **Heat Exchangers: Thermal-Hydraulic Fundamentals and Design** (Eds. S. Kakac, A.E. Bergles, and F. Mayinger), Hemisphere Publishing Corp., New York, pp. 819-842, 1981.

6. Kraus, A. and Bar-Cohen, A., **Thermal Analysis and Control of Electronic Equipment**, Hemisphere Publishing Corp., Washington, D.C., 1983.

7. Chu, R.C., Heat transfer in electronic systems, **Proceedings of the Eighth International Heat Transfer Conference**, San Fransisco, California, Vol. 1, pp. 293-305, 1986.

8. Sparrow, E.M., Neithammer, J.E., and Chaboki, A., Heat transfer and pressure drop characteristics of arrays of rectangular modules encountered in electronic equipment, **Int. J. Heat Mass Transfer**, Vol. 25, pp. 961-972, 1982.

9. Sparrow, E.M., Vemuri, S.B., and Kadle, D.S., Enhanced and local heat transfer, pressure drop, and flow visualization for arrays of block-like electronic components, **Int. J. Heat Mass Transfer**, Vol. 27, pp. 689-699, 1983.

10. Kishimoto, T., Sasaki, E., and Moriya, K., Gas cooling enhancement technology for integrated circuit chips, **IEEE Transactions on Components, Hybrids, and Manufacturing Technology**, Vol. CHMT-7, No.3, pp. 286-293, 1984.

11. Cur, N. and Sparrow, E.M., Measurements of developing and fully developed heat transfer coefficients along a periodically interrupted surface, **ASME J. Heat Transfer**, Vol. 101, pp. 211-216, 1979.

12. Sparrow, E.M., Baliga, B.R. and Patankar, S.V., Heat transfer and fluid flow analysis of interrupted-wall channels, with application to heat exchangers, **ASME J. Heat Transfer**, Vol. 99, pp. 4-11, 1977.

13. Patankar, S.V., Liu, C.H., and Sparrow, E.M., Fully developed flow and heat transfer in ducts having streamwise-periodic variation of cross-sectional area, **ASME J. Heat Transfer**, Vol. 99, pp. 180-186, 1977.

14. Patankar, S.V. and Prakash, C., An analysis of the effect of plate thickness on laminar flow and heat transfer in interrupted-plate passages, **Int. J. Heat Mass Transfer**, Vol. 24, pp. 1801-1810, 1981.

15. Sparrow, E.M. and Liu, C.H., Heat-transfer, pressure drop and performance relationships for in-line, staggered, and continuous plate heat exchangers, **Int. J. Heat Mass Transfer**, Vol. 22, pp. 1613-1625, 1979.

16. Choudhury, D., A quasi-three-dimensional calculation procedure for the prediction of flow and heat transfer in heat exchanger passages, **Ph. D. Thesis**, University of Minnesota, 1987.

17. Sparrow, E.M. and Prata, A.T., Numerical solutions for laminar flow and heat transfer in a periodically converging-diverging tube, with experimental confirmation, **Numerical Heat Transfer**, Vol.6, pp. 441-461, 1983.

18. Prata, A.T. and Sparrow, E.M., Heat transfer and fluid flow characteristics for an annulus of periodically varying cross section, **Numerical Heat Transfer**, Vol. 7, pp. 285-304, 1984.

19. Ghaddar, N.K., Korczak, K.Z., Mikic, B.B. and Patera, A.T., Numerical investigation of incompressible flow in grooved channels. Part 1. Stability and self-sustained oscillations, **J. Fluid Mech.**, Vol. 163, pp. 99-127, 1986.

20. Ghaddar, N.K., Megan, M., Mikic, B.B. and Patera, A.T., Numerical investigation of incompressible flow in grooved channels. Part 2. Resonance and oscillatory heat-transfer enhancement, **J. Fluid Mech.**, Vol. 168, pp. 541-567, 1986.

21. Kelkar, K.M. and Patankar, S.V., Numerical prediction of flow and heat transfer in a parallel plate channel with staggered fins, **ASME J. Heat Transfer**, Vol. 109, pp. 25-30, 1987.

22. Choudhury, D. and Karki, K.C., Calculation of laminar fluid flow and heat transfer in streamwise-periodic dimpled channels using generalized curvilinear coordinates, **Creare Inc.**, TN-463, Nov. 1988, presented at the AIAA Aerospace Sciences Meeting, Reno, NV, Jan. 1989, AIAA.

23. Knight, R.W. and Crawford, M.E., Numerical prediction of turbulent flow and heat transfer in channels with periodically varying cross sectional area, **ASME Proc. The 1988 National Heat Transfer Conference** (Ed. H.R. Jacobs), HTD-Vol. 96, No. 1, pp. 669-676, 1988.

24. London, A.L. and Shah, R.K., Offset rectangular plate-fin surfaces - heat transfer and flow friction characteristics, **ASME J. Engineering for Power**, Vol. 90, pp. 218-228, 1968.

25. Cur, N. and Sparrow, E.M., Experiments on heat transfer and pressure drop for a pair of colinear, interrupted plates aligned with the flow, **Int. J. Heat Mass Transfer**, Vol. 21, pp. 1069-1080, 1978.

26. Sparrow E.M. and Hajiloo, A., Measurements of heat transfer and pressure drop for an array of staggered plates aligned parallel to an air flow, **ASME J. Heat Transfer**, Vol. 102, pp. 426-432, 1980.

27. Roadman, R.E. and Loehrke, R.I., Low Reynolds number flow between interrupted flat plates, **ASME J. Heat Transfer**, Vol. 105, pp. 167-171, 1983.

28. Zelenka, R.L. and Loehrke, R.I., Heat transfer from interrupted plates, **ASME J. Heat Transfer**, Vol. 105, pp. 172-177, 1983.

29. Loehrke, R.I. and Lane, J.C., Flow through an array of interrupted, parallel plates, **Heat Transfer 1982**, Vol. 6, Hemisphere, pp. 251-262, 1982.

30. Mullisen, R.S. and Loehrke, R.I., A study of the flow mechanisms responsible for heat transfer enhancement in interrupted-plate heat exchangers, **ASME J. Heat Transfer**, Vol. 108, pp. 377-385, 1986.

31. Joshi, H.M. and Webb, R.L., Heat transfer and friction in the offset strip-fin heat exchanger, **Int. J. Heat Mass Transfer**, Vol. 30, pp. 69-84, 1987.

32. Shah, R.K. and London, A.L., **Laminar Flow Forced Convection in Ducts**, Advances in Heat Transfer, Supplement I, Academic Press, 1978.

33. Kays, W.M. and Perkins, H.C., Forced convection, internal flow in ducts, Section 7 in **Handbook of Heat Transfer**, (Eds. W.M. Rohsenow and J.P. Hartnett), McGraw-Hill Book Co., 1973.

34. Schlichting, H., **Boundary-Layer Theory**, 6th ed., McGraw-Hill Book Co., 1968.

35. Kays, W.M. and Crawford, M.E., **Convection Heat and Mass Transfer**, 2nd ed., McGraw-Hill Book Co., 1980.

36. White, F.M., **Viscous Fluid Flow**, McGraw-Hill Book Co., 1974.

37. Hinze, J.O., **Turbulence**, 2nd ed. McGraw-Hill Book Co., 1975.

38. Tennekes, H. and Lumley, J.L., **A First Course in Turbulence**, MIT Press, 1972.

39 Launder, B.E and Spalding, D.B., **Mathematical Models of Turbulence**, Academic Press, 1972.

40. Bradshaw, P., Cebeci, T. and Whitelaw, J.H., **Engineering Calculation Methods for Turbulent Flow**, Academic Press, 1981.

41. Patankar, S.V., **Numerical Heat Transfer and Fluid Flow**, McGraw-Hill Book Co., 1980.

42. Raithby, G.D. and Schneider, G.E., Elliptic systems: finite-difference method I, Section 6 in **Handbook of Numerical Heat Transfer**, (Eds. W.J. Minkowycz, E.M. Sparrow, G.E. Schneider and R.H. Pletcher), John Wiley and Sons Inc., 1988.

43. Anderson, D.A., Tannehill, J.C. and Pletcher, R.H., **Computational Fluid Flow and Heat Transfer**, McGraw-Hill Book Co., 1984.

44. Goldstein, R.J., **Fluid Mechanics Measurements**, Hemisphere Publishing Corporation, Washington, D.C., 1983.

45. Winternitz, F.A.L. and Fishcl, C.F., A simplified integration technique for pipe-flow measurement, **Water Power**, pp. 225-234, June 1957.

46. Ower, E. and Pankhurst, R.C., **The Measurements of Air Flow**, 4th ed., Pergamon Press, 1966.

47. Maltby, R.L. and Keating, R.F.A., Flow visualization in ow speed wind tunnels: current British practice, **RAE (Bedford) Tech. Note**, No. AERO.2715, August 1960.

48. Kline, S.J. and McClintock, F.A., Describing uncertainties in single-sample experiments, **Mechanical Engineering**, Vol. 75, pp. 3-8, 1953.

49. Moffat, R.J., Contributions to the theory of single-sample uncertainty analysis, **ASME J. Fluids Engineering**, Vol. 104, pp. 250-260, 1982.

50. Moffat, R.J., Using uncertainty analysis in the planning of an experiment, **ASME J. Fluids Engineering**, Vol. 107, pp. 173-182, 1985.

51. Kline, S.J., The purposes of uncertainty analysis, **ASME J. Fluids Engineering**, Vol. 107, pp. 153-160, 1985.

52. Abernethy, R.B., Benedict, R.P. and Dowdell, R.B., ASME measurement uncertainty, **ASME J. Fluids Engineering**, Vol. 107, pp. 161-164, 1985.

53. Hartnett, J.P., Koh, J.C.Y. and McComas, S.T., A comparison of predicted and measured friction factors for turbulent flow through rectangular ducts, **ASME J. Heat Transfer**, Vol. 84, pp. 82-88, 1962.

54. Jones, O.C., An improvement in the calculation of turbulent friction in rectangular ducts, **ASME J. Fluids Engineering**, Vol. 98, pp. 173-181, 1976.

55. Stanton, T.E. and Pannell, J.R., Similarity of motion in relation to the surface friction of fluids, **Phil. Trans. Royal. Soc., London**, Vol. A214, pp. 199, 1914.

56. Davies, S.J. and White, C.M., An experimental study of the flow of water in pipes of rectangular section, **Proc. Roy. Soc., London**, Vol. A119, pp. 92-107, 1928.

57. Cornish, R.J., Flow in a pipe of rectangular cross section, **Proc. Roy. Soc., London**, Vol. A120, pp. 691-700, 1928.

58. Nikauradse, J., Stromungsgesetze in rauhen rohren, **VDI-Forschungsheft**, Vol. 4, pp. 1-22, 1933 (English Translation in **NACA 1292**).

59. Colebrook, C.R., Turbulent flow in pipes with particular reference to the transition region between the smooth and rough pipe laws, **J. Instn. Civil Engineers, London**, Vol. 11, pp. 133-156, 1939.

60. Deissler, R.G. and Taylor, M.F., Analysis of turbulent flow and heat transfer in noncircular passages, **NASA Technical Report**, No. R-31, 1959.

61. Laufer, J., Investigation of turbulent flow in a two-dimensional channel, **NACA Technical Note**, No. 2123, 1950; also **NACA Technical Report**, No 1053, 1951.

62. Comte-Bellot, G., Ecoulement turbulent entre deux parois paralleles, **Publ. Sci. Tech. de Ministre de l'Air**, No. 419, 1965; also "Turbulent flow between two parallel walls", Translation by P. Bradshaw, **ARC 31 609, FM 4102**, 1969

63. Clarke, J.A., A study of incompressible turbulent boundary layers in channel flow, **ASME J. Basic Engineering**, Vol. 90, pp. 455-468, 1968.

64. Hussain, A.K.M.F. and Reynolds, W.C., Measurements in fully developed turbulent channel flow, **ASME J. Fluids Engineering**, Vol. 97, pp 568-580, 1975.

65. Prandtl, L., **Essentials of Fluid Mechanics**, Hafner, New York, 1953.

66. Brundrett, E. and Baines, W.D., The production and diffusion of vorticity in duct flow, **J. Fluid Mech.**, Vol. 19, pp. 375-392, 1964.

67. Gessner, F.B. and Jones, J.B., On some aspects of fully-developed turbulent flow in rectangular channels, **J. Fluid Mech.**, Vol. 23, pp. 689-713, 1965.

68. Launder, B.E. and Ying, W.M., Secondary flows in ducts of square cross-section, **J. Fluid Mech.**, Vol. 54, pp. 289-295, 1972.

69. Hanjalic, K. and Launder, B.E., Fully developed asymmetric flow in a plane channel, **J. Fluid Mech.**, Vol. 51, part 2, pp. 301-335, 1972.

70. El Telbany, M.M M. and Reynolds, A.J., Velocity distributions in plane turbulent channel flows, **J. Fluid Mech.**, Vol. 100 part 1, pp. 1-29, 1980.

71. El Telbany, M.M.M. and Reynolds, A.J., Turbulence in plane channel flows, **J. Fluid Mech.**, Vol. 111, pp. 283-381, 1981.

72. Ferziger, J.H., Bardina, J. and Allen, G., Overview of taxonomy: morphology of the flows and computational methods; in **The 1980-81 AFOSR-HTTM-Standford Conference on Complex Turbulent Flows: Comparison of Computation and Experiment** (Eds. S.J. Kline, B.J. Cantwell, and G.M. Lilley) , Vol. II, pp. 634-649, 1982.

73. Reynolds, W.C., Computation of turbulent flows, **Ann. Rev. Fluid Mech.**, Vol. 8, pp. 183-208, 1976.

74. Aupoix, B., Homogeneous turbulence two-point closures and applications to one-point closures, **AGARD Report**, No. 755 (Special Course on Modern Theoretical and Experimental Approaches to Turbulent Flow Structure and its Modelling), pp 3.1-3 47, 1987.

75. Rodi, W , Turbulence models and their application in hydraulics - a state of the art review, **IAHR State-of-the-Art Paper**, 1980.

76. Nallasamy, M , Turbulence models and their applications to the prediction of internal flows: a review, **Computers and Fluids**, Vol. 15, No. 2, pp. 151-194, 1987.

77. Laurence, D., Turbulence modelling through ore point closures - applications - enlightening by large scale simulation, **AGARD Report**, No. 755 (Special Course on Modern Theoretical and Experimental Approaches to Turbulent Flow Structure and its Modelling), pp. 2.1-2.34, 1987.

78. Reynolds, W.C., Fundamentals of turbulence for turbulence modeling and simulation, **AGARD Report**, No. 755 (Special Course on Modern Theoretical and Experimental Approaches to Turbulent Flow Structure and its Modelling), pp 1.1-1.66, 1987.

79. **The 1980-81 AFOSTR-HTTM-Stanford Conference on Complex Turbulent Flows: Comparison of Computation and Experiment**, (Eds. S.J. Kline, B.J. Cantwell, and G.M Lilley), Vols. I, II, and III, 1982.

80. Jones, W P. and Launder, B E., The prediction of laminarization with a two-equation model of turbulence, **Int. J. Heat Mass Transfer**, Vol. 15, pp 301-314, 1972.

81. Hanjalic, K., Velocity and length scales in turbulent flows - a review of approaches, in **The 1980-81 AFOSR-HTTM-Stanford Conference** on Complex Turbulent Flows: Comparison of Computation and Experiment (Eds. S.J. Kline, B.J. Cantwell and G M. Lilley), Vol. II, pp. 672-680, 1982.

82. Gosman, A.D. and Rapley, C.W., Fully developed flow in passages of arbitrary cross section, in **Recent Advances in Numerical Methods in Fluids** (Eds. C. Taylor and K. Morgan), Pineridge Press, Swansea, 1980.

83. Naot, D. and Shavit, A. and Wolfshtein, M., Numerical calculation of Reynolds stresses in a square duct with secondary flow, **Warme-und-Stoff**, Vol. 7, pp. 151, 1974.

84 Launder, B.E. and Ying, W.M., Prediction of flow and heat transfer in ducts of square cross-section, **Proc. I. Mech. E.**, Vol. 187, pp. 455-461, 1973.

85. Gessner, F.B. and Emery, A.F., A Reynolds stress model for turbulent corner flows - Part I: Development of the model, **ASME J. Fluids Engineering** Vol. 98, pp. 261-268, 1976.

86. Rapley, C.W., Fluid and heat flow in tubes of arbitrary cross-section, **Ph.D. Thesis**, University of London, 1980.

87. Nakayama, A., Chow, W.L. and Sharma, D., Calculation of fully developed turbulent flow in ducts of arbitrary cross-section, **J. Fluid Mech.**, Vol. 128, pp. 199-217, 1983.

88. Hanjalic, K , Two-dimensional asymmetrical turbulent flow in ducts, **Ph.D. Thesis**, University of London, 1970.

89. Jones, W.P. and Launder, B.E., The calculation of low-Reynolds-number phenomena with a two-equation model of turbulence, **Int. J. Heat Mass Transfer**, Vol. 16, pp. 1119-1130, 1973.

90. Patel, V.C , Rodi, W. and Scheuerer, G , Turbulence models for near-wall and low Reynolds number flows: a review, **AIAA Journal**, Vol. 23, No. 9, pp. 1308-1319, 1984.

91. Launder, B.E. and Sharma, B.I., Application of the energy-dissipation model of turbulence to the calculation of flow near a spinning disc, **Letters in Heat and Mass Transfer**, Vol. 1, pp 131-138, 1974.

92. Chien, K., Predictions of channel and boundary-layer flows with a low-Reynolds-number turbulence model, **AIAA Journal**, Vol. 20, No. 1, pp. 33-38, 1982.

93. Lam, C.K.G and Bremhorst, K , A modified form of the k-ϵ model for predicting wall turbulence, **ASME J. Fluids Engineering**, Vol. 103, pp. 456-460, 1981.

94. Wilcox, D.C. and Rubesin, W.M., Progress in turbulence modeling for complex flow fields including effects of compressibility, **NASA Tech. Paper**, No 1517, 1980.

95 Lam, C K G. and Bremhorst, K., A modified form of the k-ϵ model for predicting wall turbulence, **University of Queensland Department of Mechanical Engineering Research Report**, No. 3/78, Apr. 1978.

96. Hanjalic, K. and Launder, B.E., Sensitizing the dissipation equation to irrotational strains, **ASME J. Fluids Engineering**, Vol. 102, pp. 34-39, 1980.

97. Rodi, W. and Scheuerer, G., Scrutinizing the k-ε turbulence model under adverse pressure gradient conditions, **ASME J. Fluids Engineering**, Vol. 108, pp. 174-179, 1986.

98. Chieng, C.C. and Launder, B.E., On the calculation of turbulent transport downstream from an abrupt pipe expansion, **Num. Heat Transfer**, Vol. 3, 189-207, 1980.

99. Amano, R.S., Development of a turbulence near-wall model and its application to separated and reattached flows, **Num. Heat Transfer**, Vol. 7, pp. 59-75, 1984.

100. Patel, V.C. and Chen, H.C., Turbulent wake of a flat plate, **AIAA Journal**, Vol. 25, pp. 1078-1085, 1987.

101. Chen, H.C. and Patel, V.C., Practical near wall turbulence models for complex flows including separation, **AIAA Paper**, No. 87-1300, 1987.

102. Patel, V.C. and Richmond, M.C , Pressure gradient and curvature effects in turbulent boundary layers, **AIAA Paper**, No. 87-1301, 1987.

103. Iacovides, H. and Launder, B.E., PSL - an economical approach to the numerical analysis of near-wall, elliptic flow, **ASME J. Fluids Engineering**, Vol. 106, pp. 241-242, 1984.

104. Norris, R.H. and Spofford, W.A , High performance fins for heat transfer, **Trans. ASME**, Vol. 64, pp. 489-496, 1942.

105. Manson, S.V., Correlations of heat transfer data and of friction data for interrupted plane fins staggered in successive rows, **NACA Technical Note**, No. 2237, 1950.

106. Mochizuki, S. and Yoshinao, Y., Heat transfer and friction characteristics of strip fins, **Heat Transfer, Japanese Research**, Vol. 6, pp. 36-59, 1977.

107. Adarkar, D.B. and Kays, W.M., Heat transfer in wakes, **Tech. Report No. 55**, Department of Mechanical Engineering, Stanford University, 1963.

108. Mochizuki, S. and Yagi, Y., Characteristics of vortex shedding in plate arrays, in **Flow Visualization II**, (Ed. W.Merzkirch), pp. 99-103, Hemisphere Publishing Corporation, 1982.

109. McBrien, R.K., Pressure measurements for periodic fully developed turbulent flow in rectangular interrupted-plate ducts, **M. Eng. Thesis**, Department of Mechanical Engineering, McGill University, 1986.

110. McBrien, R.K. and Baliga, B.R., Module friction factors and intramodular pressure distributions for periodic fully developed turbulent flow in rectangular interrupted-plate ducts, **ASME J. Fluids Engineering**, Vol. 110, pp. 147-154, 1988.

111. Bradshaw, P., **Topics in Applied Physics**, Springer-Verlay, New York, 1976.

112. Launder, B.E. and Spalding, D.B., The numerical computation of turbulent flow, **Comp. Meth. in Appl. Mech. and Eng.**, Vol. 3, pp. 269-289, 1974.

113. Van Doormaal, J.P. and Raithby, G.D., Enhancements of the SIMPLE method for predicting incompressible fluid flows, **Numerical Heat Transfer**, Vol. 7, pp. 147-163, 1984.

114. Settari, A. and Aziz, K.A., A generalization of the additive correction methods for the iterative solution of matrix equations, **SIAM J. Numerical Anal.**, Vol. 10, pp. 506-521, 1973.

115. Raithby, G.D., Skew upwind differencing schemes for problems involving fluid flow, **Comput. Meths. Appl. Mech. Engrg.**, Vol. 9, pp. 153-164, 1976.

116. Leonard, B.P., A stable and accurate convective modelling procedure based on quadratic upstream interpolation, **Comput. Meths. Appl. Mech. Engrg.**, Vol. 19, pp. 59-98, 1979.

117. Huang, P.G., Launder, B.E., and Leschziner, M.A., Discretization of nonlinear convection processes: a broad-range comparison of four schemes, **Comput. Meths. Appl. Mech. Engrg.**, Vol. 48, pp. 1-24, 1985.

118. de Vahl Davis, G., Natural convection of air in a square cavity: a bench mark numerical solution, **Int. J. Num. Meth. in Fluids**, Vol. 3, pp. 249-264, 1983.

119. Shaw, R., The influence of hole dimensions on the static pressure measurements, **J. Fluid Mech.**, Vol. 7, pp. 550-564, 1960.

120. Langston, L.S. and Boyle, M.T., A new surface-streamline flow-visualization technique, **J. Fluid Mech.**, Vol. 125, pp. 53-57, 1982.

121. Eckert, E R.G. and Drake, R.M., **Analysis of Heat and Mass Transfer**, McGraw-Hill Book Co., 1972.

122. **ANSI/ASME PTC 19.1-1985**, Measurement uncertainty part 1: instruments and apparatus, 1985.

123. Walpole, R.E. and Myers, R.H., **Probability and Statistics for Engineers and Scientists**, 2nd ed., MacMillan Publishing Co., Inc., New York, 1978.

124. **CRAY X-MP and CRAY-1 Computer Systems - FORTRAN (CFT) Reference Manual - SR009**, Cray Research Inc., Medota Heights, Minnesota, 1986.

125. Roache, P.J., **Computational Fluid Dynamics**, Hermosa Publishers, Albuquerque, N.M., 1976.

126. Davis, R.W., Moore, E.F., and Purtell, L.P., A numerical-experimental study of flow around rectangular cylinders, **Phys. Fluids**, Vol. 27, pp. 46-59, 1984.

127. Back, L.H. and Roschke, E.J., Shear-layer flow regimes and wave instabilities and reattachment lengths downstream of an abrupt circular channel expansion, **ASME J. Appl. Mech.**, Vol. 39, pp. 677-681, 1972.

128. Shair, F.H., Grove, A.S., Petersen, E.E., and Acrivos, A., The effect of confining walls on the stability of the steady wake behind a circular cylinder, **J. Fluid Mech.**, Vol. 17, pp. 546-550, 1963.

129. Baughn, J.W., Hoffman, M.A, and Takahashi, R.K., Heat transfer downstream of an abrupt expansion in the transition Reynolds number regime, **Proc. The 23rd National Heat Transfer Conference - Denver, Colorado- August 4-7, 1985 - Fundamentals of Forced and Mixed Convection**, HTD-Vol. 42, pp. 65-71, 1985.

130. MacLennan, A.S. and Vincent, J.H., Transport in the near aerodynamic wakes of flat plates, **J. Fluid Mech.**, Vol. 120, pp. 185-197, 1982.

131. Perry, A.E , Chong, M.S., and Lim, T.T., The vortex-shedding process behind two-dimensional bluff bodies, **J. Fluid Mech.**, Vol. 116, pp. 77-90, 1982.

132. Davis, R.W. and Moore, E.F., A numerical study of vortex shedding from rectangles, **J. Fluid Mech.**, Vol. 116, pp. 475-506, 1982.

133. Durst, F., Melling, A., and Whitelaw, J.H , **Principles and Practices of Laser Doppler Anemometry**, Academic Press, 1976.

134. Baughn, J.W., Takahashi, R.K., Hoffman, M.A., and McKillop, A.A., Local heat transfer measurements using an electrically-heated thin gold-coated plastic sheet, **ASME J. Heat Transfer**, Vol. 107, pp. 953-959, 1985.

135. Neill, W.S., Local natural convection heat transfer measurements using a thin gold-film technique, **M. Eng. Thesis**, Department of Mechanical Engineering, McGill University, 1989.

136. Eckert, E.R.G. and Drake, R M., **Analysis of Heat and Mass Transfer**, McGraw-Hill Book Co., New York, 1972.

137. Thompson, J.F., Warsi, Z.U.A., and Mastin, C.W., **Numerical Grid Generation Foundations and Applications**, Elsevier Science Publ. Co., New York, 1985.

APPENDICES

APPENDIX I

GRID GENERATION

In the finite volume methods used in this work, the calculation domain is first divided into rectangular main-grid control volumes. Then all other main-grid and staggered-grid locations are determined, as described in Section 5.2.1.

The purpose of this appendix is to describe the procedure that was used to calculate the position of the rectangular main-grid control-volume faces within a calculation domain. The first part of the appendix deals with the generation of grids having nonuniform distributions of control volumes in the x- and y-coordinate directions, and the second part outlines the procedure employed to obtain the uniform grid distributions used in the grid independence tests mentioned in Section 9.1.4 and described in Appendix 6.

A1.1 NONUNIFORM GRID DISTRIBUTIONS

Each calculation domain was first divided into rectangular zones, or subdomains, in the x- and y-coordinate directions: The distribution of the respective x and y control-volume face locations within each zone was then determined. The calculation domains used in this research where divided into: (i) 1 y-zone for turbulent fully developed two-dimensional channel flows, as described in Section 5.3.2; (ii) 2 x-zones and 3 y-zones for laminar periodic fully developed flow in a two-dimensional interrupted-plate passage, in the manner stated in Section 7.3.2; and (iii) 2 x-zones and 2 y-zones for periodic fully

developed turbulent flows in two-dimensional interrupted-plate ducts, as discussed in Section 5.2.1. The general procedure that was used to determine the location of control-volume faces within each zone will be discussed next, using the calculation of y control-volume face locations within a y-zone as an example.

In the general procedure, the length of the calculation domain, Lz^T, in the y-coordinate direction was divided into N zones, each of length Lz_i, where i= 1 to N, as depicted in Fig. 109(a). Each of these zones was symmetrically subdivided into two outer layers, B and C, and one inner layer, A, that extends from lines cc to dd, as shown for Zone 2 in Fig. 109(b). Because of this symmetrical subdivision, control-volume face locations calculated in one half of a zone can be used to obtain the locations in the other half of the zone. The dimensions of control volumes were expanded from a minimum value at the outer boundaries of the zone, located at lines aa and bb with respect to Zone 2 in Fig. 109, to a maximum value in the central region of the zone: This expansion was done using a power-law formulation across the outer layers and a geometric-growth formulation across the inner layer. The y dimension of the inner layer varied from zone to zone, but the y dimension of the outer layers and the number of control volumes in them was kept the same for all zones: This ensured that there were no sudden changes in control-volume size across zone boundaries, such as lines aa and bb in Fig. 109.

With reference to the nomenclature employed in Fig. 109 and using Zone 2 in this figure as an example, the details of the general discretization process are as follows for the y-coordinate direction.

Specify:

(1) Lz, the y dimension of the zone.

(2) L^{o}, the common y dimension of all outer layers in each zone.

(3) N^{cvo}, the number of y control volumes into which each outer layer is subdivided: This value is kept the same for all y-zones in the calculation domain.

(4) N^{cvt}, the desired total number of control volumes within the particular zone of interest. N^{cvt} must be an odd number to ensure that there will be one control volume that symmetrically spans the zonal line of symmetry, line xx for Zone 2 in Fig. 109(b).

Calculate:

(5) n1, the index number of the y control-volume face located at the common boundary of Outer Layer B and Inner Layer A, shown by line cc in Fig. 109(b). This value is calculated as:

$$n1 = n0 + N^{cvo} \qquad \text{(A1-1)}$$

where n0 is the index number of the first y control-volume face at the bottom of the zone, on line aa in Fig. 109(b). If this location is the boundary of the calculation domain, then n0 = 2, otherwise, it is the number of the top-most control-volume face of the adjacent zone, Zone 1 in this case.

(6) CV_j, the y control-volume face locations in Outer Layer B. This is done using the following power-law expansion:

$$CV_j = CV_{n0} + \{(j - n0)/(n1-n0)\}^{Pow} L^o$$
$$\text{for } j = (n0 + 1) \text{ to } n1 \qquad \text{(A1-2)}$$

where Pow is the "Power-Law" expansion exponent which was assigned a value of 1.4 for the grids generated in this work.

(7) LCV_j, the y dimension of the control-volumes in Outer Layer B, given by:

$$LCV_{j-1} = CV_j - CV_{j-1}$$
$$\text{for } j = (n0 + 1) \text{ to } n1 \qquad \text{(A1-3)}$$

(8) L^{in}, the y dimension of the inner layer:

$$L^{in} = Lz - 2\,L^o \qquad \text{(A1-4)}$$

(9) N^{cvi}, the total number of y control volumes <u>desired</u> in the inner layer:

$$N^{cvi} = N^{cvt} - 2\,N^{cvo} \qquad \text{(A1-5)}$$

(10) LCV^{mx}, the desired maximum control-volume length in the inner layer:

$$LCV^{mx} = L^{in} / N^{cvi} \qquad \text{(A1-6)}$$

(11) CV_j, LCV_j, in the bottom half of Inner Layer A, from lines cc to xx in Fig. 109(b). These are calculated by doing a geometric expansion of the dimension of the last control volume in Outer Layer B:

$$CV_j = CV_{j-1} + (LCV_{j-2})\,GF \qquad \text{(A1-2a)}$$
$$LCV_{j-1} = CV_j - CV_{j-1} \qquad \text{(A1-3a)}$$
$$\text{for } j = (n1 + 1) \text{ to } n2$$

where GF is the geometric expansion factor, and n2 is the value of j for which one of the two following conditions is satisfied:

(a) $(LCV_{j-1} \geq LCV^{mx})$

or

(b) $\{(L^{in}/2) - CV_j)\} < \{(LCV_{j-1})\ GF\}$

(12) L^{ct}, the dimension of that position of the central-core region of the inner layer where control-volume faces have yet to be located:

$$L^{ct} = L^{in} - 2\ (CV_{n2-1} - CV_{n1}) \qquad \text{(A1-7)}$$

(13) N^{cvc}, the number of control volumes that can be located over the remaining central region of length L^{ct}. This number must be an integer value, and it is calculated in the following manner.

(i) If only (b) in Step (11) has been satisfied then:

$$N^{cvc} = \text{Integer value of } (L^{ct} / LCV_{n2-1}) \qquad \text{(A1-8)}$$

otherwise:

$$N^{cvc} = \text{Integer value of } (L^{ct} / LCV^{mx}) \qquad \text{(A1-8a)}$$

(ii) If N^{cvc} from (i) is an even number then, in order to ensure that symmetry in the control-volume distribution is preserved:

$$N^{cvc} = N^{cvc} - 1 \qquad \text{(A1-8b)}$$

otherwise the value calculated in (i) is used for N^{cvc}.

(14) LCV^{ct}, the length of the control volumes in the central portion of Inner Layer A:

$$LCV^{ct} = L^{ct} \; / \; N^{cvc} \qquad \text{(A1-9)}$$

(15) CV_j, LCV_j, in the remaining portion of the bottom half of Inner Layer A, between the lines cc and xx in Fig. 109(b):

$$CV_{j+1} = CV_j + LCV^{ct} \qquad \text{(A1-2b)}$$
$$LCV_{j-1} = CV_j - CV_{j-1} \qquad \text{(A1-3b)}$$
$$\text{for } j = (n2 - 1) \text{ to } (n3 + 1)$$

where

$$n3 = (n2 - 1) + \{(N^{cvc} - 1)/2)\} \qquad \text{(A1-10)}$$

(16) CV_j, LCV_j, for the upper half of the zone, from line xx to bb in Fig. 109(b). These are calculated from the values obtained for the lower half of the zone:

$$CV_{n3+j} = (CV_{n0} + Lz) - (CV_{n3+1-j} - CV_{n0})$$
$$\text{for } j = 1 \text{ to } (n3 - n0) \qquad \text{(A1-2c)}$$

$$CV_{2(n3)-1} = (CV_{n0} + Lz) \qquad \text{(A1-2d)}$$

$$LCV_j = CV_{j+1} - CV_j$$
$$\text{for } j = n3 \text{ to } \{2(n3) - 2\} \qquad \text{(A1-3c)}$$

The position of the x-zone control volume faces are calculated in an analogous fashion. The values of the variables that were used to generate the nonuniform grids in this work are given in Table 22 for each zone.

A1.2 UNIFORM GRID DISTRIBUTIONS

As was discussed in Section 9.1.4, various uniform grid distributions were employed to compute values of Re_m in Duct 3, with the specified β corresponding to the maximum flow rate in the complementary experiments, and these solutions were extrapolated using the method in [118] to calculate the grid-independent value of Re_m. The extrapolation method is discussed in detail in Appendix 6, and the details of the uniform-grid generation procedure are presented in this section.

The calculation domain was divided into the same 2 x-zones and 2 y-zones as were used to generate the nonuniform grid distributions discussed in Section A1.1. This ensured that main-grid control-volume boundaries were located at the interface between the plate surface and the fluid. The control-volume dimensions within a y-zone were calculated as follows, using the nomenclature presented in Section A1.1 and Fig. 109.

(1) Specify N^{cvT}, the number of y-direction control volumes desired across the entire y-dimension, Lz^T, of the calculation domain.

(2) Calculate N^{cvt}, the number of y control volumes located within a given zone of length Lz.

$$N^{cvt} = \text{the nearest integer value of } \left(\frac{Lz}{Lz^T} N^{cvT}\right) \tag{A1-11}$$

(3) Calculate h, CV_j, the length of the control volumes and their boundary locations, respectively:

$$h = \frac{Lz}{N^{cvt}} \tag{A1-12}$$

$$CV_j = CV_{j-1} + h \quad \text{for } j = (n0 + 1) \text{ to } (n0 + N^{cvt}) \tag{A1-13}$$

If Lz^T is an integer multiple of all Lz values, then h is the same value for all zones. For the geometry of Duct 3, this is not the case for the 2 y-zones used as $(Lz^T/Lz) = 9.06$ for the bottom zone and 1.12 for the top zone. However, by using the aforementioned procedure and by choosing an appropriate value of N^{cvT}, the h values of the two zones can be made almost equal. The average of these two h values is the value used in Table 23 for each uniform y-grid distribution, and it was the value used for the extrapolation of Re_m. The differences in h values for the two y-zones of the same grid from the average of these two values in all cases was less than 0.07 percent.

The 2 x-zones used have the same x dimensions, and the value of h is therefore the same for both zones. These values are also shown in Table 23 for the uniform grid distributions, and they were used in Appendix 6 in the extrapolation procedure used to obtain grid-independent values of Re_m.

APPENDIX II

PERFORMANCE CHARACTERISTICS OF THE AIR BLOWER

The air blower used in this research was operated in the suction mode. It is a centrifugal-type, constant speed, blower (Regenair R7100A). The blower is driven by a 10 HP AC motor (550 volts, 3 phase, 60 Hz) with a rotor speed of 3450 rpm, and it has a no-load air flow capacity of 660 m^3/hr when operated in the suction mode. A more complete description of the physical and operational characteristics of the blower are given in the manufacturer's "GENERAL SPECIFICATIONS" sheet presented on the next page. It should be noted that the 460 volts line voltage specified for the 3 phase motor unit in the specification sheet was changed to 550 volts in this application.

REGENAIR. R7100A

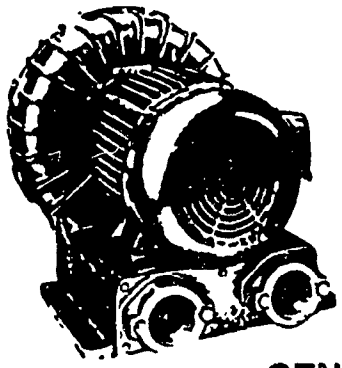

- Maximum ambient 104°F. (40°C)
- 2871 RPM @ 50 Hz.; 3450 RPM @ 60 Hz.
- Solid line on graph indicates continuous duty performance
- See graph for minimum air flow for continuous operation
- UL recognized and CSA certified motors
- Specifications subject to change without notice
- Net weight 277 lbs. (125.9 kg.)

GENERAL SPECIFICATIONS

Motor Specifications: R7100A

Three Phase Nominal Voltages, 208-230/460V 60 Hz., 200/380 50 Hz. • FLA @ 60 Hz. 24.8/12.4 • 10 HP • TEFC • Class B Insulation

Blower Limitations for Continuous Duty: R7100A

50 Hz. max. pressure/vacuum 85/70 in H_2O
50 Hz. max. flow 350 cfm
60 Hz. max. pressure/vacuum 100/95 in H_2O
60 Hz. max. flow 420 cfm

PERFORMANCE CURVES

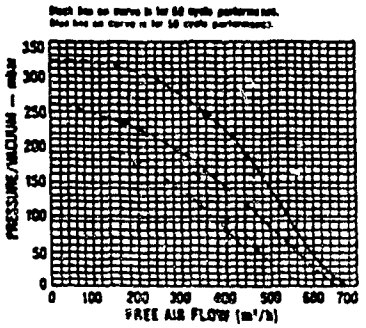

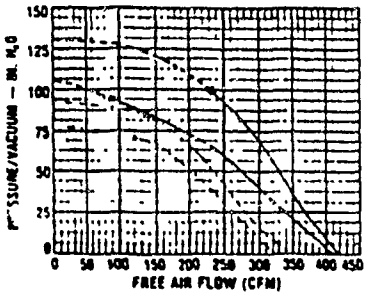

Pressure
Vacuum
Intermittent
*Recommended maximum duty

Note: On all drawings
Metric
U.S./Imperial

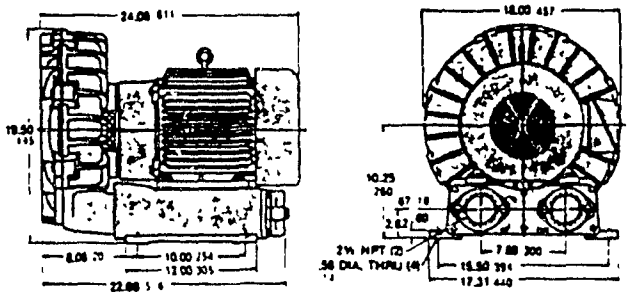

APPENDIX III

CALIBRATION OF THE BAROCEL PRESSURE TRANSDUCER

All differential pressures of less than 1 kPa were measured using an Integral Barocel Pressure Transducer (Datametrics Model 590-D-1-kPa-2Q8-V1X-4D). A cut-away sketch of this pressure transducer is shown in Fig. 110. This unit has a full scale range of 0 to 1 kPa and an output signal of 0 to 10 volts DC. Other details of the specifications provided by the manufacturer can be found in [109].

The manufacturer's calibration curve for the Barocel pressure transducer is shown in Fig. 111: It shows that the output signal of 0 to 10 volts is linearly proportional to positive differential pressures applied across the Barocel's diaphragm. Since this calibration curve was supplied with the unit at the time of its purchase, some four years prior to this work, a calibration was done in the Heat Transfer Laboratory to verify the accuracy of the curve given in Fig. 111. This procedure is outlined briefly in the following text.

The Barocel pressure transducer was calibrated using an Askania manometer (Model WS-Minimeter). This manometer has a full scale range of 0 to 100 mm with a resolution of 0.01 mm, and the manometer fluid is distilled water. When converted to Pascals, the uncertainty in the manometer reading was $\pm$ 0.1 Pa. The Barocel pressure transducer and the manometer were connected in parallel and measurements of differential pressures ranging from 0 2 Pa to 900 Pa were recorded with both units. The final value of the Barocel output voltage for a given pressure differential was obtained by using the following procedures: 60 readings

were taken over an interval of 13 seconds, and the average zero-pressure output signal of the Barocel was subtracted from the arithmetic mean of the 60 readings to obtain the zero-corrected Barocel output voltage. Since the calibration measurements were of steady static pressure differentials, it was assumed that the any uncertainty in the Barocel output signal would be due to fluctuations that were caused by the unit itself, and not due to any intrinsic fluctuations in the pressures being measured. A quantitative measure of this uncertainty was obtained by calculating the standard deviation of the 60 readings taken to obtain each zero-corrected Barocel output voltage Three sets of pressure measurements were made, ranging from. 10 Pa to 900 Pa; 1 Pa to 10 Pa; and 0.2 Pa to 1 Pa The pooled standard deviation, Eq. 6.6, of all recorded output voltages for each range were doubled and used as the estimate of uncertainty in the recorded zero-corrected output voltage. From this data, a value of $\pm$ 500 μV was established as a conservative estimate of the uncertainty in the voltage output signal of the Barocel pressure transducer, for measurements ranging from 0.2 Pa to 900 Pa.

The results of the calibration tests for the three pressure ranges already mentioned are shown in Figs. 112(a) to (c) . The solid line is from the manufacturer's calibration curve, Fig. 111, and it has a slope of 1.000×10^{-2} V/Pa. The data points from the present calibration, o, are shown to agree with this line, within the limits of uncertainty that are also plotted. In Figs. 112(a) and (b), the uncertainty in the data points is barely discernable on the plots: The slope of the least-squares (best-fit) line to the data, in both figures, differs from 1.000×10^{-2} V/Pa by less than 0.02%. At differential pressures less than 1 Pa, it is shown from the data in Fig. 112(c) that the Barocel output

begins to deviate from its linear behaviour. However, within the limits of uncertainty, the data points still show agreement with the manufacturer's calibration line.

From this calibration, it was concluded that for the range of pressure differentials measured in this work, the uncertainty in the output voltage of the Barocel can be given as $\pm \delta V_{cal} = \pm 500\ \mu V$.

APPENDIX IV

FLOW VISUALIZATION PAINTS

This appendix consists of two sections: The first section gives a brief description of the substances from which the flow visualization paints were prepared; and the second section presents the basic recipes used to make these paints.

A4.1 PROPERTIES OF THE PAINT CONSTITUENTS

As discussed in Section 6.5.5, two types of kerosene based flow visualization paints were used. Titanium dioxide, TiO_2, was used as the pigment in one paint, and fluorescent orange Day-glo pigment was used in the other. In addition, when required, Oleic acid ($C_{18}H_{34}O_2$) was used as an additive to control the extent of flocculation by pigment particles in the kerosene. The properties of these substances are listed in this section.

Kerosene

Pure odourless kerosene was used (Fisher Scientific K10-4). After refining, less than 1% of the aromatic content remained and the combustible flash point, as specified by the manufacturer, was 63.3 °C (146 °F).

Titanium Dioxide Pigment: TiO_2

The TiO_2 pigment used was an opaque fine white powder (Fisher Scientific T-315). The content analysis of the powder, supplied by the manufacturer, is as follows:

TiO_2 Formula Weight	79.90
Water Soluble Salts	0.12%
Arsenic (As)	0.4 ppm
Iron (Fe)	0.01%
Lead (Pb)	0.005%
Zinc (Zn)	0.01%

Day-glo Pigment

The Day-glo pigment used was a fluorescent orange powder (Day-glo Corp., A-15-N Blaze Orange). The physical properties of this pigment were specified by the manufacturer as:

Specific Gravity	1.36
Average Particle Size (microns)	3.5 - 4.0
Softening Point	115-120 °C
Decomposition Point	195°C
Oil Absorption (g/100g pigment)	47

Oleic Acid: $C_{18}H_{34}O_2$

Purified oleic acid was used (Fisher Scientific A-222). As specified by the manufacturer, this substance has a formula weight of 282.47, low linoleic acid content, and a maximum of 5% polyunsaturates.

A4.2 PAINT RECIPES

The composition of the TiO_2 and Day-glo paints was based on combinations given in [47]. The recipes presented in this section were found to work well for the particular circumstances prevailing in this work. As explained in Section 6.6.4, the basic recipes presented here

were often "fine-tuned" during the application procedures employed in this work.

TiO_2 Paint

By weight, the composition of this paint was 1 part TiO_2 to 4 parts kerosene to 1 part Oleic acid. Slight changes in the amount of Oleic acid were often necessary to fine-tune the quality of the streak patterns produced as flow rates varied.

Day-glo Paints

Three different basic paint recipes were used in order to provide required adjustments as the flow rates varied: (i) for flows with $Re_m < 25 \times 10^3$, 1 part Day-glo powder to 4.5 parts kerosene, by weight, plus 2 drops Oleic acid; (ii) for $Re_m \simeq 25 \times 10^3$, 1 part Day-glo powder to 3 parts kerosene, by weight; and (iii) for $Re_m \simeq 30 \times 10^3$, 1 part Day-glo powder to 2 parts kerosene, by weight.

APPENDIX V

SAMPLE CALCULATION: MODULE REYNOLDS NUMBER

In this appendix, a sample calculation is presented to demonstrate the method used to obtain final experimental results and corresponding overall uncertainties. A general description of these procedures has been given in Section 6.6. As an example, the calculation of the module Reynolds number, Re_m, and its uncertainty, $\pm \delta Re_m$, is done for the minimum flow rate, Run 1 in Table 16, in Duct 3. The calculation of Re_m is discussed first, and this is followed by that of δRe_m.

A5.1 CALCULATION OF Re_m

Re_m is defined in Eq. (2-45) as:

$$Re_m = \frac{\rho D_h \bar{U}_m}{\mu} \tag{2-45}$$

where $\bar{U}_m$ and D_h are given as:

$$U_m = \frac{\dot{m}}{2\rho bH} \tag{2-47}$$

$$D_h = 2H \tag{8-3}$$

Using Eq. (6-3), the experimental value of $\dot{m}$ is ca culated:

$$\dot{m} = \rho U_{ft} A_{ft} \tag{6-3}$$

In the above equations, the area of the flow metering cross section, A_{ft}, was calculated using the internal radius of the flow tube, measured during flow-rate calibration tests; values of b and H were obtained from

measurements of the test section dimensions after final assembly; and the measured values of the ambient atmospheric pressure, and the air temperature and static gauge pressure in the flow metering cross section, were used to calculate values of μ and ρ, as described in Section 6.6.2 The values of A_{ft}, b, μ, and ρ are shown in Table 24.

The average fluid velocity through the flow metering cross section, U_{ft} in Eq. (6-3), was calculated from ten measured values of P_{dyn}, using the ten-point log-linear rule [45]: The ten measurement locations along the internal diameter of the flow tube are shown in Fig. 113. In terms of the ten values of P_{dyn}, U_{ft} can be expressed as:

$$U_{ft} = \left(\frac{2}{\rho}\right)^{1/2} \frac{\Lambda}{10} \qquad \text{(A5-1)}$$

where

$$\Lambda = \left[\sum_{i=1}^{i=10} \{P_{dyn}{}^{1/2} \ (1 + CF_{wpx})\}_i \right] (1 + CF_{lgln}) \qquad \text{(A5-2)}$$

The CF_{wpx} and CF_{lgln} terms in Eq. (A5-2) are correction factors. As the pitot stagnation probe approaches the wall of the flow metering tube, the wall-probe interaction causes deflection of the flow and results in a negative error in the pressure measurement [46]. From the data in [46], a wall-proximity correction factor, $(CF_{wpx})_i$, was estimated at each of the 10 measurement points shown in Fig. 113. The CF_{lgln} correction factor accounts for the estimated error in the average flow calculated using the ten-point log-linear integration technique. For the flow rates of this investigation, the value of CF_{lgln} was estimated from the results provided in [45]. The values of the $(CF_{wpx})_i$ and CF_{lgln} correction factors are given in Table 25.

Correction factors were also used in the calculation of P_{dyn}. The value of P_{dyn} at any one of the 10 locations shown in Fig. 113 is calculated using the following equation:

$$(P_{dyn})_i = 100\ (V_{dyn} - V_{zero})_i\ (1 - CF_{trb} - CF_{vs} + CF_{algn}) \quad \text{for } i = 1 \text{ to } 10 \qquad \text{(A5-3)}$$

The errors in the measured values of $(P_{dyn})_i$ due to the turbulence in the flow, viscosity effects, and possible slight misalignment of the pitot tube with the flow direction were accounted for by the CF_{trb}, CF_{vs}, and CF_{algn} correction factors, respectively. The values of CF_{trb} and CF_{algn} were estimated from the data in [119] and [46], respectively. These values are given in Table 25, and they are the same at all ten measurement locations. The value of CF_{vs} depends on the value of a Reynolds number that is based on the local velocity, U, and the internal diameter of the pitot stagnation tube. The appropriate values are given in Table 25: They were obtained by interpolation of the data presented in [46].

In Eq. (A5-3), V_{dyn} and V_{zero} are the output voltages from the Barocel pressure transducer that correspond to the $(P_{stag} - P_{static})$ differential pressure measurement and the averaged zero-reading, discussed in Sections 6.6.2 and 6.6.1, respectively. The factor of 100 is to convert Volts to Pascals. In this example, $V_{zero} = (1840 \pm 454) \times 10^{-6}$ V and the values of $(V_{dyn})_i$ are shown in Table 25, along with the corresponding values of $(P_{dyn})_i$ calculated using Eq. (A5-3).

Substituting the appropriate values, presented in Tables 24 and 25, a value for Λ can be calculated using Eq. (A5-2), and it is given in Table 24.

Substitution of Eqs. (2-47), (8-3), (6-3), (A5-1), and (A5-2) into Eq. (2-45) allows Re_m to be expressed as:

$$Re_m = \frac{(2\rho)^{1/2} A_{ft} \Lambda}{10 \mu b} \qquad (A5\text{-}4)$$

This particular formulation facilitates the calculation of the uncertainty in Re_m, $\pm \delta Re_m$, discussed in the next section of this appendix. Using the values given in Table 24, the value of Re_m in this example was calculated to be 4.997×10^3.

A5.2 CALCULATION OF δRe_m

The method of Constant Odds Combination [48,49], discussed in Section 6.6.3, was used to calculate the magnitude of the uncertainty in Re_m, δRe_m. Starting from Eq. (A5-4), analogous to the derivation of Eq. (6-4), an expression for δRe_m can be derived . After some rearranging of terms, this expression can be written as:

$$\delta Re_m = Re_m \left\{ \left(\frac{\delta\mu}{\mu}\right)^2 + \left(\frac{\delta b}{b}\right)^2 + \frac{1}{4}\left(\frac{\delta\rho}{\rho}\right)^2 + \left(\frac{\delta A_{ft}}{A_{ft}}\right)^2 + \left(\frac{\delta\Lambda}{\Lambda}\right)^2 \right\}^{1/2} \qquad (A5\text{-}5)$$

The values of $\delta\mu$, δb, $\delta\rho$, and δA_{ft} were calculated from the estimated uncertainty in the measurements used to obtain these values and, when necessary, with the use of Eq. (6-4). The squared values of

$(\delta\mu/\mu)$, $(\delta b/b)$, $(\delta\rho/\rho)$, and $(\delta A_{ft}/A_{ft})$ are presented in Table 24. The calculation of $\delta\Lambda$ is not as simple as the other aforementioned δ values, as is evident from the equation for Λ, Eq. (A5-2). $\delta\Lambda$ is calculated using the same assumptions and procedures as those used to calculate δRe_m. In the calculation of δRe_m, Λ, is then treated as an independent variable having a normal distribution and 20 to 1 odds for $\delta\Lambda$.

$\underline{\delta\Lambda}$

Using Eq. (6-4), the magnitude of the uncertainty in Λ, as given by Eq. (A5-2), can be written as:

$$\delta\Lambda = \Bigg[\Big[\sum_{i=1}^{i=10} \frac{1}{2}\{P_{dyn}^{-1/2}\delta P_{dyn}\,(1 + CF_{wpx})\}_i \Big]^2 (1 + CF_{lgln})^2 + \Big[\sum_{i=1}^{i=10} \{P_{dyn}^{1/2}\,\delta CF_{wpx})\}_i \Big]^2 (1 + CF_{lgln})^2 + \Big[\sum_{i=1}^{i=10} \{P_{dyn}^{1/2}\,(1 + CF_{wpx})\}_i \Big]^2 \delta CF_{lgln}^2 \Bigg]^{1/2} \qquad \text{(A5-6)}$$

The uncertainties in all the CF correction factors used in Eqs. (A5-2) and (A5-3) were conservatively approximated as ± 100 percent of the respective values given in Table 25.

The uncertainty in values of $(P_{dyn})_i$, as given by Eq. (A5-3), was calculated using Eq. (6.4), and can be expressed as:

$$(\delta P_{dyn})_i = \left[P_{dyn} \left\{ \frac{(\delta V_{dyn}^2 + \delta V_{zero}^2)}{(V_{dyn}-V_{zero})^2} + \frac{(\delta CF_{trb}^2 + \delta CF_{vs}^2 + \delta CF_{aln}^2)}{(1-CF_{trb}-CF_{vs}+CF_{aln})^2} \right\}^{1/2} \right]_i$$

for i = 1 to 10 (A5-7)

The uncertainty in V_{dyn} is due to (i) the random uncertainty in the Barocel output signal, δV_{cal}, mentioned in Section 6.5.1 and calculated in Appendix 3; and (ii) the random uncertainty, δV_{dP}, in the magnitude of the pressure differential that is being measured. The procedure for obtaining δV_{dp} has been described in Section 6.6.3. In this example, δV_{cal} and δV_{dp} have values of 500 μV and 623 μV, respectively, and are combined to give δV_{dyn} in the following way:

$$\delta V_{dyn} = \{ (\delta V_{cal})^2 + (\delta V_{dp})^2 \}^{1/2} \quad \text{(A5-8)}$$

From the values given in Table 25, the values of $(\delta P_{dyn})_i$ were calculated using Eq. (A5-7). The results are listed as the $\pm$ uncertainties in $(P_{dyn})_i$ values in the same table.

$\delta\Lambda$ was calculated using Eq. (A5-6) and the data in Table 25: The value of $(\delta\Lambda/\Lambda)^2$ is given in Table 24.

$\underline{\delta Re_m}$

δRe_m was calculated from Eq. (A5-5) using the value of Re_m calculated in Section A5.1 and the values given in Table 24 for $(\delta\mu/\mu)^2$, $(\delta b/b)^2$, $(\delta\rho/\rho)^2$, $(\delta A_{ft}/A_{ft})^2$, and $(\delta\Lambda/\Lambda)^2$: δRe_m = 96.21. Therefore,

$Re_m = 4.997 \times 10^3 \pm 1.92$ % for Run 1 in Duct 3. From the values of the terms in Eq. (A5-6), as presented in Table 24, it is seen that the uncertainty in A_{ft} and A are the dominant factors in determining δRe_m.

The complete uncertainty analysis presented in this appendix was incorporated into the general software of the data acquisition system and was, therefore, performed for each flow rate. Similar procedures were used to determine the uncertainties in the pressure-drop data that is also reported in this thesis.

APPENDIX VI

EXTRAPOLATION OF Re_m TO A GRID-INDEPENDENT VALUE

As discussed in Section 9.1.4, to determine the accuracy of the solutions obtained for the interrupted-plate duct flows of this study, it is necessary to establish how well these solutions approach true grid-independent values. The grid-independent value of Re_m was calculated for the maximum flow rate in Duct 3, Run 6 in Table 19, and used to obtain a quantitative estimate of the numerical accuracy of the corresponding Re^m value reported in Table 19: This estimate was used as a conservative estimate of the accuracy in all other interrupted-plate duct solutions, for the reasons discussed in Section 9.1.4. The extrapolation method used to obtain the grid-independent value of Re_m is described in this appendix.

Employing the extrapolation method presented by de Vahl Davis [118], the grid-independent value of Re_m, Re_{mt}, can be found from the following equation set:

$$Re_{mt} = (Re_m)_i + C\,(h_i)^n \qquad i = 1,2,3 \qquad \text{(A6-1)}$$

where the subscript i indicates values obtained with one of three different grid spacings; h is the characteristic control-volume length of a grid; C is a constant assumed to be independent of h_1, and n is the order of the truncation error for the numerical method used Re_{mt}, C, and n are unknowns in this set of equations. The value of h is constant in a given coordinate direction for the grid distribution of interest. From the set of equations given by Eq. (A6-1), the following relation

can be obtained and used to solve for the value of n:

$$\frac{(Re_m)_2 - (Re_m)_1}{(Re_m)_3 - (Re_m)_2} = \frac{(h_1)^n - (h_2)^n}{(h_2)^n - (h_3)^n} \qquad \text{(A6-2)}$$

With this value of n, the value of C can be calculated as:

$$C = \frac{(Re_m)_2 - (Re_m)_1}{(h_1)^n - (h_2)^n} \qquad \text{(A6-3)}$$

In the present extrapolation, the values of h_i were different for the x- and y-coordinate directions of the grids that were used. To perform this extrapolation for Re_m, using Eqs. (A6-1) to (A6-3), values of Re_m were required from nine different x-y grid combinations: Three uniform x-grid distributions, X1, X2, and X3, and three uniform y-grid distributions, Y1, Y2, and Y3, were used. A value of Re_{mt} was obtained for a fixed x-grid distribution, by extrapolating values of Re_m obtained for the three y-grid distributions: For example, values of Re_m calculated using grid distributions of X1 x Y1, X1 x Y2, and X1 x Y3, were used with the values of $(h_1)_{Y1}$, $(h_2)_{Y2}$, and $(h_3)_{Y3}$ to solve for n_{X1} and C_{X1}, and then calculate a value of $(Re_{mt})_{X1}$. Extrapolated Re_m values were obtained in this manner with respect to the changing y-grid distributions, to obtain values for $(Re_{mt})_{X1}$, $(Re_{mt})_{X2}$, and $(Re_{mt})_{X3}$. Using Eqs. (A6-1) to (A6-3) in a similar fashion, these values of $(Re_{mt})_{Xi}$ were then extrapolated in the x-coordinate direction to obtain the final extrapolated value of Re_{mt}. If this were the true grid-independent value, the same value of Re_{mt} would be obtained by doing the extrapolation in the other grid-direction (i.e. extrapolating first with respect to changing x-grid distributions and then extrapolating these $(Re_{mt})_{Yi}$

values with respect to changing y-grid distributions). In addition, it would be expected that the value of n should always be close to 2, since the numerical method becomes second order accurate as $h_i \longrightarrow 0$ [41,125].

In the present study, values of Re_m were calculated for three uniform x- and three uniform y-grid distributions: The number of grid points for each was X1 = 100, X2 = 124, X3 = 146, Y1 = 147, Y2 = 174, and Y3 = 201. The corresponding h_i values are given in Table 23, in nondimensional form, and details of the general grid-generation procedure are given in Appendix 1. The computed values of $(Re_m)_{X_1,Y_1}$ are shown in Table 26, as are the extrapolated $(Re_{mt})_{X_1}$ and $(Re_{mt})_{Y_1}$ values. The calculated values of n ranged from 0.5 to 5.0, indicating that true quadratic convergence had not been achieved with the grids used. The reason for this is probably due to the fact that with the coarsest grids, Eqs. (A6-1) are not quite valid, thus contaminating the extrapolated solution. This is demonstrated in the results shown in Table 26, where oscillations are observed in the value of $(Re_{mt})_{X_1}$ as the y-grid spacing becomes finer, making it impossible to extrapolate to an accurate value of Re_{mt}. The obvious solution to this problem is to conduct additional runs using finer grids, however, the financial resources to do so were not available, since CPU times in excess of 120 minutes were required for each such run. Due to this restriction, it was assumed that the contamination of the extrapolated solutions had been caused by grids with either the coarsest x or y distributions, X1 and Y1. Grids that had either X2 or X3, and Y2 or Y3 distributions were assumed to be sufficiently fine that a value of n = 2 could be assumed. Assuming this value of n, the values of $(Re_{mt})_{X_1}$ and $(Re_{mt})_{Y_1}$ could be calculated by solving Eqs. (A6-3) and (A6-1). The results of these calculations are

shown in Table 27, where two values of Re_{mt} are given: One was extrapolated from the $(Re_{mt})_{Xi}$ values and the other from the $(Re_{mt})_{Yi}$ values. These two Re_{mt} values differ by less than $\pm$ 0.004 percent from the average of the two values, $Re_{mt} = 27.27 \times 10^3$, which is reported as the grid-independent value of Re_m for Run 6 in Duct 3. This verifies that the assumptions required to make this extrapolation from the available data were indeed reasonable.

FIGURES

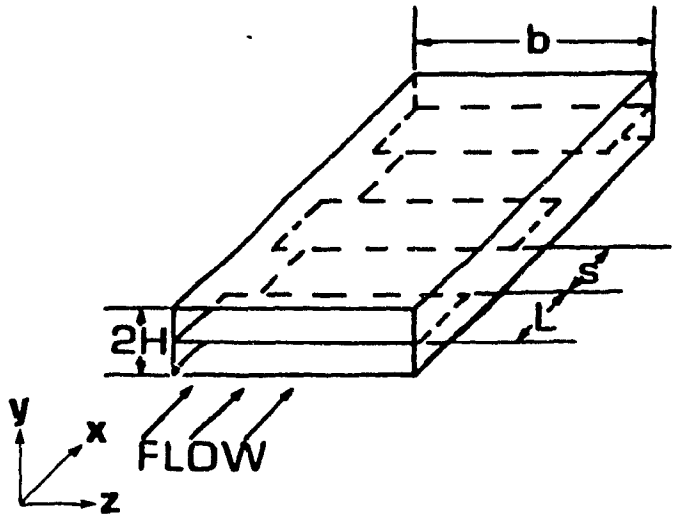

Figure 1: Straight rectangular interrupted-plate duct.

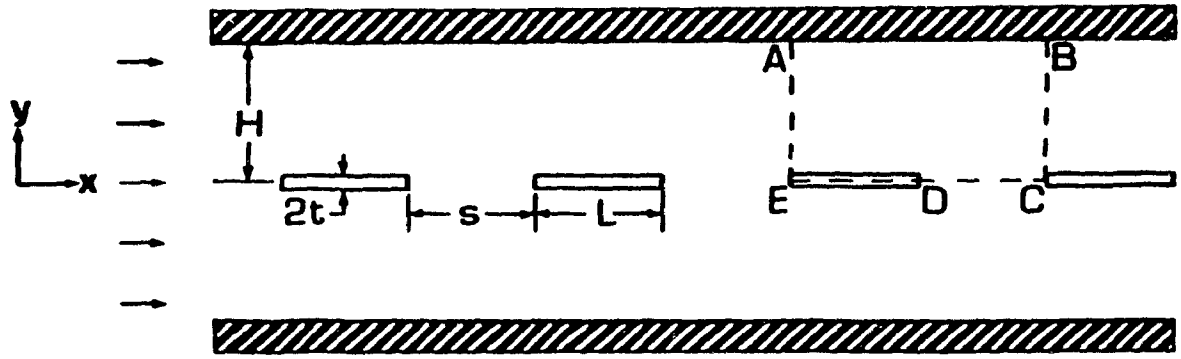

Figure 2: Cross section of a rectangular interrupted-plate duct, associated nomenclature, and representation of a geometrically similar module ABCDE.

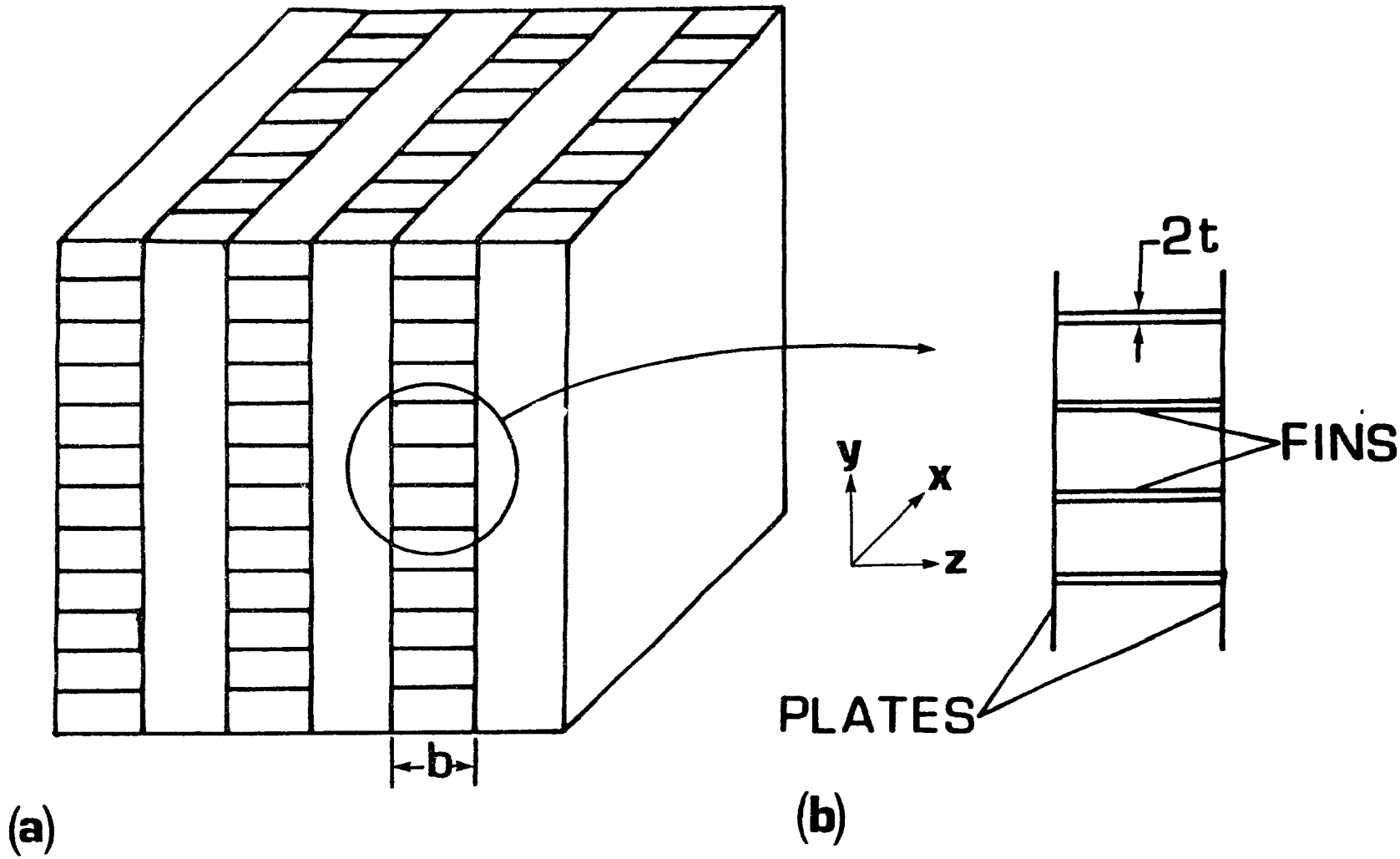

Figure 3: (a) Schematic representation of a compact heat exchanger core; and (b) details of rectangular plate-fin flow passages.

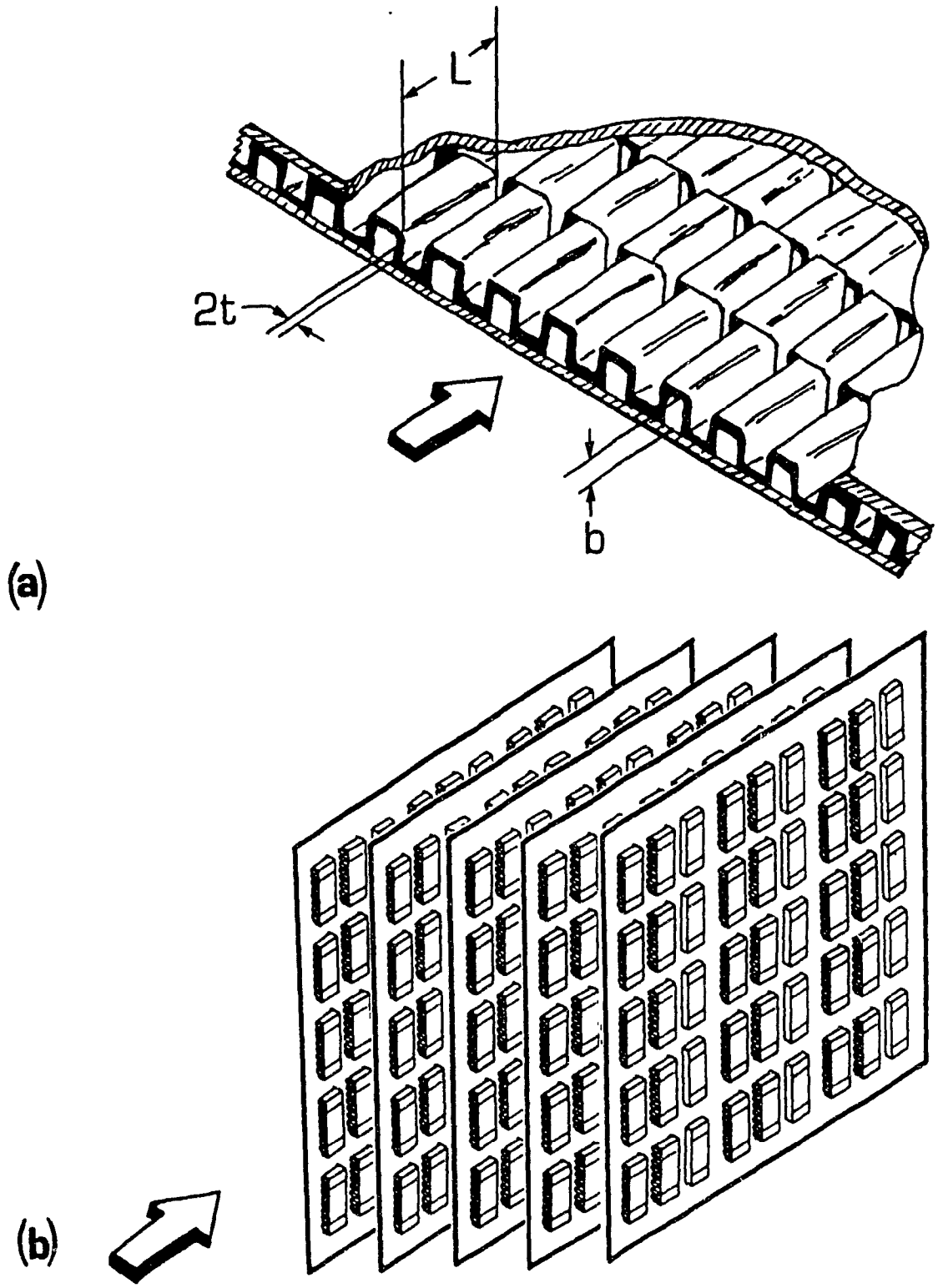

Figure 4: (a) Typical rectangular offset-fin arrangement in a compact heat exchanger core [4]; and (b) array of electronic modules deployed along circuit boards that are stacked in parallel.

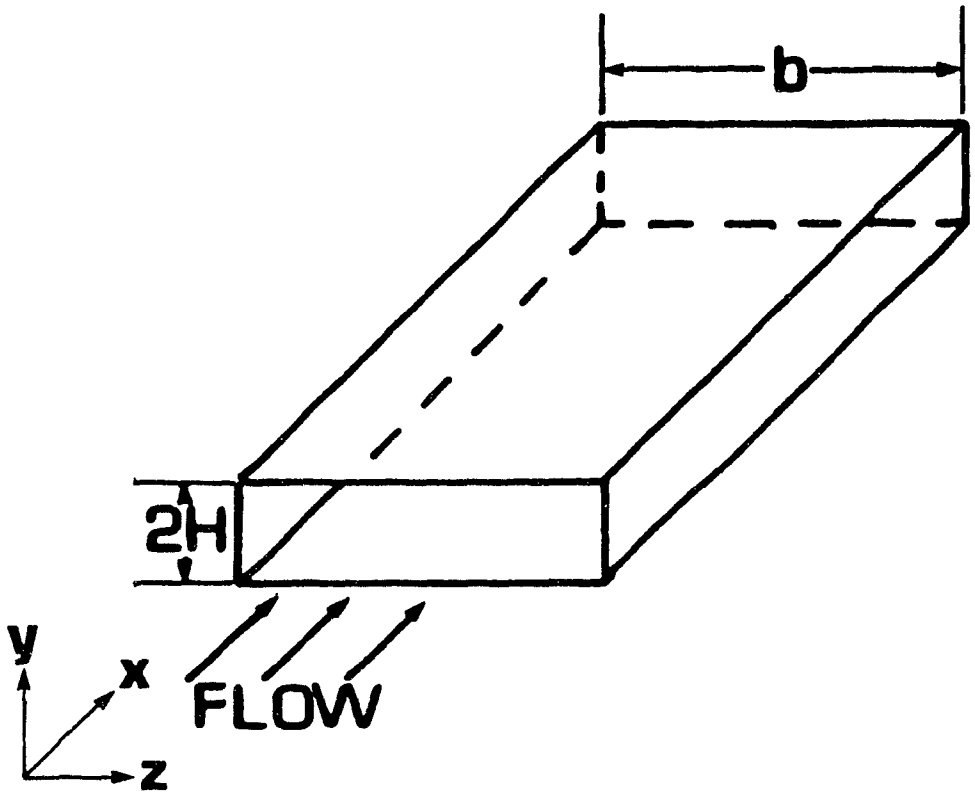

Figure 5: Straight rectangular duct.

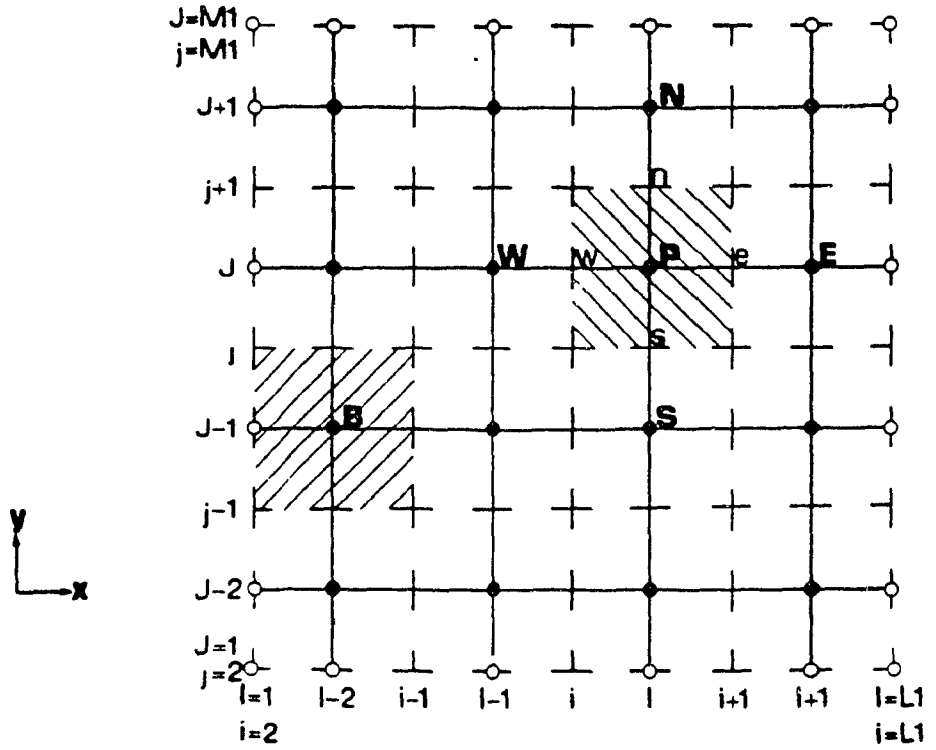

Figure 6: Locations of grid points relative to their associated control-volume faces in a two-dimensional calculation domain. Shown in this diagram are: internal grid points (●); boundary grid points (○); control-volume face locations (— — —), numbered as i=2 to L1 in the x direction and j=2 to M1 in the y direction; main-grid lines (——), numbered as I=1 to L1 and J=1 to M1 in the x and y directions, respectively; an internal control volume (▨), associated with point P; and a boundary control volume (▨), associated with point B.

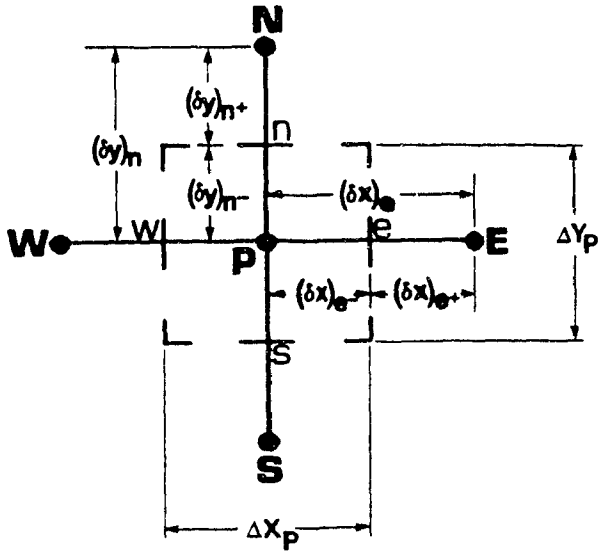

Figure 7: Schematic of the control volume associated with node P in Fig. 6. Distances between neigbouring nodes and control-volume faces are shown: $(\delta x)_{e-} = \Delta X_P/2$ and $(\delta y)_{n-} = \Delta Y_P/2$.

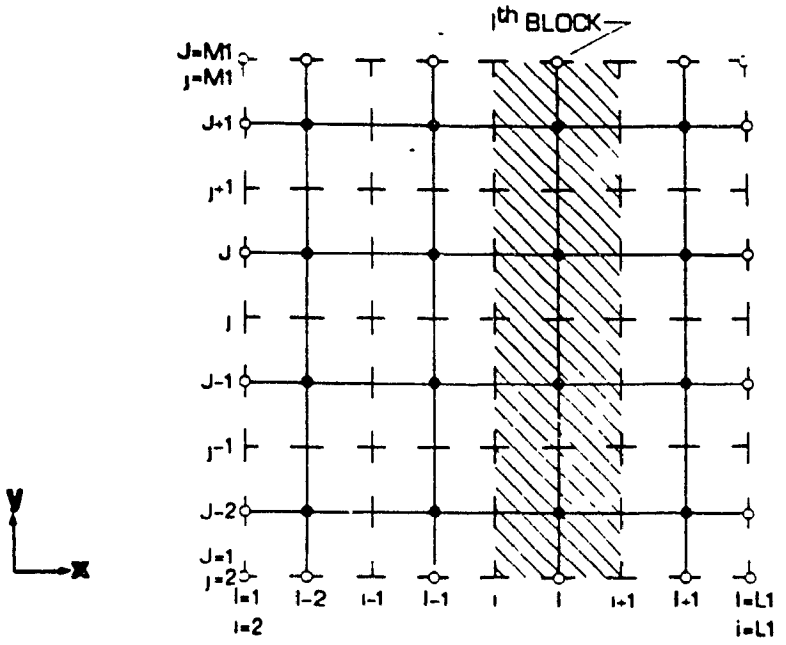

Figure 8: Block correction along grid lines of constant I.

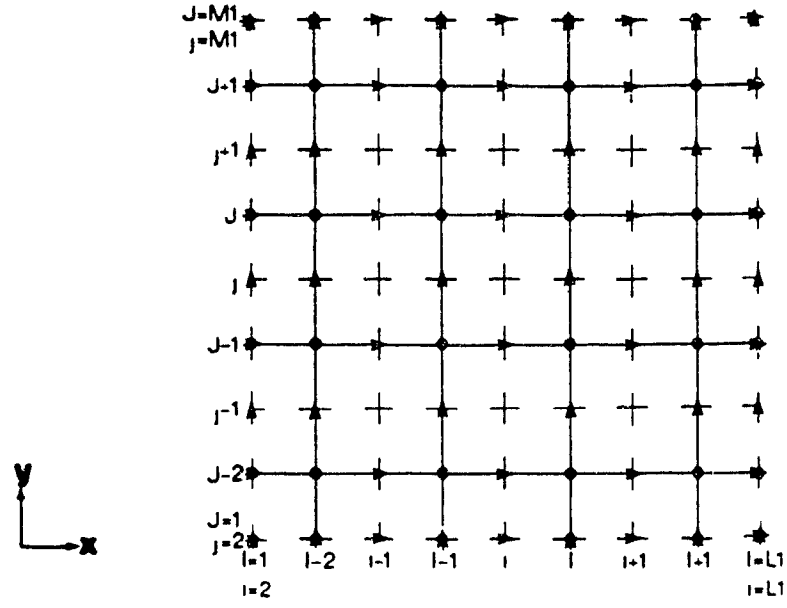

Figure 9: Staggered locations for U (➔) and V (▲) velocities: control-volume face locations (– – –); main-grid lines (———); and main-grid points (●).

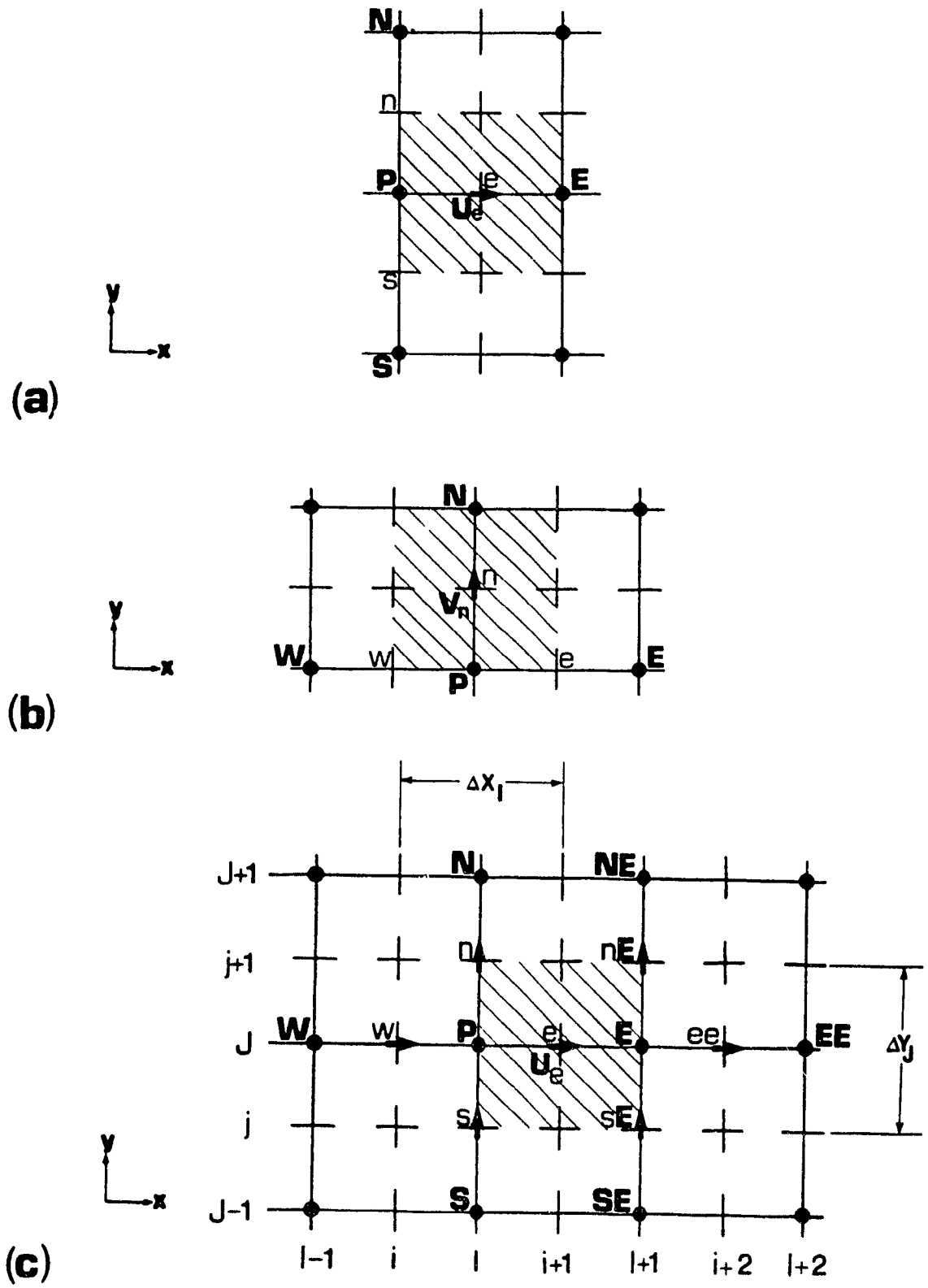

Figure 10: Staggered momentum control volumes for: (a) U velocity; (b) V velocity; and (c) U_e velocity showing neigbouring node and velocity locations.

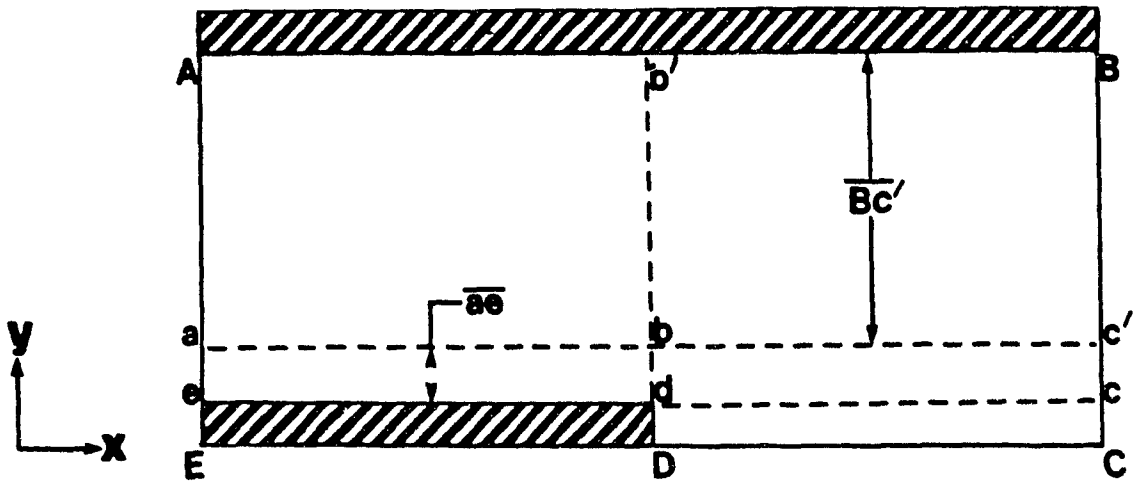

Figure 11: Positions and distances within the geometric flow module ABCDE.

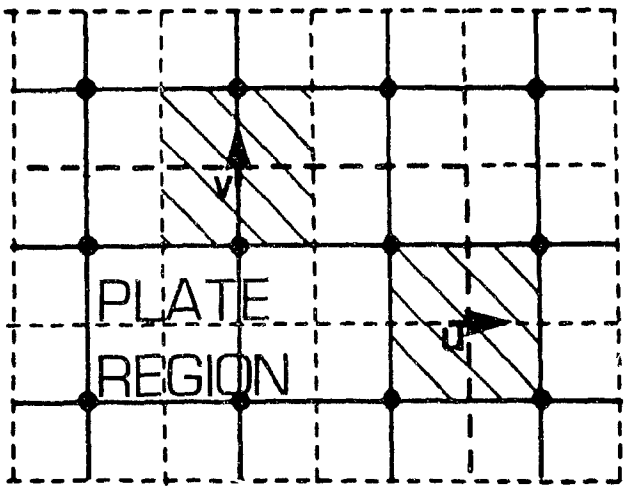

● main-grid points

——— main-grid lines

------ control-volume face locations

– – – – control-volume faces located on the plate surface

▨ velocity control volume located at the plate surface

Figure 12: Location of U and V velocities at a plate surface-fluid interface: U velocity (→) and V velocity (↑). The plate region is in the bottom left-hand corner of the figure, enclosed by the bold-dashed lines which indicate the location of its horizontal and vertical surfaces

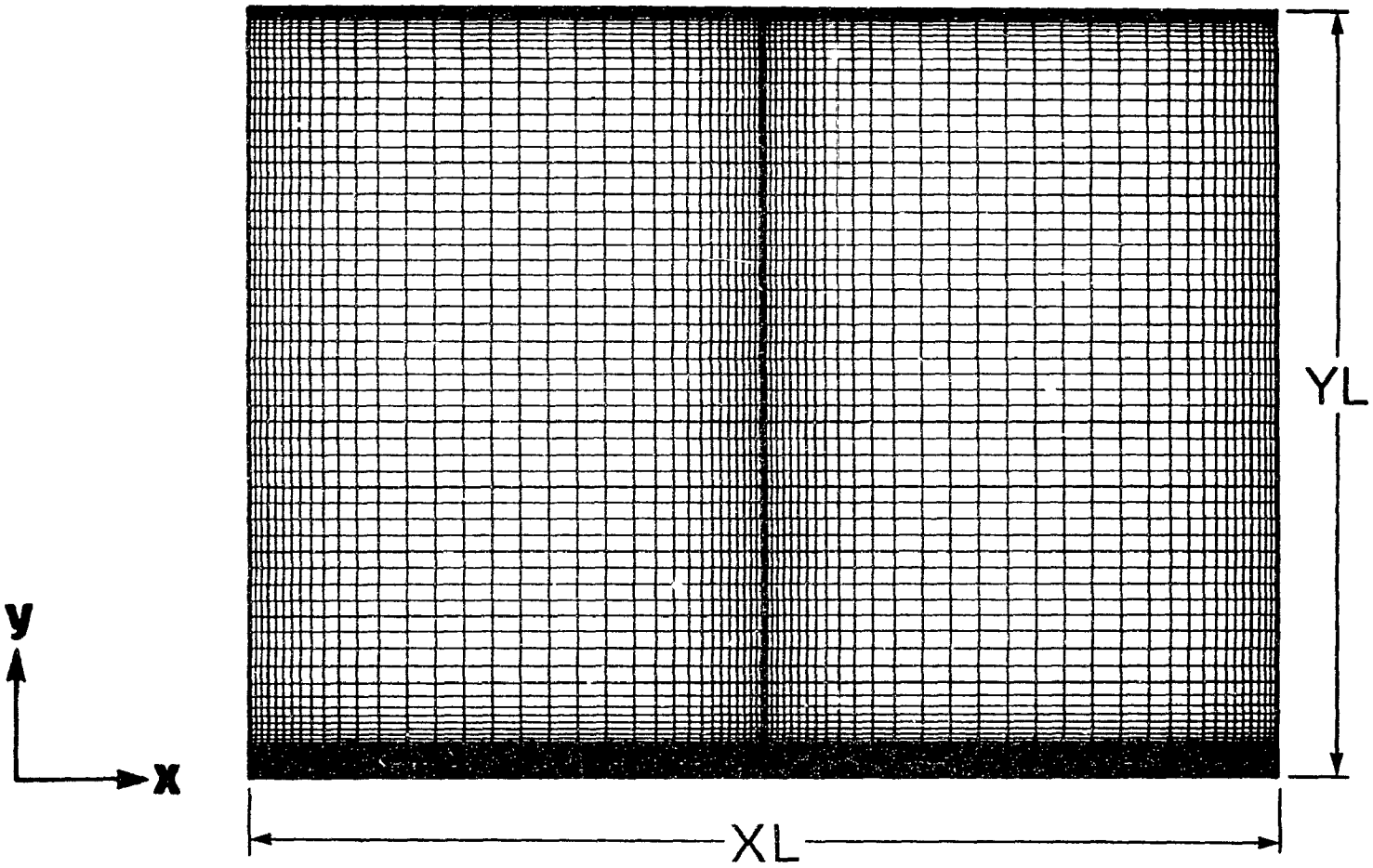

Figure 13: Control-volume locations in the domain discretization used for the turbulent periodic fully developed flow simulations in Duct 1: 72x78 x-y grid. This figure is not to scale, as the y dimensions have been expanded relative to the x dimensions in order to aid the visual aspect of the presentation (true scale is XL:YL = 4:1).

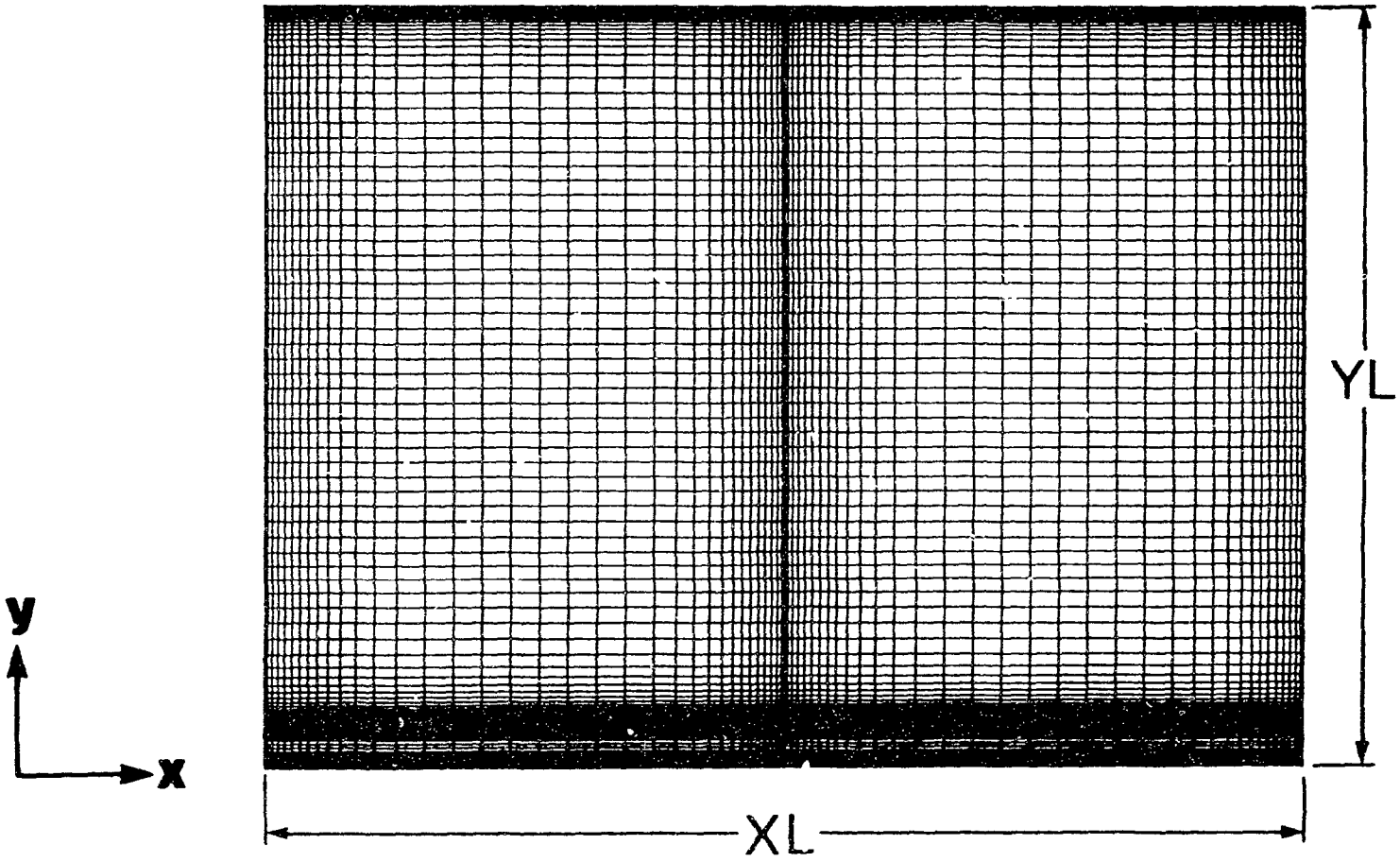

Figure 14: Control-volume locations in the domain discretization used for the turbulent periodic fully developed flow simulations in Duct 2: 72x100 x-y grid. This figure is not to scale, as the y dimensions have been expanded relative to the x dimensions in order to aid the visual aspect of the presentation (true scale is XL:YL = 4:1).

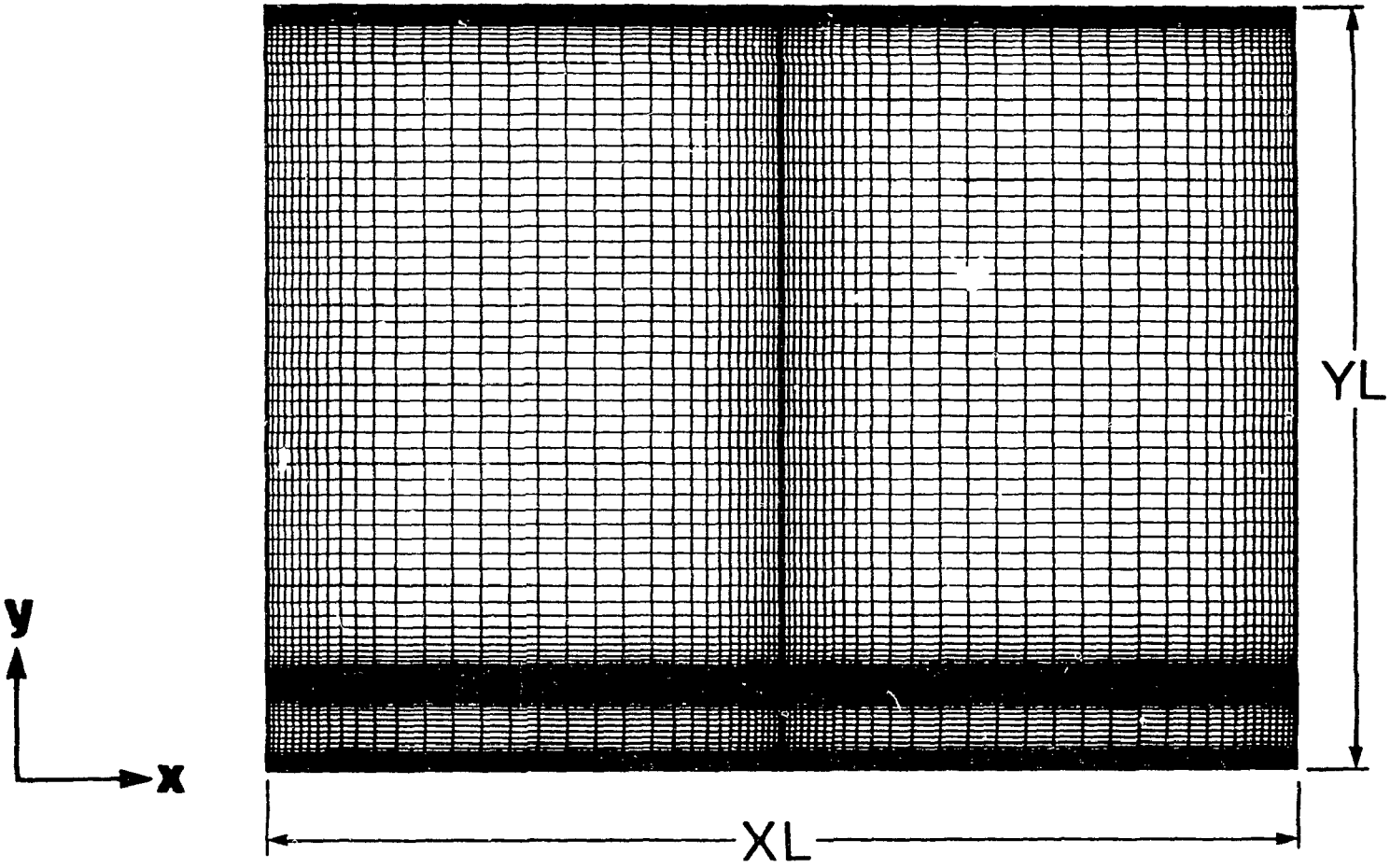

Figure 15: Control-volume locations in the domain discretization used for the turbulent periodic fully developed flow simulations in Duct 3: 72x100 x-y grid. This figure is not to scale, as the y dimensions have been expanded relative to the x dimensions in order to aid the visual aspect of the presentation (true scale is XL:YL = 4:1).

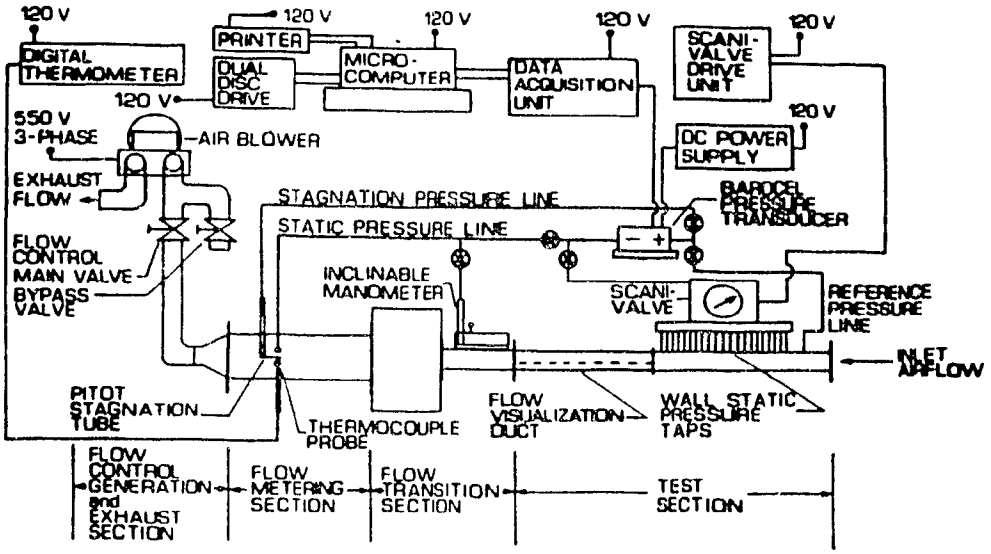

Figure 16: Schematic of the overall experimental setup.

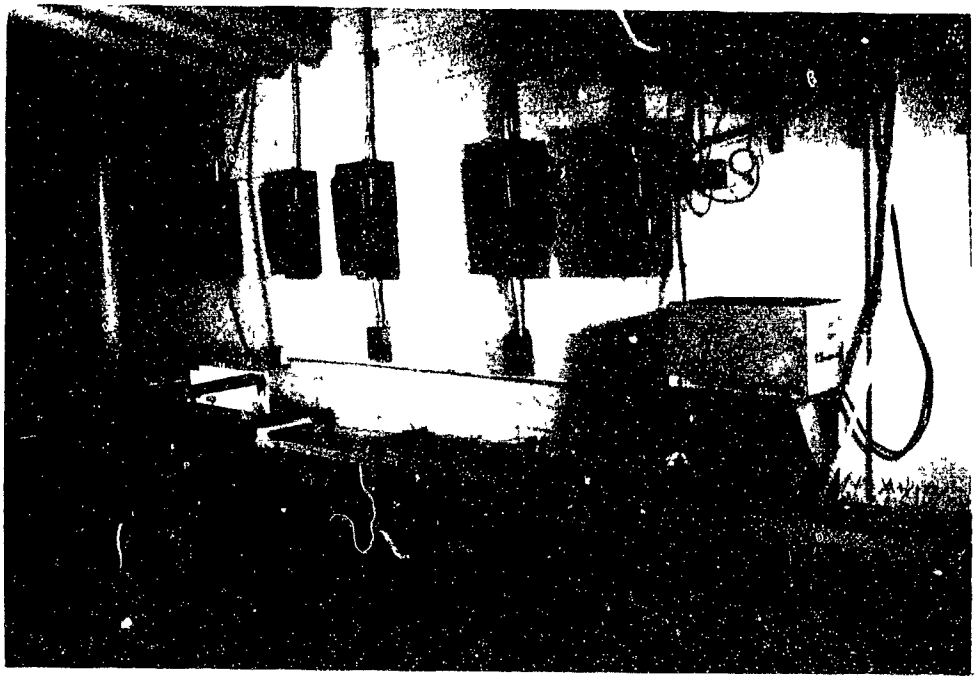

Figure 17: Photograph of the experimental flow facility, showing from right to left: the aluminum duct and the acrylic flow visualization duct of the test section; followed by the flow redevelopment duct and flow adjustment box of the flow transition section; the flow metering section; and some of the black colored rubber and plastic ducts, and two flow control valves of the flow control, generation, and exhaust section. The Barocel pressure transducer is mounted in the protective wooden casing visible in the middle right-hand portion of the photograph, just above the aluminum duct. The air flow is from right to left.

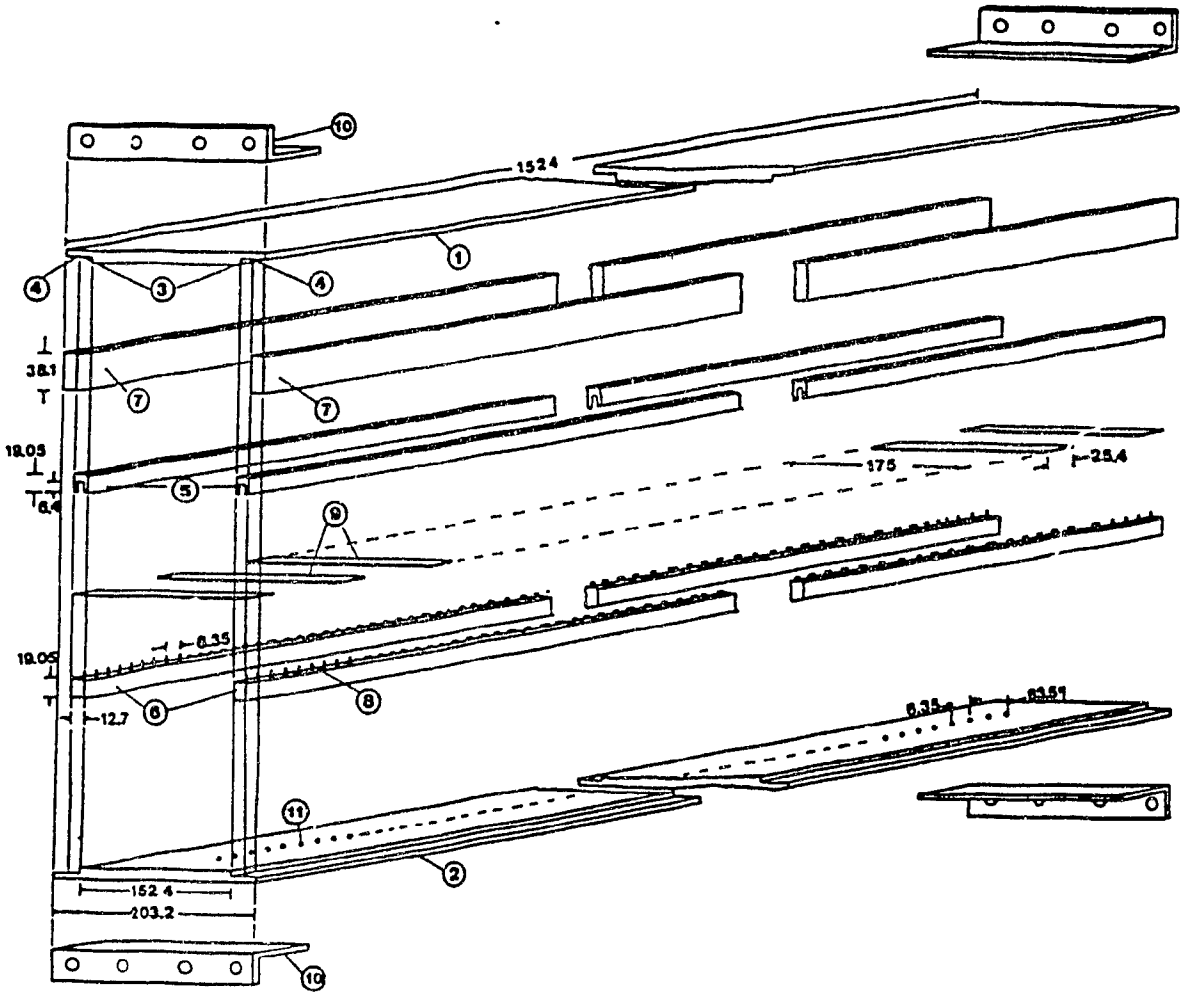

Figure 18: An exploded view of the aluminum section of Duct 3: (1) top wall; (2) bottom wall; (3) location and alignment shoulders for inner side walls; (4) location and alignment shoulders for outer side walls; (5) upper set of inner side walls; (6) lower set of inner side walls; (7) outer side walls; (8) steel dowel pins used for positioning of the interrupted plates; (9) interrupted plates; (10) aluminum angles used for attachment of the duct to the rest of the flow circuit; and (11) static pressure tap holes.

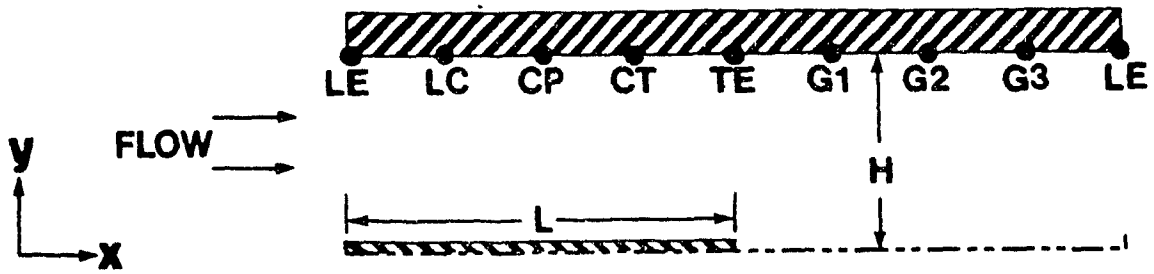

Figure 19: Intramodule wall static pressure measurement locations LE, LC, CP, CT, TE, G1, G2, G3, and LE. The length of the geometric module is (2L) and nominal spacing between adjacent pressure measurement points is (L/4).

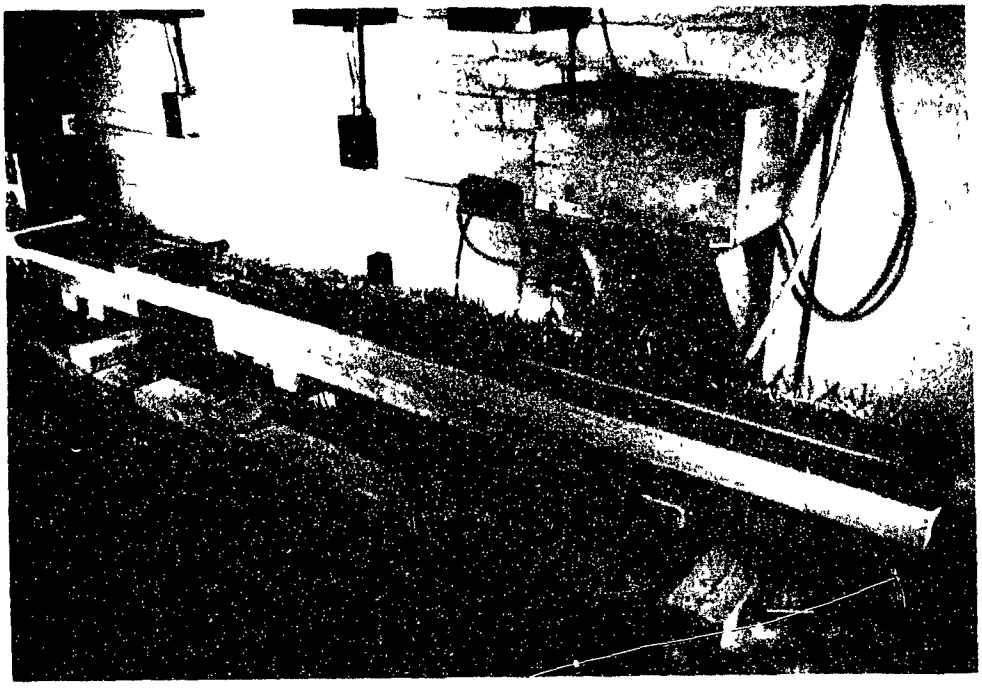

Figure 20: Photograph of an assembled interrupted-plate rectangular duct test section, showing the aluminum duct on the right and the downstream acrylic flow visualization duct on the left.

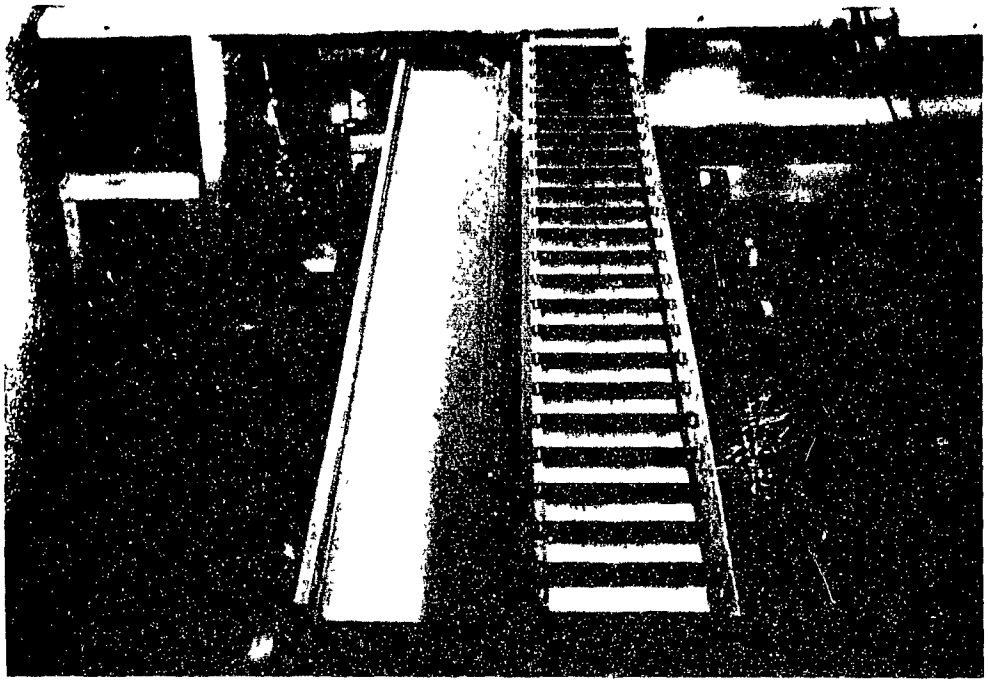

Figure 21: Photograph of a disassembled aluminum interrupted-plate duct, showing the top and bottom plates, the inner and outer side walls, and the array of colinear interrupted plates.

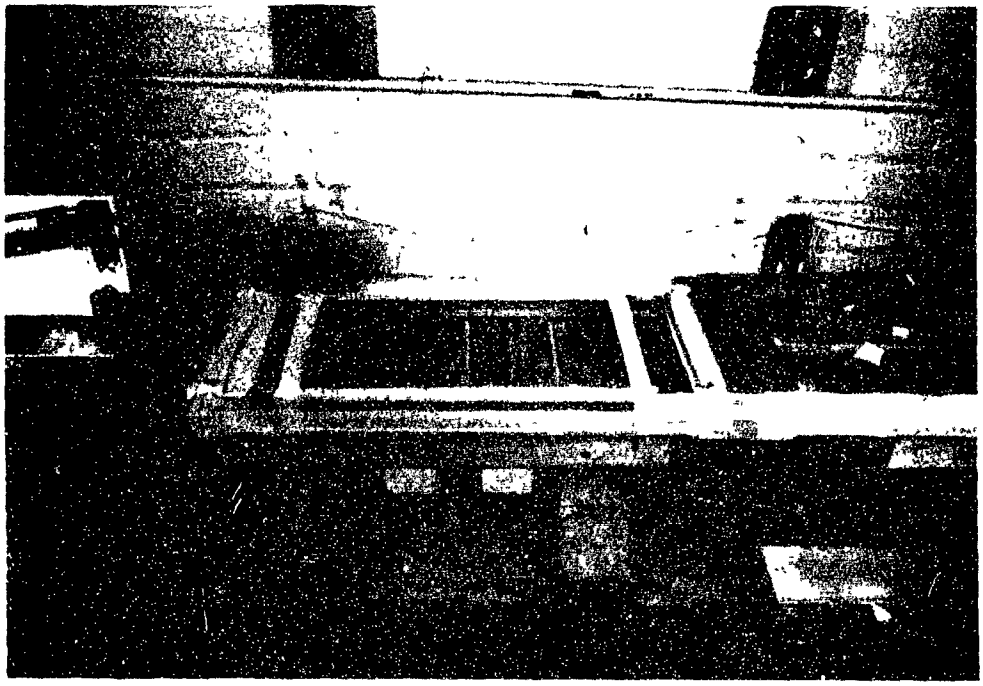

Figure 22: Photograph of the acrylic flow visualization duct, sealed and mounted in the flow facility. The colinear array of plates are clearly seen along the duct's length: The three orange colored plates were painted with Day-glo paint for surface flow visualization.

Figure 23: Photograph showing the acrylic duct with the central top section removed to allow easy access to the array of interrupted plates.

Figure 24: Photograph showing the acrylic duct and the removal of one of the interrupted plates used in the surface flow visualization studies.

Figure 25: Close-up view, from above, of the acrylic duct test section with the central top plate section and one of the plates removed. Details of the duct inner side walls, the plates and dowel pins used to construct the colinear interrupted-plate array, and the interplate spacers used to fill the gaps between plates along the inner side walls, are clearly seen.

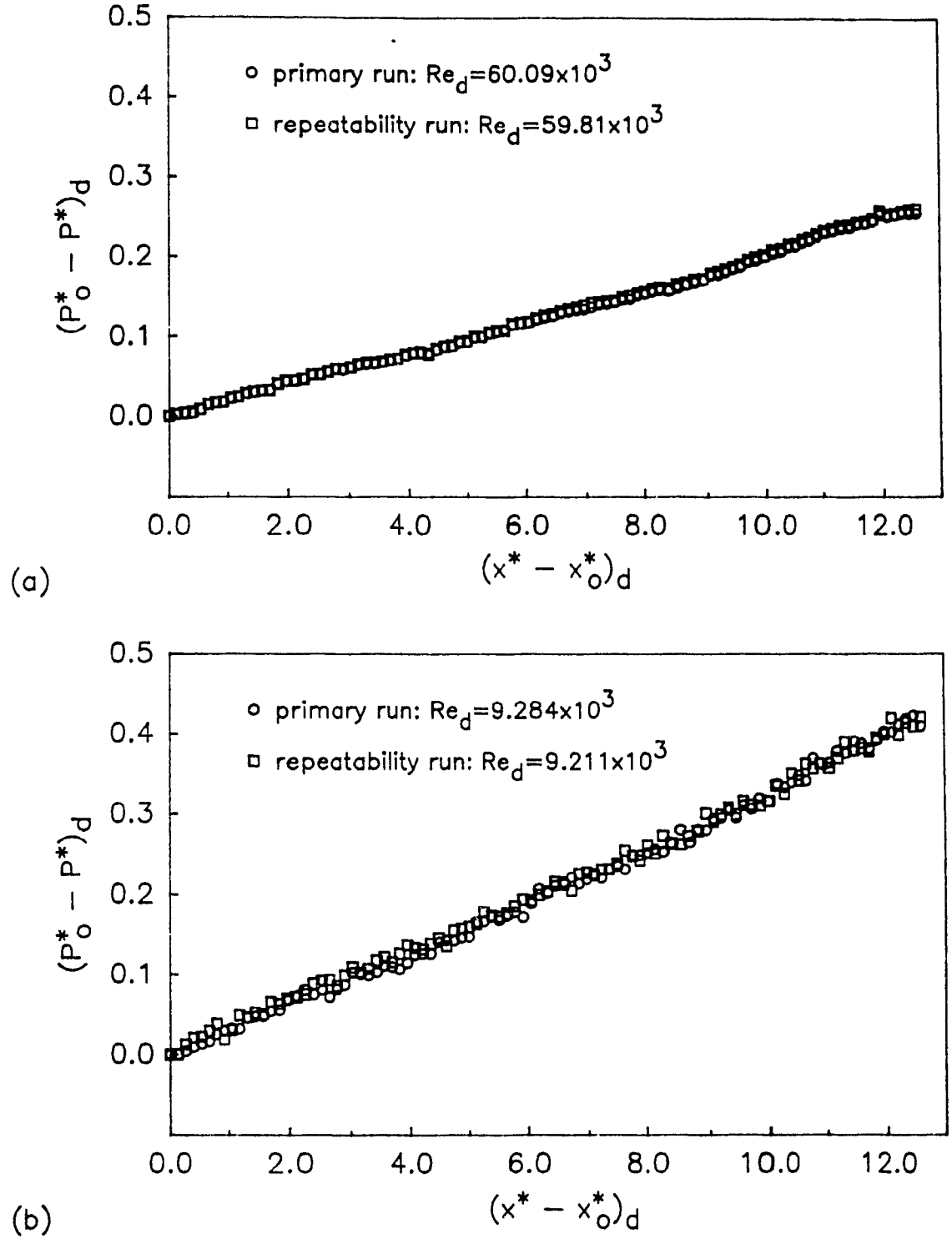

Figure 26: Repeatability checks of time-mean wall static pressure measurements for fully developed flow in a straight rectangular duct: (a) maximum flow rate; (b) minimum flow rate. The maximum uncertainty in $(P^*_o - P^*)_d$ values is ± 0.012 in (a) and ± 0.024 in (b); and the maximum uncertainty in $(x^* - x^*_o)_d$ values is less than ± 0.019 in both (a) and (b).

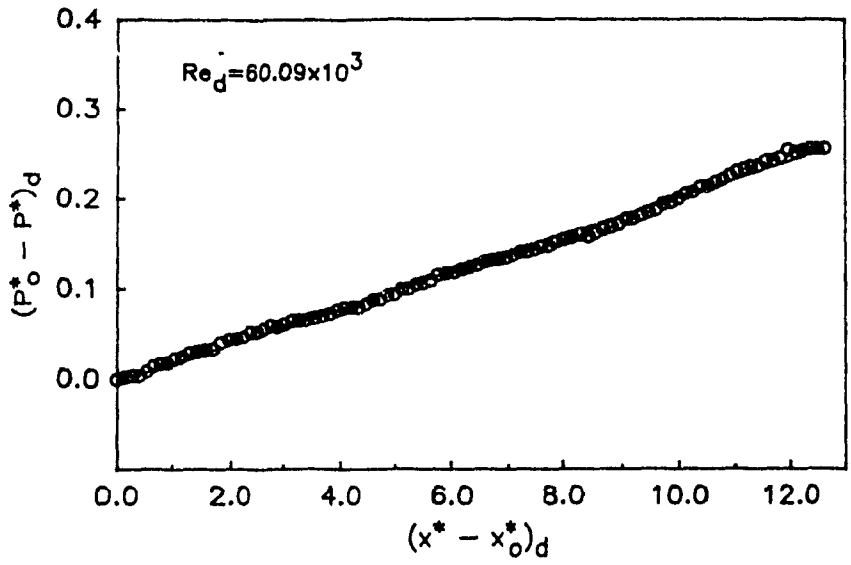

Figure 27: Least-squares straight line fitted to the $(P^*_o - P^*)_d$ versus $(x^* - x^*_o)_d$ data for fully developed duct flow: maximum flow rate. The maximum uncertainty in $(P^*_o - P^*)_d$ values is ± 0.012 and is less than ± 0.019 in $(x^* - x^*_o)_d$ values.

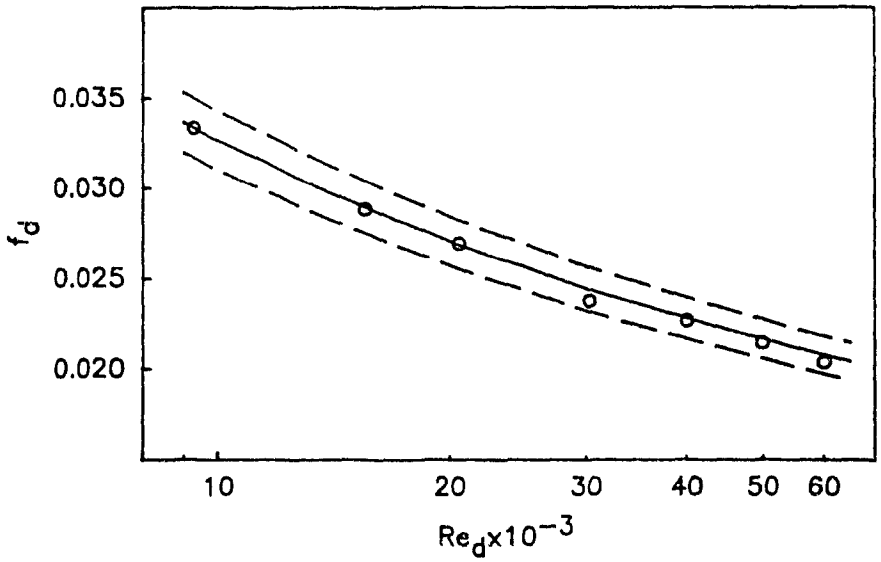

Figure 28: Friction factor - Reynolds number results for fully developed duct flows: o denotes the experimental results of this investigation ; (————) denotes the results obtained from the PJ correlation [54]; and (— — — —) denotes ± 5% deviation in the PJ correlation values. The uncertainty in all experimental f_d and Re_d values is less then ± 5.00% and ± 2.35%, respectively.

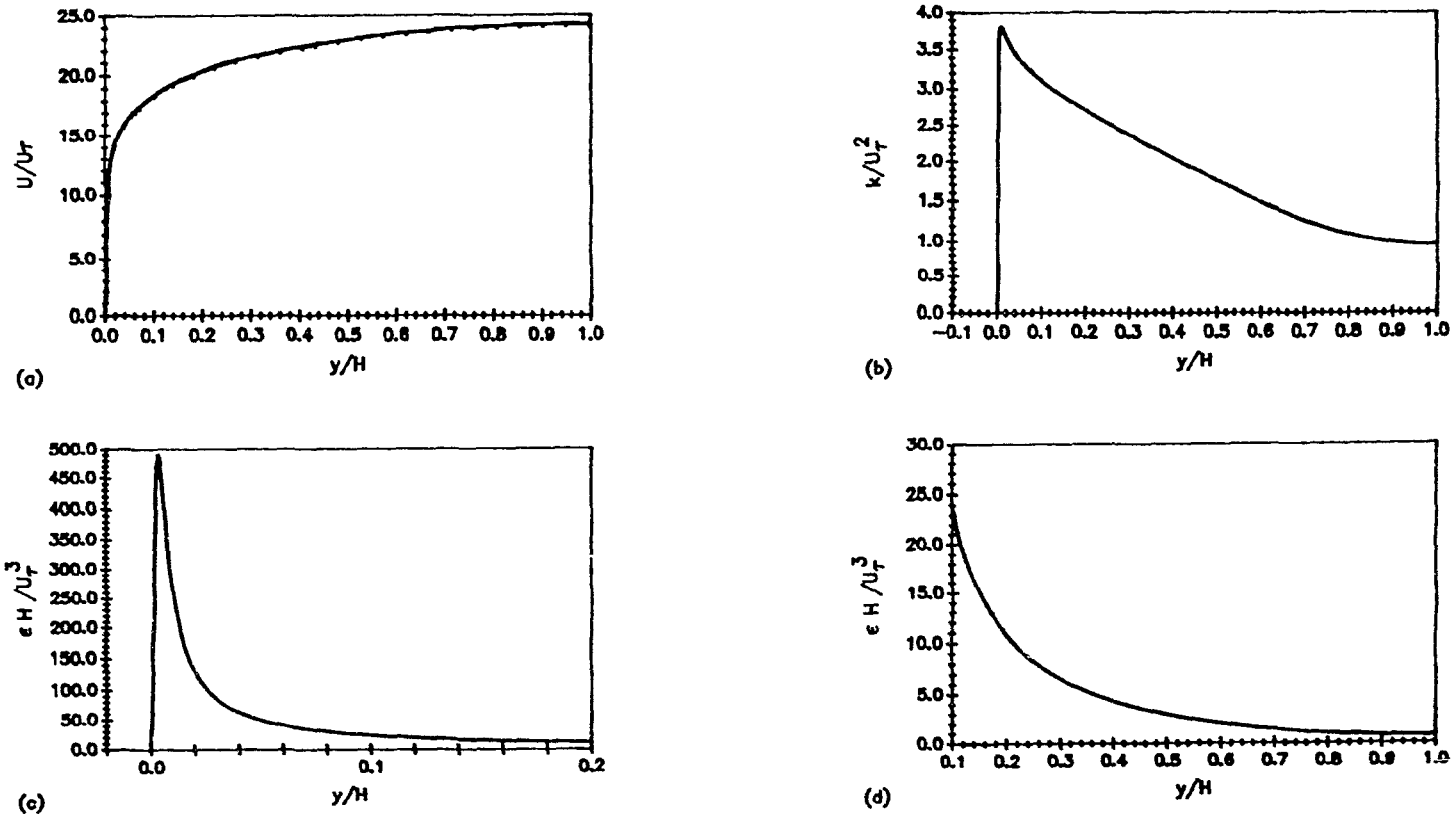

Figure 29: Results of grid-independence checks done with the JL [89] k-ε model of turbulence for $Re_{fric} = 10.5 \times 10^3$: M1 = 193 (———), M1 = 153 (—— – – ——), M1 = 133 (– – –), and M1 = 93 (·····). Shown are profiles of: (a) U/U_τ; (b) k/U_τ^2; and $(\epsilon H)/U_\tau^3$ for (c) $0 \leq y/H \leq 0.2$, and (d) $0.1 \leq y/H \leq 1.0$.

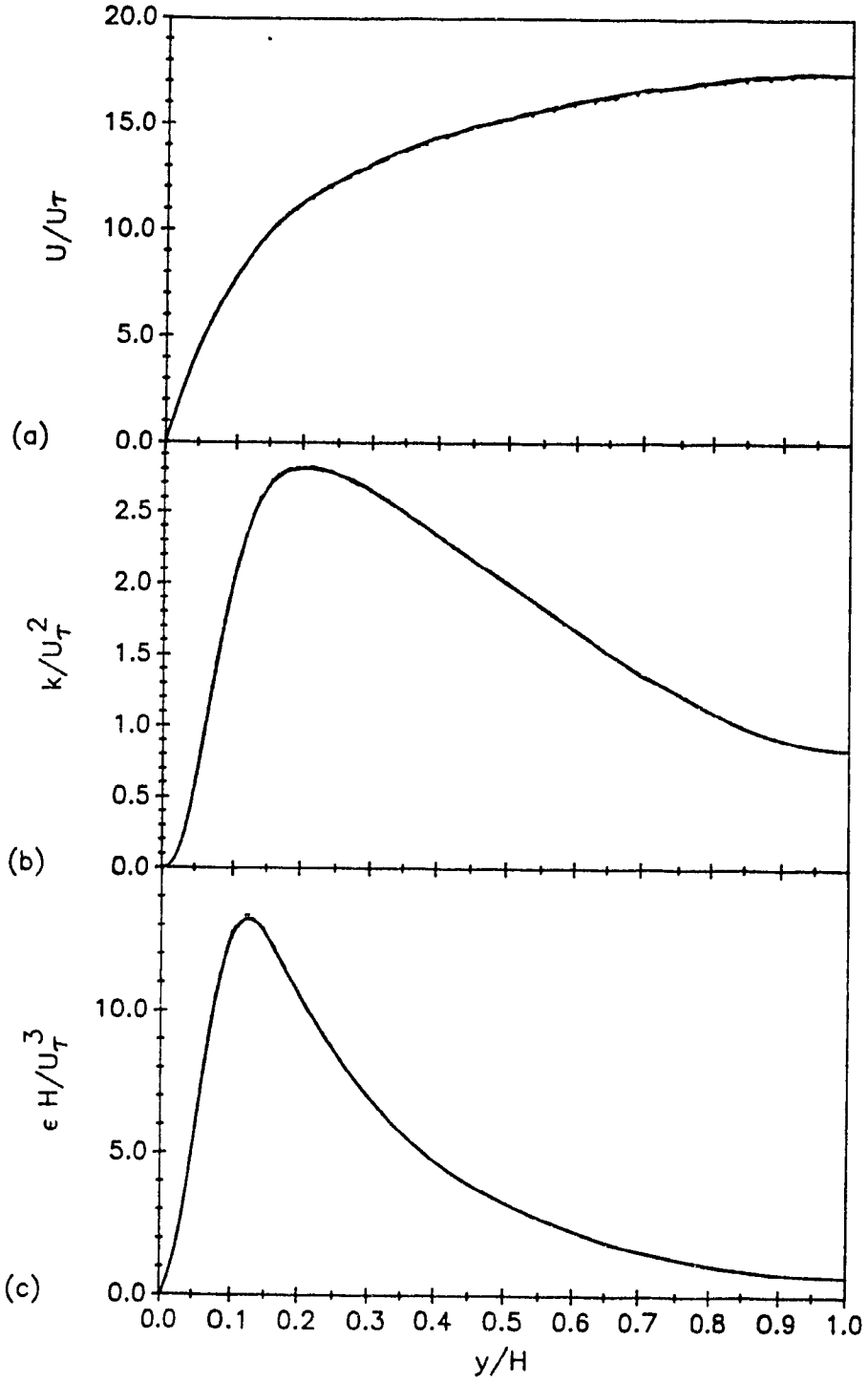

Figure 30: Results of grid-independence checks done with the JL [89] k-ϵ model of turbulence for $Re_{fric} = 3.72 \times 10^2$: M1 = 161 (———), M1 = 141 (——— — — ———), M1 = 101 (— — —), and M1 = 81 (·····). Shown are profiles of: (a) U/U_τ; (b) k/U_τ^2; and (c) $(\epsilon\ H)/U_\tau^3$.

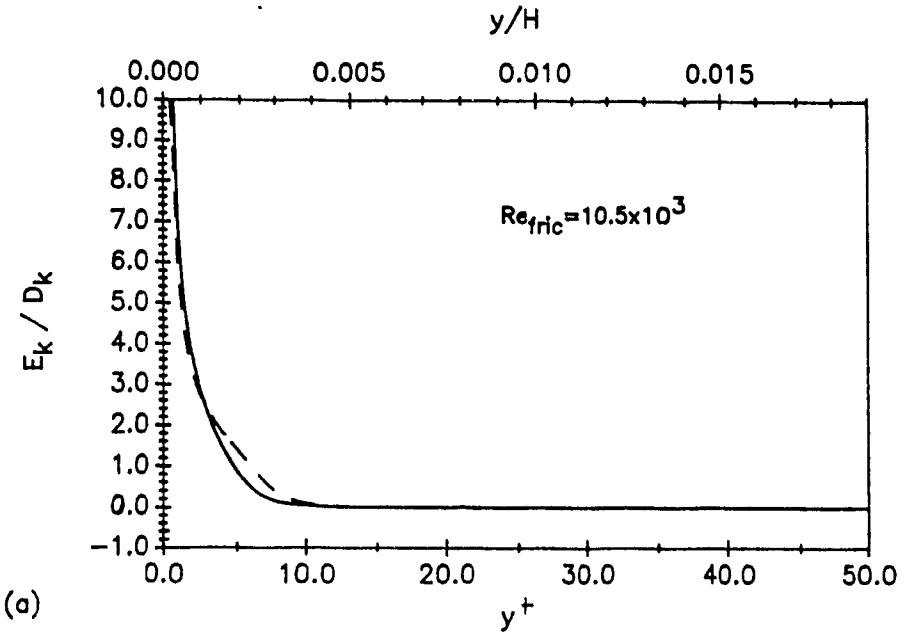

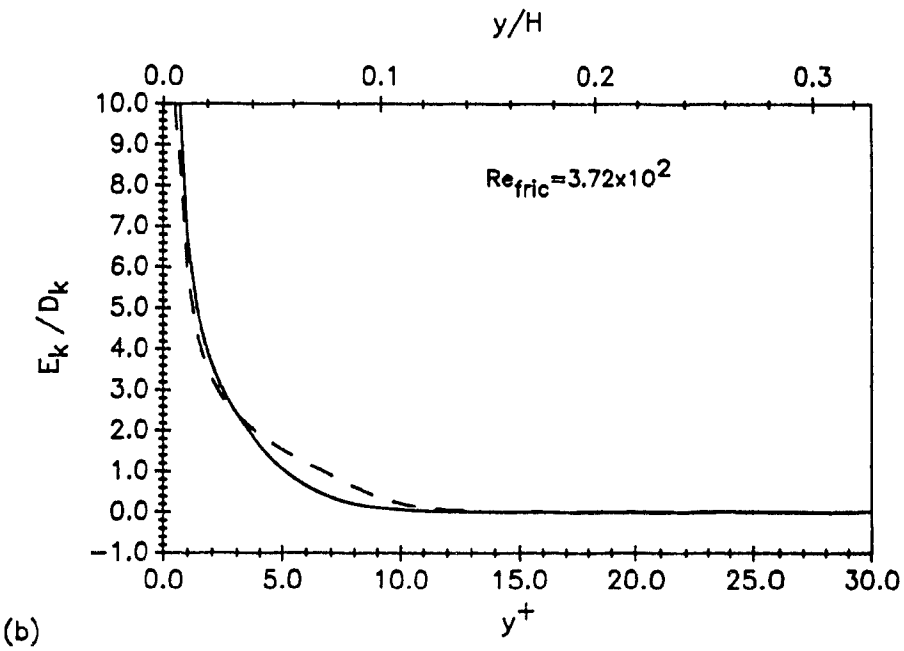

Figure 31: Behaviour of the E_k term relative to the D_k term in the k equation, Eq. (3-14), of the JL (———) [89] and LS (– – –) [91] turbulence models for fully developed duct flow calculations: (a) maximum Reynolds number; and (b) minimum Reynolds number.

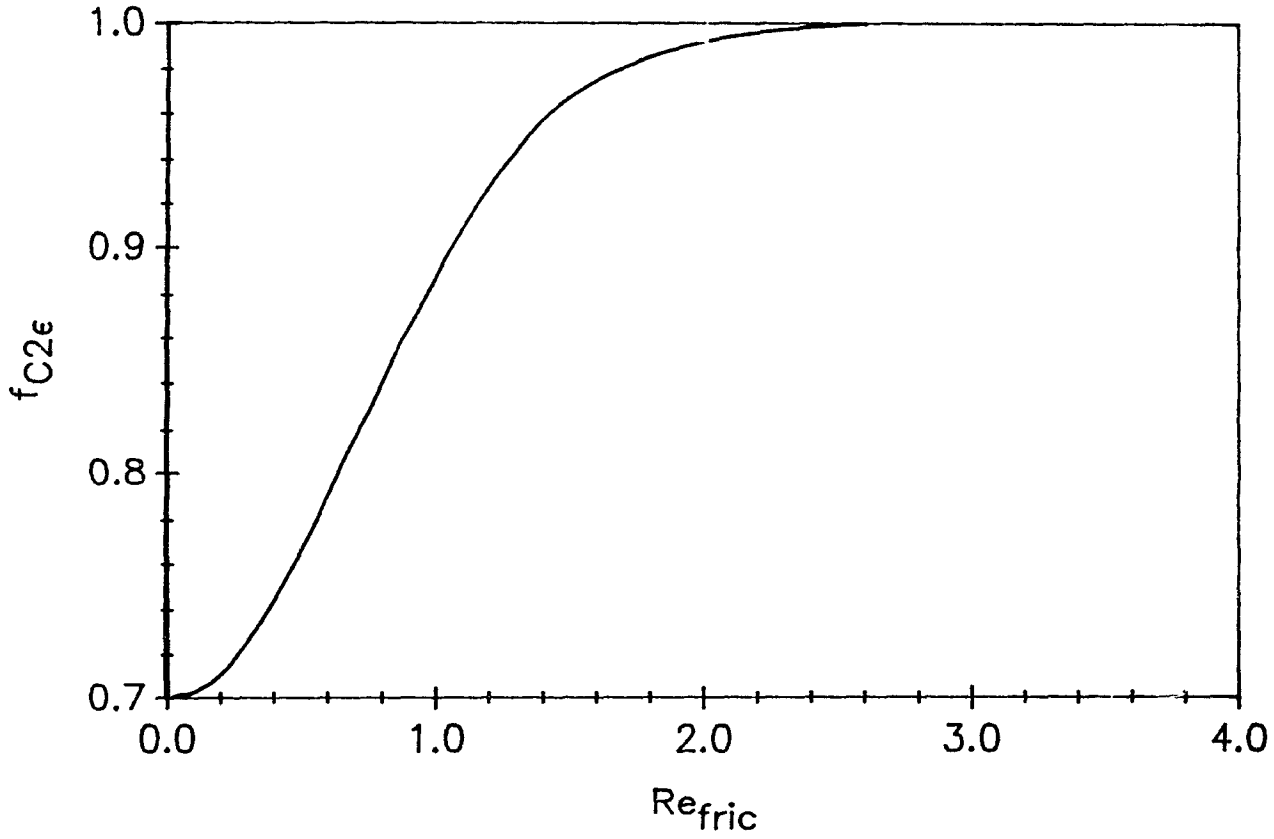

Figure 32: Behaviour of $f_{C2\epsilon}$ as a function of Re_t in the JL [89] and LS [91] turbulence models.

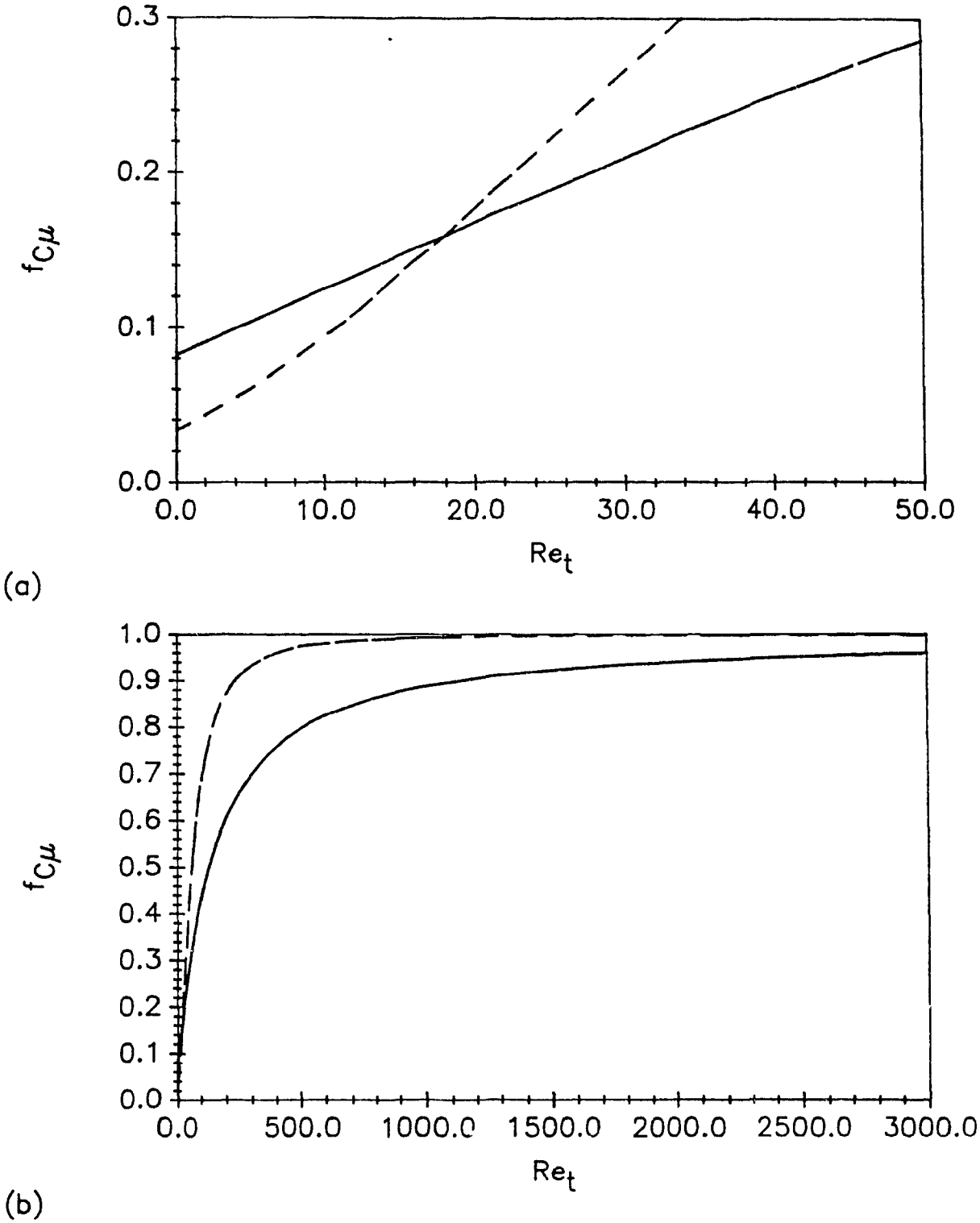

Figure 33: Behaviour of $f_{c\mu}$ as a function of Re_t in the JL (———) [89] and LS (– – –) [91] models of turbulence: (a) $0 \leq Re_t \leq 50$; and (b) $0 \leq Re_t \leq 3000$.

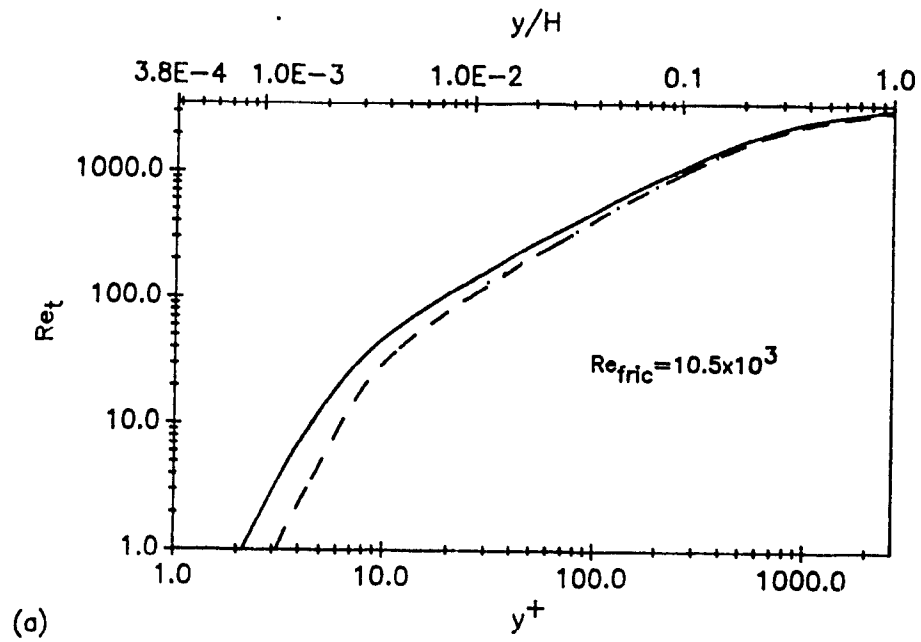

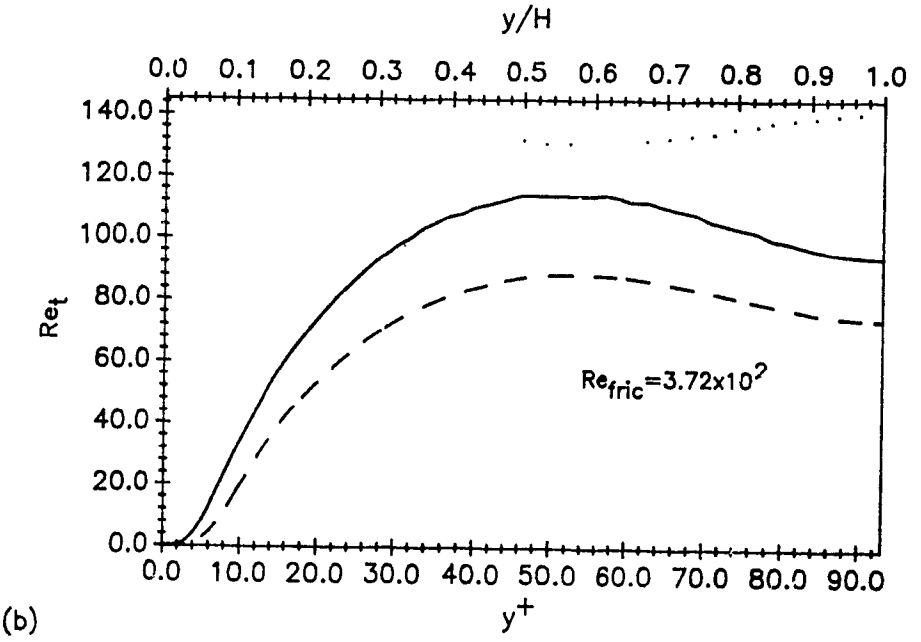

Figure 34: Profiles of Re_t obtained with the JL (———) [89], LS (– – –) [91], and ST (·····) [75] models of turbulence: (a) maximum Reynolds number; and (b) minimum Reynolds number.

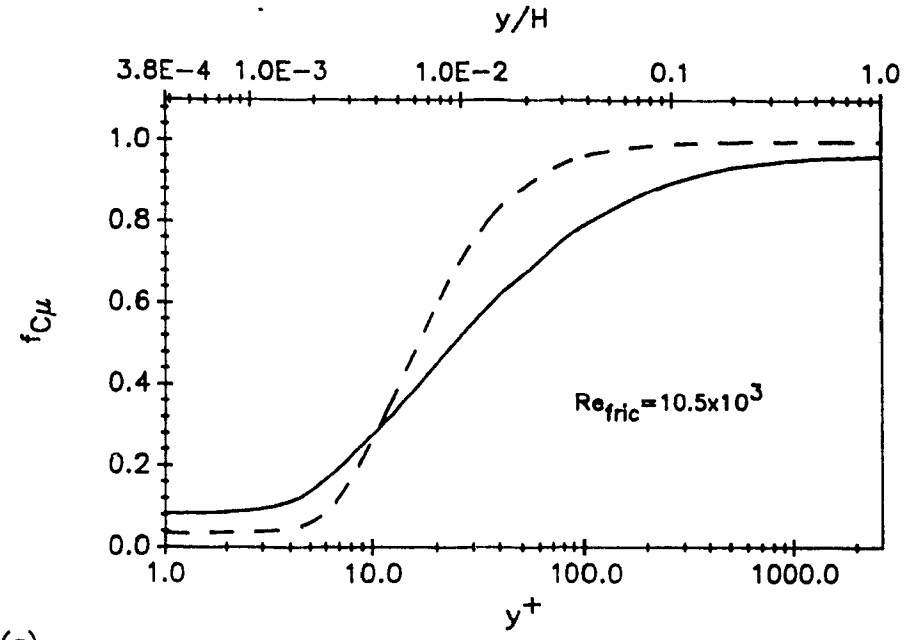

(a)

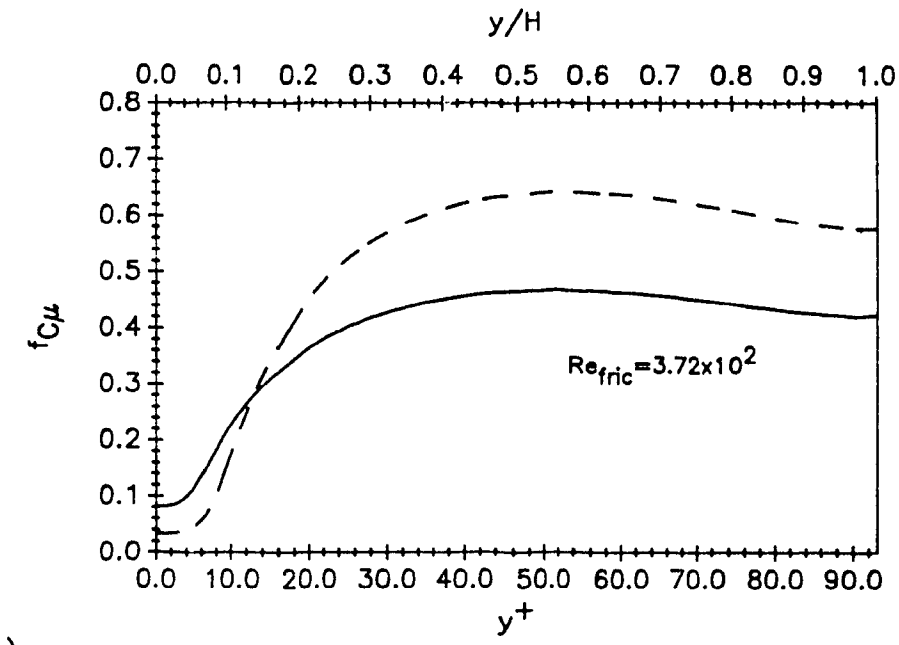

b)

Figure 35: Profiles of $f_{c\mu}$ calculated with the JL (———) [89], and LS (– – –) [91] models of turbulence: (a) maximum Reynolds number; and (b) minimum Reynolds number.

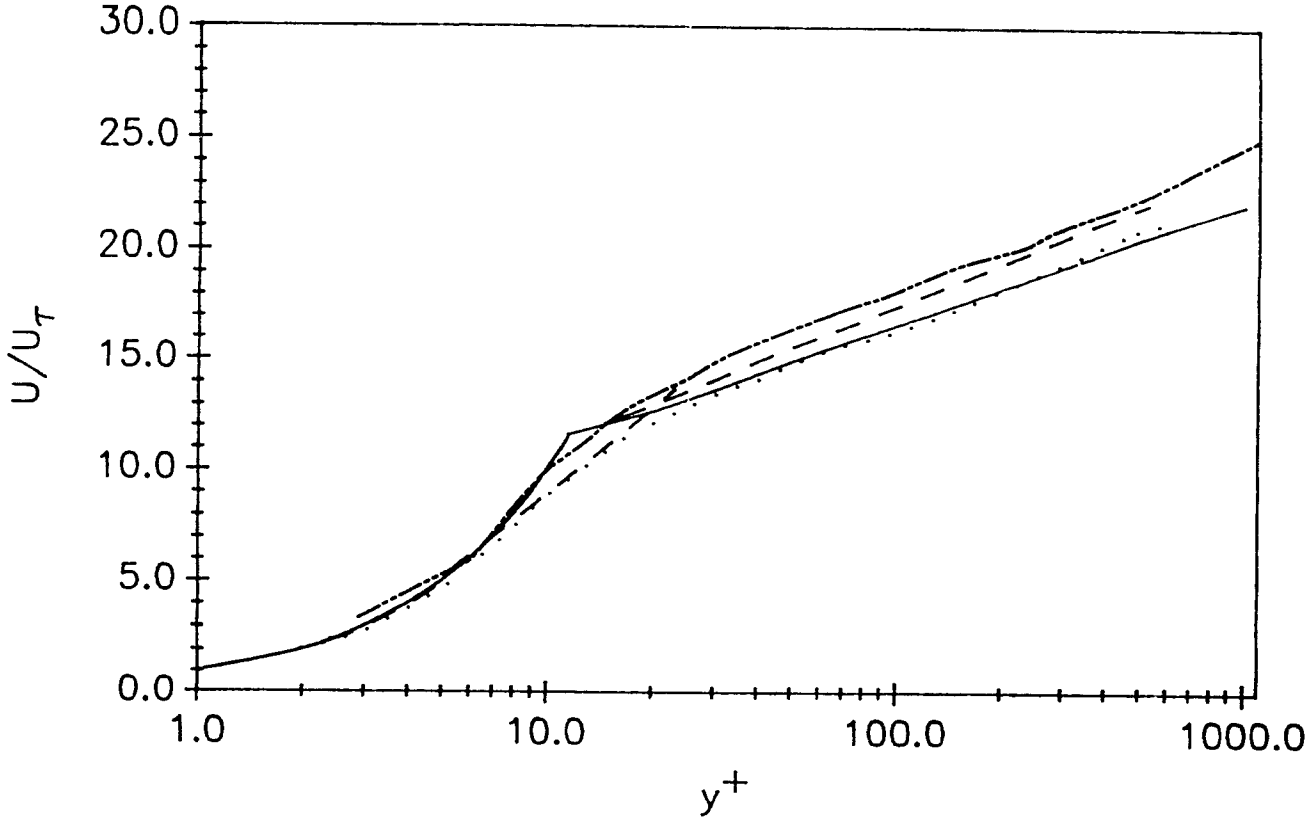

Figure 36: U velocity distributions of wall bounded shear flows: Eq. (7-11) for $y^+ \leq 11.5$ (———), Eq. (3-29) for $y^+ > 11.5$ (———); and experimental measurements of Comte-Bellot (—— – – ——) [62] with $Re_H = 57.0 \times 10^3$; Clark (– – –) [63] with $Re_{max} = 15.2 \times 10^3$; and Hussain and Reynolds (·····) [64] with $Re_{max} = 13.8 \times 10^3$.

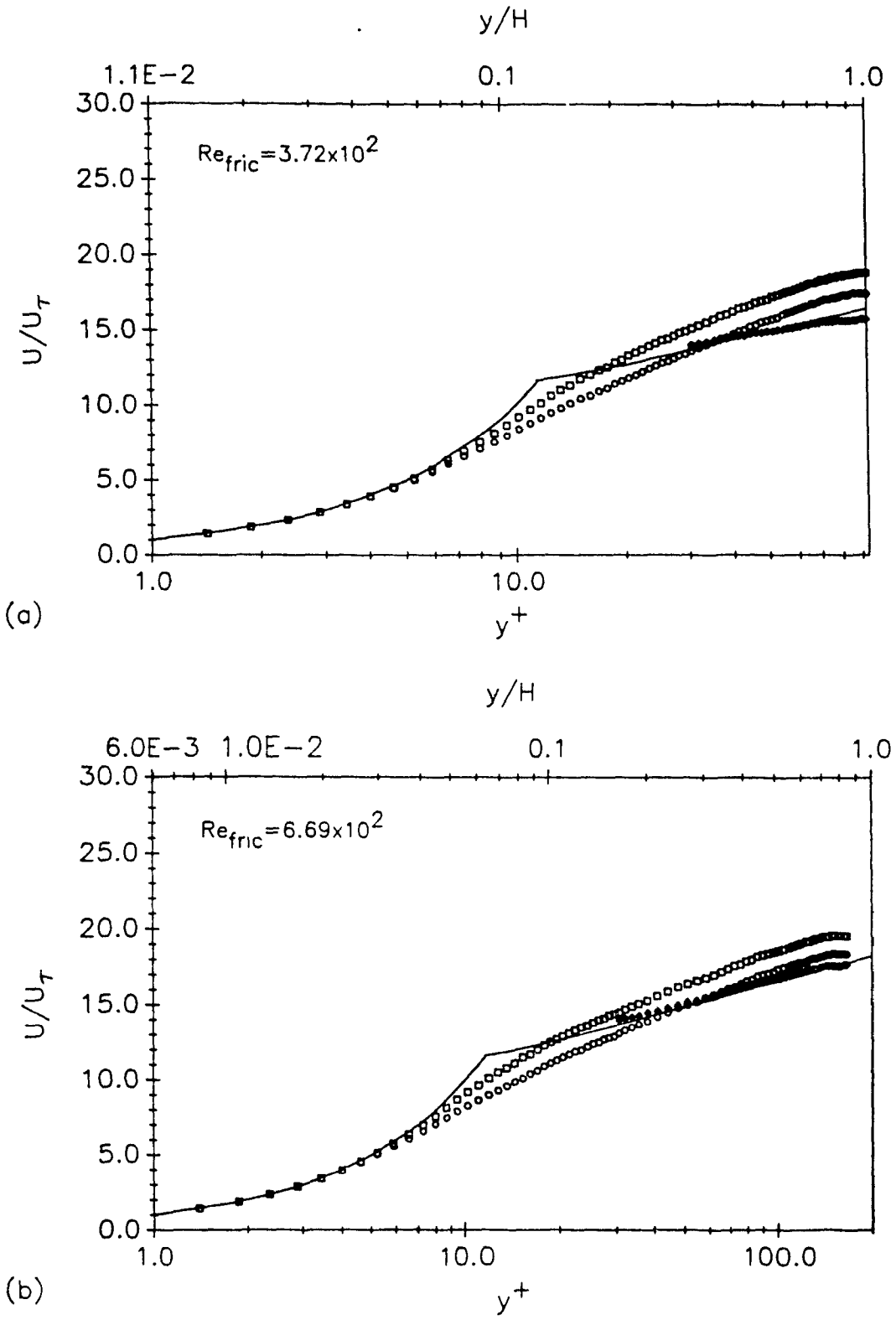

Figure 37: U velocity distributions of two-dimensional channel flows calculated with the JL model ○ [89], the LS model □ [91], and the ST model ◆ [75]. Eqs. (7-11) and (3-29) are plotted (———) for $y^+ \leq 11.5$ and $y^+ > 11.5$, respectively: (a) and (b).

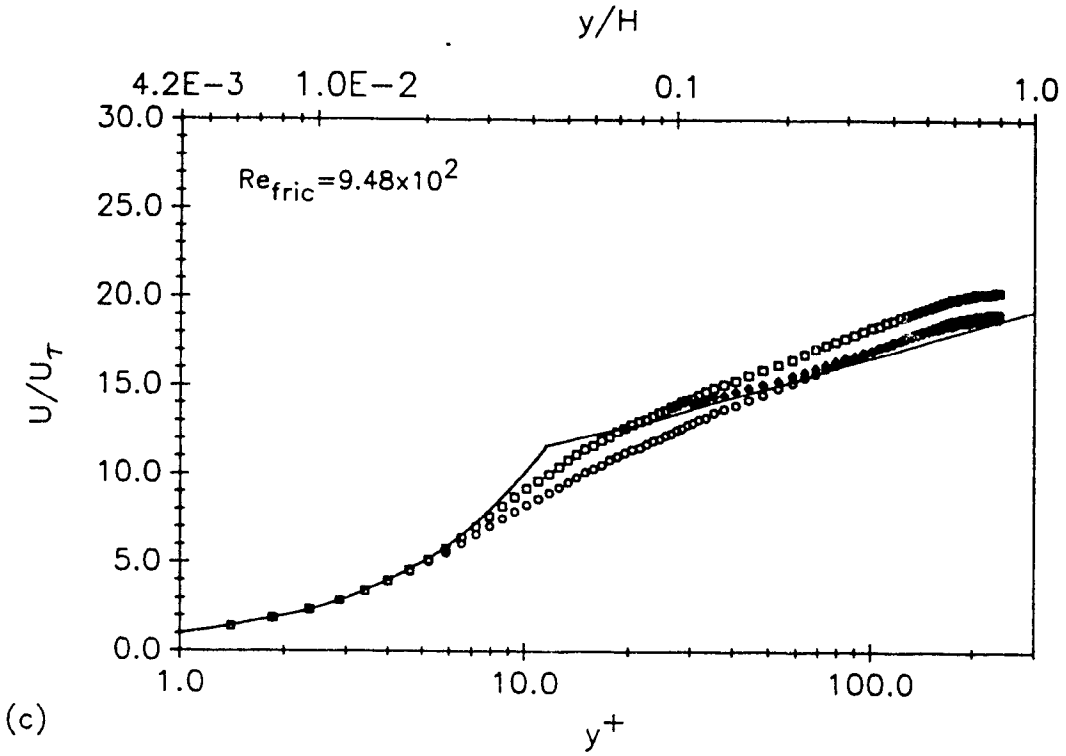

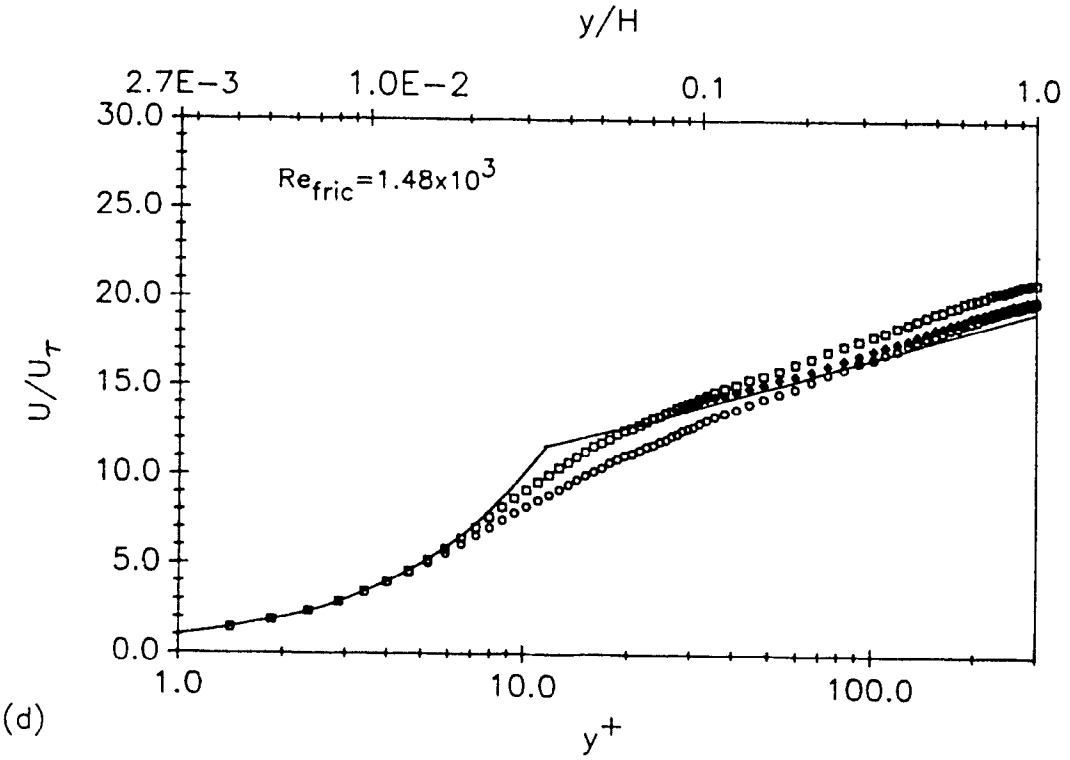

Figure 37: U velocity distributions of two-dimensional channel flows calculated with the JL model ○ [89], the LS model □ [91], and the ST model ◆ [75]. Eqs. (7-11) and (3-29) are plotted (———) for $y^+ \leq 11.5$ and $y^+ > 11.5$, respectively: (c) and (d).

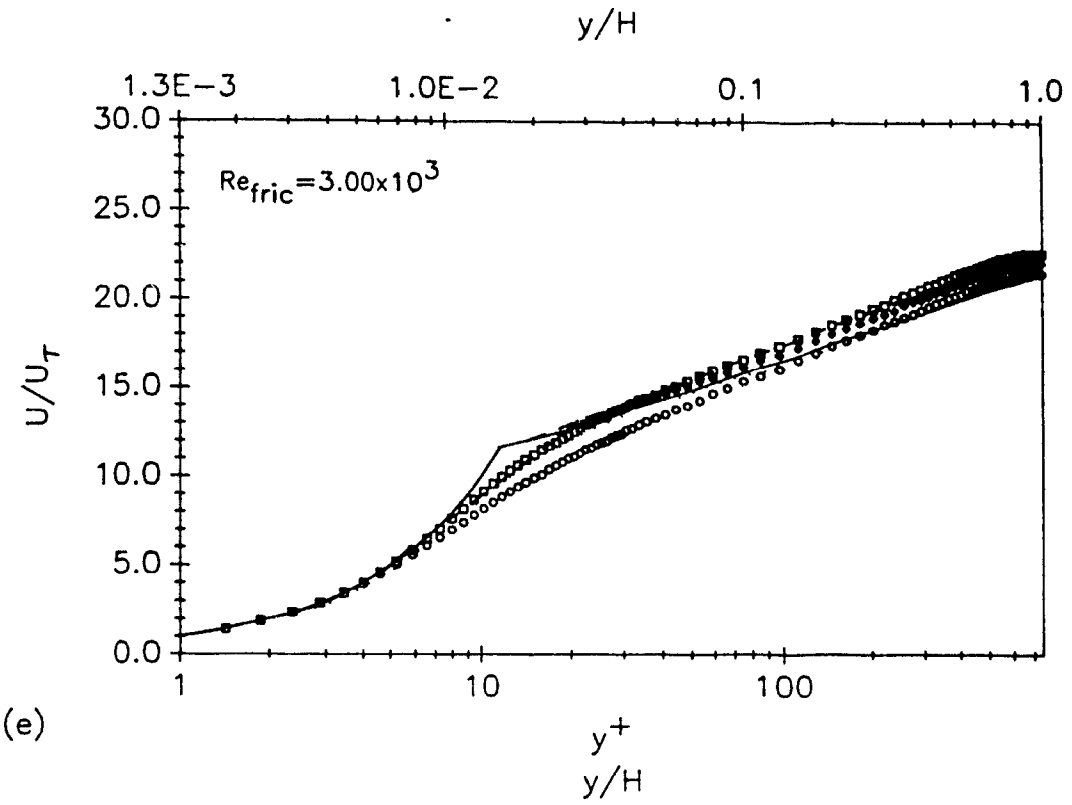

(e)

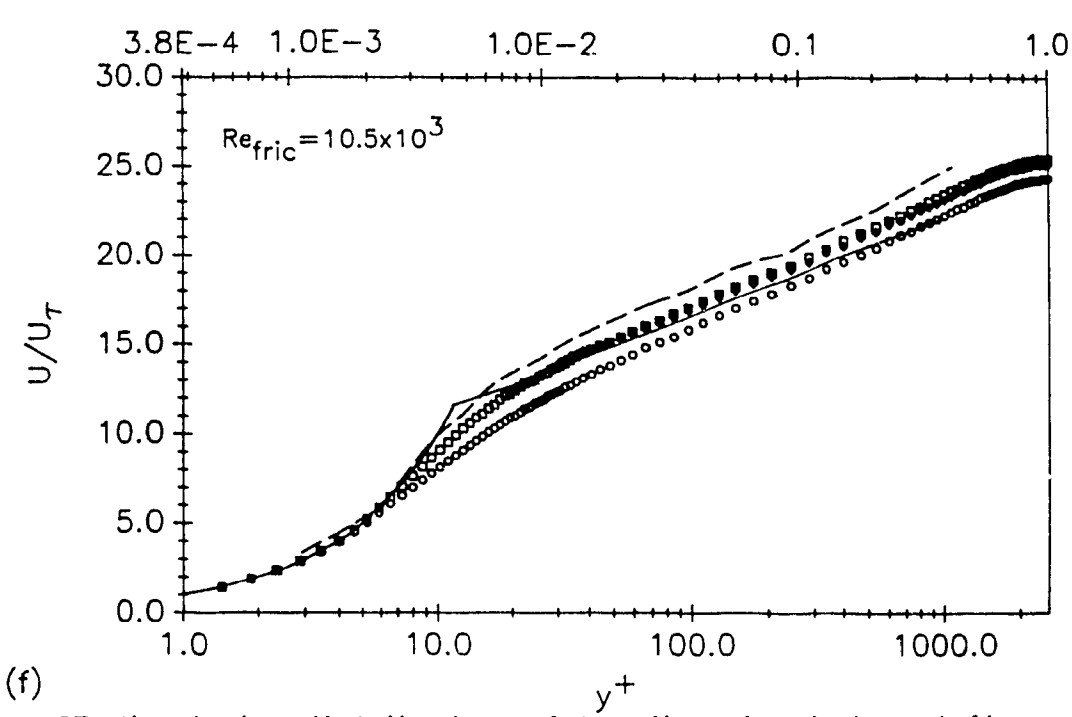

(f)

Figure 37: U velocity distributions of two-dimensional channel flows calculated with the JL model ○ [89], the LS model □ [91], and the ST model ◆ [75]. Eqs. (7-11) and (3-29) are plotted (———) for $y^+ \leq 11.5$ and $y^+ > 11.5$, respectively: (e) results of Clark (— — —) [63] with $Re_{max} = 15.2x10^3$, and Hussain and Reynolds (·····) [64] with $Re_{max} = 13.8x10^3$; and (f) Comte-Bellot (— — —) [62] with $Re_H = 57.0x10^3$.

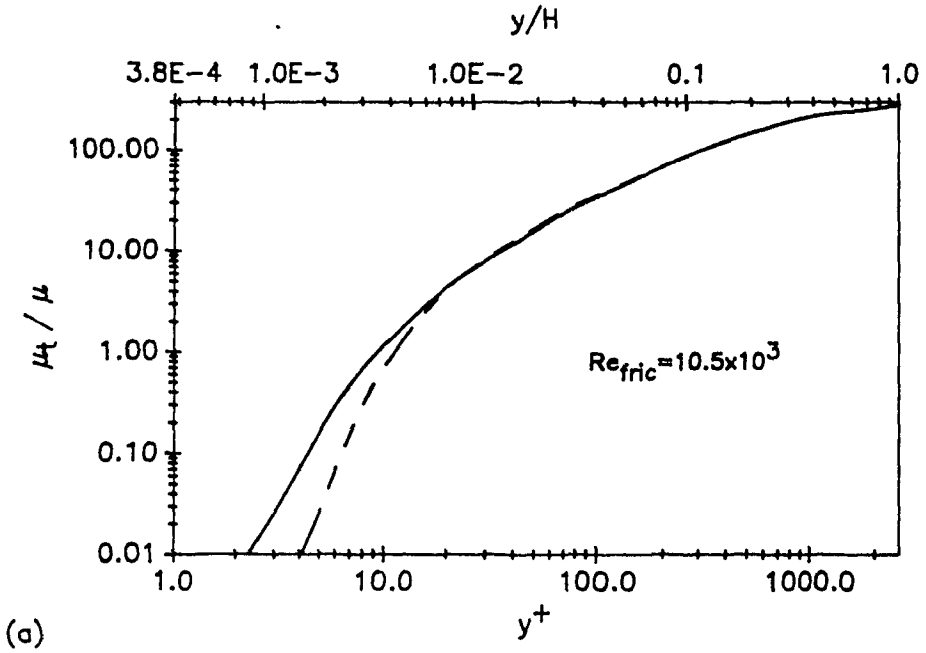

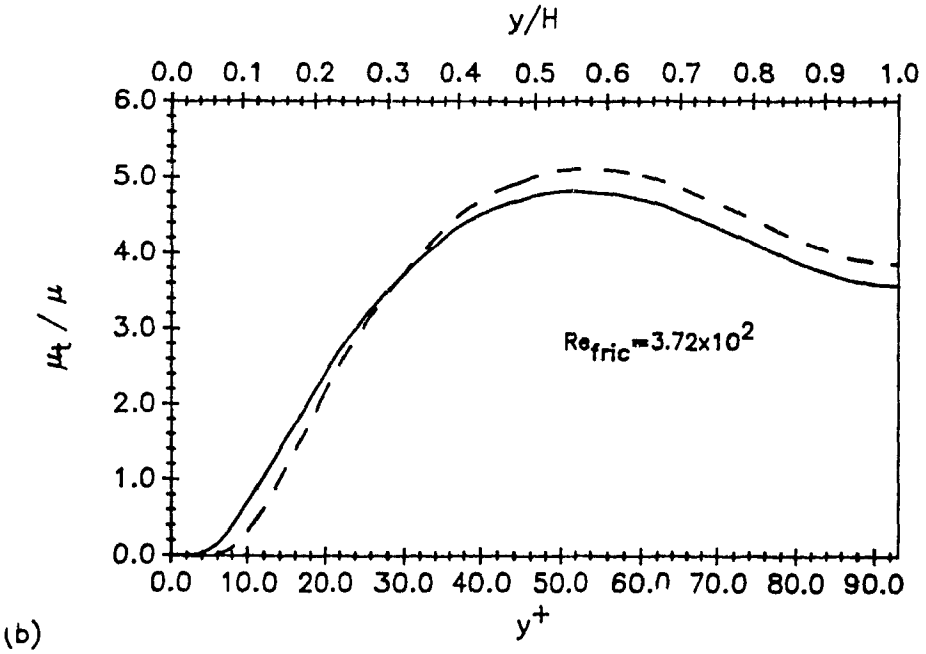

Figure 38: Profiles of μ_t/μ in two-dimensional channel flows calculated with the JL (———) [89] and LS (— — —) [91] models: (a) maximum Reynolds number; and (b) minimum Reynolds number.

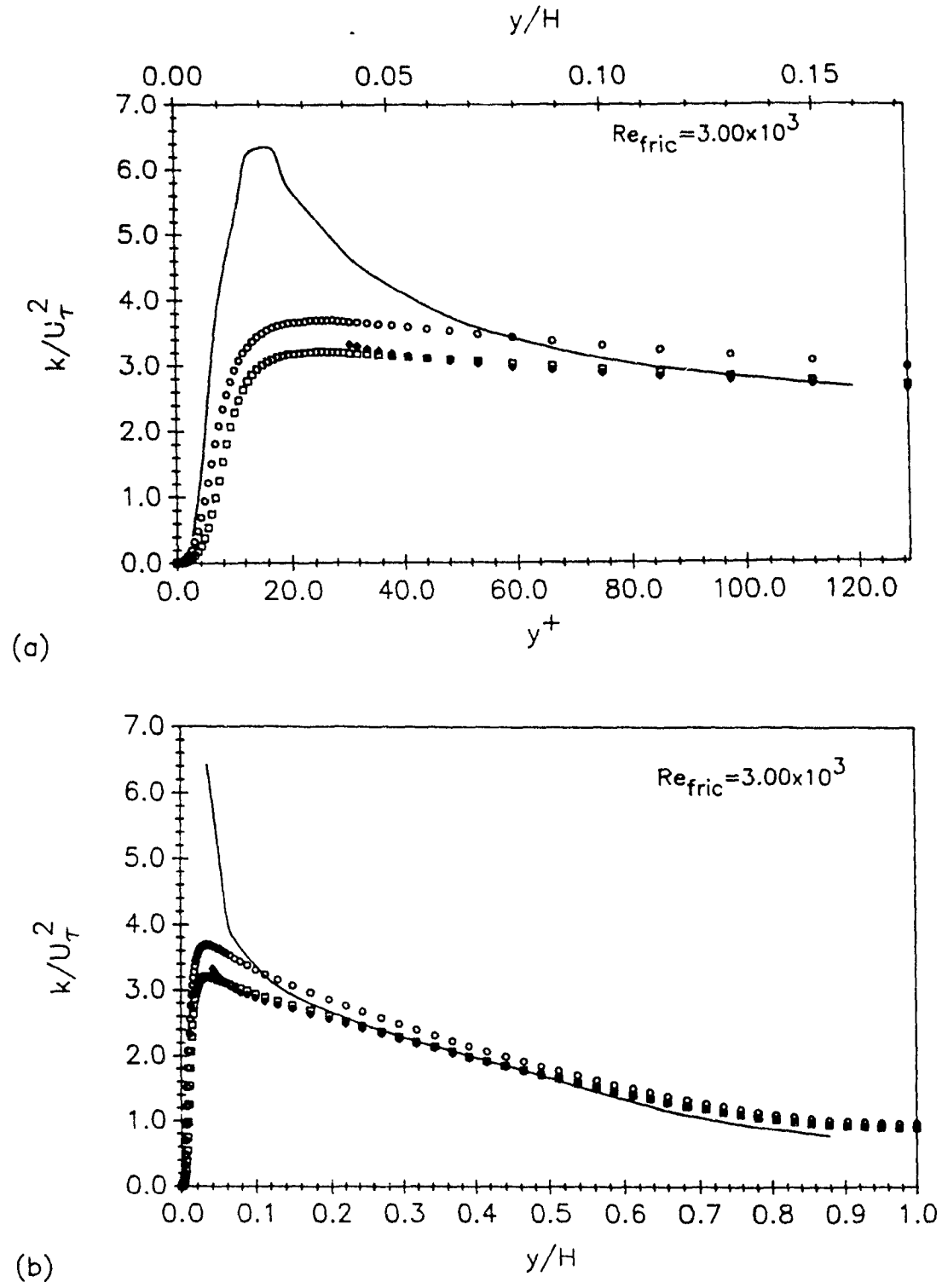

Figure 39: Profiles of mean turbulent kinetic energy in two-dimensional channel flow. Plots show the results obtained with the JL ○ [89], LS □ [91], and ST ◆ [75] models with $Re_{fric} = 3.00 \times 10^3$; and the experimental data of Clark (—— [63] with $Re_{max} = 15.2 \times 10^3$: (a) near-wall profiles; and (b) profiles across the channel half-height, $0 \leq y/H \leq 1.0$.

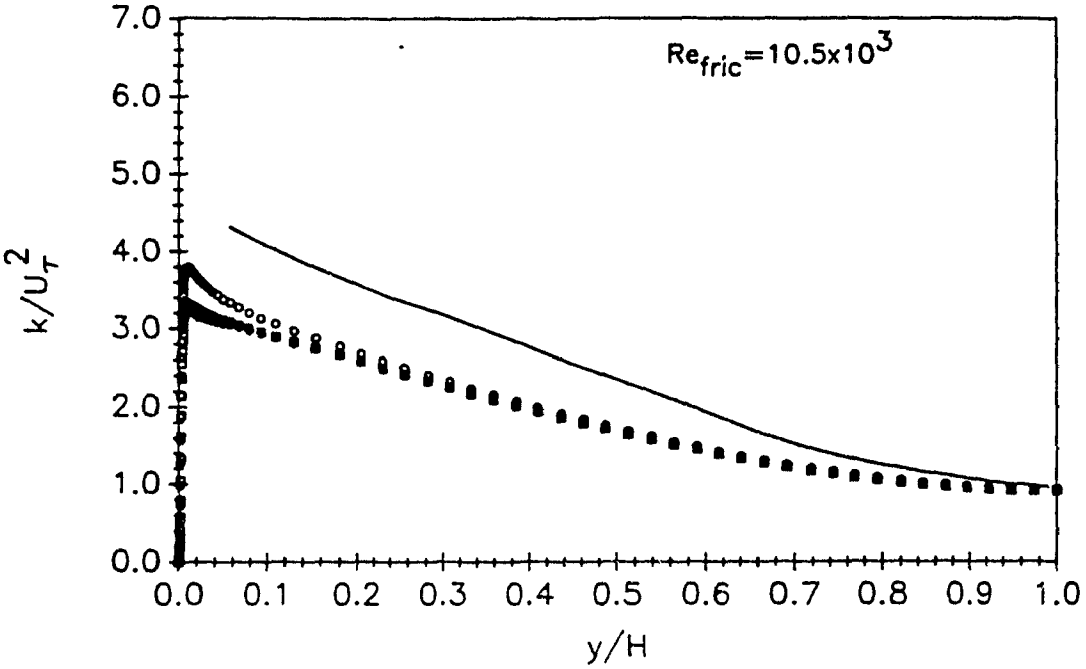

Figure 40: Profiles of mean turbulent kinetic energy in two-dimensional channel flow. Plots show the results of computations done with the JL ○ [89], LS □ [91], and ST ◆ [75] models with $Re_{fric} = 10.5x10^3$; and the experimental data of Comte-Bellot (———) [62] with $Re_H = 57.0x10^3$.

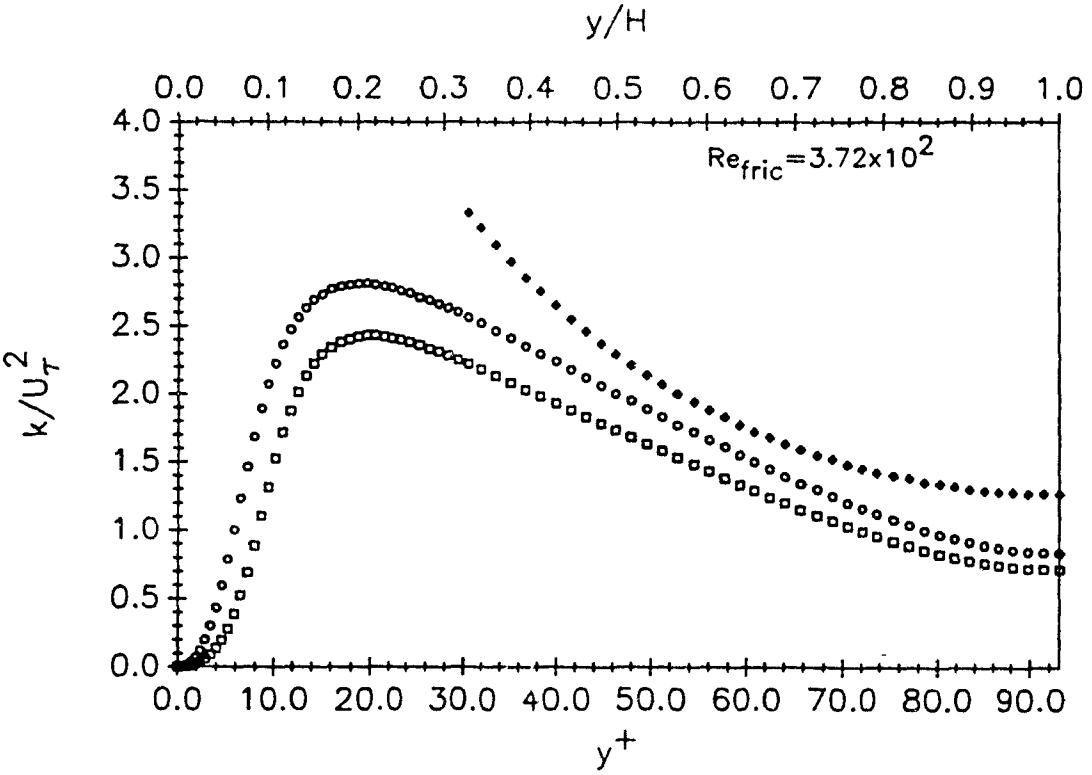

Figure 41: Profiles of mean turbulent kinetic energy in two-dimensional channel flow. Plots show the results of computations done with the JL ○ [89], LS □ [91], and ST ◆ [75] models with $Re_{fric} = 3.72x10^2$.

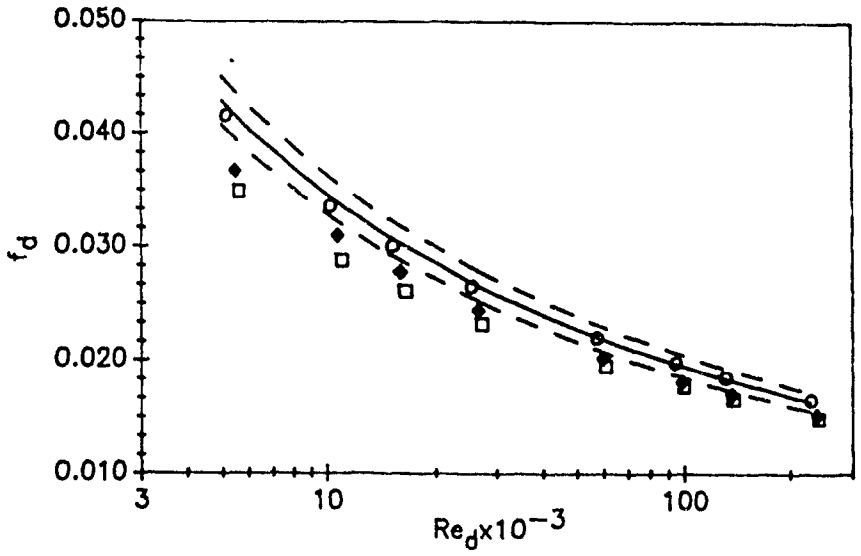

Figure 42: Friction factor - Reynolds number results of the computations for fully developed channel flows: JL model ○ [89]; LS model □ [91]; ST model ◆ [75]; (————) denotes the results obtained from the PJ correlation [54]; and (— — — —) denotes ± 5% deviation in the PJ correlation values.

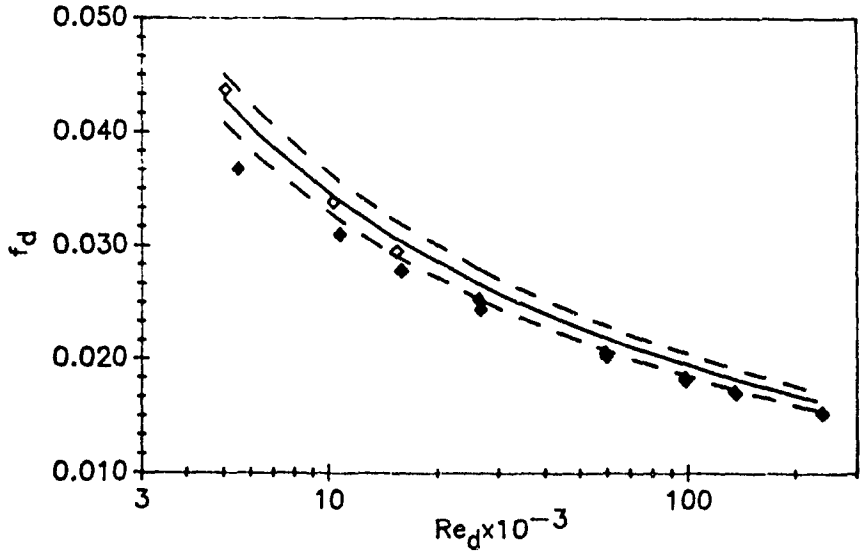

Figure 43: Friction factor - Reynolds number results obtained with the ST model [75] using the prevailing assumption ◆ and the two-piece near-wall velocity profile integration ◇ methods. (————) denotes the results obtained from the PJ correlation [54], and (— — — —) denotes ± 5% deviation in the PJ correlation values.

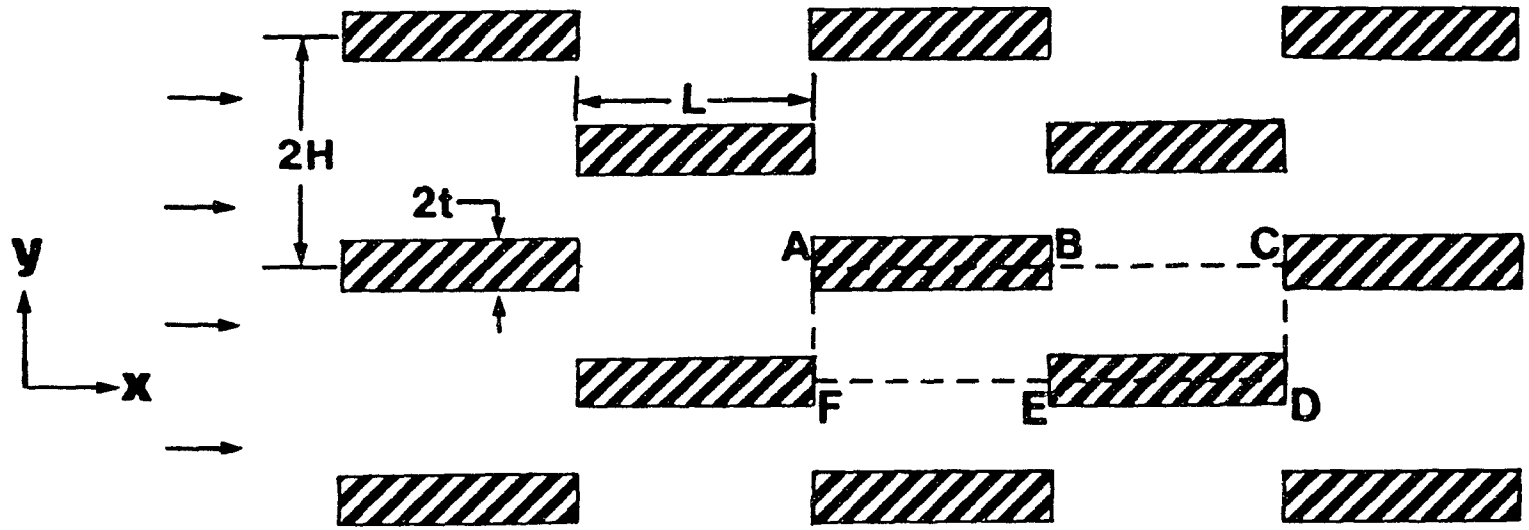

Figure 44: An interrupted-plate passage showing associated nomenclature and a geometrically similar module, ABCDEF.

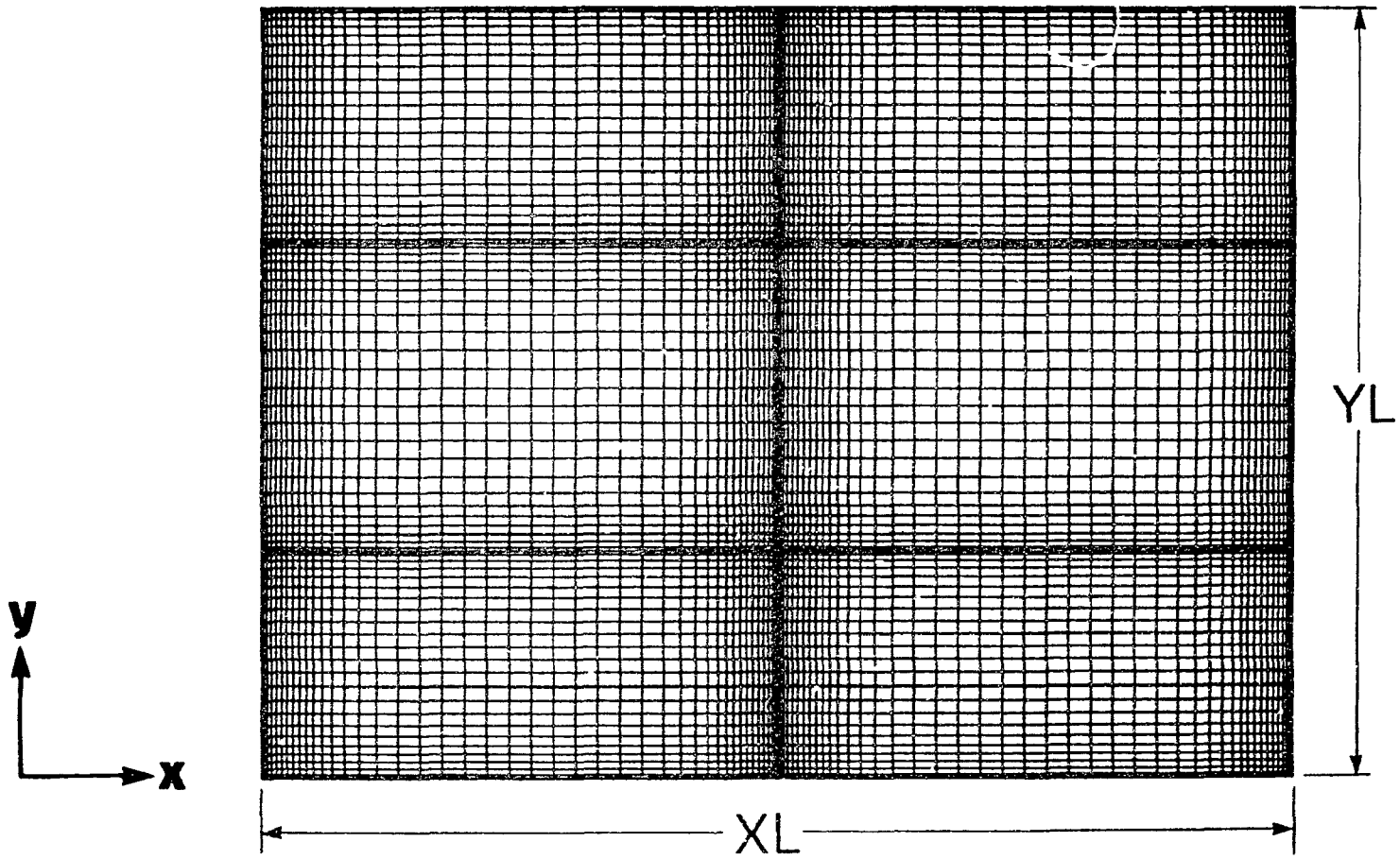

Figure 45: Control-volume locations in the domain discretization used for laminar periodic fully developed flow simulations. This figure is not to scale as the y dimensions have been expanded relative to the x dimensions to allow a clear representation of the relative changes in y-direction control-volume dimensions (true scale is XL:YL= 4:1).

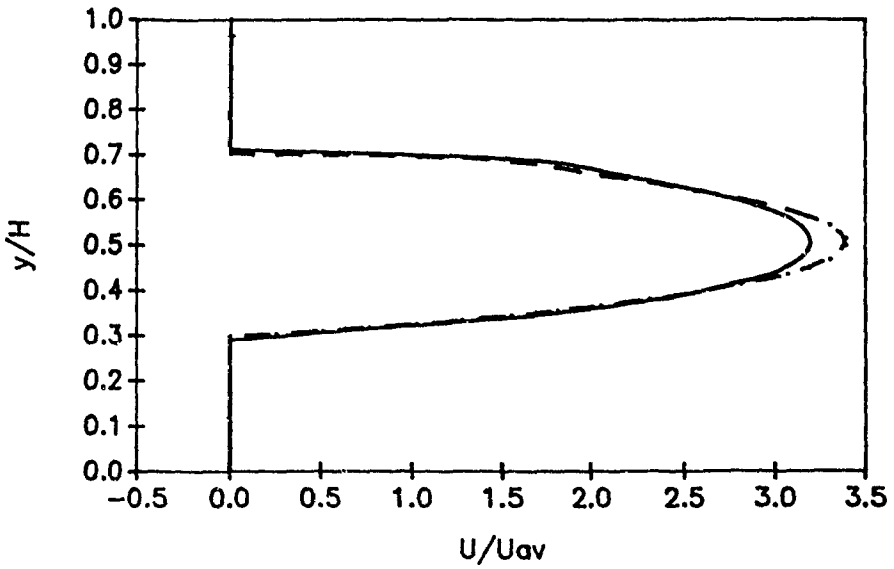

Figure 46: Results of grid checks for laminar periodic fully developed flow: Profiles of nondimensional U velocities at the inlet plane of module ABCDEF in Fig. 44 are shown for Re_s=2000 and x-y grids of 56x11 (———), 88x73 (— — —), and 112x105 (·····).

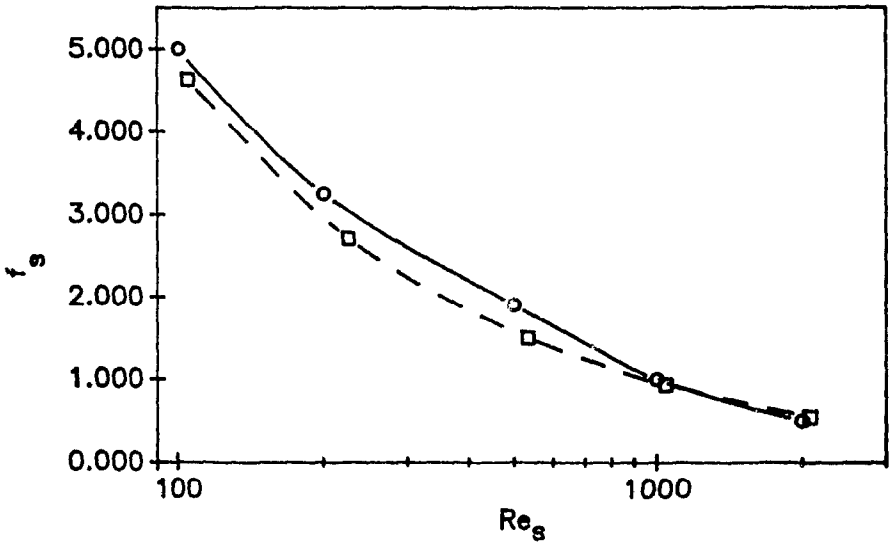

Figure 47: Friction factor - Reynolds number plots for laminar periodic fully developed flow in an interrupted-plate passage with L/H = 1.0 and t/H = 0.3: numerical results of this investigation (□— — —□) and of Patankar and Prakash [14] (o ——— o).

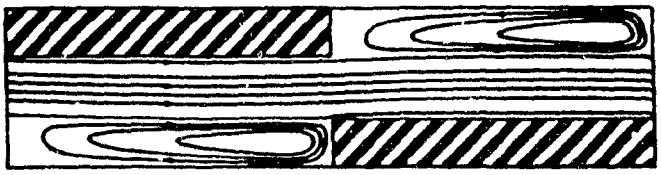

Re_s = 2000

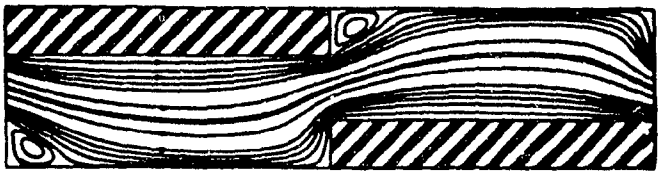

Re_s = 100

(a)

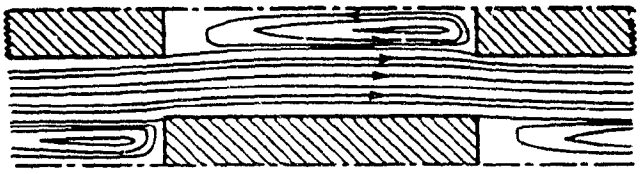

Re_s = 2000

Re_s = 100

(b)

Figure 48: Module streamline plots for maximum and minimum values of Re_s: (a) this investigation; and (b) Patankar and Prakash [14].

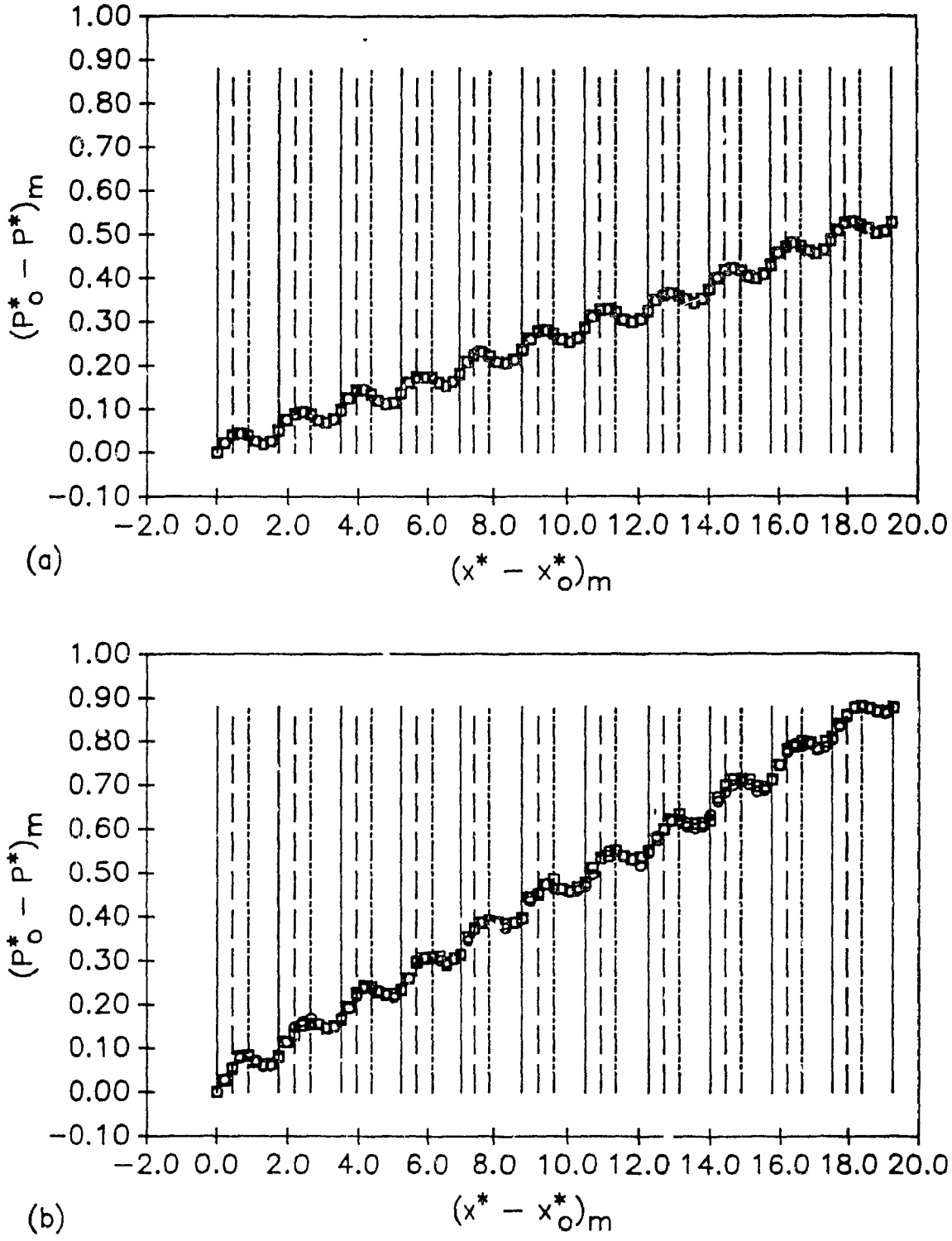

Figure 49: Repeatability checks on time-mean wall static pressure measurements for periodic fully developed flow in Duct 1 showing the initial run (○) and the repeated run (□) for maximum and minimum flow rates: (a) $Re_m = 33.49 \times 10^3$ (○), $Re_m = 33.50 \times 10^3$ (□); and (b) $Re_m = 5.432 \times 10^3$ (○), $Re_m = 5.398 \times 10^3$ (□). The maximum uncertainty in $(P^*_o - P^*)_m$ values is ± 0.024 in (a) and ± 0.046 in (b); and it is ± 0.041 in the $(x^* - x^*_o)_m$ values in both (a) and (b).

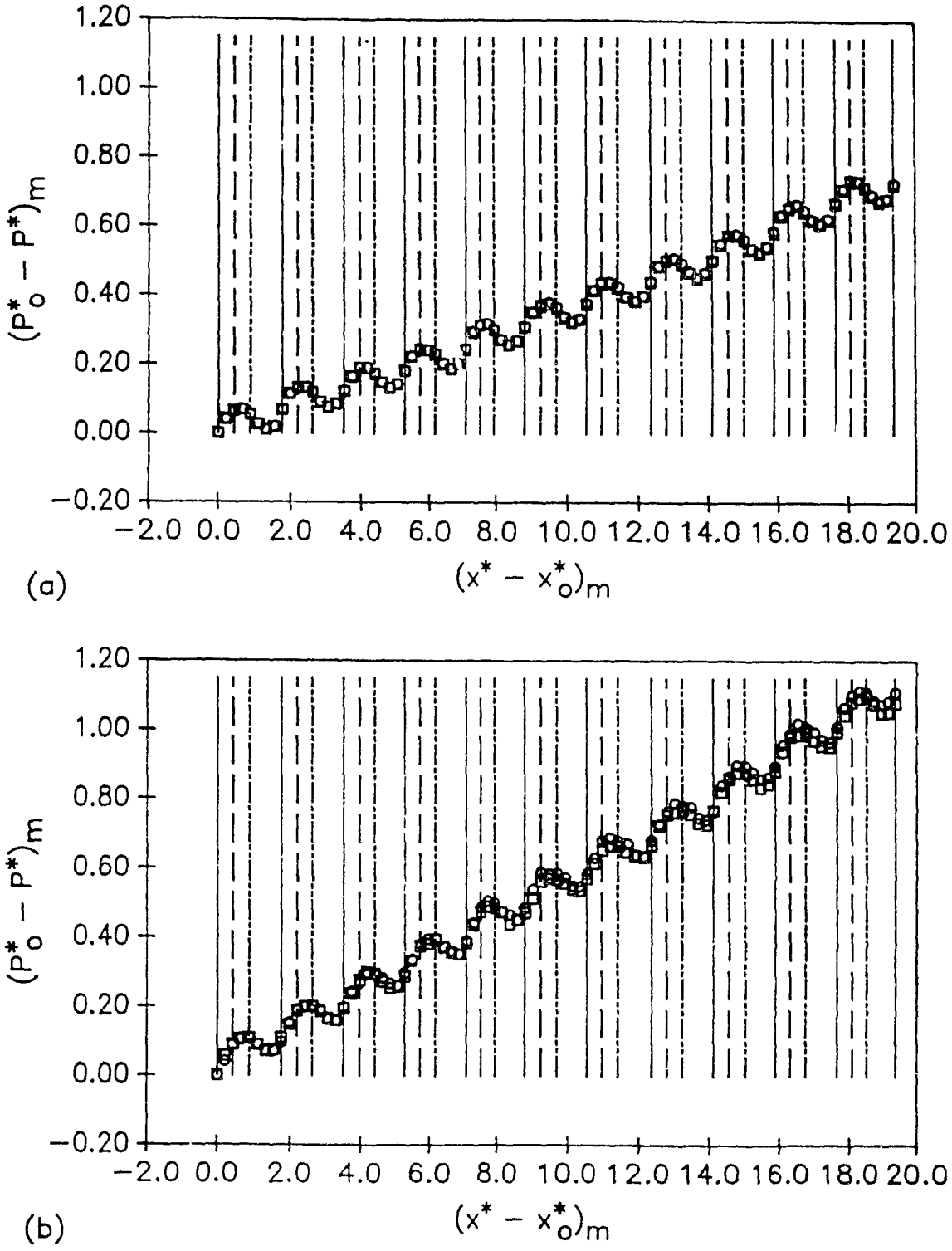

Figure 50: Repeatability checks on time-mean wall static pressure measurements for periodic fully developed flow in Duct 2 showing the initial run (○) and the repeated run (□) for maximum and minimum flow rates: (a) $Re_m = 32.93 \times 10^3$ (○), $Re_m = 32.70 \times 10^3$ (□); and (b) $Re_m = 5.397 \times 10^3$ (○), $Re_m = 5.388 \times 10^3$ (□). The maximum uncertainty in $(P^*_o - P^*)_m$ values is ± 0.033 in (a) and ± 0.058 in (b); and it is ± 0.041 in the $(x^* - x^*_o)_m$ values in both (a) and (b).

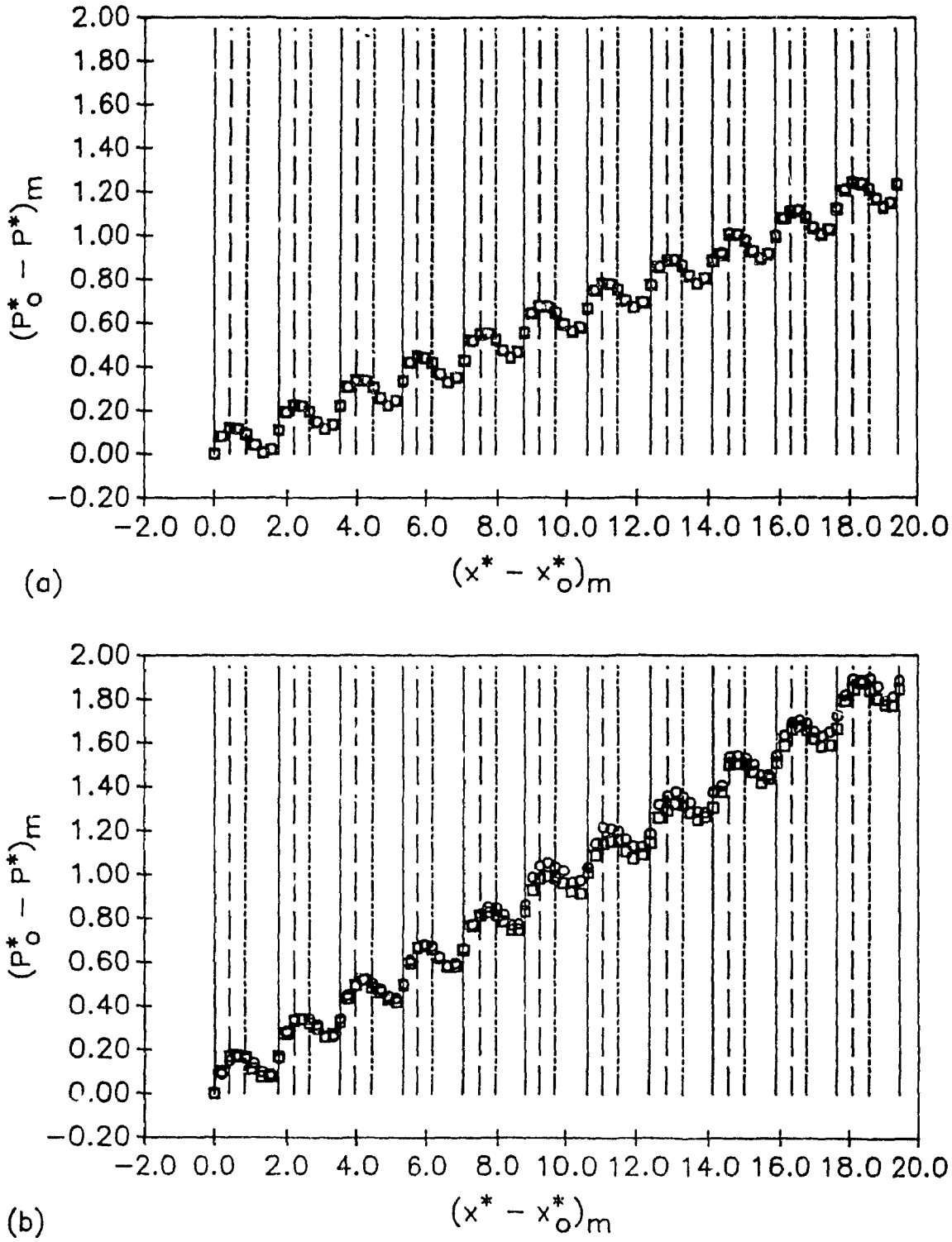

Figure 51: Repeatability checks on time-mean wall static pressure measurements for periodic fully developed flow in Duct 3 showing the initial run (○) and the repeated run (□) for maximum and minimum flow rates: (a) $Re_m = 32.32 \times 10^3$ (○), $Re_m = 32.15 \times 10^3$ (□); and (b) $Re_m = 4.997 \times 10^3$ (○), $Re_m = 4.980 \times 10^3$ (□). The maximum uncertainty in $(P^*_o - P^*)_m$ values is ± 0.055 in (a) and ± 0.11 in (b); and it is ± 0.041 in the $(x^* - x^*_o)_m$ values in both (a) and (b).

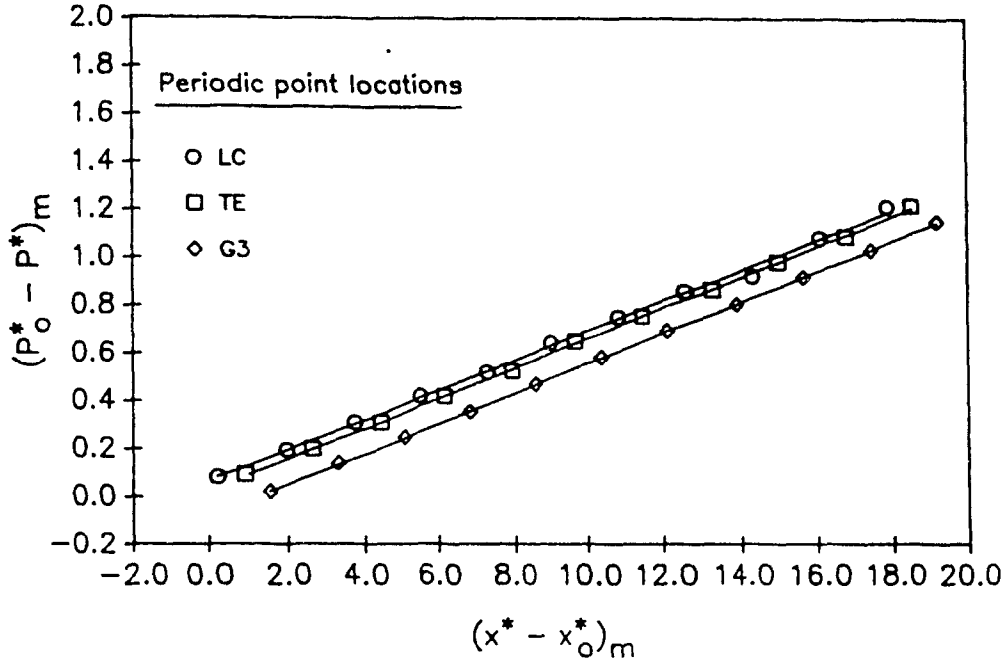

Figure 52: Least-squares straight lines fitted to the $(P^*_o - P^*)_m$ vs. $(x^* - x^*_o)_m$ data points for the LC, TE, and G3 locations of Duct 3 for $Re_m = 32.32 \times 10^3$.

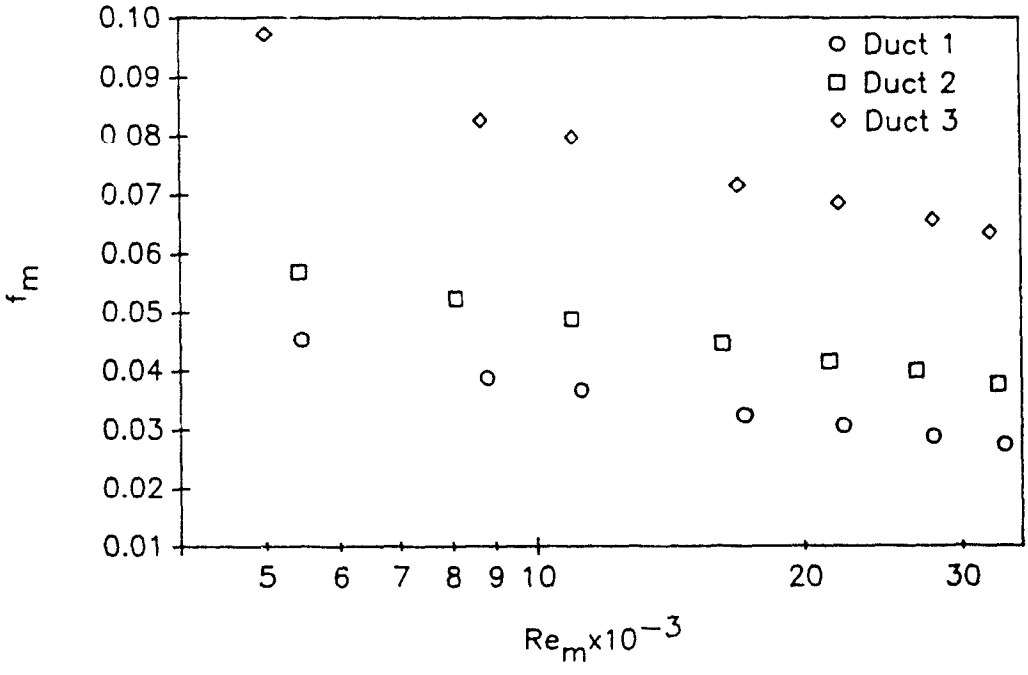

Figure 53: Module friction factor vs. Reynolds number (f_m vs. Re_m) results from the experimental investigations performed with Ducts 1, 2, and 3.

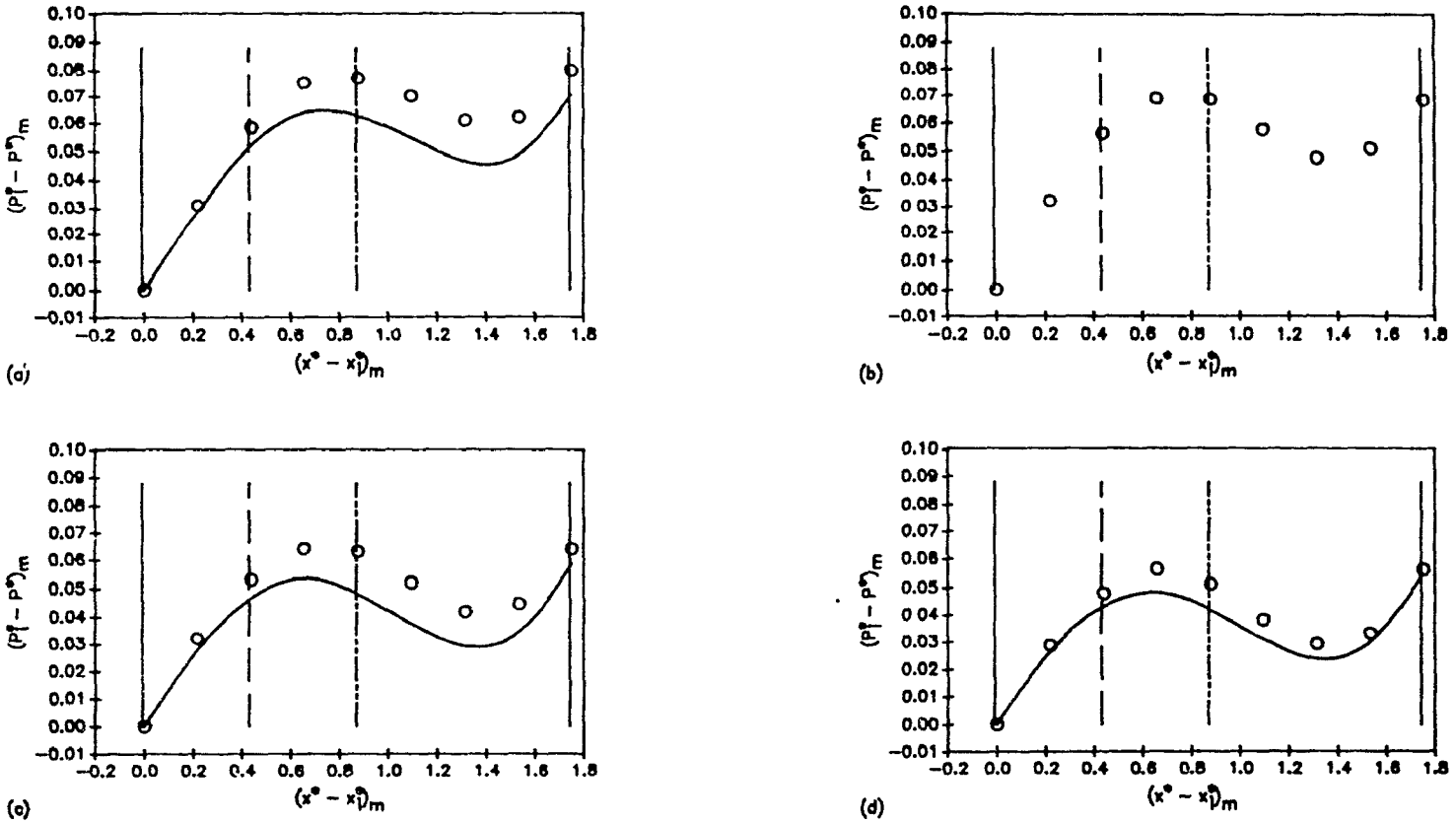

Figure 54: Intramodular time-mean wall static pressure distributions in Duct 1. For the experimental data (o) of each graph, the (i) run number, (ii) Re_m, and the maximum uncertainties in (iii) $(P^*_i - P^*)_m$ and (iv) $(x^* - x^*_i)_m$ values are, respectively:
(a) 1, 5.432×10^3, $\pm$ 6.8×10^{-3}, and $\pm$ 1.3×10^{-3};
(b) 2, 8.806×10^3, $\pm$ 3.6×10^{-3}, and $\pm$ 1.3×10^{-3};
(c) 3, 11.22×10^3, $\pm$ 2.2×10^{-3}, and $\pm$ 1.3×10^{-3}; and
(d) 4, 17.17×10^3, $\pm$ 1.3×10^{-3}, and $\pm$ 1.3×10^{-3}.
Numerical data (——) is shown for Runs 1,3, and 4: See Table 19 for Re_m values.

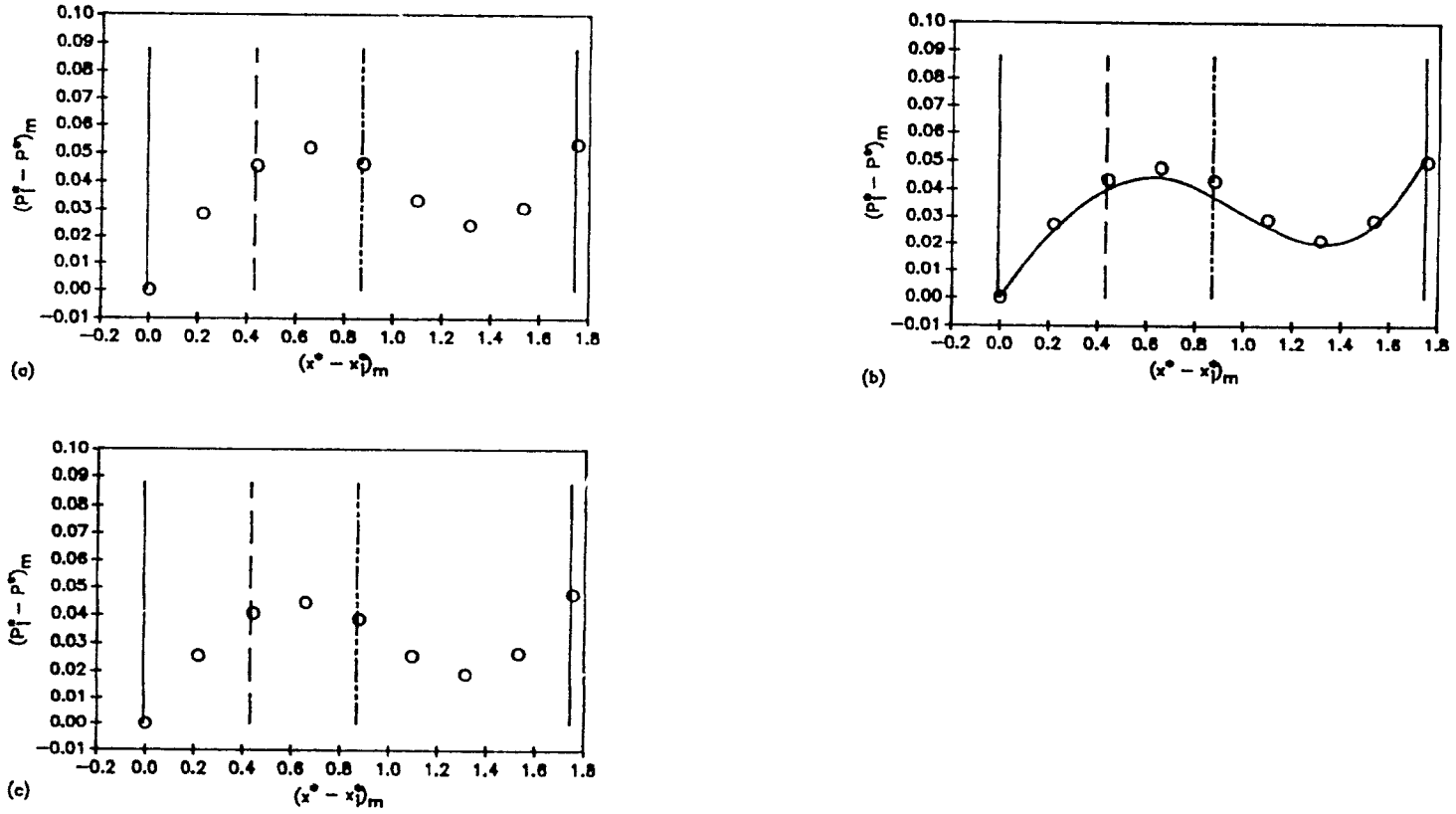

Figure 55: Intramodular time-mean wall static pressure distr'butions in Duct 1. For the experimental data (o) of each graph, the (i) run number, (ii) Re_m, and the maximum uncertainties in (iii) $(P^*_i - P^*)_m$ and (iv) $(x^* - x^*_i)_m$ values are, respectively:
(a) 5, 22.06×10^3, $\pm 1.5 \times 10^{-3}$, and $\pm 1.3 \times 10^{-3}$;
(b) 6, 27.81×10^3, $\pm 1.2 \times 10^{-3}$, and $\pm 1.3 \times 10^{-3}$; and
(c) 7, 33.49×10^3, $\pm 8.3 \times 10^{-4}$, and $\pm 1.3 \times 10^{-3}$.
Numerical data (——) is shown for Run 6: See Table 19 for Re_m value.

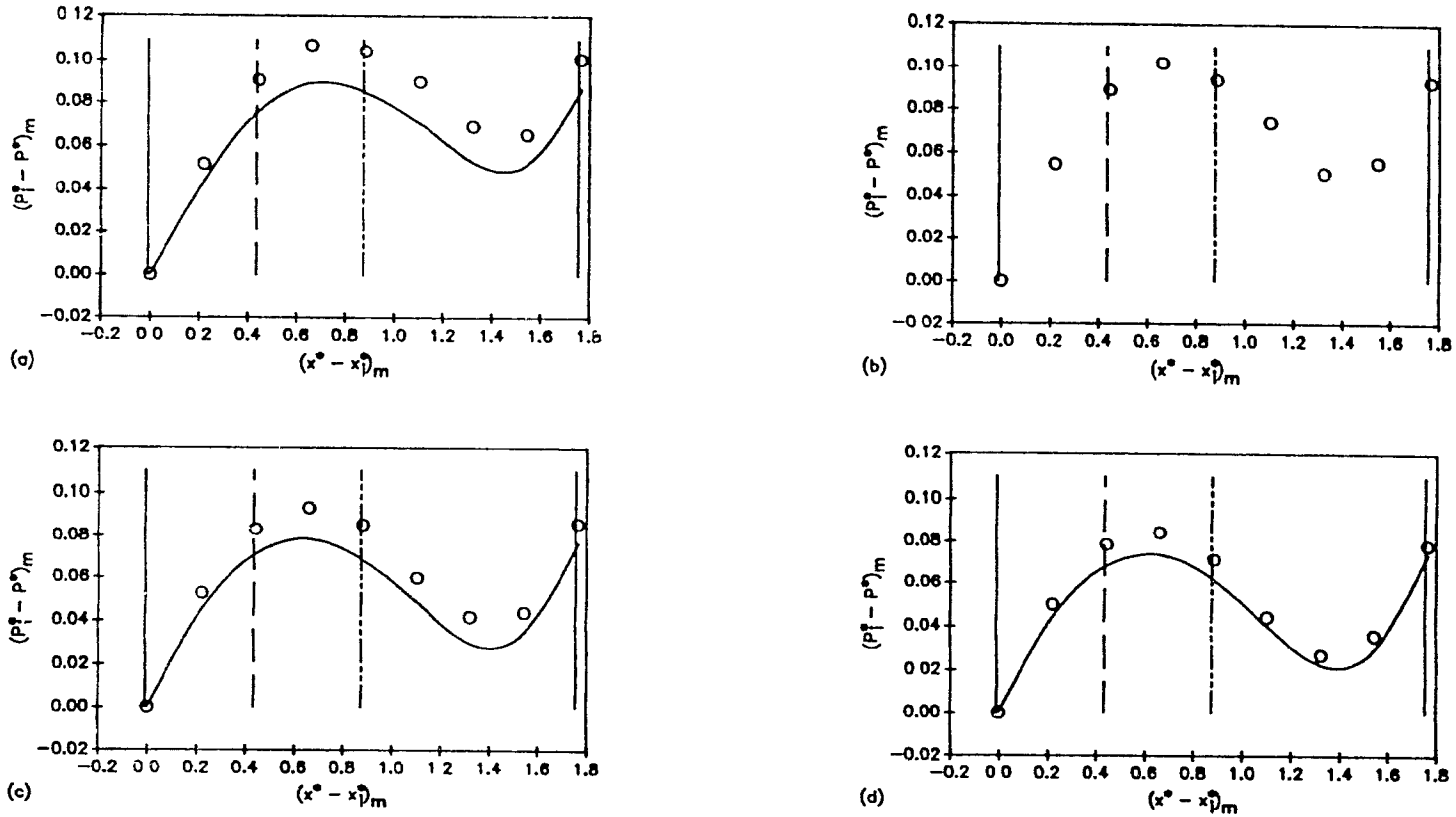

Figure 56: Intramodular time-mean wall static pressure distributions in Duct 2. For the experimental data (o) of each graph, the (i) run number, (ii) Re_m, and the maximum uncertainties in (iii) $(P^*_i - P^*)_m$ and (iv) $(x^* - x^*_i)_m$ values are, respectively:
(a) 1, 5.397×10^3, $\pm 7.7 \times 10^{-3}$, and $\pm 1.3 \times 10^{-3}$;
(b) 2, 8.087×10^3, $\pm 3.1 \times 10^{-3}$, and $\pm 1.3 \times 10^{-3}$;
(c) 3, 10.94×10^3, $\pm 2.4 \times 10^{-3}$, and $\pm 1.3 \times 10^{-3}$; and
(d) 4, 16.28×10^3, $\pm 1.4 \times 10^{-3}$, and $\pm 1.3 \times 10^{-3}$.
Numerical data (——) is shown for Runs 1,3, and 4: See Table 19 for Re_m values.

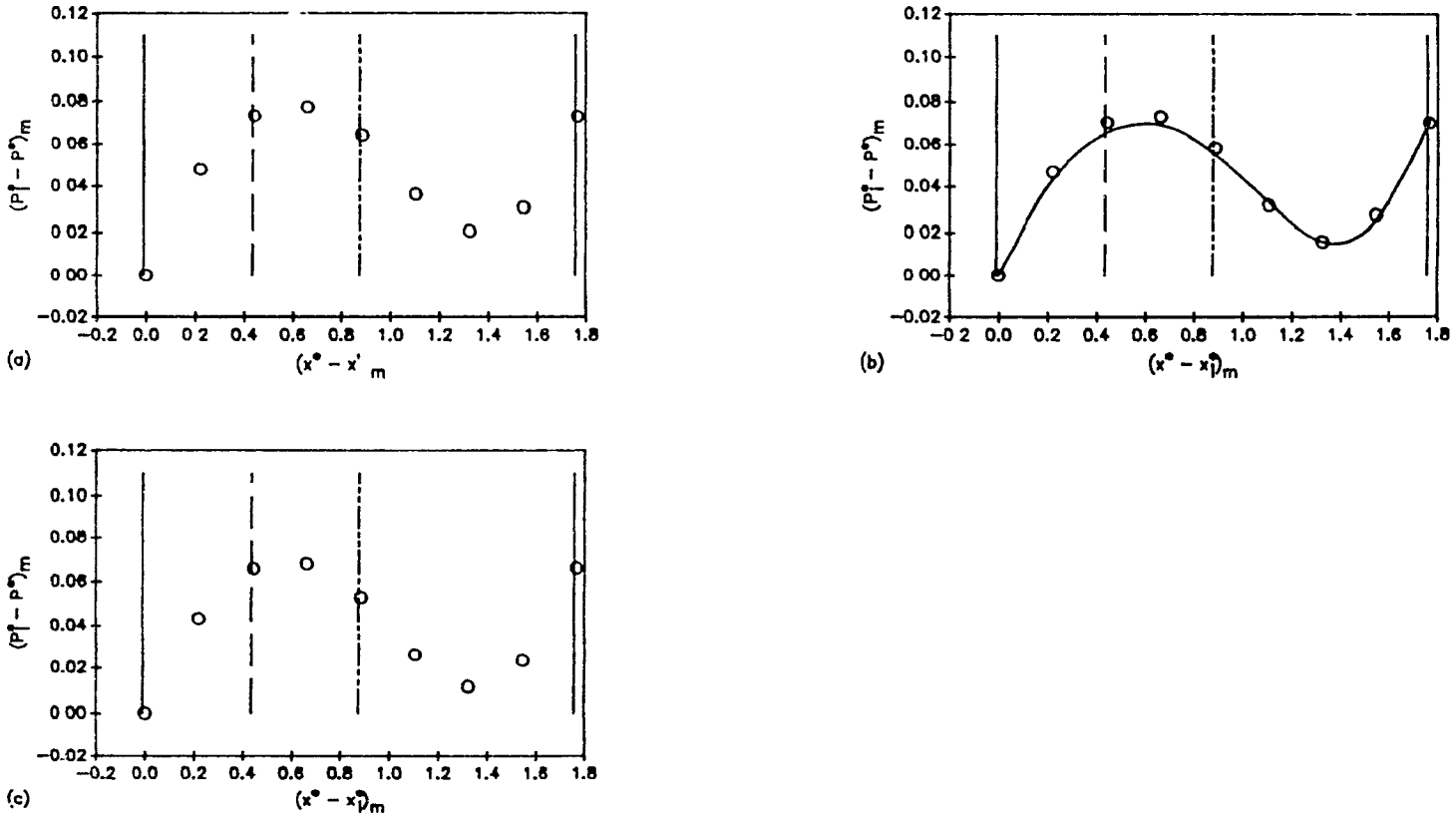

Figure 57: Intramodular time-mean wall static pressure distributions in Duct 2. For the experimental data (o) of each graph, the (i) run number, (ii) Re_m, and the maximum uncertainties in (iii) $(P^*_i - P^*)_m$ and (iv) $(x^* - x^*_i)_m$ values are, respectively:
(a) 5, 21.33×10^3, $\pm$ 1.2×10^{-3}, and $\pm$ 1.3×10^{-3};
(b) 6, 26.62×10^3, $\pm$ 1.2×10^{-3}, and $\pm$ 1.3×10^{-3}; and
(c) 7, 32.93×10^3, $\pm$ 1.0×10^{-3}, and $\pm$ 1.3×10^{-3}.
Numerical data (——) is shown for Run 6: See Table 19 for Re_m value.

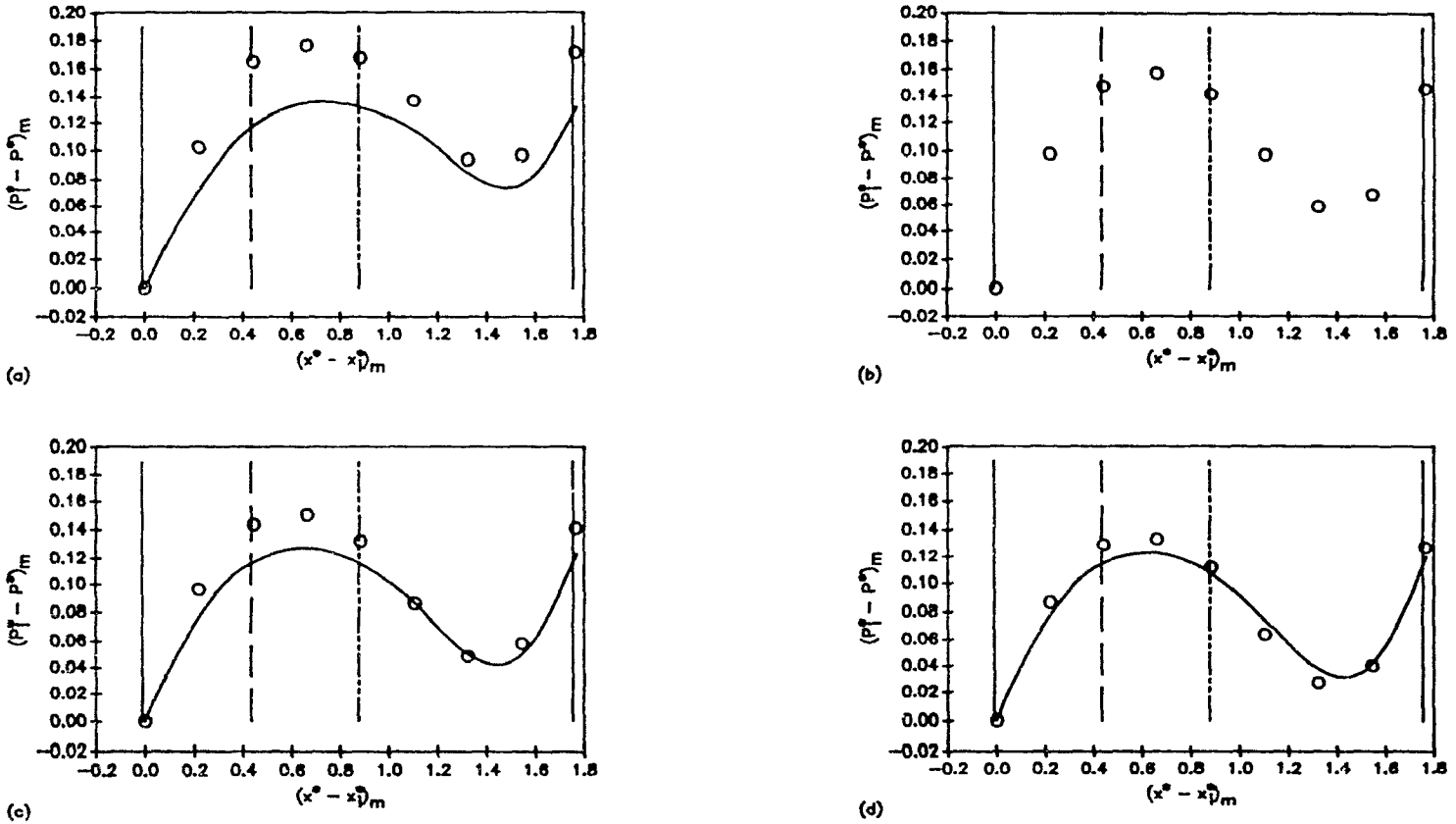

Figure 38: Intramodular time-mean wall static pressure distributions in Duct 3. For the experimental data (o) of each graph, the (i) run number, (ii) Re_m, and the maximum uncertainties in (iii) $(P^* - P^*)_m$ and (iv) $(x^* - x^*_t)_m$ values are, respectively:
(a) 1, 4.997×10^3, $\pm 1.5 \times 10^{-2}$, and $\pm 1.3 \times 10^{-3}$;
(b) 2, 8.682×10^3, $\pm 3.2 \times 10^{-3}$, and $\pm 1.3 \times 10^{-3}$;
(c) 3, 10.98×10^3, $\pm 2.9 \times 10^{-3}$, and $\pm 1.3 \times 10^{-3}$; and
(d) 4, 16.93×10^3, $\pm 2.1 \times 10^{-3}$, and $\pm 1.3 \times 10^{-3}$.
Numerical data (——) is shown for Runs 1,3, and 4: See Table 19 for Re_m values.

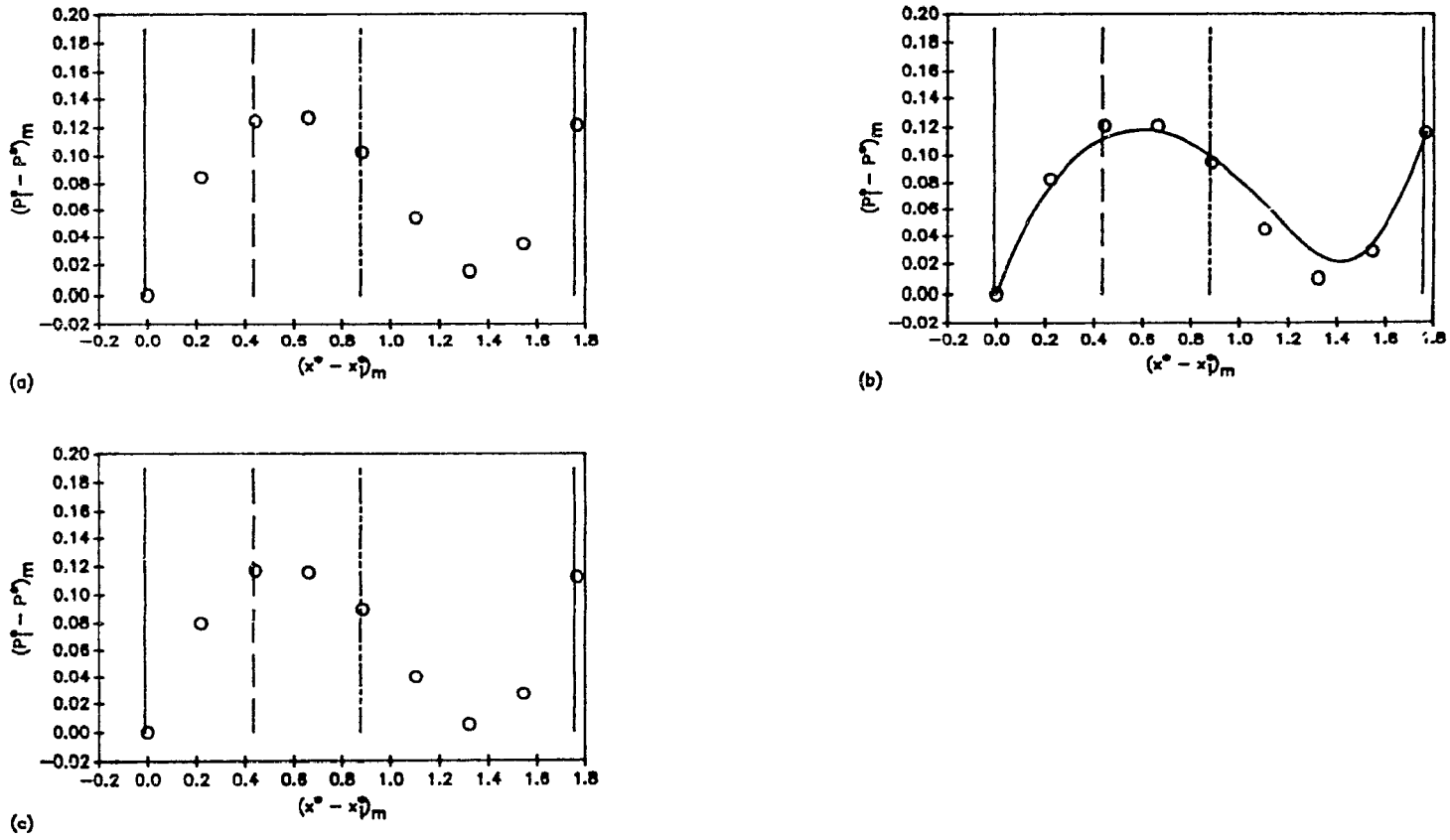

Figure 59: Intramodular time-mean wall static pressure distributions in Duct 3. For the experimental data (o) of each graph, the (i) run number, (ii) Re_m, and the maximum uncertainties in (iii) $(P^*_i - P^*)_m$ and (iv) $(x^* - x^*_i)_m$ values are, respectively:
(a) 5, 21.85×10^3, $\pm$ 1.9×10^{-3}, and $\pm$ 1.3×10^{-3};
(b) 6, 27.84×10^3, $\pm$ 1.8×10^{-3}, and $\pm$ 1.3×10^{-3}; and
(c) 7, 32.32×10^3, $\pm$ 1.6×10^{-3}, and $\pm$ 1.3×10^{-3}.
Numerical data (——) is shown for Run 6: See Table 19 for Re_m value.

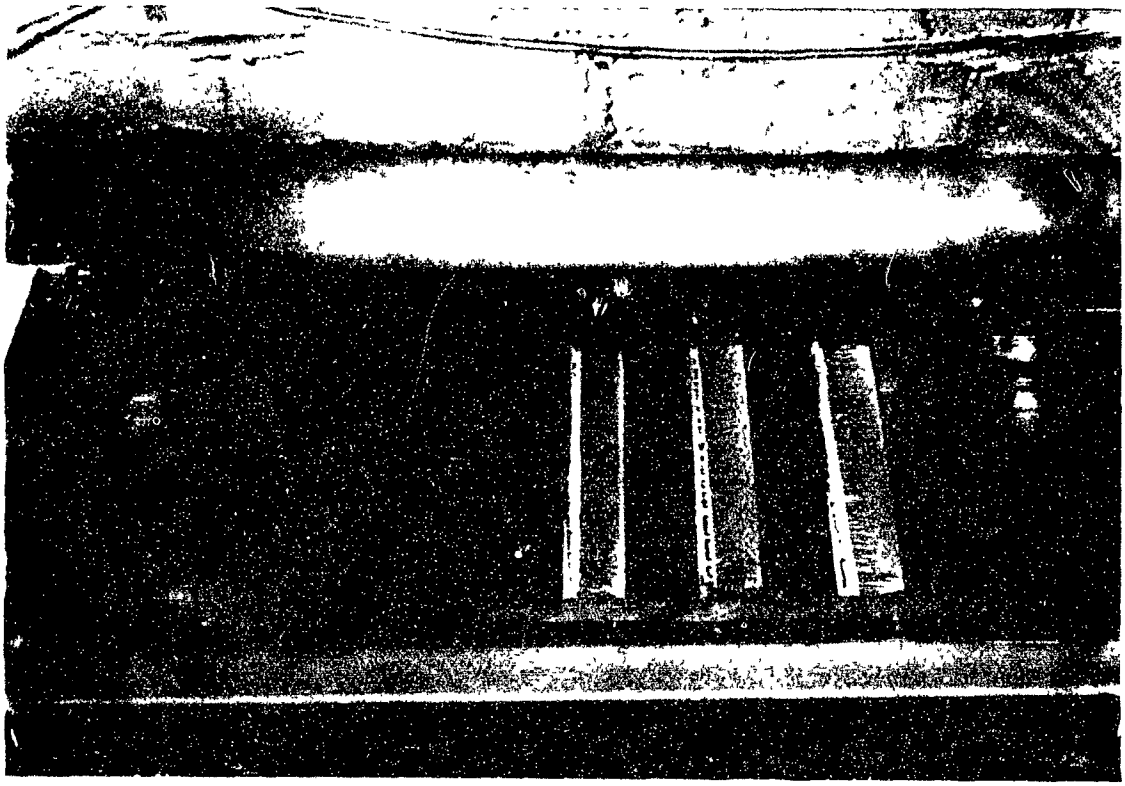

Figure 60: Surface streamline patterns on plates in the fourth, fifth and sixth periodic modules downstream of the start of the flow visualization section in Duct 2 for Run 2, $Re_m = 8.087 \times 10^3$: The main-flow direction is from right to left.

Figure 61: Plate-surface streamline pattern for periodic fully developed turbulent flow in Duct 1 with $Re_m = 5.432 \times 10^3$: The main-flow direction is from top to bottom.

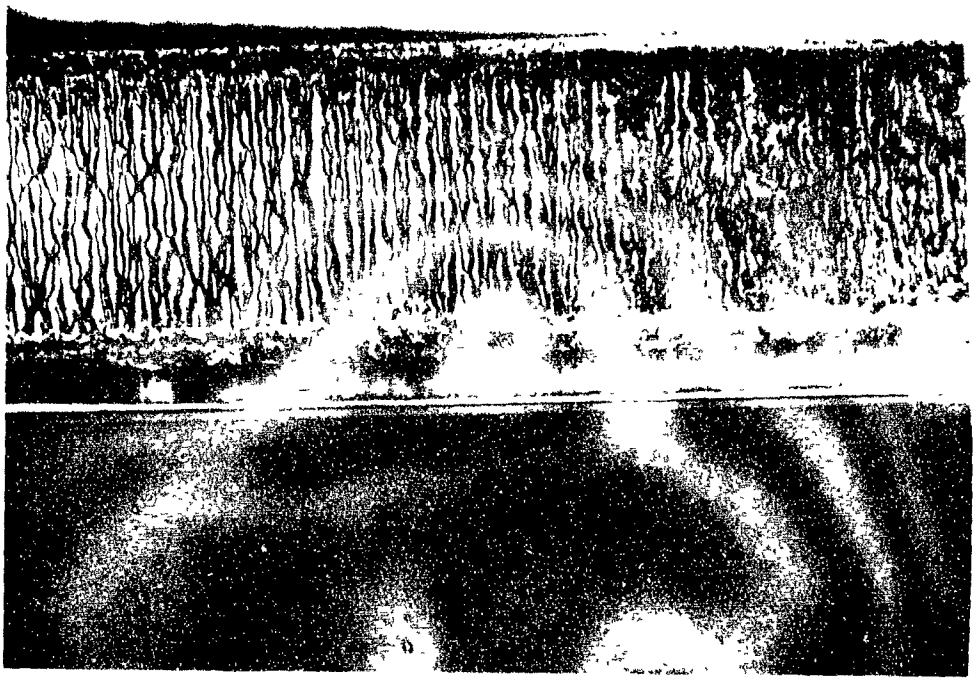

Figure 62: Plate-surface streamline pattern for periodic fully developed turbulent flow in Duct 1 with $Re_m = 8.806 \times 10^3$: The main-flow direction is from top to bottom.

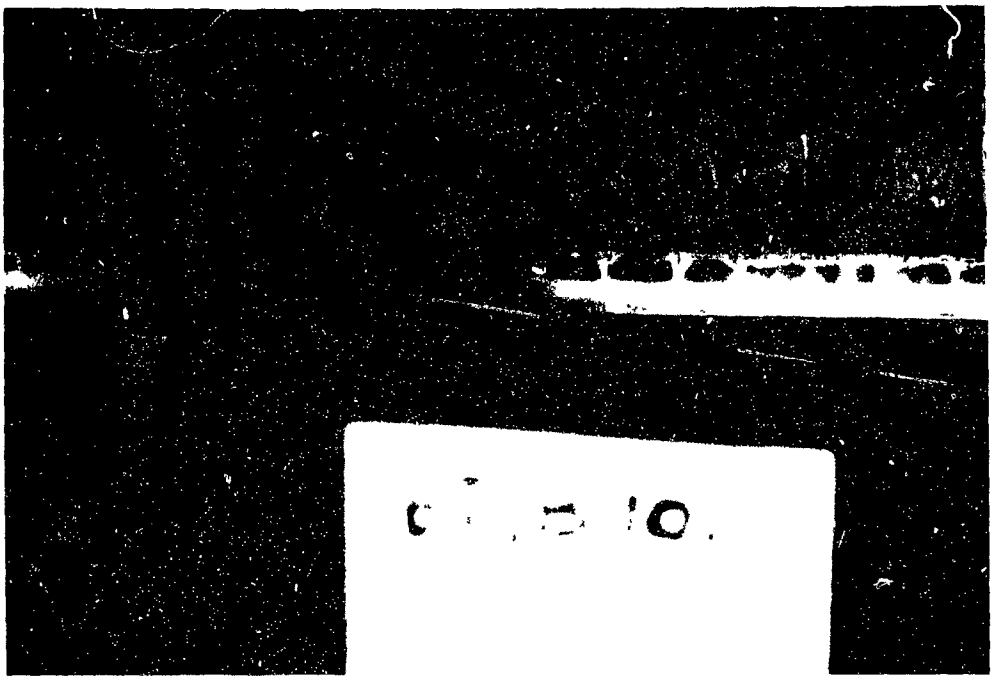

Figure 63: Plate-surface streamline pattern for periodic fully developed turbulent flow in Duct 1 with $Re_m = 11.22 \times 10^3$: The main-flow direction is from top to bottom.

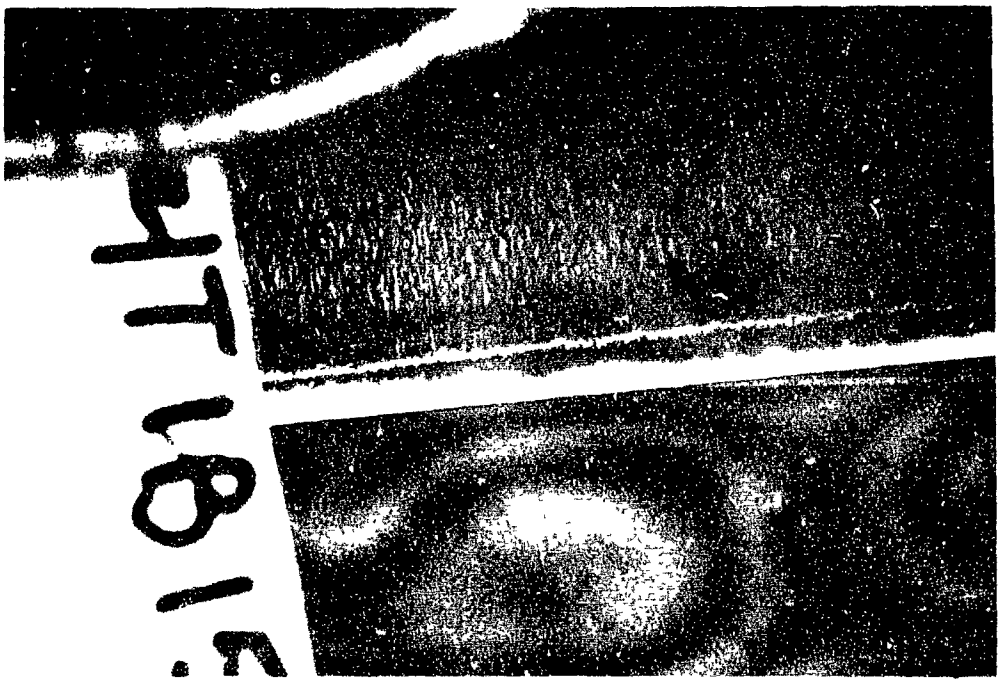

Figure 64: Plate-surface streamline pattern for periodic fully developed turbulent flow in Duct 1 with $Re_m = 17.17 \times 10^3$: The main-flow direction is from top to bottom.

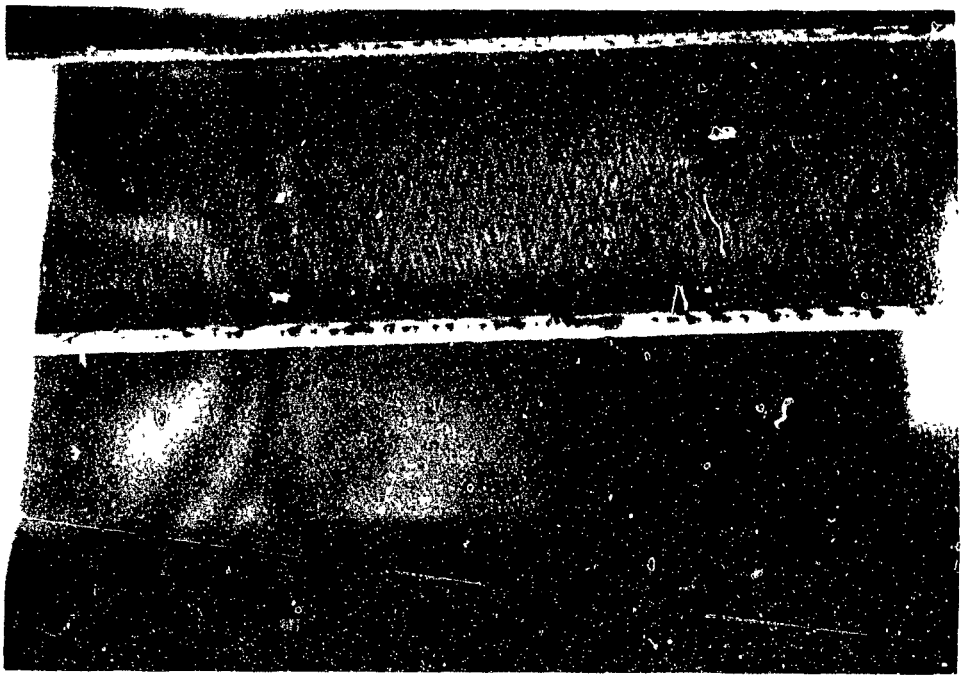

Figure 65: Plate-surface streamline pattern for periodic fully developed turbulent flow in Duct 1 with $Re_m = 22.06 \times 10^3$: The main-flow direction is from top to bottom.

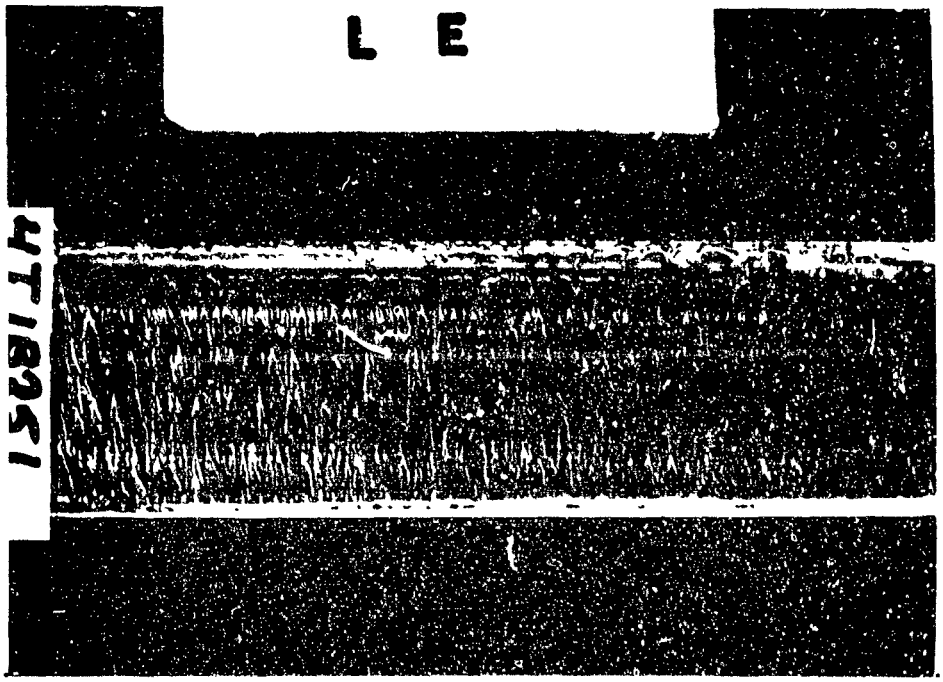

Figure 66: Plate-surface streamline pattern for periodic fully developed turbulent flow in Duct 1 with $Re_m = 27.81 \times 10^3$. The main-flow direction is from top to bottom.

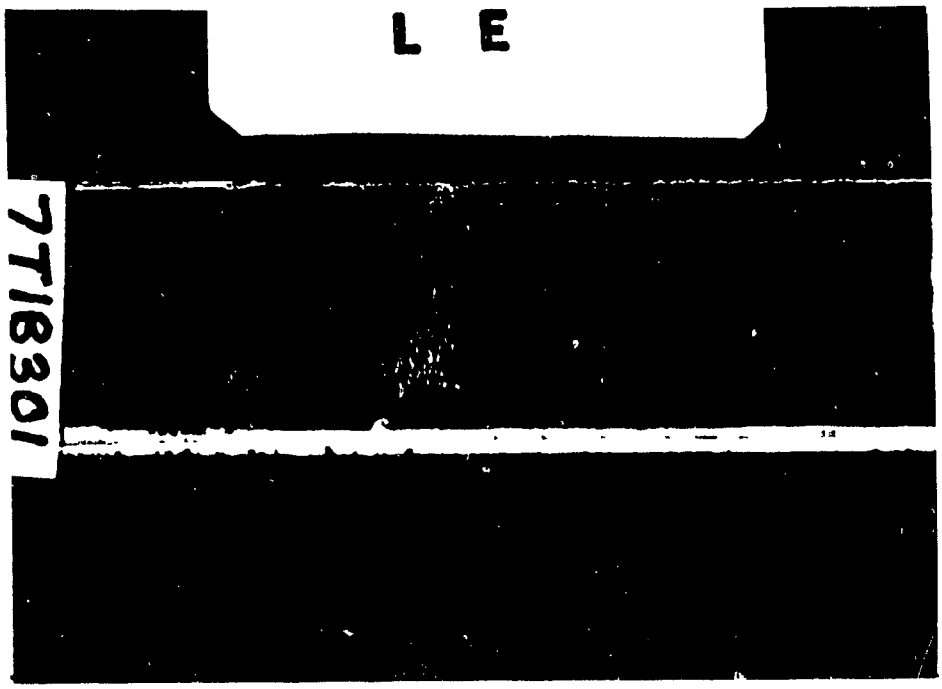

Figure 67: Plate-surface streamline pattern for periodic fully developed turbulent flow in Duct 1 with $Re_m = 33.49 \times 10^3$: The main-flow direction is from top to bottom.

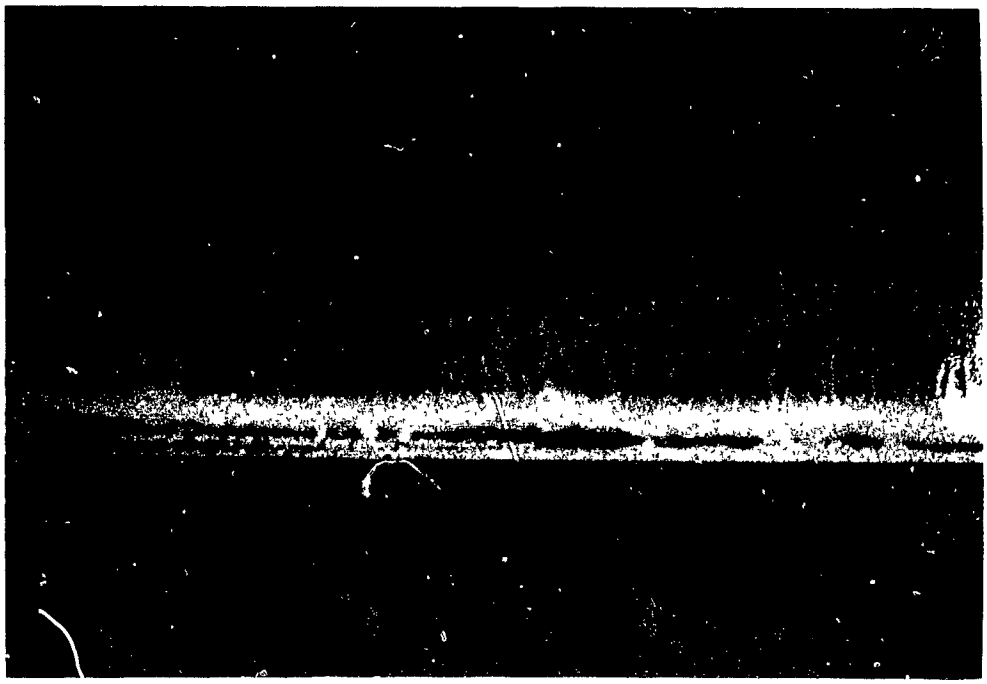

Figure 68: Plate-surface streamline pattern for periodic fully developed turbulent flow in Duct 2 with $Re_m = 5.397 \times 10^3$: The main-flow direction is from top to bottom.

Figure 69: Plate-surface streamline pattern for periodic fully developed turbulent flow in Duct 2 with $Re_m = 8.087 \times 10^3$: The main-flow direction is from top to bottom.

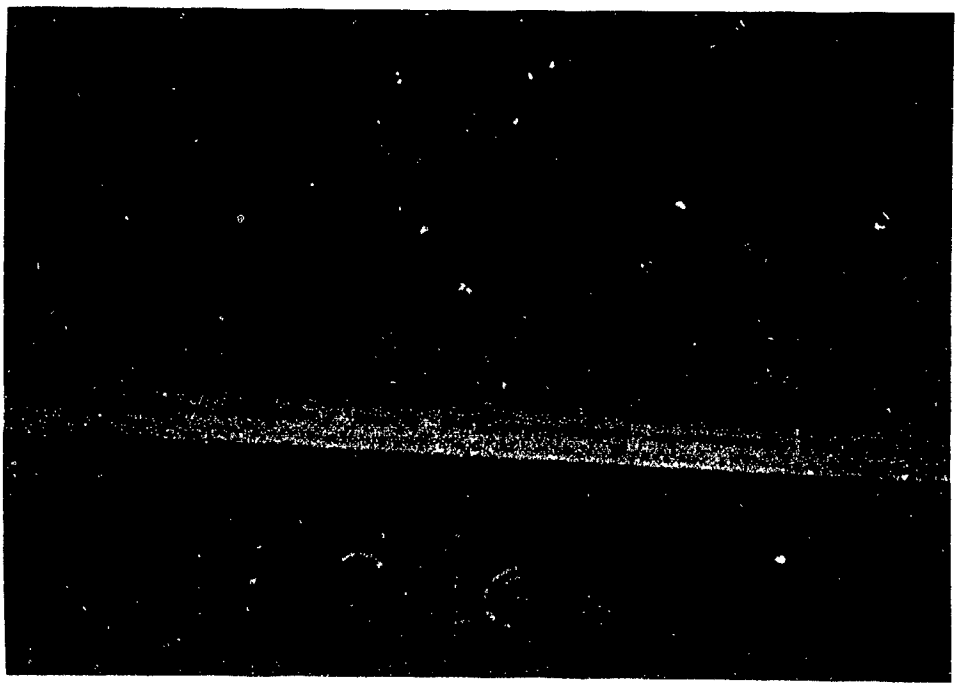

Figure 70: Plate-surface streamline pattern for periodic fully developed turbulent flow in Duct 2 with $Re_m = 10.94 \times 10^3$: The main-flow direction is from top to bottom.

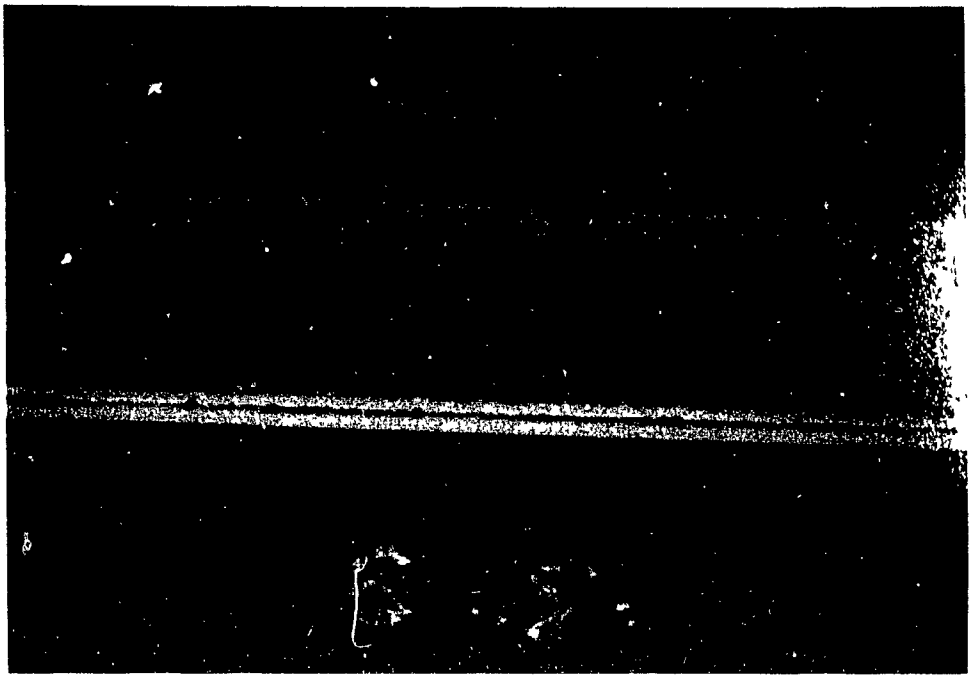

Figure 71: Plate-surface streamline pattern for periodic fully developed turbulent flow in Duct 2 with Re_m = 16.28x10^3. The main-flow direction is from top to bottom.

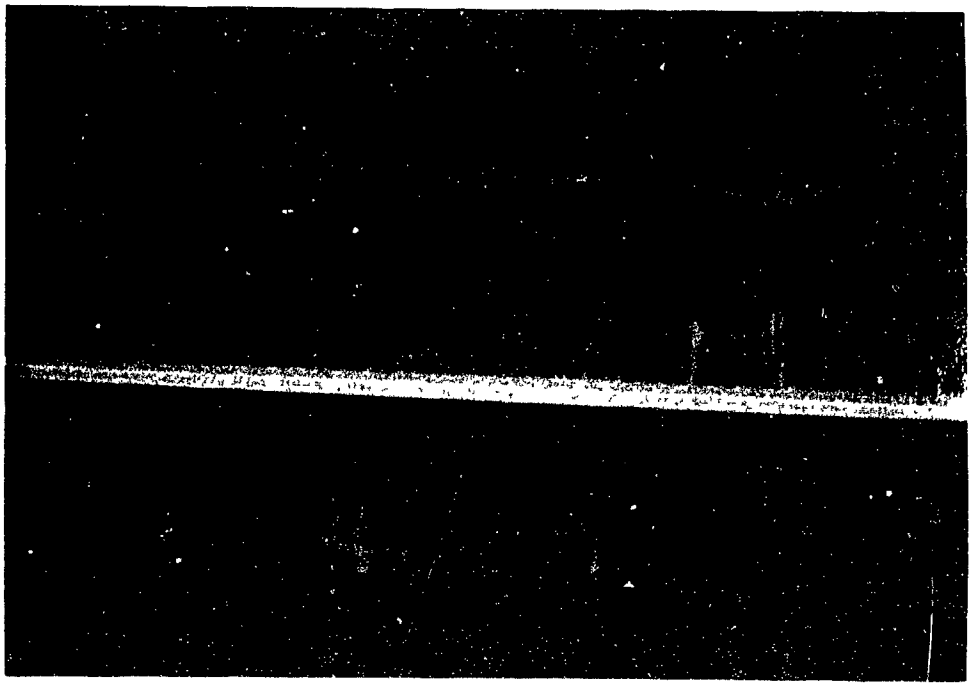

Figure 72: Plate-surface streamline pattern for periodic fully developed turbulent flow in Duct 2 with Re_m = 21.33x10^3: The main-flow direction is from top to bottom.

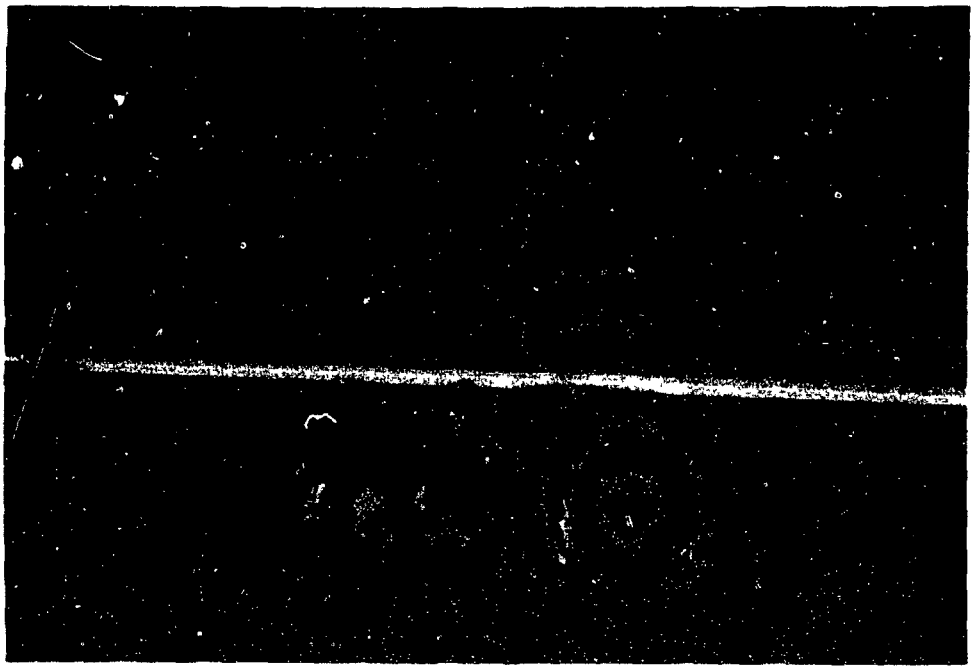

Figure 73: Plate-surface streamline pattern for periodic fully developed turbulent flow in Duct 2 with $Re_m = 26.62 \times 10^3$: The main-flow direction is from top to bottom.

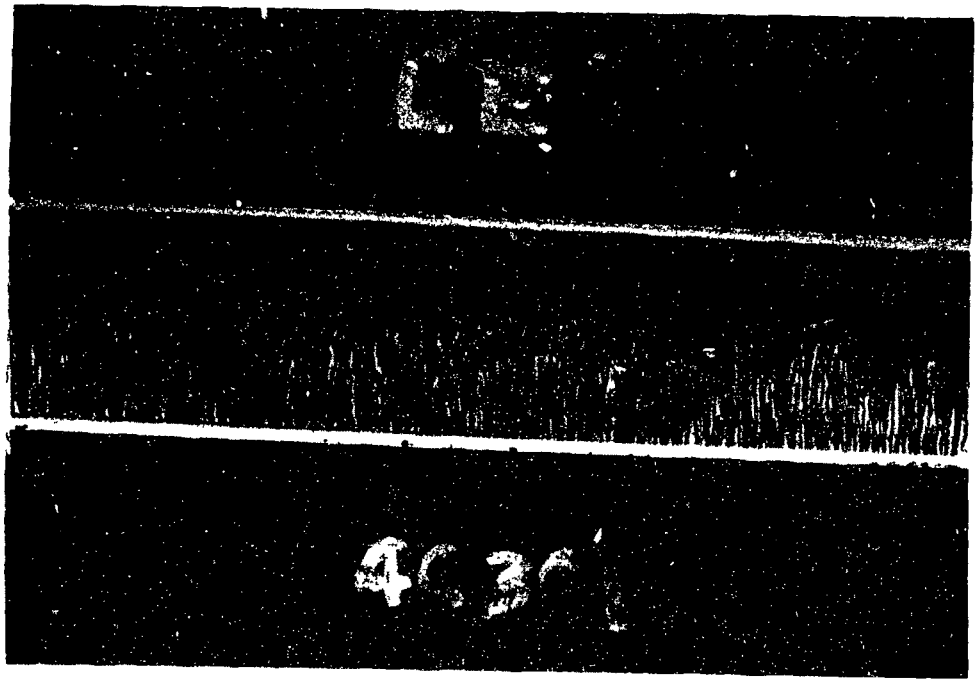

Figure 74: Plate-surface streamline pattern for periodic fully developed turbulent flow in Duct 2 with $Re_m = 32.93 \times 10^3$: The main-flow direction is from top to bottom.

Figure 75: Plate-surface streamline pattern for periodic fully developed turbulent flow in Duct 3 with $Re_m = 4.997 \times 10^3$: The main-flow direction is from top to bottom.

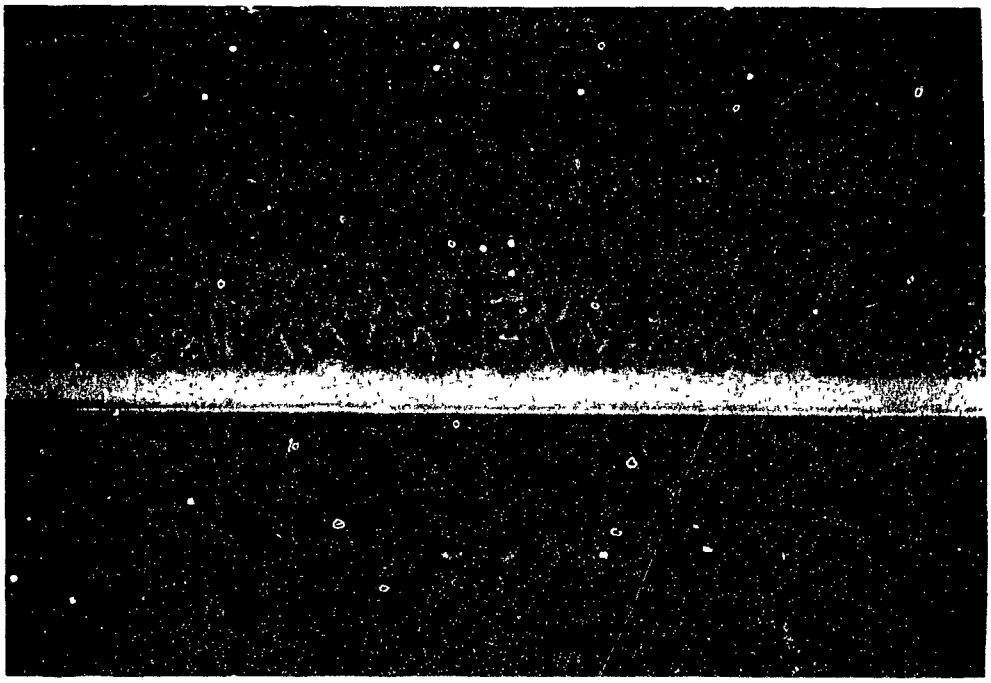

Figure 76: Plate-surface streamline pattern for periodic fully developed turbulent flow in Duct 3 with $Re_m = 8.682 \times 10^3$: The main-flow direction is from top to bottom.

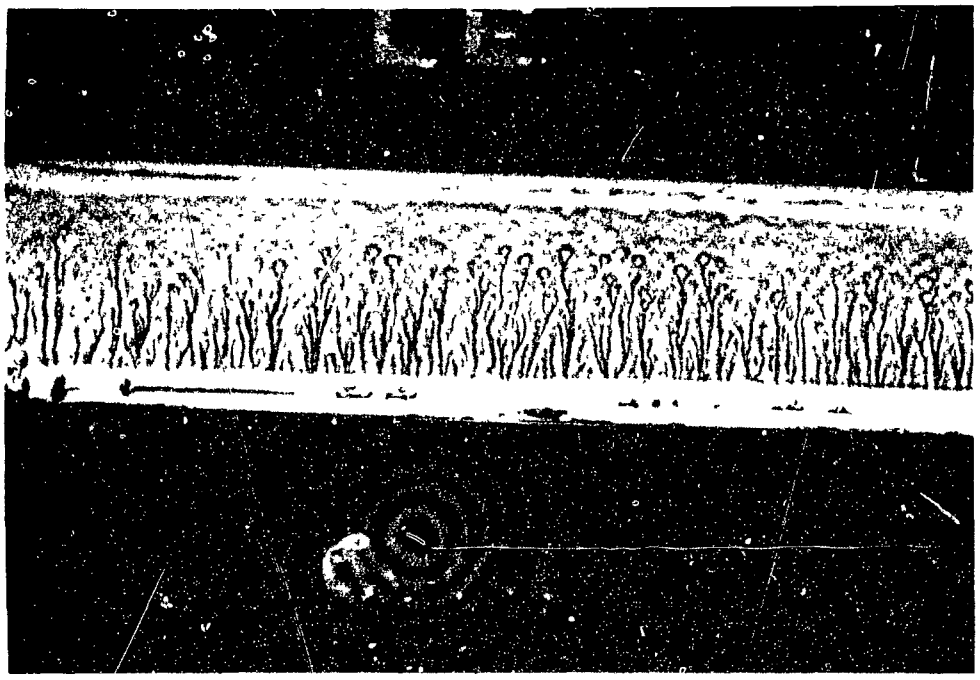

Figure 77: Plate-surface streamline pattern for periodic fully developed turbulent flow in Duct 3 with $Re_m = 10.98 \times 10^3$: The main-flow direction is from top to bottom.

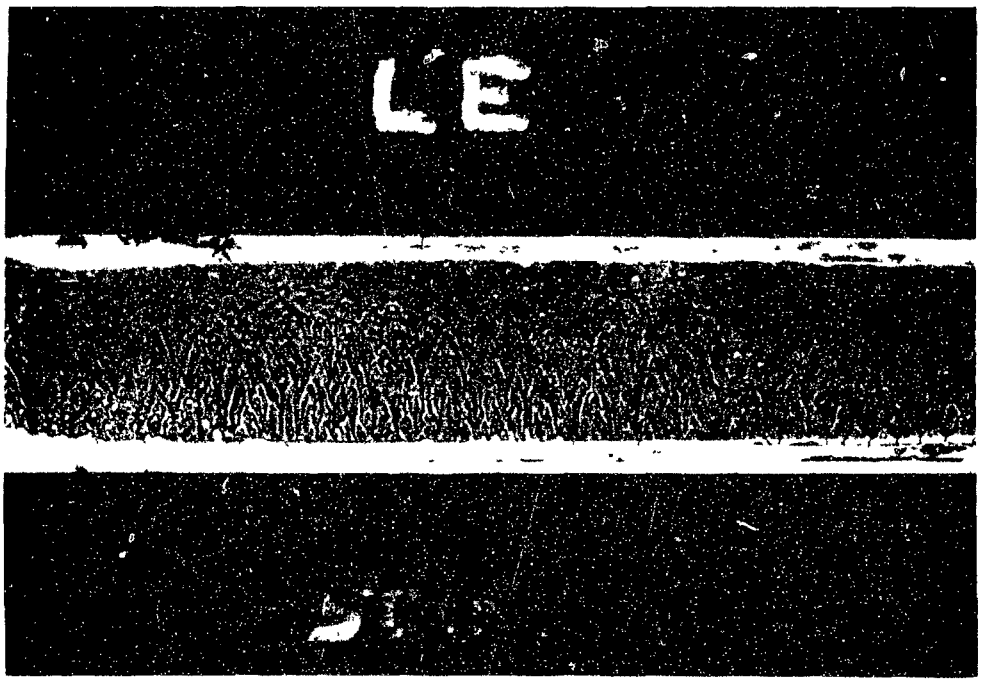

Figure 78: Plate-surface streamline pattern for periodic fully developed turbulent flow in Duct 3 with $Re_m = 16.93 \times 10^3$: The main-flow direction is from top to bottom.

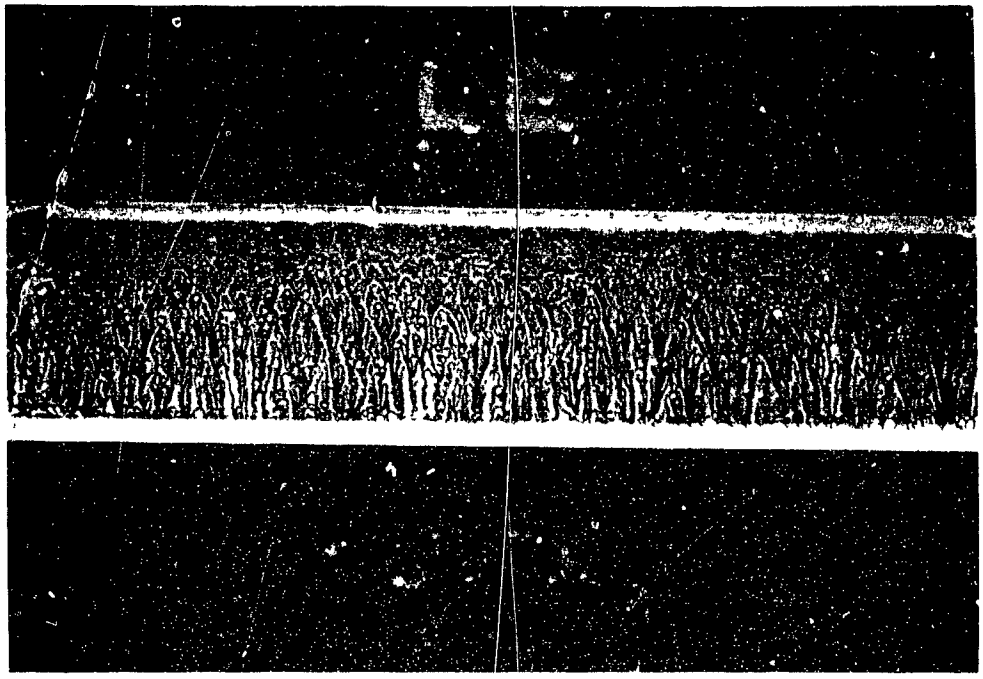

Figure 79: Plate-surface streamline pattern for periodic fully developed turbulent flow in Duct 3 with $Re_m = 21.85 \times 10^3$: The main-flow direction is from top to bottom.

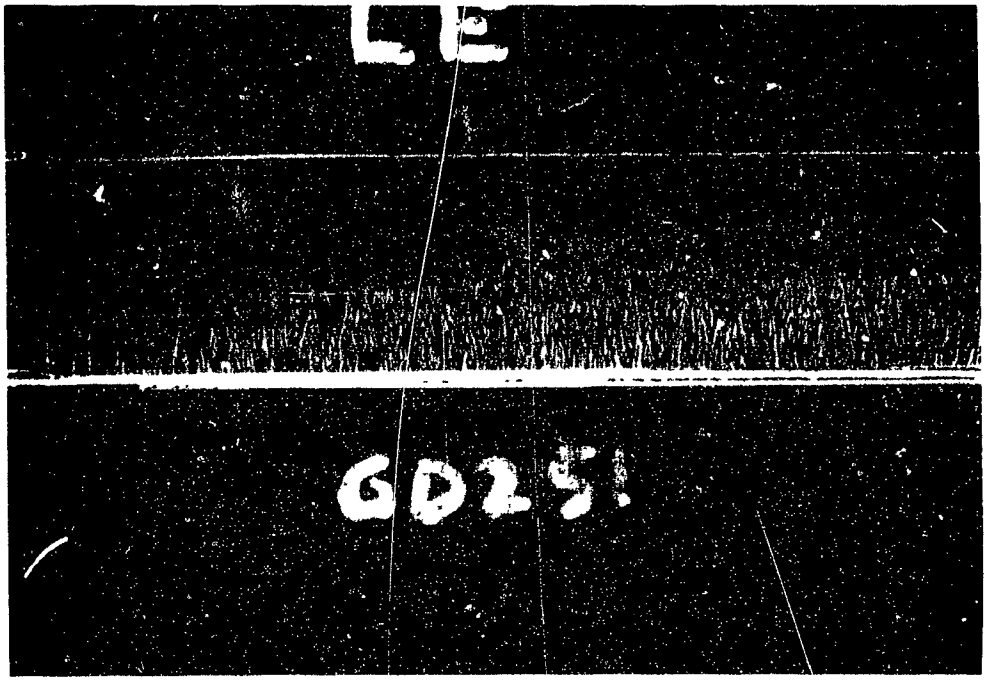

Figure 80: Plate-surface streamline pattern for periodic fully developed turbulent flow in Duct 3 with $Re_m = 27.84 \times 10^3$: The main-flow direction is from top to bottom.

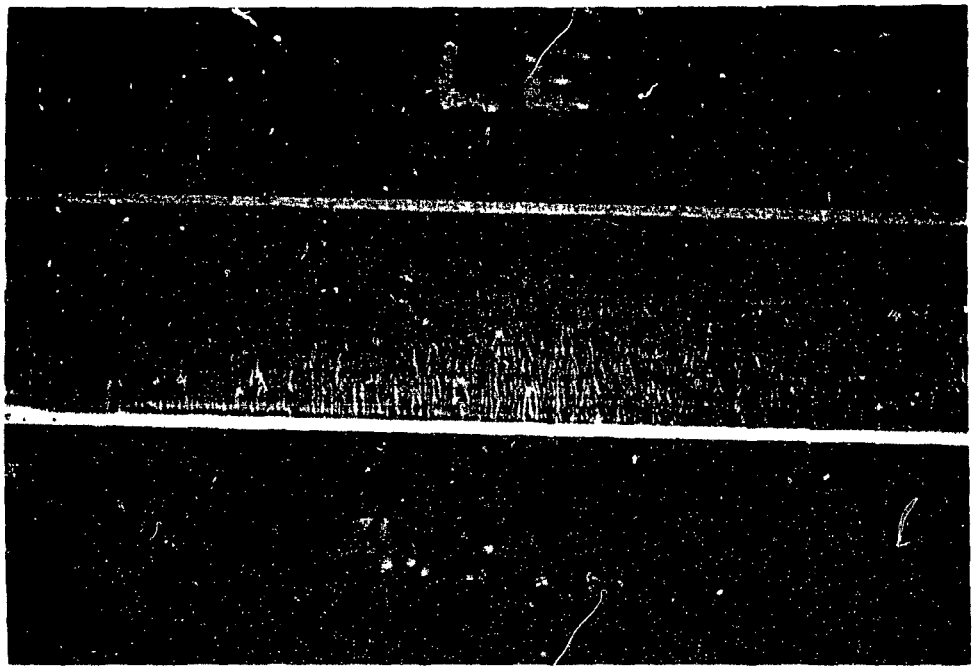

Figure 81: Plate-surface streamline pattern for periodic fully developed turbulent flow in Duct 3 with $Re_m = 32.32 \times 10^3$: The main-flow direction is from top to bottom.

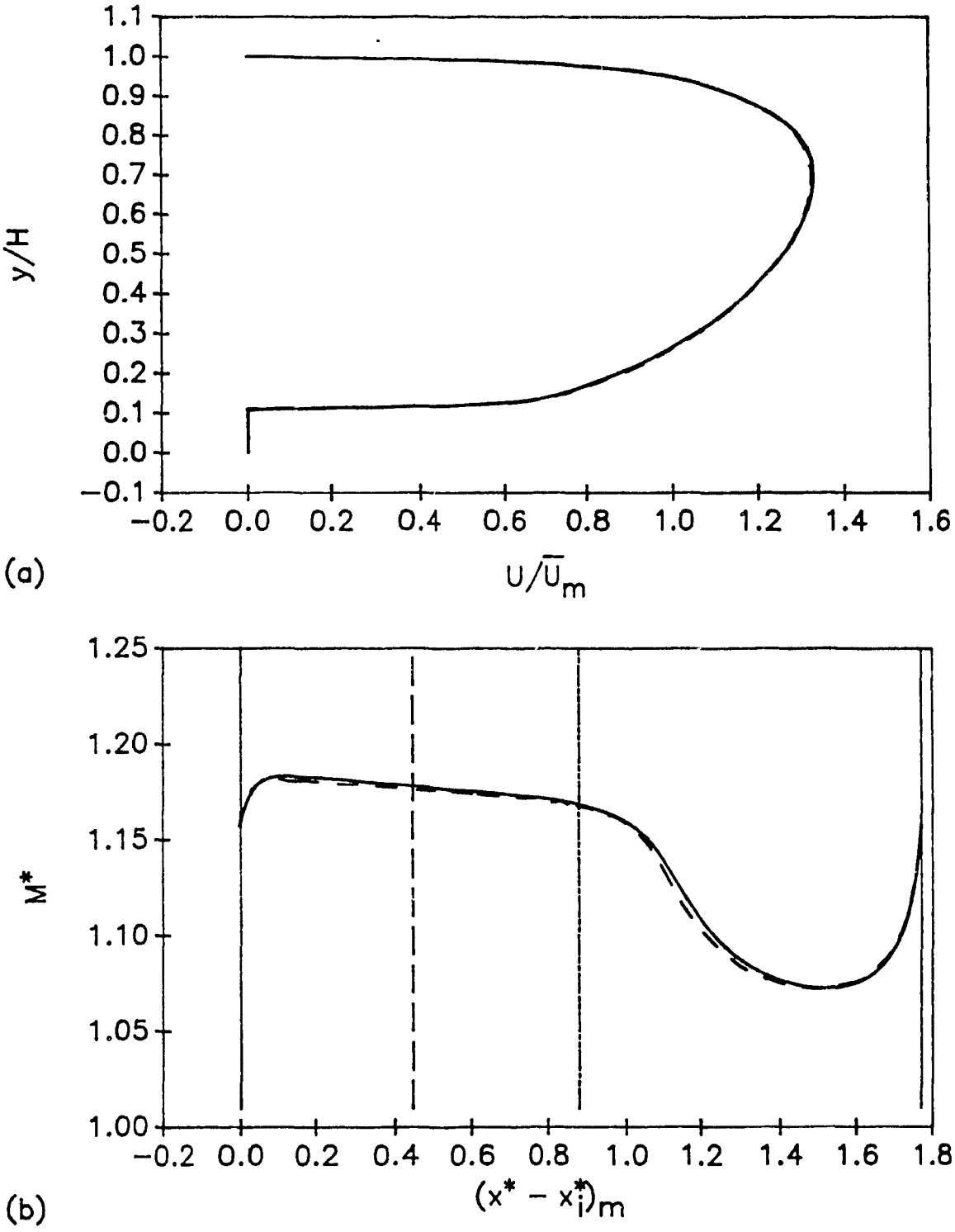

Figure 82: Comparison of nondimensional results obtained from numerical simulations using x-y grids of 146x201 (———) with uniform spacing, and 72x100 (— — —) with nonuniform spacing, for the maximum flow rate in Duct 3: (a) U profiles at $(x^*-x_i^*)_m = 0.8854$; and (b) M^* profiles.

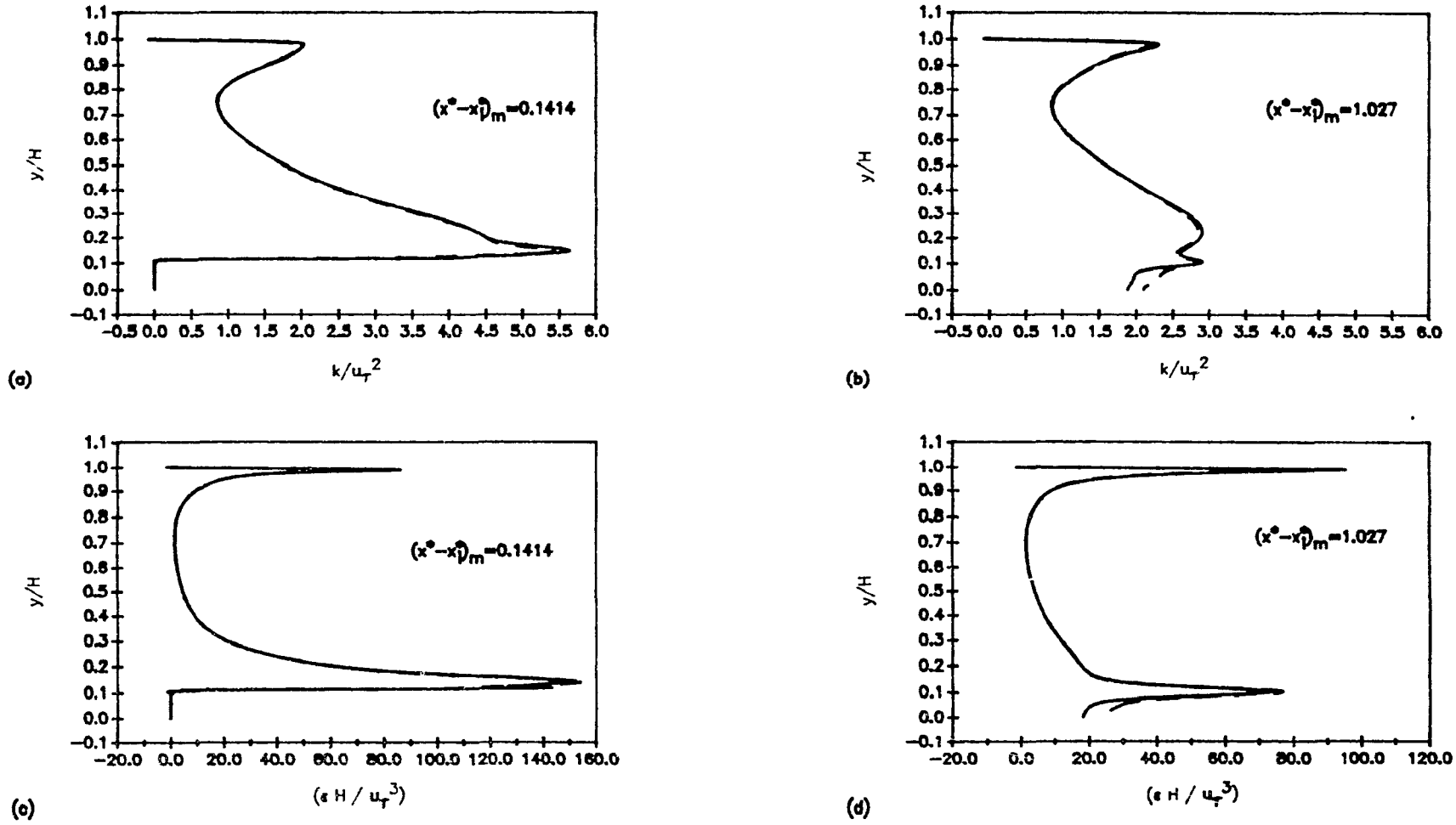

Figure 83: Comparison of nondimensional results obtained from numerical simulations using x-y grids of 146x201 (———) with uniform spacing, and 72x100 (— — —) with nonuniform spacing, for the maximum flow rate in Duct 3: k profiles at $(x^* - x^*_i)_m$ = (a) 0.1414 and (b) 1.027; and ϵ profiles at $(x^* - x^*_i)_m$ = (c) 0.1414 and (d) 1.027.

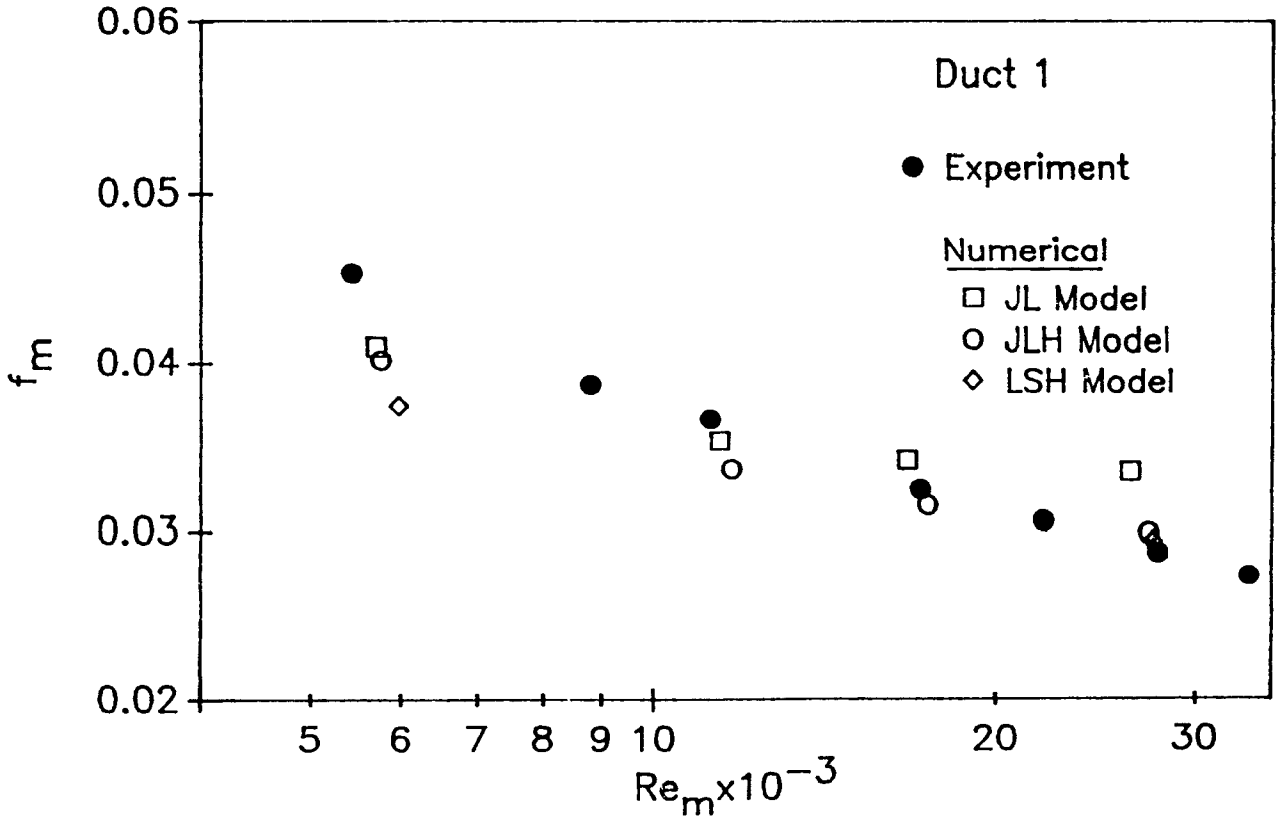

Figure 84: Module friction factor vs. Reynolds number values for Duct 1: Comparison of results from experiments, and computations with the JL, JLH, and LSH versions of the k-ε turbulence model.

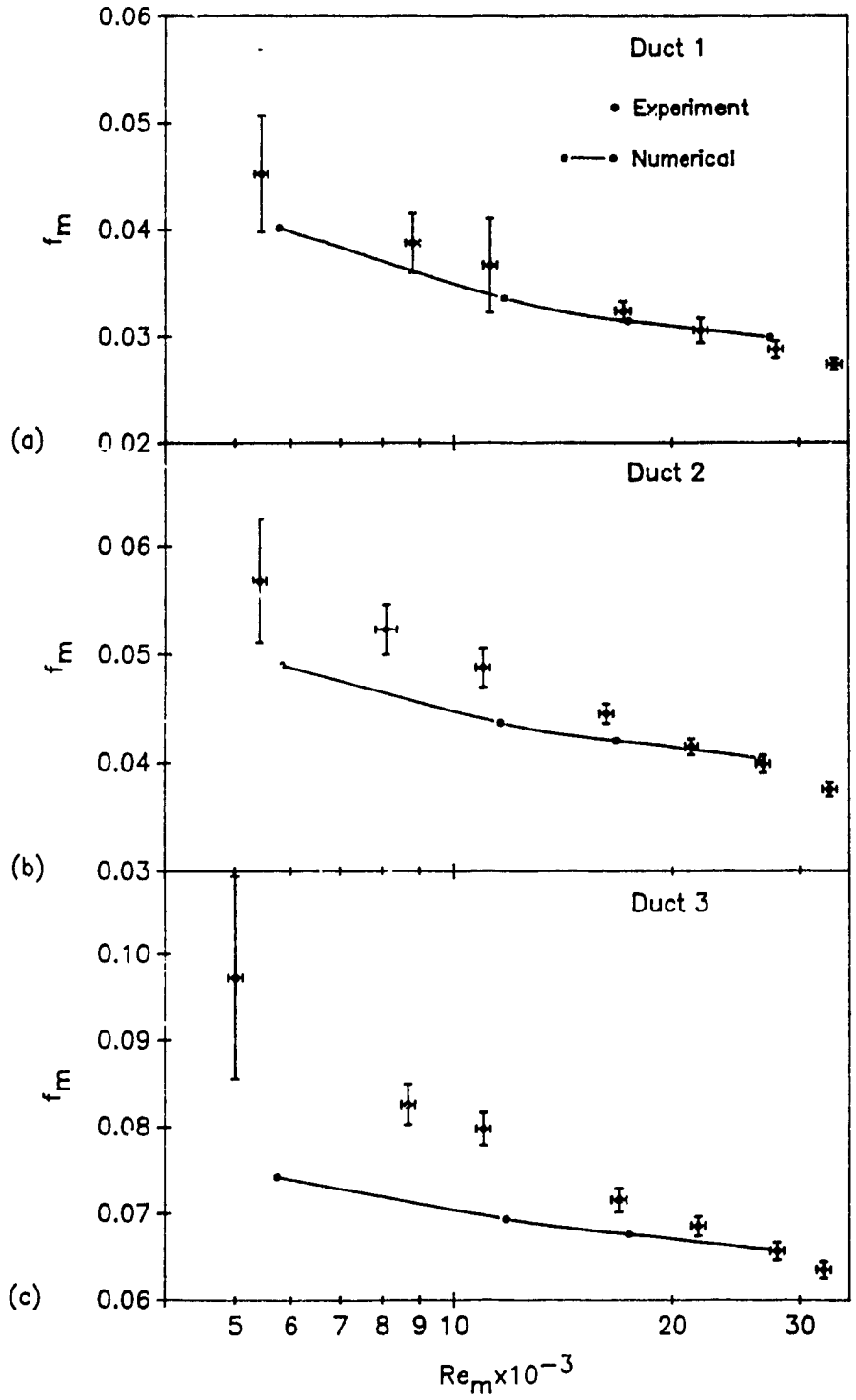

Figure 85: Module friction factor vs. Reynolds number results from the experimental (●) and the numerical (○——○) investigations: (a) Duct 1; (b) Duct 2; and (c) Duct 3. The uncertainty in the experimental data is shown by the error bars.

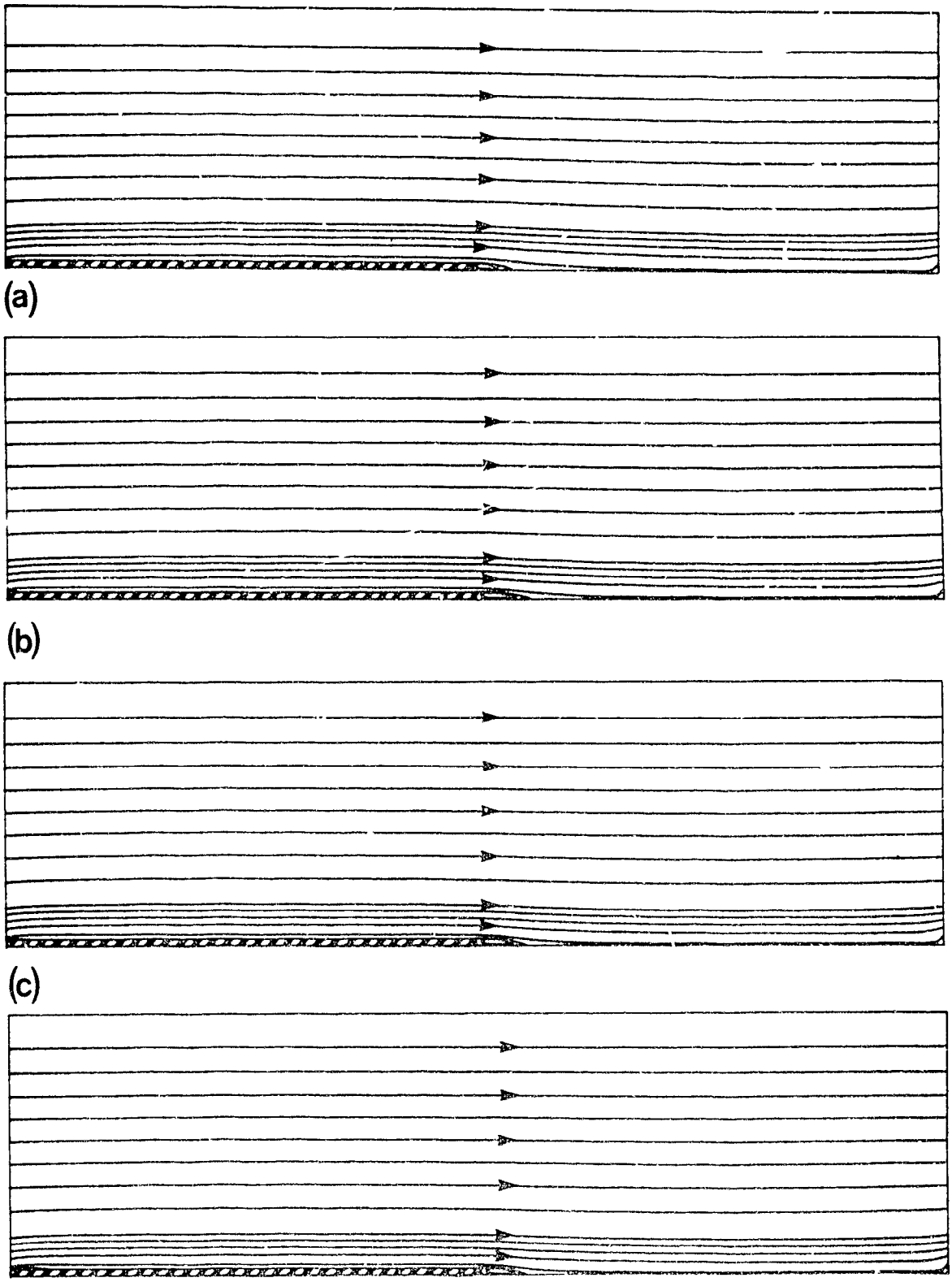

Figure 86. Streamline plots for Duct 1: (a) Run 1, $Re_m = 5.764 \times 10^3$; (b) Run 3, $Re_m = 11.72 \times 10^3$; (c) Run 4, $Re_m = 17.42 \times 10^3$; and (d) Run 6, $Re_m = 27.27 \times 10^3$. (Diagrams are not to scale, true horizontal:vertical dimensions = 4:1.)

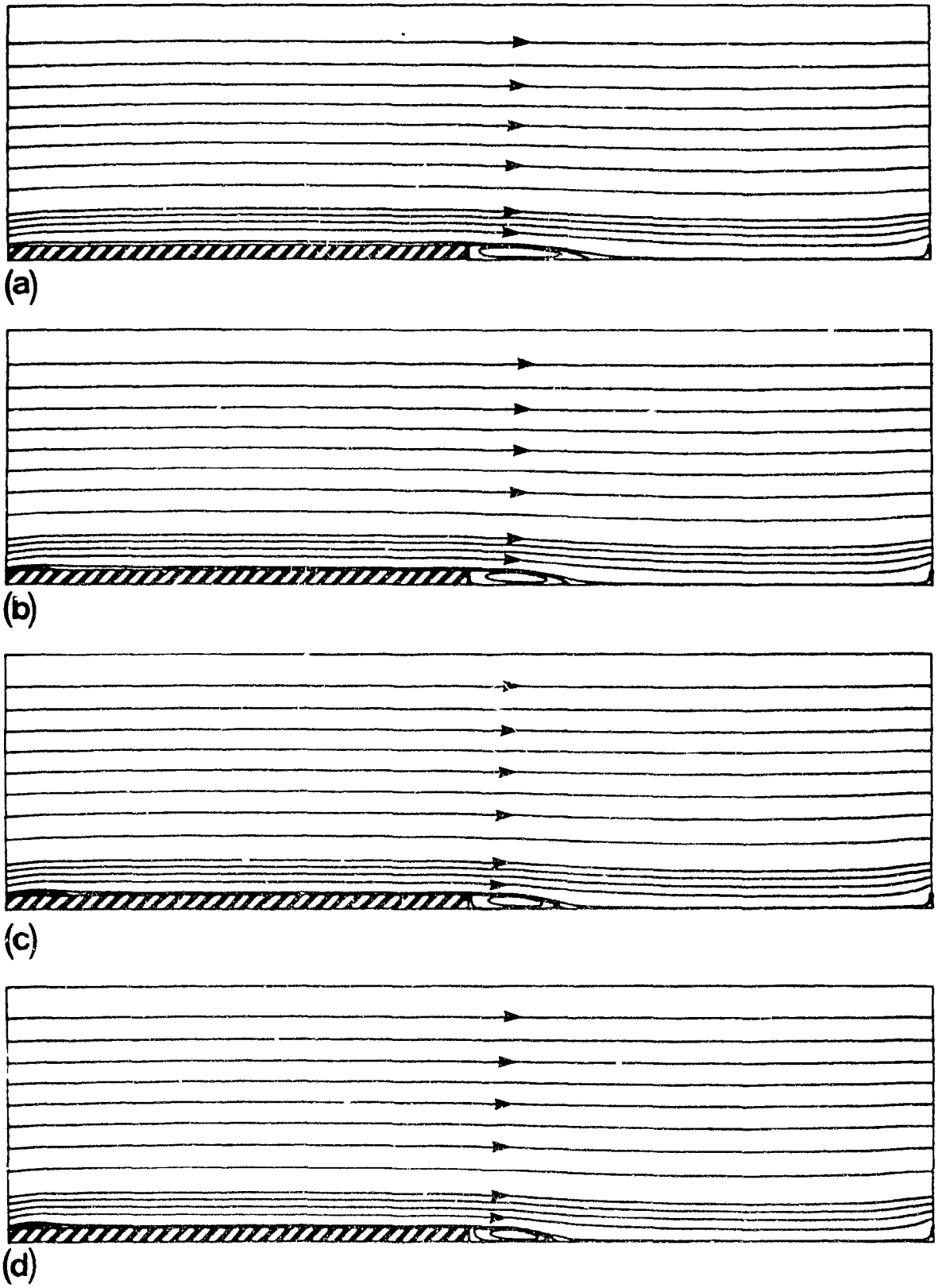

Figure 87. Streamline plots for Duct 2: (a) Run 1, $Re_m = 5.809 \times 10^3$; (b) Run 3, $Re_m = 11.56 \times 10^3$; (c) Run 4, $Re_m = 16.76 \times 10^3$; and (d) Run 6, $Re_m = 26.47 \times 10^3$. (Diagrams are not to scale, true horizontal:vertical dimensions = 4:1.)

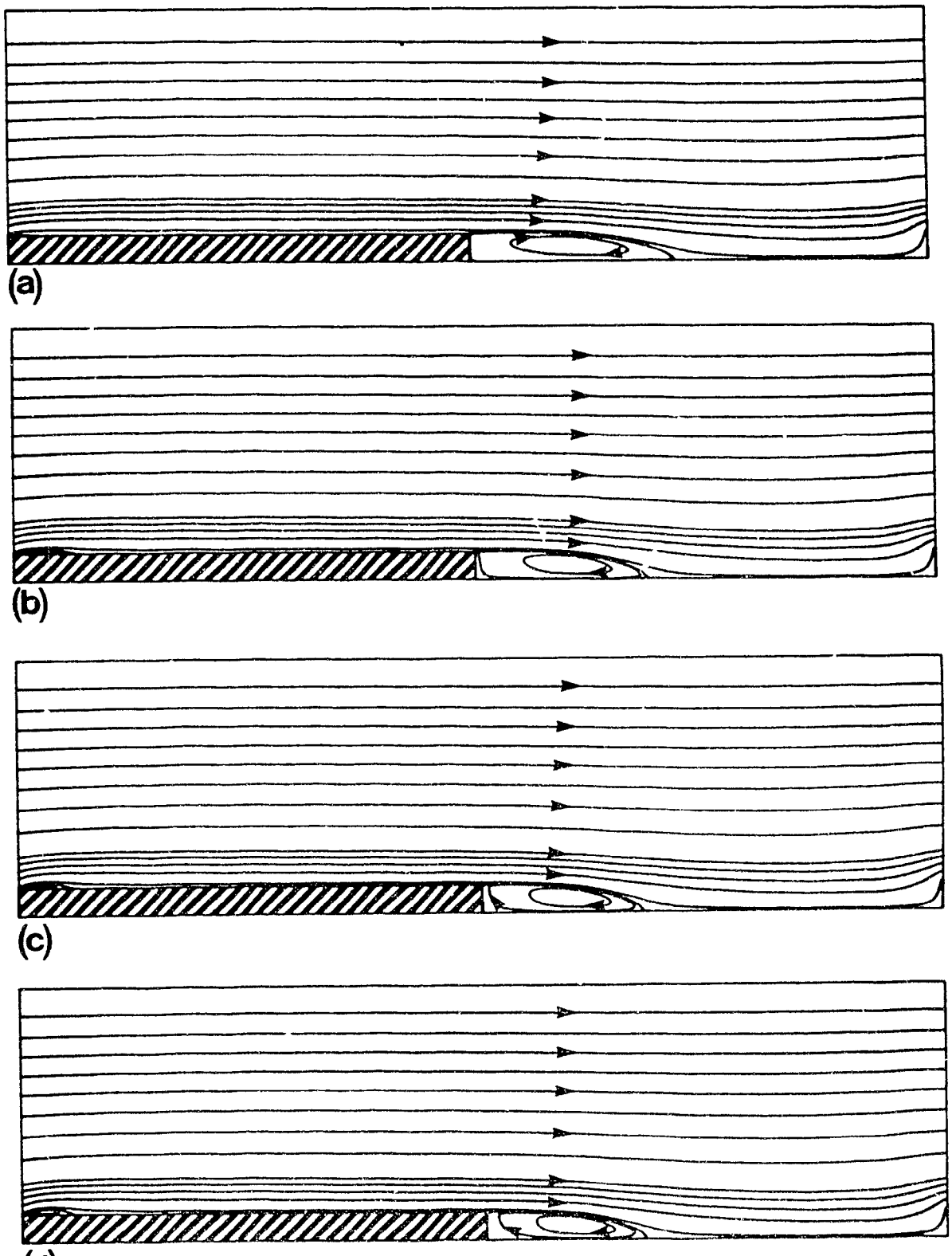

Figure 88: Streamline plots for Duct 3: (a) Run 1, $Re_m = 5.718 \times 10^3$; (b) Run 3, $Re_m = 11.78 \times 10^3$; (c) Run 4, $Re_m = 17.42 \times 10^3$; and (d) Run 6, $Re_m = 27.84 \times 10^3$. (Diagrams are not to scale, true horizontal:vertical dimensions = 4:1.)

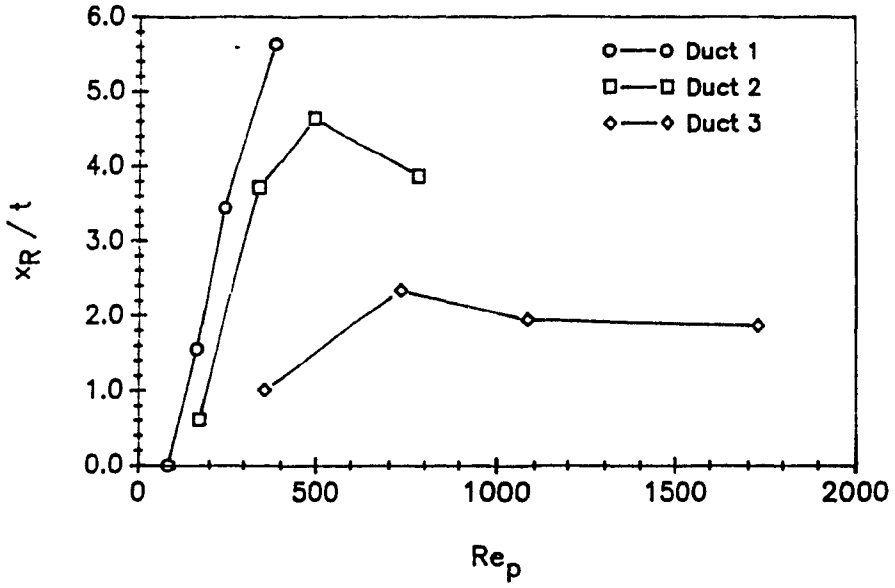

Figure 89: Variation of nondimensional stream-wise lengths of leading-edge recirculation zones, as a function of plate Reynolds number.

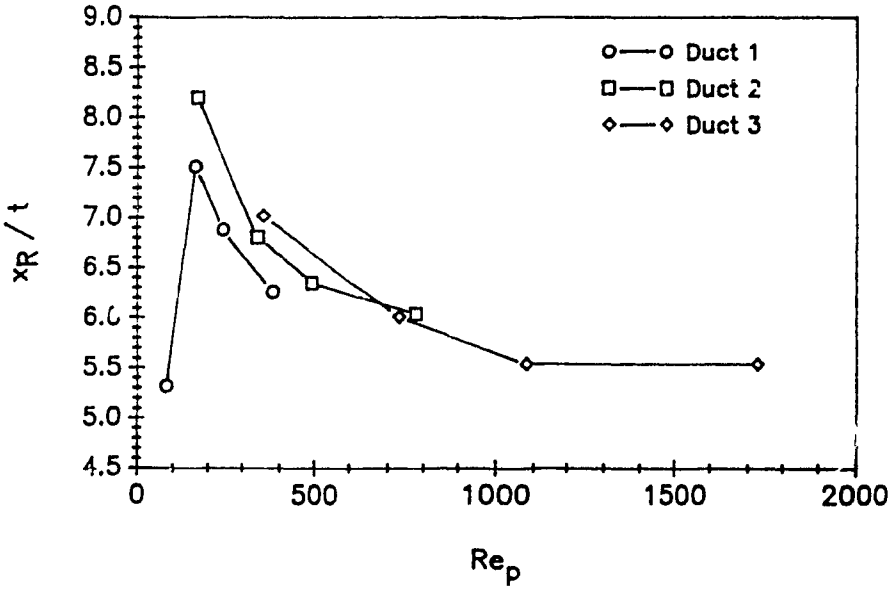

Figure 90: Variation of nondimensional stream-wise lengths of trailing-edge recirculation zones, as a function of plate Reynolds number.

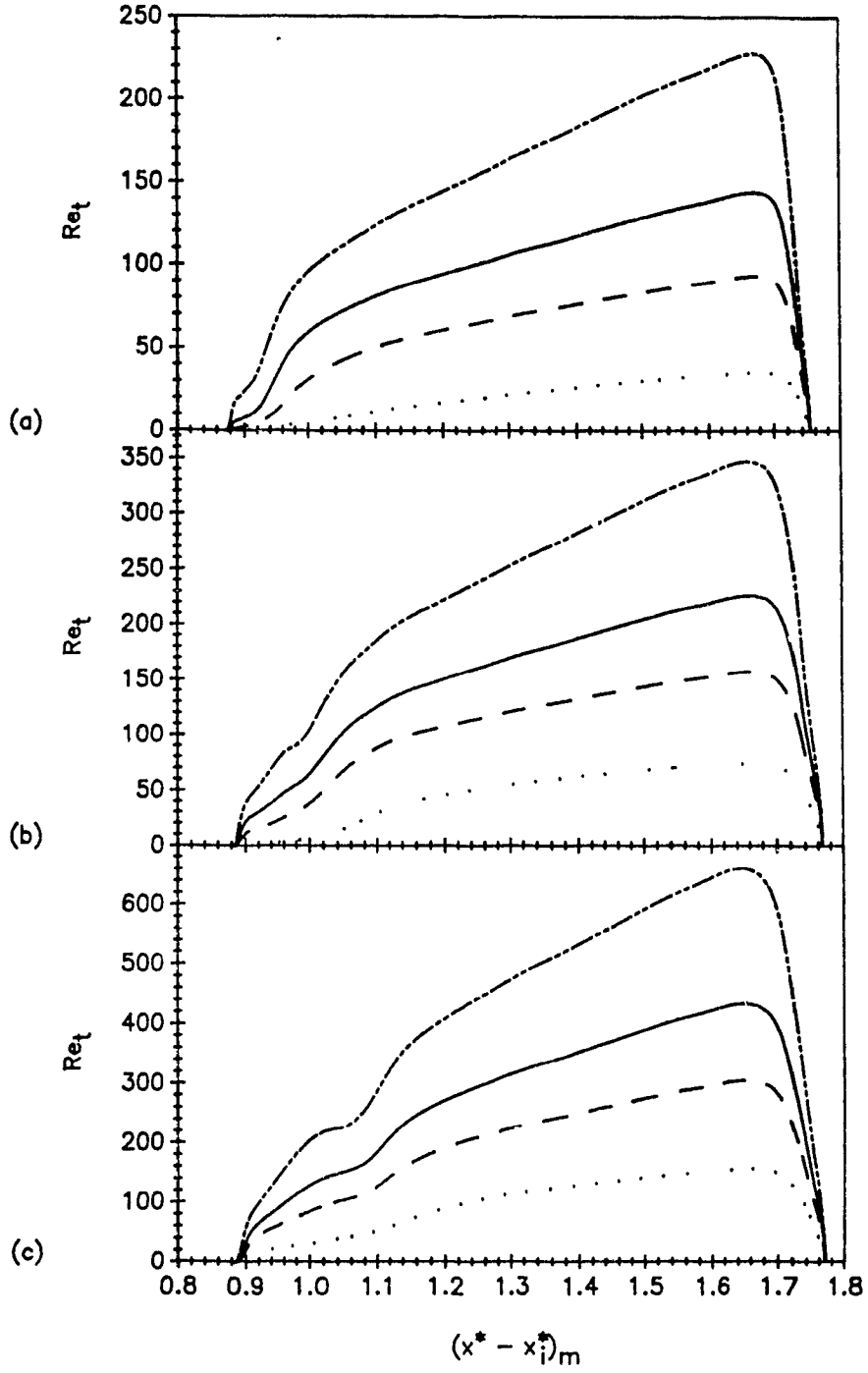

Figure 91: Streamwise profiles of Re_t in the interplate gap (y/t = 0.5). Profiles for Run 1 (·····), Run 3 (— — —), Run 4 (———), and Run 6 (—— — — ——) are shown for each of Ducts 1 to 3. The respective values of Re_m for Runs 1, 3, 4, and 6, are: (a) 5.764×10^3, 11.72×10^3, 17.42×10^3, and 27.27×10^3 in Duct 1; (b) 5.809×10^3, 11.56×10^3, 16.76×10^3 and 26.47×10^3 in Duct 2; and (c) 5.718×10^3, 11.78×10^3, 17.42×10^3 and 27.84×10^3 in Duct 3.

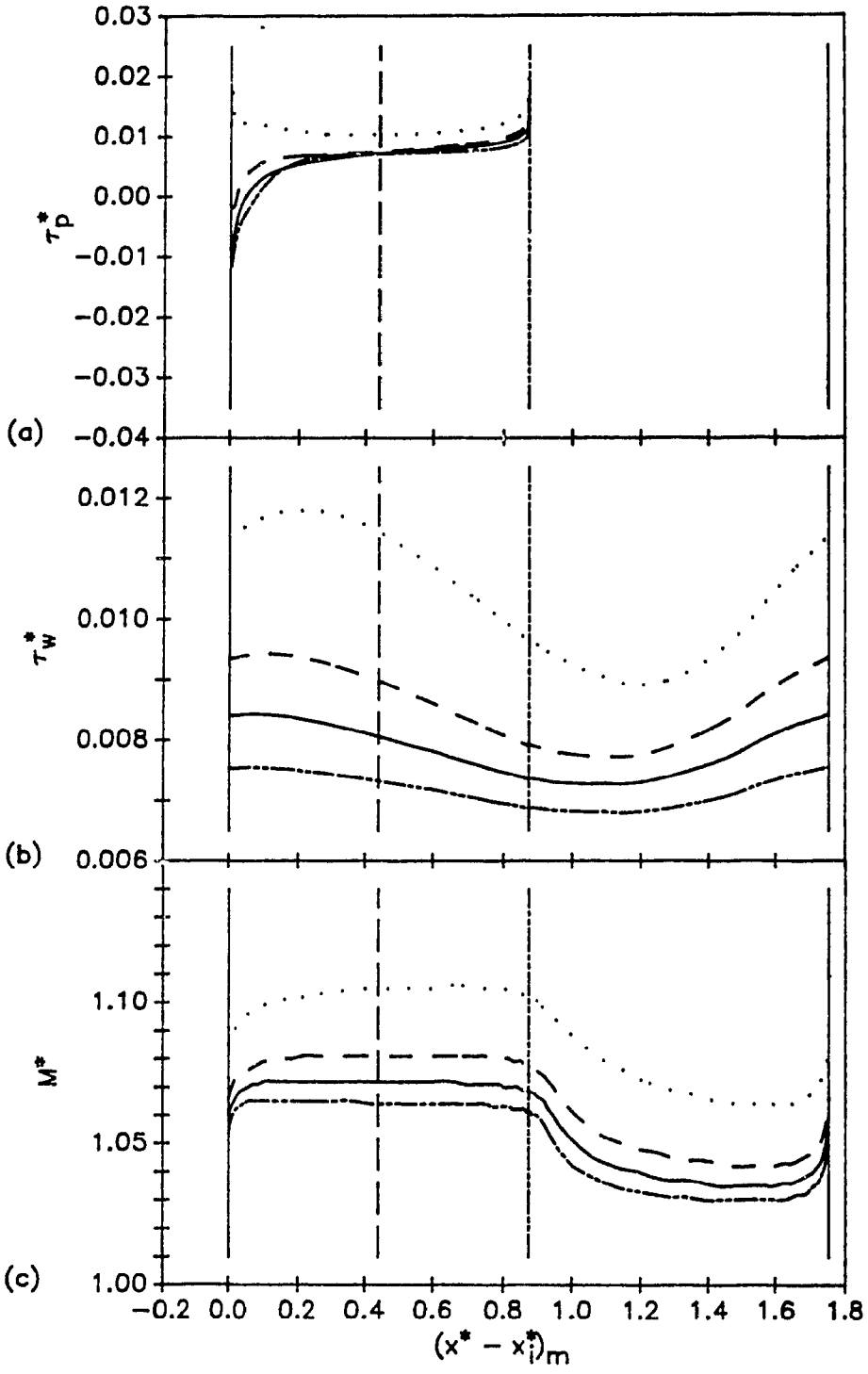

Figure 92: Axial profiles of nondimensional variables in Duct 1 with Re_m = 5.764x10^3 (·····), 11.72x10^3 (— — ·-), 17.42x10^3 (———), and 27.27x10^3 (—— — — ——): (a) nondimensional plate shear stress; (b) nondimensional wall shear stress; and (c) nondimensional axial momentum flux.

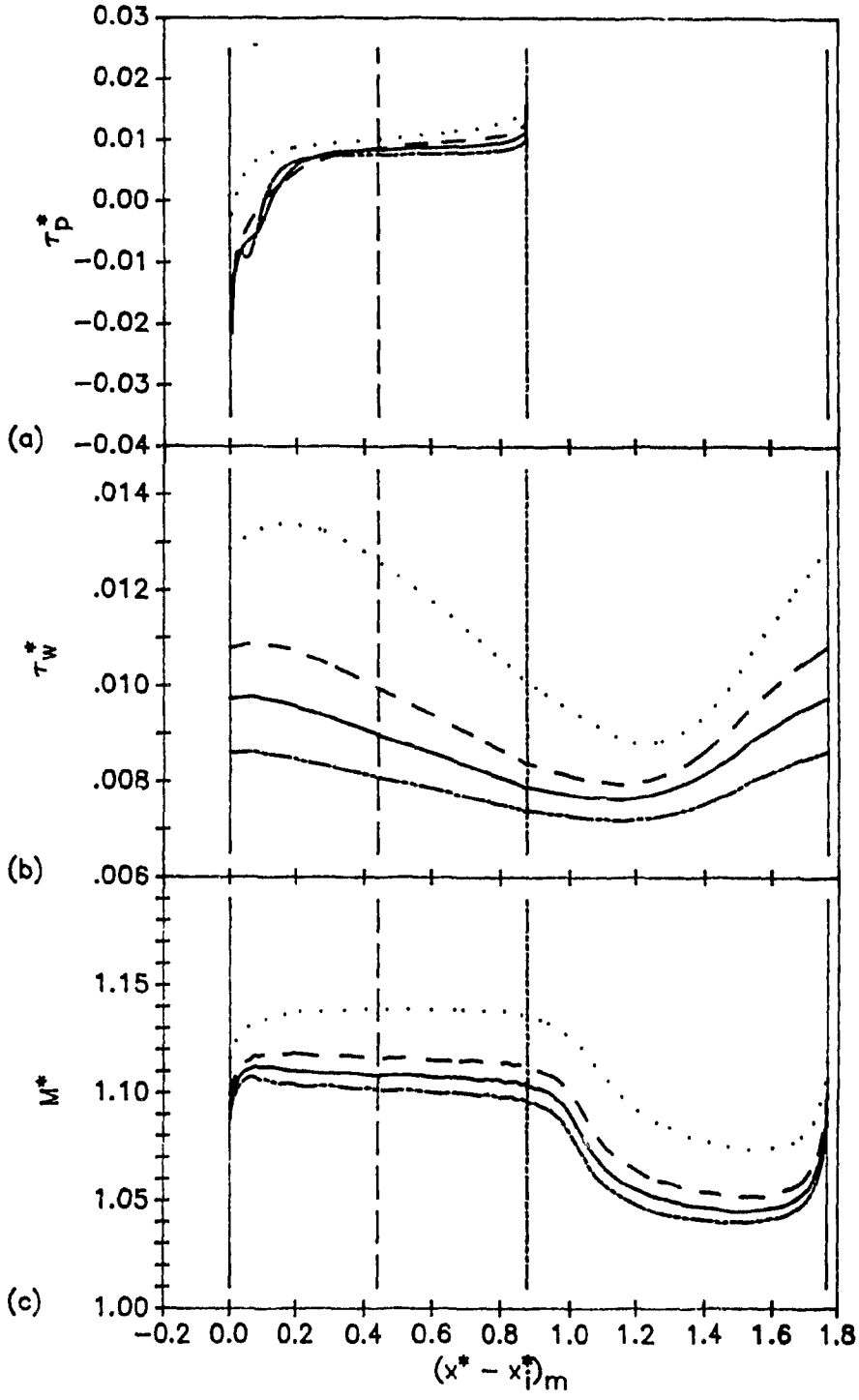

Figure 93: Axial profiles of nondimensional variables in Duct 2 with Re_m = 5.809×10^3 (·····), 11.56×10^3 (– – –), 16.76×10^3 (———), and 26.47×10^3 (—— – – ——): (a) nondimensional plate shear stress; (b) nondimensional wall shear stress; and (c) nondimensional axial momentum flux.

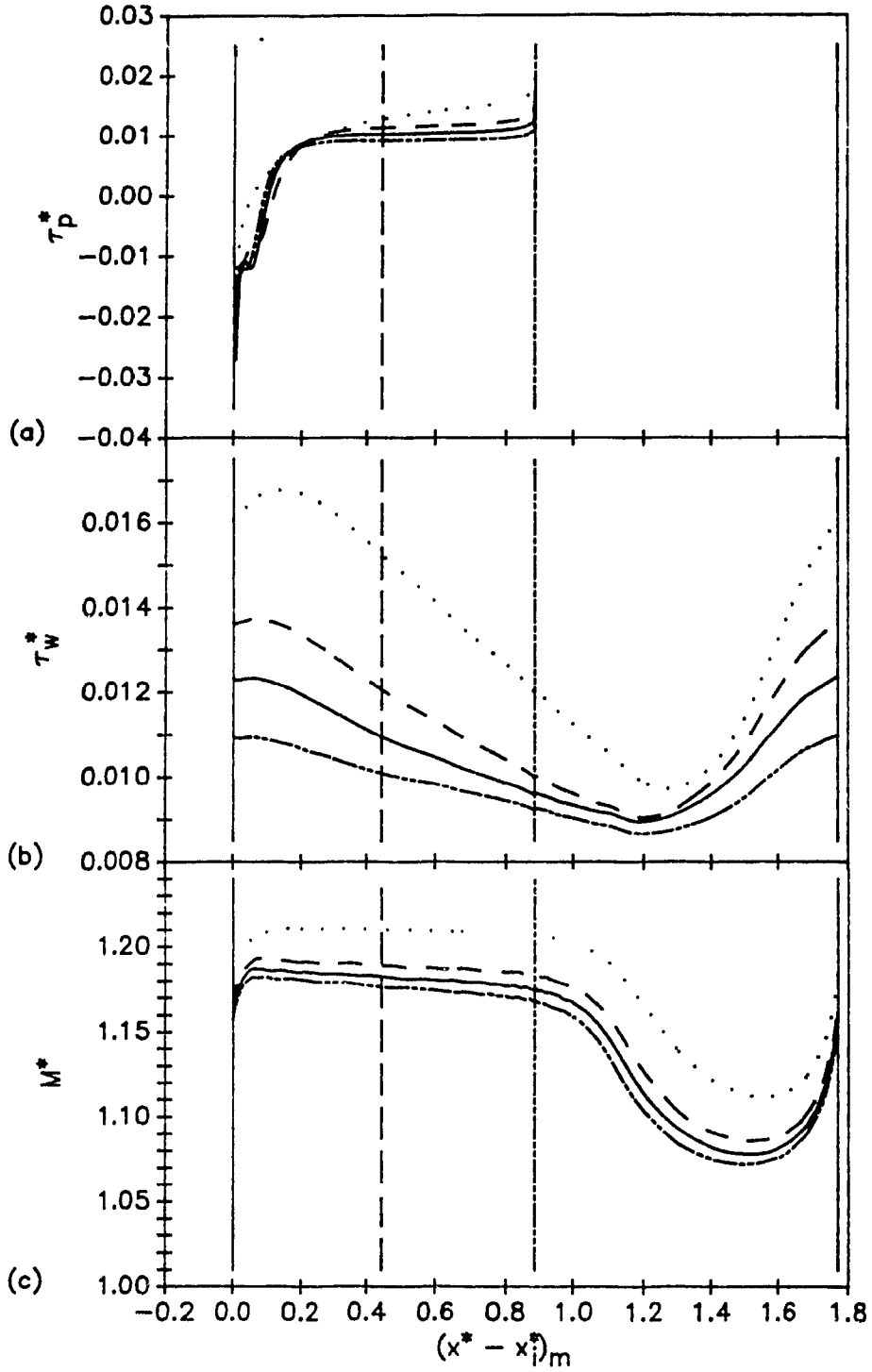

Figure 94: Axial profiles of nondimensional variables in Duct 3 with Re_m = 5.718×10^3 (·····), 11.78×10^3 (— — —), 17.42×10^3 (———), and 27.84×10^3 (—— — — ——): (a) nondimensional plate shear stress; (b) nondimensional wall shear stress; and (c) nondimensional axial momentum flux.

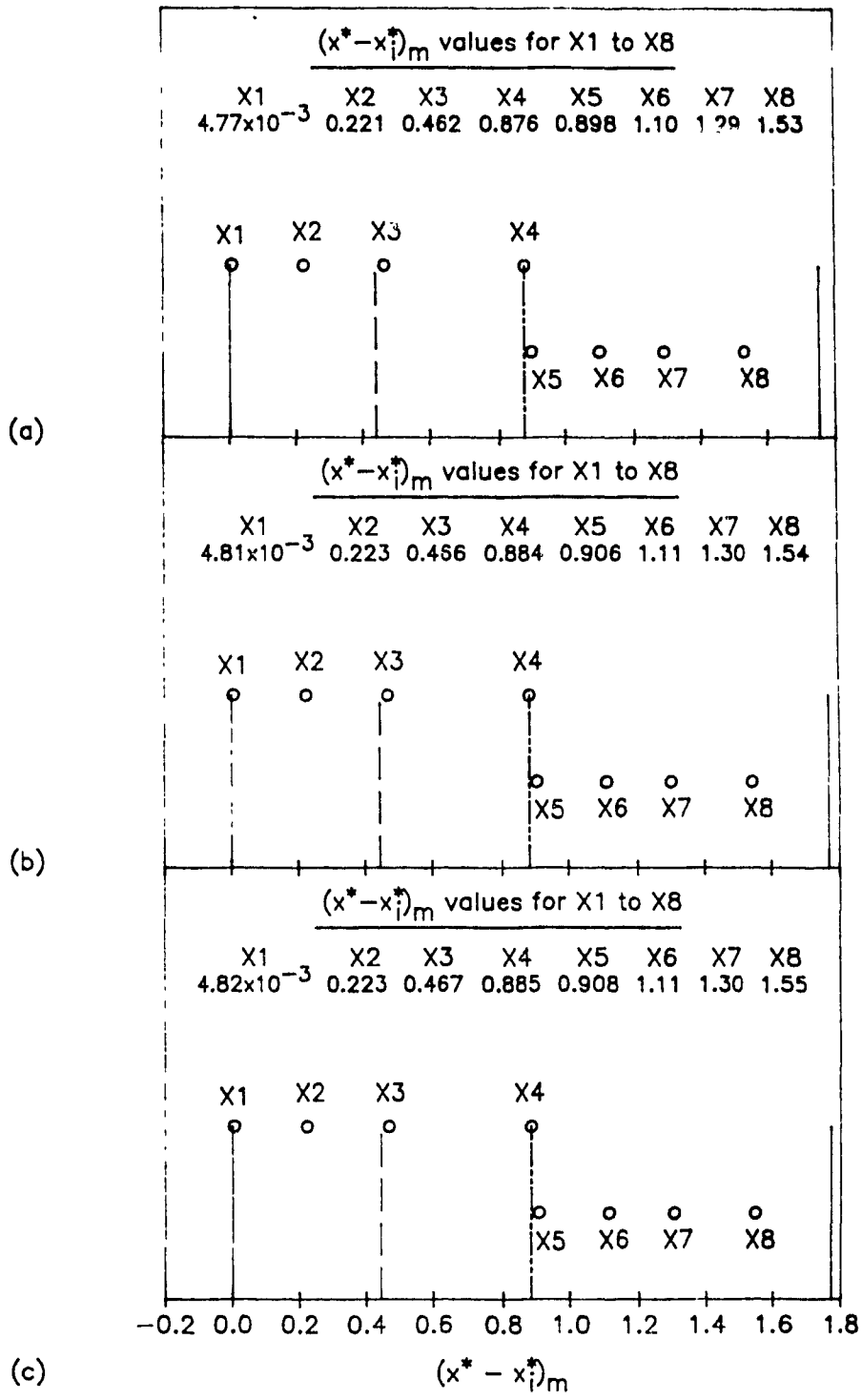

Figure 95: The eight intramodular locations, X1 to X8, for the U velocity plots presented in Figs. 96 to 101: (a) Duct 1; (b) Duct 2; and (c) Duct 3.

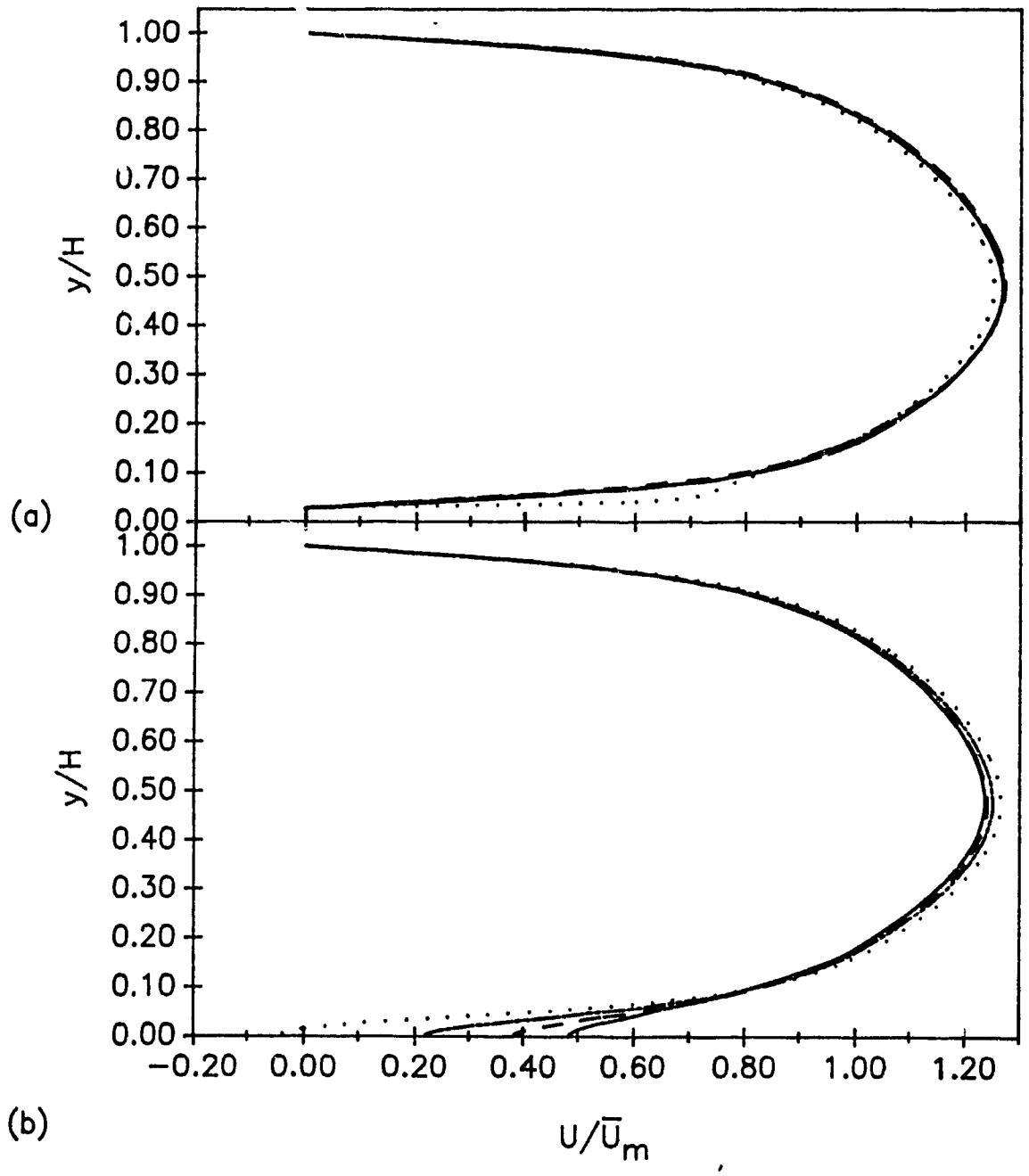

Figure 96: Nondimensional U velocity profiles for Duct 1, $Re_m = 5.764 \times 10^3$, at: (a) X1 (·····), X2 (—— – – ——), X3 (– – –), and X4 (———); and (b) X5 (·····), X6 (—— – – ——), X7 (– – –), and X8 (———). (Refer to Fig. 95 for locations of X1 to X8.)

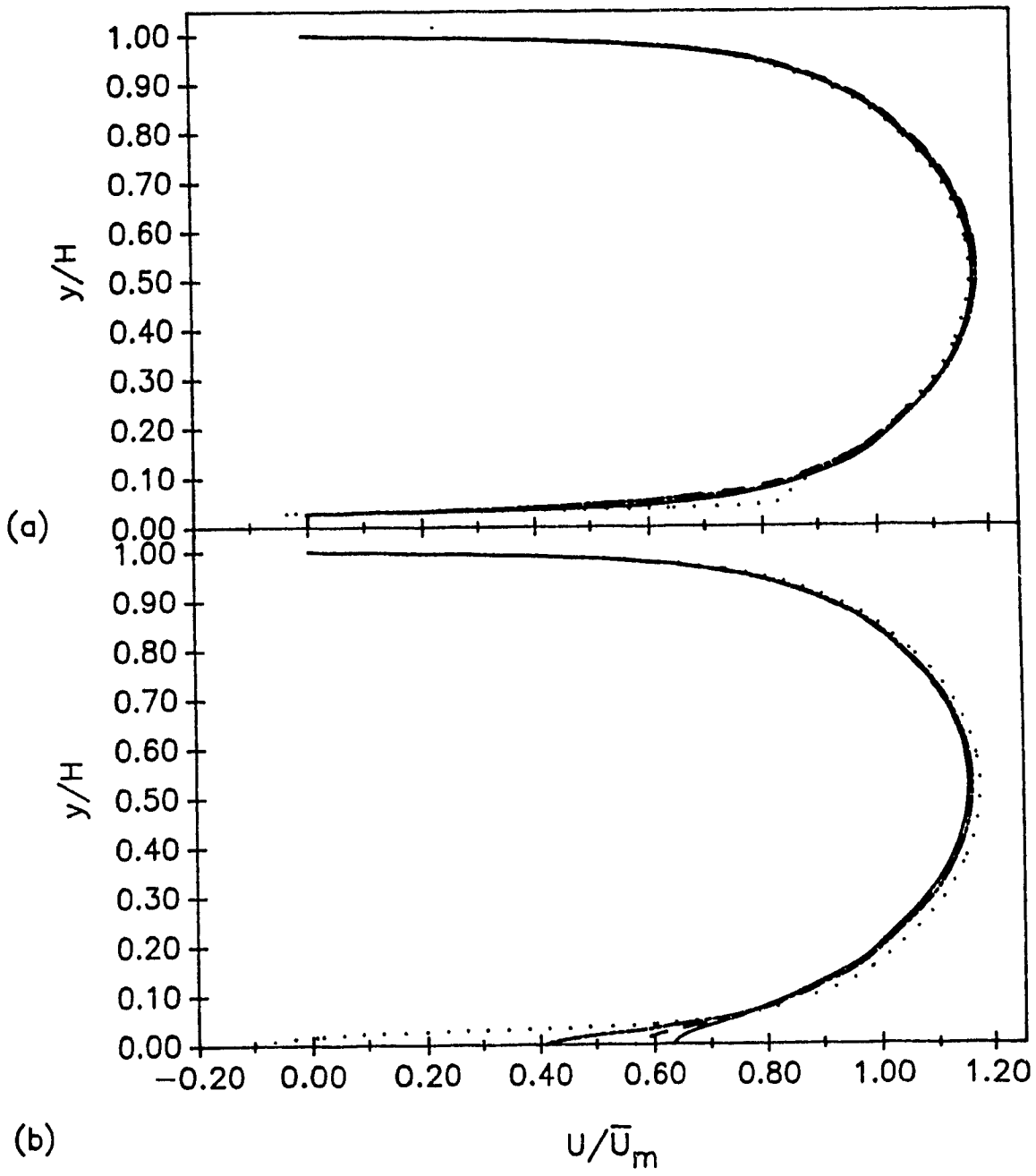

Figure 97: Nondimensional U velocity profiles for Duct 1, $Re_m = 27.27 \times 10^3$, at: (a) X1 (·····), X2 (—— – – ——), X3 (– – –), and X4 (———); and (b) X5 (·····), X6 (—— – – ——), X7 (– – –), and X8 (———). (Refer to Fig. 95 for locations of X1 to X8.)

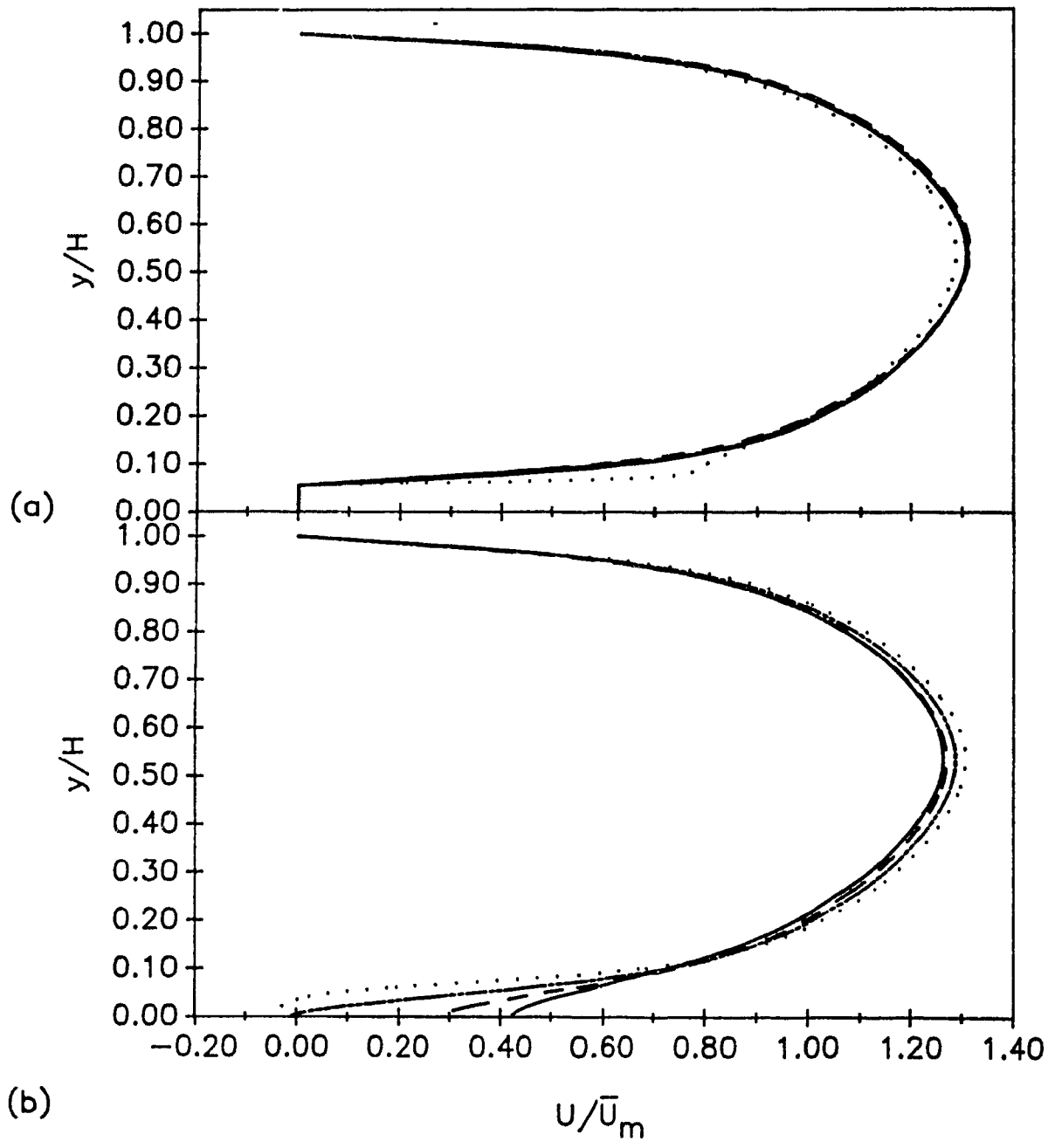

Figure 98: Nondimensional U velocity profiles for Duct 2, $Re_m = 5.809 \times 10^3$, at: (a) X1 (·····), X2 (—— – – ——), X3 (– – –), and X4 (———); and (b) X5 (·····), X6 (—— – – ——), X7 (– – –), and X8 (———). (Refer to Fig. 95 for locations of X1 to X8.)

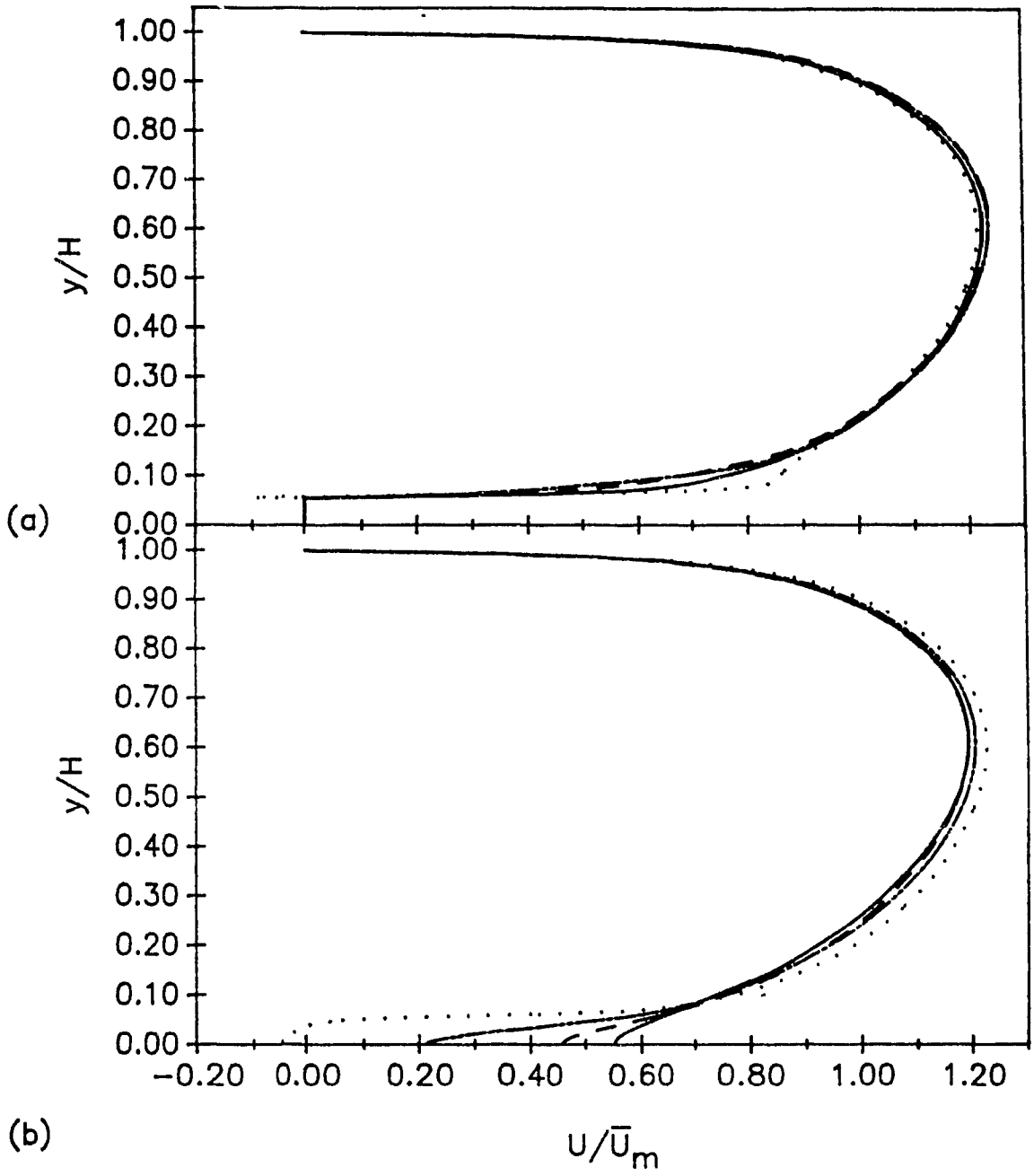

Figure 99: Nondimensional U velocity profiles for Duct 2, $Re_m = 26.47 \times 10^3$, at: (a) X1 (·····), X2 (— — — —), X3 (— — —), and X4 (———); and (b) X5 (·····), X6 (— — — —), X7 (— — —), and X8 (———). (Refer to Fig. 95 for locations of X1 to X8.)

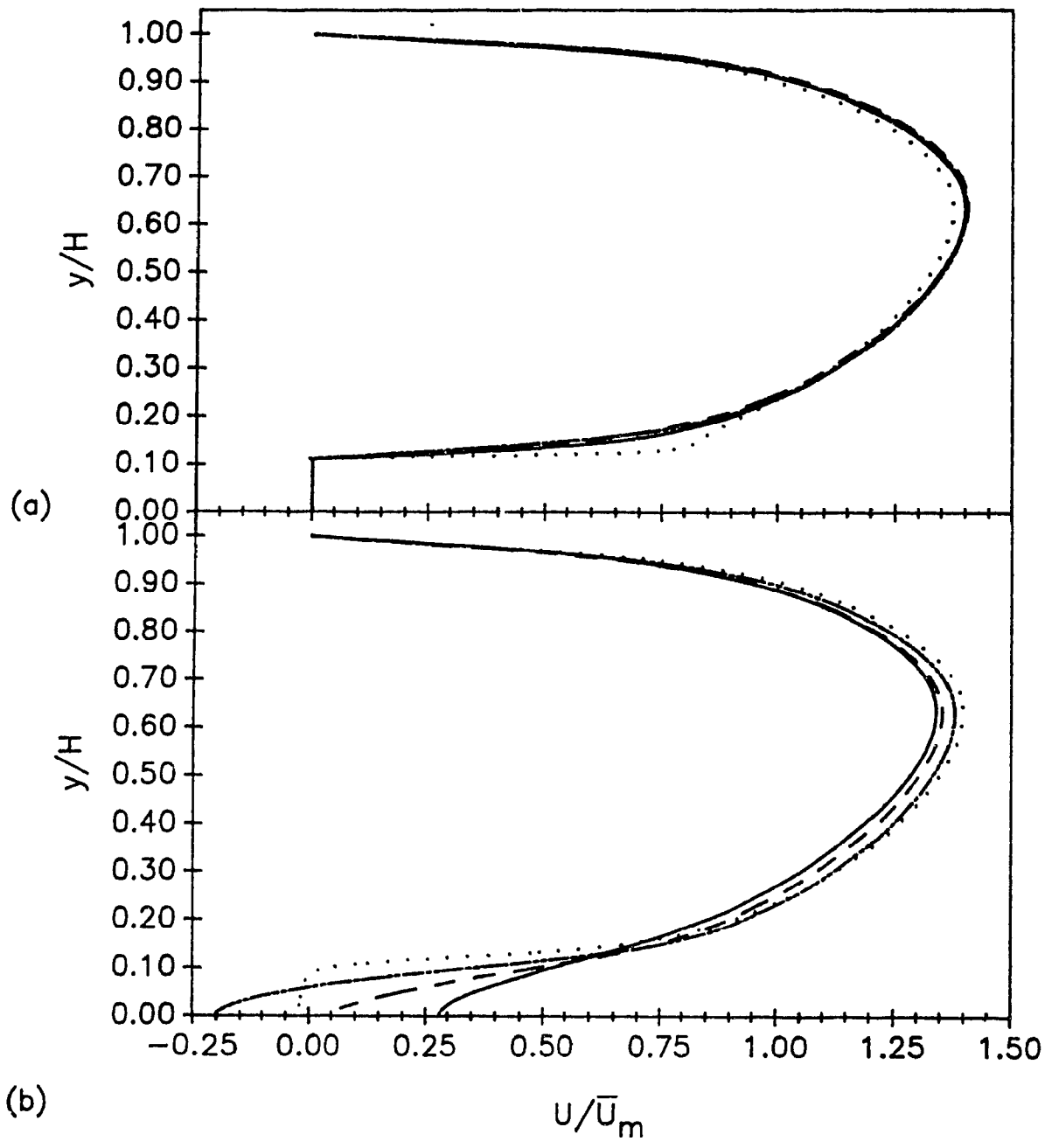

Figure 100: Nondimensional U velocity profiles for Duct 3, $Re_m = 5.718 \times 10^3$, at: (a) X1 (·····), X2 (—— – – ——), X3 (– – –), and X4 (———); and (b) X5 (·····), X6 (—— – – ——), X7 (– – –), and X8 (———). (Refer to Fig. 95 for locations of X1 to X8.)

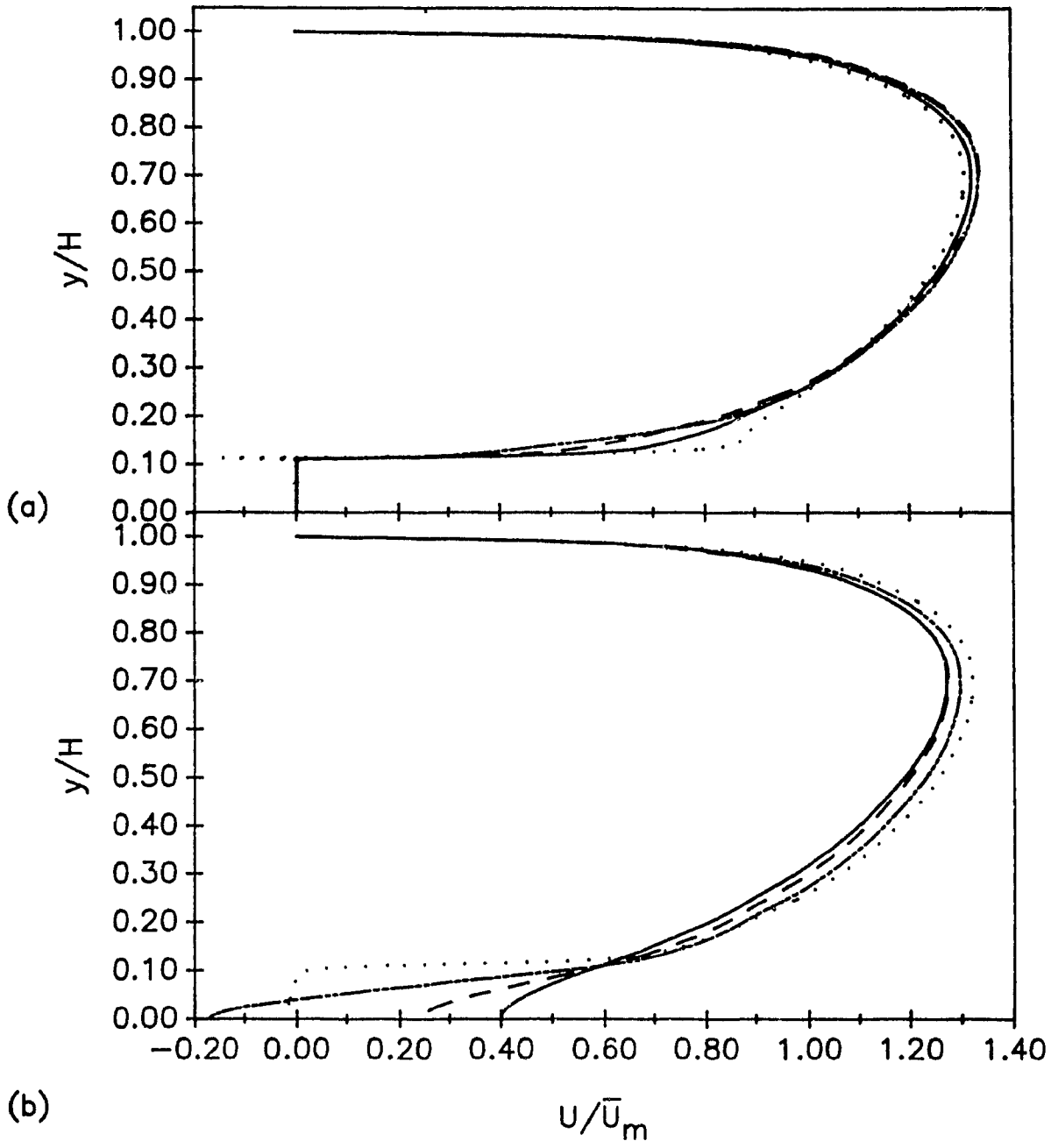

Figure 101: Nondimensional U velocity profiles for Duct 3, $Re_m = 27.84 \times 10^3$, at: (a) X1 (·····), X2 (—— – – ——), X3 (– – –), and X4 (———); and (b) X5 (·····), X6 (—— – – ——), X7 (– – –), and X8 (———). (Refer to Fig. 95 for locations of X1 to X8.)

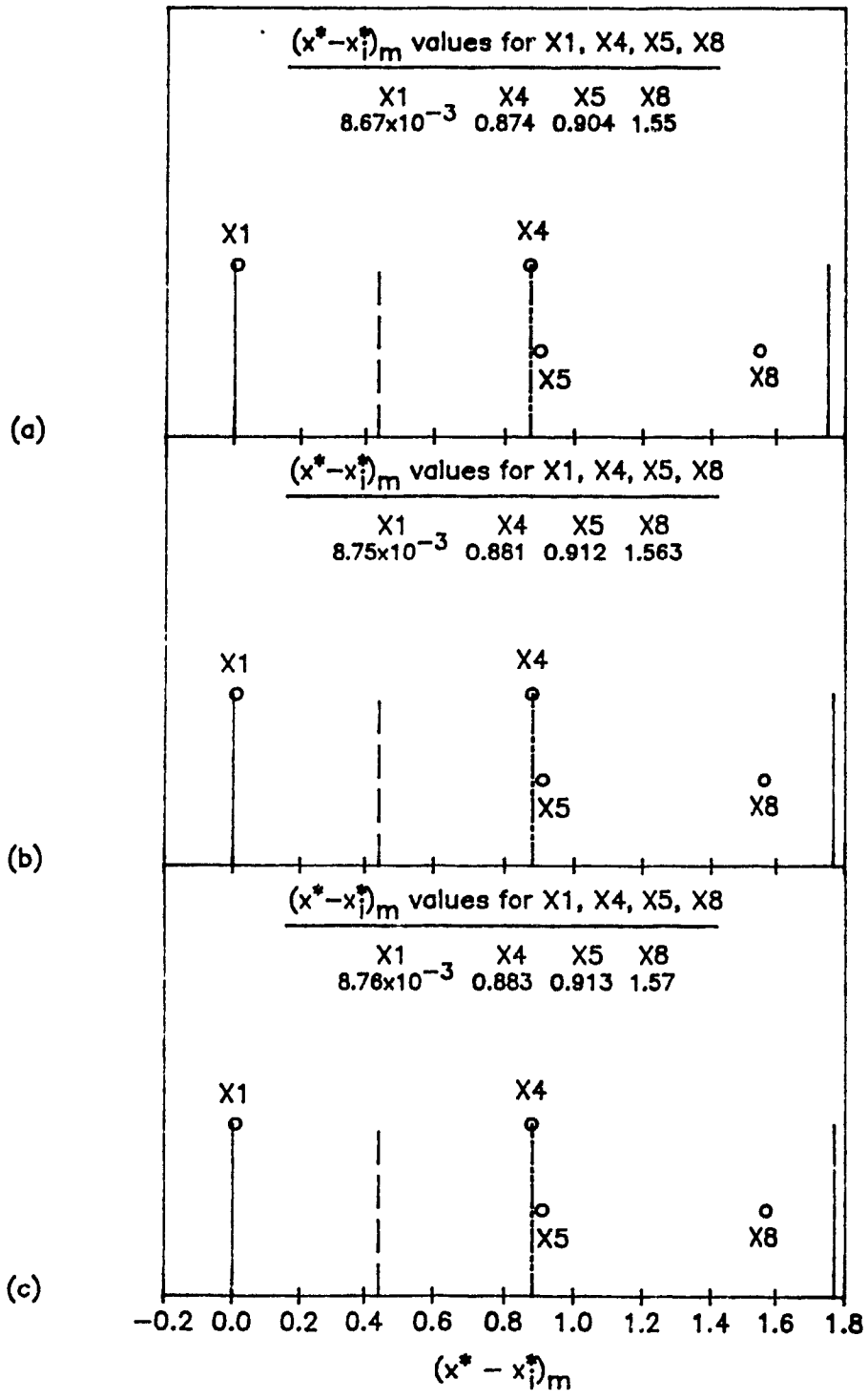

Figure 102: The intramodular locations, X1, X4, X5, and X8, for the profile plots of k and Re_t presented in Figs. 103 to 108: (a) Duct 1; (b) Duct 2; and (c) Duct 3.

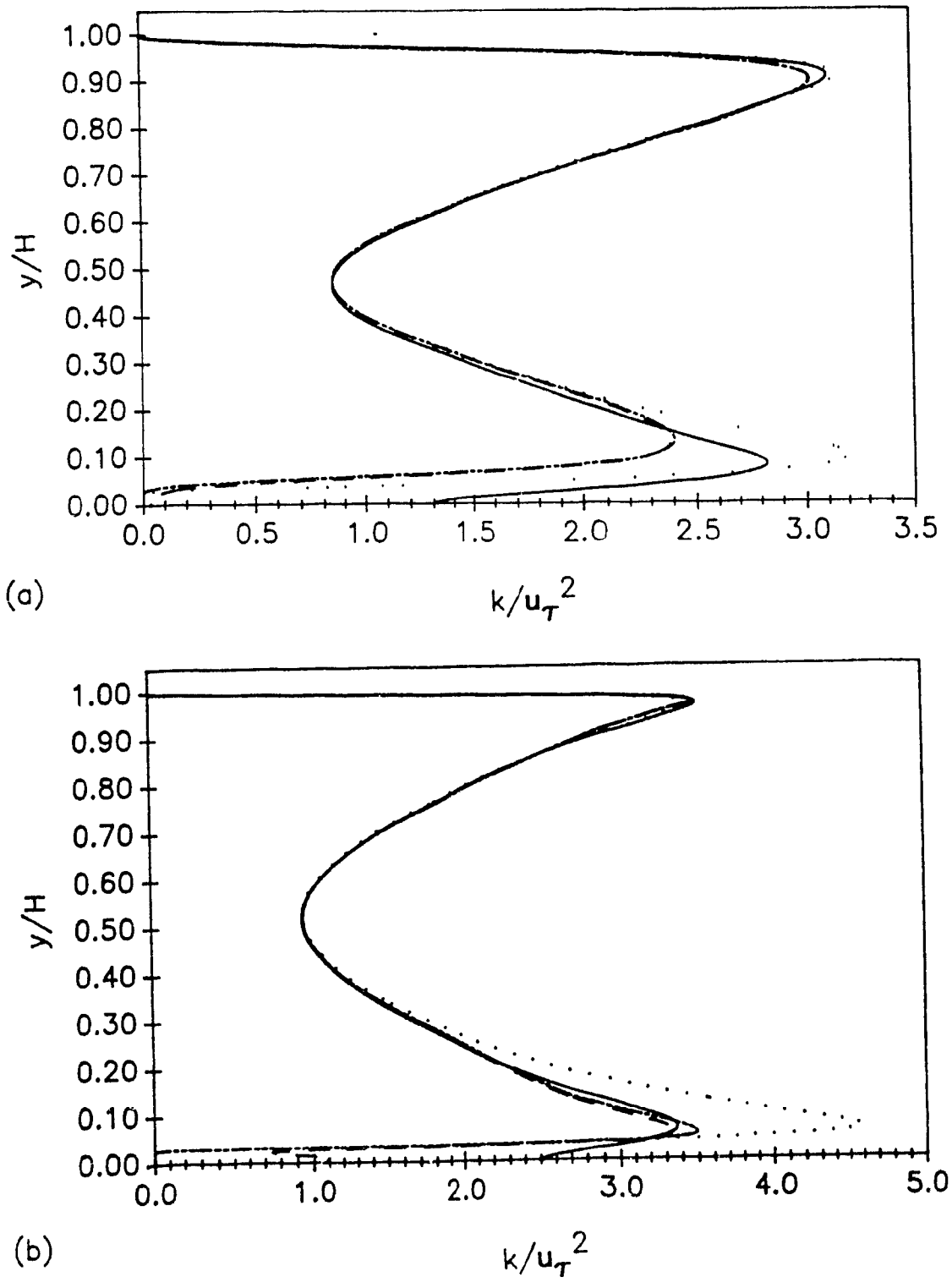

Figure 103: Nondimensional mean turbulence kinetic energy, k, profiles in Duct 1 at X1 (·····), X4 (—— – – ——), X5 (– – –), and X8 (———): (a) $Re_m = 5.764 \times 10^3$; and (b) $Re_m = 27.27 \times 10^3$. (Refer to Fig. 102 for locations X1, X4, X5, and X8.)

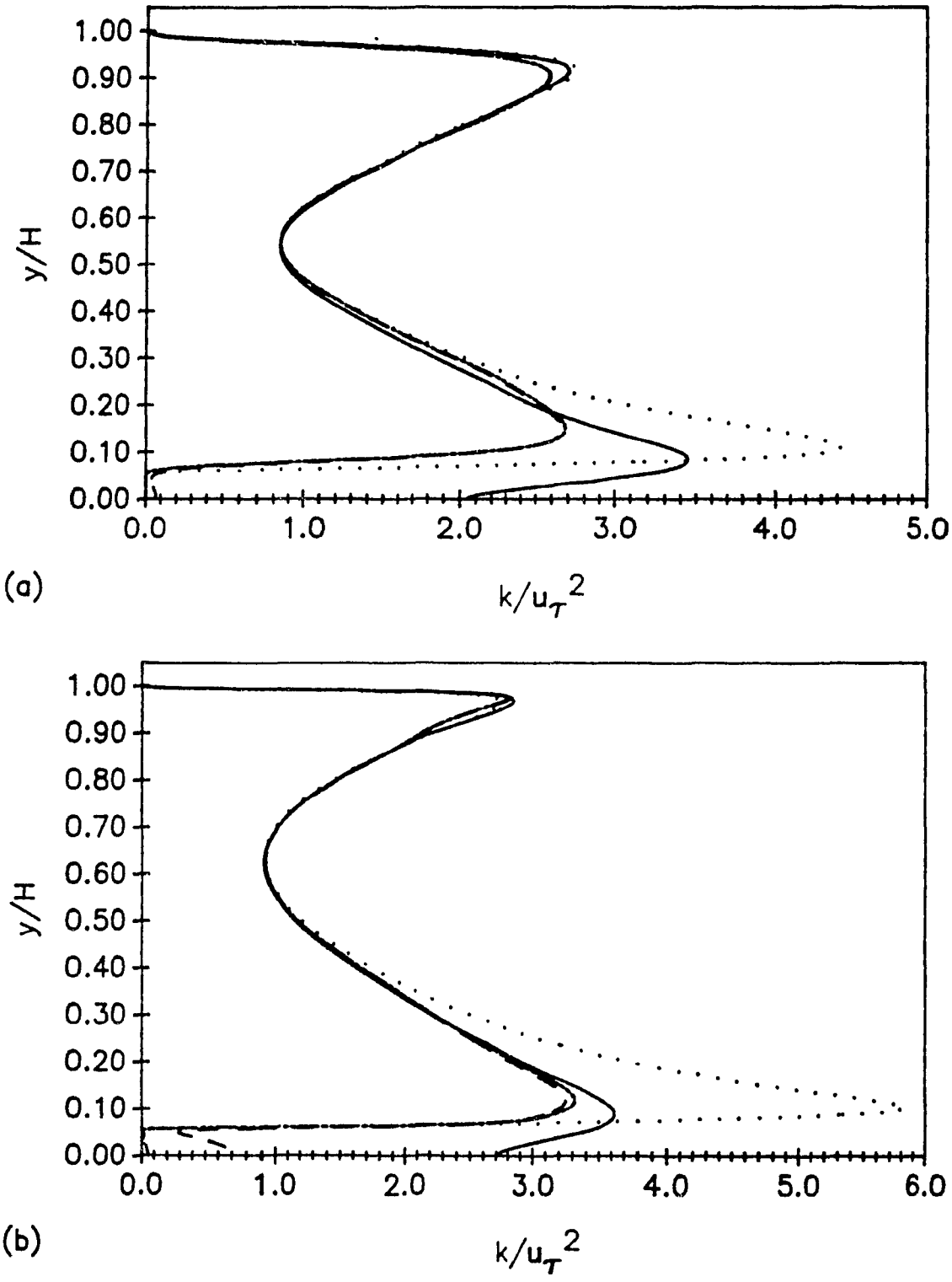

Figure 104: Nondimensional mean turbulence kinetic energy, k, profiles in Duct 2 at X1 (·····), X4 (—— – – ——), X5 (– – –), and X8 (———): (a) $Re_m = 5.809 \times 10^3$; and (b) $Re_m = 26.47 \times 10^3$. (Refer to Fig. 102 for locations X1, X4, X5, and X8.)

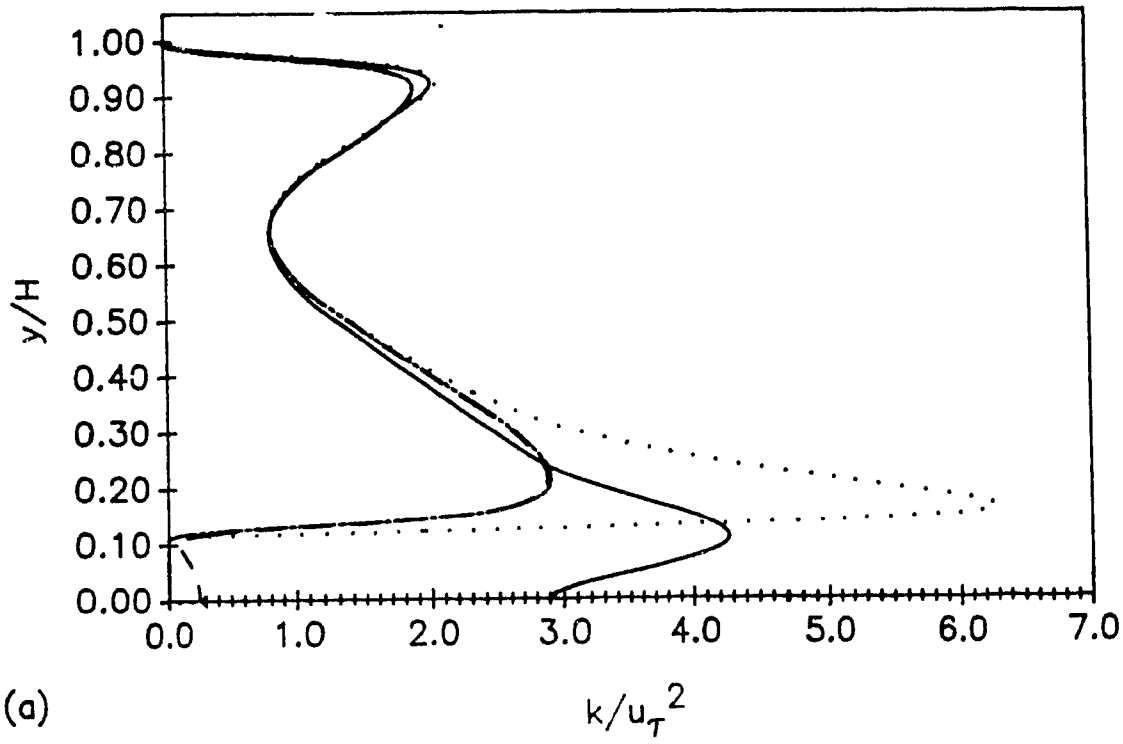

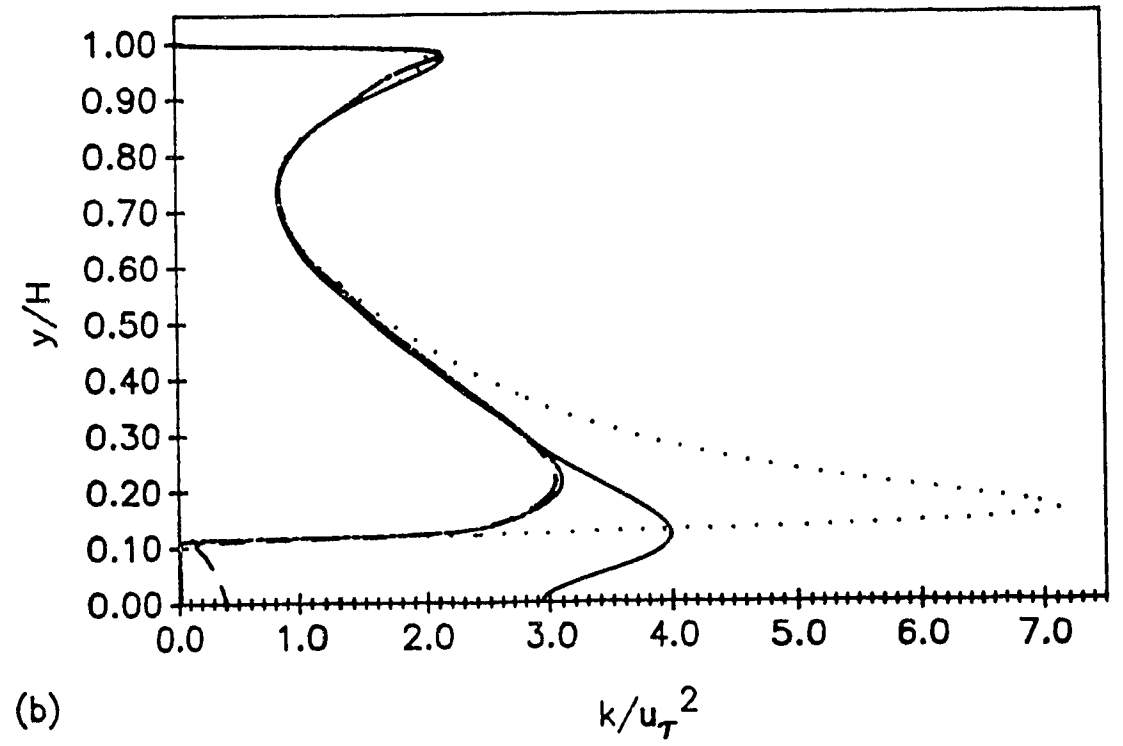

Figure 105: Nondimensional mean turbulence kinetic energy, k, profiles in Duct 3 at X1 (·····), X4 (—— – – ——), X5 (– – –), and X8 (———): (a) $Re_m = 5.718 \times 10^3$; and (b) $Re_m = 27.84 \times 10^3$. (Refer to Fig. 102 for locations X1, X4, X5, and X8.)

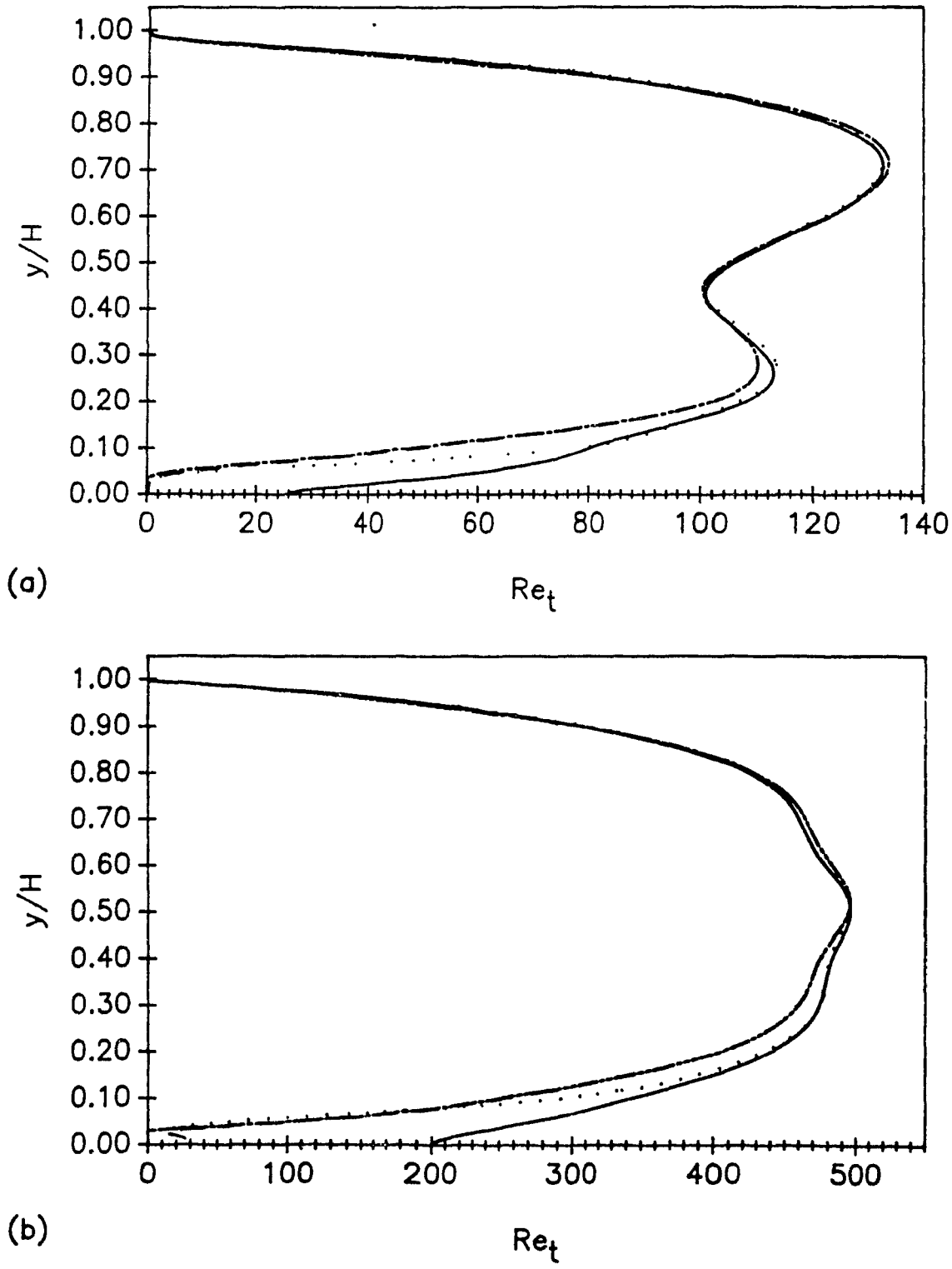

Figure 106: Profiles of turbulence Reynolds numbers, Re_t, in Duct 1 at X1 (·····), X4 (—— – – ——), X5 (– – –), and X8 (———): (a) $Re_m = 5.764 \times 10^3$; and (b) $Re_m = 27.27 \times 10^3$. (Refer to Fig. 102 for locations X1, X4, X5, and X8.)

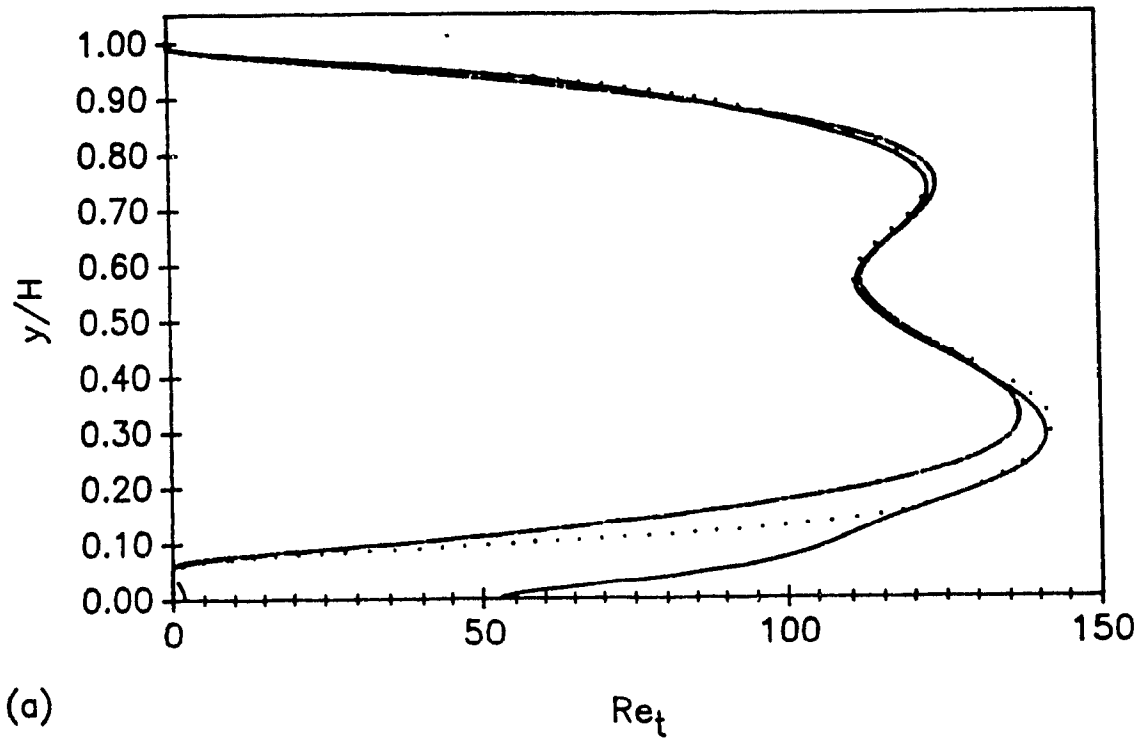

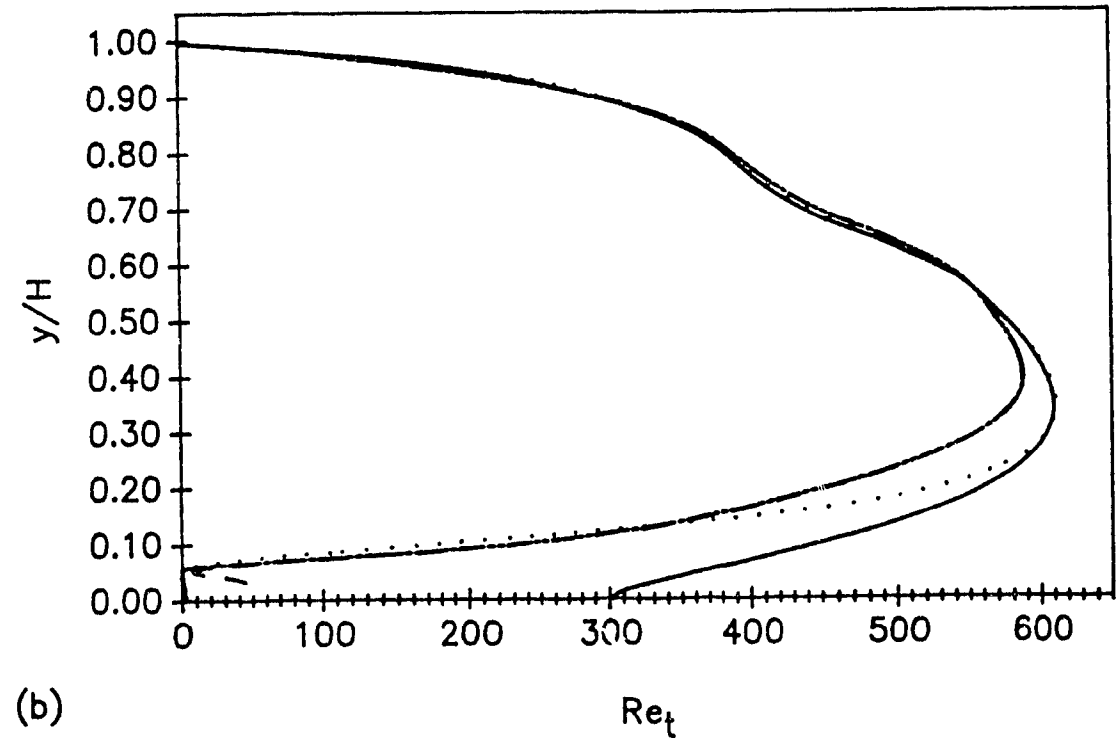

Figure 107: Profiles of turbulence Reynolds numbers, Re_t, in Duct 2 at X1 (·····), X4 (—— – – ——), X5 (– – –), and X8 (———): (a) $Re_m = 5.809 \times 10^3$; and (b) $Re_m = 26.47 \times 10^3$. (Refer to Fig. 102 for locations X1, X4, X5, and X8.)

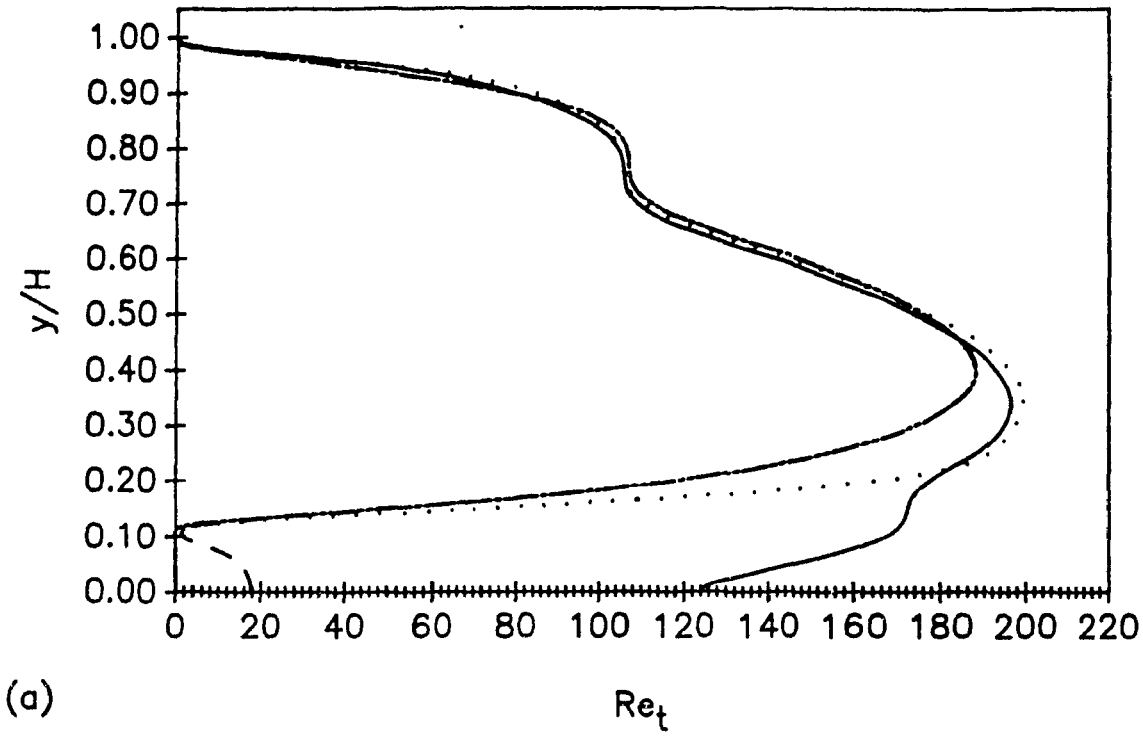

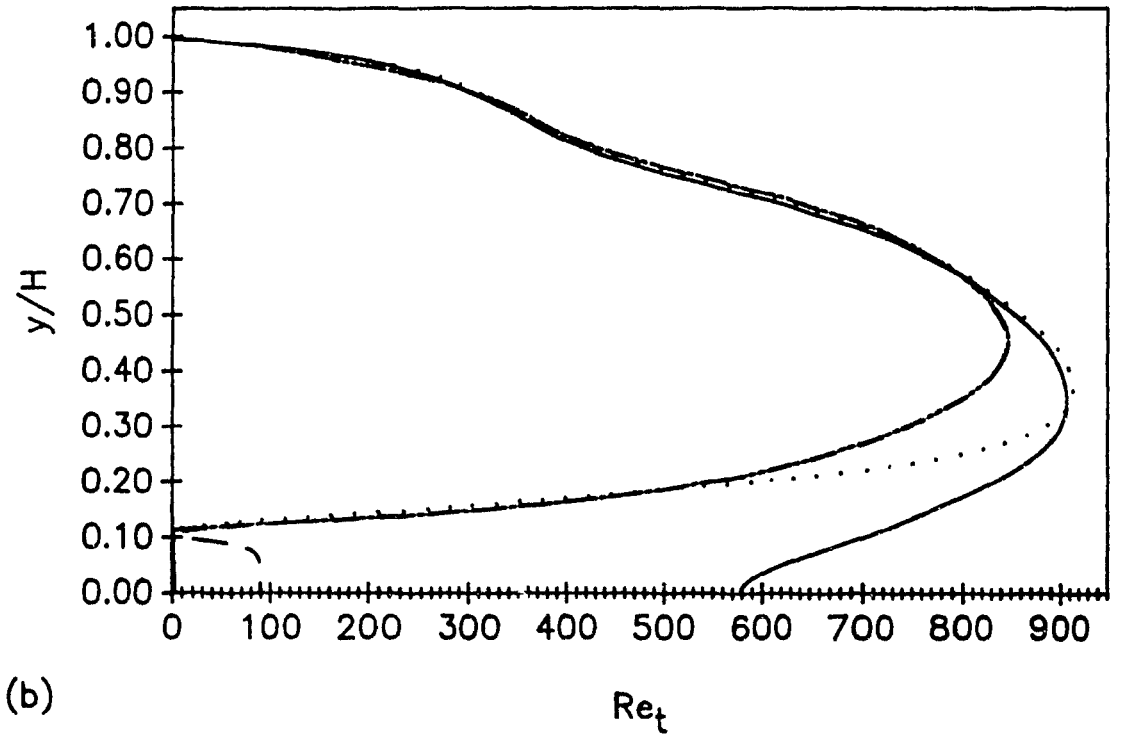

Figure 108: Profiles of turbulence Reynolds numbers, Re_t, in Duct 3 at X1 (·····), X4 (—— – – ——), X5 (– – –), and X8 (———): (a) $Re_m = 5.718 \times 10^3$; and (b) $Re_m = 27.84 \times 10^3$. (Refer to Fig. 102 for locations X1, X4, X5, and X8.)

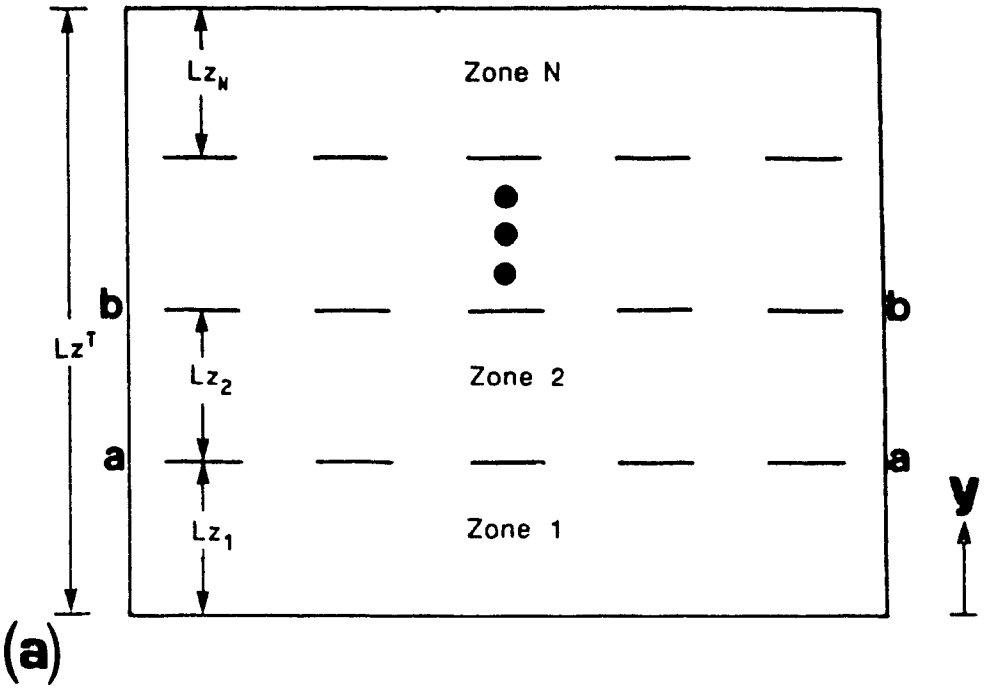

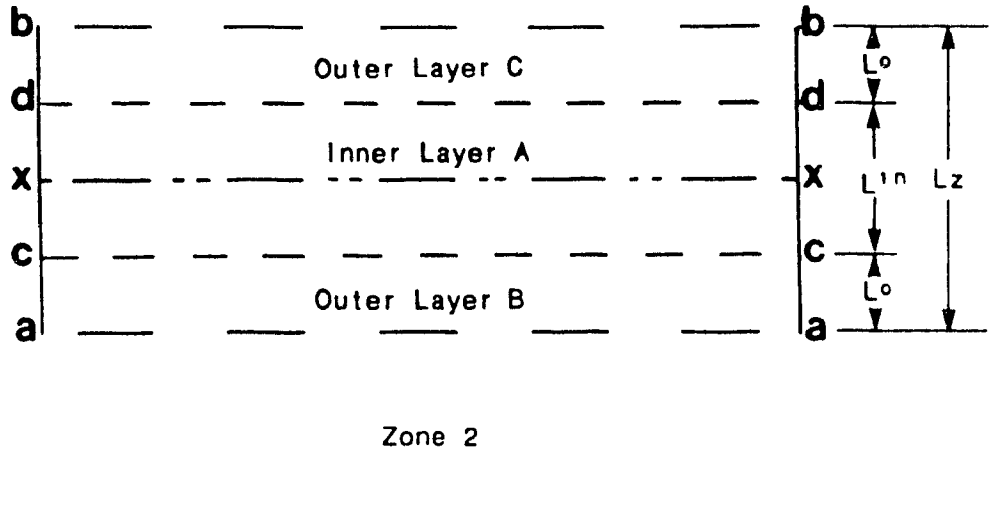

Figure 109: Division of a calculation domain, in the y-coordinate direction, for purposes of grid generation: (a) division into zones; and (b) subdivision of Zone 2 into layers.

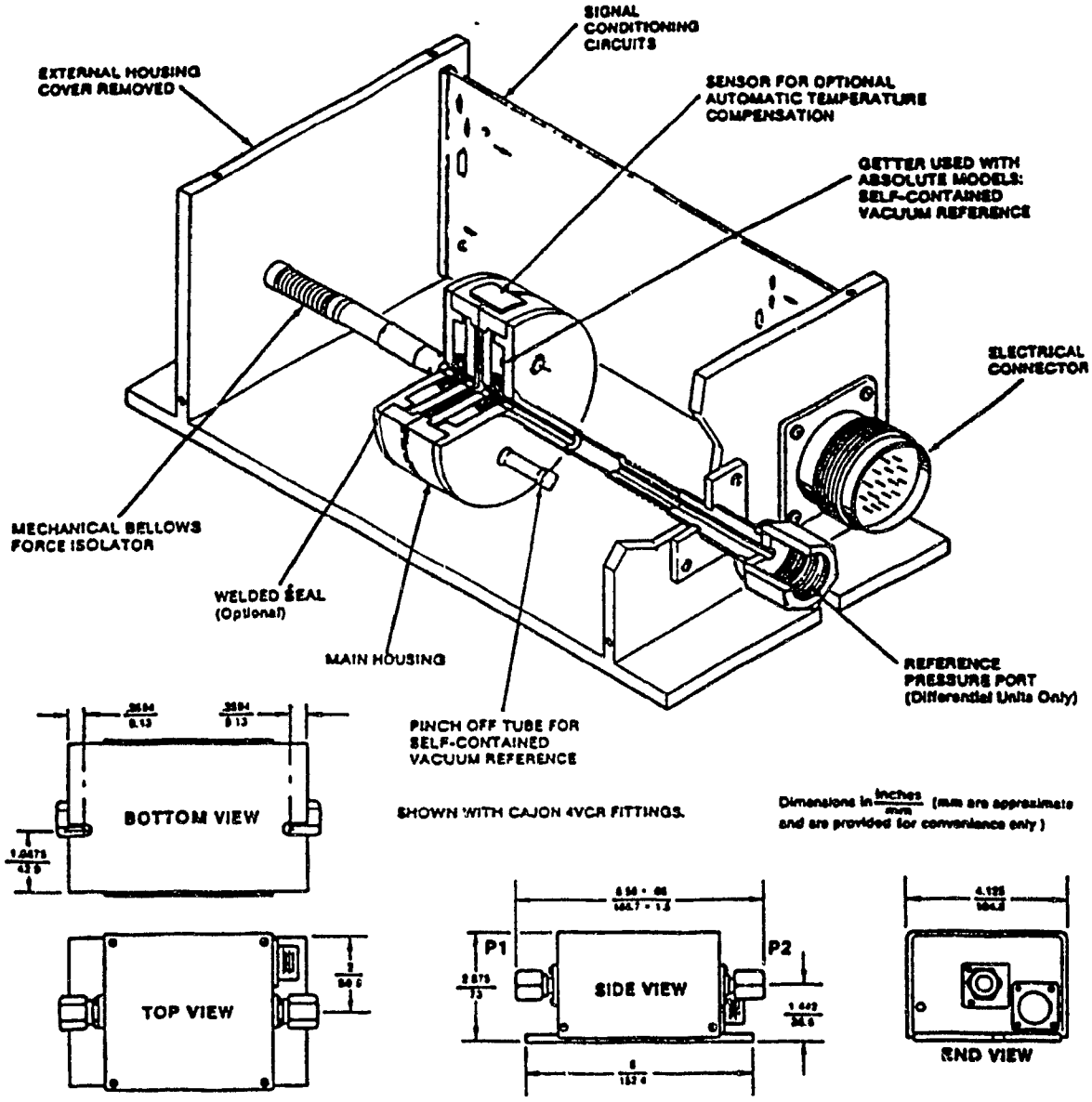

Figure 110: Cut-away sketch and dimensions of the Integral Barocel Pressure Transducer.
(Datametrics Model 590-D-1-kPa-208-V1X-4D).

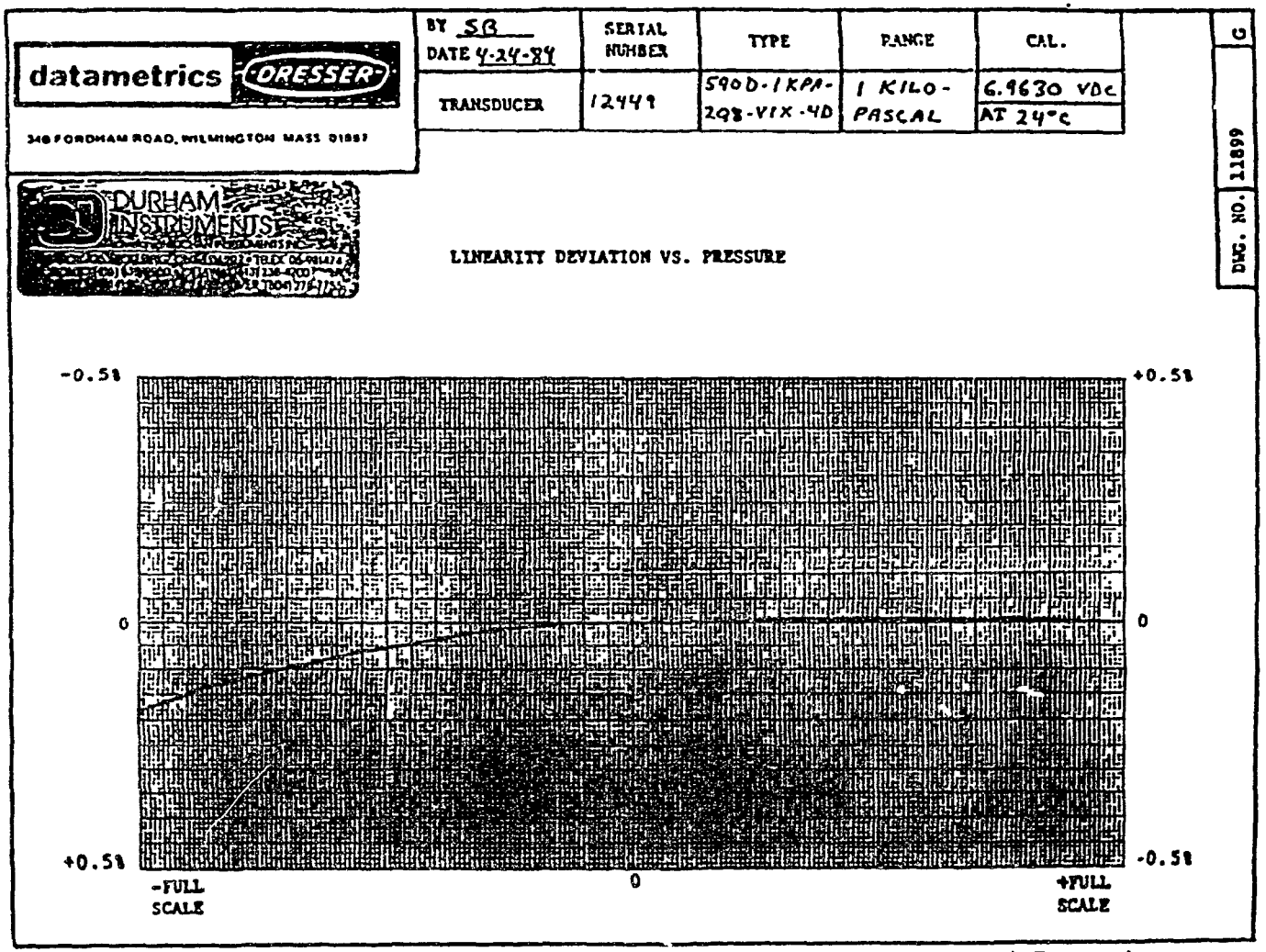

Figure 111: Manufacturer's calibration curve for the Integral Barocel Pressure Transducer.
(Datametrics Model 590-D-1-kPa-2Q8-V1X-4D).

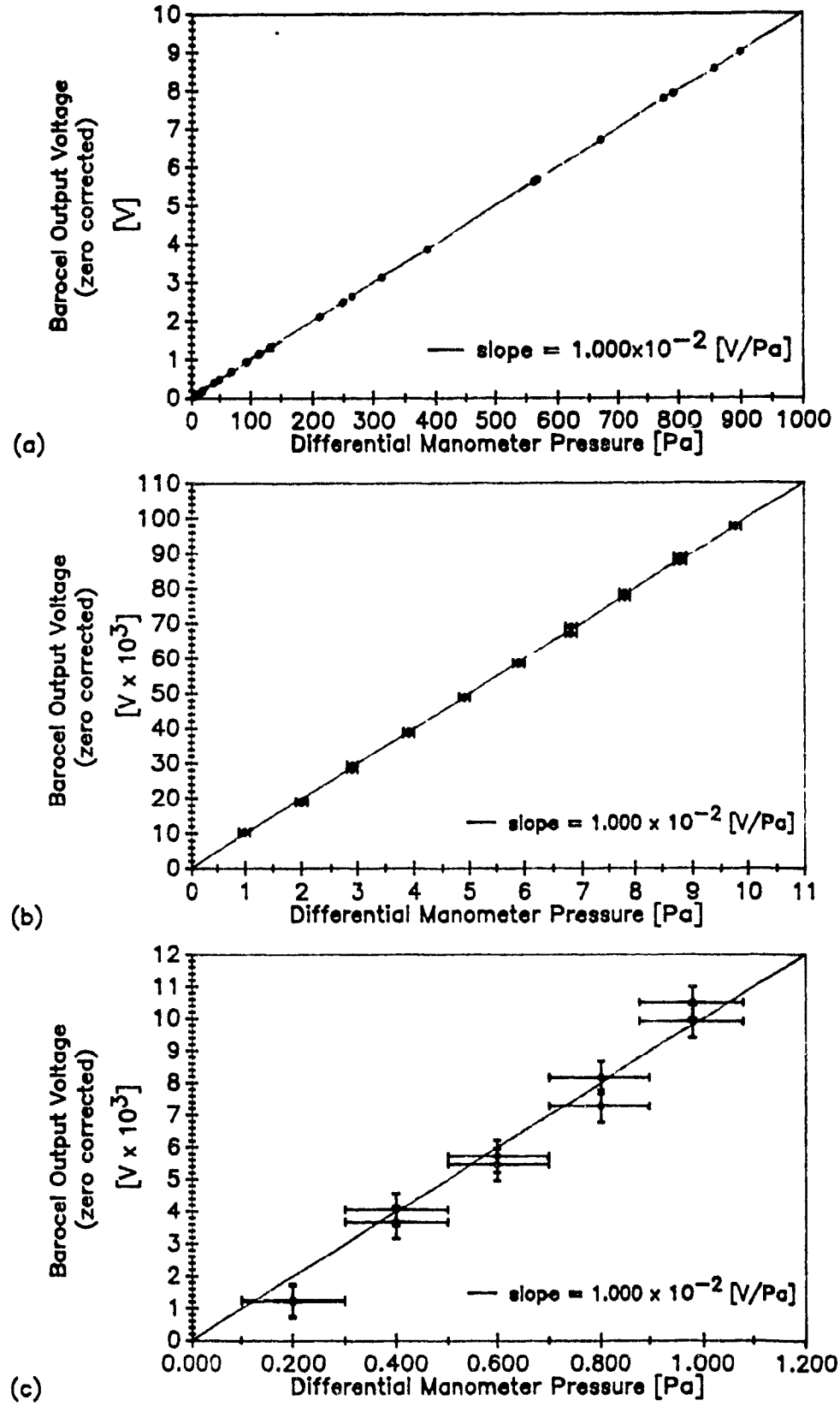

Figure 112: Results of calibration tests for the Integral Barocel Pressure Transducer. Results are shown for three ranges: (a) 10 Pa to 900 Pa; (b) 1 Pa to 10 Pa; and (c) 0.2 Pa to 1 Pa.

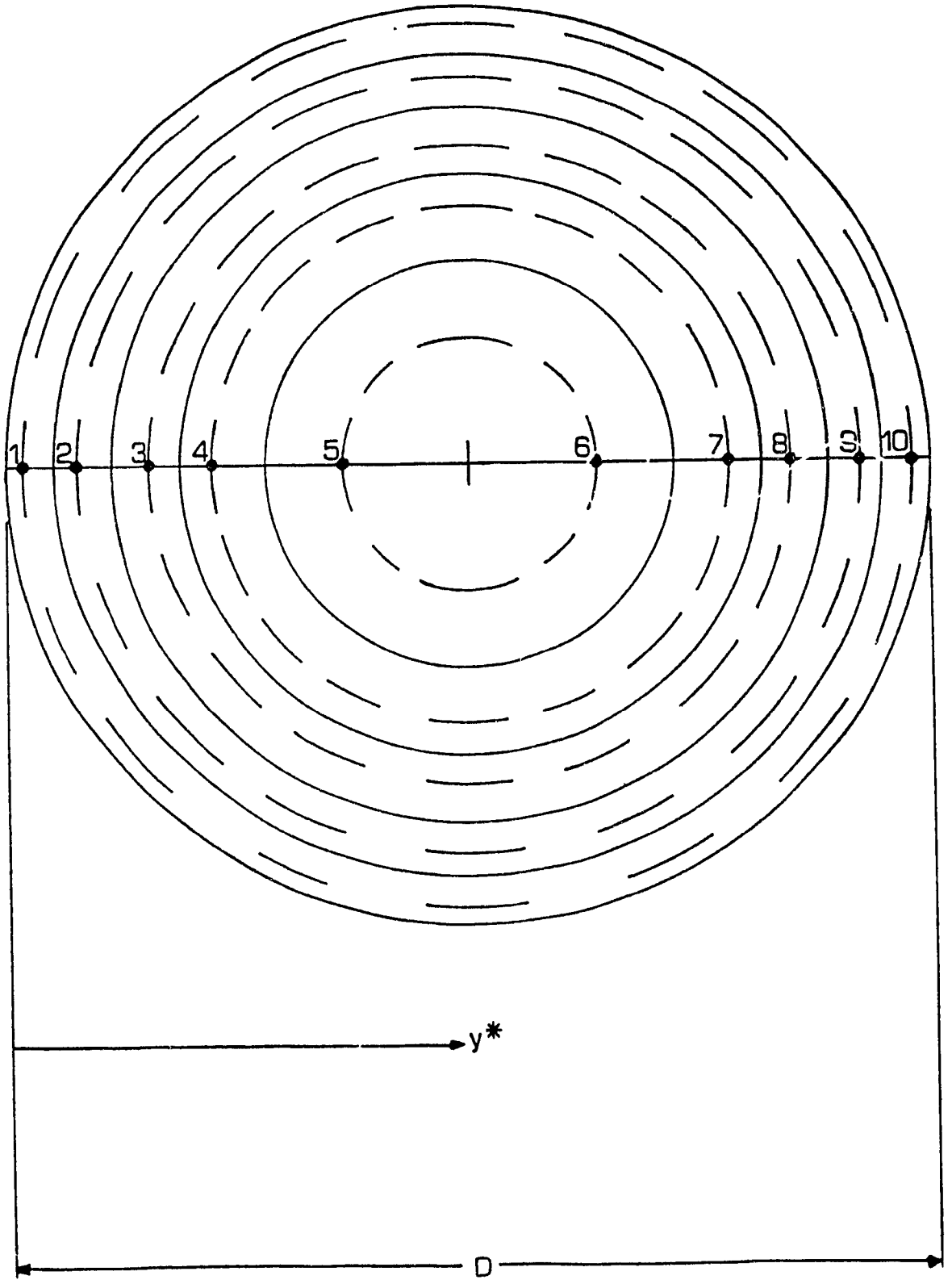

Figure 113: Sampling points used in the ten-point log-linear method. D is the internal diameter of the flow metering tube and $y^* = \{$(distance from the inner tube wall) / D$\}$: Values of y^* for the sampling points shown are given in Refs. [45] and [109].

TABLES

Table 1

Values of the constants used in the k-ϵ models of turbulence [112].

C_μ	$C_{1\epsilon}$	$C_{2\epsilon}$	σ_k	σ_ϵ
0.09	1.44	1.92	1.0	1.3

Table 2

Functions for the k-ϵ models. Models are designated by the following two-letter codes:

ST - standard or high-Reynolds-number [75]
JL - Jones and Launder [80,89]
LS - Launder and Sharma [91]
CH - Chien [92]
LB - Lam and Bremhorst [93]

Model	$f_{c\mu}$	$f_{c1\epsilon}$	$f_{c2\epsilon}$	E_ϵ	E_k	ϵ at wall
ST	1.0	1.0	1.0	0	0	‡
JL	$\exp\left\{\frac{-2.5}{(1+0.02Re_t)}\right\}$	1.0	$1-0.3\exp\{-(Re_t)^2\}$	$\frac{2\mu\mu_t}{\rho}\left(\frac{\partial^2 U_i}{\partial x_j \partial x_k}\right)^2$	$2\mu\left\{\frac{\partial(k^{1/2})}{\partial x_j}\right\}^2$	0
LS	$\exp\left\{\frac{-3.4}{(1+0.02Re_t)^2}\right\}$	1.0	$1-0.3\exp\{-(Re_t)^2\}$	$\frac{2\mu\mu_t}{\rho}\left(\frac{\partial^2 U_i}{\partial x_j \partial x_k}\right)^2$	$2\mu\left\{\frac{\partial(k^{1/2})}{\partial x_j}\right\}^2$	0
CH	$1-\exp(-0.0115\ y^+)$	1.0	$1-0.22\exp\left\{-\left(\frac{Re_t}{6}\right)^2\right\}$	$2\frac{\epsilon}{y^2}\exp(-0.5y^+)$	$2\mu\frac{k}{y^2}$	0
LB	$\{1-\exp(-0.0165\ Re_y)\}^2 \times\left(1+\frac{20.5}{Re_t}\right)$	$1+\left(\frac{0.05}{f_\mu}\right)^3$	$1-\exp\{-(Re_t)^2\}$	0	0	$\mu\frac{\partial^2 k}{\partial y^2}$

‡ near-wall ϵ value is specified using wall functions.

Table 3

Cross-sectional and modular dimensions of interrupted-plate rectangular duct test sections (Ducts 1 to 3).†

Duct No.	b (mm)	H (mm)	L (mm)	t (mm)	s (mm)	λ = b/H	L^* = L/H	t' = t/H	s^* = s/H
1	152.54	14.50	25.45	0.40	25.36	10.52	1.755	0.027	1.749
2	152.46	14.40	25.45	0.80	25.36	10.59	1.767	0.056	1.761
3	152.52	14.40	25.50	1.59	25.30	10.59	1.771	0.110	1.757

† 1. Values of H and t were calculated from measured values of 2H and 2t.
2. The uncertainty in all values of b, H, L, and s, is less than ±1.0% of the reported value.
3. The uncertainty in all values of t is ±0.01 mm.
4. The uncertainty in all values of λ, L^*, and s^* is less than ±1.1% of the reported value.
5. The uncertainty in all values of t^* is less than ±0.0014.

Table 4

Locations of the centers of the wall static pressure tap holes for the aluminum duct portion of the test section.†

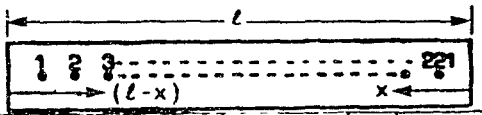

Hole No	(ℓ-x)‡ (mm)	Hole No	(ℓ-x)‡ (mm)	Hole No	(ℓ-x)‡ (mm)	Hole No	(ℓ-x)‡ (mm)	Hole No	(ℓ-x)‡ (mm)	Hole No	(ℓ-x)‡ (mm)	Hole No	(ℓ-x)‡ (mm)	Hole No	(ℓ-x)‡ (mm)	Hole No	(ℓ-x)‡ (mm)	Hole No.	(ℓ-x)‡ (mm)
1	62 99	26	221 61	51	380 50	76	539 33	101	698 16	126	856 97	151	1015 86	176	1174.64	201	1333.45
2	69 09	27	227 97	52	386 85	77	545 83	102	704 64	127	863.36	152	1022 16	177	1181.01	202	1339.81
3	75 45	28	234 25	53	393 34	78	552 17	103	710 96	128	869.73	153	1028 63	178	1187.33	203	1346.19
4	81 84	29	240 63	54	399 65	79	558 57	104	717 40	129	875 91	154	1035.01	179	1193.70	204	1352.53
5	88 16	30	247 00	55	405 92	80	564 90	105	723 48	130	882 52	155	1041 20	180	1200.07	205	1358.90
6	94 57	31	253 34	56	412 26	81	571 20	106	730 07	131	888.74	156	1047.61	181	1206.52	206	1365.17
7	100 98	32	259 73	57	418 71	82	577 64	107	736 53	132	895 16	157	1053 98	182	1212 78	207	1371.43
8	107 25	33	265 98	58	424 92	83	583 91	108	742 69	133	901 54	158	1060 30	183	1219.18	208	1377.85
9	113 73	34	272 44	59	431 34	84	590 34	109	749 04	134	907 89	159	1066 60	184	1225.54	209	1384.19
10	119 94	35	278 94	60	437 72	85	596 66	110	755 38	135	914.21	160	1073 02	185	1231.90	210	1390.57
11	126 37	36	285 19	61	444.16	86	602 88	111	761 78	136	920.51	161	1079 44	186	1238 17	211	1397.01
12	132 65	37	291.63	62	450 44	87	609 30	112	768 08	137	926 92	162	1085 77	187	1244.50	212	1403 23
13	139 06	38	297 88	63	456 75	88	615.68	113	774 40	138	933 26	163	1092.11	188	1250 91	213	1409 65
14	145 31	39	304 20	64	463 20	89	621 95	114	780 84	139	939 59	164	1098.39	189	1257 27	214	1415.90
15	151 65	40	310 50	65	469 42	90	628 48	115	787 10	140	945 93	165	1104 92	190	1263 56	215	1422.37
16	158 06	41	316 89	66	475 94	91	634.75	116	793 43	141	952.31	166	1111 07	191	1269.93	216	1428.77
17	164 36	42	1.. 18	67	482 18	92	641 04	117	799 89	142	958 65	167	1117 46	192	1276 23	217	1435.05
18	170 79	43	329 67	68	488 60	93	647 35	118	806 15	143	965 00	168	1123 86	193	1282.62	218	1441.35
19	177 20	44	336 09	69	495 00	94	653 85	119	812 61	144	971 45	169	1129 98	194	1288.99	219	1447.72
20	183.61	45	342 44	70	501 38	95	660 17	120	818 98	145	977 78	170	1136.41	195	1295.18	220	1454.14
21	189 85	46	348 76	71	507 54	96	666 51	121	825 31	146	984 13	171	1142.90	196	1301.70	221	1460.55
22	196 23	47	355 23	72	514 09	97	672 88	122	831.55	147	990 48	172	1149 38	197	1307.95		
23	202.50	48	36 49	73	520 40	98	679 16	123	837 86	148	996.88	173	1155.51	198	1314.38		
24	208.91	49	367 76	74	526 80	99	685.50	124	844 34	149	1003.07	174	1162 04	199	1320.66		
25	215 28	50	374 25	75	533.10	100	691 83	125	850 60	150	1009.47	175	1168.32	200	1326.94		

† (ℓ-x) dimension is shown in the table as the pressure tap hole positions were measured with the respect to the exit plane of the aluminum duct section, at x=ℓ.

‡ Tolerances on all (ℓ-x) values are less than ±0.10 mm.

Table 5

Cross-sectional dimensions of the rectangular duct test section.†

b (mm)	2H (mm)	ξ = b/2H
152.57 (±0.10)	28.74 (±0.05)	5.309 (±0.010)

† Refer to Fig. 5 for a description of the nomenclature.

Table 6

Fully developed turbulent flow in the rectangular duct: repeatability checks.

Re_d Range	Run No.	Re_d† x 10^{-3}	f_d†† x 10^2	Correlation‡ Coefficient	% Deviation in Re_d‡‡	% Deviation in f_d‡‡‡
$(Re_d)_{min}$	1	9.284	3.336	0.9978	-0.77	-2.34
	2	9.211	3.258	0.9978		
$(Re_d)_{max}$	1	60.09	2.039	0.9978	-0.47	1.57
	2	59.81	2.071	0.9980		

† Uncertainty in Re_d values is less than ± 2.35%.
†† Uncertainty in all f_d values is less than ± 5.00%.
‡ Correlation coefficient for $(P_o^* - P^*)_d$ vs. $(x^* - x^*_o)_d$ data points [123].
‡‡ (% deviation in Re_d) = $(Re_{d2} - Re_{d1}) / Re_{d1}$ x 100%.
‡‡‡ (% deviation in f_d) = $(f_{d2} - f_{d1}) / f_{d1}$ x 100%.

Table 7

Fully developed turbulent flow in the rectangular duct: comparison of friction factors with those obtained using the Prandtl-Jones correlation [54].ǂ

Re_d $x10^{-3}$	f_d $x10^2$	$(f_d)_{PJ}$ $x10^2$	% Deviation from $(f_d)_{PJ}$
9.284	3.336	3.321	0.45
15.46	2.887	2.900	-0.45
20.57	2.697	2.698	-0.04
30.28	2.379	2.454	-3.06
40.05	2.272	2.298	-1.13
49.87	2.145	2.184	-1.79
60.09	2.039	2.095	-2.67

ǂ 1. Uncertainty in Re_d values is less than ± 2.35%.
2. Uncertainty in f_d values is less than ± 5.00%.
3. Estimated uncertainty in $(f_d)_{PJ}$ values is ± 5% [54].
4. (% Deviation from $(f_d)_{PJ}$) = $\{f_d - (f_d)_{PJ}\}/(f_d)_{PJ}$ x 100%.

Table 8

Nominal values of Re_d and the corresponding values of Re_{fric} and M1, the number of grid points used in the numerical investigation of fully developed turbulent flow in a two-dimensional channel.

$(Re_d)_{nom}$ $x10^{-3}$	Re_{fric} $x10^{-3}$	M1 = (number of grid points)	
		JL and LS models	ST model
5.00	0.372	161	81
10.0	0.669	165	85
15.0	0.948	169	89
25.0	1.48	173	93
56.2	3.00	181	101
92.8	4.69	185	105
129.	6.30	189	109
228.	10.5	193	113

Table 9

Values of Re_d and f_d calculated from the solutions obtained with the JL [89], LS[91], and ST [75] models.

	JL model				LS model				ST model			
Re_{fric} $\times 10^{-3}$	Re_d $\times 10^{-3}$	f_d $\times 100$	$(f_d)_{PJ}$ $\times 100$	% Diff. in f_d †	Re_d $\times 10^{-3}$	f_d $\times 100$	$(f_d)_{PJ}$ $\times 100$	% Diff. in f_d †	Re_d $\times 10^{-3}$	f_d $\times 100$	$(f_d)_{PJ}$ $\times 100$	% Diff. in f_d †
0.372	5.16	4.16	4.17	-0.240	5.64	3.49	4.07	-14.2	5.50	3.67	4.10	-10.5
0.669	10.3	3.36	3.42	-1.75	11.1	2.88	3.35	-14.0	10.8	3.10	3.38	-8.28
0.948	15.4	3.01	3.07	-1.95	16.6	2.61	3.01	-13.3	16.1	2.78	3.03	-8.25
1.48	25.6	2.65	2.69	-1.49	27.4	2.32	2.65	-12.4	26.7	2.44	2.66	-8.27
3.00	57.3	2.20	2.22	-0.900	60.8	1.95	2.19	-11.0	59.8	2.02	2.20	-8.18
4.69	94.3	1.98	1.99	-0.500	99.7	1.77	1.96	-9.69	98.5	1.81	1.97	-8.12
6.30	131.	1.85	1.85	0.000	138.	1.66	1.83	-9.29	137.	1.70	1.83	-7.10
10.5	231.	1.65	1.65	0.000	243.	1.49	1.63	-8.59	241.	1.52	1.63	-6.75

† (% Diff. in f_d) = { f_d - $(f_d)_{PJ}$ } / $(f_d)_{PJ}$ x 100%.

Table 10

Values of Re_d and f_d obtained with the ST model [75] when using a two-piece velocity profile to calculate near-wall ($y^+ < 30$) flow rates.

Re_{fric} x 10^{-3} §	Re_d x 10^{-3}	f_d x 100	$(f_d)_{PJ}$ x 100	% Diff. in f_d †
0.372	5.04	4.37	4.20	4.05
0.669	10.3	3.38	3.42	-1.17
0.948	15.6	2.95	3.06	-3.59
1.48	26.3	2.53	2.68	-5.60
3.00	59.4	2.05	2.20	-6.82
4.69	98.0	1.83	1.97	-7.11
6.30	136.	1.71	1.84	-7.06
10.5	240.	1.53	1.63	-6.13

† % Diff. in f_d = [f_d - $(f_d)_{PJ}$] / $(f_d)_{PJ}$ x 100%.

Table 11

Effect on the the overall rate of convergence when employing different k and ϵ equation source term formulations in the JL model. Procedure A was used with all source term combinations listed. (Refer to Section 7.2.2 for details.)

Re_{fric} x 10^{-3}	Normalized Execute Units †			
	S^k_1-S^ϵ_1	S^k_1-S^ϵ_2	S^k_2-S^ϵ_1	S^k_2-S^ϵ_2
0.372	1.00	1.00	0.970	0.970
1.48	1.00	1.40	1.03	1.19
3.00	1.00	1.30	0.840	1.10
10.5	1.00	4.72	2.58	2.49

Values shown are the number of execute units required, normalized by the execute units required for the S^k_1-S^ϵ_1 combination at the same value of Re_{fric}.

Table 12

Effect on the the overall rate of convergence when employing different k and ϵ equation source term formulations in the ST model. Procedure A was used with all source term combinations listed, and all relaxation parameters, α's, are 1.0. (Refer to Section 7.2.2 for details).

Re_{fric} x 10^{-3}	Normalized Execute Units †			
	S^k_1-S^ϵ_1	S^k_1-S^ϵ_2	S^k_2-S^ϵ_1	S^k_2-S^ϵ_2
0.372	1.00	1.75	NC ‡	4.00
10.5	1.00	NC ‡	NC ‡	NC ‡

† Values shown are the number of execute units required, normalized by the execute units required for the S^k_1-S^ϵ_1 combination at the same value of Re_{fric}.

‡ NC - no convergence achieved

Table 13

Re_s and f_s values used to determine the input value of β for the periodic fully developed laminar flow calculations.

Re_s from [14]	f_s from [14]
100	0.500
200	1.00
500	1.90
1000	3.25
2000	5.00

Table 14

Periodic fully developed turbulent flow in Ducts 1 to 3: repeatability checks.

Duct No.	Re_m Range	Run No.	Re_m † x 10^{-3}	f_m †† x 10^2	Correlation ‡ Coefficient	% Deviation in Re_m ‡‡	% Deviation in f_m ‡‡‡
1	$(Re_m)_{min}$	1	5.432	4.522	> 0.9993	-0.63	0.84
		2	5.398	4.560	> 0.9995		
	$(Re_m)_{max}$	1	33.49	2.735	> 0.9990	0.03	0.00
		2	33.50	2.735	> 0.9990		
2	$(Re_m)_{min}$	1	5.397	5.678	> 0.9991	-0.17	-2.32
		2	5.388	5.546	> 0.9990		
	$(Re_m)_{max}$	1	32.93	3.756	> 0.9985	-0.70	-0.61
		2	32.70	3.733	> 0.9985		
3	$(Re_m)_{min}$	1	4.997	9.723	> 0.9990	-0.34	-2.60
		2	4.980	9.470	> 0.9993		
	$(Re_m)_{max}$	1	32.32	6.352	> 0.9990	-0.53	-0.52
		2	32.15	6.319	> 0.9988		

† Uncertainty in Re_m values is less than ± 2.25%.

†† The estimated experimental uncertainty in f_m values is less than or equal to ± 2.00% and ± 12% of the reported values corresponding to Re_{max} and Re_{min}, respectively.

‡ Correlation coefficients for $(P_o^* - P^*)$ vs. $(x^* - x^*_o)$ data points [123]. The value shown is the minimum value obtained for the sets of periodic data points used to calculate local f_m values.

‡‡ (% deviation in Re_m) = $(Re_{m2} - Re_{m1}) / Re_{m1} \times 100\%$.

‡‡‡ (% deviation in f_m) = $(f_{m2} - f_{m1}) / f_{m1} \times 100\%$.

Table 15

Deviation of local friction factors from the average friction factor calculated for the various module Reynolds numbers of Ducts 1, 2, and 3. (See Table 16 for average friction factor values, f_m, and uncertainty in Re_m values.)

		% Deviation of local f_m values from average f_m value †								Correlation
	$Re_m \times 10^{-3}$	f_{mLE}	f_{mLC}	f_{mCP}	f_{mCT}	f_{mTE}	f_{mG1}	f_{mG2}	f_{mG3}	Coefficients ‡
Duct 1	5.432	0.28	0.54	-0.42	-0.23	-0.61	0.26	0.07	0.11	≥ 0 9993
	8.806	0 28	0.14	0 14	0.47	-1.54	0.08	-0.50	0.94	≥ 0 9993
	11.22	-0.58	0.06	0.09	0.27	0 24	0.18	-0.13	-0.12	≥ 0.9994
	17.17	-0.08	-0 06	0.24	0.17	-0.32	0 21	-0.03	-0 14	≥ 0 9992
	22.06	-0.37	-0.50	0 13	0.42	-0 10	0.25	0.05	0 12	≥ 0 9992
	27.81	-0 18	-0 21	-0 33	0.12	-0 36	0 73	-0 13	0.37	≥ 0.9989
	33 49	-0 24	-0.42	-0 22	0 10	-0 42	0 65	0 25	0.30	≥ 0.9990
Duct 2	5 397	-0 08	0 67	-0 07	0 65	-0 37	-0.43	-0 62	0 26	≥ 0.9991
	8 087	0 15	-0.24	-0 24	-0.31	-0 60	0.28	0.81	0.15	≥ 0 9990
	10 94	0.02	-0.24	-1 02	0.27	-0 13	0.32	0 39	0.39	≥ 0 9988
	16 28	0 19	-0.06	0.16	0 04	-0 53	-0 24	0 03	0.41	≥ 0 9987
	21.33	-0 02	-0.22	-0.25	-0.31	-0.25	0 20	-0 04	0 89	≥ 0 9986
	26.62	-0 13	-0.35	-0 37	-0.31	-0 28	0.19	0 45	0 80	≥ 0 9986
	32 93	0 01	-0.52	-0.18	-0 16	-0.48	0.02	0 51	0 81	≥ 0.9985
Duct 3	4.997	0 57	-0.88	0 97	0.06	-0.05	-0.53	-0.52	0.38	≥ 0 9990
	8 682	-0 13	-0.38	0.01	0.35	-0.25	-0.33	0.32	0 40	≥ 0 9995
	10.98	0 15	-0 71	-0 06	0.06	-0 07	0.26	-0 17	0.54	≥ 0.9994
	16 93	0.30	-0.85	0.02	0 22	0.09	-0.06	0 12	0.17	≥ 0 9994
	21.85	0.30	-0 98	-0 03	0.42	-0.20	-0.13	0.02	0.59	≥ 0.9992
	27.84	0.09	-1.00	0.19	-0 04	-0 27	0.10	0.53	0 41	≥ 0.9992
	32 32	0 28	-1.35	0.19	0 15	-0 01	0.18	0 19	0 37	≥ 0 9990

† % Deviation in local f_m from average f_m = $(f_{m\,local} - f_m) / f_m \times 100\%$

‡ Correlation coefficients for periodically spaced $(P^*_o - P^*)$ vs. $(x^* - x^*_o)$ data points [123]. The value shown is the minimum value obtained from all 8 sets of the periodic data points used to calculate the local value of f_m.

Table 16

Experimental values of module Reynolds number, Re_m and corresponding module friction factor, f_m, values for periodic fully developed turbulent flow in interrupted-plate rectangular ducts: Ducts 1, 2, and 3.

Run No.	Duct 1			Duct 2			Duct 3		
	Re_m † $\times 10^{-3}$	f_m $\times 10^2$	$\pm f_m$ †† %	Re_m † $\times 10^{-3}$	f_m $\times 10^2$	$\pm f_m$ † %	Re_m † $\times 10^{-3}$	f_m $\times 10^2$	$\pm f_m$ †† %
1	5.432	4.522	12.	5.397	5.678	10.	4.997	9.723	12.
2	8.806	3.871	7.1	8.087	5.227	4.4	8.682	8.257	2.8
3	11.22	3.664	4.5	10.94	4.874	3.7	10.98	7.975	2.4
4	17.17	3.234	2.8	16.28	4.453	2.0	16.93	7.157	1.9
5	22.06	3.056	3.7	21.33	4.146	1.8	21.85	6.854	1.6
6	27.81	2.875	2.9	26.62	3.990	2.0	27.84	6.569	1.6
7	33.49	2.735	2.0	32.93	3.756	1.7	32.32	6.352	1.5

† Uncertainty in Re_m values is less than ± 2.25%.

†† $\pm f_m$ (%) = (± uncertainty in f_m) / f_m x 100%.

Table 17

Reynolds number, Re_k, and corresponding module friction factor, f_k, values for periodic fully developed turbulent flow in Ducts 1, 2, and 3.‡

Duct 1		Duct 2		Duct 3	
Re_k † $\times 10^{-3}$	f_k $\times 10^2$	Re_k † $\times 10^{-3}$	f_k $\times 10^2$	Re_k † $\times 10^{-3}$	f_k $\times 10^2$
7.238	5.467	7.191	6.374	6.654	9.114
11.74	4.748	10.78	5.868	11.56	7.740
14.95	4.494	14.58	5.472	14.62	7.476
22.87	3.967	21.70	4.999	22.55	6.709
29.40	3.748	28.43	4.654	29.08	6.425
37.06	3.526	35.47	4.479	37.07	6.158
44.63	3.355	43.88	4.216	43.04	5.954

† Uncertainty in Re_k values is less than ± 3.00%.
‡ f_k values derived from f_m values of Table 16, using Eq. (8-3).

Table 18

Intramodular $(P^*_i - P^*)_m$ vs. $(x^* - x^*_i)_m$ data points corresponding to the minimum and maximum flow rates in Ducts 1, 2, and 3.‡

Duct 1			Duct 2			Duct 3		
$(x^*-x^*_i)_m$ x10	$(P^*_i-P^*)_m \times 10^2$		$(x^*-x^*_i)_m$ x10	$(P^*_i-P^*)_m \times 10^2$		$(x^*-x^*_i)_m$ x10	$(P^*_i-P^*)_m \times 10^2$	
	$Re_m = 5.432 \times 10^3$	$Re_m = 33.49 \times 10^3$		$Re_m = 5.397 \times 10^3$	$Re_m = 32.93 \times 10^3$		$Re_m = 4.997 \times 10^3$	$Re_m = 32.32 \times 10^3$
0.000	0.000	0.000	0.000	0.000	0.000	0.000	0.000	0.000
2.186	3.105	2.565	2.201	5.191	4.348	2.201	10.35	7.985
4.396	5.857	4.007	4.427	9.079	6.758	4.427	16.98	11.71
6.578	7.523	4.469	6.624	10.73	6.805	6.624	18.58	11.56
8.776	7.699	3.860	8.837	10.47	5.306	8.837	16.84	8.948
10.96	7.006	2.570	11.04	8.982	2.605	11.04	13.70	3.954
13.14	6.087	1.909	13.23	6.900	1.177	13.23	9.960	0.5086
15.34	6.192	2.672	15.45	6.528	2.362	15.45	9.799	2.670
17.53	7.971	4 783	17.66	10.09	6.615	17.66	17.22	11.268

‡ 1. Uncertainty in all Re_m values is less than ± 2.25%.
2. The maximum uncertainty in $(x^* - x^*_i)_m$ values is less than $\pm 1.3 \times 10^{-3}$.
3. The maximum uncertainty in the $(P^*_i - P^*)_m$ values ranges from a minimum value of $\pm 8.3 \times 10^{-4}$ for Duct 1, with $Re_m = 33.49 \times 10^3$, to $\pm 1.5 \times 10^{-2}$ for Duct 3, with $Re_m = 32.32 \times 10^3$.

Table 19

Numerical values of module Reynolds number, Re_m and corresponding module friction factor, f_m, for periodic fully developed turbulent flow in interrupted-plate rectangular ducts: Ducts 1, 2, and 3.

Run No.	Duct 1		Duct 2		Duct 3	
	Re_m † $\times 10^{-3}$	f_m $\times 10^2$	Re_m † $\times 10^{-3}$	f_m $\times 10^2$	Re_m † $\times 10^{-3}$	f_m $\times 10^2$
1	5.764	4.018	5.809	4.901	5.718	7.425
3	11.72	3.356	11.56	4.368	11.78	6.935
4	17.42	3.143	16.76	4.204	17.42	6.762
6	27.27	2.989	26.47	4.035	27.84	6.570

† Difference between reported Re_m values and grid-independent values is estimated to be less than 2% of the grid-independent values.

Table 20

Percent deviation of numerical values of Re_m in Table 19 from corresponding experimental values in Table 16. ‡

Run No.	Duct 1	Duct 2	Duct 3
1	7.90	7.63	14.4
3	4.46	5.67	7.28
4	1.46	2.95	2.69
6	-1.94	-0.563	0.00

‡ (Percent deviation) = (Numerical - Experimental) / Experimental x 100%

Table 21

Values of stream functions corresponding to streamlines plotted in Figs. 86(a) to 88(d) for Ducts 1, 2, and 3. In these figures, Streamline Number 1 is the uppermost horizontal line followed by Streamline number 2 immediately below it, followed by the streamlines below it which are numbered 3 to 14 in the same manner. Streamline Number 14 is located immediately above the horizontal surface of the plate.

Streamline No.	Stream Function Values $(m^2/s) \times 10^4$											
	Duct 1				Duct 2				Duct 3			
	Re_m = 5.764 $\times 10^3$	Re_m = 11.72 $\times 10^3$	Re_m = 17.42 $\times 10^3$	Re_m = 27.27 $\times 10^3$	Re_m = 5.809 $\times 10^3$	Re_m = 11.56 $\times 10^3$	Re_m = 16.76 $\times 10^3$	Re_m = 26.47 $\times 10^3$	Re_m = 5.718 $\times 10^3$	Re_m = 11.78 $\times 10^3$	Re_m = 17.42 $\times 10^3$	Re_m = 27.84 $\times 10^3$
1	432.1	878.9	1306.	2044.	420.6	882.2	1285.	2016.	423.3	866.7	1282.	2090.
2	388.9	791.0	1176.	1840.	378.5	794.0	1156.	1814.	381.0	780.0	1154.	1881.
3	345.7	703.1	1045.	1636.	336.5	705.7	1028.	1613.	338.6	693.4	1026.	1672.
4	302.5	615.2	914.5	1431.	294.4	617.5	899.4	1411.	296.3	606.7	897.4	1463.
5	259.3	527.3	783.8	1227.	252.4	529.3	770.9	1210.	254.0	520.0	769.2	1254.
6	216.0	439.4	653.2	1022.	210.3	441.1	642.4	1008.	211.6	433.3	641.0	1045.
7	172.8	351.6	522.6	817.8	168.2	352.9	513.9	806.3	169.3	346.7	512.8	835.8
8	129.6	263.7	391.9	613.3	126.2	264.6	385.5	604.8	127.0	260.0	384.6	626.9
9	86.42	175.8	261.3	408.9	84.12	176.4	257.0	403.2	84.66	173.3	256.4	417.9
10	43.21	87.89	130.6	204.4	42.06	88.22	128.5	201.6	42.33	86.67	128.2	209.0
11	32.76	66.79	99.35	155.6	31.71	66.54	96.93	152.1	32.05	65.66	97.12	158.5
12	22.31	45.70	68.07	106.6	21.35	44.87	65.37	102.6	21.77	44.65	66.04	108.1
13	11.86	24.60	36.78	57.75	11.00	23.19	33.81	53.05	11.49	23.64	34.96	57.70
14	1.417	3.502	5.498	8.855	.6416	1.519	2.251	3.538	1.207	2.626	3.880	7.273

Table 22

Values of variables used in the generation of the nonuniform x and y grids that were employed in the simulations of turbulent fully developed channel flow (Turb.F.D.Ch.Flow), and laminar and turbulent periodic fully developed (P.F.D.) flows. (See Appendix 1 for further details).

Grid / Variable	Turb. F.D. Ch.Flow	Laminar P.F.D. Interrupted-Plate Passage Flow			Turbulent P.F.D. Interrupted-Plate Duct Flow						
	1 y zone	2 x zones	3 y zones		2 x zones	2 y zones					
						Bottom			Top		
		Upstrm & Dwnstrm	Top & Bottom	Middle	Upstrm & Dwnstrm	Duct 1	Duct 2	Duct 3	Duct 1	Duct 2	Duct 3
GF	1.2	1 2	1.2	1.2	1.2	1.2	1.2	1.2	1.2	1.2	1.2
L^o/Lz^T	$\left(\frac{60}{Re_{fric}}\right)^{\ddagger}$	0.05	0.06	0.06	0.05	5.45×10^{-3}	1.11×10^{-2}	2.21×10^{-2}	5.45×10^{-3}	1.11×10^{-2}	2.21×10^{-2}
N^{cvo}	40	10	6	6	8	3	7	9	3	7	9
Lz/Lz^T	1.000	0.500	0.300	0.400	0.500	0.027	0.973	0.056	0.944	0.110	0.890
N^{cvt} : specify	159	41	23	27	33	7	13	17	93	97	87
calculate	‡‡	43	23	25	35	11	23	29	65	75	69

‡ Corresponds to a distance of $y^+ = 30$ from the channel wall.

‡‡ See Table 8: $N^{cvt} = (M1 - 2)$ for JL and LS models;
$N^{cvt} = \{(N^{cvt})_{JL\ model} - 2(N^{cvo})\}$ for ST model.

Table 23

Uniform X and Y grid distributions used in Appendix 6.

Grid	Number of Grid Points	h/Lz^T
X1	100	1.020×10^{-2}
X2	124	8.196×10^{-3}
X3	146	6.945×10^{-3}
Y1	147	6.899×10^{-3}
Y2	174	5.813×10^{-3}
Y3	201	5.022×10^{-3}

Table 24

Values of variables, denoted as η_i in this table, used in the sample calculation of $Re_m \pm \delta Re_m$. (See Appendix 5 for details.)

η_i	Value of η_i	$(\delta\eta/\eta)_i^2$
A_{ft}	6.204×10^{-3} [m^2]	1.210×10^{-4}
b	0.1525 [m]	4.299×10^{-7}
μ	1.782×10^{-5} [kg/(m-s)]	1.545×10^{-7}
ρ	1.203 [kg/m^3]	1.432×10^{-8}
Λ	14.11 [$Pa^{1/2}$]	2.485×10^{-4}

Table 25

Values of variables, and their associated uncertainties, used in the calculation of A and ± A terms in Eqs. (A5-2) and (A5-6), respectively.

ǂ M.P.L.	CF_{lgln} $x10^3$	CF_{trb} $x10^2$	CF_{algn} $x10^2$	CF_{wpx} $x10^3$	CF_{vs} $x10^3$	V_{dyn} (v) $x10^6$	P_{dyn} (Pa)
1	5.0 ±5.0	1.0 ±1.0	1.0 ±1.0	2.5 ±2.5	20.32 ±20.32	11569 ±799	0.9531 ±0.09319
2	5.0 ±5.0	1.0 ±1.0	1.0 ±1.0	0.0 ±0.0	14.29 ±14.29	20516 ±799	1.841 ±0.09806
3	5.0 ±5.0	1.0 ±1.0	1.0 ±1.0	0.0 ±0.0	12.69 ±12.69	24509 ±799	2.238 ±0.1004
4	5.0 ±5.0	1.0 ±1.0	1.0 ±1.0	0.0 ±0.0	11.80 ±11.80	26903 ±799	2.476 ±0.1018
5	5.0 ±5.0	1.0 ±1.0	1.0 ±1.0	0.0 ±0.0	11.28 ±11.28	28373 ±799	2.625 ±0.1028
6	5.0 ±5.0	1.0 ±1.0	1.0 ±1.0	0.0 ±0.0	11.36 ±11.36	28128 ±799	2.600 ±0.1026
7	5.0 ±5.0	1.0 ±1.0	1.0 ±1.0	0.0 ±0.0	11.85 ±11.85	26786 ±799	2.465 ±0.1018
8	5.0 ±5.0	1.0 ±1.0	1.0 ±1.0	0.0 ±0.0	12.53 ±12.53	24937 ±799	2.280 ±0.1007
9	5.0 ±5.0	1.0 ±1.0	1.0 ±1.0	0.0 ±0.0	14.15 ±14.15	20846 ±799	1.874 ±0.09827
10	5.0 ±5.0	1.0 ±1.0	1.0 ±1.0	2.5 ±2.5	21.33 ±21.33	11079 ±799	0.9042 ±0.09299

ǂ M.P.L. = measurement point location (see Fig. 113).

Table 26

Values of $(Re_m)_{X,Y}$ obtained using uniform X-Y grid distributions, and values of $(Re_{mt})_X$ and $(Re_{mt})_Y$ extrapolated from these values using the method described in Appendix 6.

X	Y = 147	Y = 174	Y = 201	$(Re_{mt})_X$ ‡
100	27105	27036	26945	→ 26739
124	27317	27171	27115	→ 27063
146	27398	27265	27208	→ 27143
$(Re_{mt})_Y$ ‡	28086	28551	27500	

‡ Re_{mt} values were extrapolated from the Re_m values.

Table 27

Extrapolation of $(Re_m)_{X,Y}$ values, to grid-independent value of Re_{mt}, assuming n = 2 in Eq. (A6-1).

X	Y = 174	Y = 201	$(Re_{mt})_X$ ‡	
124	27171	27115	→ 26950	
146	27265	27208	→ 27040	
			27270	
$(Re_{mt})_Y$ ‡	27504	27445	→ 27269	→ 27270 = Re_{mt} ‡‡

‡ Re_{mt} values were extrapolated from the Re_m values.
‡‡ estimated grid-independent value of Re_{mt}